Regulation of Alzheimer pathology by amyloid seeds : from toxic effects to therapeutic opportunities, in mouse model of amyloidosis

Marina Celestine

THESE DE DOCTORAT

NNT : 2023UPASL010

Regulation of Alzheimer pathology by amyloid seeds : from toxic effects to therapeutic opportunities In mouse model of amyloidosis

Régulation de la pathologie Alzheimer par des variants de l'amyloïde-β : des effets toxiques et des opportunités thérapeutiques dans un modèle murin de l'amyloïdose

Thèse de doctorat de l'Université Paris-Saclay

École doctorale n° 568: Signalisations et réseaux intégratifs en biologie (BIOSIGNE)
Spécialité de doctorat : Neurosciences
Graduate school : Life Science and health
Référent : Faculté de medecine

Thèse préparée au sein du **Laboratoire de Maladies Neurodégénératives, (Université Paris-Saclay, CEA, CNRS)**
sous la direction de **Marc DHENAIN**, Directeur de recherche, CNRS, CEA Paris-Saclay,
le co-encadrement de **Anne-Sophie HERARD**, Chargé de recherche, CEA Paris-Saclay

Thèse soutenue à Paris-Saclay, le 2 mars 2023, par

Marina CÉLESTINE

Composition du Jury

Membres du jury avec voix délibérative

Claire PAQUET Professeure, Practicien hospitalier, Université Paris	Présidente
Claire MEISSIREL Directeur de recherche, INSERM, Université de Lyon	Rapporteur & Examinatrice
Benoît DELATOUR Directeur de recherche, CNRS, Université de Paris	Rapporteur & Examinateur
Nicolas SERGEANT Directeur de recherche, INSERM, Université de Lille	Examinateur
Elisabeth TRAIFFORT Directeur de recherche, INSERM, Université Paris-Saclay	Examinatrice

A ma fille Naëmy,

ACKNOWLEDGMENT

Je tiens à remercier les membres du jury pour avoir accepté d'examiner mon travail de thèse. En particulier, je remercie Claire Meissirel et Benoît Delatour pour leur rôle de rapporteur. Je remercie également Claire Paquet, Nicolas Sergeant et Elisabeth Traiffort pour avoir accepté d'être examinateurs lors de la soutenance.

Tout à bord, je tiens à remercier les fondations Vaincre Alzheimer et France Alzheimer pour avoir financé le projet ATAUME, ce qui a permis la réalisation de ce projet dans le cadre de ma thèse.

Je remercie tous les partenaires du projet ATAUME avec qui j'ai beaucoup échangé et auprès de qui j'ai énormément appris. En particulier, je remercie l'équipe de Alain Buisson à Grenoble qui a produit les peptides et a réalisé les expériences *in vitro*. Je tiens à remercier tout d'abord Alain pour son expertise sur les différentes mutations de l'amyloïde-beta et sur l'environnement synatique ; et sans qui le projet ATAUME n'aurait sans doute pas existé. Merci à Muriel Jacquier-Sarlin pour son aide dans la réalisation et l'interprétation des résultats de biochimie. Merci à Eve Borel pour la production des peptides. Cette collaboration a été très enrichissante et motivante pour moi et pour le projet.

Je remercie aussi Philippe Hantraye, Emmanuel Brouillet et Gilles Bonvento pour leur accueil au sein de MIRCen et du Laboratoire des maladies neurodégénératives.

Je remercie énormément mon directeur de thèse, Marc Dhenain et ma co-directrice de thèse, Anne-Sophie Hérard pour leur encadrement, soutien et conseil depuis mon master jusqu'à ma thèse. Vous avez toujours été présent et très à l'écoute peu importe le moment où je vous sollicitais. Je vous remercie pour votre confiance en moi face à ce projet ce qui m'a permis d'acquérir une grande autonomie qui me servira pour la suite de ma carrière. Mes remerciements également à toute l'équipe MIINDT. Merci à Luc Bousset pour m'avoir fait découvrir l'univers de la microscopie électronique et de l'étude biochimique de l'amyloïde. Merci à Mehdi Kabani pour son expertise sur l'extraction protéique. Merci à Thierry Delzescaux et Nicolas Souedet pour leur gentillesse et leur humour mais aussi de m'avoir formé sur Anatomist et Brain Visa. Merci à Fanny Petit qui m'a beaucoup aidé en fin de thèse.

Merci à tous les membres de MIRCen pour leur joie de vivre et leur gentillesse. Je remercie Martine Guillermer et Mylène Gaudin pour m'avoir aidé dans les inoculations des souris. Même à la dernière minute, vous avez toujours pu vous libérer pour moi. Merci à Julien Mitja pour ses nombreux conseils sur l'élevage des souris et pour son aide précieuse sur le comportement des souris. Merci à Caroline Jan et Pauline Gipchtein pour leur aide sur l'histologie des tissus. Je tiens également à remercier Karine Cambon, Géraldine Liot, Carole Escartin et Maria-Angeles Carríllo de Sauvage pour avoir pris le temps

de répondre à mes nombreuses questions et me conseiller sur mes manips. Merci aussi à Noëlle Dufour pour sa joie de vivre et son énergie positve ; et à Marie-Claude Gaillard pour son soutien.

Un grand merci à tous mes amis MIRCeniens : Fanny, Jean-Baptiste, Suzanne, Océane, Mathilde, PA, Pauline, Emma, Amélie, Yohann et Myriam. Vous avez rendu mes quatres années de thèse HYPER AGREABLES !!! Je n'oublierais pas tous ces moments de rire, de folie et de galère qu'on a partagés ensemble. L'ambiance à MIRCen était vraiment parfaite grâce à vous tous et elle m'a permise d'apprécier la vie au labo chaque jour. Merci aussi à tous les autres étudiants de MIRCen qui contribuent à cette bonne ambiance. Et je souhaite que les futurs étudiants aient la chance de vivre ce que j'ai vécu auprès de vous tous.

Enfin, je tiens à remercier mes amis proches et ma superbe famille de m'avoir toujours soutenu pendant ma thèse. Merci à ma sœur et à mon frère pour leurs conseils bienveillants. Merci à mes parents pour leurs nombreux encouragements. Merci à mon compagnon pour être rester toujours présent à mes côtés. Pour finir, merci à ma tendre et chaleureuse fille, Naëmy, qui a enjolivé ma dernière année de thèse et à qui je dédie tout ce beau travail.

ABSTRACT

La maladie d'Alzheimer (MA) est caractérisée par l'accumulation cérébrale de peptides β-amyloïdes (Aβ) et de protéine tau mal conformés, associés à une neuroinflammation excessive et à des altérations synaptiques, menant à la perte neuronale et au déclin cognitif. Les mutations dans la séquence de l'$Aβ_{1-42}$ induisent des variations de sa structure et de ses propriétés biochimiques qui peuvent être délétère ($Aβ_{1-42}$ -Osaka, $Aβ_{osa}$) ou protectrices ($Aβ_{1-42}$ -muté, $Aβ_{ice}$). L'origine de ces effets variables est, cependant, encore mal connue. Nous souhaitons donc en déterminer les mécanismes d'action et identifier une nouvelle stratégie thérapeutique en mimant l'effet des variants protecteurs.

Nous avons inoculé $Aβ_{osa}$ et $Aβ_{ice}$ dans l'hippocampe (partie du cerveau importante pour la mémoire) de souris transgéniques $APP_{SWE}PS1_{dE9}$ âgées de 2 mois qui sécrètent continuellement de l'Aβ endogène. Nous avons ensuite évalué l'impact des différents variants de l'Aβ sur plusieurs domaines : i) les fonctions cérébrales englobant les performances de mémorisation et la connectivité cérébrale ; ii) le développement pathologique des lésions de la MA (amyloïde et tau) ; iii) le processing de la protéine précurseur de l'amyloïde (APP) et les espèces d'Aβ sécrétées ; iv) la densité synaptique ; v) la neuroinflammation. Les souris ayant reçu ces deux variants ont été comparées à des souris ayant reçu soit une solution contrôle (PBS) soit de l'$Aβ_{1-42}$ non muté ($Aβ_{WT}$). Cette étude multimodale nous a permis d'identifier des cibles potentielles de chacun des variants sur un large spectre d'événements pathologiques déjà identifiés chez les patients.

Nous avons montré qu'à une même concentration, l'Aβ a des impacts fonctionnels différents dépendant de sa structure primaire. Ces impacts se maintiennent 4 mois après l'inoculation et nous permettent de différencier les variants selon leur toxicité : toxique, modéré et protecteur. L'$Aβ_{OSA}$ entraîne de sévères déficits mnésiques et une perte de connectivité cérébrale associés à une perte synaptique sans modulation de la pathologie Tau. Ces altérations fonctionnelles sont, en fait, induites par une accélération de l'amyloïdose se traduisant par une augmentation des plaques amyloïdes, une forte production d'oligomères Aβ préfibrillaires et fibrillaire ainsi qu'un excès de *processing* de l'APP résultant en une augmentation des fragments C-terminaux (CTF-β et CTF-α). Alors que les souris $APP_{SWE}PS1_{dE9}$ inoculées avec du PBS présentent des pertes de mémoire spatiale, l'inoculation de l'$Aβ_{ice}$ restaure un phénotype normal en préservant la mémoire spatiale, la connectivité cérébrale et la densité synaptique. Chez ces souris, l'amyloïdose n'est pas modifiée mais la pathologie Tau est réduite, suggérant de possibles relations entre ce variant et Tau. L'$Aβ_{ice}$ semble moduler des éléments de la pathologie Aβ endogène qui peuvent constituer de nouvelles cibles importantes pour traiter la maladie.

L'impact fonctionnel à long terme d'une inoculation unique d'Aβ sur une cascade d'évènements pathologiques n'a jamais été démontré. De plus, en choisissant différents variants de l'Aβ, nous espérons trouver diverses cibles de l'Aβ dépendant uniquement de sa structure, ce qui apporterait des explications sur l'hétérogénéité de la MA. Finalement, en utilisant des variants protecteurs, nous mettons en évidence des mécanismes d'action pouvant être utilisés comme des outils thérapeutiques.

TABLE OF CONTENTS

ABBREVIATIONS

AD: Alzheimer's disease

AICD: APP IntraCellular Domain

AMPA: α-amino-3-hydroxy-5-methyl-4-isoxazolepropionic acid

APOE: Apolipoprotein E

APP: Amyloid Precursor Protein

ARIA: amyloid-related imaging abnormalities

ATP: Adenosine Triphosphate Protein

Aβ: β-amyloid peptide

BACE1: β-site amyloid precursor protein cleaving enzyme 1

BBB: blood–brain barrier

BDNF: brain derived neurotrophic factor

BOLD: blood-oxygen-level dependent

CAA: cerebral amyloid angiopathy

CSF: cerebrospinal fluid

CEST: Chemical Exchange Saturation Transfer

CNS: central nervous system

CompCor: component-based noise correction

CTF: C-terminal fragment

DAMPs: damage-associated molecular patterns

DMN: default mode network

dHb: deoxyhemoglobin

DWI: Diffusion weighted imaging

EPSP: excitatory postsynaptic potential

FAD: familial Alzheimer's disease

FC: Functional connectivity

FDG: F-fluorodeoxyglucose

FDA: Food and Drug Administration

fMRI: functional magnetic resonance imaging

GABA: Gamma-aminobutyric acid

GWAS: Genome-Wide Association Study

GE-EPI: Gradient echo echo-planar imaging

Hb: hemoglobin

HRF: Hemodynamic Response Function

HSP: heparan sulfate proteoglycans

IPMS: immunoprecipitation and mass spectrometry

IL: interleukin

iNOS: inducible nitric oxide synthase

IWG: International Working Group

ISF: interstitial fluid

LTD: Long-term depression

LTP: Long-term potentiation

LRP1: Low-density lipoprotein receptor-like protein 1

MRI: magnetic resonance imaging

MTL: medial temporal lobe

mGluR5: metabotropic glutamate receptor 5

MAPT: microtubule associated protein tau

MCI: mild cognitive impairments

MMSE: Mini-Mental State Examination

MTBD: microtubule-binding domain

NINCDS-ADRDA: Neurological and Communicative Diseases and Stroke - Alzheimer's disease and Related Disorders Association

NFT: neurofibrillary tangles

NTs: Neuropil threads

NMDA: N-methyl-D-aspartate

NMR: Nuclear Magnetic Resonance

PAMPs: pathogen-associated molecular patterns

PET: positron emission tomography

PCC: posterior cingulate cortex

PHF: paired-helical filaments

PiB: Pittsburgh Compound-B

PrPc: cellular protease-resistant prion protein

PSEN: Presenilin

P-tau181P: phosphorylated tau epitope in threonine 181

RAGE: Receptor for Advanced Glycation Endproducts

SAD: sporadic Alzheimer's disease

SNR: signal-to-noise ratio

TE: echo time

TR: repetition time

T-tau: total tau

ThT: thioflavine T

TREM2: Triggering receptor expressed on myeloid cells 2

VEGF: Vascular Endothelial cell Growth Factor

VGLUT1: Vesicular Glutamate Transporter 1

LIST OF FIGURES

LIST OF TABLES

INTRODUCTION

Chapter 1 – Alzheimer's disease overview

Alzheimer's disease (AD) is the most widespread form of dementia in the world. It is characterized by a progressive neurodegeneration leading to a progressive disability in doing normal daily tasks. In most cases, the first signs of AD start over 65 years. Thus, for a long time, AD manifestations were hidden by the low population lifespan. During the XXth century, medical progress and lifespan extension revealed an emergence of AD cases in the elderly population and AD became a worldwide issue for public health.

The most common clinical symptoms of AD affect cognitive abilities like memory loss, inability to learn new things, difficulty with language, poor judgment and mood and personality changes. This form of dementia is the main cause of patient dependence. Physical, psychological, social and economic consequences are weighty for AD patients but, also, for their caregivers and more generally for the society.

AD is a heterogeneous disease as regards to its biology. The presence of extracellular senile plaques composed of aggregated β-amyloid (Aβ) peptides and intracellular neurofibrillary tangles (NFT) composed of misfolded tau proteins in the brain remain the primary neuropathological criteria for AD diagnosis. In the last decade, other hallmarks, as the activation of the neuroinflammatory cells and the synaptotoxicity, were demonstrated to play a central role in the pathogenesis of AD. However, how the crosstalk between all AD hallmarks affects disease progression is still unclear.

Despite the rise of the scientific and medical community interest in AD, there is still no cure for this devastating disease. Most of the available drugs help to control symptoms without changing the disease progression. Recently, Lecanemab has received an approval as a curative therapy for AD from the U.S. Food and Drug Administration (FDA). This is the first drug that showed an efficient disease-modifying effect. This drug aims to remove the early accumulation of Aβ protofibrils from the brain and to hinder the cognitive decline progression. This therapy highlights the importance of both the Aβ pathology and the need for early detection of AD.

1.1 General context

1.1.1 Before Alzheimer's disease

AD has occurred in human history long before it was named. It was included in a bigger category called "dementia". The transcription of Ebers Papyrus, the earliest medical text, revealed that 2000 years before Christ, Egyptian physicians associated the mental disorders as memory decline and attention troubles (distinctive feature of AD) to aging. During Ancient Greece, Pythagoras (philosopher and mathematician) divided the lifetime into six stages: infancy, adolescence, adulthood, middle age, senescence and old age. The last two phases of life were described as an inevitable period of decline and decay of the mind and the body, where the mental capacities return to a baby mental state (Berchtold and Cotman, 1998; Halpert, 1983). Additionally, Hippocrates (father of medicine) and Plato (philosopher) also recognized that aging was the main cause of dementia. It was during Ancient Roma that Marcus Tullius Cicero (philosopher and politician) pointed out that an active mental life could prevent mental deterioration thus, dementia was not an inevitable consequence of aging (Yang et al., 2016). Unfortunately, the end of Roman Empire and the Middle Age slowed down the progress of studies on dementia as dementia and other mental health illnesses were considered as punishment of God for sins committed during life. The diagnosis of dementia was then accepted in the Modern Age and several neurologists began to discover pathological features of dementia that will be associated to AD later on.

1.1.2 Discovery of AD

Alois Alzheimer, a German psychiatrist and neurologist, was interested in the development of senile dementia and neuropathology. At this time, these features were mainly associated with neurosyphilis or vascular disease. In 1901, he was intrigued by a new patient, Auguste Deter, a 51-year-old woman who presented clinical symptoms of progressive cognitive disorders different from anterior known features. Alzheimer fully documented the process and the aspects of her memory decline. Additionally to memory troubles, Auguste Deter was disoriented in time and space (**Figure 1A**) and she suffered from paranoia, auditory hallucinations and psychological disability (Maurer et al., 1997). She could not write her own name or remember objects that were presented to her just before (Alzheimer et al., 1995) (**Figure 1B**). Finally, she died of pneumonia in 1906. The autopsy of her brain revealed brain atrophy and two particular neuropathological lesions: tangles of fibrils within the cytoplasm of neurons and extracellular senile plaques (**Figure 1**). Alzheimer concluded about a "disease of cerebral cortex" and described for the first time the main lesions of AD that will be named later on as neurofibrillary tangles (NFT) and amyloid plaques.

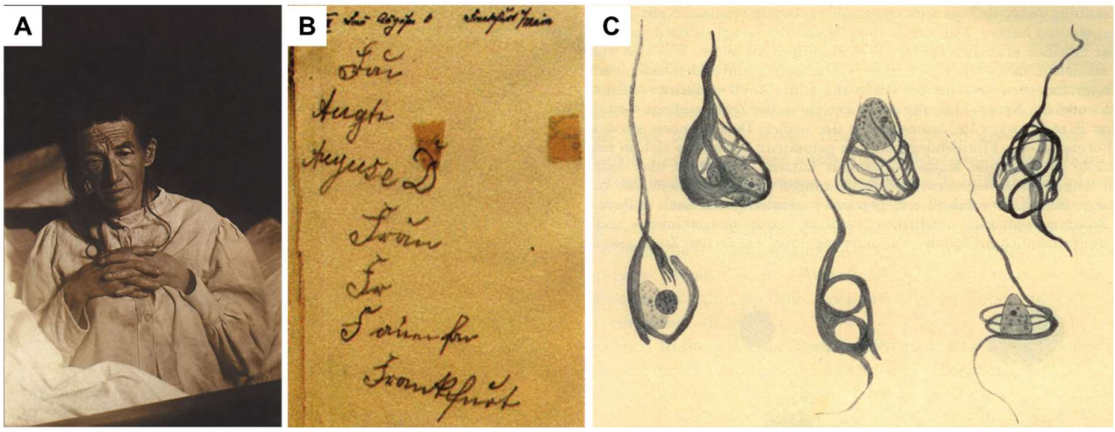

Figure 1: The discovery of AD

A. Picture of Mrs. August Deter, patient of Dr. Alois Alzheimer. **B.** Auguste Deter's handwriting. **C.** Neurofibrillary tangles from Auguste Deter, drawn by Alois Alzheimer above the caption '*Peculiar fibrillary changes of the nerve cells. Progressed stage of disease*'. From (Alzheimer et al., 1995).

Indeed, the proteins associated with these lesions were identified only in the 80's. The American pathologist, George Glenner, discovered the Aβ peptides as the major component of the amyloid plaques (Glenner and Wong, 1984a). In the meantime, the Belgian neuropsychiatrist Jean-Pierre Brion identified the presence of an accumulation of abnormally phosphorylated Tau proteins in NFT (Brion, 2006; Brion et al., 1985; Grundke-Iqbal et al., 1986). Further discoveries about genetic mutations responsible for familial AD (FAD) transmission and allelic risk factors were also revealed. Many studies to understand AD markers were thus conducted and many treatments has been proposed. However, the complexity of AD physiology and clinical symptoms only lead yet to a daily growing knowledge about the crosslinking between AD markers.

1.1.3 Epidemiology of AD: a worldwide dementia

Since AD discovery, the number of people being afflicted has logically risen due to the improvement of its diagnosis. According to The World Alzheimer Report, there are over 55 million people worldwide living with dementia in 2020. Every 3 seconds, someone in the world develops dementia. AD accounts for 60-80% of dementia cases. The number of AD patients is predicted to double within the next two decades, leading to major social and economic challenges for the patients' relatives and for the society (2020 Alzheimer's disease facts and figures, 2020).

This rise of AD cases is more important in developing countries as the elderly population is growing faster. The cumulative incidence of AD has been estimated to increase from about 5% by age 70 to 50% by age 90. In France, more than 1,175,000 people suffer from AD according to France Alzheimer.

They estimate over 200,000 new patients every year, making AD an immeasurable issue for public health.

Over the last decades, studies about AD have gained more prominence as the number of publications on the topic and associated proteins has sharply increased (**Figure 2**). Today, finding a cure for AD is a challenge that our societies have to overcome.

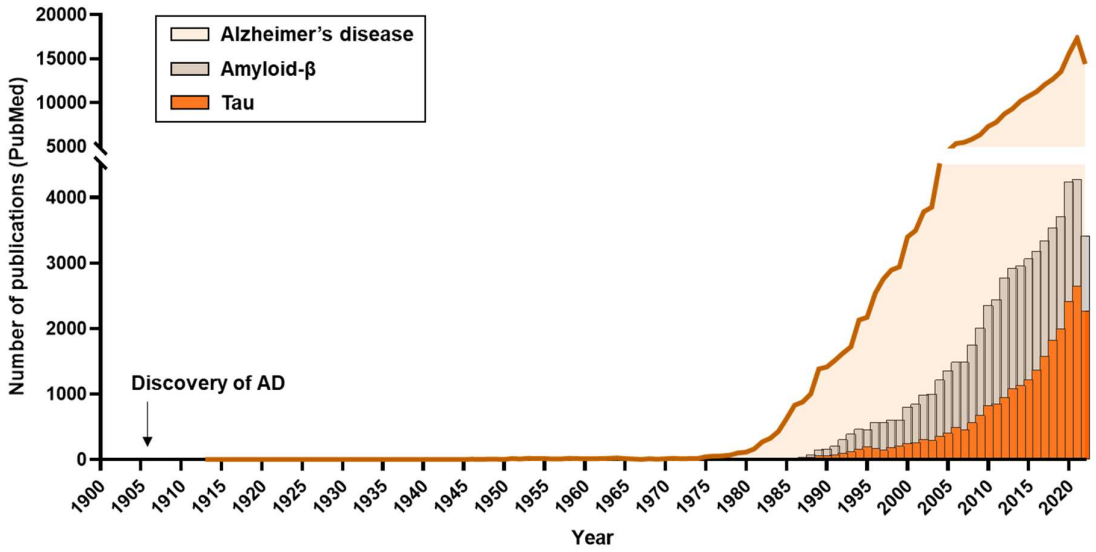

Figure 2: Number of publications about AD since its discovery

1.2 Clinical aspects of AD

1.2.1 Symptoms

AD is a slowly progressive disorder combining cognitive symptoms and neuropsychiatric troubles.

1.2.1.1 Memory dysfunctions

Progressive loss of memory is among the first symptoms reported by AD patients. This loss of memory disrupts daily life. Affected people are unable to learn new things, they usually forgot relatively new facts such as recent conversations, ask the same questions over and over, do not remember the names of objects or misplace items in the house. With progression of the disease, amnesia becomes more severe and they can forgot their personal history leading to a complete loss of their autonomy. For example, it can be difficult to remember the names of people they know and to recognize their family and friends.

At early stages of the disease, a person with AD may be aware of having difficulty remembering things. Progressively, the symptoms worsen, patients are not aware of the severity of memory

loss and associated memory deficits to age. Thus, it becomes difficult for the caregivers to convince patients to accept their help.

1.2.1.2 Spatial and temporal disorientation

Patients can get lost or wander. They may not know what time or day it is. They may have troubles understanding something if it is not happening immediately. Sometimes, they may forget where they are or how they got there.

1.2.1.3 Alteration of executive functions

Attention deficits and alteration of working memory associated to degeneration of frontal subcortical circuits lead to impaired executive functions as making judgements and decisions, problem solving, thinking and reasoning.

1.2.1.4 Mood disorders

Changing in mood such as obsessive, repetitive or impulsive behavior is frequent with AD patients. They can feel increasingly anxious, frustrated or agitated. One of the first signs of AD that August Deter developed was delusions. She accused her husband of adultery for no apparent reason and became aggressive with him (Alzheimer et al., 1995). AD patients are prone to paranoia and suspicious about careers or family members. As a result, they may have trouble keeping up with their close environment or favorite activity.

1.2.1.5 Aphasia

Aphasia-related problems with speech or language arise from the **inability to comprehend or formulate language**. AD patients have trouble following or joining a conversation. They may stop in the middle of a conversation without knowing how to continue or they may repeat themselves. They may struggle with vocabulary, have trouble in naming a familiar object or use the wrong name. As a result, they withdraw from hobbies, social activities or other engagements.

1.2.1.6 Apathy

Apathy is the loss of motivation in doing daily tasks leading to emotional deficits due to an impairments of fronto-striatal circuits, specifically involving the anterior cingulate cortex (Nobis and Husain, 2018). As apathy worsens, AD patients show poor judgement and may struggle with making decisions.

1.2.1.7 Agnosia

Agnosia is the impairment of the ability to recognize familiar stimuli or sensory modality (visual, auditory, tactile, olfactory, gustative), despite normal perception of those stimuli. For example, AD patients may not recognize faces of familiar persons, objects, sounds or tastes.

1.2.1.8 Apraxia

Apraxia, inducing gesture impairments, is the difficulty in completing familiar tasks even though patient has normal sensation and motor control.

1.2.2 Continuum of AD

AD is a gradual neurodegenerative disease. The progression of the disease from asymptomatic to complete dementia is called the continuum of AD manifestations (**Figure 3**). Within this continuum, there are 3 phases: preclinical AD, mild cognitive impairments (MCI) and dementia. The last phase is further divided in 3 parts: mild dementia, moderate dementia and severe dementia which reflect the disability for patients to keep doing daily activities. The time spent in each phase varies from one patient to another depending on several individuals' factors as age, genetics, gender, etc.

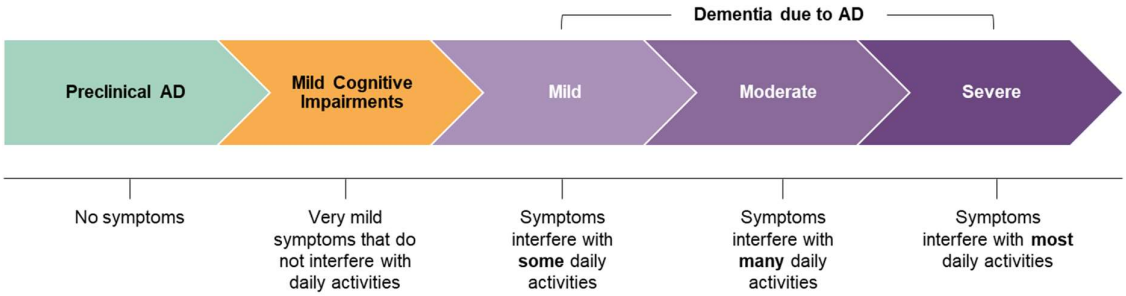

Figure 3: Continuum of AD

AD continuum is divided into three phases: preclinical AD characterized by biomarker-positive changes without symptoms occurrence, mild cognitive impairments (MCI) associated with subtle cognitive changes and AD dementia qualified as mild, moderate or severe depending on the severity of symptoms interference with daily activities. Adapted from (2020 Alzheimer's disease facts and figures, 2020).

During **preclinical** phase of AD, early brain changes occur at molecular levels. The Aβ peptides and tau proteins abnormally accumulate in the brain without causing any cognitive disorder. This asymptomatic phase can last 10 to 20 years. At this stage, early biological disturbances can be compensated by the brain, which precludes the distinction between AD patients and healthy individuals after clinical examination. However, some tools can be used as biomarkers of early AD such

as abnormal levels of Aβ in cerebrospinal fluid (CSF) or decreased metabolism of glucose measurable by positron emission tomography (PET) scans. The accuracy and the reproducibility of these methods vary between patients due to the individual heterogeneity of the disease. Actually, not all individuals with AD-related early brain changes develop MCI and dementia. Thus, developing biomarkers of the preclinical phase to earlier diagnose patient with AD is a major goal of current research. The earliest AD is detected, the easiest the disease could be slowed and stopped before the advent of major biological perturbations causing cognitive deficits.

The **MCI** phase, also called the prodromal AD, is the predementia phase of cognitive impairment. During this phase, neurobiological changes continue to progress. Individuals start to have mild disturbances in episodic memory and thinking but these subtle symptoms do not interfere with daily activities. The apparition of these symptoms is caused by the inability of the brain to compensate molecular changes as brain atrophy and synaptic loss that are strongly correlated with cognitive decline. Recent studies have shown that 32% of MCI individuals develop AD dementia within five years (Mitchell and Shiri-Feshki, 2009; Ward et al., 2013), which indicates that not all MCI patients convert to dementia. In many cases, the symptoms of MCI remain stable and sometimes individuals revert to normal cognition (Jongsiriyanyong and Limpawattana, 2018). In fact, the MCI stage of AD is a prodromal transitional state between normal aging and AD, where curative therapeutics can have a crucial impact to reverse disease progression. An efficient diagnosis of this stage may allow identification of individuals who are more predictable to develop AD.

Cognitive changes during **AD dementia** worsen and they can be completely distinguished from normal age-related cognitive changes. During this phase, symptoms interfere progressively with daily activities and AD patients lose their autonomy. First, they suffer from **mild dementia**, although memory starts to be impaired, they can still drive, go to work but, sometimes, they require few assistances for some activities. Then, in the **moderate** stage of AD dementia, individuals have troubles to perform routine tasks, to communicate and they have mood disorders (aggressivity, depression…). Most of the AD symptoms reported by the caregivers appear during this stage which can be long. Finally comes the **severe** stage of AD dementia characterized by a complete loss of autonomy, where patients cannot do any daily activities without help. As a result, they are vulnerable to other pathologies like pneumonia which is the major contributing cause of death among AD patients.

1.2.3 Diagnosis

Several studies indicated that 65 and older individuals can survive from four to ten years after the diagnosis of AD dementia, yet some live as long as 20 years with dementia. Even if the progression of AD is slow and uncertain, an accurate diagnosis of AD is useful for comparative studies of patients,

including patients in clinical trials. Nowadays, the diagnosis of AD addresses the medical history of the patient, a clinical examination, several neuropsychological testing and some laboratory assessments. Because AD dementia is often underdiagnosed, the diagnosis is based on standardized criteria that must progress with the advance in AD knowledge.

1.2.3.1 Clinical diagnosis

Twenty years ago, a work group composed of the National Institute of Neurological and Communicative Diseases and Stroke (NINCDS) and the Alzheimer's disease and Related Disorders Association (ADRDA) established and described the clinical criteria for the diagnosis of AD (McKhann et al., 1984). These criteria relied on functional, psychiatric and neurologic assessments which demonstrated a continuing decline of cognitive function compared to previous performance. Moreover, these criteria depended on the exclusion of systemic disease or other deficits that can cause dementia. The diagnosis of AD was categorized in three items: **possible AD** (atypical clinical course of dementia), **probable AD** (memory impairments and, at least, disability in one non-amnestic domain) and **definite AD** (clinical and histopathologic evidences). Although these criteria allowed distinction between AD and others dementias, clinicians were able to diagnose AD only in the presence of dementia which lowered the sensitivity and specificity of the diagnosis as we know that AD starts long before symptoms appear. Thus, based on the advances in the understanding of AD, diagnosis criteria were revised in 2011 by NINCDS-ADRDA. They now include the formalization of earlier disease stages (MCI and preclinical AD). According to the new proposal, memory impairment is not necessarily required. The cognitive or behavioral disorders should involve **at least two** of the following domains for probable AD: memory, executive function, speech, visual-spatial ability and change in personality.

Alternatively, the Diagnostic and Statistical Manual of Mental Disorders 5th edition (**DSM-5**) defined criteria for **major neurocognitive disorder** (previously called dementia) that are also used for AD diagnosis. They are based on the identification of a gradual decline of cognitive functions in **one or more** cognitive domains including learning and memory, language, executive function, complex attention, perceptual-motor and social cognition. These deficits should interfere with independence in daily activities and they are not due to any other psychiatric or neurologic disorders.

In practice, how clinicians can address the cognition inabilities? Several standardized neuropsychological tests which investigate mental flexibility and executive functioning have been developed. The Mini-Mental State Examination (MMSE) is the most commonly used in clinic and research. It associates a cognitive score from 0 to 30 (most severe dementia) to patients. Another surprisingly simple test is the Clock Drawing test. AD patients show early deficits in semantic memory

which lead to difficulties in visual spatial processing and misrepresentation of clock numbers (**Figure 4**).

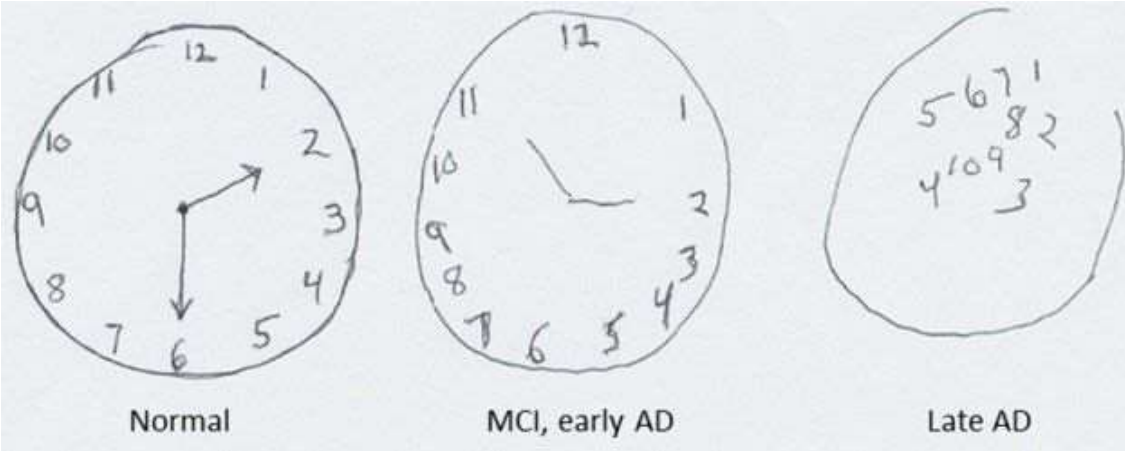

Figure 4: Clock Drawing test in healthy elderly individual, early AD and late AD

AD patients progressively loose the capacity to accurately place the clock numbers.

Atypical forms of AD may not be detected following the above criteria of classical AD diagnosis. Thus, additionally to clinical examination, complementary exams as neuroimaging and blood test are always recommended to confirm the diagnosis and exclude alternative causes of dementia, especially for the asymptomatic phase of AD.

1.2.3.2 Post-mortem diagnosis: neuropathology

The gold standard of definitive AD diagnosis remains the neuropathology studies of brain lesions after the death of the patient. It relies on the identification of the two hallmarks of AD: Aβ deposits and NFTs. In 2012, the National Institute on Aging-Alzheimer's Association (NIA-AA) recommended to evaluate the degree of AD-associated neuropathological changes using an **"ABC" score** based on the morphology and density of AD lesion features (Hyman et al., 2012). This score is based on 3 criteria: the distribution of amyloid plaques according to Thal phases ("**A**" for **Amyloid**), the presence of NFTs related to Braak stage ("**B**" for **Braak**) and the semi-quantitative evaluation of neuritic plaques based on the Consortium to Establish a Registry for AD ("**C**" for **CERAD**). Together, the 3 criteria help to define a score that reflects the level of neuropathological changes as "not", "low", "intermediate" or "high". However, during preclinical and MCI stages of AD, only a proportion (20-40%) of non-demented individuals display enough amyloid plaques and NFTs within their brain that fit with these criteria. Additionally, half of individuals with cerebrovascular or metabolic disease present the same neuropathological lesions and unfortunately may be diagnosed as AD. Thus, because of these comorbidities, neuropathological changes are not sufficient to diagnose AD. Fortunately, ante-mortem

diagnosis of AD is now possible since several AD biomarkers in the brain and in the biological fluids has been explored.

1.2.3.3 Biomarkers of AD

A biomarker is a characteristic that "can be measured and evaluated as an indicator of normal biological processes, pathological processes or pharmacologic responses to a therapeutic intervention" (Lashley et al., 2018). Current AD biomarkers rely on brain scanning, CSF protein examination and blood test. Rapid advances in the development of ultra-sensitive assays may enable individuals on the AD spectrum to be distinguished from healthy controls.

1.2.3.3.1 Classification of biomarkers: benefits and limitations

According to NIA-AA Research Framework, AD is defined as "a biologic construct that is identified by biomarkers in living people", which enlarges the diagnosis of AD from a syndromal to a biological and possibly asymptomatic aspect (Jack et al., 2018). A new classification of AD biomarkers has been proposed to simplify diagnosis. The **ATN classification system** groups the detection of amyloid pathology (**A**), tau pathology (**T**) and neurodegeneration or neuronal injury (**N**). In this system, Aβ biomarkers determine whether or not an individual is in the AD continuum while pathologic tau biomarkers determine if a patient who is in AD continuum has AD. The last biomarkers serve as an indication of staging severity and are not specific to AD. Each biomarker is binarized into normal (-) or abnormal (+) items which lead to eight different biomarkers profiles (**Table 1**). Then, each patient is assigned to one or more biomarker categories: (1) individuals with normal AD biomarkers (A-T-N-); (2) patients in the AD continuum (any A+ combination); and (3) patients with a normal amyloid biomarker but with abnormal T or (N), or both, also called "Suspected Non-Alzheimer's Pathophysiology" (or SNAP).

<table>
<tr><th colspan="2" rowspan="2"></th><th colspan="3">Cognitive Stage</th></tr>
<tr><th>Cognitively unimpaired</th><th>Mild Cognitive Impairment</th><th>Dementia</th></tr>
<tr><td rowspan="8">Biomarker Profile</td><td>$A^- T^- (N)^-$</td><td>Normal AD biomarkers</td><td>Normal AD biomarkers with MCI</td><td>Normal AD biomarkers with dementia</td></tr>
<tr><td>$A^- T^+ (N)^-$</td><td colspan="3" rowspan="3">Suspected Non-Alzheimer's Pathophysiology (SNAP) change</td></tr>
<tr><td>$A^- T^- (N)^+$</td></tr>
<tr><td>$A^- T^+ (N)^+$</td></tr>
<tr><td>$A^+ T^- (N)^-$</td><td rowspan="4">Preclinical AD</td><td rowspan="4">AD with MCI</td><td rowspan="4">AD with dementia</td></tr>
<tr><td>$A^+ T^- (N)^+$</td></tr>
<tr><td>$A^+ T^+ (N)^-$</td></tr>
<tr><td>$A^+ T^+ (N)^+$</td></tr>
</table>

Table 1 : ATN biomarkers

Each cognitive stage of AD can be associated with ATN biomarker profile. (-) and (+) represent respectively normal and abnormal biomarker.

The standardization of diagnosis criteria through this classification may ensure the diagnosis of symptomatic patients and evaluate the probability that asymptomatic patients develop AD, using continuous measures of biomarkers. This approach may facilitate the enrollment of patients in clinical trials whenever they have classical or typical AD. Moreover, the flexibility to add new discovered biomarkers when there are validated and available makes possible the personalized medicine of each pathologic change for each patient. The use of biomarker-based diagnosis in everyday clinical practice is still under debate. The main limitation of this classification relies on its purely biological definition of AD which can lead to consider as an AD patient any individual positive for AD biomarkers but without AD symptoms. This confusion between the presence of AD lesions and AD symptoms rises the existential question about when we could really consider an asymptomatic individual as an AD patient. The International Working Group (IWG) which contests the new definition, proposed to consider these individuals more like **at-risk for progression to AD** and recommended to use clinical-biological diagnosis (Dubois et al., 2021).

1.2.3.3.2 Currently available AD biomarkers

The first neurodegenerative change is the cerebral atrophy. It mainly occurs in the medial temporal lobe which includes the hippocampus (region of memory) and entorhinal cortex and then, spreads through other cortical regions as sensory-motor and visual areas. In clinical settings, structural magnetic resonance imaging (MRI) measured the regional atrophy in patients with pre-existing MCI to confirm positive diagnosis of AD. The accuracy of this diagnosis depends on the measured regions and the topographical progression of atrophy as normal aging leads also to a reduced volume of hippocampus and other areas. Longitudinal assessment of cerebral atrophy allows to follow the progression of the disease meanwhile as the clinical signs increase. Thus, patients suspected of AD display a typical pattern of atrophy distinguishable from cognitively normal elderly with 80-90% accuracy (**Figure 5**). Non-invasive volumetric MRI-based techniques remain the modality of choice to evaluate brain changes caused by other dementias and some affected regions are similar with those showing AD associated-brain changes. In the last decade, multimodal MRI analysis - from white matter diffusion studies to brain region networking evaluation - has emerged in research settings. These novel developments may help to find specific AD criteria with high predictive value that can be applicable in clinical settings.

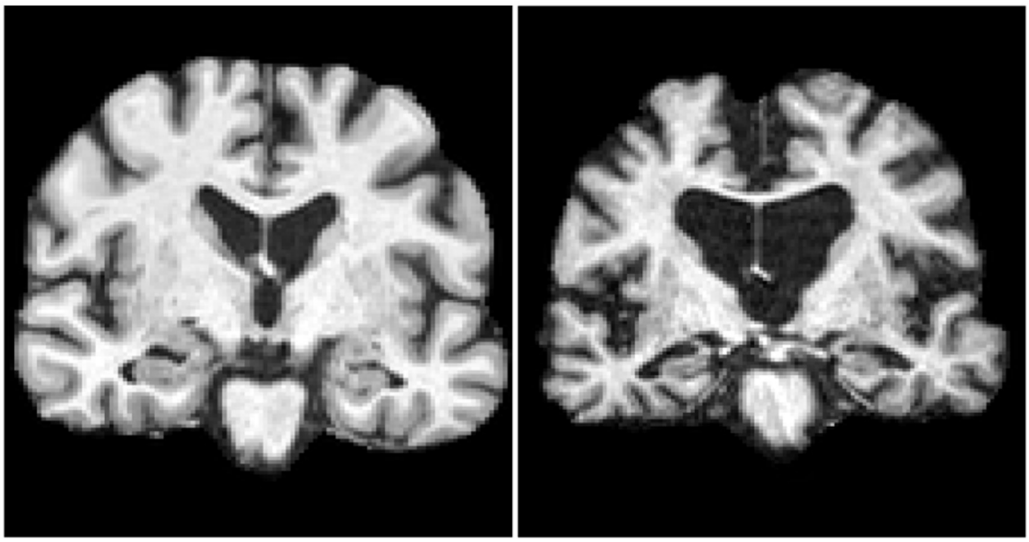

Figure 5: Brain atrophy is observed in AD patients compared to healthy individual

Brain MRI samples of a healthy person (left) (male, 84.8 years) and an AD patient (right) (female, 71.8 years). Increased atrophy in the medial temporal lobe and the enlarged ventricles are apparent. Adapted from (Ledig et al., 2018).

Neurodegeneration can also be evaluated using PET imaging which allows to measure brain metabolites in the living human brain. F-fluorodeoxyglucose (FDG)-PET measures glucose uptake in neurons and glial cells and is sensitive to synaptic dysfunction. Several studies have shown AD-associated hypometabolism in the temporo-parietal and posterior cingulate cortex of AD patients. Accurate interpretation of FDG-PET allows to distinguish AD from other dementia and from cognitively normal elderly individuals. Hippocampal FDG-PET changes occur in the early stages of AD, before first symptoms appear. Thus, non-invasive longitudinal metabolic assessment allows to detect the decline from normal to MCI or AD.

Another early molecular brain change detected by PET imaging is the increase of Aβ. The thioflavine T derivative Pittsburgh Compound-B (PiB) is a tracer of Aβ used clinically to detect progressive deposition of fibrillary Aβ plaques in patients' brain (**Figure 6**). However, brain amyloidosis has been shown to be strongly associated with dementia (Ossenkoppele et al., 2015) and Aβ plaques have been found in cognitively normal elderly individuals (Marchant et al., 2012). Thus, positive amyloid PET is more an exclusive predictive value of AD diagnosis (Scheltens et al., 2016) and needs complementary diagnosis. Tau PET is a new modality which evaluates the binding of fluorinated ligands to tau fibrillary aggregates (**Figure 6**). A combination of amyloid and tau PET imaging could help to confirm AD diagnosis. However, additionally to the difficulty to bind all pathological isoform of Tau, Tau PET suffers from off-target

binding (Makaretz et al., 2018). New Tau ligands are under validation in research settings (Marquié et al., 2015).

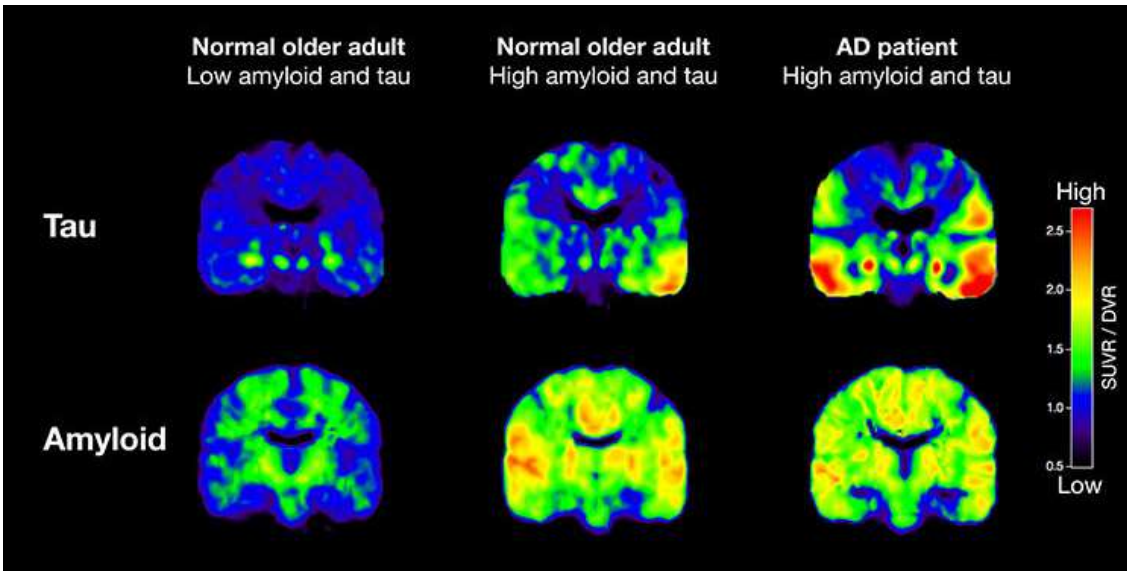

Figure 6: Accumulation of amyloid Carbon 11-labeled PiB and Tau-PET in AD patient

AD patients display higher amyloid and Tau burden. From **(Schöll et al., 2016)**

Ante-mortem AD neuropathologic diagnosis can be performed using CSF assessment of AD lesions. Aβ arising from the endoproteolytic cleavage of amyloid precursor protein (APP), is secreted into the extracellular space and continuously released within CSF. CSF Aβ is a core biomarker candidate of AD. $A\beta_{42}$ is more prone to aggregate and is a major component of amyloid deposits. During AD, cortical accumulation of Aβ leads to sequestration of $A\beta_{42}$ within senile plaques causing a decrease of its release in the CSF (Lashley et al., 2018; Olsson et al., 2016). In contrast, cortical neuronal loss induce high level of total tau (T-tau) in CSF. Additionally, tangle-containing neurons release phosphorylated tau (P-Tau) that can also be measured in CSF (Buerger et al., 2006). The most widely measured phosphorylated tau epitope is threonine 181 (P-tau181P). Despite a sensitivity and a specificity of **CSF biomarkers** reaching 85-90% for detecting AD, protein concentration does not always correlate with PET imaging (Blennow et al., 2010; Buerger et al., 2006; Lashley et al., 2018). While PET imaging measures amyloid plaque load and tau deposits accumulating over time, CSF biomarkers measure the level of production and clearance of Aβ and phosphorylated tau at a given time. CSF biomarkers are used to decipher pathological state at different stages of AD (Andreasen et al., 1999). Low CSF $A\beta_{42}$ is associated with increased CSF T-Tau and P-Tau levels in prodromal AD, in patients with MCI, as well as in asymptomatic AD-risk ones, compared to healthy controls with good accuracy (Olsson et al., 2016). Recently, a comparative study showed that lower CSF $A\beta_{42}$ is a strong prognostic factor of AD-associated mortality (Boumenir et al., 2019). Thus, using CSF biomarkers, future cognitive decline in

healthy individuals can be predicted and the progression of cognitively impaired patients to dementia can also be known.

1.2.3.3.3 Challenges in the development of new biomarkers

AD is characterized by a continuum of pathological changes without any clear distinction between AD patients and cognitively normal elderly individuals. One of the aims of biomarker-based diagnosis is to separate, with high performance, AD from healthy controls on the one hand and prodromal AD with MCI from stable MCI on the other hand. Emerging evidence have shown that AD develops 10 to 20 years before symptoms appear, which indicates that at one point AD-risk patients and healthy individuals are clinically indistinguishable. A current challenge for our societies is to detect the most of AD-risk patients in a general population that does not present any symptoms at the time of diagnosis. Rapid non-invasive diagnosis tests need to be developed for primary care and even future population screening.

While CSF collection is invasive and impressive for patients, blood collection is more accessible in routine practice. Recent studies have shown the ability to detect, in the plasma, Aβ species from brain of AD patients. Abnormal levels of plasmatic $A\beta_{42}$ and $A\beta_{40}$ were associated with AD. However, measuring CNS-specific proteins in routine blood diagnosis is under debate because of their weak reliability due to their low concentration in the plasma. Additionally, platelets and other extra-cerebral tissues also secrete Aβ in the plasma that interfere and prevent higher concordance between plasma Aβ level and cerebral β-amyloidosis (Olsson et al., 2016; Zetterberg, 2015). Encouragingly, assessment of plasma $A\beta_{42}/A\beta_{40}$ ratio - by combining immunoprecipitation and mass spectrometry (IPMS) - showed promising results for predicting AD at individual level (Nakamura et al., 2018). Indeed, reduced plasma $A\beta_{42}/A\beta_{40}$ ratio was demonstrated to correlate with brain amyloid-β PET burden and levels of CSF $A\beta_{42}$ in pre-symptomatic, MCI and AD patients (Nakamura et al., 2018). The quantification of $A\beta_{42}/A\beta_{40}$ ratio, rather than separate levels of $A\beta_{42}$ and $A\beta_{40}$, allows to normalize Aβ level for biologically induced Aβ variations. Interestingly, the study of a cohort including cognitively normal elderly individuals showed that amyloid-negative individuals with positive plasma $A\beta_{42}/A\beta_{40}$ have 15-fold higher risk to develop brain Aβ PET burden (Schindler et al., 2019). This finding indicates that plasma $A\beta_{42}/A\beta_{40}$ ratio can predict earlier brain amyloidosis rather than amyloid PET. Although underlying causes of theses associations are still unclear, it is essential to consider that blood-brain exchange of Aβ has a crucial role in early stages of AD.

Regarding tau pathology, plasma levels of tau phosphorylated at residue 181 (P-tau181) and residue 217 (P-tau217) appear to be specific biomarkers of AD as they were found significantly higher in AD compared to others tauopathies or neurodegenerative diseases (Leuzy et al., 2022; Palmqvist et al.,

2020; Thijssen et al., 2020). Plasma P-tau level changes occur before symptom onsets and increase with progression from prodromal to late AD suggesting that this measure can predict AD development (**Figure 7**)(Janelidze et al., 2020). Importantly, plasma P-tau level changes were strongly associated with amyloid PET, tau PET and CSF P-tau (Janelidze et al., 2020; Mattsson et al., 2016; Palmqvist et al., 2020). The measures enabled to detect amyloid PET-negative individuals who converted to amyloid PET-positive indicating that plasma P-tau becomes positive earlier than PET targets. Although, plasma P-tau level increase occurs before tau aggregation and amyloid burden, it occurs after CSF and plasma Aβ changes, which is in accordance with hypothesis of early Aβ-induced tau changes in AD. As a result, plasma P-Tau combined with plasma $A\beta_{42}/A\beta_{40}$ are good candidate biomarkers for preclinical and symptomatic AD. Now, research needs to optimize the blood-based assays for high precision population screening and determine their potential role in clinical care.

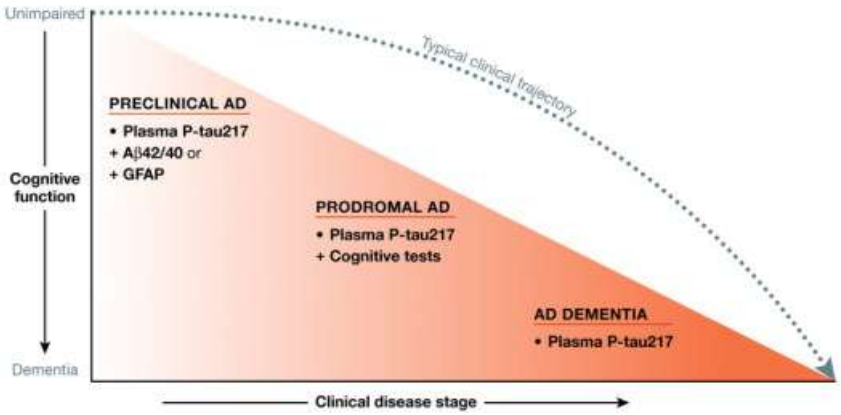

Figure 7: Plasma-based biomarkers across the clinical continuum of AD

The most promising plasma biomarker or plasma biomarker combination is represented within each stage of the disease. (From (Leuzy et al., 2022)).

Among the existing biomarkers used, urinary analysis has also been considered for AD diagnosis. A propensity-score match study revealed that high arsenic or low dimethylarsinic acid levels (predominant urinary metabolites) are associated with increased AD-risk which indicates that urinary biomarkers are promising candidate for AD diagnosis (Yang et al., 2018).

Despite its invasiveness, CSF biomarker yet remains the gold standard to detect and follow AD-related proteins. Thus, research aims to find novel CSF biomarker candidates. One such biomarker is Aβ oligomers that have a central role during early AD-induced toxicity. Because of their presence in physiological conditions, their threshold of detection in AD patients overlaps with healthy control and CSF is poorly concentrated in Aβ oligomers. Fortunately, ultra-sensitive Aβ oligomer assays have been developed and show high precision to discriminate AD patients from cognitively normal elderly

individuals (Savage et al., 2014). Synaptic biomarkers are also promising as synaptic dysfunction occurs early in AD. High CSF synaptic proteins have been shown to correlate with progression of AD clinical severity (Kvartsberg et al., 2015).

Improve diagnosis and prognosis in AD, using ultra-sensitive biomarker-based assays, might enable to identify patients who could benefit from AD-targeted disease-modifying agents by decreasing the time, cost and risk of drug trial.

1.2.3.3.4 Time-course of major AD pathophysiological events

AD is a progressive age-related disorder that start 15 to 20 years before the onset of clinical symptoms. The effect of each pathophysiological event on brain increases either simultaneously or consecutively and can be detected as a biomarker (**Section 1.2.3.3**). Longitudinal studies of AD patients' biomarkers allowed to propose a model of AD evolution based on the clinical course (**Figure 8**) (Long and Holtzman, 2019). Accumulation of Aβ occurring during preclinical phase is the first event of the disease. It can be detected by a reduction of $A\beta_{42}$ in CSF and plasma coming with an increased signal of amyloid PET imaging. At meantime, microglia and astrocyte changes occurred and cortical hypometabolism is observed in FDG-PET imaging. Then, while Aβ deposition spreading reaches all the brain structures, increased NFT tau pathology is observed in tau PET imaging and CSF P-tau levels increase. The spreading of tau leads to synaptic dysfunction and neurodegeneration. The first symptoms start to appear from subtle symptoms to dementia. Longitudinal imaging of hippocampal volume loss (MRI) enables to follow these neurodegenerative changes. At the onset of cognitive impairments the brain Aβ build-up reaches a plateau (Long and Holtzman, 2019). As a result, progression of cognitive impairment correlates with tau pathology and hippocampal atrophy but not with amyloid deposition. Regarding the first event of AD, whether it is Aβ-related toxicity or microglia/astrocyte dysfunction that initiates the pathology remains unclear. One hypothesis can be that cooperation between Aβ and neuroinflammatory actors, during the preclinical phase, facilitates the progression to MCI stage and, then, the increase of tau pathology aggravates the disease and amplifies the severity of clinical symptoms until complete dementia. Interestingly, regarding the topography of tau and amyloid deposits, another model has been proposed where tau pathology starts even before Aβ deposits in some cortical regions involved in AD. The timeline of apparition of AD pathological events led to many hypotheses on AD origins that will be discussed in **Chapter 2**.

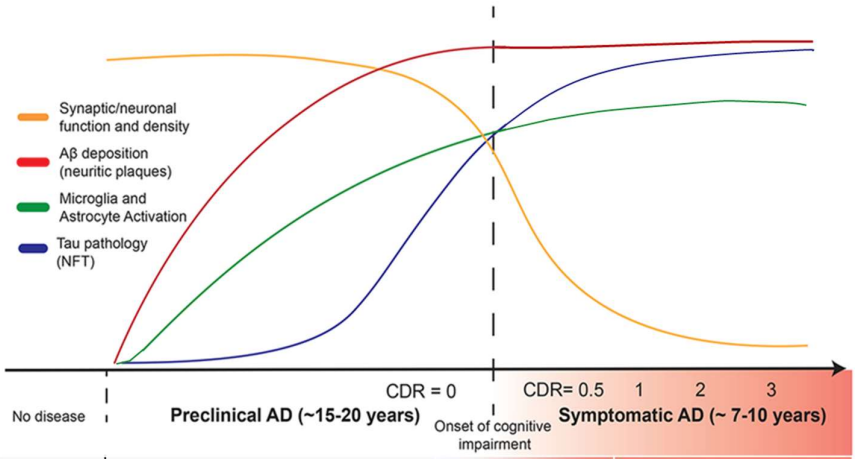

	No disease	Preclinical AD		MCI	Dementia
		Stage1	Stage 2		
Aβ CSF/plasma	-	+	+	+	+
Aβ PET	-	-	+	+	+
Tau CSF/plasma	-	-	+	+	+
Tau PET	-	-	+	+	+
Neurodegeneration (FDG-PET, sMRI)	-	-	-	+	+
Subtle Cognitive decline	-	-	-	+	-
Major cognitive decline	-	-	-	-	+

Figure 8: Timeline of the apparition of AD biomarkers in relation to clinical course

The horizontal axis represents the clinical stages of AD: preclinical AD, MCI and dementia. The vertical axis represents the degree of each biomarker during disease progression. The level of Aβ in CSF and plasma is the first biomarker that becomes positive (+). CDR : Clinical Dementia Rating Adapted from (Long and Holtzman, 2019).

1.3 Different forms of AD

AD is a multifactorial disorder that can be classified into two categories: familial and sporadic forms. Genetic factors are responsible for familial forms of AD (FADs) that represent 1% of AD patients. FADs are rare autosomal dominant diseases resulting in an early onset of the pathology, between 30 and 60 years, and are more aggressive. Accumulation of multiple genes and environmental risk factors throughout life are responsible for developing complex sporadic forms of AD (SADs) that represent the majority of AD cases (99%). SADs result in late onset of pathology and are more challenging to study because of the wide heterogeneity among patients.

1.3.1 Familial forms

FADs are due to genetic mutations transmitted through families indicating that at least one first-degree relative of the patient has a history of AD. These mutations have been identified in 3 main genes coding for proteins involved in Aβ production: APP, Presenilin 1 (PSEN1) and Presenilin 2 (PSEN2). These mutations are directly involved in the accumulation, aggregation and stability of Aβ in the brain by influencing its structure and its regulation. For several decades and until now, the study of FADs enabled the major advances in AD mechanism deciphering.

1.3.1.1 Mutation in presenilin PSEN1/PSEN2

PSEN1 and PSEN2 are two homologous genes coding for two proteins that have around 67% of homology (Piaceri et al., 2013). Linkage analysis revealed their implication in the majority of FAD cases. Both are subunits that form the catalytic core of the γ-secretase complex which is involved in C-terminal cleavage of APP resulting in the generation of Aβ isoforms. Most of the mutations in presenilin genes are autosomal dominant missense mutations leading to amino acid substitution. While PSEN2 mutation is rare, PSEN1 mutation accounts for up to 50% of FADs. Both mutations disturb Aβ regulations. The mechanism by which PSEN mutations induce neurodegeneration and alteration of cognitive functions remains unclear. Several hypotheses have been proposed. On the one hand, PSEN mutations have been suggested to duplicate γ-secretase activity resulting in a toxic increase in Aβ synthesis and $A\beta_{42}/A\beta_{40}$ ratio. On the other hand, PSEN mutations would lead to a loss of physiological presenilin function that is important for learning and memory, as animal models bearing these mutations were found to mimic better neurodegeneration of AD than animal models bearing Aβ overproduction-based mutations (Shen and Kelleher, 2007).

1.3.1.2 Mutations in APP

The first mutation causing the FADs was identified in the APP gene on chromosome 21 as patients with Down's syndrome showed similar neuropathological features as AD patients. The duplication of chromosome 21 leads to a gain function of APP gene associated with a cerebral accumulation of Aβ in these individuals (Goate et al., 1991). The discovery of mutations on APP gene at the origin of the FADs has brought a lot to our understanding of the disease. Nowadays, more than 50 mutations have been identified in APP. They are located outside or inside the Aβ sequence and mostly near or around α-, β- or γ-secretase cleavage sites, which are the enzymes responsible for APP cleavage and Aβ production. Depending on their location, mutations can: enhance Aβ production (*Swedish*, *Flemish*); change $A\beta_{42}/A\beta_{40}$ ratio and induce selective production of highly toxic isoforms of Aβ (*Taiwanese, Artic, Dutch*); modulate Aβ folding and aggregation properties (*Osaka, Iowa, Italian*) (Bi et al., 2019). Interestingly, mutations in the N-terminal domain of Aβ lead to a decrease of Aβ levels and have protective

properties on cognition (Di Fede et al., 2012; Jonsson et al., 2012). These APP mutations will be further detailed in **Section 3.3.1**. Regarding that mutations in APP gene induced specific properties, FADs have been useful for understanding the widespread heterogeneity observed in AD patients. Multiple animal models bearing these familial mutations have been developed to guide AD research and test disease-modifying therapies.

1.3.2 Sporadic form and risk factors

The majority of AD origins cannot be explained by one single event but by a huge number of sequential events that patients progressively acquire during their life. Unsurprisingly, age is a major risk factor for succumbing to AD. Sporadic late onset AD is an age-related multifactorial disease which complexity relies on multiple genetic and environmental factors that interact with each other and badly influence disease threshold to develop AD**.**

1.3.2.1 Genetic susceptibility

The best known susceptibility gene involved in AD is the Apolipoprotein E (APOE) gene that codes for a lipoprotein binding amyloid proteins. APOE is a polymorphic gene meaning that three alleles (APOE2, APOE3, APOE4) exist at this locus and gradual AD risk depends on the expressed alleles. Individuals that carry APOE2 allele, have a lower risk to develop AD. APOE3 does not have any influence on AD risk. In contrast, APOE4 has been associated with higher AD risk (**Figure 9**). One copy of this allele increases by 3-fold the risk to develop AD and two copies increase it by 12-fold, indicating that either in homozygous state or in heterozygous state, APOE4 has a predominant role in the predisposition to AD. APOE is an apolipoprotein involved in the transport and homeostasis of cholesterol. Correlation between increased brain cholesterol and production of Aβ has been found in AD patients. Recently, super-resolution imaging of the mouse brain showed that the transport of cholesterol by APOE from astrocytes to neurons, contributes to maintain Aβ plaques around neurons and determines the production of Aβ (Wang et al., 2021). Thus, APOE4 allele carrying has been associated with the increase of Aβ plaques. Moreover, the discovery of APOE in senile plaques and intracellular NFTs revealed that APOE was enabled to bind Aβ and play a role in formation of Aβ oligomers and fibrils (Castano et al., 1995). The elimination of Aβ oligomers through CSF and plasma was found reduced in AD patients bearing the APOE4 allele, indicating that APOE is involved in the sequestration and the accumulation of Aβ in the brain (Tai et al., 2013). Other studies have highlighted the own neurotoxic effects of APOE independently of Aβ (Piaceri et al., 2013).

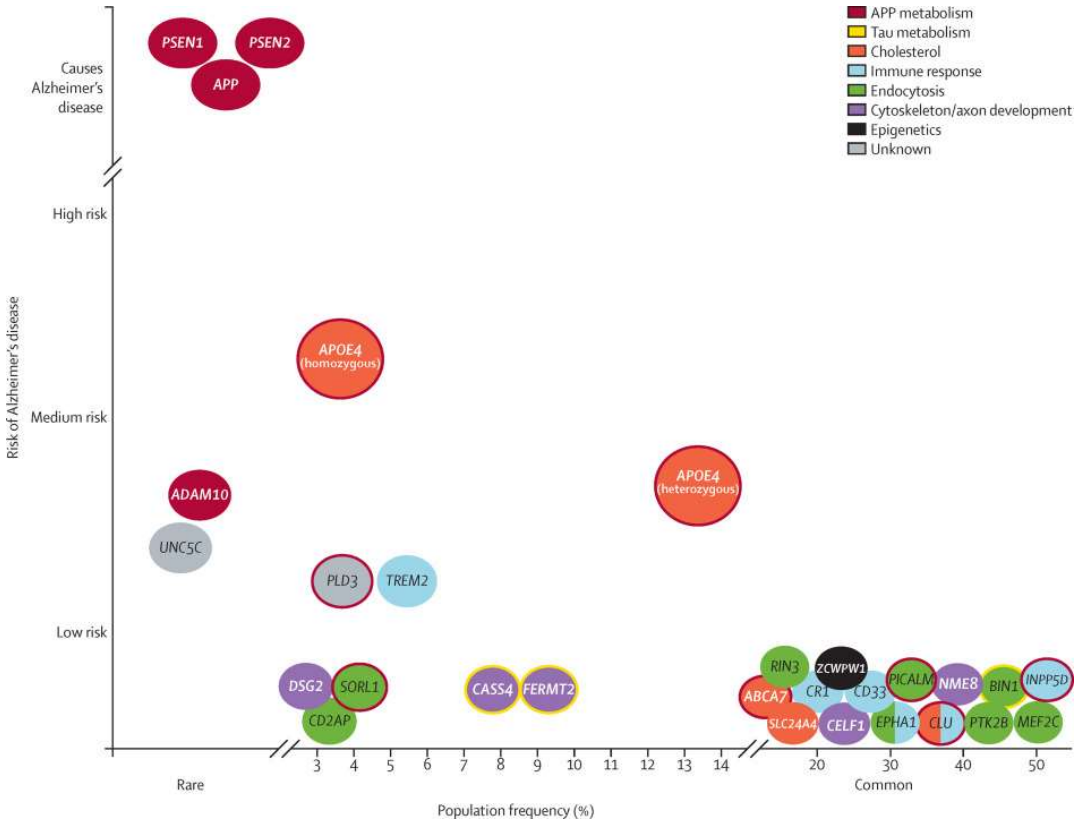

Figure 9: Genetic landcape of AD

Representation of AD-associated genes including causative genes (APP, PSEN1 and PSEN2) and susceptibility genes with high, medium and low risk factors. The colours in the key show the pathways in which these genes are implicated. (Scheltens et al., 2016).

Although APOE gene is the best documented susceptibility gene for AD, over 60% of SADs are not associated with APOE suggesting that other factors contribute to the development of AD. In fact, large-scale Genome-Wide Association Study (GWAS) enabled to identify more than 30 genetic loci involved in predisposition for AD (**Figure 9**). Most of the genes were clustered within the main three pathways: immune system-inflammatory response, cholesterol-lipid metabolism and endocytosis (**Figure 9**). Among them, mutation in Triggering receptor expressed on myeloid cells 2 (TREM2) gene, coding for a microglial receptor involved in Aβ clearance, has been associated with increased AD risk to carriers. Interestingly, a rare TREM2 variant (R47H) prevents TREM2-mediated early microglial response to Aβ phagocytosis and plaque compaction. The discovery of many genes involved in microglial and immune cell function has reconsidered the role of this cell type in the progression of AD and new mechanism hypothesis of AD has emerged.

1.3.2.2 Lifestyle-related factors

The wide clinical spectrum of SAD cases makes unclear the etiology of this disease. As causal genetic susceptibility was not found in all SAD patients, the role of environment as a putative risk factor has gained importance during the last decade. Particularly, bacteria and virus infections have been shown to alter Aβ pathology. Chronic oral exposure to a periodontal pathogen has been shown to induce accumulation of Aβ in the brain of WT mice (Ilievski et al., 2018). Moreover, the herpes virus has been observed more frequently in AD brains than in healthy brains supporting that the neuroinflammation response is altered in AD. Moreover, lifestyle choice appears to be a determinant factor in AD developing risk. Social context, as high education and physical activity, contributes in modulating the risk of AD. As high cholesterol level is a concomitant sign of AD, having an unhealthy diet (eating saturated fats, lots of sugar and salt) affects biological mechanisms such as inflammation and oxidative stress and, finally, leads to the development of metabolic disorders (obesity, diabetes) that underlie AD. Furthermore, increasing evidence suggests that consumption of alcohol and tobacco aggravates AD risk. Vascular background (cardiovascular diseases) is also linked to lifestyle comorbidities and, as a result, increases the incidence of AD. Epidemiological studies on the effect of environmental pollutants on the predisposition to develop AD revealed AD aggravation in presence of some neurotoxic metals (mercury, aluminum, arsenic) and pesticides that enhance Aβ accumulation, Tau phosphorylation and impairment of cognitive functions (Rahman et al., 2020). Hence, it is critical to establish public health strategies, achievable for all societies, to enable healthy lifestyle at individual level and to enhance environmental protection rules.

1.4 Pathophysiology of AD

AD patient autopsy revealed the presence of two main disease-related neurohistopathological lesions: extracellular senile plaque composed of aggregated Aβ peptide and intraneuronal accumulation of hyperphosphorylated Tau protein matting in NFTs. Additionally, growing evidence suggested that neuroinflammatory activation and synaptic deterioration play a pivotal role in AD pathophysiology. Deciphering the role of each AD hallmark is crucial in the understanding of the disease.

1.4.1 Amyloidosis

1.4.1.1 Formation and clearance of Aβ peptide

An imbalance between production and clearance of Aβ is responsible for its accumulation and aggregation throughout the brain.

Aβ peptide is the main constituent of amyloid plaque. Aβ is generated from APP, a transmembrane protein produced in neurons, which can be proteolytically cleaved through non-amyloidogenic α-secretase or amyloidogenic β-secretase pathways (**Figure 10**) (Haass et al., 2012). Initial APP cleavage by β-site amyloid precursor protein cleaving enzyme 1 (BACE1, β-secretase enzyme) at the N terminus of Aβ sequence releases a large N-terminal secreted APP-β fragment and the membrane-bound C99 fragment also called CTF-β. C99 fragment is further cleaved by the γ-secretase that allows the formation of several truncated Aβ species depending on the location of γ-cleavage. $Aβ_{40}$ and $Aβ_{42}$ are the more predominant isoforms of Aβ found in AD patients. Alternatively, to this amyloidogenic pathway, the physiological pathway, including the α-cleaving site within the Aβ sequence of APP, precludes Aβ generation and yields soluble N-terminal APPα (sAPPα) and C-terminal fragment α (CTF-α) production. The CTF-α is further processed by γ-secretase to generate P3 which contains the 17-42 Aβ fragment and a final C-terminal fragment called APP IntraCellular Domain (AICD) (**Figure 10**).

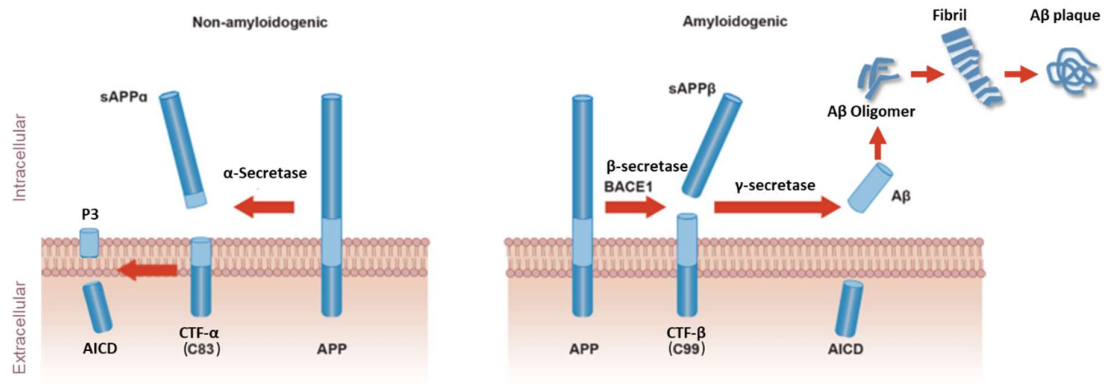

Figure 10: APP processing and generation of Aβ

Amyloid Precursor Protein (APP is a single transmembrane protein. In the non-amyloidogenic pathway (left), APP is cleaved by α-secretase to yield CTF-α and extracellularly released sAPPα. CTF-α is subsequently cleaved resulting in the release of P3 fragment. In the amyloidogenic pathway (right), APP is first cleaved by β-secretase (BACE1). CTF-β fragment is subsequently cleaved by γ-secretase composed of PSEN1 or 2. This proteolytic processing releases Aβ into the extracellular space that will further aggregates into oligomers, fibrils and finally Aβ plaque. APP intracellular domain (AICD) from the initial α- or β-secretase cleavage is released into intracellular space. Adapted from (Hampel et al., 2021).

The mechanism of Aβ elimination from the brain, mostly invalidated in SAD, is unclear. Pathways that are known to be involved in clearing soluble Aβ include transport across the blood–brain barrier (BBB), phagocytosis, enzymatic degradation and perivascular drainage.

AD-related pathology is not exclusively related to Aβ occurrence but is thought to be due to unbalanced of APP cleavage products. The first β-cleavage of APP initiates the neurodegenerative process as it has been suggested a predictive role of β-CTF accumulation in cognitive alteration in transgenic mouse (Lauritzen et al., 2016). Despite the numerous clinical trial failures in targeting secretases in the amyloidogenic pathway, concepts that look for new therapeutic targets across the secreted fragment from the non-amyloidogenic pathway have emerged to resolve AD pathology. The sAPP-α appears to be a potential candidate as low levels of sAPPα were reported in patients with mild cognitive impairment and AD (Lannfelt et al., 1995). Additionally, in APP transgenic mouse model, modulation of hippocampic sAPPα by gene transfer was shown to rescue spatial memory impairment and synaptic alteration (Fol et al., 2016). This results were strongly supported by *in vitro* studies demonstrating a protective role of sAPPα against neuron death (Copanaki et al., 2010) and excitotoxicity (van der Kant and Goldstein, 2015). So far, the underlying protective mechanisms of this pathway still need to be elucidated. In pathological conditions, direct interaction between Aβ and α-secretase were proposed to contribute to modulation of non-amyloidogenic pathway (Marcello et al., 2019).

1.4.1.2 Neuropathology

Post-mortem analysis of AD patients' brain revealed the presence of **extracellular amyloid plaques** and **intracellular amyloid**, in the parenchyma, whereas accumulation of Aβ deposits around blood vessel wall were responsible for **cerebral amyloid angiopathy** (CAA).

1.4.1.2.1 Parenchymal amyloid plaques

Investigating the morphology of Aβ aggregates in the parenchyma led to the description of different types of Aβ plaques: diffuse, fibrillary and dense-cored plaques (**Figure 11**). **Diffuse** plaques are highly variable in size (from 50 µm to several hundred µm), irregular in shape and without distinct edges. As they are mainly composed of $A\beta_{40}$, amyloid dyes cannot enable their visualization and they have been usually revealed using antibodies against Aβ. This amorphous deposits have been found in large numbers in cognitively unimpaired patients during the preclinical AD (Duyckaerts et al., 2009). Late stage of AD is associated with the presence of numerous **fibrillar** plaques which are composed of central mass of Aβ with compact spoke-like fibril bundles (Dickson and Vickers, 2001). The last form of plaques has been described as **dense-cored** plaques characterized by a compacted central core of Aβ surrounded by an outer sphere of Aβ. They adopt either a reticular or radial shape and are smaller than the other forms of Aβ plaques. These focal deposits mainly contain $A\beta_{42}$ species and thus, are highly reactive to amyloid aggregate dyes as Congo Red and Thioflavine S.

A common phenomenon in AD is the association between Aβ plaques and clusters of dystrophic neurites. A detailed exploration of this association showed that dense-cored plaques composed of radiating amyloid fibrils can be surrounded with neuritic components as tau filaments, Aβ oligomers and activated glial cells in order to form large **neuritic plaques also called senile plaques** (DeTure and Dickson, 2019; Duyckaerts et al., 2009).

Although Aβ is the major component of senile plaques, various proteins, lipids and cells can bind to Aβ deposits and contribute to highly pathogenic clusters surrounding neurons. Among these molecules, emerging evidence have shown that heparan sulfate proteoglycans - membrane receptors of growth factors - induce tau abnormal phosphorylation and facilitate tau spreading, which initiates tau pathology in AD.

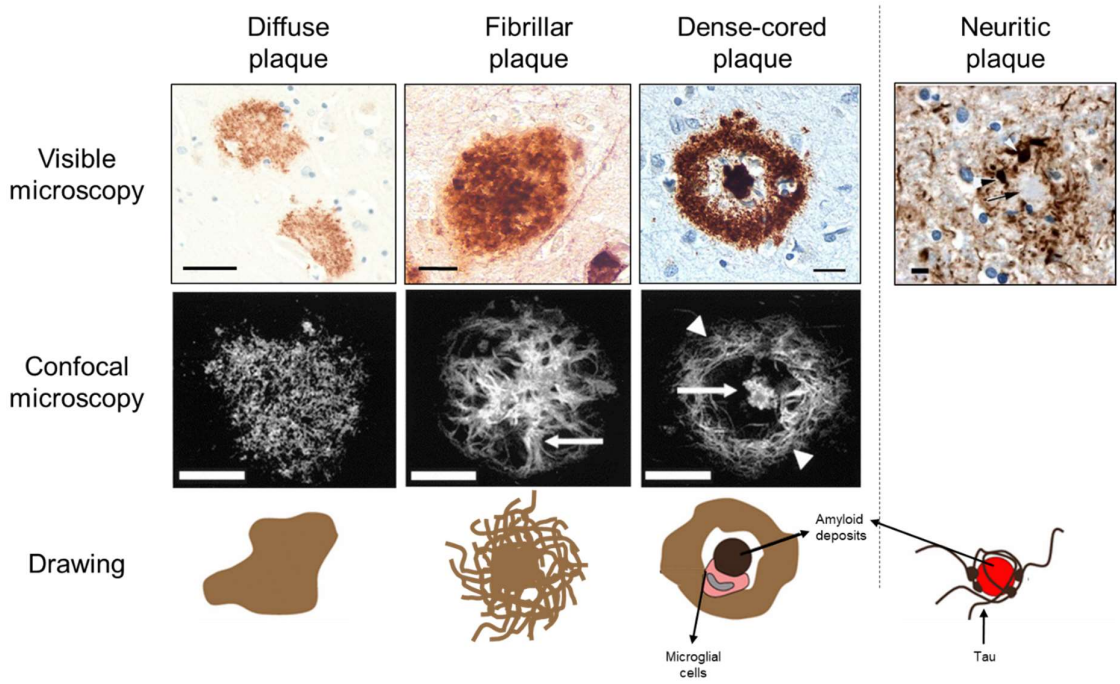

Figure 11: Pattern of amyloid depositions in the brain parenchyma

Different types of amyloid plaques can be visualized on visible (scale bar= 40µm) and confocal microscopy (scale bar = 20µm). Adapted from (DeTure and Dickson, 2019; Dickson and Vickers, 2001; Duyckaerts et al., 2009; Walker, 2020)

1.4.1.2.2 CAA

Physiopathological study of FAD patients bearing the *Dutch* mutation in APP gene enabled the identification of severe inherited cerebral hemorrhages linked to Aβ causing CAA (Biffi, 2022; Levy et al., 1990). Although CAA can develop separately from AD, around 80% of AD patients present features of CAA in their brain that are associated with early and severe AD dementia. This vascular disorder is

characterized by amyloid deposition within the walls of leptomeningeal and cortical blood vessels, with specific predilection for arterioles over capillaries and veins (**Figure 12**). The vascular deposition is predominantly made of $A\beta_{40}$ and is particularly found in the occipital cortex. For several decades, mechanism by which Aβ secreted by neurons can accumulate within blood vessels has triggered many questioning. Abnormal perivascular drainage of Aβ through interstitial fluid (ISF) and increased BBB permeability has been suggested to have a major role in the accumulation of Aβ within the vessel wall. An alternative hypothesis proposed that Aβ-mediated astrocyte dysfunction impaired CSF-ISF exchange involved in perivascular Aβ elimination via the glymphatic system (Greenberg et al., 2020).

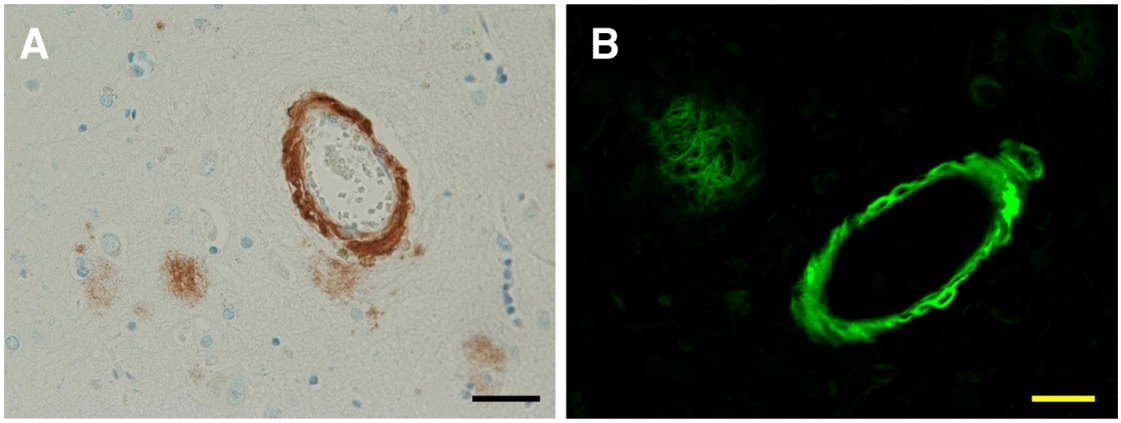

Figure 12: Cerebral Amyloid Angiopathy

Amyloid deposition within the wall of vessels lead to cerebral Amyloid Angiopathy (CAA) that can be visualized in frontal cortical sections using Aβ antibody labeling (a) or Thioflavin S staining (b) Scale bars= 40 µm (DeTure and Dickson, 2019).

1.4.1.2.3 Intracellular amyloid

Numerous studies have confirmed that intracellular accumulation of Aβ is an early event in AD and may be a source for extracellular deposits (Gouras et al., 2010, 2000; LaFerla et al., 2007; Tomiyama et al., 2008). Indeed, growing evidence supported that intraneuronal Aβ build up precedes extracellular plaque formation in AD patients and its levels decrease as extracellular plaques accumulate. The main question remains about the origin of the intracellular Aβ pool. One hypothesis is that endocytoliticly generated Aβ is not secreted, resulting in a sequestration of Aβ in neurons. The release of Aβ is strongly dependent on the localization of APP along with the β- and γ-secretases and, thus, can occur in several cellular compartments. Aβ cleavage can occur either at plasma membrane, leading to Aβ release in extracellular medium, or in trans-Golgi network, endoplasmic reticulum, endosomal membranes, lysosomal membranes and mitochondrial membranes. Alternative hypothesis proposed that secreted Aβ from extracellular pools can be uptaken by the cell to feed Aβ intracellular pools. Internalization of Aβ is mediated through interaction with Aβ-binding protein receptors present at the cell surface like

metabotropic glutamate receptor 5 (mGluR5). Additionnaly, N-methyl-D-aspartate (NMDA) receptor antagonist limits neuronal Aβ uptake, prevents microglial activation and reduces Aβ-mediated toxicity.

Inside neurons, Aβ is predominantly aggregated as oligomeric Aβ assemblies which have been described as the most pathological forms of Aβ (**Figure 13**). This intraneuronal Aβ has been associated to tau phosphorylation, neuronal loss and to the development of synaptic pathology at the origin of cognitive deficits (Gouras et al., 2010; Ripoli et al., 2014). Thus, emerging questioning has been addressed to know whether extracellular or intracellular Aβ were the most deleterious in AD pathogenicity. Recently, a study of Aβ pathology propagation from diseased to healthy neurons brought to light the crucial role of cooperation between extracellular and intracellular Aβ in synaptic alterations. Treatment of healthy primary cortical neurons with exogenous Aβ oligomers increased the amyloidogenic processing of APP which led to intracellular accumulation of newly produced Aβ oligomers in the synaptic terminal where it exerted its toxicity (Rolland et al., 2020). The release of extracellular Aβ oligomers promoted the spreading of synaptopathology through a vicious cycle.

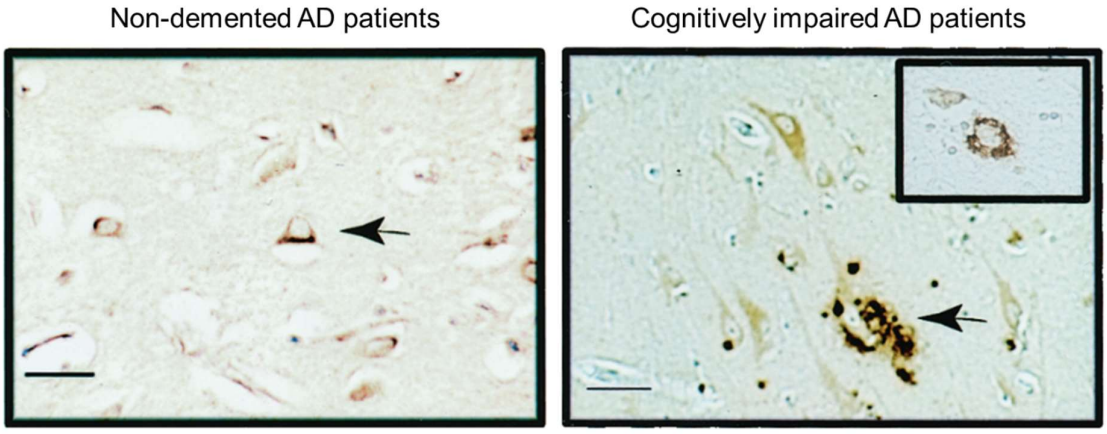

Figure 13: Intracelluar Aβ were found in AD cases and healthy controls

Representation of $A\beta_{42}$ labeling in the entorhinal cortex of a 79-year-old subject without dementia (left) and an 83-year-old cognitively impaired subject (right). The arrow indicates a neuron with intracellular staining. Increased staining with higher intensity was found in AD case compared to age-matched control. Scale bar = 40 µm. (Gouras et al., 2000).

1.4.1.3 Amyloid deposits' progression pattern: Thal phases

Amyloid deposits are absent at the beginning of the disease and gradually appear with aging through a typical topographical distribution. Thal and colleagues described five hierarchical phases for amyloid deposition pattern (**Figure 14**). First, Aβ deposits are found exclusively in the neocortex (phase 1), then disease spreads to allocortical and limbic brain regions, including the hippocampus, entorhinal cortex and cingulate gyrus (phase 2). The phase 3 is characterized by the occurrence of amyloid plaques in

subcortical areas such as thalamus, hypothalamus, striatum and the basal forebrain, while phase 4 displays amyloid deposits in the midbrain and the medulla oblongata as well as in several brainstem nuclei. Finally, during the phase 5, Aβ plaques reach the cerebellum and the pons (Thal et al., 2015, 2002).

Figure 14: Topographic distribution of amyloid deposition according to the Thal phases

Red areas in Thal phases depicts the brain regions with the initial accumulation of Aβ. Continued deposition in the same areas are shown in darker colors in the subsequent stages, with the new areas showing Aβ in red in each phase. Pre-clinical stages: In phase 1, neocortical regions including association cortices are first affected (phase 1); additional accumulation is seen in allocortical and limbic regions (phase 2); subcortical areas are then reached out (phase 3). Clinical stages: midbrain, brainstem and cerebellum are the last regions to display Aβ accumulation in late phases 4 and 5.

1.4.2 Tauopathy

1.4.2.1 Tau protein

Tau protein name comes from Tubulin associated unit. Tau is a microtubule-binding protein encoded by the MAPT gene on chromosome 17 (Binder et al., 2005). Tau is divided into four domains: N-terminal domain containing two alternatively spliced N-terminal insert, proline-rich domain (PRD), microtubule-binding domain (MTBD) including four imperfectly repeated motifs and C-terminal tail. Six distinct isoforms of this protein are produced in the adult human brain through alternative splicing in the microtubule associated protein tau (MAPT) gene which contains 16 exons coding for a 441-residue polypeptide. Tau isoforms are distinguished by either the absence (0N) or presence of two (2N) or one (1N) of the N-terminal inserts encoded by exon 2 and 3; and the presence (4R) or absence (3R) of the second of the four C-terminal microtubule-binding repeats encoded by exon 10. This gives rise to a total of six isoforms: 2N4R, 1N4R, 0N4R, 2N3R, 1N3R and 0N3R (**Figure 15**). The 3-repeat (3R) tau isoforms are mainly produced during development while the 4-repeat (4R) tau isoforms are produced only in adulthood. Both are maintained in a balanced ratio (1:1) in adult human brains. Impaired ratio has been involved in AD as well as in other tauopathies.

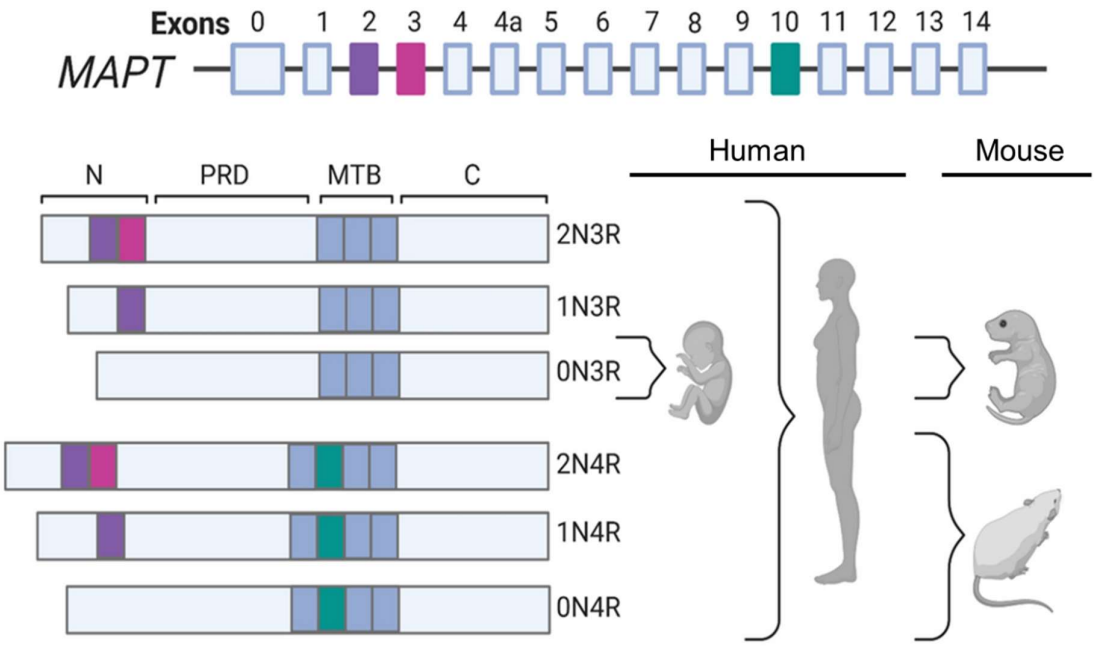

Figure 15: Tau isoforms

Tau is encoded by the MAPT gene on chromosome 17 (top). The alternative splicing of exons 2, 3, and 10 generates 6 Tau isoforms. Inclusion of exon 10 (green) produces Tau with 4 microtubule-binding (MTB) domains (4R). The absence of exon 10 producing tau with 3 MTB domains (3R). Tau can include (2N or 1N) or exclude (0N) amino-terminal inserts through regulation of exons 2 (purple) and 3 (pink). While all isoforms are expressed in adult humans and exclusively the 4R isoforms in the adult mouse, the human and mouse fetal brain only expresses 0N3R tau. Adapted (Kent et al., 2020).

Compared to Aβ, the role of Tau has been largely elucidated over the last decade. In physiological conditions, tau is found primarily in the axons of mature neurons where it regulates the dynamic instability of microtubules and plays an important role in axonal transport of cargo proteins from the soma to axon terminals by interacting with motility proteins such as dynein and kinesin. Although many *in vitro* studies supported the idea that Tau contributes to microtubule stabilization and neuronal architecture maintenance, MAPT knockout or knockdown in mouse models and in primary neurons does not impair microtubule assembly or axonal transport (Guo et al., 2017). This finding suggested that compensatory mechanisms may arise from other microtubule associated proteins (MAP). Tau participates to neuronal cell signaling pathways by binding to transmembrane receptors. Furthermore, the identification of Tau within the cell nucleus revealed a pivotal role as DNA-binding protein allowing DNA repair mechanism, gene expression and epigenetic regulation. Interestingly, Tau translocation to nucleus regulates the expression of glutamatergic transporter proteins, as Vesicular Glutamate

Transporter 1 (VGLUT1), leading to a control of neuronal excitability. The role of Tau in neuronal development, synaptogenesis and synaptic plasticity has been demonstrated as it induces synaptic response to brain-derived neurotrophic factor (BDNF) which facilitate spine growth. Moreover, Tau knockdown in murine models showed that new-born granule neurons in the dentate gyrus failed to migrate normally and had both disrupted postsynaptic densities and mossy fiber terminal formation during hippocampus neurogenesis (Kent et al., 2020; Pallas-Bazarra et al., 2016).

Tau is subject to numerous post-translational modifications including phosphorylation, acetylation, ubiquitination, sumoylation, methylation, glycation and truncation. Tau phosphorylation is a common feature of AD. Tau can be phosphorylated by protein kinases at 82 residues. Aberrant phosphorylation due to pathological mutations in kinases results in decreased microtubule binding affinity in addition to increased propensity of tau to aggregate. Hyperphosphorylated tau can be found in somatodendritic compartments and post-synaptic densities where it alters synaptic function by reducing glutamate receptor trafficking and synapse pruning.

1.4.2.2 Neuropathology of post-mortem AD brain

In AD, tau is found as aggregated and filamentous deposits inside neurons. Subcellular compartmentalization of Tau location revealed different types of deposits: NFTs in the soma, neuropil threads (NTs) in the dendrites and neuritic plaques (NPs) mainly in axonal processes (Duyckaerts et al., 2009). NFTs correspond to abnormal formation of paired helical filaments (PHFs) of Tau mainly detected by AT8 monoclonal antibodies which recognize phosphorylated epitopes at serine and threonine residues (**Figure 16**). Several evidence suggested that NFTs strongly correlate with cognitive decline in AD compared to amyloid deposits. Besides AD, NFTs have been identified in over 20 different neurodegenerative diseases like tauopathies and frontotemporal dementia. NTs are composed of dendritic and axonal processes containing filamentous Tau including PHFs and straight filaments of Tau (**Figure 16**). NTs may represent the majority of tau burden in AD and they are thought to originate from neurons containing NFTs. Gallyas silver staining enables their visualization in the brain of AD patients. Cored NPs containing Tau-positive neurites and a central zone of dense amyloid have already been described in **Section 1.4.1.2**. Dystrophic neurites are thought to originate from neurons bearing NFTs in their soma and can contain neurofilament proteins. They are mostly heterogenous. Degenerating mitochondria, lysosomal bodies and vesicles can also accumulate in NPs, playing a central role in alteration of trafficking and protein degradation pathways (**Figure 16**) (DeTure and Dickson, 2019).

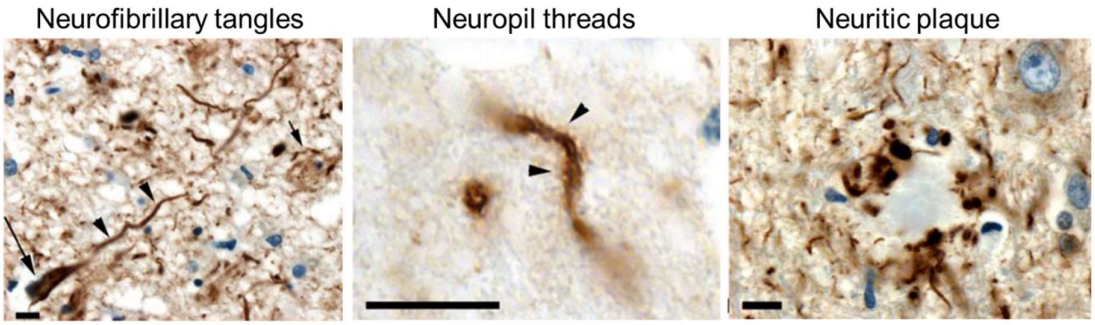

Figure 16: Tau deposits in AD brain

Accumulation of Tau aggregates are shown within either the cell body of neurons as NFTs (arrow) or the dendritic shaft as NTs (arrowheads) or within the immediate vicinity of amyloid plaques in NP. Scale bars: 10µm. Adapted from (Duyckaerts et al., 2009).

1.4.2.3 Progression of Tau pathology: Braak stages

The most widely used staging scheme for progression of NFTs and NTs in AD brains was proposed in 1991 by Heiko and Eva Braak. First, Tau pathology is largely confined to the transentorhinal and perirhinal cortex (stage I). Then, the CA1 region of the hippocampus is affected (stage II). The pathology spreads to the entire hippocampus and reaches the subiculum followed by limbic structures such as the thalamus, the temporal cortex and the fusiform gyrus (stage III). The Braak Stage IV is characterized by massive development of neurofibrillary pathology in neocortical associative areas and further increases in amygdala, thalamus and claustrum. Cognitive decline starts to appear in AD patients. NFTs reach out the isocortical areas as frontal cortices, superolateral and occipital territories and the peristriate region (stage V). Finally, primary sensory areas including striate areas as well as motor and visual regions become involved (stage VI) (**Figure 17**) (Braak et al., 2006; Braak and Braak, 1991). The typical temporal-spatial progression of Tau pathology in AD brain demonstrates the consistence of Tau-mediated AD spreading though neuron-to-neuron pathway.

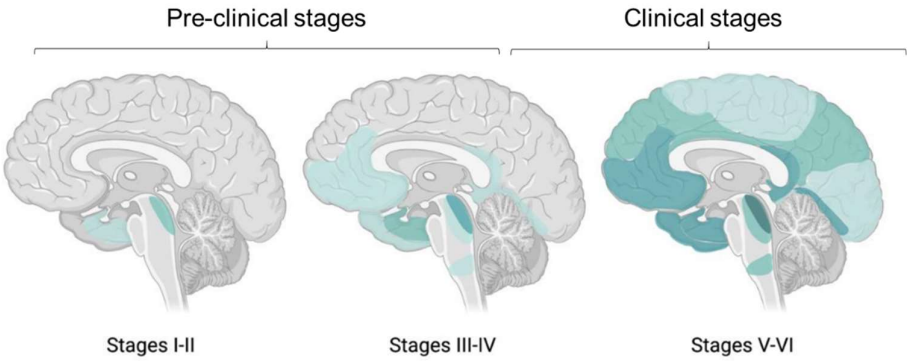

Figure 17: Topographic distribution of Tau deposition according to the Braak stages

Green areas in Stage I-II depicts cortical regions with the initial accumulation of Tau during the early pre-clinical stages, including the transentorhinal and entorhinal cortex. Additional accumulation is seen in hippocampal region, basal forebrain and thalamus associated with the involvement of the amygdala, putamen and accumbens nucleus during Stages III-IV. The isocortex and temporal lobe, and most of association cortices have Tau accumulation in late phase clinical Stages V-VI. Adapted from (Goedert et al., 2014).

1.4.3 Neuroinflammation

Neuroinflammation exerted by astrocytes and microglial cells plays a central role in the pathogenesis of AD. Reactive glial cells are associated with amyloid plaques and NFTs. However, it was uncertain whether microgliosis and astrogliosis reflect a beneficial, detrimental or inconsequential activity in AD.

1.4.3.1 Astrogliosis

1.4.3.1.1 Physiological function of astrocytes

Astrocytes are the most abundant glial cells and are involved in multiple essential brain functions. Astrocytes regulate formation, maturation and elimination of synapses and are central for maintaining synaptic transmission and information processing by neural circuit functions. Astrocytes are involved in reuptake and recycling of neurotransmitters. They provide metabolic support to neurons and assist neurogenesis. They are responsible for brain homeostasis by maintaining extracellular ion balance. They form biochemical support of endothelial cells of the BBB and they regulate the cerebral blood flow. When brain injuries occur, astrocytes become activated and so called reactive astrocytes. Reactive astrocytes increase neuroprotection and trophic support of stressed neurons. They isolate the damaged areas from the rest of the brain by forming a glial scar. Then, they participate to BBB reconstruction and repair process.

1.4.3.1.2 Reactive astrocytes in AD

Loss of astroglial function and reactivity contributes to AD. Hippocampal morphological and phenotypic alterations of astrocytes occur early in AD prior to amyloid plaques and NFTs depositions. These changes are highly heterogeneous and region-specific. Astrocytes undergo degeneration and atrophy at the early stages of pathological progression. Absence of reactive astrocytes in some brain regions such as the entorhinal cortex coincides with higher vulnerability of these regions to AD pathology (Rodríguez-Arellano et al., 2016). Indeed, chronic astrogliopathology leads to a loss or remodeling of basic astroglial functions and facilitates the development of AD. For example, alteration of brain homeostasis contributes to early cognitive deficits. Morphological atrophy of astroglial cells reflects a decrease in their territorial domains meaning that astrocytes are not anymore able to cover

neurons and synapses located in these domain. Thus, a reduction of astroglial homeostatic support is observed and the performance and survival of neurons decrease. Furthermore, astrocyte-synaptic contacts are abolished, which affects functional activity of synapses by weakened synaptic transmission and plasticity. As synaptic deficit is an early event in AD, this finding claims that astrocyte activation may occur early in AD even before amyloid deposition (Fuller et al., 2009; Orre et al., 2014; Verkhratsky et al., 2010). Histopathological analysis of post-mortem AD brains revealed that, at later stage of AD, hypertrophic reactive astrocytes accumulate around and are associated with neuritic plaques.

Hypertrophic reactive astrocytes are characterized by increased expression of glial fibrillary acidic protein (GFAP). In the 3xTg mouse model of AD, reactive GFAP-positive astrocytes were found around senile plaques and associated with perivascular Aβ deposits (Rodríguez and Verkhratsky, 2011; Verkhratsky et al., 2010). Growing evidence demonstrates that theses reactive astrocytes produce pro-inflammatory factors that can be regulated by Aβ. Some studies have shown that astrocytes release cytokines, interleukins, nitric oxide and other cytotoxic molecules upon exposure to Aβ (Gitter et al., 1995; Speciale et al., 2003). The synergistical action of Aβ and these cytokines on astrocytes exacerbates the neuroinflammatory response (LaRocca et al., 2021). Aβ has been shown to bind several astrocytic receptors like receptor for advanced glycation endproducts (RAGE) and low-density lipoprotein receptor-like protein 1 (LRP1) that activate pro-inflammatory signaling pathways. Recently, these pro-inflammatory “disease-associated astrocytes” have been shown to accumulate and facilitate AD progression (Habib et al., 2020). Together, these findings suggest a possible cytokine-like effect of Aβ in AD. Interestingly, in transgenic mouse bearing APP mutations, prior to amyloid deposition, up-regulation of inducible nitric oxide synthase (iNOS) by reactive astrocytes was found to prepare an environment that favors the development of future amyloid plaques (Heneka et al., 2015).

Levels of Aβ in the brain are regulated by innate immune response which in turn, can be it-self activated by Aβ. Astrocytes have a potential role in internalizing and degrading Aβ. The clearance of parenchymal soluble Aβ by astrocytes occurs by paravenous drainage across BBB or by enzymatic degradation (Ueno et al., 2014). Impaired function and atrophy of astrocytes manifest in the reduction of proteolytic clearance of Aβ. Astrocyte-mediated clearance of Aβ requires APOE and depends on a signaling pathway involving astrocytic water channel aquaporin-4. For several decades, it was thought that neuronal cells were the major source of Aβ. However, growing evidence showed that astrocytes can secrete a pool of Aβ that significantly contributes to brain amyloid burden (Frost and Li, 2017).

1.4.3.2 Microglia

1.4.3.2.1 General function

Microglial cells are the macrophages of the central nervous system (CNS) and are responsible for innate immune response. Under a resting state, microglial cells serve as resident phagocytes that dynamically survey the environment using their long ramifications. They play a crucial role in tissue maintenance, injury response and defense against pathogens. Microglia releases trophic factors including BDNF which aims at protecting synapses and ensures maintenance and plasticity of neuronal circuits though synapse remodeling. During normal brain development, a massive elimination of unwanted neurons and synapses, called synapse pruning, is required to ensure correct neuron connectivity (Paolicelli et al., 2011). Microglia mediates synaptic engulfment and sculpts synaptic connections during synapse pruning by involving the classical pathway of complement. Microglia-synapse interactions also contribute to memory formation.

Microglia becomes activated following exposure to pathogen-associated molecular patterns (PAMPs) and/or endogenous damage-associated molecular patterns (DAMPs). Once activated, microglia migrates to brain lesions and undergoes chronic morphological changes. Microglia ramifications shorten, somas widen and microglial cells adopt an amoeboid or round morphology. Additionally, microglia-secreted factors change from neurotrophic factors to cytotoxic molecules such as proinflammatory cytokines, reactive oxygen species, proteinases and complement proteins that may cause neuronal damage.

1.4.3.2.2 AD-associated microglia

Human genetic studies identified that the majority of risk genes for AD are highly expressed by microglia (Lambert et al., 2013; Srinivasan et al., 2016). Among them, the discovery of AD-associated variants in TREM2, a receptor protein selectively and highly expressed by microglia, brings to light an impairment of microglial activation. In TREM2, R47H loss-of-function mutation prevents the protective effect of microglia against AD as it reduces the ability of microglia to phagocyte pathogens as Aβ (Jay et al., 2017; Ulrich et al., 2017; Yeh et al., 2017). The activation of microglia exerts beneficial or deleterious aspects depending on the stage of AD. Early AD is associated with a protective role of microglia while in late AD high activation of microglia contributes to synaptic dysfunction.

Controversial role of the effects of microglia on AD physiopathology has been reported in the literature that strengthens the counteracting effects in the early and late stages of AD. On the one hand, evidence have shown that microglia protects against the incidence of AD as alteration of its activity has been associated with increased AD risk, in particular impairment of Aβ-toxicity response (Yeh et al., 2016). Moreover, microglia is involved in uptake and clearance of Aβ, in phagocytose of insoluble

Aβ deposits and in the initiation of chemotaxis (Hansen et al., 2018). Additionally, several studies in mouse models of AD and human AD brains described an accumulation of microglia around amyloid plaques. Microglia has been suggested to form a protective barrier around amyloid deposits that compacts Aβ fibrils into dense-cored plaques (potentially less toxic), prevents the attachment of new Aβ and reduces axonal dystrophy around the amyloid plaques (Condello et al., 2015; Yuan et al., 2016). On the other hand, activated microglia has been shown to be neurotoxic for neurons. Acute inflammation has a protective role in defending against brain injury such as the presence of Aβ plaques. However, chronic and persistent activation of microglia makes it incapable of removing amyloid plaques. Unfortunately, microglia ability to secrete pro-inflammatory cytokines that can injure neurons directly is maintained. As a result, an imbalance between the pro- and anti-inflammatory cytokines is created and may impair dendritic spines and also disrupt microglial clearance of Aβ.

Additionally, microglia has been shown to exacerbate Tau pathology, mediate engulfment of synapse and activate neurotoxic astrocytes (Leyns and Holtzman, 2017; Spangenberg and Green, 2017). Evidence have been shown that Aβ and Tau are directly linked to microglia-mediated toxicity that will be discussed in **Section 2.3.1**.

1.4.4 Synaptopathy

1.4.4.1 The excitatory glutamatergic synapse

Transmission of nervous messages from one neuron to another occurs through synaptic transmission between pre- and postsynaptic elements separated by a gap called the synaptic cleft. In the excitatory glutamatergic synapses, the presynaptic element is rich of numerous small vesicles which contains excitatory (glutamate) or inhibitory (Gamma-Aminobutyric Acid, GABA) neurotransmitters that can be released in the synaptic cleft. The postsynaptic element contains several ion channels and neurotransmitter receptors. The majority of the excitatory neurotransmission in the CNS is carried out by glutamatergic excitatory synapses which are abundant in the hippocampus and the cortex. When the action potential arrives, membrane depolarization induces the opening of voltage-dependent calcium channels. Calcium influx provokes the fusion of glutamate-containing vesicles to the presynaptic membrane followed by the release of glutamate in the synaptic cleft. Then, glutamate binds to postsynaptic receptors and induces an influx of cations (Na^+,K^+,Ca^{2+}) leading to excitatory postsynaptic potential (EPSP) responsible for the transmission of nervous signal. Two categories of glutamate postsynaptic receptors were described: **metabotropic receptors** coupled to G proteins and **ionotropic receptors** coupled to ion channels including α-amino-3-hydroxy-5-methyl-4-isoxazolepropionic acid (AMPA), N-methyl-D-aspartate (NMDA) and kainate receptors. Metabotropic receptors are involved in the regulation of neuronal excitability and inhibition of glutamate release.

AMPA receptors mediate fast excitatory synaptic transmission. Kainate receptors contribute to the modulation of glutamate release and are involved in epilepsy mechanism. Finally, NMDA receptors take part in the induction of synaptic plasticity which is central for learning and memory.

In 1888, morphology of synapses was first described by Ramón y Cajal as tiny protrusions from dendrites, which form functional contacts with neighboring axons. The dendritic spines are composed of spine head and spine neck. Dendritic spines are highly heterogenous structures in term of number, size and shape, which constantly change in response to neuronal activity. This particular feature of dendritic spines is crucial for synaptic plastic. Spines can adopt three different shapes categorized as mushroom, thin or stubby (**Figure 18**). Compelling evidence have suggested that this different shapes of spine reflect different developmental stages and/or altered synaptic strength (Hayashi and Majewska, 2005; Yuste and Bonhoeffer, 2001). Strong synaptic connections are associated with mature spines with larger head, as mushrooms, while immature spines with small head contribute to weak synaptic connections, as thin. Stubby spines are intermediates in the process of maturation.

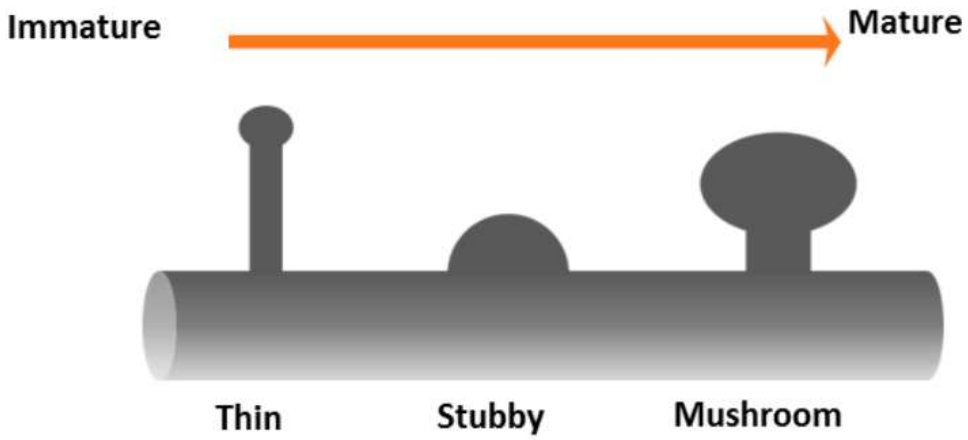

Figure 18: Schematic representation of the maturation of dendritic spines

1.4.4.2 Reduction of synaptic density and synapse morphological changes

It appears that synaptic loss precedes neuronal loss and is strongly correlated with cognitive decline in AD patients. The projection of neurons belonging to septal-hippocampal and basal forebrain-neocortical cholinergic pathways are abolished in AD (Whitehouse et al., 1982). Investigation of the alterations that occur in synapses and axons during AD revealed particular dysfunction of excitatory cholinergic and glutamatergic synapses while deficits in several neurotransmitters (GABA, serotonin, somatostatin) increase as the disease progresses (Selkoe, 2002). Transmitter alterations result from axonal dysfunction affecting the presynaptic terminals. Proteins involved in synaptic vesicle trafficking and neurotransmitter recycling as well as structural elements of synapses are thought to be strongly

affected during AD. It has been shown that impaired axonal transport due to Tau dysfunction facilitates the mislocation of Tau in dendritic spines. These pathogenic changes of synapse terminals contribute to alter synaptic transmission and, thus, impair synaptic function. Morphological analysis of synapses showed that synaptic damages are related to a decrease in synaptic density in the hippocampus and medial temporal lobes. Biopsy of AD brains revealed a decrease of 15-35% in the number of synapses per cortical neuron (Davies et al., 1987). This quantification is assimilated to the number of dendritic spines near excitatory synapses in most of *in vivo* imaging studies. Additionally to the number spines, their shape also influences synaptic activity by allowing or not neuronal connections and communications, which are crucial for developing cognition function. Spine structure can be classified, according to three-dimensional morphology, as thin, stubby and mushroom. While newly formed spines are thin, immature and dynamic structures, stubby spines are transitional structures that can enlarge and become mushrooms, the most stable and mature kind of spines. The volume of spines is proportional to the density of their receptors which is strongly correlated to efficient synaptic transmission. Indeed, high synaptic stimuli increase the volume of spines whereas low synaptic stimuli cause a decrease in spine volume (Hayashi and Majewska, 2005). In AD, a reduction in mature spine density is accompanied by an increased appearance of immature spines due to the presence of Aβ (Ortiz-Sanz et al., 2020). Despite an important loss of synapses in early stages of AD, the remaining synapses become larger and more robust indicating that compensatory synaptic mechanisms take place to ensure a cognitive reserve.

1.4.4.3 Loss of synaptic function

Memory loss is a very common symptom of AD and is strongly associated with synaptic alterations. Many studies investigated whether synaptic dysfunction and damage in AD were driven by early subtle pathological brain changes. Learning and memory require persistent changes in neuronal circuits which rely on synaptic plasticity. Thus, evaluating synaptic plasticity at hippocampal synapses appears to be a good marker to estimate memory dysfunction. Long-term potentiation (LTP) is defined as a long-lasting increase in synaptic transmission induced by either a short high-frequency stimulation delivered to presynaptic afferents or pharmacological treatments (Tv and Gl, 1993). Following electrical or biochemical stimulation, the slope or amplitude of EPSP is measured and represents the depolarization of the postsynaptic membrane due to the release of glutamate from presynaptic compartment (**Figure 19**). Glutamate binding to postsynaptic receptors provokes the expulsion of Mg^{2+} from ion channels of postsynaptic NMDA receptors, allowing strong calcium influx into the neuron. Strong Ca^{2+} influx activates various protein kinase signaling cascades leading to recruitment of more glutamate-binding AMPA receptors accompanied by an increased volume of spines to facilitate rapid synaptic responses.

Deficits in LTP have been found in still undemented future AD patients, which is in line with the apparition of hippocampal LTP impairments prior to behavioral deficits in AD transgenic mice.

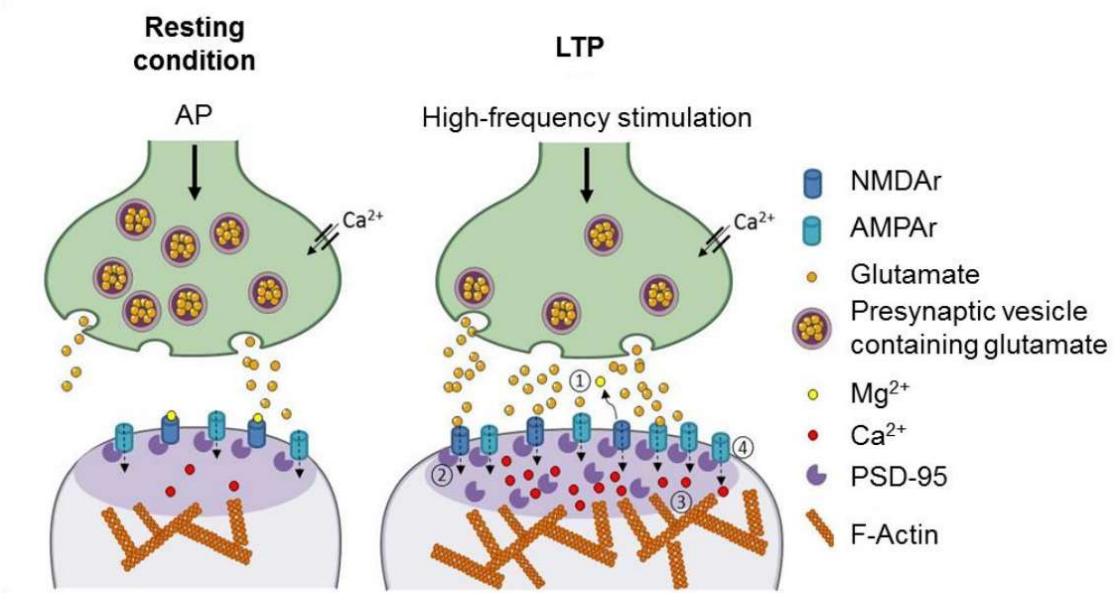

Figure 19: Synaptic mechanism of LTP generation

Under resting condition, NMDAr are blocked by Mg^{2+} ions. High-frequency stimulation induces the release of glutamate from the presynaptic compartment. Glutamate binds to NMDA and AMPA receptors inducing post-synaptic depolarization and subsequent ejection of Mg^{2+} ion along with the induction of Ca^{2+} influx. The latter is involved in the activation of several signaling pathways leading to an enlargement of post-synaptic element by the recruitment of more membrane receptors to the spine.

Long-term depression (LTD) is another form of synaptic plasticity. Unlike LTP, LTD is a long-lasting decrease of synaptic transmission induced by low-frequency stimulation which leads to a moderate depolarization activating phosphatase enzymes, instead of kinases, and results in the endocytosis of AMPA receptors and a decrease in dendritic spine volume.

While LTP is strongly correlated to memory consolidation, LTD is essential for cognitive flexibility (Jacobsen et al., 2006; Tv and Gl, 1993). Both are strongly affected during AD because of the internalization and endocytosis of AMPA and NMDA receptors. Disruption of LTP or LTD assessment may provide insight into synaptic failure by estimating synapse modulation.

1.4.5 Functional alterations

Memory impairment is due to neuronal loss in the perforant pathway of the medial temporal lobe (MTL) consistent with early NFTs involvement (Hyman et al., 1984). The MTL is composed of several

subregions including the hippocampus, entorhinal cortex and perirhinal cortex. Recently, the ability to perform functional magnetic resonance imaging (fMRI) studies during memory tasks brings to light the alterations of large-scale neuronal communications in clinical AD. Converging evidence suggests that specific neural networks are vulnerable to AD and most of the affected networks were involved in memory encoding and retrieval, additionally to executive function. Episodic memory impairment occurs early in AD and is supported by alterations of neural networks including the MTL network and the default mode network (DMN). DMN is metabolically active at rest and decreases in activity during cognitive tasks. It includes the posterior cingulate cortex (PCC) extending into the precuneus, lateral parietal, and medial prefrontal regions. DMN regions such as the precuneus and PCC are thought to be preferred accumulating region of amyloid deposition in AD. **During memory tasks**, while fMRI activation in MTL regions is abolished, abnormal activation of DMN was reported in cognitively impaired AD patients compared to control subjects (Golby et al., 2005; Machulda et al., 2003; Rombouts et al., 2005; Sperling et al., 2010). Consistently, decreases in hippocampal activity were also observed in AD patients. Regions demonstrating aberrant response to DMN activity overlap with high amyloid burden in AD. Interestingly, other groups reported particular patterns of functional connectivity in prodromal AD patients compared to normal elderly individuals and AD patients in task-related fMRI. Instead of network activity loss, paradoxical hippocampal hyperactivation was observed suggesting either the enrollment of compensatory mechanisms to maintain memory performance that lead to subtle cognitive impairments or the existence of excitatory mechanisms that take place early in the disease and cause neuronal failure (Dickerson et al., 2005; Hämäläinen et al., 2007). **At rest**, decreases in DMN functional connectivity allow to distinguish AD patients from cognitively normal elderly individuals (Greicius et al., 2004). This study highlighted a strong implication of hippocampus in the impairment of functional connectivity and showed a disruption of functional connectivity between the hippocampus and the PCC. The pattern of functional connectivity at cerebral rest is more complex and depends on the stage of AD. Evidence for the involvement of compensatory mechanisms during the progression of AD is emerging. Longitudinal resting-state studies have shown an increase in functional connectivity within posterior DMN in MCI patients compared to healthy controls. Then, connectivity in these regions decreases and frontal DMN shows an increased connectivity (Bai et al., 2011). In AD patients, posterior DMN connectivity decreases first and frontal DMN increases compared to healthy controls (Damoiseaux et al., 2012). Finally, AD patients display an overall activity decrease in the entire DMN. These findings support the hypothesis that hyperconnectivity precedes hypoconnectivity within the DMN and the passage from one connectivity state to the other may point out the early phase of brain dysfunction.

Several studies have also proposed resting-state fMRI setting as a biomarker of early AD as functional alterations in memory circuits and DMN have been observed in cognitively unimpaired AD patients even though they were amyloid PET positive (Damoiseaux, 2012; Sperling et al., 2010). Recently, longitudinal analysis of AD patients combining structural MRI and resting-state fMRI identified two distinct networks, belonging to the MTL network, strongly associated with differences in Tau and amyloid burden during AD progression. This finding supports previous investigations, showing a relationship between functional connectivity disruptions and spreading of disease though specific networks, and highlights the ability to predict the progression of AD (Flores et al., 2022).

Chapter 2 – Hypothesis of AD and therapeutic strategy

2.1 The amyloid cascade

2.1.1 Amyloid cascade hypothesis

The identification of Aβ peptides as the major constituents of senile plaques established the primacy of Aβ in AD pathogenesis (Glenner and Wong, 1984a, 1984b). The **amyloid cascade hypothesis** was proposed for the first time in 1992 by Hardy and Higgins. This hypothesis placed the accumulation of Aβ peptides in the brain as the central event in AD pathology (Hardy and Higgins, 1992). The imbalance between Aβ production and Aβ clearance results in Aβ aggregation and formation of insoluble plaques, which trigger a cascade of deleterious changes including NFT formation, neuronal death, vascular damage and, ultimately, clinical dementia. Furthermore, Aβ accumulation was suggested to initiate a process that may take several decades to produce the final pathology (Hardy and Higgins, 1992).

The initiation of AD pathological cascade by Aβ is strongly supported by neuropathological and human genetic evidences. Rare FADs are directly due to autosomal-dominant mutations in genes involved in amyloid pathways (Bi et al., 2019; Hatami et al., 2017; Piaceri et al., 2013). As these mutations cause an increase in Aβ plaque deposition, this pathological event is sufficient for the development of Tau pathology and neurodegeneration in the carrier. This discovery brings to light the pathological contribution of Aβ in AD pathogenesis. Aβ is a proteolytically derived product of APP. Most of FAD mutations identified in the APP gene result in the increased level of hydrophobic $A\beta_{42}$ and changes in the $A\beta_{42}/A\beta_{40}$ ratio. Moreover, missense mutations occurring within Aβ sequence have been shown to modulate Aβ aggregation properties, either yielding toxic damages or conferring protective effects. The central role of APP in AD was further confirmed by the discovery that increased number of copies of APP gene induce higher prevalence of AD, in particular in Down's syndrome (Sleegers et al., 2006). Furthermore, the most common form of early-onset FAD was linked to mutations of presenilin, which altered cleavage of APP to generate more aggregate-prone $A\beta_{42}$ and/or less $A\beta_{40}$, emphasizing the importance of Aβ peptides in AD. Finally, animal models bearing FAD mutations display AD-like features as amyloidosis, synaptic dysfunctions and memory impairments.

Only a tiny part of AD cases can be explained by familial mutations. Most of AD cases are sporadic, meaning that a specific event or series of events rising Aβ deposition may occur according to the amyloid cascade hypothesis. Pathological genetic variability altering Aβ has been found in SAD patients. The allele ε4 of APOE gene is a genetic risk factor that reduces Aβ clearance and increases Aβ production, whereas the allele ε2 of APOE has been demonstrated protective in SAD (Corder et al.,

1994). Interestingly, reversing APOE effect in transgenic APP mouse model was sufficient to reduce cerebral Aβ deposition and downstream events (Bales et al., 1997). Altogether, these data provide complementary evidence for the amyloid cascade hypothesis.

Spatial and temporal disconnection between amyloid and Tau spreading was demonstrated (Thal et al., 2002) in human neuropathological studies. Aβ deposition occurs in a step-wise manner, starting in neocortex, and then spreading to hippocampus while Tau pathology starts from hippocampus before spreading to the neocortex. The presence of Tau in some brain areas before amyloid deposition and its high correlation with cognitive decline begs the question whether Tau may initiate the pathology in this areas (Duyckaerts et al., 2009). However, several studies have suggested a potential temporal Aβ–Tau synergy in some brain areas (**Figure 20**). Tau pathology was shown not to progress from the entorhinal cortex to the neocortex without co-occurring amyloid pathology (Pontecorvo et al., 2019), placing Tau pathology downstream of amyloid pathology. Several findings deriving from mouse models converge toward a synergy between soluble forms of Aβ and Tau to exert synaptic toxicity. Furthermore, unlike APP mutations that could induce Tau pathology, genetic mutations in Tau are strongly associated with frontotemporal lobe dementia without reproducing amyloid deposition. Additionally, crossing Tau transgenic and APP transgenic mice or inoculating $A\beta_{42}$ into Tau transgenic mice leads to Tau pathology and neurodegeneration. This was also demonstrated recently in our team by intrahippocampal inoculation of AD-brain extracts harboring Aβ and tau fibrils into Aβ-plaque bearing mice, leading to seeding of aggregated human Tau in NPs and NFTs in the entorhinal cortex (Lam et al., 2022). In contrast, amyloid pathology remained unaffected in mice bearing Tau pathology (Hurtado et al., 2010; Pooler et al., 2015) which, again, strongly supports the amyloid cascade hypothesis. Aβ has been described to be highly neurotoxic and to increase intraneuronal calcium concentration, leading to the hyperphosphorylation of Tau and the formation of PHFs, the main components of NFTs. Accumulation of Aβ has also been involved in caspase-mediated Tau cleavage and Tau modifications leading to microtubule destabilization and formation of NFTs. Moreover, another research group postulated that amyloid pathology may drive the spreading of Tau pathology responsible for neuronal loss either through direct Aβ-Tau interaction or in an indirect and continuous Aβ load-dependent manner (Karran et al., 2011, p. 2), suggesting a mechanistic link between Tau and Aβ. Together, these data strongly argue that AD is an Aβ-facilitated tauopathy responsible for disturbance of cerebral function.

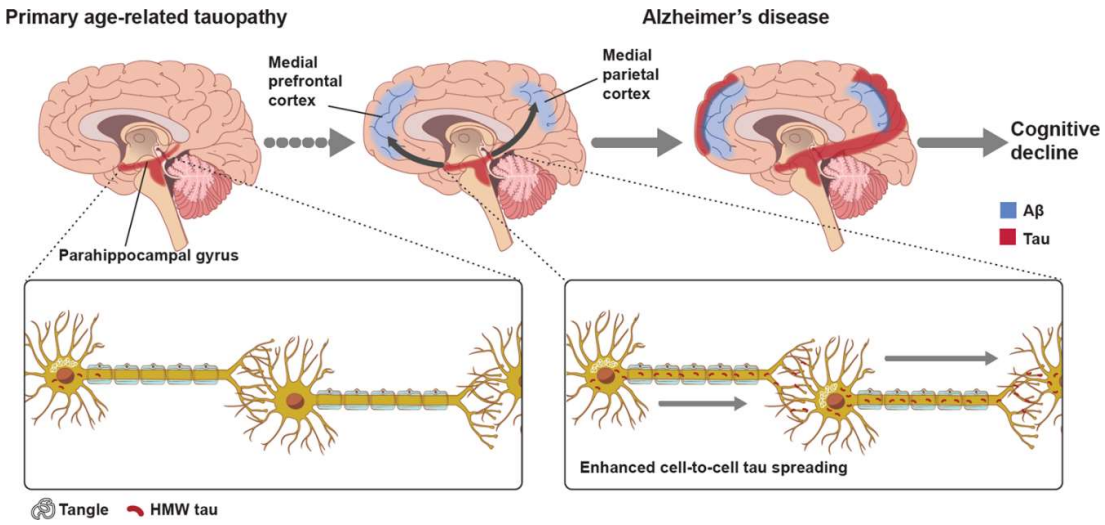

Figure 20: Synergy between Aβ and Tau pathology

NFTs (red) and Aβ deposits (blue) coincide in the neocortical areas in the brain of AD subjects (top), supporting amyloid-β dependent Tau propagation across neocortical regions. Inter-neuronal spreading of Tau (bottom) is favored by Aβ in AD brains. From (Hampel et al., 2021).

Initially, senile plaques containing Aβ were considered to initiate deleterious events and cause AD. However, although fibrillary Aβ has been demonstrated to produce deleterious changes in neuronal culture and following inoculation in mouse models, growing evidence encourages redefining the nature of pathogenic Aβ forms. Amyloid plaques might not be the most relevant pathological Aβ species. Recently, the amyloid cascade hypothesis has been upgraded as Aβ deposition and cognitive alterations are not linear neither in AD patient nor mouse model of AD (**Figure 21**) (Karran and De Strooper, 2022). Additionally, whether the presence of Aβ plaques in the brain is deleterious or protective remains controversial. While severely impaired AD patients did not always present with brain amyloid deposition, the presence of amyloid plaques has been found in cognitively normal individuals (Nordberg, 2008; Terry et al., 1991; Villemagne et al., 2008). Altogether, these findings support the idea that insoluble plaques may not trigger the pathological events. Instead, it appears that soluble forms of multimeric Aβ species are more toxic than amyloid plaques. This gave rise to the "Oligomer hypothesis" claiming that these neurotoxic oligomers of Aβ are mainly responsible for activation of neuroinflammation and synaptotoxicity, which would be causative of memory deficits.

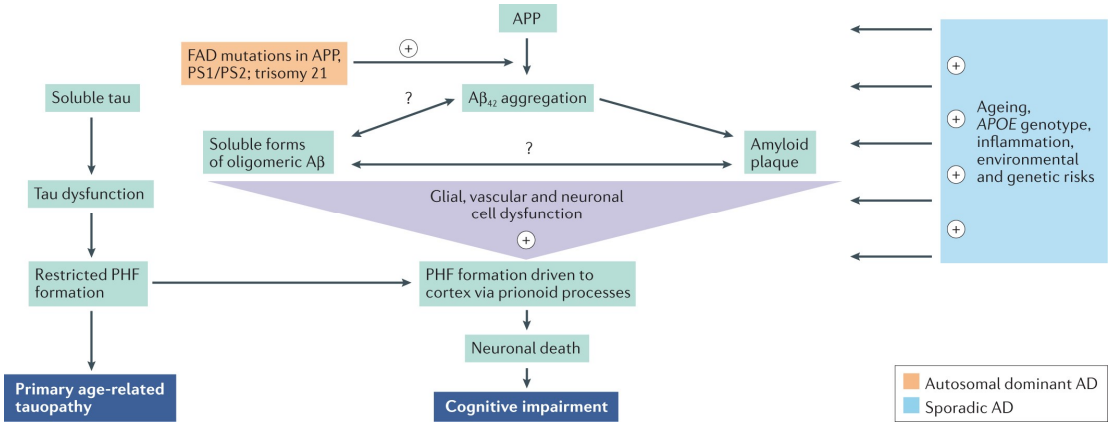

Figure 21: Upgraded amyloid cascade hypothesis (Karran and De Strooper, 2022)

There is also an emerging interest in the observations that Aβ accumulates intracellularly in mouse models of AD, as well as in human AD brains, and could contribute to disease progression (Bayer and Wirths, 2010; Gouras et al., 2000; LaFerla et al., 2007; Tomiyama et al., 2008). This extends the amyloid hypothesis. Many functional studies supported the central role of cellular aspects in the disease process. This "cellular phase" of AD incriminated dysfunctions of neuronal network, alteration of neurovascular units and impaired astrocyte and microglia physiological functions. The "cellular phase" of AD is preceded by a "biochemical phase" characterized by abnormal accumulation of aggregated Aβ and hyperphosphorylated Tau intracellularly and/or extracellularly. This process is described as slow and progressive, initially tolerated by the brain and ultimately responsible for alteration in aggregated protein clearance resulting in complex cellular damages evolving over decades. Brain could not compensate anymore the failure of physiological cellular functions and cellular homeostatic breakdown, leading to neurodegeneration (De Strooper and Karran, 2016).

Taken together, the available data strongly support the central role of aberrant Aβ accumulation in AD pathogenesis. Ongoing studies aimed to clarify the underlying mechanism by which Aβ drives the pathological cascades and to propose therapeutics strategies to anticipate/counteract the development of the disease.

2.1.2 Aβ-directed therapeutic strategies

Despite the announcement of the amyloid cascade hypothesis, several clinical trials using amyloid-lowering agents have been conducted to resolve AD pathogenic primacy and slow down disease progression. The three main approaches were: active or passive **Aβ immunization**, **γ-secretase inhibitors** and **BACE1 inhibitors**. The goals of these Aβ-directed therapies were to reduce amyloid-β production, facilitate amyloid-β clearance and prevent amyloid-β aggregation.

2.1.2.1 Increased Aβ clearance: passive and active Aβ immunization

Disease-modifying therapies that can change the underlying pathophysiology of AD with Aβ vaccines or anti-Aβ antibodies have been developed successively and assessed in clinical trials. Active and passive Aβ immunotherapies aimed to mediate clearance of existing Aβ either by targeting Aβ plaque or soluble Aβ. The goal of active immunization is to inoculate Aβ fragments into patients in order to stimulate the immune system so as to produce antibodies against Aβ, allowing massive Aβ clearance from the brain. The first successful active vaccine against Aβ (AN-1792) was developed in 1999 and was composed of synthetic full-length human $Aβ_{42}$. Significant decrease in amyloid deposition was observed in vaccinated mice at older age and the development of amyloid pathology was prevented in young mice (Schenk et al., 1999). This immunotherapy aborted in phase II because of the development of unexpected inflammatory reactions in patients. Indeed, one drawback of active immunization is a large variability in efficacy, which is due to the inability to control the immune system response, as the level of produced antibody is variable from patient to patient. Additionally, post-mortem studies revealed the presence of severe Tau pathology in vaccinated patients even despite amyloid plaque clearance.

Passive immunotherapy consists in the infusion of monoclonal antibodies against a specific epitope of Aβ. Several monoclonal antibodies have been designed successively to target soluble or insoluble Aβ via binding to various Aβ epitopes (**Figure 22**). Six of them have been advanced to phase III clinical trials and tested in patients with mild to moderate AD. The first one is **Bapineuzumab**, which targets the N-terminal region of Aβ peptide and is able to bind fibrillar, oligomeric and monomeric forms of Aβ triggering microglial phagocytosis of Aβ (Demattos et al., 2012). Bapineuzumab induced a decrease of amyloid deposits to baseline but without improving cognition. It was also associated with amyloid-related imaging abnormalities (ARIA) edema and microhemorrhages (Salloway et al., 2014). Another antibody, **Gantenerumab**, has been tested in a cohort of asymptomatic and symptomatic patients. Gantenerumab is a fully human IgG1 antibody, binding a conformational epitope, that targets N-terminal and mid-domain Aβ epitopes on amyloid plaques (Bohrmann et al., 2012). It does not bind to soluble Aβ (**Figure 23**). Amyloid deposition was removed and low CSF $Aβ_{42}$ levels were observed in patients. Even if asymptomatic patients did not develop cognitive alterations following Gantenerumab treatment, symptomatic patients have not shown signs of clinical improvement, hence, the drugs was not considered as efficient. Two anti-Aβ antibody approaches have directly targeted soluble Aβ instead of amyloid plaques and have been tested in phase III clinical trials (Karran and De Strooper, 2022). **Solanezumab** targets the mid-domain of Aβ peptide and binds predominantly to Aβ monomers. Although Solanezumab was able to lower CSF levels of $Aβ_{40}$ significantly, there was no significant effect on $Aβ_{42}$, on brain amyloid PET signal or on cognitive decline. **Crenezumab** binds to oligomers, fibrillar

and other forms of Aβ resulting in a rapid increase of Aβ in periphery which was not efficacious enough to remove amyloid plaques and lacked clinical efficacy too.

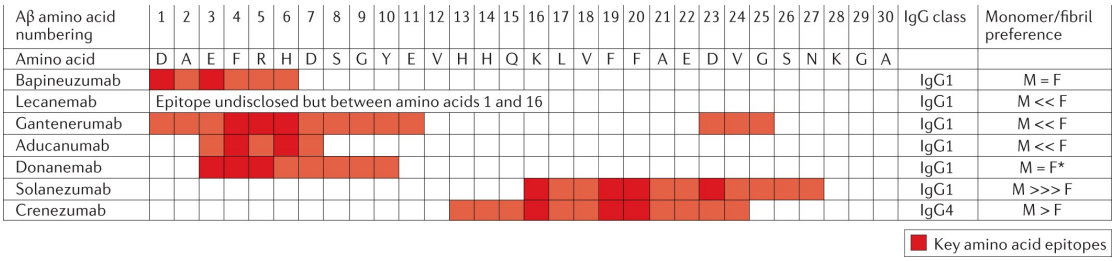

Figure 22: Aβ epitopes of monoclonal antibodies tested in clinical trials against AD

The epitope recognized by the antibodies are stained in red (key amino acid) or orange. The efficiency on Aβ monomer (M) or fibril (F) removal is indicated in the last column. From (Karran and De Strooper, 2022).

Recently, **Aducanumab** developed by Biogen and Eisai, provided therapeutic benefits to patients. Aducanumab targets N-terminus amino acids 3–7 of the Aβ peptide and is specific for soluble oligomers and insoluble fibrils (**Figure 23**). Although it has shown a dose-dependent reduction of Aβ plaques, the study was not sufficiently powered to detect clinical changes and the FDA concluded to end the studies. Further investigations will be done to elucidate whether this therapy has actual clinical benefits or not and will be resume in a final report by 2030 (Karran and De Strooper, 2022). Importantly, following the discovery of Aducanumab, other monoclonal antibodies targeting the different forms of Aβ have been developed such as **Lecanemab** (Leqembi | ALZFORUM, n.d.). Lecanemab showed encouraging results in patients with early AD in clinical trials called 'the Clarity AD" which is a double-blind, parallel-group, randomized study. Lecanemab is a humanized IgG1 monoclonal antibody that binds with high affinity to Aβ soluble protofibrils rather than amyloid plaques (**Figure 23**). This antibody has successfully passed the phase III of clinical trials, which should reinforce the importance of targeting Aβ in disease-modifying therapies. Lecanemab showed a decrease in brain amyloid burden and, importantly, reduced clinical decline by 27% on the global cognitive and functional scale compared with placebo at 18 months. Unfortunately, side effects as ARIA edema and microhemorrhages were observed in few treated patients and need to be further investigated and controlled. The Eisai laboratory, that developed this drug, plans to submit a marketing authorization application to the European Medicines Agency by the end of March 2023.

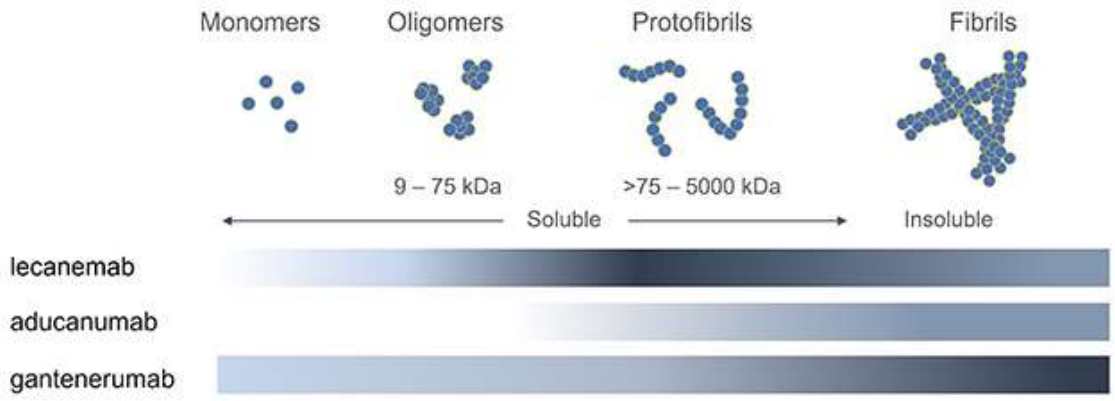

Figure 23: Monoclonal therapeutic antibodies exhibit distinct binding selectivity toward Aβ species

Lecanemab binds most strongly (dark gray) to protofibrils, while aducanumab and gantenerumab favor fibrils.

2.1.2.2 Decreasing Aβ production: secretase inhibitors

Several clinical trials with drugs aimed at preventing Aβ formation by inhibiting β- or γ- secretases, the enzyme ensuring the proteolytic cleavage of APP. In mouse models of AD, BACE1 inhibition limits the formation of new plaques but does not prevent the growth of established plaques (Ridler, 2018). Thus, one of the therapeutic strategies was to use BACE1 inhibitors in a primary preventive treatment in order to reduce the production of Aβ at early stage of AD and, afterwards, ensure clearance of established Aβ with monoclonal anti-Aβ antibodies. A clinical trial called "TRAILBLAZER-ALZ" tested this hypothesis by combining the Lilly BACE1 inhibitor LY3202626 with Donanemab, a monoclonal antibody that targets a pyroglutamate form of Aβ aggregated in plaque. Despite a significant reduction of amyloid burden, this combination therapy failed to improve cognitive impairments. A number of drugs has been developed to test the efficiency of BACE1 inhibitors in AD patients. Among them, **Verubecestat**, was tested in phase III clinical trials in patients with prodromal and mild to moderate AD. It significantly reduced the cerebral Aβ production by up to 75%. However, Verubecestat significantly worsen cognitive decline and the administration of this drug has been associated with severe side effects such as suicidal ideation, weight loss and sleep disturbance. Subsequently, other BACE inhibitors in clinical development have also failed or were interrupted because of these side effects. Indeed, these drugs inhibited both BACE1 and its homologue BACE2 that targets substrates other than APP, mostly important for physiological functions. The deletion of BACE1 in mice led to myelination deficits, seizures and cognitive impairments. Thus, it may be difficult to block BACE1 activity without creating unwanted off-target effects.

Several γ-secretase inhibitors have also been tested clinically as disease-modifying therapies for AD. Among them, **Semagacestat** was tested in phase III clinical trials in patients with mild to moderate AD. It led to a modest reduction in Aβ production, increased incidence of skin cancer and worsened cognition compared to placebo. These side-effects were due to the inhibition of other substrates belonging to Notch signaling pathways mainly involved in developmental and homeostatic processes. **Avagacestat** did not alter Notch's signaling pathway but was aborted in phase II as it failed to demonstrate therapeutic benefit and caused adverse effects too. Modulators of γ-secretase that alter APP processing without affecting other substrates, as **Tarenflurbil**, have also been developed but did not exhibit any benefits on cognition.

Nowadays, strong suppression of Aβ production via secretase inhibitors or modulators without engendering severe side effects remains a huge challenge in clinical trials.

2.1.2.3 Aβ neurotoxicity shielding

The primary focus of efforts was to develop drugs that mediate a therapeutic disease-modifying effect by targeting Aβ itself or its production. However, it seems that Aβ-targeting is not effective if it is not coupled with efficient inhibitors of Aβ neurotoxic properties. In the last decade, others therapeutic strategies that counteract the toxic effects of Aβ have been proven more promising in slowing or delaying the progression of AD than Aβ-directed therapies.

Mounting evidence has demonstrated that Aβ exerts negative impacts on local synapse density, morphology and functioning, resulting in the decrease of synaptic plasticity and the loss of synapses strongly correlated with cognitive impairments. Thus, factors that hinder the synaptotoxicity of Aβ were investigated in several studies. Among them, the **Vascular Endothelial cell Growth Factor** (VEGF) appears to be a promising candidate as it has been shown to play a potential neuroprotective role in AD. Evidences show that VEGF and its receptor VEGFR 2 increase the postsynaptic responses mediated by NMDA in hippocampal neurons, which allows the formation of new synaptic sites and improves synaptic plasticity (De Rossi et al., 2016). In contrast, silencing of VEGFR2 in neurons abolished hippocampal LTP, impaired synaptic transmission and memory consolidation (De Rossi et al., 2016). VEGF levels, normally found in higher amounts in the brain, decreased in the CSF of AD patients meaning that some factors impede its eliminations through CSF. Intriguingly, early accumulation of Aβ biomarkers has been associated with increased VEGF brain level, resulting in reduction of hippocampal atrophy and cognitive decline (Hohman et al., 2015). However, this neuroprotective effect seems to disappear during AD progression. A potential explanation is that VEGF is located in the close vicinity of amyloid plaques during AD progression. Sequestration of VEGF into amyloid plaques may interfere with its protective role. Recently, VEGF treatment has been demonstrated to increase synaptic

transmission on hippocampal slices from APP/PS1 transgenic mice after exogenous application of Aβ oligomers (Martin et al., 2021). This finding suggests that VEGF is able to reverse the synaptic damage initiated by toxic Aβ oligomers. Indeed, VEGF has been shown to selectively bind to Aβ oligomers and counteract their neurotoxic effects. Thus, synthetize Aβ-binding domain of VEGF seems to be an encouraging therapeutic tool for AD.

The discovery of a naturally-occurring variant of Aβ carrying the **A2V substitution** ($Aβ_{A2V}$), which protects heterozygous carriers from AD, allowed to design a novel therapeutic strategy for AD based on the ability of $Aβ_{A2V}$ to interact with wild-type Aβ, interfering with its nucleation or nucleation-dependent polymerization, through conformational changes and assembly (Di Fede et al., 2012, 2009). Di Fede and colleagues have designed a synthetic peptide derived from $Aβ_{A2V}$ sequence, retaining only the protective properties of the peptide residing in 6 N-terminal amino acids of the Aβ mutated sequence, and entirely composed of D-amino acids to increase its stability *in vivo* (Di Fede et al., 2012). *In vitro* studies have shown strong anti-amyloidogenenic properties of the synthetic peptide by hindering oligomer production and preventing amyloid fibril formation. In a first *in vivo* study, the six-mer mutated D-isomer peptide [Aβ1-6_{A2V}(D)] was linked to the HIV TAT peptide, widely used for brain delivery, which enables the peptide to cross the BBB. The constructions were then infused via intraperitoneal administration in Aβ plaque-bearing mice (APP_{swe}/$PS1_{δE9}$) to prevent *in vivo* amyloidogenesis, Aβ-dependent neurotoxicity and synaptic dysfunctions. Short-term treatment with this synthetic peptide showed encouraging results by presenting successful outcome. Unfortunately, after 5 months, reverse effects on cognition and Aβ production were obtained in mice, mostly due to side effects of the TAT carrier which promoted amyloidogenesis and hindered the anti-amyloidogenic properties of Aβ1-6_{A2V}(D) (Di Fede et al., 2016). Recently, intranasal brain delivery of Aβ1-6_{A2V}(D) peptide alone in a double transgenic mouse model of AD revealed an effective outcome as it prevented the oligomerization of wild type Aβ and counteracted the synaptic damages associated with amyloidogenesis (Catania et al., 2022).

Interestingly, in 2012, *Jonsson et al.* identified a natural protection against sporadic late-onset AD in human carriers, the **A2T mutation** in Aβ sequence (Jonsson et al., 2012; Kero et al., 2013). This missense mutation, mostly found in Icelandic population, confers protection against neurotoxicity, avoiding cognitive decline and also presenting with anti-amyloidogenic effects (Benilova et al., 2014). By changing the Aβ structure, $Aβ_{A2T}$ can bind to wild-type Aβ to hinder its toxicity. Recently, the CRISPR prime editing approach was used to introduce the A2T mutation in human cell genome (Tremblay et al., 2021). The effect of A2T editing still needs to be assessed in biological organism. This approach raises the question whether the protective properties is exhibited by the DNA mutation or by the

peptide it-self. These protective genetic variant of Aβ could be used to develop new therapeutic strategies that take advantage of its biological mechanism of action against Aβ neurotoxicity.

2.1.3 Why did Aβ-directed therapies failed?

The amyloid cascade hypothesis has dominated the AD field during the last 25 years. However, therapeutic approaches aiming at decreasing Aβ levels have failed to demonstrate clinical efficacy. Most of them failed at phase 3 of clinical trials in patients with mild-to-moderate symptomatic AD (Long and Holtzman, 2019). Several clinical trials have been stopped because of the detection of severe side effects and anti-Aβ therapy responders were not different from placebo-treated controls (Ricciarelli and Fedele, 2017a). These failures deeply question the reliability of the amyloid cascade hypothesis. A number of reasons can explain the failure of anti-Aβ therapies and can answer to the following questions: when, what and how?

First, **when** therapies must be applied? Several comments suggested that the treatment has been administered too late in the disease course. Aβ pathology is reaching a plateau in the brain prior the onset of clinical symptoms meaning that the onset of amyloid deposition may occur 15-20 years before cognitive alterations are diagnosed. At late stage of AD, irreversible synaptic and neuronal loss have occurred yet and the pathological events become difficult, if not impossible, to reverse. Indeed, most of anti-Aβ therapies were effective in removing senile plaques from the brain of mild-to-moderate symptomatic AD but failed to abolish cognitive alterations. At this stage, the biological phases of the disease including amyloid and Tau accumulation were already too advanced. Thus, the early toxic effects of Aβ on downstream events were not targeted. Disease-modifying treatments might be at their most effective level when initiated very early in the course of AD, before amyloid plaques and neurodegeneration become too widespread, which requires an accurate diagnosis of AD. So far, any current diagnosis tool enabled highly sensitive and massive screening of potentially AD patients among a wide population. Accurately identifying toxic Aβ species in AD prevention drug trials will help to recruit cognitively normal AD-risk participants for clinical trials.

Second, **what** should therapies target? Whether pathological cascade is triggered by amyloid plaques, Aβ monomers or oligomers is not clearly defined. Recently, amyloid plaques have been described as a reservoir for Aβ oligomers that are thought to be the most pathological forms of Aβ (Hong et al., 2018). Thus, disaggregation of amyloid plaques, like in anti-Aβ therapies, might release oligomer species that would be more damaging for synaptic environment. Researchers need to keep in mind that not all Aβ species are toxic and some of them can even be protective at low concentration, and thus they should not be targeted by the therapy. Another controversial effect of therapeutic approaches has been shown. Therapies targeting the α- or γ-secretases reduce Aβ accumulation but fail at reducing cognitive

decline and, more importantly, induce side effects by removing indispensable enzymatic functions. Thus, it appears crucial to deeply assess potential targets in order to find the “good” one.

Finally, **how** would therapies mediate benefit? The mechanism by which Aβ affects cognitions is still unclear. Whether it is direct or through sequential events is poorly understood. Different pathways have been submitted: induction of Tau pathology, activation of neuroinflammation or direct alteration of synapses. A combination of all pathways is also possible. Recently, Karran and De Strooper proposed an Aβ threshold hypothesis to explain how the pattern of Tau pathology can be heterogeneous from an individual to another and why it is highly dependent on amyloid response (Karran et al., 2011; Karran and De Strooper, 2022; Pontecorvo, et al., 2019). According to this hypothesis, it exists an **amyloid threshold** that determines if an individual will or not developed AD. Below the threshold, individuals have a variable response to amyloid leading to poor damage in the brain. In contrast, when Aβ aggregates reach the threshold, they initiate or accelerate the spreading of Tau and AD starts to develop. Thus, therapeutic strategies using soluble and insoluble Aβ aggregate lowering drugs toward non-pathological levels will certainly mediate a clinical benefit.

2.2 Tau hypothesis

The amyloid hypothesis posits a linear cascade initiated by Aβ and leading to dementia but incompatible with clinical observations. Tau pathology itself can cause neuronal loss. Moreover, it has also been reported that reduction in endogenous levels of Tau in APP transgenic mice can reverse Aβ-mediated toxicity. Together, these observations gave Tau pathology a pivotal role in AD and allowed the emergence of Tau hypothesis in AD etiology.

2.2.1 Tau propagation hypothesis

In AD, abnormal phosphorylation of Tau leads to disassembly and destabilization of microtubules. Once released, mislocalized Tau induces impairment of microtubule regulation (Zempel and Mandelkow, 2014). Tau becomes hyperphosphorylated which reinforces its stability *in vivo* and hinders its degradation. Hyperphosphorylation of Tau facilitates its aggregation into filamentous PHFs that form NFTs. Normal Tau can be sequestered into tangles of filaments, which favor the pathology. Aberrant interaction of hyperphosphorylated Tau with filamentous actin induces improper stabilization of actin leading to axon damage (Fulga et al., 2007) and synaptic impairment (Bardai et al., 2018; Cabrales Fontela et al., 2017). Moreover, the presence of NFTs inside neurons is highly toxic for the axons and is responsible for neuronal loss. The amount of PHFs and NFTs has been demonstrated to correlate with the severity of neuronal damage and cognitive impairment in AD patients. Mutation of human Tau in mouse models of Tauopathy induce severe synaptic and memory

impairment as well as tau hyperphosphorylation and pre-tangle formation (Van der Jeugd et al., 2012). Interestingly, when pro-aggregant Tau is switched-off, synapses are recovered and cognition is rescued although insoluble murine Tau is still present. This reversible effect of Tau may reflect the early phase of AD, when the brain can still compensate molecular changes, suggesting an early impact of Tau pathology in the course of the disease.

Despite Aβ has been shown to be a causal factor in FADs, Tau pathology has been proposed to be an initiating factor in SAD. Progression of AD is strongly associated with Tau pathology, rather than Aβ accumulation, which strongly supports the "Tau hypothesis" in the origin of AD. Furthermore, neuropathological evidences demonstrated that Tau lesions arise prior to the appearance of amyloid plaques in the human brain, especially targeting glutamate projection neurons in the association cortex (Braak and Del Tredici, 2014; Johnson et al., 2016). Indeed, post-mortem analysis of AD brains helped to describe Braak stages describing Tau pathology spreads during AD progression while causing cognitive defects (See **Chapter 1**). Tau pathology begins very early in the entorhinal region before arising in the interconnected hippocampal area and association cortices. Within the cerebral cortex, Tau causes rapid neurodegeneration that correlates with the first symptoms of AD. In several studies, aging rhesus macaques have been used to model late-onset of AD as they exhibit both human-like Tau and amyloid pathology (Arnsten et al., 2019; Paspalas et al., 2018). The researchers took advantage of the ability to assess early Tau phosphorylation states by immunoelectron microscopy in this model in order to follow the progression of the disease from the entorhinal cortex to the dorsolateral prefrontal cortex. They showed patterns of Tau pathology progression similar to human's (Paspalas et al., 2018). Interestingly, accumulation of abnormally phosphorylated Tau mostly affected glutamatergic synapses localized in the prefrontal association cortex but not in the sensory cortex. In addition to abnormal Tau accumulation, these synaptic damages were strongly related to calcium dysregulation. These data corroborate human data analysis, indicating the occurrence of Tau pathology within vulnerable neurons belonging to specific brain areas. Interestingly, Tau pathology degree of severity correlates with the number of cortico-cortical glutamatergic connections, expanding over brain evolution and lifespan (Arnsten et al., 2021).

Neuropathological studies from primate brains revealed that the pattern of Tau pathology spreading is consistent with neuronal networks, meaning that phosphorylated Tau may spread from neuron to neuron. In 2009, Clavaguera et al. presented the first evidence of neuron-to-neuron spreading of Tau, in a mouse model of Tauopathy (Clavaguera et al., 2009). In this study, brain extracts containing hyperphosphorylated Tau from Tau transgenic mice were inoculated into the brain of mice expressing the wild type form of human Tau and developing late Tau pathology. They found an acceleration of Tau pathology at the inoculum site but also into interconnected regions. Tau spreading was suggested

to occur through “prion-like” mechanism (**Figure 24**). This mechanism would involve the transfer of abnormal Tau seeds from a “donor cell” to a “recipient cell” and facilitate newly generated Tau seeds by incorporating normal Tau, thus, driving to a vicious circle. This mechanism has been also proposed to explain the spreading of amyloid pathology that will be further discussed in **Chapter 3**.

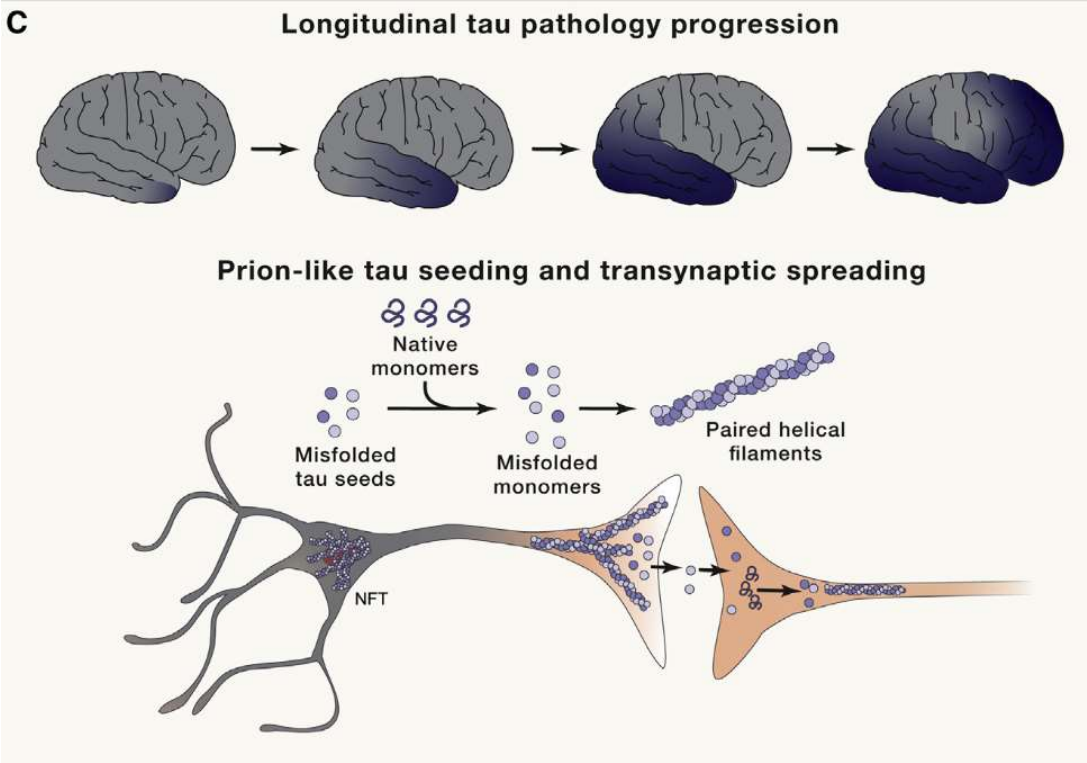

Figure 24: Inter-neuronal spreading of Tau pathology

Misfolded tau seeds transform native monomers into toxic Tau monomers that are prone to aggregate and form PHFs and NFTs. These aggregates can dissociated to form new seeds that are involved in inter-neuronal spreading. From (Long and Holtzman, 2019).

Taken together, analyses of human and non-human primate brains revealed that Tau pathology early affects vulnerable neurons and spreads via seeding using interconnected glutamatergic projection neurons belonging to the same network. Interestingly, cross-talk between amyloid hypothesis and Tau hypothesis has been demonstrated. Phosphorylated Tau can increase the production of Aβ. In addition, the presence of Tau has been shown to be essential for Aβ-induced synaptic toxicity.

2.2.2 Therapeutic strategies

According to the Tau hypothesis, Tau is an essential target for developing disease-modifying therapies. One of the first strategies to reduce Tau pathogenicity was to inhibit kinases that mediate abnormal

Tau hyperphosphorylation. Thus, several Tau kinase inhibitors have been developed. Among them, GSK-3 inhibitors showed reduction of Tau phosphorylation, amyloid deposition and neuronal loss in transgenic mice. However, no beneficial effect on cognition was observed in AD patients (Gong and Iqbal, 2008; Wang et al., 2007). The upregulation of Tau phosphatases is another approach to drive dephosphorylation of Tau (Tian and Wang, 2002). So far, Tau-based clinical trials have not yet produced positive findings. Many adverse side effects were even observed in patients as kinases and phosphatases are involved in many signaling pathways (Goedert et al., 1995; Gong and Iqbal, 2008; Sontag et al., 2014). Immunotherapy to facilitate Tau clearance also failed, however, anti-sense oligonucleotide (ASO)-based treatments reducing Tau expression showed promising results in preclinical studies (Long and Holtzman, 2019).

2.3 Other hypothesis of AD

With the improvement of knowledge about AD pathophysiology, numerous hypotheses have been developed in the last decade to explain the etiology of AD. Four hypotheses that are related to Aβ accumulation are described below. These hypotheses were used to develop drugs, essentially symptomatic therapies, and were tested in clinical trials.

2.3.1 Inflammatory hypothesis

The inflammatory hypothesis of AD postulates that the sustained inflammation in the brain, characterized by activation of astrocytes and microglia, leads to neurodegeneration and ultimately AD. Dual function of brain inflammation has been described in the literature. While acute response of the immune system is neuroprotective at early stages of AD, chronic activation of inflammatory cells, especially microglia, accelerates the development of amyloid and Tau pathology (Kinney et al., 2018). Elevated levels of interleukin-1 (IL-1), a pro-inflammatory cytokine, has been demonstrated to be responsible directly for the increased APP production and Aβ load and indirectly for the activation of the kinase that triggers phosphorylation of Tau (Goldgaber et al., 1989; Quintanilla et al., 2004). Furthermore, long-term anti-inflammatory treatments have been shown to provide protective benefits against AD by reducing by 50% the risk for developing AD (Kinney et al., 2018).

Numerous investigations report that immune-related proteins and cells were located in the vicinity of amyloid plaques. In particular, microglia has been suspected to drive the initiation of AD, as most of genetic risk factors of AD were found involved in microglial functions. Activated microglia proliferates more around senile plaques and neurons with NFTs in AD than in normal individuals. Fibrillary Aβ can bind to microglial receptors, which activates the release of inflammatory factors and, in turn, can either favor Aβ production or enhance Aβ clearance depending on the stage of disease (Liu et al., 2019). A

number of investigations showing controversial role of microglia during AD, from neuroprotective to detrimental role, have supported the microglia hypothesis of AD. Microglia is thought to mediate phagocytosis of Aβ and to form a barrier around amyloid plaques in order to protect the brain against plaque-associated neurotoxicity (Condello et al., 2015). However, prolonged activation of microglia exacerbates the neuroinflammation, contributing to neuronal loss and leading to the activation of more microglia. Additionally, several studies have reported that microglia is involved in both phagocytosis and release of Tau aggregates (Asai et al., 2015; Clayton et al., 2021; Dejanovic et al., 2018; Hopp et al., 2018; Perea et al., 2020; Zhu et al., 2022). This mechanism was suggested to be mediated by the accumulation of amyloid plaques that transform microglia into neurodegenerative microglia which exhibits enhanced phagocytosis of plaques, apoptotic neurons and dystrophic neurites containing aggregated and phosphorylated Tau. Recently, Clayton et al. established the relationship between phagocytic microglia, amyloid plaques and Tau propagation in promoting disease progression (Clayton et al., 2021). They showed that the depletion of plaque-associated microglia in transgenic APP mouse model reduces the amount of extracellular vesicles containing Tau aggregates while increasing amyloid plaques and neuritic plaques (**Figure 25**). Thus, for the first time, plaque-associated microglia was shown to enhance Tau spreading, resulting in progression of AD (Clayton et al., 2021; Gratuze et al., 2021; Pascoal et al., 2017). Importantly, some research groups suggested that AD heterogeneity is strongly related to phagocytose state of microglia, which varies from an individual to another. In an individual, the more microglia is defective, the more pathological events are getting worse, meaning that microglia may be the origin of pivotal point from reversible physiological state to irreversible pathological state leading to AD (Edwards, 2019).

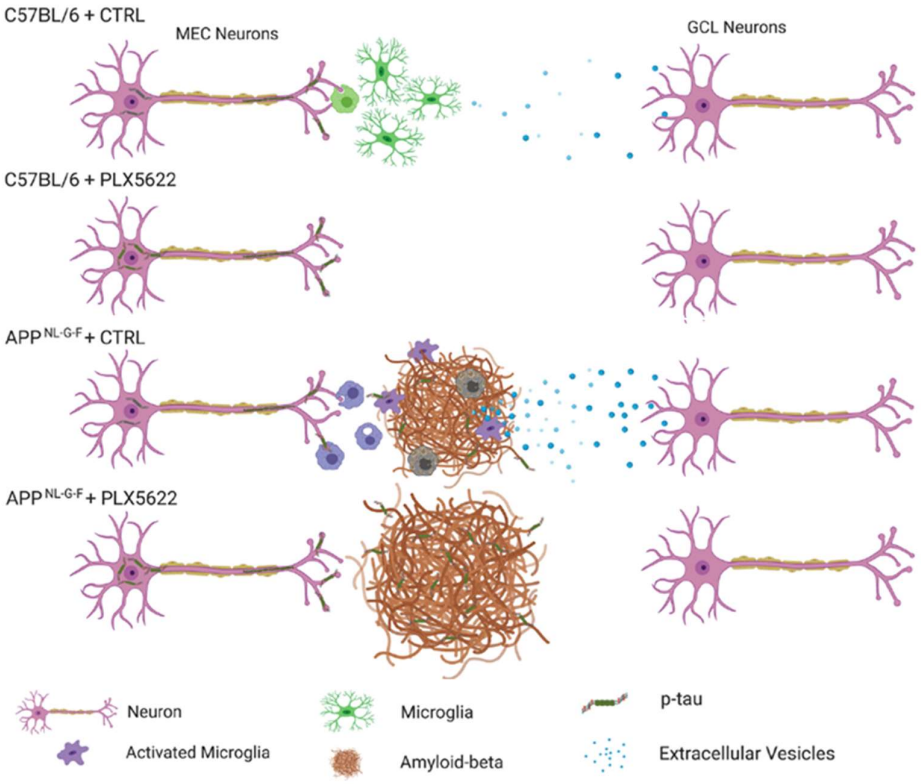

Figure 25: Aβ plaque-associated microglia accelerates Tau spreading in a mouse model of AD.

In the WT mouse brain, Tau propagation is sensitive to microglia. In APP^{NL-G-F} mouse brains, Aβ plaque-associated microglia are highly phagocytic and hyper-secrete Tau-seeding extracellular vesicles, resulting in enhanced Tau propagation. Both Aβ plaques and Tau-associated neuritic plaques are increased following microglia depletion while Tau propagation is inhibited. This suggests an active role of microglia on compaction and clearance of protein aggregates and Tau propagation. From (Clayton et al., 2021).

2.3.2 Infectious hypothesis

The infectious hypothesis proposes that stimulation of innate immune response by various bacterial and viral pathogens may precipitate AD (Sjogren et al., 1952). Intracerebral infection by microbes has been shown to induce Aβ aggregation and deposition, as an antimicrobial defense mechanism where Aβ coats microbial particles to fight the infection. The enrollment of amyloid seeding in the antimicrobial protection initiates the amyloid cascade (Moir et al., 2018). Recently, one type of the herpes simplex virus, HSV-1, has been shown to trigger $Aβ_{42}$ fibrillization *in vitro* by nucleating aggregation via contact with the viral surface (Ezzat et al., 2019). Moreover, HSV infections have been associated with an increase of dementia risk. These findings and several studies strongly support the hypothesis that infectious exposition to HSV can caused AD (Carbone et al., 2014; Itzhaki, 2014;

McNamara and Murray, 2016). Thus, anti-HSV therapies, as **Valaciclovir,** have been developed to counteract the effect of the virus. These drugs have been demonstrated to reduce Aβ and phosphorylated Tau accumulation, which may change the course of the disease. Valaciclovir was tested in positive HSV patients with mild cognitive impairment and completed phase II trial for AD treatment (Valacyclovir | ALZFORUM, n.d.).

2.3.3 The vascular hypothesis of AD

Investigators have suspected that initial vascular damage may be involved in the onset and progression of AD. Many functional studies in humans and mouse models of AD support the vascular hypothesis. Neuroimaging studies in AD patients have demonstrated the presence of vascular lesions in their brain preceding the onset of neurodegeneration. Multiple genetic investigations have shown that neurovascular pathology increased the risk for developing AD (Attems and Jellinger, 2014). Indeed, deletion of APOE in mice, a major genetic risk factor for AD, has been demonstrated to mediate detrimental effects on endothelial cells and pericytes localized around capillaries, resulting in failure of the BBB (Bell et al., 2012) also seen in human APOE4 carriers. In mouse models of AD, microvasculature dysfunction was found in the neocortex prior to Aβ accumulation. Hypoperfusion and hypoxia are observed in AD patients and are associated with alteration of the BBB, which has been proposed to play a pivotal role in the initiation of AD. Hypoxia is a common feature of vascular diseases which leads to degeneration of pericytes. Hypoxia has been shown to trigger Aβ accumulation by increasing BACE1 expression levels (Zhang et al., 2018) and by affecting Aβ clearance (Winkler et al., 2014). In addition to aberrant angiogenesis, impairments of BBB compromise the elimination of Aβ and Tau from the brain resulting in their accumulation and sometimes cause vascular damage as CAA (Zlokovic, 2011). Traumatic brain injury models display a decreased cerebral blood flow also called hypoperfusion that contributes to accumulation of secreted Tau (Iliff et al., 2014).

While vascular damages participate to Aβ accumulation, mounting evidence suggests that Aβ accumulation leads to severe vascular damages manifesting as CAA. Additionally, Aβ can induce the constriction of the cerebral arteries, a major cause of hypoperfusion. This vicious circle may accelerate the occurrence and course of AD.

2.3.4 Cholinergic hypothesis

The cholinergic hypothesis was suggested over 20 years ago and proposes that dysfunction of acetylcholine containing neurons play a major role in cognitive impairments in AD (Davies and Maloney, 1976). The concentration of acetylcholine and the activity of choline acetyltransferases, the enzymes involved in acetylcholine synthesis, have been found reduced in the amygdala, hippocampus

and cortex in AD patients. Furthermore, degeneration of cholinergic neurons in the nucleus basalis of Meynert, and other septal nuclei projecting to the cortex, was observed during AD progression (Bartus et al., 1982). The cholinergic deficit was associated with early attention and memory dysfunction in AD. Thus, three cholinesterase inhibitors (Donepezil, Rivastigmine and Galantamine) were approved by FDA to increase synaptic levels of acetylcholine and reverse memory defects. Although they improve cognitive status of patients, they essentially treat symptoms without changing the occurrence or progression of AD. Recently, the long-term use of these inhibitors was associated with disease-modifying benefits which encourages further studies of the role of the cholinergic pathways in the course of the disease (Hampel et al., 2019).

2.4 A unifying hypothesis of AD

Despite amyloid cascade hypothesis has been proposed, several questions have emerged about the sequence of pathological events following Aβ accumulation that lead to AD. It is misunderstood whether the delay between the onset of amyloid plaque build-up and disease diagnosis is due to a complete dissociation of the two events or to a cascade of events governed by the degree of Aβ accumulation. Furthermore, although Aβ-mediated synaptoxicity has been proven, the direct impact of Aβ on neuronal network is unclear. Another important question is why neurodegeneration and cognitive impairment do not occur in absence of Tau pathology. Frances A. Edwards proposed a "unifying hypothesis" of AD where the initial rising of Aβ concentration triggers Tau tangles and neurodegeneration in a microglia-dependent manner (Edwards, 2019). The author described a progressive pathological mechanism in which brain tries initially to contain molecular disturbances in restricted areas but, the increased amount of pathological proteins and their spreading make these disturbances irreversible and lead to the pathological state. Four actors play a crucial role in this mechanism: soluble Aβ, synaptic impairments, Tau tangles and microglia dysfunctions. It has been suggested that AD occurs in the following stages:

1) Initial increase in Aβ concentration depends on elevated glutamatergic synaptic activity and leads to plaque seeding. Toxic soluble Aβ is found inside and around senile plaques;

2) Synaptic loss is localized in the immediate vicinity of amyloid plaques;

3) Microglia is attracted to plaques by activation of TREM2. Effective response of microglia removes damaged synapses by phagocytosis;

4) As amyloid load increases, axons close to plaques are vulnerable to Aβ-mediated synaptic toxicity which causes phosphorylation of Tau at multiple points along the axon. Modification of Tau leads to its dissociation from microtubules and formation of NFTs;

5) The loss of normal Tau functions induces the dysfunction of the whole axon and, thus, contributes to the loss of synapses and to neurodegeneration;

6) The loss of axons and the spreading of the pathology cause network impairments.

First, the initial rising of Aβ concentration appears as a reversible early brain change and is not necessarily deleterious (**stage 1**). Several studies have reported physiological role of $A\beta_{40}$ and $A\beta_{42}$ at low concentration in hippocampal synaptic transmission and neuronal activity (Wu et al., 1995; Yuede et al., 2016) which, in turn, favor synaptic release of Aβ. Despite its physiological role, high concentration of Aβ was reported to strongly precipitate synaptic alteration. In the unifying hypothesis, the synaptic loss is suspected to exacerbate Aβ release, which could cause spreading of damages (**stage 2**). Fortunately, plaque-associated microglia has been reported to exert a protective role at early stages of the disease (Condello et al., 2015). Microglia limits synaptic damages to the immediate vicinity of the plaques in order to protect the axons, which could slow network disruption (**stage 3**) (**Figure 26**). Microglia-mediated synaptic pruning has been largely demonstrated to enhance neuron connectivity during neurodevelopment (Paolicelli et al., 2011). However, the microglia-mediated synaptic phagocytose during AD has often been considered as detrimental and responsible for neurodegeneration (Spangenberg and Green, 2017). Interestingly, according to Edwards point of view, it is preferable to lose synapses than the entire axon and, thus, all mechanisms that save the axons will slow the disease. Consequently, the apparition of symptoms is highly dependent on stage 3. It was suggested that there is a tolerance of individual for amyloid load, which is highly related to genetic-mediated microglia efficiency. This hypothesis is strongly supported by genome-wide association studies identifying several microglial genes as risk factors of AD (Scheltens et al., 2016). Indeed, without efficient phagocytic microglia, damages spread more quickly and symptoms appear (**Figure 26**).

The pathological mechanisms could be stopped at stage 3, however, it is likely that gradual increase of Aβ plaques together with cross-talk between Aβ-mediated synaptoxicity and Tau contribute to exacerbate the pathology (**stage 4**).

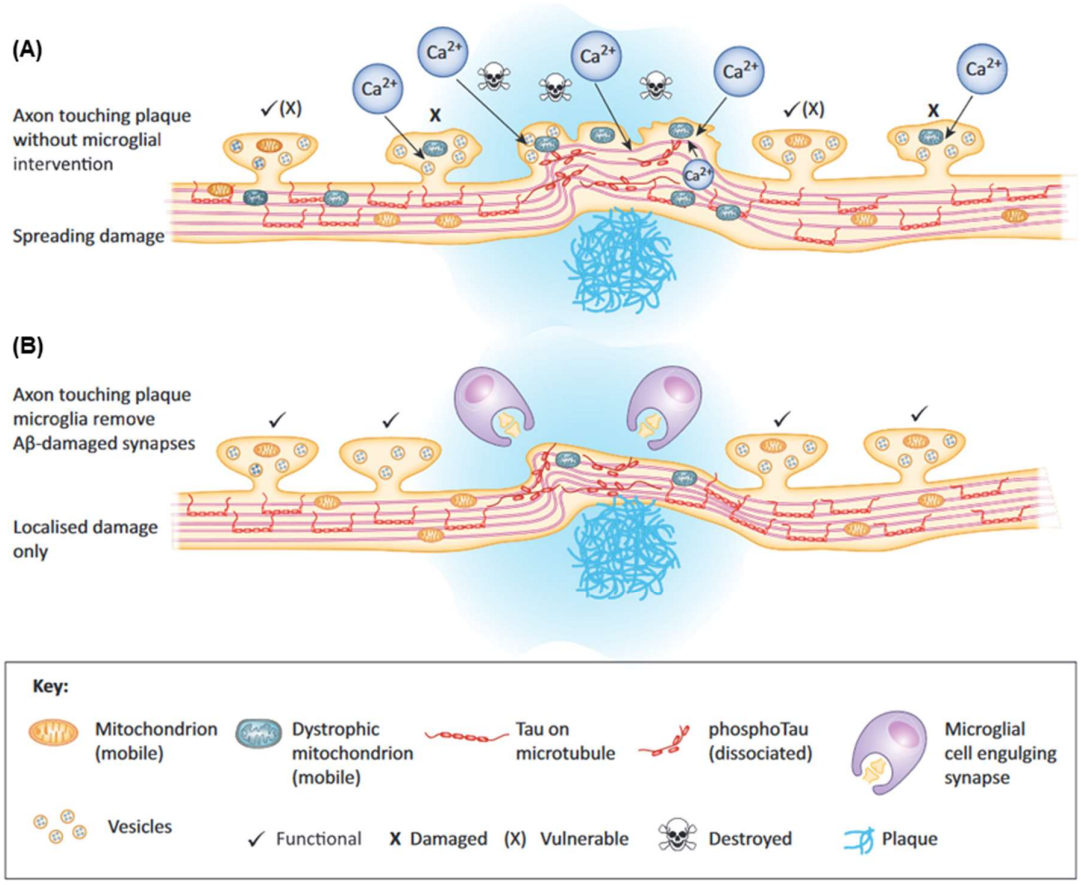

Figure 26: Efficient microglial response slows the progression of AD by limiting the spreading of synaptic damage.

A. Synapses on axons in the immediate vicinity of plaques are damaged by a high concentration of soluble Aβ. This damage is mediated by dissociation of phosphorylated Tau from microtubule and Ca^{2+} influx which causes mitochondrial damage. Spreading of damaged mitochondria causes ongoing synaptic damage up- and downstream the axon at a distance away from the plaque. **B.** If microglia removes damaged synapses promptly, damage may be restricted to the immediate vicinity of the plaques.

The unifying hypothesis of AD argues that the different hallmarks of AD (Aβ, Tau, synapse, microglia, neuronal network) should further be studied as a whole since each of them constitutes a small part of the pathological puzzle. The global view of the disease progression is consistent with many findings in AD patients and may help to design new therapies. Indeed, this hypothesis highlights two main targets that should be considered in future studies: early Aβ accumulation and microglia genome, this latter supposing to enlarge diagnosis of AD through personalized medicine.

Chapter 3 – AD heterogeneity: Insight from the proteinopathy concept

3.1 Sporadic AD heterogeneity

Although AD patients converge to a final common clinico-pathological endpoint, AD is heterogeneous as regard to its origins, lesions and clinical course. Age variability at onset marks differences between early-onset (FADs) and late-onset (SAD) AD. As described in **Section 1.3**, early-onset AD due to familial mutations in key genes shows more pronounced pathologic compounds that arrive earlier in patient life, while multiple sporadic events acquiring during lifespan are responsible for late-onset AD. Intra-subtype heterogeneity has been found across FAD and SAD patients. Variability between FAD patients is mostly due to the localization of the genetic mutations and their study can help understanding the pathogenicity of SAD heterogeneity, which will be further discussed in **Section 3.3**. Instead, we will focus on sporadic subtypes that represent the most complex and abundant cases of AD heterogeneity. First, inter-individuals variability affect cognitive profiles. Indeed, clinical subtypes of AD were classified into amnestic and non-amnestic variants. An association between age at onset and clinical presentation exists since non-amnestic subtypes can have earlier onset of AD. Variability in the rate of disease progression has also been observed among AD patients defining the classical forms of AD evolving in approximately 10 years and the rapidly progressive forms of AD evolving in 2 to 5 years following the diagnosis. AD heterogeneity impedes the development of effective drugs as it may arise from different triggering targets that may require different therapies. This variability also reduces the power of statistical analysis in clinical trials. Further understanding of SAD syndrome is needed to facilitate personalized AD medicine, which could greatly enable clinical trials targeting specific AD subtypes.

3.1.1 Clinical heterogeneity

In 1969, Mc Donald made the first observation of clinical variability among patients suffering from senile dementia (McDonald, 1969). He distinguished patients who showed predominant memory dysfunction, late age of onset and slow disease progression from non-amnestic patients having predominant difficulties with language, visuospatial construction and cortical sensation and showing severe progression of the disease. These two distinct atypical subtypes were respectively termed 'benign memory dysfunction of aging group' and 'parietal group'. Later on, longitudinal follow-up of larger AD patient cohorts demonstrated that atypical subtype syndromes remained distinct over time supporting the existence of distinct AD variants. Additional support for AD heterogeneity was provided

by PET studies that showed variable topographic distributions of Aβ and Tau deposition as well as specific brain atrophy and hypometabolism/hypoperfusion patterns for each clinical variant.

Numerous atypical subtypes were then identified, including both **amnestic presentations** such as pure amnestic temporal of AD and **non-amnestic presentations** such as logopenic primary progressive aphasia (LPPA), posterior cortical atrophy (PCA), and the frontal variant of AD (Lam et al., 2013). These atypical subtypes of AD differed from typical AD in the age of onset, cognitive profile and rate of disease progression. **Pure amnestic temporal AD variant** is a late-onset AD syndrome with slower rates of cognitive decline than in typical AD (Butters et al., 1996). It is associated with focal temporal lobe dysfunction and predominant hypoperfusion in the mesiotemporal lobes. Neuropathologically, neocortical areas are not affected as atrophy, senile plaques and NFTs are limited to the limbic areas (Armstrong et al., 2000). **LPPA** is a potential 'language variant' of AD due to left parietal atrophy and left posterior temporal and inferior parietal hypoperfusion strongly associated with Aβ deposition (Lam et al., 2013). This syndrome is associated with a younger age of onset and faster rate of decline with preservation of memory. Patients present slow speech rate with difficulties in repetition (Gorno-Tempini et al., 2008). Neuropathologically, there is a prominent Tau regional distribution of NFTs within the left neocortex. Conversely, **PCA** shares similar pathological pattern but is characterized by visuospatial and visuoperceptual symptoms due to an affection of the right parietal lobe. An atypical predominant occurrence of NFTs is found in occipital regions (Scialò et al., 2019). Interestingly, Rasmussen et al. have identified distinct amyloid conformations between PCA and typical AD (Rasmussen et al., 2017). Finally, **frontal AD variant** is an extremely rare early-onset syndrome associated with executive dysfunction and prominent behavioral symptoms. Neuropathologically, there is a predominance of NFTs in the frontal regions ten-fold higher than in typical AD (Scialò et al., 2019).

3.1.2 Neuropathology-defined subtypes of AD

AD subtypes have also been defined based on cortical atrophy measures (Noh et al., 2014; Shiino et al., 2006; Whitwell, 2018), postmortem NFTs counts (Murray et al., 2011) and Tau retention in PET scans (Whitwell, 2018). Based on these neuropathological and neuroimaging data, different subtypes have been described.

Previous studies have suggested anatomical and neuropathological heterogeneity in AD. A post-mortem study identified three AD subtypes based on the distribution of NFT: **typical AD**, with NFTs in the hippocampus and association cortex; **limbic-predominant AD,** with NFTs predominantly in hippocampus; and **hippocampal-sparing AD**, with NFTs predominantly in the association cortex (Murray et al., 2011). Several investigations of atrophic patterns using voxel-based morphometry study

reported three subtypes likely corresponding to the post-mortem subtypes (Shiino et al., 2006; Whitwell, 2018). These AD subtypes were shown to exhibit different clinical presentations, rate of disease progression and demographic characteristics (Murray et al., 2011; Noh et al., 2014; Whitwell, 2018). They also have been found in neuroimaging studies using Tau-PET (Whitwell et al., 2018). Recently, MRI studies have consistently identified a fourth subtype displaying **minimal brain atrophy** (Ferreira et al., 2020, 2019). In 2020, Ferreira et al published a meta-analysis on the four AD subtypes based on the distribution of Tau-related pathology and brain atrophy patterns (Ferreira et al., 2020). They investigated inter-subtype differences by comparing age at onset, sex distribution, years of education, global cognitive status, disease duration, APOE ε4 genotype, and CSF biomarkers (**Figure 27**). First, they observed different proportion of AD subtypes. While typical AD is the most frequent subtype (55%), limbic-predominant, hippocampal-sparing and minimal atrophy AD had a frequency of 21%, 17%, and 15%, respectively. The four subtypes do not differ substantially in disease duration. Instead, similarity between hypometabolism and specific patterns of brain atrophy were found for each subtype. Tau-related pathology was highly correlated with the pattern of brain network dysfunction of each subtype. The three atypical subtypes showed similar CSF $A\beta_{42}$ levels and amyloid load. In contrast, regional distribution of Aβ deposition was different between subtypes. We briefly described below the three atypical atrophy-defined subtypes of AD:

- **Limbic-predominant** variant is a late-onset disease more frequent in female and APOEε4 carriers (Ferreira et al., 2020). Patients display bilateral focal Tau-PET binding in the temporal lobes sparing the posterior cingulate (Whitwell, 2018). Amyloid pathology assessed by PET-imaging mostly affects the medial frontal and parietal cortices compared with typical AD (Whitwell, 2018);

- **Hippocampal-sparing AD** includes highly educated individuals that present earliest disease onset compared to other AD subtypes with a higher severity. APOE ε4 non-carriers and male are more frequently affected (Ferreira et al., 2020). While the regional distribution of Tau-PET binding is similar to typical AD, amyloid pathology affects both frontal and parietal cortices with higher severity compared to typical AD (Whitwell, 2018). Hypometabolism was found in prototypic AD regions and was greater than in typical AD. More intense neurodegeneration and more aggressive disease progression was observed while preservation of cognitive status indicated a high capacity of brain reserve (*i.e* capacity of the brain to compensate severe pathological events) in these patients (Ferreira et al., 2020). Finally, atypical non-amnestic presentations previously described (**Section 3.1.2**) are more common in these patients.

- **Minimal brain atrophy** exhibits several pathological patterns. Patients show high level of abnormal CSF p-Tau and T-Tau, atrophy, hypometabolism in the parietal cortex and low cognitive reserve (Ferreira et al., 2017). It was suggested that Tau-related pathology and neurodegeneration may be sufficient to disrupt key brain networks at the root of dementia symptoms in those patients (Ferreira et al., 2019).

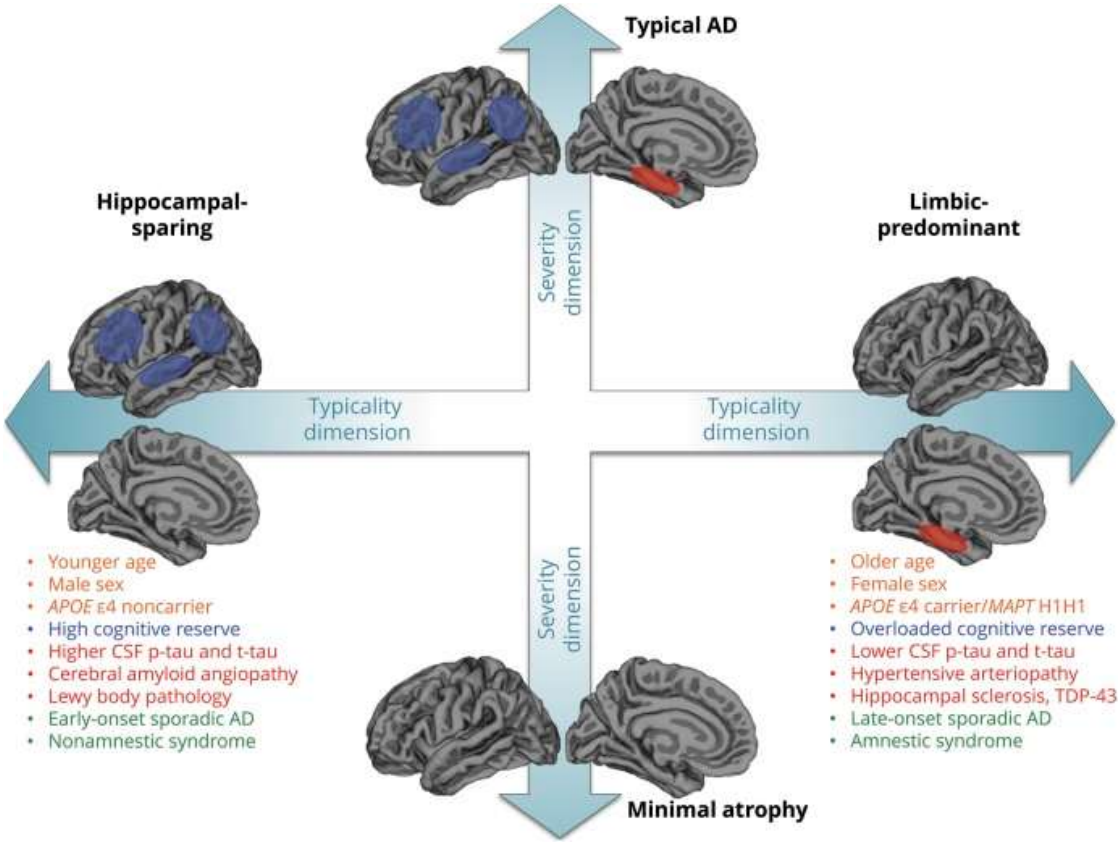

Figure 27 : Atrophy-defined subtypes of AD

Representation of 4 distinct subtypes: typical AD, limbic-predominant AD, hippocampal-sparing AD, and minimal atrophy AD. Their localization on the graph depends on their typicality and severity deviation from typical AD. The blue and red ellipsoids on the brains represent the regions defining these 4 subtypes according to previous studies. The studied factors are listed below each brain representation: the risk factors, including age, sex, and APOE (orange); the protective factors, including cognitive reserve (blue); brain pathologies including AD pathologies and concomitant non-AD pathologies (red); the age at onset and the cognitive presentation (green). From (Ferreira et al., 2020)

To conclude, polymorphism of regional distribution of Aβ and Tau gave rise to distinct AD variants. However, AD-associated pathology rarely occurs in isolation. Patients with AD pathology have concomitant pathologies such as Lewy body pathology. Risk factors, protective factors and

concomitant non-AD brain pathologies were suggested to contribute to the heterogeneity within AD by inducing brain regional vulnerability along the lifespan (Ferreira et al., 2020). Hence, spatial deposition polymorphism of different pathological hallmarks is induced which partly contributes to divergent clinico-pathologic presentations of AD.

3.1.3 Polymorphism of disease progression rate

Disease progression rate is defined by the rate of cognitive decline as well as the survival time of an individual diagnosed for AD. The mean survival time of typical AD patients is 8 to 10 years with MSME score declining of 3 points per year. Post-mortem studies identified a new AD subtype called rapidly progressive AD (rpAD) that evolves in less than 3 years following the diagnosis with cognitive decline of 6 points per year in MSME test (**Figure 28**).

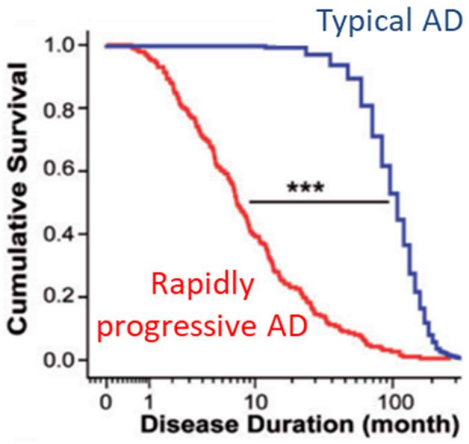

Figure 28: Disease progression rate of typical AD and rapidly progressive AD (rpAD)

The severity of the rpAD variant is due to an early impairment of the frontal lobe leading to early executive dysfunction, motor impairments and language deficits. The faster decline of cognition was also associated with dysfunctions in memory and non-memory domains such as attention and visuospatial construction. Higher CSF levels of phopho-Tau and lower $A\beta_{42}$ CSF burden were also reported. Hypometabolism was found too in several brain areas including the left angular, temporal and frontal cortices, unlike in typical AD. Although the regional distribution of Aβ deposits and NFTs is similar in rpAD and typical AD, conformational heterogeneity of protein aggregates was reported. Aβ fibrils isolated from rpAD brains showed atypical morphology distinct from typical AD Aβ fibrils (Qiang et al., 2017). Furthermore, rpAD brains contain higher levels of large Aβ conformers with low stability that were suggested to dissociate, therefore facilitating Aβ spreading, which strongly contributes to

accelerate disease progression (Cohen et al., 2015). These findings strongly support that Aβ conformers are one of the main culprit of AD heterogeneity.

3.2 Prion hypothesis of AD

3.2.1 Prion diseases

3.2.1.1 Overview

Mammalian prions are pathogens responsible for a family of fatal neurodegenerative diseases in humans and animals known as transmissible spongiform encephalopathies or prion diseases. During the 1950s, "Kuru", the first prion disease, was discovered by D. Carleton Gajdusek in the Fore linguistic group of the Eastern Highlands of Papua New Guinea. This community practiced a form of endocannibalism in which people ate the brains of dead relatives as part of a funeral ritual. It was also the first human prion disease experimentally transmitted to non-human primates through the intracerebral inoculation of pathological brain homogenates (**Figure 29**) (Gajdusek et al., 1966). The persistence of clinical and neuropathological phenotype after several passages in the non-human primate strongly argues for the existence of a transmissible agent in the human diseased brain. There are many prion diseases in humans including Creutzfeldt-Jakob disease (CJD), familial fatal insomnia, Gerstmann−Sträussler−Scheinker disease, which result in different diseases characterized by different age of onset. Scrapie in sheep and goats, bovine spongiform encephalopathies (BSE) in cattle, chronic wasting disease (CWD) in cervids have also been identified. BSE can cross the species barrier to humans, leading to variant CJD (vCJD).

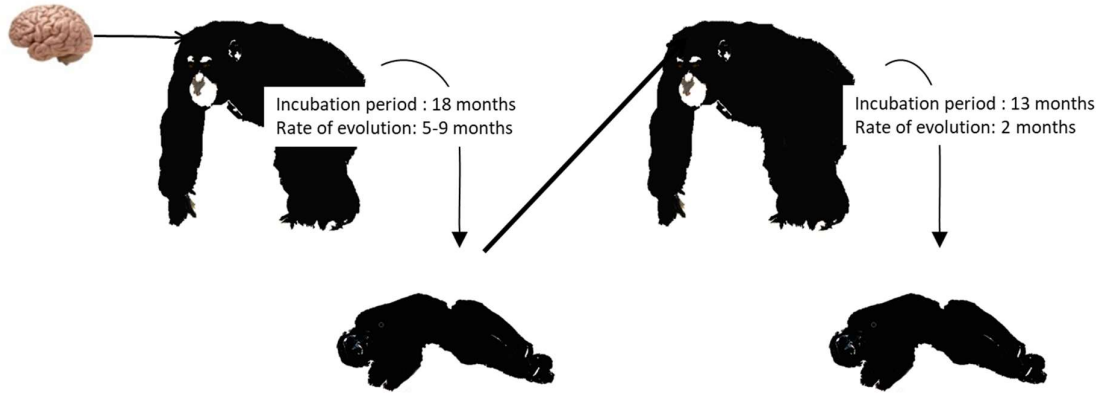

Figure 29: The transmission of Kuru-like syndrome to chimpanzee

Brain-extracts from Kuru patients were experimentally inoculated in the brain of chimpanzees. Further passages from infected chimpanzee to another chimpanzee host were conducted. The incubation period and the rate of evolution for each passage are indicated. After several passages, the Kuru

pathological phenotype was maintained and the rate of disease evolution was reduced (Gajdusek et al., 1966).

The term prion, derived from the words “protein” and “infectious,” was latter introduced by Stanley Prusiner in 1982 to define “a small proteinaceous infectious particle” lacking nucleic acids (Prusiner, 1982). It is now thought that prion diseases are associated with the accumulation in the brain of an abnormal, partly protease-resistant, isoform of a host-encoded glycoprotein known as prion protein (PrP^{C}) ubiquitously expressed. The soluble α-helical PrP^{C} can conformationally rearrange to an infectious isoform PrP^{Sc}, in reference to scrapie, which has a β-sheet structure. PrP^{C} and PrP^{Sc} share the same amino acid sequence but differ in their conformational and aggregation state (Collinge, 2005). During the pathogenesis, PrP^{Sc} can act as a “seed” as it can recruit and impose its particular conformation to PrP^{C} misfolding into further PrP^{Sc} and allowing the auto-catalytic formation PrP^{Sc} as well as the spreading of the disease from cell to cell. This linear elementary mechanism which constitutes the base of the prion paradigm has been proposed to be at origin of the accumulation of PrP^{Sc} aggregates in the CNS, causing neuronal dysfunction and fatal irreversible degeneration through either gain of cytotoxic PrP^{Sc} functions or loss of PrP^{C} cytoprotective functions (Halliday et al., 2014). Since then, several experimental transmission studies in animal models have demonstrated the potential infectivity of prion diseases.

3.2.1.2 Concept of prion strains

In prion diseases, transmission is characterized by the occurrence of a "strain effect" leading to distinct phenotypes. Compelling evidences have suggested that phenotypic polymorphism of prion disease is mainly due to the possibility of PrP^{Sc} assemblies to adopt different conformations, at the tertiary and quaternary levels with different pathobiological properties, defined as prion strains (Aguzzi et al., 2007; Colby and Prusiner, 2011; Collinge and Clarke, 2007). These differences in PrP^{Sc} structure have been assumed to induce prion specific templating activity and various levels of prion resistance to conventional degradation techniques. Thus, prion strains exhibit different incubation times, histopathological lesions and clinical manifestations.

3.2.2 AD is a proteinopathy

A proteinopathy is a disease involving a native protein that can adopt pathological conformations responsible for the disease. Each conformation of the protein can be associated with specific features of the pathology. Additionally, these abnormally folded proteins are able to seed and propagate resulting in possible transmission of the pathology by inoculation of these pathological seeds. In the last decade, mounting evidences described below, have supported the hypothesis that AD, like prion disease, is a proteinopathy. Furthermore, the polymorphism of Aβ conformation states has been

suspected to be one of the main culprit of AD clinical heterogeneity. So far, conformational heterogeneity is difficult to target rendering anti-conformational drugs ineffective.

3.2.2.1 Nucleation-dependant polymerization mechanism

In physiological condition, Aβ is continuously produced throughout life without causing any pathological changes. Aβ peptides are generated under several isoforms called **Aβ proteoforms**. In AD, Aβ peptides aggregate in an aberrant manner. It has been proposed that Aβ aggregation follows a nucleation-dependent polymerization process, which is concentration and time-dependent (**Figure 30**). This mechanism consists of two phases: the initial nucleation phase or "lag phase" and the elongation phase (Eisele, 2013). The nucleation phase is slow and thermodynamically unfavorable, occuring only under certain circumstances (peptide concentration, pH, temperature, genetic mutations). During the nucleation phase, the random-coiled Aβ monomers adopt an alternative, misfolded conformation rich in β-sheet structure. These conformations are prone to self-aggregate, initiating the pathological process. Aβ monomers further aggregate into various types of assemblies, including oligomers, protofibrils and amyloid fibrils. During oligomerization, small oligomeric assemblies form multimeric nucleus that serve as templates to rapidly incorporate other Aβ monomers and form larger aggregates (elongation phase). Initial oligomerization process from the pool of Aβ monomers is called the primary nucleation. Alternatively, heterogeneous contacts between monomers and fibrils contribute to the secondary nucleation where another pool of Aβ oligomers are generated (Glabe, 2008; Lee et al., 2017). The nucleation phase is the rate-limiting step of fibrillization (Cohen et al., 2013). However, fibril fragmentation generates another pool of Aβ oligomers contributing to accelerate this vicious circle.

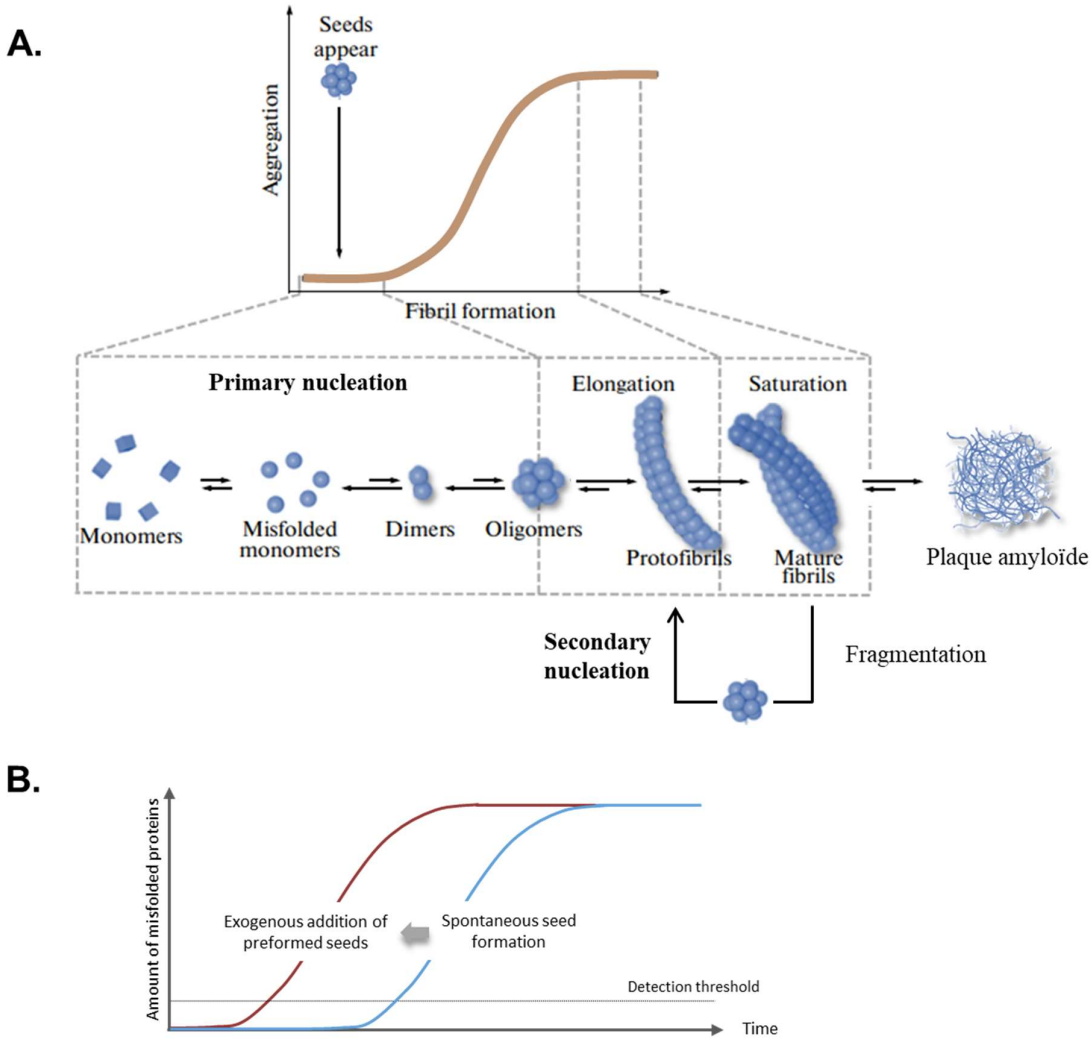

Figure 30: Aβ nucleation-dependent seeding and template misfolding

A. Aβ formation starts with a slow nucleation phase (aggregation of the protein into a seed) that may go through a series of intermediate states until the initial segment of the amyloid spine is formed. Monomers or oligomeric structures are then bonded to the ends of the initial amyloid seed by conformational conversion. With increasing length, and depending on the conformational stability of the amyloid spine, the growing fibril can eventually break, either spontaneously or actively through cellular processes. In this way, amyloid formation becomes self-propagating through the generation and spread of new Aβ seeds. The kinetics of amyloid fibril formation is a function of the rate of nucleation, growth, and fragmentation. **B.** The lag time that precedes protein aggregation *in vitro* can be greatly shortened by the addition of pre-formed exogenous seeds. Adapted from (Kulikova et al., 2015).

Although each aggregation state participates to Aβ build-up, the key issue is "which of these assembly states accumulate in disease and are more closely associated with AD pathogenesis?". While Aβ fibrils

are insoluble and can further assemble into amyloid plaques, soluble Aβ oligomers spread throughout the brain and has been shown to be causative of AD pathogenesis.

3.2.2.2 AD pathology is transmissible by inoculation of amyloid seeds: Prion-like hypothesis

Prion-like spreading of disease within the brain is not unique to PrP. The mechanism of nucleation and propagation of abnormally folded proteins in AD has been proposed to have some similarity with prion diseases. An expanding body of evidence argues that the formation of Aβ "prions" is involved in the pathogenesis of AD. Neuropathology study of AD brains revealed that Aβ deposition follows a stereotypical progression instead of emerging randomly (Thal et al., 2002). During the last decade, several cases of potential iatrogenic contamination with compounds containing Aβ pointed the first evidence that Aβ is a "prion-like" protein. Patients who received cadaver-sourced human growth hormone during childhood developed cerebral amyloidosis and severe CAA without carrying any genetic susceptibility associated with the development of early Aβ pathology (Jaunmuktane et al., 2015). The recent analysis of administered materials revealed that batches of hormones were contaminated with misfolded Aβ seeds (Duyckaerts et al., 2018) suggesting Aβ self-propagation in the host.

Greatest evidence for prion-like template misfolding of Aβ comes from various experimental transmission of Aβ pathologies in transgenic mice overexpressing human APP through the intracerebral inoculation of AD brain-derived Aβ aggregates (Eisele et al., 2010, 2009; Meyer-Luehmann et al., 2006; Watts et al., 2014; Ye et al., 2015). The inoculation of brain homogenates containing Aβ was sufficient to accelerate β-amyloidosis in the host, in the form of parenchymal plaques and vascular Aβ similar to AD-associated lesions. Since Aβ deposition appears after a lag period of incubation and does not occur in host lacking endogenously expressed Aβ, it was assumed that is was coming from a seeding process rather than from the inoculum itself (Jucker and Walker, 2011; Walker et al., 2016). Similarly, Aβ-rich brain extracts from aged transgenic mice were demonstrated to induce build-up of Aβ in the host (Meyer-Luehmann et al., 2006). The reduction of the lag phase was shown to be highly dependent on Aβ seed concentration (Morales et al., 2015) supporting the idea that more seeds will more efficiently recruit Aβ peptides for template misfolding (Eisele, 2013). Additionally, lower APP overexpression was demonstrated to extend the lag phase (Meyer-Luehmann et al., 2006). Importantly, the removal of Aβ aggregates in AD brain extracts, by immunodepletion or chemical denaturation, prevents the transmission of Aβ pathology meaning that Aβ is the self-propagating component allowing the development and acceleration of the pathology in the host (Eisele et al., 2009; Meyer-Luehmann et al., 2006).

In addition to Aβ lesions, the inoculation of AD-brain extracts can induce long-term cognitive alterations as well as synaptic impairments in rodents (Lam et al., 2022) or in primates (Gary et al., 2019; Lam et al., 2021). Notably, our group showed that brain function defects were strongly associated with Aβ and Tau depositions in the host brain. Additionally, in rodents, both Aβ and Tau pathologies were induced in the hippocampus, close to the inoculation site but also in distant connected areas such as the entorhinal cortex (Lam et al., 2022). These data strongly support the existence of a self-propagating mechanism of proteinopathic seeds from neuron to neuron. However, although models based on brain extract inoculation offer a unique opportunity to assess the relationships between AD lesions during the course of the disease, they also impede the investigation of Aβ seed pathological impacts, as it is difficult to dissociate the respective roles of Aβ and Tau in AD downstream events. Furthermore, the high seeding potency of AD brain extracts may be facilitated by co-factors present in the donor brain that can also modulate the pathology.

Therefore, inoculation of highly purified brain-derived Aβ or synthetic Aβ fibrils formed *in vitro* was proposed to evaluate the self-propagating properties of Aβ (Stöhr et al., 2012). Synthetic Aβ was sufficient to induce cerebral β-amyloidosis in young APP transgenic mice, definitely proving that misfolded Aβ by itself promotes prion-like propagation of the disease (Stöhr et al., 2012). Although synthetic Aβ peptides are less bioactive than brain-derived misfolded Aβ, acute functional alterations were shown in wild-type mice following synthetic Aβ oligomer inoculation, suggesting that synthetic Aβ oligomers share some similarities with brain-derived Aβ (Balducci et al., 2010; Epelbaum et al., 2015). However, the persistence of self-propagation and the functional impact of seeding of synthetic Aβ at long-term have not yet been reported. Interestingly, it was reported that *in vitro* synthetic or recombinant Aβ can form different Aβ aggregates that can be induced either by mutations within the Aβ sequence or by chemical changes of Aβ (Stöhr et al., 2014). Notably, the inoculation of different Aβ polymorphs, with distinct structural motifs, in transgenic mice was shown to induce structural differences in AD-like lesions in the host (Stöhr et al., 2014), bringing forward the notion of Aβ strains.

3.2.2.3 Strain concept: each conformation is associated to a pathology

Aβ can form a number of β-sheet-rich structures with distinct conformations (strain). Each conformation is supposed to give rise to a specific disease and associated pathology. This hypothesis relies on the possibility that Aβ seeds can transform an endogenous strain into a pathogenic strain that allows propagation of the pathology and yields different phenotypes. Aβ prion strain-specific biological information is encompassed within different conformations of Aβ protein aggregates. Studies of Aβ oligomers and fibrils generated *in vitro* showed that synthetic Aβ can aggregate into structurally diverse amyloid fibrils, which retain their conformational properties and cellular toxicities after repeated passage (Petkova et al., 2005). Further convincing evidences were demonstrated by

histological studies of AD brains and transgenic mice models. Aβ deposits were shown to be highly heterogeneous in their appearance, which reflects polymorphism of molecular composition and/or conformation of the aggregated Aβ. Furthermore, when different extracts derived from either APP/PS1 (Swedish FAD mutation) or APP23 (Artic FAD mutation) transgenic mice were used as inoculum, the features of plaque morphology of the donor brain was replicated into the host (Watts et al., 2014). Thus, distinct conformations of Aβ aggregates have been described as forming either spontaneously from synthetic Aβ or by Aβ aggregates from AD brains. These findings strongly indicate that each Aβ conformer adopts a specific aggregation pathway that leads to phenotypic variability observed among AD patients (Ladiwala et al., 2012). The heterogeneity of AD could, thus, potentially be explained by the existence of multiple Aβ strains.

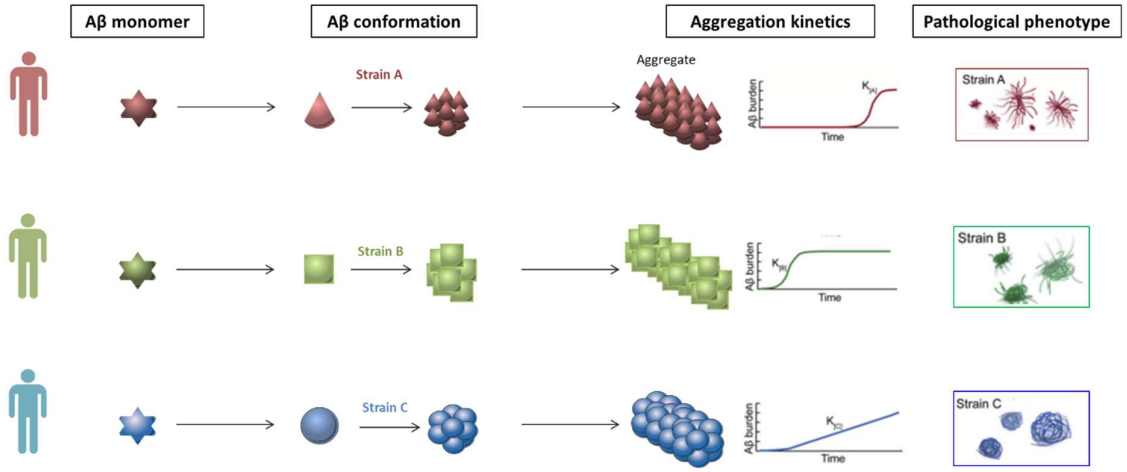

Figure 31: Conformational strains of Aβ could explain the heterogeneity in AD

Distinct structural variants of misfolded Aβ (strains) lead to different aggregation properties and different pathological phenotypes. Adapted from (Condello et al., 2018).

3.2.3 Pathological transconformation of a native protein in AD

Recent advances in structural biology techniques allowed to assess the tridimensional structure of protein involved in several diseases. It has been demonstrated that a same sequence of amino acids can fold differently giving rise to several conformations of the protein called **alloforms**. Initially described in prion diseases, protein conformation has a pivotal role in the characterization of "the strain" responsible for the proteinopathy. Misfolding of the native protein could lead to cellular interaction changes resulting in the modification of the protein physiological functions, inducing pathological events.

One way to investigate misfolded protein structures is to use cryo-electron microscopy and atomic force microscopy. Aβ has been shown to exhibit different conformations that exert proteopathic stress

on different brain cells. While the factors that influence Aβ conformations remain unclear in SAD, genetic mutations within Aβ sequence in FAD have been clearly identified as responsible for pathological transconformation of Aβ (See **Section 3.3**). These mutated forms of Aβ adopt different conformations that lead to different aggregation properties and different toxicity, making study of familial AD more informative to explain the complexity of AD heterogeneity.

3.2.3.1 Monomer: Aβ proteoforms and Aβ alloforms

Aβ monomers gathers a group of ~4 kDa-peptides ranging in size from 37 to 49 residues called **Aβ proteoforms**. $Aβ_{40}$ and $Aβ_{42}$ are the most predominant forms. Despite the small structural difference between them, they exhibit different properties *in vitro* and *in vivo.* $Aβ_{42}$, the major constituent of senile plaque, is more aggregation-prone and more toxic than $Aβ_{40}$, which is less hydrophobic. The inaccurate secretase-dependent cleavages of APP also generate a variety of Aβ proteoforms. These Aβ fragments can emerged from either the amyloidogenic or the non-amyloidogenic pathway leading to distinct degree of neurotoxic properties. Each of these peptides is likely to possess a different thermodynamic landscape to convert into a misfolded protein. Recent advances in mass spectrometry enable to detect numerous Aβ proteoforms in the brain or in biological fluids (blood, CSF) of AD patients such as $Aβ_{43}$, $Aβ_{5\text{-}40}$, $Aβ_{17\text{-}40/42}$ also called p3 fragments (Di Fede et al., 2018; Portelius et al., 2010). Interestingly, it was reported that the concentration of each Aβ proteoform was different between AD patients independently of AD etiology, suggesting that Aβ proteoform profiles can be used as new classification compounds for AD (Di Fede et al., 2018). The different Aβ proteoform profiles led to distinct disease phenotypes, suggesting that heterogeneity of Aβ proteoforms might partly explain AD heterogeneity. In addition to expressed level polymorphism, the degree of Aβ toxicity has been shown to vary between Aβ proteoforms depending on either their ability to self-aggregate into oligomeric forms or their physiological role (Fu et al., 2017). The cleavage of $Aβ_{40}$ or $Aβ_{42}$ by BACE-1 provides the formation of the intermediate fragment $Aβ_{34}$ that is further degraded by metalloprotease enzymes to achieve amyloid clearance. Alteration of BACE-1 expression levels has been shown to increase the level of cerebral $Aβ_{34}$ by preventing its degradations. Interestingly, measurement of $Aβ_{34}$ in the CSF of cognitively normal individuals at risk for AD allowed to distinguish patients that later converted to AD from those who did not (Liebsch et al., 2019). While the toxicity of many Aβ proteoforms was associated with pre-clinical markers of neurodegeneration, the presence of some Aβ proteoforms were shown to protect against Aβ-induced synaptotoxicity and ultimately AD. Aβ C-terminal hydrophobic domain has been demonstrated to largely contribute to its aggregation and neurotoxicity compared to the N-terminal hydrophilic domain (Glabe, 2008; Haass and Selkoe, 2007). An N-terminal Aβ fragment produced via α-secretase-related pathway and found in the CSF (Portelius et al., 2010) was shown to act as a neuromodulator on synapses, reversing Aβ toxicity (Lawrence et al.,

2014). Similar effects were obtained with the shorter hexapeptide Aβ core fragment. Interestingly, the intrahippocampal inoculation of these fragments in adult 5XFAD mice showed to reverse Aβ-triggered synaptic plasticity deficits and to rescue memory (Forest et al., 2021, 2018).

Mounting evidence suggested that the toxicity and the abnormal aggregation of Aβ species in AD highly depend on monomeric Aβ conformation (Das et al., 2015; Ladiwala et al., 2012). The native Aβ protein has an initial α-helical conformation that is thermodynamically stable and non-amyloidogenic. The hydrophobic C-terminal of Aβ triggers the transformation from α-helical to β-sheet structure, which is more prone to aggregate (Mirza et al., 2014). These conformational changes of the native protein are kinetically unfavorable but play a key role in determining the state of protein aggregation in AD and may occur during the early stages of the disease. Several studies have identified a huge number of **Aβ alloforms** that comprise either α-helix or β-sheet conformers due to dynamic and rapid structural state transitions (Sgourakis et al., 2011; Yang and Teplow, 2008). The lack of existence of a stable fold and the propensity of Aβ to aggregate into higher molecular assemblies complicates the study of Aβ monomer structure and dynamics. Therefore, the identification of the Aβ alloforms in AD patients remains challenging. As Aβ conformation is the culprit of the disease initiation, structure-based therapeutic developments are in progress and may call on personalized medicine.

3.2.3.2 Aβ oligomer: structure, classification and toxicity

3.2.3.2.1 Toxicity

Pro-aggregated Aβ monomer recruits other Aβ molecules to form different soluble Aβ oligomeric assemblies ranging from low molecular weight - such as dimers, trimers and tetramers - to higher molecular weight including hexamers and dodecamers. Emerging evidence has demonstrated that cerebral and plasmatic levels of soluble Aβ oligomers correlate better with dementia than insoluble amyloid deposit load (Lue et al., 1999; McLean et al., 1999). Aβ oligomer-triggered toxicity has also been shown in mouse models of AD. Unlike amyloid plaques, AD brain-derived Aβ oligomers can induce Tau hyperphosphorylation, alter synaptic plasticity (Hughes et al., 2020; S. Li et al., 2011) and initiate cognitive decline in exposed rodent (Jin et al., 2011; Shankar et al., 2008). Interestingly, intracerebroventricular injection of high molecular weight Aβ oligomers induces transient memory impairment whereas injection of low molecular weight ones causes severe cognitive impairment and synaptic damage (Shankar et al., 2008). These results were also shown in wild-type mice in which high molecular weight Aβ oligomers dissociate into low molecular weight Aβ oligomers, activate microglial response and inhibit hippocampal LTP (Yang et al., 2017). The quantification of lactate dehydrogenase (LDH) released from cells after exposition to Aβ oligomers enabled to know the cytotoxic ability of these small Aβ assemblies. Those experiments revealed that neurotoxicity activity of small Aβ

assemblies increased proportionally with oligomer order (Ono et al., 2009). Indeed, dimers and trimers were three times more toxic than monomers, while tetramers were 13 times more toxic (tetramers > trimers > dimers> monomers).

The mechanisms by which Aβ oligomers can prompt toxic effects is complex. Aβ oligomers could bind to different cell membrane receptors, be internalized into cells or accumulate in extracellular compartments. It was suggested that toxic oligomers expose hydrophobic surfaces that disturb membranes, exposing the cytoplasm to the extracellular space, causing undesirable calcium flux and ultimately cell death (Iadanza et al., 2018).

Taken together, these data reinforce the "Oligomer Hypothesis", according to which Aβ oligomers but not monomers or fibrils were responsible for synaptic dysfunction and memory loss in AD. Elucidating and counteracting Aβ-associated toxicity could advance development of new diagnostic tools and influence AD drug discovery toward Aβ oligomer targeting. Furthermore, identifying the most deleterious Aβ assemblies in AD patients may provide insight into the molecular subtypes of AD.

3.2.3.2.2 Structure

Structural analysis of Aβ oligomers has been conducted to understand their toxicity. Electron microscopy and atomic force microscopy have identified spherical aspect of Aβ oligomers that measure between ∼3 and 10 nm. Although Aβ monomers were largely unstructured, the quaternary structure of an Aβ oligomer depends on the order-dependent arrangement of its constitutive monomers. Mainly composed of β-sheet structures with a stable core. Aβ oligomers are highly heterogeneous and differ in size, morphology, aggregation mode, toxicity and appearance time in the brain. A spectrum of Aβ oligomers has been described ranging in molecular size from 4 to 100 kDa.

3.2.3.2.3 Classification

In vitro, Aβ oligomers appear at early stage during nucleation-dependent process and disappear as mature fibrils are formed, indicating that Aβ oligomers are an intermediate transient structure enrolled in fibrils formation and elongation. However, the formation of Aβ oligomers is much more complex and leads to a highly heterogeneous population of Aβ oligomers in the living brain. Some progress on elucidating the mechanism responsible for the diversity of Aβ forms and understanding their associated functional characterization have been made. Several studies were conducted to find the better classification. In addition to their heterogeneity, Aβ oligomers are unstable in solution and the method of their isolation differs between research groups, which can lead to different structural variants of Aβ oligomers that did not reflect AD-associated polymorphism. For several decades, the size of Aβ oligomers was used to categorize them. Small oligomers such as dimers and trimers were reported to be more toxic as they can spread easily and bind to different cell targets involving several

signaling pathways (Jin et al., 2011; Shankar et al., 2008). However, the size of Aβ oligomers do not properly reflect their conformation or aggregation state known to be strongly associated with pathogenesis. Although conformationally distinct Aβ oligomers can show overlapping size distributions, they display mutually exclusive generic epitopes associated with specific aggregation states that can be recognized by conformation-dependent antibodies (Kayed et al., 2007). At least two classes of Aβ oligomers were highlighted based on their underlying structural organization: the **prefibrillar** oligomers and **fibrillar** oligomers (Ashe, 2020; Glabe, 2008; Kayed et al., 2007; Liu et al., 2015).

Prefibrillar oligomers arise from monomers assemblies (**Figure 32**) and are recognized by A11 antibodies (Kayed et al., 2007). They vary in size from tetramers to 20-mers. They appear early in the course of AD, before plaque deposition. They are kinetic intermediates in fibril assembly. Indeed, prefibrillar oligomers further aggregate with each other to form protofibrils that ultimately become mature fribrils. In order to convert into a fibrillar state, they undergo conformational change, mainly consisting in an increased content of antiparallel β-sheets (Diociaiuti et al., 2021; Glabe, 2008; Lee et al., 2017). Interestingly, inhibition of prefibrillar oligomers did not hinder fibril formation suggesting that an alternative pathway may generate fibrils (Kayed et al., 2007).

Fibrillar oligomers share similar epitopes with Aβ fibrils and, thus, are recognized by OC-antibodies as they contain in-register β-sheet structures (Kayed et al., 2007). They emerge after plaque deposition and accumulate in the immediate vicinity of dense-core plaques (Ashe, 2020; Liu et al., 2015). Fibrillar oligomers are coming from secondary nucleation where addition of monomers to the end of fibrils induces monomer conformational changes to fibrillar oligomers (**Figure 32**). Furthermore, with increased length, fibril fragmentation occurs and generates soluble fibrillar oligomers, the fibril seeds or small piece of fibrils (Glabe, 2008; Lee et al., 2017).

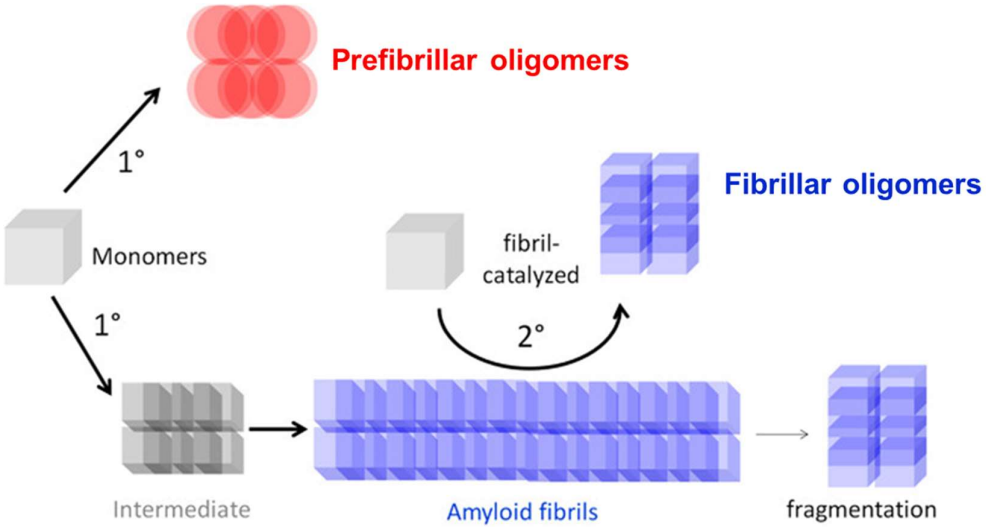

Figure 32: Formation of prefibrillar and fibrillar oligomers. From (Ashe, 2020).

It is not clear whether prefibrillar or fibrillar oligomers are the primary pathological species responsible for AD pathogenesis. As prefibrillar oligomers were reported in human AD brain earlier than fibrillar oligomers, they have been considered the most toxic species responsible for synapse damage and subsequent amyloid toxicity. Furthermore, multiple studies have shown that prefibrillar oligomers, in particular Aβ*56, are responsible for memory dysfunction in AD mouse models (Billings et al., 2007; Cheng et al., 2007). *Tomic et al.* observed higher amounts of fibrillar oligomers in the brain of AD patients compared to control elderly individuals. In contrast, prefibrillar oligomers levels were similar in both cohorts (Tomic et al., 2009). Fibrillar oligomers are also predominant in mice bearing increasing amyloid dense-core plaques (Liu et al., 2015). This finding is mainly due to their temporal, spatial and structural relationship to amyloid fibrils and their association to amyloid plaques. In addition, fibrillar oligomers were shown to better correlate with cognitive decline in AD than prefibrillar oligomers, indicating that transient prefibrillar oligomers may represent a non-toxic pool of oligomers (Tomic et al., 2009). Controversially, transgenic mice that exclusively produce fibrillar oligomers had intact cognition suggesting that fibrillar oligomers confined into amyloid plaques does not impair cognition (Liu et al., 2015). Based on the collection of current findings, there is growing consensus that both types of oligomers are harmful for brain function but at varying degrees, through distinct neuronal signaling pathways and depending on their distribution in the brain (Ashe, 2020). Both have shown to interact with dendritic spines causing synaptic deficits. Prefibrillar oligomers, independent to temporal and spatial distribution of Aβ fibrils, have more potential to diffuse and, thus, cause global neural dysfunction in AD. It has been demonstrated that they induce the formation of oligomer-triggered Tau toxicity, which may explain why they have been associated with dementia. In contrast, fibrillar

oligomers, sequestered within the “toxic halo” of dense-core plaques, do not diffuse and induce focal neurological dysfunction as much as these toxic spheres extend. Thus, they might interfere with neural networks in AD patients bearing high plaque density.

Others type of oligomer have been described: Aβ-derived diffusible aggregates (ADDLs) and globulomers. These biggest structures that were classified as fibrillary oligomers, alter synaptic plasticity, induce mislocalization of Tau to dendrites and mediate memory dysfunctions. Conformation-dependent antibodies can specifically recognize these distinct assembly states (Glabe, 2008).

3.2.3.3 Aβ fibrils: structure and toxicity

The amyloid structure of Aβ fibrils was known well before its amino acid sequence was deciphered from AD brain isolated proteins. The initial stages of amyloid fibrils formation involve a heterogeneous ensemble of monomers or/and oligomeric intermediates. These amyloid fibrils can further associate with each other to form amyloid plaques, or dissociate and release fibrillar oligomers as previously described (See **Section 3.2.1.1**). X-ray diffraction studies have shown that amyloid fibrils are highly ordered structures. They adopt the canonical cross-β structure, which consist of sets of β-sheets with β-strands arranged perpendicularly to the fibril axis and stabilized by hydrogen bonds (Eisenberg and Jucker, 2012; Sunde et al., 1997). Fibril cross-β structures can display a parallel or antiparallel organization. Dyes that positively stain β-sheets secondary structures, such Congo red, are used to reveal amyloids fibrils. When viewed under polarized light, a characteristic red/green birefringence of amyloid fibrils is observed. Electron microscopy studies have shown that the diameter of amyloid fibrils is about ∼7–10 nm.

NMR spectroscopy studies have reported structural polymorphism of Aβ fibrils in AD patients (Lu et al., 2013; Qiang et al., 2017) that was associated with various amyloid morphologies (Condello et al., 2018; Watts et al., 2014). Isolated Aβ fibrils showed distinct sizes, concentrations and conformational characteristics, which correlate with duration and severity of disease. Such diversity may explain different clinical presentations leading to strong heterogeneity between AD patients (Lu et al., 2013; Paravastu et al., 2009; Qiang et al., 2017). The wide variety of amyloid structures were mainly due to the different intrinsic organization of α-helices and β-strands. Recent studies have demonstrated that a same protein sequence can conduct to different fibril morphologies meaning that oligomer and fibril formations are pivotal steps responsible for the structural diversity of Aβ fibrils (Iadanza et al., 2018). This was illustrated by the possibility to produce different $A\beta_{40}$ fibrils *in vitro* under different conditions. Additionally, differences in fibril characteristics can partly explain the distinct topologic distribution of amyloid plaques observed across patients. Amyloid morphologies may affect the ability of fibrils to

spread to different sites, depositing in different locations. They can also cause different cellular effects presumably due to different molecular bindings (Iadanza et al., 2018).

3.3 Phenotypic polymorphism in Familial AD can explain AD heterogeneity

Several questions are pending about how structural polymorphisms of Aβ aggregates can affect disease onset, disease progression and clinical presentation. It is widely accepted that variation in APP sequence can directly influence variability in both age of onset and disease duration in numerous FADs. In this part, we will describe several evidences showing that the study of FADs can contribute to answer to this question.

3.3.1 Different forms of mutated Aβ

For several decades, clinical classification of AD has relied on the age at onset of the pathology. Early-onset FAD is an uncommon form of AD that shows an autosomal dominant pattern of inheritance associated with numerous mutations in genes governing Aβ regulation. Although, most of FAD-associated mutations caused severe AD pathogenesis, some of them are inherited in a recessive Mendelian manner. In 2019, Bi *et al.* listed 69 missense mutations within the APP gene (Bi et al., 2019). Most of them were pathogenic or are "unclear" and two mutations were reported to be protective (Jonsson et al., 2012). The wide range of FAD-associated mutations conducted phenotypic polymorphism among FAD patients (**Table 2**). There is an increasing understanding of the influence of FAD mutation in Aβ conformational diversity. FAD-associated mutations can occur either near α- or β-cleavage site, affecting Aβ production, or within Aβ sequence, affecting Aβ conformation. Almost all of pathogenic mutations result in a single phenotype, an increase in either the total amount of Aβ or the relative proportion of $Aβ_{1-42}$ (Esler and Wolfe, 2001; Glabe, 2008; Hardy, 2017; Jonsson et al., 2012; Selkoe, 2001). The resultant accumulation of Aβ is identical to what is observed in the SAD but occurs earlier in life. Thus, the study of FAD-associated mutations is relevant in understanding of common sporadic AD heterogeneity.

3.3.1.1 Mutation affecting Aβ production

Mutations near the β-cleavage site such as *Swedish* (KM670/671NL), *Taiwanese* (D678H), *Leuven* (E682k) and *Flemish* (A692G) mutations exacerbate BACE1 cleavage toward the β-site leading to an increase of total secreted Aβ and ultimately, changes in $Aβ_{42}/Aβ_{40}$ ratio (**Table 2**) (Bi et al., 2019). Overall, these mutations induce a heavy load of amyloid plaques and sparse Tau pathology in the form of pre-tangles rather than NFTs. Various levels of cognitive alteration were shown in patients and can be associated with synaptic and neuronal loss. The most commonly explored mutation in AD research field is the **Swedish mutation** (KM670/671NL). MRI studies have shown that patients exhibit cortical

atrophy and cerebral blood flow reduction. Pathologically, this mutation induces NFTs and amyloid plaque burden as well as concomitant pathologies such as Lewy body pathology and CAA (Bi et al., 2019). Regarding APP processing end-products, it was reported an increase of intracellular Aβ and CTF-β while α-CTF-α levels remained constant in cellular models. The Swedish mutation induces a general increase of both $A\beta_{42}$ and $A\beta_{40}$ production and secretion without changing $A\beta_{42}/A\beta_{40}$ ratio (Axelman et al., 1994; Bi et al., 2019). Several transgenic mouse models expressing a humanized APP gene with the Swedish mutation (APP_{swe}) were designed such as APP23 (M670/671NL) and Tg2576 mouse models. The **APP_{swe}/$PS1_{dE9}$ mouse model** has been largely used to investigate the role of Aβ in AD-associated pathology. This mouse model, created on a C57BL/6J background, overexpresses the human APP gene and a human PS1 gene, lacking exon 9, under the mouse prion promoter (Jankowsky et al., 2004). These mutations lead, as expected, to an overproduction of Aβ and an increase in the $A\beta_{42}/A\beta_{40}$ ratio. This model begins to develop amyloid plaques by 4 months of age with a progressive increase in plaque deposition until 12 months of age in the cortex and hippocampus (Garcia-Alloza et al., 2006). Synaptic alterations (Viana da Silva et al., 2016) and neuroinflammation process were also described as well as memory impairment associated with aging (Huang et al., 2016). Onset of each AD-like feature can differ from a lab to another one.

FAD mutations falling near the γ-cleavage was demonstrated to alter C-terminal residues to selectively produce amyloidogenic $A\beta_{42}$ and increase the $A\beta_{42}/A\beta_{40}$ ratio (Suárez-Calvet et al., 2014). These mutations modify the structure and dynamics of the transmembrane domain of APP in order to make it more vulnerable to γ-secretase therefore shifting toward Aβ overproduction. Numerous mutations have been identified at γ-cleavage site including *Austrian*, *German*, *French*, *Iberian*, *Florida*, *Indiana*, *London* and *Australian* (**Table 2**). Interestingly, AD patients with the London mutation showed intra-subtype diversity depending on their ethnic origin as Chinese AD patients develop a more aggressive form than Western Europ AD patients (Zhang et al., 2017). Additionally, the *Austrian* and *Iberian* mutations were associated with neuronal loss and activation of microglia and astrocytes (**Table 2**) (Bi et al., 2019).

3.3.1.2 Mutations affecting Aβ conformation

FAD-associated mutations within the Aβ sequence in amyloid conformation lead to a wide range of disease phenotypes by creating mutated forms of Aβ (Chong et al., 2013). Each mutated Aβ has its own degree of toxicity, aggregation properties and localization inside/outside the cell. The properties of mutated Aβ are strongly related to the localization of the mutation. FAD-associated mutation within Aβ sequence can occur either in the C-terminal domain or N-terminal domain or in central core region of Aβ (**Figure 33**). Several studies demonstrated that the position of the FAD-associated mutation

within the Aβ sequence influences differently the 3D structural conformation of the peptides that may underlies their pathological phenotypic diversity.

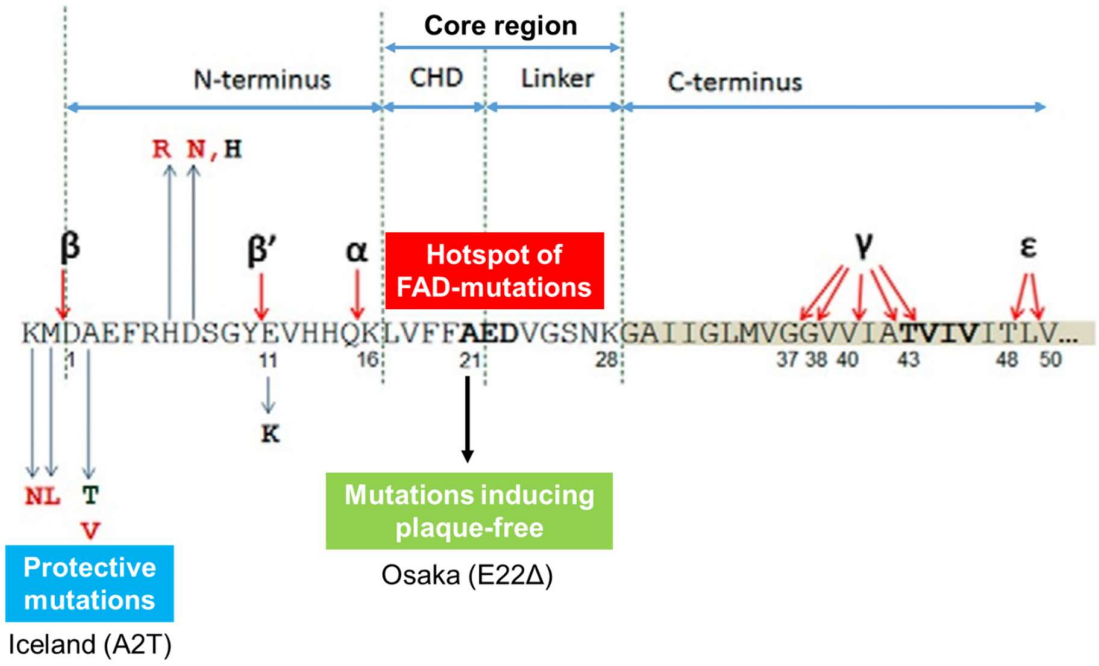

Figure 33: The localization of some FAD-associated mutations on the Aβ sequence

3.3.1.2.1 Hotspot of FAD-associated mutation in Aβ core region

A hotspot of FAD mutations was described in the core region of Aβ (residues 21-30) that enhances Aβ misfolding and toxicity, and changes aggregation propensity (Dai et al., 2018; Lazo et al., 2005). Numerous mutations have been identified including *Osaka* (E693Δ), *Dutch* (E693Q), *Italian* (E639K), *Artic* (E693G) and *Iowa* (D694N) mutations. The majority of these mutations leads to severe dementia associated with concomitant pathologies that distinguish these mutations from others causing only AD dementia (Bi et al., 2019; Grabowski et al., 2001). One of the earliest discovered forms of FAD is the *Dutch* variant characterized by an early-onset, severe CAA with recurrent and fatal intracerebral hemorrhages by 50 years of age. The deposition of amyloid in the cerebral vasculature is associated with an unique clinical feature causing recurring seizures (van Duinen et al., 1987; Haan et al., 1990; Luyendijk et al., 1988; Van Broeckhoven et al., 1990). In contrast, at the same locus, the Arctic variant mutation leads to late-onset AD with an early generation of small Aβ assemblies with increased stability (Lam et al., 2011; Nilsberth et al., 2001; Päiviö et al., 2004; Whalen et al., 2005). Most of these mutations lead to amyloid burden except for *Osaka* mutation that enhances intraneuronal accumulation of Aβ but no extracellular amyloid deposits (Tomiyama et al., 2008). Further details about these interesting AD features are provided in **Section 3.3.1.2.2**. Additionally, while *Dutch*, *Italian*, *Artic* mutations were reported to decrease the $A\beta_{42}/A\beta_{40}$ ratio and change total secreted Aβ whereas

the *Iowa* (D694N) mutation instead of changing $A\beta_{42}/A\beta_{40}$ ratio, accelerate their polymerization (Grabowski et al., 2001; Iwanowski et al., 2015; Mok et al., 2014). Thus, mutations occurring in the same domain of Aβ conduct to different clinical expression and distinct neuropathology.

3.3.1.2.2 FAD mutation increasing Aβ oligomerisation

The ***Osaka* mutation** was initially found in a Japanese pedigree where only homozygous carriers suffer from severe dementia, indicating that this mutation is recessive (Tomiyama et al., 2008). This mutation consists in the deletion of codon 693 of the APP gene, resulting in mutant Aβ that lacks the 22nd glutamate ($A\beta_{osa}$). Human *Osaka* carriers have AD-like cognitive deficits in the absence of cerebral amyloid plaques (Kulic et al., 2012; Tomiyama et al., 2008; Tomiyama and Shimada, 2020). Thus, accumulated Aβ that is usually found within senile plaques is not a prerequisite for the disease progression. Instead, small oligomeric aggregates of Aβ may play a key role in the onset and progression of the disease. These mechanisms were experimentally confirmed by previous *in vitro* studies revealing that *Osaka* mutation has a very unique characteristic that promotes Aβ oligomerization but does not form amyloid fibrils (Jang et al., 2013; Poduslo and Howell, 2015). Furthermore, the *Osaka* mutation led to an accumulation of intracellular Aβ rather than extracellular Aβ deposition resulting in an early neuronal dysfunction (Jang et al., 2013; Kulic et al., 2012; Ovchinnikova et al., 2011; Umeda et al., 2017). Transgenic mice expressing $A\beta_{osa}$ displayed intraneuronal accumulation of Aβ oligomers followed by synaptic and cognitive impairment, Tau hyperphosphorylation, glial activation and neurodegeneration but not amyloid plaques (Kulic et al., 2012; Tomiyama et al., 2010; Tomiyama and Shimada, 2020). Recently, for the first time, a prominent Tau burden was found in *Osaka* patients compared to early and late SAD patients (**Figure 34**) indicating that $A\beta_{osa}$ triggers Tau accumulation at early stage of the disease without forming senile plaques (Shimada et al., 2020). $A\beta_{osa}$ can exert its toxicity in different biological compartments either by extracellularly damaging synapses or by causing intraneuronal Aβ accumulation that is highly toxic for the neuron.

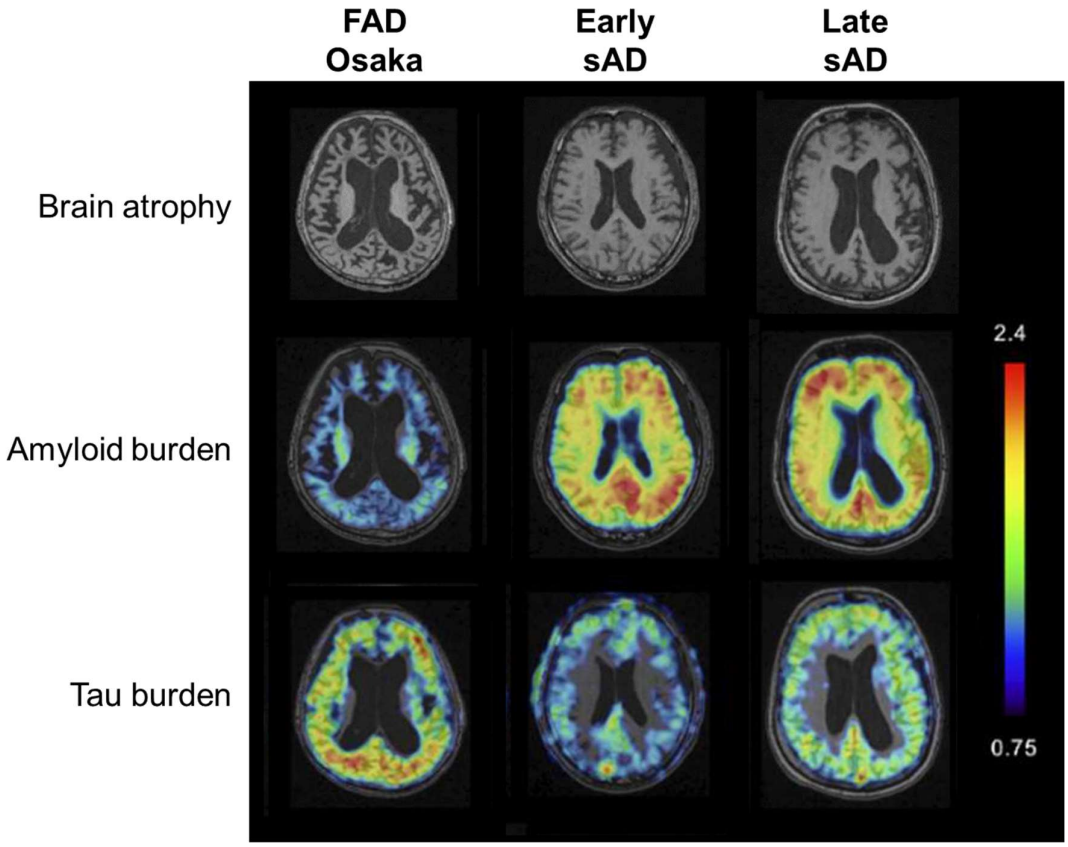

Figure 34: Characteristic features of Osaka-FAD patients compared to sporadic AD patients.

Anatomical scans, amyloid PET using ^{11}C-PiB tracer and Tau PET using ^{11}C-PBB3 tracer were obtained from a patient with familial Alzheimer's disease with Osaka mutation (FAD Osaka); a patient with early sporadic Alzheimer's disease (early SAD) and a patient with advanced stage SAD (late SAD). The Osaka-FAD patient had severely advanced brain atrophy including most of the cerebral cortex and brain stem resulting in prominent ventricular enlargement. Only negligible amounts of amyloid deposition were detected in cerebral cortex whereas both the early and advanced SAD patients had highly elevated amyloid burden. In Osaka-FAD patient, Tau burden was observed in the cerebral cortex and the cerebellar cortex, whereas the SAD patients had much less tau accumulation. Adapted from (Shimada et al., 2020).

3.3.1.2.3 FAD mutation leading to protective properties

Previous studies have indicated that the Aβ N-terminal domain is non-toxic (Forest et al., 2018; Whitson et al., 1989). Indeed, the hydrophilic N-terminal domain was found to exhibit neuromodulatory agonist-like properties through binding to nicotinic acetylcholine receptors that can rescue LTP inhibition and enhance contextual fear conditioning performance in exposed WT mice (Lawrence et al., 2014). FAD-associated mutation in N-terminal domain of Aβ can either inhibit its naturally benefic effects, such as *English* (H6R), *Taiwan* (D7H) or *Tottori* (D7N) mutations, or enhance

the protective properties of this domain. Missense mutation at the second amino acid residue of the Aβ sequence was reported to have a crucial dual impact on AD risk. The substitution of the alanine to valine (A2V) mutation is AD causative with amyloid brain deposition at homozygous state and protective at heterozygous state (Di Fede et al., 2016, 2012, 2009; Murray et al., 2016; Zheng et al., 2015). In contrast, the substitution of the alanine to threonine (A2T), called ***Icelandic* mutation**, has been reported to protect against AD-like cognitive defects by reducing Aβ aggregation properties and reversing Aβ neurotoxicity (Benilova et al., 2014; Guyon et al., 2020; Jonsson et al., 2012; Maloney et al., 2014). This mutation reduces the cleavage of APP by BACE1 lowering Aβ accumulation *in vitro* (Kero et al., 2013; Maloney et al., 2014). These findings were consistent with lower monomer concentration found in the plasma of A2T carriers providing protection against AD (Bussy et al., 2019; Martiskainen et al., 2017). Regarding the formation of mutated Aβ ($Aβ_{ice}$) oligomers, an *in vitro* study showed that it forms oligomers with lower molecular weight than wild type Aβ (Limegrover et al., 2021). Decreased binding affinity of these oligomers for synaptic receptors was found and inhibition of cellular vesicle trafficking was reported, indicating that $Aβ_{ice}$ is able to modulate cellular trafficking rate (Limegrover et al., 2021). Recently, knock-in rats carrying the *Icelandic* mutation were generated to study the effect of *Icelandic* variant on APP metabolism (Tambini et al., 2020). Western blot analysis of young rat brain homogenates showed an increase of α-processing with higher levels of sAPPα and a reduction of β-cleavage with lower levels of sAPPβ and CTFs- β suggesting that this variant favors the non-amyloidogenic pathway by affecting APP cleavage enzyme and reducing the amyloidogenic pathway (Tambini et al., 2020). Although the protective effect of this variant was confirmed, one dementia case was reported. Neuropathological analysis of the 104-years-old patient showed little amyloid pathology and dementia (Kero et al., 2013). Dementia was attributed to likely hippocampal sclerosis rather than AD-causal features and slight parenchymal plaque pathology suggested that this variant protects against amyloid pathology and AD.

At the same locus, A2V and A2T (*Icelandic*) mutations differs in biophysical behaviors including the kinetics of aggregation, the initial monomer conversion to an aggregation prone state, the abundances and size of oligomers, and adopted conformations (Murray et al., 2016; Zheng et al., 2015). Difference in the evolution of the secondary structures also results in fibrils of different morphologies (Colombo et al., 2017). These distinct features have been shown to differently influence synaptic activity (Murray et al., 2016). These point mutations affected differently the N-terminal domain of Aβ. A comparative study suggested that the conformational landscape of Aβ monomer contributing to the early-stage aggregation mechanism differs between the two mutated forms of Aβ (Das et al., 2015). They showed that the A2V-$Aβ_{42}$ monomers engaged the N-terminus in interaction with the central and C-terminal region of Aβ causing a hydrophobic cluster (Das et al., 2017, 2015; Murray et al., 2016). In contrast,

the A2T-$A\beta_{ice}$ N-terminus is preferentially engaged in an unusual ionic interaction that hinders the stabilization of the β-hairpin conformation and inhibits formation of small synaptotoxic species serving as aggregation seeds. This comparative study reported strong evidences that Aβ sequence changes impacting the nucleus site for Aβ monomer misfolding contribute to variable aggregation pathway even if the mutation occurs at the same locus (Hatami et al., 2017). Interestingly, although Aβ conformations are different between both mutations, cross-interactions with wild-type Aβ through formation of heterodimers were shown to exhibit similar properties. Mixtures of both wild-type Aβ x A2V-Aβ and wild-type Aβ x A2T-$A\beta_{ice}$ peptides were reported to postpone fibril formation and protect against their toxicity (Nguyen et al., 2016). The mechanism by which this Aβ variant shift wild type Aβ toxicity is unclear. Das et al. suggested that the inhibition of toxicity may rely on the intrinsic structure of the heterodimers (Das et al., 2017). Determining how subtle changes in the primary structure of Aβ translate into either dramatic or benefic changes will provide essential insight into AD etiology.

	Name	Mutation	Neuropathological features				APP processing		
		APP	MRI	NFTs	Amyloid plaques	Concomittant pathology	Intracellular Aβ	α-CTF	β-CTF
Mutations affecting α-cleavage	Swedish	KM670/ 671NL	Cortical atrophy CBF reduction	X	X	Lewy bodies CAA	Increase	unchanged	Increase
	Tottori	D678N	Cortical atrophy CBF reduction	Not avalaible		Non	unchanged		unchanged
	Taiwanese	D678H	Cortical atrophy CBF reduction			Non	unchanged		Increase
	Leuven	E682K	Hippocampal atrophy			Non		unchanged	Increase
	-	K687N	cortical atrophy			Non		Decrease	Decrease
	Flemish	A692G	Cortical atrophy	X	X	CAA hemorrhagic infarction		unchanged	Increase
N-terminal domain of Aβ	Icelandic	A673T	Protective			Non			Decrease
		A673V	Cortical atrophy	X	X	Non			Increase
Hotspot of mutations	Osaka	E693Δ	Cortical atrophy CBF reduction Cortical glucose metabolism reduction	X		Non	Increase		
	Artic	E693G	Cortical atrophy CBF reduction	X	X	CAA	Increase		
	Italian	E693K	Cerebral hemorrhages Multi-infarct encephalopathy Leukoaraisosis		X	CAA			
	Dutch	E693Q	Cerebral hemorrhages		X	CAA	Increase	Increase	Increase
	Iowa	D694N	Cerebral hemorrhages	X	X	CAA		unchanged	unchanged
Mutations affecting γ-cleavage	Austrian	T7141		X	X	CAA	Increase	Increase	Increase
	German	V715A	Parieto-occipital hypometabolism	Not avalaible		Non		unchanged	unchanged
	French	V715M	Cortical atrophy Hypometabolism			Non	Decrease	Increase	unchanged
	Iberian	I716F	Cortical atrophy CBF reduction	X	X	Lewy bodies CAA			Increase
	-	I716T		Not avalaible		Non			unchanged
	Florida	I716V	Cortical atrophy			Non		Decrease	unchanged
	Indiana	V717T		X	X	CAA		Increase	
	-	V717G	Cortical atrophy	X	X	CAA		Decrease	
	London	V717I		X	X	Lewy bodies CAA	Increase	Increase	Increase
	Indiana-2	V717L	Cortical atrophy CBF reduction	X	X	CAA		Increase	Increase
	Australian	L723P	Cortical atrophy	Not avalaible		Non			
	-	K724M	Cortical atrophy			Non			
	Belgian	K724N	Cortical hypometabolism		X	hemorrhage		unchanged	unchanged

Table 2: Summary of FAD mutations features (adapted from (Bi et al., 2019))

Aβ				Aggregation		AD-like feature				Transgenic mice avalaible
Level of Aβ40	Level of Aβ42	Total secreted Aβ	ratio Aβ42/40	Aβ40	Aβ42	Microglia activation	Astrocyte activation	Neuronal loss	Synaptic loss	
Increase	Increase	Increase	unchanged			X	X	X	X	Yes
unchanged	unchanged	unchanged	unchanged		Increase					No
Increase	Increase	Increase	Decrease	Increase	Decrease					No
Increase	Increase	Increase	Decrease							No
Increase	Increase	Increase	Increase	Increase						No
Increase	Increase	Increase	Increase	Decrease	Decrease	X	X	X		No
Decrease	Decrease	Decrease	unchanged	Decrease	Decrease					Yes
Increase	Increase	Increase	unchanged	Increase		X	X	X		No
Decrease	Decrease	Decrease	unchanged	Increase	Increase	X	X		X	Yes
unchanged	Decrease	Increase	Decrease	Increase	Increase		X	X		Yes
unchanged	Decrease	Increase	Decrease		Increase					No
Decrease	Decrease	unchanged	Decrease	Increase		X	X			Yes
unchanged	unchanged	unchanged	unchanged	Increase	Increase		X			
			Increase			X	X	X		Yes
			Increase							
		Decrease	Increase							
Decrease	Increase	Decrease	Increase			X	X	X		No
Decrease	Increase	unchanged	Increase							
unchanged	Increase	unchanged	Increase							No
Decrease	Increase		Increase							Yes
Decrease	Increase		Increase							Yes
Decrease	Increase	Decrease	Increase			X		No		Yes
Decrease	Increase		Increase							Yes
			Increase							Yes
Unchanged	Increase		Increase							No
Decrease	Increase		Increase							

3.3.2 Heterogeneity of neuropathological lesions in FAD

The phenotypic polymorphism associated with FAD mutations within Aβ relies on the preferred conformational states adopted by Aβ variants. Each conformation favors cellular targets and induces particular pathology outcomes. There are multiple evidence showing polymorphic Aβ aggregation. A comparative analysis of the aggregation behavior of 11 synthetic $A\beta_{40}$ variants showed distinct kinetic aggregation patterns and conformational polymorphisms resulting in distinct structural variants of synthetic Aβ fibrils (**Figure 35**) (Hatami et al., 2017). Isolation and characterization of fibrils from patients also suggest that fibril morphology varies from patient to patient (Iadanza et al., 2018).

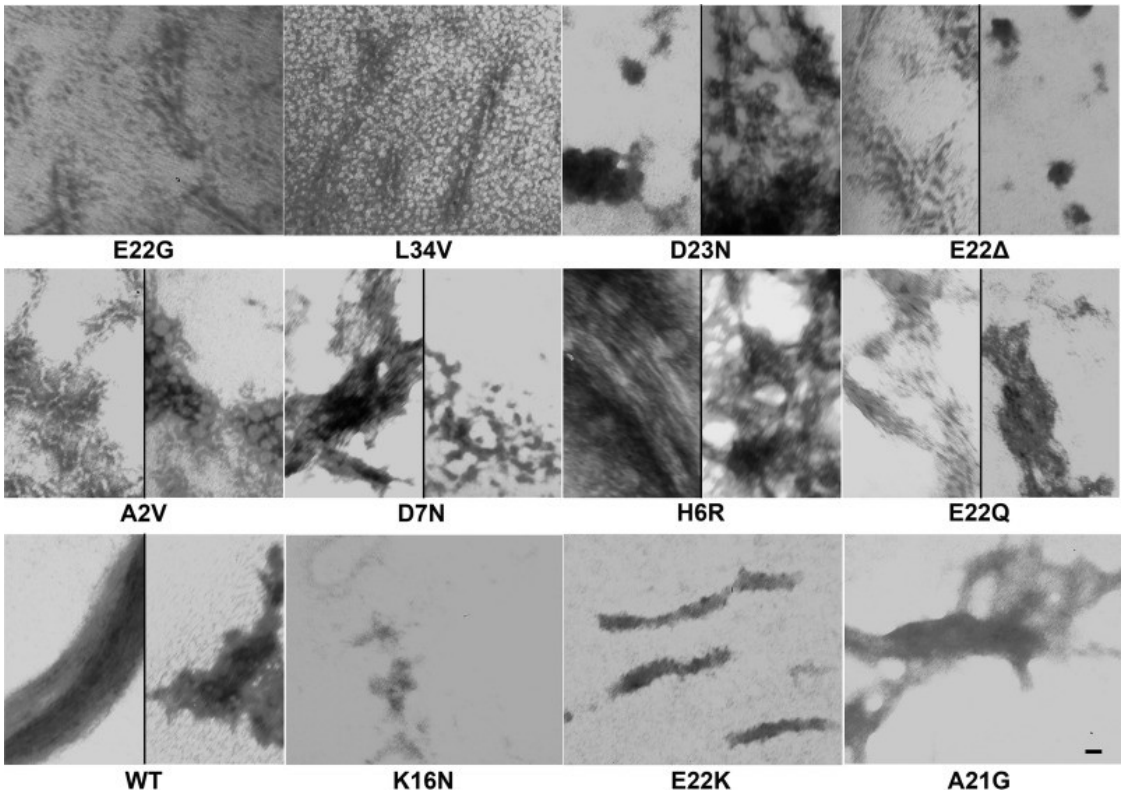

Figure 35: Various synthetic $A\beta_{40}$ variants lead to different morphologies of Aβ aggregates

One of the most interesting features of the FAD mutations within the Aβ sequence is that they lead to distinct aspect of neuropathological lesions that can be detectable by histopathological analysis in humans and animal models. It is widely accepted that the morphology of Aβ plaques differ across APP transgenic mouse models. While APP23 mice exhibit fairly large Aβ deposits consisting of congophilic amyloid cores with diffuse penumbras and diffuse Aβ deposition, $APP_{swe}/PS1_{dE9}$ mice develop small, compact and highly congophilic Aβ deposits (Heilbronner et al., 2013). The induction of different Aβ morphotypes in a given transgenic mouse was also obtained after intracerebral inoculation of

aggregated Aβ-containing brain extracts from two different sources (Condello et al., 2018; Stöhr et al., 2014; Watts et al., 2014). These experimental transmissions of amyloidosis were widely used to demonstrate the concept of prion-like templated misfolding of Aβ. In human studies, Di Fede et al. compared neuropathological and biochemical phenotypes in patients with FAD and SAD (Di Fede et al., 2018). They found different aspects of Aβ deposits between FAD patients and between FAD and SAD patients (**Figure 36**). Interestingly, they also assessed the pattern of expressed Aβ isoforms and showed different expressed levels in AD subtypes, suggesting that Aβ depositions may differ in biochemical composition (Di Fede et al., 2018). The different Aβ morphotypes and soluble Aβ profiles allowed defining distinct AD molecular subgroups.

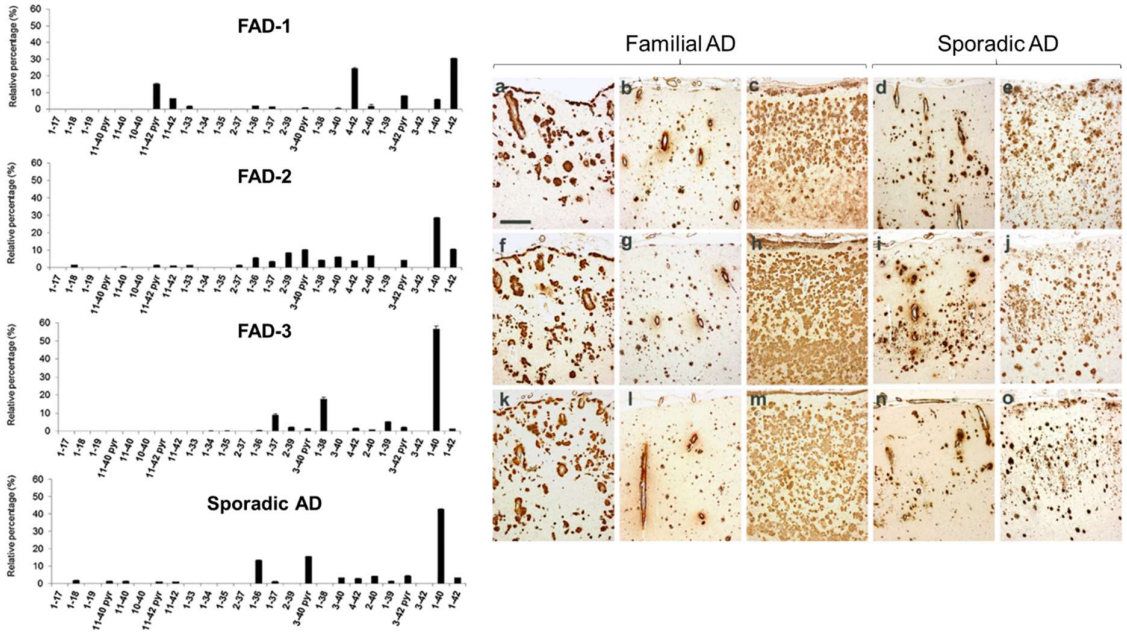

Figure 36: Molecular subtypes in familial and sporadic AD

(**Left panel**) Relative percentage of Aβ isoforms measured in human brains defined a representative profile for each AD subgroup (n = 3, mean relative percentages ± SEM). (**Right panel**) Immunohistochemical study (4G8 antibody) performed in: the frontal cortex (**a,b,c,d,e**); temporal cortex (**f,g,h,i,j**); occipital cortex (**k,l,m,n,o**). Differences in amyloid-related pathology of AD cases: (**a,f,k**) APP_{A673V} (FAD-1); (**b,g,l**) APP_{A713V} (FAD-2); (**c,h,m**) $PS1_{P117A}$ (FAD-3); (**d,i,n**) sAD carrying the ApoE ε4/ε4 genotype ; (**e,j,o**) sAD carrying the ApoE ε3/ε3 genotype. Scale bar = 400 um. Adapted from (Di Fede et al., 2018)

Aβ depositions can also differ in binding of amyloid conformation-sensitive dyes. The use of conformation-sensitive dyes previously allowed to discriminate various prion strains. A new class of amyloid dyes called the luminescent conjugated oligothiophenes (LCOs) was developed. These flexible amyloid-binding dyes exhibit spectral fluorescence emission properties depending on its binding to the

β-sheet structures of amyloid fibrils, which offers the possibility to assess amyloid conformation. Rasmussen *et al.* used this approach to decipher the dominant Aβ conformation in postmortem brain tissues from 40 cases of FAD and SAD (Rasmussen et al., 2017). They found different LCO amyloid spectra among FAD and SAD subtypes and defined clusters of patients with similar amyloid conformational variants, suggesting that the clinical heterogeneity among AD patients is due to variation in the molecular architecture of aggregated Aβ. In FAD cases, mutations within the Aβ sequence seemed to define distinct Aβ prion conformations responsible for a unique pathology in the carriers. Investigation of amyloid structural heterogeneity in patients bearing the *Swedish*, *Dutch* or *Arctic* mutations (occurring at the same locus) showed high inter-subject variability and low intra-subject variability that allowed distinguishing patients with high sensitivity (Condello et al., 2018). These findings strongly support the hypothesis of the existence of Aβ prion strains in FAD. The existence of intra-subject variability suggests that Aβ prion conformations are more complex and may not give rise to a unique pathology. Conformational differences of variant Aβ morphotypes using conformation-sensitive amyloid-binding dyes were also assessed in APP transgenic mouse models. While fluorescence images revealed bright yellow–greenish colors for the Aβ deposits in APP23 mice, the amyloid plaques in $APP_{swe}/PS1_{dE9}$ mice showed a reddish appearance (Heilbronner et al., 2013).

The heterogeneous molecular architecture of Aβ variants observed in FAD patients allows identification of different molecular strains of Aβ aggregates responsible for the distinct subtypes of AD. Importantly, although this phenotypic diversity is most striking in FAD, this methodology can be extended to the SAD that display a larger heterogeneity in clinical presentations. The link between Aβ conformation and clinical phenotypes remains unclear but still evident. There is an immediate need to develop non-invasive tools that can detect pathological Aβ conformations in AD patients. Tools that are more sensitive will result in earlier AD detection, providing a longer period for therapeutic interventions.

3.3.3 Complexity of conformations

As AD is a proteinopathy, conformational changes of pathogenic proteins were suggested to be the key event of AD pathological process that may explain the heterogeneity among AD patients. Despite the emerging interest in Aβ conformations, the remaining question is, whether individual express a unique Aβ conformation or multiple Aβ conformations. Spectral discrimination of distinct Aβ conformations in AD patients using conformation-sensitive fluorescent probes showed that complete intra-subject homogeneity of emission spectra is not found among all patients suggesting that some patients may exhibits more than one Aβ conformation (Condello et al., 2018). Diversity in Aβ fibrils along the disease evolution supports the idea of the co-existence of a mixture of several conformations

in a single brain. It is crucial to develop therapy that can target the specific deleterious Aβ conformation responsible for pathological effect in each individual. The conformational diversity in one strain is complex. Amyloid proteins are able to form hetero-oligomeric assemblies (Das et al., 2015). Cross-interaction between amyloid conformations may give a higher impact on AD pathophysiology than a unique conformation as suggested by the seeded properties of Aβ (Heilbronner et al., 2013; Jucker and Walker, 2011; Walker et al., 2016; Watts et al., 2014). Understanding the underlying mechanism by which the dominance/recessiveness of amyloid strains is governed may highlight new therapeutic targets. The underlying genetic mechanism associated with FAD mutation can allow the studying this concept. Most Aβ mutations caused familial AD with dominant inheritance. In this case, wild-type form of Aβ subsisted with the mutated form of Aβ resulting in a large Aβ population diversity composed of homo-interaction and hetero-interaction. The impact of the mutated forms on wild-type form can be either deleterious or beneficial. Giving the importance of conformation-interaction in a prion-like mechanism of AD pathogenesis, there is an important need to look for dominant non-deleterious amyloid strains that can be used to interfere with pathological amyloid conformation.

Chapter 4 – Experimental evaluation of brain function and diffusion parameters by MRI

4.1 Principle of MRI

Magnetic resonance imaging (MRI) is a non-invasive and non-ionizing technique based on the principle of nuclear magnetic resonance (NMR). This mechanism arises from a fundamental quantum property of atomic nuclei (electron, proton, and neutron) to possess a "spin" angular momentum, which has been discovered in 1946 by Bloch and Purcell. The spin represents the magnetic moment of the particle in rotation on itself. For clinical MRI acquisitions, the hydrogen nucleus (a single proton) is widely used because of its abundance in water and fat. The hydrogen atom is composed of a positive and a negative pole capable of acting like a bar magnet with a north and a south pole that allow to detect the NMR signal. At rest, the orientation of protons is random but they can be influenced by an external magnetic field. MRI scanner is a giant magnet that generate a strong magnetic field called B0. When protons are placed in this magnetic field, their spin can either align with the field (parallel) or flip to orient against the direction of the field (anti-parallel) (**Figure 37A**). In addition to aligning with the magnetic field produced by the MRI scanner, the spins also rotate along their own axes like a stable spinning top in rotation. This movement is called **spin precession**. The speed of precession is proportional to the strength of the applied magnetic field B0 and depends on the gyromagnetic ratio (γ), which is a constant of the proton. It is characterized by the frequency of precession (ω) defined by the Larmor equation as:

$$\omega = \gamma \cdot B0$$

When a radiofrequency (RF) radiation is applied to the frequency of precession of the spin, a **phenomenon of nuclear resonance** occurs (**Figure 37B**). The transfer of energy between the RF pulses and the group of spins within the magnetic fields induces the rotation of the spin in phase toward the transverse plane following a flip angle α. The angle depends on the strength and duration of the RF pulse. This brief synchronization also called **excitation stage** is the transverse magnetization of the protons causing the RMN signal. When the RF radiation is interrupted, the protons will recover or return to their original state of orientation with the magnetic field and asynchronous precession: it is the **relaxing stage** (**Figure 37C**)**.** This return of each nucleus to its thermal equilibrium is going with the emission of RF radiation called Free Induction Decay (FID) signal, which constitute the signal recorded by RMN (**Figure 37D**).

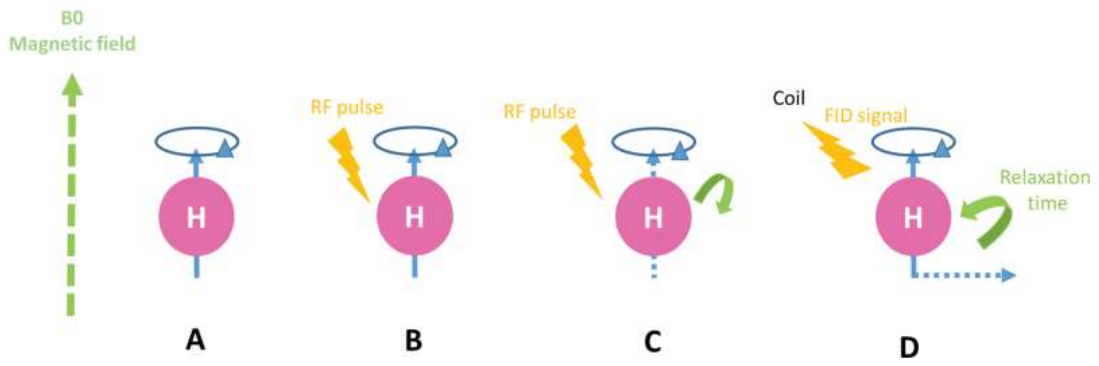

Figure 37 : Principle of MRI

(A) When placed in a strong magnetic field B0, protons align themselves parallel or antiparallel with the direction of B0. (B) The application of a RF pulse B1 at the same frequency of B0 allows the longitudinal magnetization to tilt away from B0 (resonance). (C) Once the RF signal stops, spinning protons returns to equilibrium (relaxation) such that it aligns again with B0. (D) During relaxation, proton loses energy by emitting a RF signal Free Induction Decay (FID) which can be measured by a coil placed around the object being imaged and subsequently reconstructed to obtain 3D gray-scale MR images. From (Ella et al., 2019).

Depending on the chemical properties of a tissue, spins exhibit different relaxation properties. The **longitudinal relaxing** is the regrowth of the longitudinal element following a characteristic time constant T1. T1 contrast is better to represent tissue as it depends on the mobility of particles containing hydrogen nucleus. T1 is shorter for biggest particles. Along time, the magnitude of the magnetization decreases following the transversal axis. The **transversal relaxing** is due to the dephasing of spin. Indeed, spin-spin interactions contribute to the heterogeneity of magnetic field and frequency of precession. The difference in spin frequency causes an acceleration of the dephasing. The fall of the transversal magnetization follows an exponential curve characterized by the time constant T2, which is shorter than T1. T2* represents the local inhomogeneity of the magnetic field and the tissue susceptibility. During relaxation, protons loose energy by emitting the FID signal detected by the receiver coil of MRI scanner, which can be reconstructed to obtain three-dimensional (3D) gray-scale MR images. Localization of the signal in the 3D space is ensured by magnetic field gradients. First, a gradient to select slice on the *z* axis of the tissues is applied, then the second gradient encodes the frequency of the spins towards *x* axis. Finally, the third gradient encodes the phase of spins belonging to the same column through the *y* axis of the tissue. The MRI acquisition allowed filling the K-space matrix arising from the Fourrier Transform of the spatial coding of the frequential image.

Finally, the acquisition parameters in MRI sequence have to be chosen to correspond to the constraints of the spatial resolution (voxel size) and the desired signal quality (signal-to-noise ratio, SNR). To create an average image, the emission of FID signal is repeated several times and the time between two excitatory RF pulses is called the repetition time (TR). The TR represents the limit of extension of the longitudinal magnetization regrow. Another parameter called echo time (TE) can be set during the acquisition of MRI sequence. The TE is the time between the beginning of the first RF pulse (excitation pulse) and half TR (signal peak). In addition to the choice of RF pulses, these two parameters allow to weight contrast of the future image. Indeed, when TE and TR are short, the relaxation properties will follow the T1 relaxing constant. In contrast, long TE and TR are sensitive to the T2 relaxing constant. The various relaxation properties of the protons in the tissues toward T1 and T2 relaxing constant provide different contrasts of the image (**Figure 38**). When looking at anatomical images, T1 weighted imaging produces high intensity within the white matter (bright), medium intensity within the gray matter and low signal intensity within the brain ventricles (dark). In contrast, white matter is dark on T2 weighted imaging and the grey matter is bright.

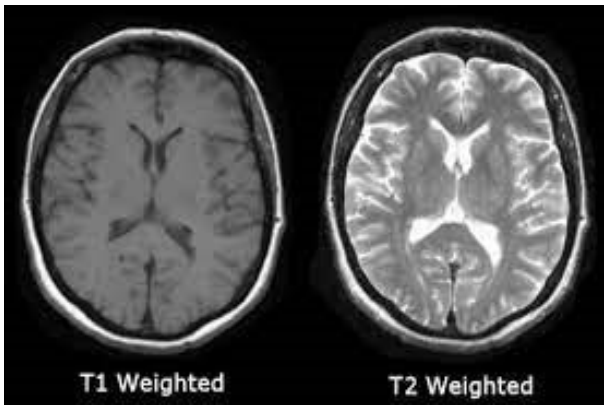

Figure 38: T1 and T2-weighted images

CSF is dark on T1-weighted imaging and bright on T2-weighted imaging.

Modification of acquisition parameters will also provide different types of images that can be used to detect several pathological signs. Indeed, MRI is a highly multimodal imaging approach. MRI can be used to measure indirectly brain activity through the detection of functional change associated with blood flow oxygenation. The functional MRI (fMRI) is based on the ability of deoxyhemoglobin to act as an endogenous contrast agent that reduces the signal in T2-weighted images when its concentration increases. Encoded images are used to reveal functional connectivity between brain regions. The random movements of water protons can also be detected by diffusion weighted imaging (DWI) sequences revealing anatomical details about tissue architecture and mapping the main white matter tracts of the brain. The detection of brain metabolites is also possible towards chemical exchange

saturation transfer (CEST) imaging. These three sequences have been largely used to elucidate the mechanisms of neurodegenerative disorders.

4.2 Resting-state fMRI

4.2.1 BOLD signal

The fMRI is an indirect measure of brain activity in high temporal resolution. It relies on the facts that neuronal activations are tightly coupled with cerebral hemodynamic responses. Indeed, neuronal metabolism depends on the blood oxygen level because the production of energy to form adenosine triphosphate (ATP) from glucose is strongly aerobic. The hemoglobin (Hb), a protein that have magnetic properties, carries molecules of oxygen (O_2) in the blood. Two states of Hb can be found in the blood: oxyhemoglobin, when O_2 is attached to Hb, or else deoxyhemoglobin (dHb). Neuronal activations induce an increase in O_2 consumption and blood flow. As increase in blood flow is more important than elevated O_2 consumption, neuronal activations induce an increase in oxyhemoglobin compared to deoxyhemoglobin level in activated regions (**Figure 39**). The ability to detect this change in fMRI relies on the fundamental difference in the magnetic properties of oxyhemoglobin and deoxyhemoglobin. While diamagnetic oxyhemoglobin negligibly affects the magnetic resonance, the reduced level of paramagnetic deoxyhemoglobin, which acts as an endogenous contrast agent detected by MRI, temporally increases T2* signal. This is called the blood-oxygen-level dependent (BOLD) signal discovered in 1990 by Ogawa et al. A slight T2* weighted change around 1-5% occurs (Gore, 2003). Thus, BOLD contrast is weak and MRI acquisition is needed to be repeated several times in order to map functional changes. Gradient echo-echo planar imaging (GE-EPI) sequence that has a high acquisition speed was used as the gold standard to maximize BOLD sensitivity.

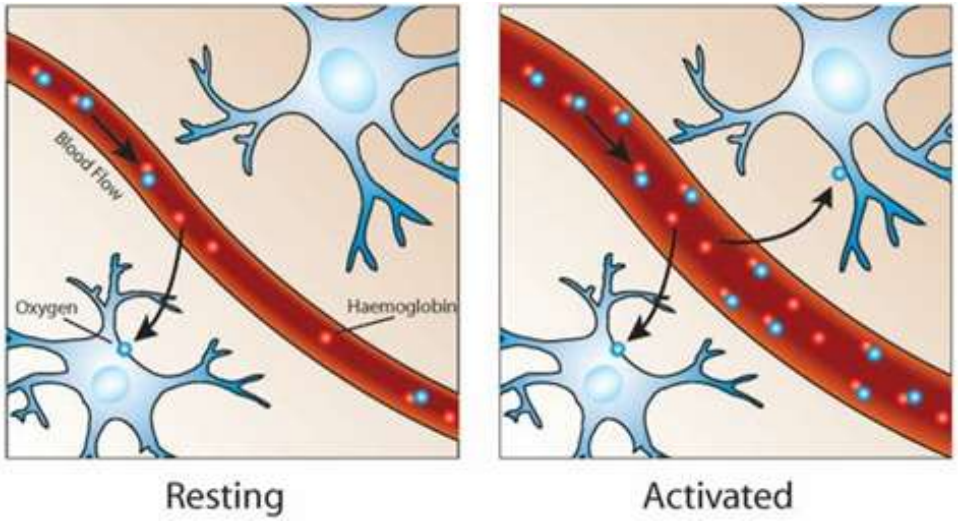

Figure 39: BOLD signal mechanism, magnetic susceptibility to vascular oxygenation.

Following brain activity, the cerebral blood flow is increased, leading to an increase of oxyhemoglobin and a decrease of deoxyhemoglobin that reveal the BOLD signal. Oxygen is represented in blue and hemoglobin in red.

The BOLD signal has been widely used in humans and in rodents for functional exploration of the brain during a task or at rest. The BOLD signal can be expressed in response to various stimulations such as a sensory stimulation or performance of a motor/cognitive task. The hemodynamic response function (HRF) characterizes the BOLD signal generated following a stimulus. The HRF has been described to follow a sigmoid curve starting with a small initial dip, followed by a tall peak, and then a variable post-stimulus undershoot (Barth and Poser, 2011) (**Figure 40**). The initial dip, commonly observed at very high field (from 7.0T) might represent the gap between the time of neuronal activations and the measured hemodynamic response. The mechanism causing this interval is unclear and two possible theories have been speculated: the early extraction of blood oxygen and/or an increase of local cerebral blood volume. During the main peak of the BOLD signal, neurovascular coupling contributes to a local increase of cerebral blood flow and volume to meet immediate metabolic needs resulting in an increased ratio of oxygenated to deoxygenated hemoglobin with increased MR signal constituting the BOLD response. The post-stimulus undershoot is the decrease of the BOLD signal after the stimulus. It may reflect the slow arterial blood volume recovery and an increase of the cerebral blood flow overcompensating for the oxygen increase. Interestingly, when stimuli are repeated, the positive dominant peak becomes a plateau and a small overshoot is observed. To conclude, the BOLD signal is assumed to indirectly measure the neuronal activity in a process called neurovascular coupling.

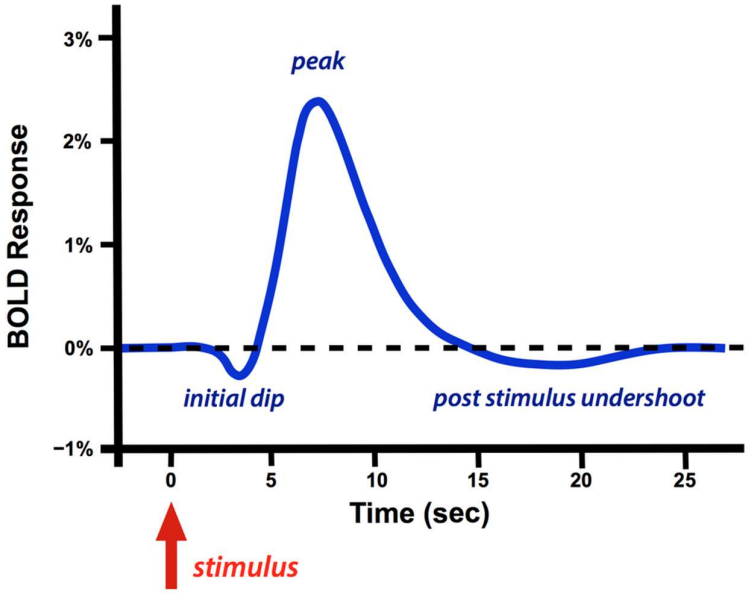

Figure 40: Hemodynamic Response Function (HRF)

Following a stimulus, the typical hemodynamic response demonstrates a small negative initial dip then a positive dominant peak and, finally, a post-stimulus undershoot.

In the absence of an overt task, the measure of BOLD fluctuation allows to investigate how spatially distinct regions of the brain are functionally connected. This technique called resting-state fMRI is widely used to identify functional brain networks and to detect subtle functional changes in diseased brain.

4.2.2 From BOLD signal to resting-state functional connectivity

Functional connectivity (FC) between brain regions is defined as the level of co-activation in spontaneous neuronal activation patterns of these regions, measured through a hemodynamic response function (Buckner and Vincent, 2007; Greicius et al., 2003; Gusnard et al., 2001). The discovery that the functional communications between brain regions can be measured during rest, provided new important insights in the core organization of the human brain (van den Heuvel and Hulshoff Pol, 2010). Biswal and colleagues demonstrated for the first time, a high correlation between the neuronal activation of the left and right hemispheric regions of the primary motor network during rest, revealed by the measure of fMRI BOLD time-series correlation in these regions (Biswal et al., 1995, 1997). These correlations originate from the low frequency oscillations (~ 0.01–0.1 Hz) of fMRI signal during rest emerging from anatomically separated brain regions (Biswal et al., 1995, 1997; Cordes et al., 2001; Lowe et al., 2008). Following these pioneering observations, several studies have replicated this technique to reveal multiple connected brain areas. In 2001, Raichle et al. described a large-scale

brain network of interacting structures that ensure the baseline state of brain areas called default mode network (DMN) (Raichle et al., 2001). Other functional networks such as the primary visual network or cognitive networks were further reported and will be described in **Section 4.2.4**. Together, these findings suggest that during rest, the brain is not passive but rather brain regions keep communicating in a spontaneously coordinated manner to elaborate large-scale organization of brain connected areas. This gave rise to the emerging concepts of resting-state functional networks.

4.2.3 Analysis of functional MRI

4.2.3.1 Preprocessing

The extraction of the BOLD fMRI signal is crucial to measure the underlying neural activity. To ensure the validity and the interpretability of results, fMRI raw data undergo several critical preprocessing steps described below. The preprocessing steps aim at reducing nuisance signals and noise, to remove particular imaging artifacts and to ensure the accurate anatomical localization of signals. Preprocessing reduces false positive signal without inducing excessive false negative signal. Preprocessing steps can be divided into two groups addressing either the **signal localization** by co-registration and spatial normalization or **artifacts** removal such as slice-timing correction, head-motion correction, and susceptibility distortion correction. Denoising of fMRI signal has been shown to enhance functional connectivity specificity in human and animal model studies (Grandjean et al., 2020).

- **Intra-subject registration**

MR sequences of a same subject are sometimes acquired during different sessions like in longitudinal studies, which results in head motion between the different protocol runs. An image registration process between sessions is necessary to merge aligned functional information. Anatomical misregistration across individuals can lead to false negatives correlation reducing statistical power.

- **Spatial normalization**

In order to enable group comparisons, all subject-space functional scans need to be aligned into a common space defined using a reference atlas or an average of anatomical images from the study. Inaccurate spatial normalization can, for instance, cause signal activation observed outside the brain.

- **Head motion correction**

Head motion occurs as slow degree changes from the original position of the head, for example, by involuntary movements of subjects. Motions cause a spatial misalignment in the source of the BOLD signal measured in all voxels. This artefact can generate the misinterpretation of the results of

activation and functional connectivity analyses. Head motion parameters can be estimated and removed from times series (Figure 41).

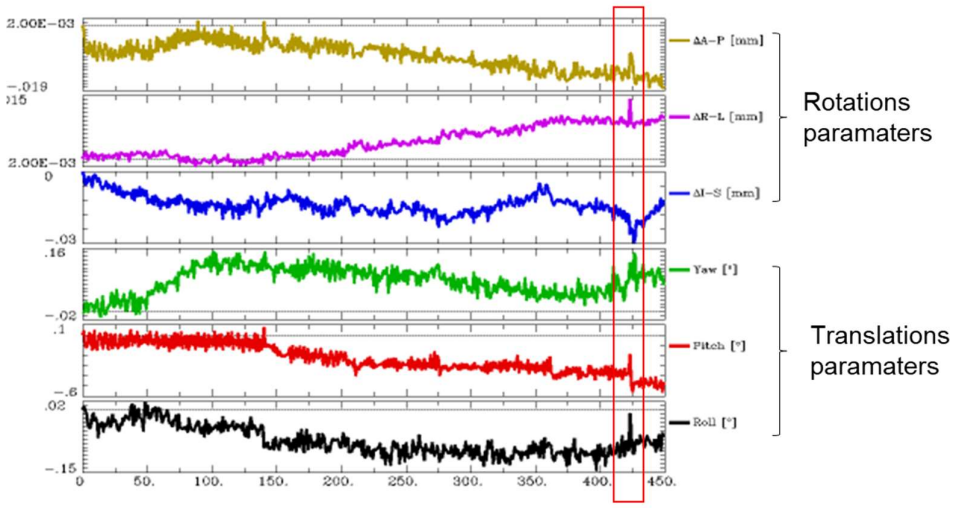

Figure 41: Estimation of head motion parameters

During EPI frame registration to the reference image, head motion parameters, combining 3 translation and 3 rotation realignment parameters, can be estimated and further saved into a matrix file. Motion spikes (red box) are then identified and excluded from time series.

- **Slice-timing correction**

Functional MRI images are the combination of multiple 2D slices into a single 3D volume. During MR acquisition, all brain slices cannot be acquired instantaneously resulting in an accumulation of offset delays between the first slice and all remaining slices equivalent to the repetition time. These temporal offsets between slices must be corrected in order to accurately analyze time series signal.

- **Spatiotemporal filtering**

Time series fMRI contain very slow frequency fluctuations that may be unrelated to the signal of interest. The goal of temporal filtering is to increase the SNR by choosing a lower and upper bound for a band-pass filter. Then, signal from frequencies outside the specified frequency will be removed. Resting functional connectivity has been shown to be most prominent between 0.01 to 0.1 Hz bands (Cordes et al., 2001).

- **Susceptibility distortion correction**

Fast MR acquisitions like EPI suffer from susceptibility distortion due to the inhomogeneity of high magnetic fields. An estimation of field variance map (also called voxel-shift map) during the acquisition allows correcting this artefact.

- **Calculation of confounds**

Confounds commonly include motion parameters, framewise displacement, spatial standard deviation of the data after temporal differencing, and global signals. Estimation of confounds can originate either from the addition of experimental time series such as physiological recordings and equipment-related noise or from statistical algorithm such as the component-based noise correction (CompCor) (Behzadi et al., 2007). This latter approach supposes that voxel time series with a relatively high temporal standard deviation is associated with physiological noise.

- **White matter/CSF signal removal**

Average signal from all voxels within a white or cerebro spinal fluid (CSF) mask is calculated. Mean white matter and CSF time series are removed from the raw data through linear regression. Vascular signal regression can also be performed.

Several tools has been implemented to perform the individual steps of preprocessing described above in human studies. These tools are readily available in software packages such as AFNI (Cox, 1996), ANTs (Tustison et al., 2014), FSL (Smith et al., 2004), Nilearn (Abraham et al., 2014), and SPM (Friston, 2007). Despite the wealth of accessible software, it can be difficult to switch from one to another one. Thus, pipelines that encompass the most of preprocessing steps has been developed in python library such as SAMMBA-MRI from our group (Celestine et al., 2020) and RABIES (Desrosiers-Gregoire et al., 2022). These tools are appropriate for preclinical studies.

4.2.3.2 Analysis of resting-state functional MRI data

Several methods to process resting-state fMRI data have been proposed: atlas-based correlation analysis, seed-based analysis (Andrews-Hanna et al., 2007; Biswal et al., 1995; Cordes et al., 2001; Fransson, 2005; Larson-Prior et al., 2009; Song et al., 2008) and spatial decomposition analysis including independent component analysis (Beckmann et al., 2005; Calhoun et al., 2001; van de Ven et al., 2004) and dictionary learning. All these approaches examine the existence and extent of functional connections between brain regions.

Seed-based analysis

Seed-based analysis is commonly used to find functional networks in the brain. This method is based on the extraction of average resting-state time-series of a region of interest (ROI) called the “seed” (Biswal et al., 1997; Cordes et al., 2001). The seed is a small area chosen by the experimenter that can be either a sphere corresponding to the coordinates of brain regions or a region from brain atlas. Then, functional connectivity is calculated as the correlation between resting-state time-series of the selected seed region and the resting-state time-series of all other voxels of the brain (**Figure 42**). This

voxel-wise analysis allows to explore all functional connectivity to a specific brain region revealing functional networks that share similar patterns of activity. The result of seed-based analysis is a connectivity map showing Z-scores for each voxel indicating the correlation strength of its time series with the time series of the seed. Spatial connectivity map is further statistically compared between individuals and between groups through dual regression analysis to identify subject-specific networks based on networks identified at the group level. The main limitation of this approach relies on the simplicity of the obtained result. Although functional connectivity maps provide a clear view of which regions the seed is functionally connected with, the functional connectivity is restricted to the seed region and do not allow to explore functional connections patterns on a whole-brain scale.

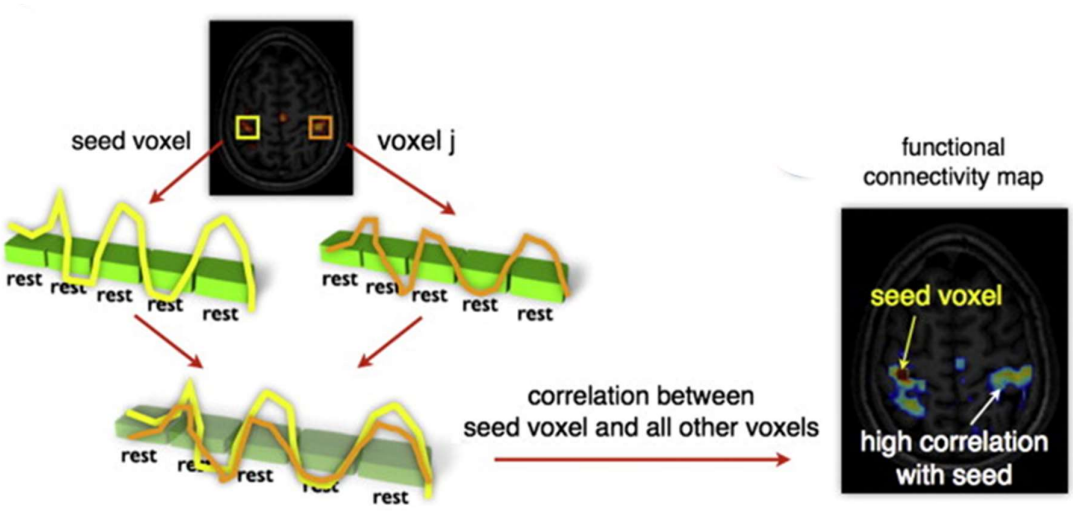

Figure 42: Principle of seed-based analysis (van den Heuvel and Hulshoff Pol, 2010)

Atlas-based correlation analysis

The principle of atlas-based correlation analysis is similar to seed-based analysis. Instead of extracting the signal from a unique seed, time series is extracted from a group of voxels based on an atlas parcelation. Correlation between the neuronal activity of several atlas-based brain areas allows to perform connectivity matrices and to evaluate the functional connectivity of each area.

Several "model-free" methods have been suggested to find general patterns of connectivity across brain regions. Here, we will described the two main algorithms that were developed to explore connectivity patterns without defining *a priori* seed region: **independent component analysis** and **dictionary learning**. Both approaches are based on the spatial decomposition of the whole-brain signal to reconstruct functional network.

- **Independent component analysis** (ICA) was the first computational algorithms developed to extract distributed sets of regions demonstrating correlated fluctuating activity in order to identify networks of functionally related regions in a blind-source manner. This approach suppose that the brain is organized into different spatial or temporal sources of resting-state signal called components that are maximally **independent** from each other. This powerful method is applied to whole-brain voxel-wise data and enable direct comparison between subject groups. The purpose of ICA is to find a linear representation of non-Gaussian data so that the components are statistically independent (Hyvärinen and Oja, 2000). Thus, a same region cannot be included in several networks. Yet various axonal projections and neurons within the same region are involved in different networks. As a result, ICA can only reveal networks with partial neuro-anatomical overlaps (Zhang et al., 2019).

- **Dictionary learning** aims at finding a sparse representation of the input data that can form a linear combination of elements called atoms instead of component. The decomposed fMRI signal is extracted in a dense matrix where the rows represent the time points and the columns contain the brain voxels. The dictionary relies on a sparsity principle meaning that instead of having independent atoms as in ICA method, a same voxel can belong to different atoms which maximizes the sparse representations of the dataset.

The main limitation of spatial decomposition approaches is that the number of components or atoms is determined prior starting the analysis leading to a potential artefact as it forces the algorithm to separate the brain into an estimated number of functional networks. Fortunately, strong overlap of multiple networks such as DMN or the primary motor network has been found using either seed-based analysis or ICA-based methods. This findings also suggest that the functional connectivity between brain regions during resting-state forms robust networks.

4.2.4 Functional network organization of the human brain

Since the discovery that communication between brain regions during rest can give rise to functional sub-networks, a wide range of functional resting-state networks has been described in the human brain (**Figure 43**) (Beckmann et al., 2005; Damoiseaux et al., 2006; Fox and Raichle, 2007; Raichle, 2011; Thomas Yeo et al., 2011). These resting-state networks consist of anatomically separated, but functionally linked brain regions that express a highly correlated neuronal activity during rest. The continuous integration of information across different regions of the brain play a key role in complex cognitive processes that are altered in several brain disorders. We listed below some resting-state functional networks that was found to be disturbed during the course of AD.

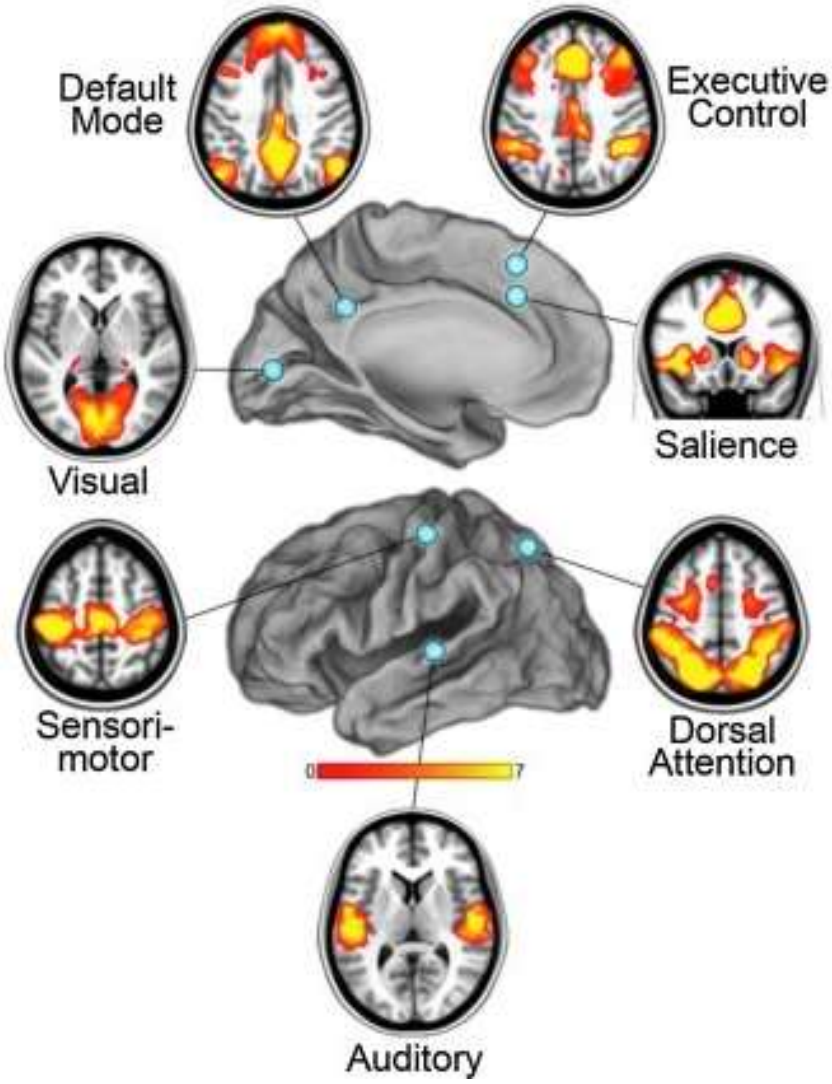

Figure 43: Seven functional networks in the human brain (Raichle, 2011)

The DMN is the most studied network. It was first described by Raichle et al. in 2001 as the functional communication of the posterior cingulate cortex (PCC), medial prefrontal cortex (mPFC), and the parietal regions (PTL) (Raichle et al., 2001). The entorhinal cortex, the thalamus and the hippocampal formation are sometimes attached to this network. The DMN is particularly engaged during rest and is deactivated during a task (Raichle et al., 2001). An interesting feature of the DMN is that it exhibits a pattern of anticorrelation with the parietal/frontocortical areas activated during tasks which referred to the DMN as the "task-negative network". Although the precise function of DMN is still incompletely understood, it is generally believed that DMN is involved in the wandering mind and supports cognitive functions such as mindfulness, self-referential and introspective state (Gusnard et al., 2001). It has also

been found to be active during remembering, imaging the future, and making social inferences (Buckner and DiNicola, 2019; Buckner and Krienen, 2013). More than 90% of the energy consumed by the brain is used to support the DMN. This network continues to be active during sleep and persists during light anesthesia (Raichle, 2009) making easier its study in animal models. Compelling evidence have shown that dysfunction of the DMN may contribute to widespread brain disconnection leading to several diseases. Failure to reduce DMN activity may result in interference causing symptoms in major depression. In AD patients, findings of decreased DMN connectivity are associated with a **preferential deposition site for Aβ within this network**.

The salience network (SN) is a large-scale network embedding the anterior insula and dorsal anterior cingulate cortex. It can also be detected at rest. The SN plays an important role in emotional information processing, communication, social behavior, and self-awareness (Menon and Uddin, 2010). It has been associated with cognitive regulation, particularly in helping the brain to decrease DMN activity. Interestingly, when salient stimuli are detected, the SN organizes the switch between the central executive network and the DMN. Furthermore, this network mediates dynamic interactions between other large-scale brain networks implicated in mindfulness. It facilitates the access to working memory, attention or motor systems. It is divided in two submodules: the ventral and the dorsal salience networks. While the ventral salience network is involved in the affective function like empathic functions, the dorsal salience network ensures the executive function such as moral reasoning. Dysfunctions of the SN are associated with neuropsychiatric disorders. Importantly, **functional disconnection between the two submodules of this network** drives neuronal deficits causing **cognitive impairment in early AD** (He et al., 2014).

The executive control network (ECN) has traditionally been considered to be located in the superior and middle prefrontal cortex, anterior cingulate cortex, paracingulate gyri and ventrolateral prefrontal cortex. More recently, studies have reported the involvement of subcortical regions such as the thalamus in network functioning. The ECN is especially active during tasks but can still be active during rest. This network contributes to extrinsic awareness that regulates executive functions involving intellectual activities and participation in cognitive control such as working memory, reasoning, and decision-making for goal-directed behavior and planning (Connolly et al., 2016; Qin et al., 2009). **Altered ECN connectivity** has been shown in patients with attention-deficit and hyperactivity, in addition to **AD patients**.

The attention network is strongly related to communication between the dorsal frontoparietal system involved in voluntary attention and the ventral frontoparietal system associated with the detection of unexpected stimuli. The dorsal attention network is composed of the intraparietal sulcus and the

frontal eye field. This network contributes to the control of attention in response to cognitive stimuli, which is responsible for the endogenous attention orienting ("top-down") process. The ventral attention network includes the ventral frontal cortex and the temporo-parietal junction. This network allows the reorientation ("bottom-up") of the attention following new stimuli (Vossel et al., 2014). A resting-state functional MRI study in **AD patients** revealed that the **dorsal attention network is impaired** in patients while the **ventral attention network remains intact** (R. Li et al., 2011). It suggests that AD patients would perform poorly on attentional-related tasks such as selecting proper objects or giving appropriate responses to learning rules. However, they might still have the ability to reorient to novel information.

The sensory-motor network (SMN) displays high interhemispheric correlations (homotopic connectivity) due to synchronous functional activation of the precentral and postcentral gyri (Brodmann areas 1, 2 and 3), detected at rest and during a motor task such as finger tapping. It was the first functional network described by Biswal et al. using seed-based analysis. The SMN is mainly composed of the primary sensory cortex and the primary motor cortex that are responsible for processing of sensory information and motor coordination. Alteration of the SMN is associated with amyotrophic lateral sclerosis, a type of motor neuron disease leading to abnormal voluntary control of muscle movement. An increase of the SMN activity causing sensory and motor dysfunction has been found to **precede the onset of cognitive impairments and dementia in AD patients**. The possibility to include the SMN activity into the diagnostic criteria for AD is still under debate (Albers et al., 2015).

The visual network is divided in three networks: (1) the primary visual network which is involved in processing information of static and moving objects, (2) the dorsal visual network associated with spatial awareness and guidance of actions and (3) the ventral visual network associated with object recognition (James et al., 2003; Nassi and Callaway, 2009). It is composed of the primary visual cortex and the precuneus region as well as non-visual areas such as the occipito-temporal cortex and superior parietal cortex. The primary visual cortex receives inputs from the thalamus. The main function of the visual network is to provide visuo-spatial attention or visual attention. Thus, dysfunction of the visual network might disturb spatial attention. Progressive **reduction of visual network connectivity is observed in AD** patients (Huang et al., 2021).

The basal ganglia network (BGN) is composed of the dorsal striatum, caudate-putamen nucleus, pallidum, subthalamic nucleus and substantia nigra. The BGN are a group of subcortical nuclei, which integrate information from cortical areas and in turn project their outputs back to the cerebral cortex (Afifi, 2003). Particularly detected at rest, the BGN have a pivotal role in motor and non-motor functions such as emotional and cognitive processes. In general, changes in BGN functional

connectivity are commonly found in Parkinson's disease, as the dorsal striatum, main structure impacted in the disease, has been suggested to be a main node of this network. Several studies have demonstrated a strong relationship between cognitive decline and BGN alteration. In **AD patients**, **aberrant functional connectivity of the BGN**, especially in the caudate and amygdala was found **during cognitive decline** making the BGN a potential target in the disease (Xiong et al., 2022).

Even if we cannot list all the existing resting-state functional networks, it is important to keep in mind that the precise boundaries of networks are arbitrary and do not absolutely overlap with anatomical boundaries. Furthermore, functional networks comprise overlapping positively correlated regions that are known to share a common function, supporting the relevance of communications between networks. For example, the retrosplenial cortex of the DMN communicates with the frontal eye field component of the dorsal attention network. The alteration of this communication is associated with several brain disorders. The underlying mechanism between network communication and spatiotemporal trajectories and how cross-network signaling is implemented remains to be understood.

4.2.5 Common functional networks in the mouse brain

Despite a growing interest in the resting-state fMRI field, few studies have been conducted to elucidate large-scale functional networks present in animal models. Prominently, the detection of subtle functional alterations in animal models may contribute to understand the complex cognitive processes that become progressively impaired over the course of AD. In rodent studies, several functional networks have been commonly identified from resting-state fMRI data in anesthetized mice (Grandjean et al., 2020, 2017b, 2017a; Stafford et al., 2014; Zerbi et al., 2015) and awake mice (Gutierrez-Barragan et al., 2022). Relevant large-scale resting-state networks were highlighted using ICA with different numbers of components (15 to 40) or seed-based analysis. Sforazzini et al. explored the functional architecture of the mouse brain by varying the number of ICA components. While high level (20 components) was associated with dissociated brain region, low level (5 components) encompassed widespread networks (Sforazzini et al., 2014). They highlighted homologous networks such as DMN-like, the somatosensory and the salience network. Zerbi et al. used a hierarchical clustering method to find 23 relevant functional networks including bilateral cortical and subcortical regions. They further separated the somatosensory/motor network into sensorimotor, visual, olfactory and auditory network. They also described non-cortical networks such as the limbic system network, the basal ganglia and cerebellar network (**Figure 44**) (Zerbi et al., 2015). Similarities and differences with human networks will be discussed below.

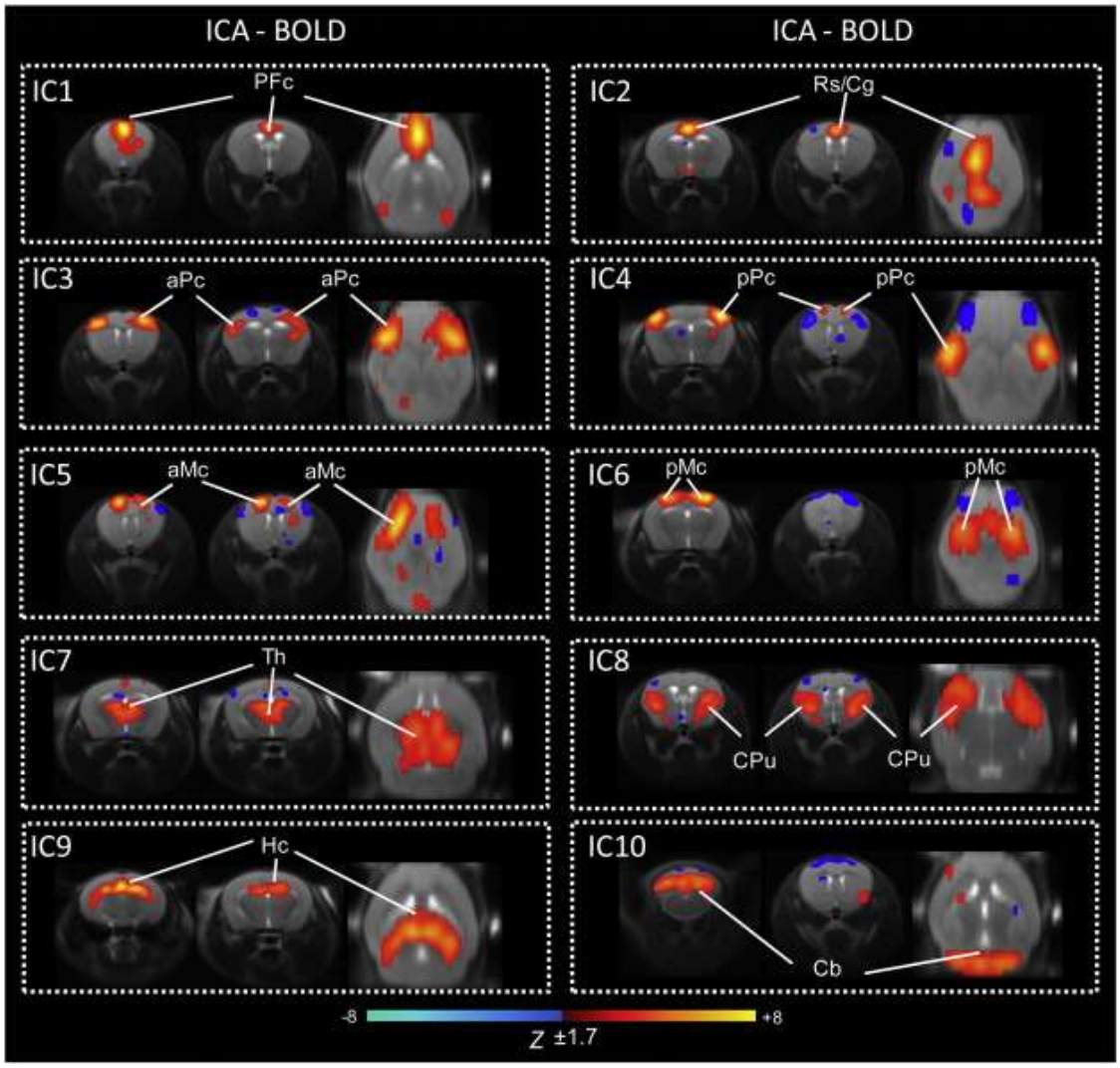

Figure 44: Spatial maps of ten individual components (IC) identified by ICA-BOLD

ICA components are represented overlaid on anatomical template in the coronal and horizontal view. Functionally-correlated and anti-correlated oscillation signals are shown in red/yellow and blue, respectively : IC1, pre-frontal cortex; IC2, cingulate/retrosplenial cortex; IC3 and IC4, anterior and posterior parietal (somatosensory) cortex; IC5, anterior motor cortex; IC6, posterior motor cortex; IC7, thalamus; IC8, caudate putamen; IC9, dorsal hippocampus; IC10, cerebellum and brain stem. Abbreviations: aMc, anterior motor cortex; aPc, anterior parietal cortex; Cb, cerebellum; Cg, cingulate cortex; CPu, caudate-putamen; Hc, dorsal hippocampus; PFc, prefrontal cortex; pMc, posterior motor cortex; pPc, posterior parietal cortex; Rs, retrosplenial cortex; Th, thalamus. From (Zerbi et al., 2015)

A DMN homologous to human has been reported in rodent (Grandjean et al., 2020; Sforazzini et al., 2014; Whitesell et al., 2021; Zerbi et al., 2015) which was found anti-correlated with the parietal/frontal areas (Gozzi and Schwarz, 2016; Schwarz et al., 2013) and exhibited a passive role

during tasks (Li et al., 2015) consistent with human DMN features. Cross-species comparison have suggested that the human cortical DMN anatomy is comparable with the rodent DMN regarding molecular, anatomical and functional level (**Table 3**) (Coletta, 2020; Whitesell et al., 2021). However, depending on the methodological approaches used, the regions included in the DMN are different. While Stafford et al. included the cingulate areas, the parietal cortex, the orbitofrontal cortex and somatosensory components in the DMN (Stafford et al., 2014), Sforazzini et al. added the nucleus accumbens and the prelimbic cortex in this network (Sforazzini et al., 2014) (**Figure 45**). Other studies detected a DMN-like network gathering also the caudate putamen, the medial entorhinal cortex, the retrosplenial cortex, the parasubiculum and the thalamus (Zerbi et al., 2015) as well as the temporal association areas and the ventral hippocampus (Grandjean et al., 2020)). The existence of such networks was for a long time under debated. Other structural connectome methods, such as the use of anterograde tracer mapping axonal projections allowed to confirm the relevance of DMN anatomical structure in mice. They showed that DMN regions in mice appear to be preferentially interconnected (Whitesell et al., 2021). Although similarities in DMN neuroanatomical organizations has been found, cross-species differences in the DMN still exist. For example, the precuneus, found in the human DMN, do not have anatomical equivalence in mice but its functional role in human is closed to the role of retrosplenial cortex in mice. As in AD patient, **aberrant activity of the DMN has been found in a mouse model of AD** (Adhikari et al., 2020; Damoiseaux, 2012; Grandjean et al., 2014a; Shah et al., 2016, 2013; Zerbi et al., 2014).

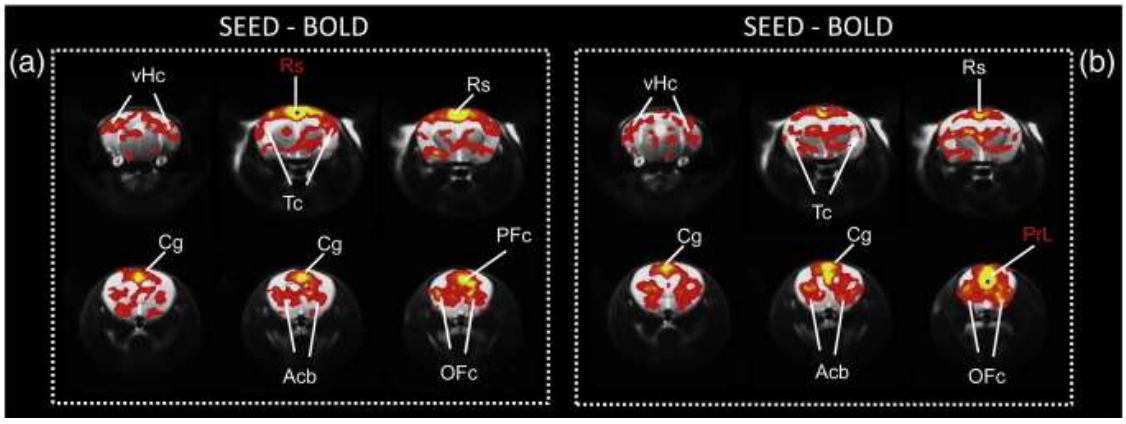

Figure 45: Characterization of DMN-like network in mice identified using (a) the retrosplenial cortex (Rs) and (b) the prelimbic area (PrL) as a seeds. (Sforazzini et al., 2014)

Several evidences have revealed the existence of the salience network, evolutionarily conserved from human to mice (Gozzi and Schwarz, 2016; Grandjean et al., 2020; Mandino et al., 2022). This network

in mice showed anatomical similarities with humans as it included the insula, the dorsal anterior cingulate cortex, and the amygdala (**Table 3**) (Grandjean et al., 2020; Mandino et al., 2022). In addition, a potential homologous of ECN was also identified in mice, called the lateral cortical network. This network shares similar areas as the somatosensory/motor network and was postulated to perform the central executive function in rodents (Gozzi and Schwarz, 2016; Grandjean et al., 2020; Mandino et al., 2022). As previously discussed, the SMN is separated in different domains responsible for movement and sensory abilities in mice while in human, they were all grouped into a single somatomotor network (Thomas Yeo et al., 2011). Thus, dual functions of this network were found in rodent. Mice survival depends on a fundamental network called the olfactory network, responsible for the sense of smell and pheromone-based communication (Huilgol and Tole, 2016). One can expect that this network is more selected by evolution processes in rodent than in human. Indeed, in humans, it serves multiple functions either olfactory sensory perception or non-sensory functions such as emotion. The olfactory network is composed of the piriform cortex, the orbital cortex and the glomerular layer of the olfactory bulb in mice while it is further decomposed into limbic and frontal systems in human (**Table 3**). Despite the enlarged olfactory bulbs and the presence of the accessory olfactory bulbs in rodents, the rodent limbic networks exhibits similar functions than in human meaning that the processing of emotions and other social cues are similar. This discovery allowed to study limbic responses to social cues in mouse models of human pathology affecting social domains (Sokolowski and Corbin, 2012). Although several homologous networks were defined, some human networks such as the attention network have not yet been discovered in rodents. One hypothesis can be that these networks are encompassed in other large networks such as the DMN that make it impossible to distinguish them (Gozzi and Schwarz, 2016).

Human networks	Anatomical regions	Mouse networks	Anatomical regions	References
Default mode network (DMN)	Cingulate cortex / retrosplenial cortex	**DMN**	Cingulate cortex, retrosplenial cortex	*Sforazzini et al., 2014; Mandino et al., 2021*
	Precuneus posterior			
	Prefrontal cortex		Prefrontal and orbito-frontal cortex, prelimbic cortex	
	Parietal and temporal lobes		Temporal cortex	
	Parahippocampal cortex		Ventral-hippocampus, dorsal striatum, dorsolateral nucleus of the thalamus	
Somatomotor	Motor cortex	**Sensory, motor**	Motor cortex	*Zerbi et al., 2015*
	Auditory cortex	**Sensory, auditory**	Dorsal and ventral auditory cortex	
	Somatosensory cortex posterior insular cortices	**Somatosensory**	Upper lip region, barrel field, hindlimb region, and forelimb region in primary somatosensory cortex	
Limbic	Orbital frontal cortex	**Sensory, olfactory**	Piriform cortex, medial orbital cortex, and glomerular layer of the olfactory bulb	*Zerbi et al., 2015*
	Temporal pole	**Limbic system (non-cortical)**	Cingulate cortex area 1, 2, and retrosplenial cortex Ventral and dorsal hippocampus, amygdala	*Zerbi et al., 2015*

Visual	Visual cortex	**Sensory, visual**	Visual cortex and retrosplenial dysgranular	*Zerbi et al., 2015*
Frontoparietal	Parietal and temporal lobes Dorsal, lateral, and ventral prefrontal cortex Orbital frontal cortex Precuneus, cingulate, medial posterior prefrontal cortex	**Lateral cortical network**	Primary motor, primary somatosensory, lateral striatum, ventroposterior nucleus of the thalamus	*Mandino et al., 2021*
Salience/ventral attention	Parietal operculum, temporal occipital, frontal operculum insula, lateral prefrontal cortex, medial nodes	**Salience***	Anterior insular, dorsal anterior cingulate, ventral striatum/nucleus accumbens	*Sforazzini et al., 2014; Mandino et al., 2021*

Table 3: Cross-species comparison of functional networks. Adapted from (Xu et al., 2022)

To conclude, homologous functional networks to those of human has been found in mice although the regions belonging to this network and their role were not systematically similar in mice (**Table 3**). Hence, cross-species comparison might be difficult to interpret. Additionally, there is evidence demonstrating that there are anatomical differences between the types of cells and the regional boundaries across species. For example, the border between subregions of the cingulate cortex are different from human to mice. Rats and mice exhibit also differences in cortical resting-state networks as mice can have unilateral cortical networks and rats do not. Different processing methods also contribute to network inconsistency across species. Anesthesia has a strong impact on resting-state network identification (Liang et al., 2012, 2011). Current methods used for awake mice are not efficient, as the result is lacking reproducibility and can lead to several artefacts such as motion ones. Grandjean et al. described a combination of factors allowing to identify the most "specific" and reproducible functional connectivity in the mouse brain using ICA and seed-based analysis (Grandjean et al., 2020). They found that datasets acquired "*at higher field strength, with cryoprobes, in ventilated animals and under medetomidine-isofluorane combination sedation*" provides the best combination to enhance spatial specificity of identified functional networks. They also provide criteria to remove components that do not reflect resting-state networks such as vascular/motion-associated component and single-slice artifact components. The progression of functional connectivity studies in rodents will allow exploring the functional pathological hallmarks of neurodegenerative disorders.

4.2.6 Role of Aβ in neural network dysfunctions

AD is a disconnection syndrome as it affects both local connections within networks and global links between networks (Sanz-Arigita et al., 2010; Stam et al., 2007; Supekar et al., 2008). This disconnection occurs in selectively vulnerable regions probably because of their **high degree of connectivity (hubs)** and neural activity, which favors Aβ secretion. Compelling evidences have demonstrated a strong link between Aβ and functional connectivity (Buckner et al., 2009; Elman et al., 2014; Jagust and Mormino, 2011; Myers et al., 2014). Animal studies have shown the role of Aβ in the reduction of intrinsic activity and connectivity (Bero et al., 2011; Busche et al., 2008; Grandjean et al., 2014b; Shah et al., 2016). Additionally, it has been described a high degree of spatial overlap between the spatial distribution of Aβ deposition and the spatial distribution of functional MRI networks. The detrimental effects of Aβ within-network connectivity have been demonstrated particularly in areas in connectivity hubs. Several human studies revealed that Aβ accumulation preferentially starts in the precuneus, medial orbitofrontal, and posterior cingulate cortices, regions that belong to the DMN which display high metabolic activity and high intrinsic functional connectivity (**Figure 46**) (Binnewijzend et al., 2012; Damoiseaux, 2012; Greicius et al., 2004; Seeley et al., 2009). In prodromal stages of AD, loss of DMN functional connectivity is associated with neocortical and hippocampal gray matter volume loss,

meaning that functional connectivity is directly linked to neurodegeneration. Dysfunction in DMN activity allows differentiating AD from other neurodegenerative diseases (Seeley et al., 2009; Zhou et al., 2010). The earliest Aβ accumulation is further associated with hypoconnectivity within the DMN and between the DMN and the frontoparietal network. The reduction in DMN activity can take place before Aβ biomarkers (either PET or CSF) become positive.

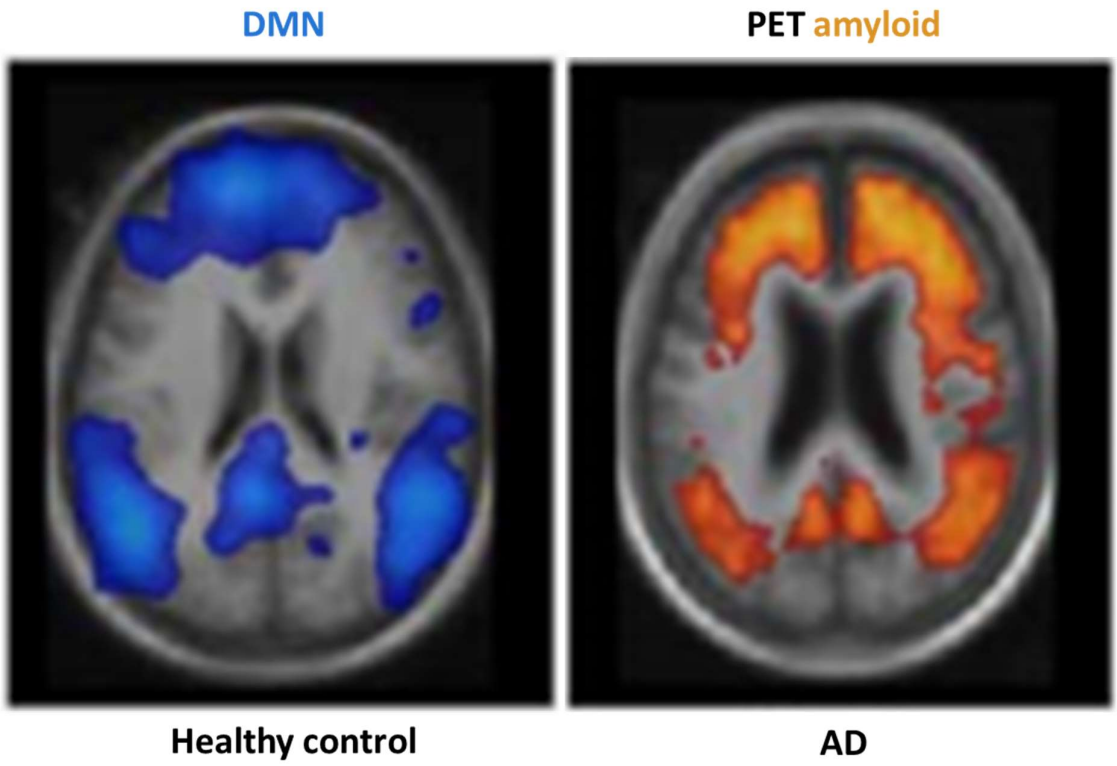

Figure 46. Colocalisation between the region of DMN (*left*) **and accumulation of Aβ deposits** (*right*)

While the DMN may be the primary target of AD-related change, it is not the only network affected. Over the course of AD progression, changes in functional connectivity have been reported in the dorsal attention network, frontoparietal control network, salience network (He et al., 2014), and sensorimotor network (Agosta et al., 2012; Brier et al., 2012; Zhou et al., 2010). Aβ pathology reduces connectivity of brain regions that are highly interconnected and exhibit high levels of neural activity which may predispose these brain regions to amyloid deposition. Thus, cortical regions showing altered functional connectivity in parietal and temporal cortex are particularly susceptible to Aβ-induced alterations. Similar alterations were found in animal models of AD. Grandjean et al. have reported that abnormal functional connectivity in the somatosensory cortex and the motor cortex of APP transgenic mice appeared in the early months before the accumulation of Aβ (Grandjean et al., 2014b). These alterations were associated with impaired microstructure of the white matter as revealed by a significant decrease of fractional anisotropy (FA, described in next section). In another

study, an unexpected pattern of functional connectivity were described in the hippocampus depending on the stage of the disease. Hypersynchronized functional connectivity was found before Aβ deposition and hyposynchronized functional connectivity at later stages (Shah et al., 2016). Interestingly, this early functional modification was reversed by treating transgenic mice with anti-Aβ antibody suggesting that soluble Aβ is responsible for these alterations prior to Aβ deposition.

Memory relies on the integration between neural networks. The reduced activity of the DMN, the central executive and the salience network in AD patients displaying elevated Aβ burden, both have been associated with worse cognitive performance. Thus, it has been postulated that Aβ pathology might cause neural network dysfunction, and this disruption causes worse memory performance. Recently, a study that used simultaneously memory tasks, functional MRI and amyloid PET have proven this direct relationship in AD patients (Li et al., 2021). They showed that cortical Aβ deposition impaired functional connectivity in the default mode, limbic, and frontoparietal networks during the retrieval of stored memory information in early AD. These findings can help to find sensitive markers that can unveil early alterations in brain function and explain Aβ-related memory deficiencies in AD patients.

4.3 Diffusion imaging

4.3.1 Principle of diffusion-based MRI

Diffusion-based MRI is designed to detect the random movements of water protons in biological tissues. Diffusion is a three-dimensional process where water proton mobility differs depending on the directions. While water molecules diffuse relatively freely in the extracellular space, their movement is restricted in the intracellular space. During their displacement, water molecules interact with tissue components, such as macromolecules, fibers, and cell membranes. Diffusion weighted imaging (DWI) is an important type of MRI that allows the mapping of *in vivo* diffusion of water molecules in biological tissues revealing anatomical details about tissue architecture. Indeed, these methods statistically evaluate the motion of water molecules providing an indirect identification of microscopic aspects that reflect the patterns in size, orientation and organization of tissues, which are predicted to be precursors to the final neurodegeneration process. A special type of DWI called diffusion tensor imaging (DTI) is widely used to map the main white matter tracts of the brain *via* tractography algorithms.

Diffusion is a three-dimensional process where water molecules can diffuse through several directions. When acquiring, each image voxel has an image intensity reflecting a measurement of the rate of water diffusion at that location. The properties of each voxel is calculated by a vector, which is a 3 x 3

symmetric matrix that features different orientation of the diffusion sensitizing gradients. This information is comprised in a 3D diffusion tensor image obtained from at least six different diffusion weighted acquisitions. Several parameters can be measured from the tensor depending on the three principal axes (**Figure 47**): the **Axial Diffusivity** (**AxD**), which represents the longitudinal diffusivity (main diffusion axes); the **Radial Diffusivity** (**RD**), which reflects the diffusion through the axis perpendicular to the longitudinal diffusivity the **Mean Diffusivity** (**MD**) which is the measure of diffusion without a selected direction. AxD, RD and MD provide information about the microstructure of tissues and have been used as potential biomarkers for neurodegenerative diseases. MD is an inverse measure of membrane density and fluid viscosity in both gray and white matter; hence, it is a good indicator of edema and necrosis (Alexander et al., 2007). RD is sensitive to white matter demyelination or dysmyelination as well as changes in axonal diameter or density. AxD is a good indicator of axonal degeneration. The interpretation of these parameters is highly depending on the nature of biological tissues. For example, a reduction of AxD can represent either demyelination process or loss of axon. The most commonly used parameter is fractional anisotropy (FA). In the brain, white matter bundles are arranged in a packed and highly directional manner. The mobility of water is hindered by axonal membranes and by myelin sheaths. Thus, the diffusion of water molecules is anisotropic as their displacement will be highly restricted to the direction of the bundle compared to other directions. FA describes fiber tract directionality and provides a value that reflects the tendency of water molecule to diffuse in a single direction within a voxel. FA value can vary from 0 (random diffusion) to 1 (highly linear diffusion) meaning that if a voxel is placed in a highly oriented white matter bundle, the FA will be close to 1; while if the tissue is most isotropic, the value will be lower. It has been shown that the difference between diffusivity along and across bundles increases with axonal density. Thus, low FA value indicates lower axonal density. FA provides an index of white matter characteristics including myelination, axonal degeneration, axonal packaging, and cytoskeletal features. The directional information can be exploited at a higher level of structure to select and follow neural tracts through the brain, a process called tractography.

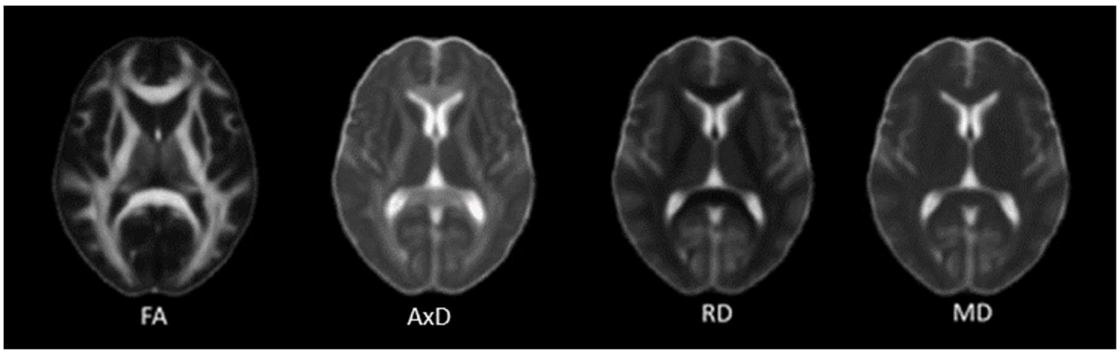

Figure 47: Maps of averaged diffusion metrics of 42 subjects in the MNI standard space.

Diffusion tensor imaging (DTI) metrics include fractional anisotropy (FA), axial diffusivity (AxD), radial diffusivity (RD), and mean diffusivity (MD). (Wu et al., 2018)

4.3.2 Diffusivity changes in AD

Diffusion MRI is a potentially important tool for probing the effects of disease and aging on brain microstructure as it is extremely sensitive to subtle pathological changes at the cellular and microstructural level. Early microstructural alterations of white matter have been detected in patients with AD. These changes occurred prior to brain atrophy and were undetectable by conventional MRI. Higher diffusivity with loss of directionality has been found in AD patients while intermediate levels of diffusivity were observed in patients with MCI. Thus, decreased FA in white matter and increased MD in gray matter regions were observed (Hanyu et al., 1998; Kantarci et al., 2011). While white mater disturbance was associated with myelin loss, decrease in axonal bundles, axonal disconnection and inflammation process (Song et al., 2004; Zerbi et al., 2013) in mouse models of AD, neuronal loss in gray matter strongly contributes to increased diffusivity (Syková et al., 2005). In human, diffusion deteriorations were predominately observed in the corpus callosum, cingulate gyrus/cingulate fiber tracts, uncinate fasciculus and inferior/superior longitudinal fasciculus (**Figure 48**) as well as in regions commonly affected in early AD including the hippocampal area, temporal area and posterior cingulate (Alves et al., 2015; Racine et al., 2014). Several studies suggested that hippocampal microstructural changes are better indicators than hippocampal atrophy to predict risk of progression from MCI to AD. The early white matter change observed in cognitively normal carriers of familial AD mutations and pre-clinical AD is the decreased of FA in the fornix. The fornix ensures the efferent projections from the CA1 and CA3 pyramidal neurons of the hippocampus and subiculum. An alteration of the fornix strongly disturbs the integrity of the hippocampus, causing subsequent memory dysfunctions. Furthermore, disturbance of diffusional measurements was strongly correlated with neuropsychological scores in cognitively impaired individuals. While positive correlation between cognitive performance and FA was described in AD patients, MD was found to negatively correlate with cognitive performance. Further analysis of FA in patients with MCI and AD revealed that the pattern of FA changes is strongly dependent on fiber tract architecture. A decrease of FA in intracortically projecting fiber tracts was opposed to an increase of FA in the corticospinal tract in MCI and AD patients suggesting these fibers do not exhibit the same properties of diffusivity (Teipel et al., 2014). Moreover, while the decrease of FA was associated with an early axonal degeneration, the increase of FA is more complex to explain. Some studies have suggested a potential explanation based on the loss of crossing fibers. Fiber crossing is a common feature of white matter organization that has been described to correspond with low FA (Alexander et al., 2011, 2007). The loss of this phenomenon may reflect a decrease in the complexity of white matter architecture resulting in an increase of

anisotropy probably because of the homogeneity of fiber orientation (Alexander et al., 2011; Alves et al., 2015; Douaud et al., 2011; Tournier et al., 2008; Tuch et al., 2002). Thus, the increase of FA can also be a feature of white matter disturbance in AD patients.

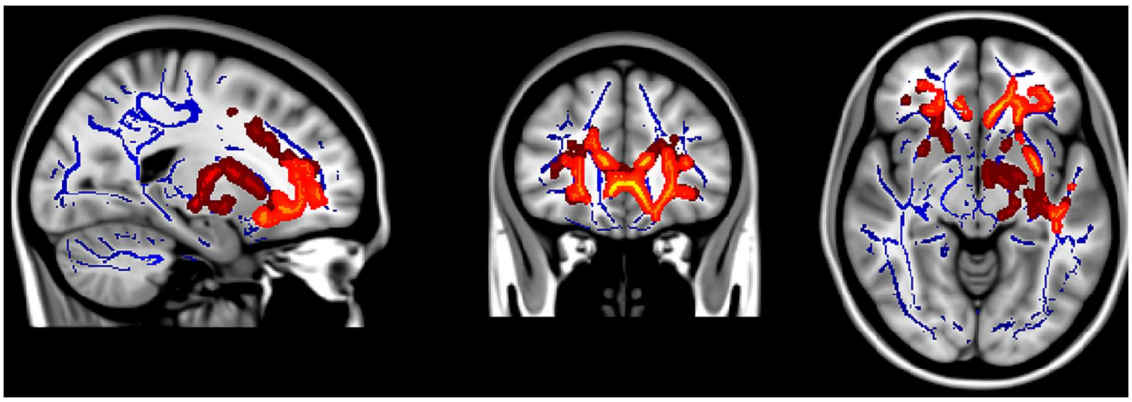

Figure 48: DTI changes in AD patients compared to healthy controls.

Voxels showing FA decreased (yellow-red) are revealed by DTI-Tract-based spatial statistics analysis overlapping on brain fiber. These areas can be observed in the corpus callosum (anterior and middle segments), anterior cingulum, and uncinate fasciculus (anterior portion). From (Alves et al., 2015)

4.3.3 Aβ burden-mediated white mater changes during AD

Some studies has demonstrated positive correlation between altered FA and increased Aβ burden. Intracerebroventricular inoculation of $A\beta_{42}$ in WT mice induced white matter changes in the optic nerves and tracts 2 months after the inoculation (Sun et al., 2014). Histological examination of mouse brains confirmed a significant loss of axons and myelin integrity, suggesting a potential role of Aβ in axon damage. However, the contribution of Aβ deposition to diffusional changes remains controversial (Thiessen, 2010). Several diffusion MRI studies in APP transgenic mice have demonstrated both increased and decreased FA and MD (Müller et al., 2013; Qin et al., 2013; Shu et al., 2013; Zerbi et al., 2013) (**Figure 49**). In humans, a multimodal study combining DTI and PiB-PET has reported that increased amyloid load was associated with higher FA in presymptomatic AD patients (Racine et al., 2014). In contrast, lower fronto-lateral gray matter MD was associated with higher amyloid burden. These findings are in contradiction with what was described in patients with MCI and AD suggesting that diffusivity changes may contribute to compensatory mechanisms prior to cognitive decline in order to response to early Aβ accumulation (Ryan et al., 2013).

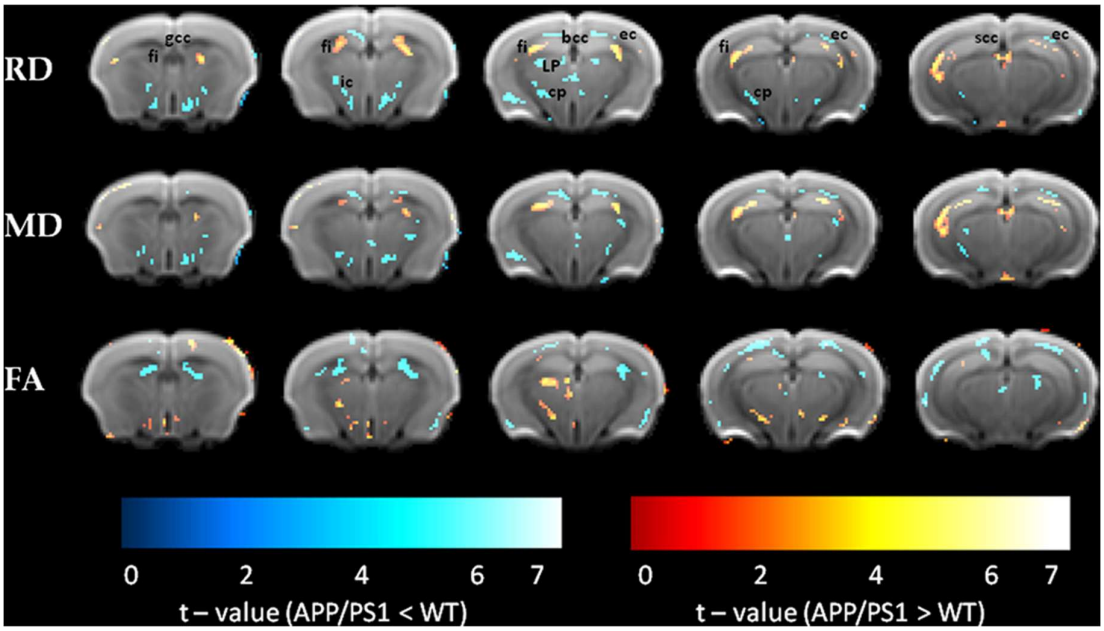

Figure 49: Voxel-based analysis indicates significant differences in diffusion parameters in transgenic $APP_{swe}/PS1_{dE9}$ mouse brains compared with wild type.

Diffusion weighted maps are overlaid with voxels that showed a significant difference ($p < 0.01$, voxel cluster size 0.05 mm^3) in radial diffusivity (RD), mean diffusivity (MD), and fractional anisotropy (FA). The voxel color indicates a negative (blue) or positive (red) change in the transgenic mice compared with the wild type mice. Increase in RD is found in the hippocampus and in the fimbria (fi), and decrease in RD is present in the corpus callosum (cc), cerebral peduncle (cp), and in the lateral posterior thalamus nuclei (LP). The MD decrease is found among others in the internal capsule (ic) and in the cc. An increased MD in the hippocampus and fi is also present. FA reduction is observed in areas such as the fi and cortex. Increases in FA are found in the cp, ic, and LP (Zerbi et al., 2013).

4.4 Chemical exchange saturation transfer (CEST) imaging

4.4.1 Principle of CEST

Chemical exchange saturation transfer (CEST) appears as a novel MRI contrast mechanism, which enables the indirect detection of macromolecules (proteins or metabolites) with exchangeable protons and exchange-related properties. Unlike traditional MRI, CEST enables the detection of signal from specified endogenous macromolecules. In biological tissues, there is a natural equilibrium between water protons and those belonging to the surrounding molecules. The CEST approach is based on the possibility to chemically exchange the hydrogen protons in the macromolecules of the biological tissues with the hydrogen protons in the free water. Image contrast can then be modulated by

applying a selective pre-saturation pulse that pre-saturate the hydrogen protons of macromolecules in the biological tissues. During acquisition, this exchange of saturated protons reduces the number of protons contributing to the water signal, resulting in a decrease in the signal of water. The reduced signal amount difference can indirectly reflect the concentration of proteins or metabolites present in the biological tissues. By saturating the sample at different frequencies around the bulk water resonance, the attenuation of water free signal can be measured using a spectrum of attenuation called Z-spectrum. In addition, CEST image is corrected by the water saturation offset reference (WASSR) to obtain a more accurate brain image and to weaken the influence of environmental factors such as magnetic field inhomogeneity.

4.4.2 Glutamate CEST imaging applications in AD

Macromolecule detected by CEST imaging are separated in three families depending on their chemical group: amide groups (-NH), amine groups (-NH2) or hydroxyl groups (-OH). The most abundant metabolite found in intracellular medium is the glutamate that contains amine group. CEST imaging of glutamate called **gluCEST** allows detecting glutamate with high sensitivity and specificity of 70%. gluCEST imaging enables the acquisition of glutamate weighted images. This approach has been widely explored in the study of neurodegenerative diseases due to the pivotal role of glutamate in neuronal metabolism and synaptic transmission. Disturbance of glutamate levels is strongly associated with cognitive abilities, learning, and memory. To our knowledge, investigating glutamate alterations with CEST has not yet been reported in AD patients. However, recent developments of gluCEST imaging allowed the quantification of glutamate at the level of the whole brain in animal models (Cai et al., 2012). Changes in glutamate levels were detected in mouse models of Huntington disease (Pépin et al., 2016; Pérot et al., 2022) and AD (Crescenzi et al., 2017; Haris et al., 2013; Igarashi et al., 2020; Liu et al., 2022). Compared to age matched WT mice, transgenic mice overexpressing a mutated form of APP ($APP_{swe}PS1_{dE9}$), analyzed with gluCEST MRI, showed a clear reduction of gluCEST contrast in all areas of the brain, in particular in the hippocampus where a glutamate decrease of ~31% was observed (Haris et al., 2013) (**Figure 50**). Recently, Igarashi et al. explored changes in gluCEST in a 5xFAD mouse model of AD at different development stages of the disease (Igarashi et al., 2020). They revealed an age-dependent decrease in gluCEST contrast in specific brain areas. The decrease in gluCEST signal begins as early as one month of age in parietal and temporal cortex, and in hippocampus. This alteration of glutamate level was detected until 15-months and spread to frontal cortex, striatum, and thalamus. Interestingly, at 7-months of age, the AD mouse model exhibited reduced gluCEST signal pattern that correlated with neurite density and synaptic loss in the parietal cortex and hippocampus while any atrophy was reported at this stage. These results indicate that gluCEST can be an early indicator of glutamatergic synapse loss and axonal impairment (Igarashi et al., 2020). Furthermore, in

a mouse model of tauopathy, it was suggested a positive correlation between gluCEST and several pathological processes occurring in the hippocampus (Crescenzi et al., 2017). At early stage of the pathology, elevated gluCEST was found in hippocampus in particular in cornu ammonis 1 (CA1) and dentate gyrus (DG), and was associated with synaptic excitotoxicity. Astrocytic activity increased to counteract the excess of glutamate as revealed by an increased GFAP-immunoreactivity. Thus, the early increase of gluCEST signal reflects an increased extracellular glutamate concentration in CNS, which is associated with activation of glial cells leading to early neuroinflammation process. The following decrease in glutamate concentration was related to a decrease in synaptic density due to reduced glutamate metabolism in synaptic mitochondria. This study demonstrated that GluCEST imaging is a marker of glutamate concentration in glial cells and at the synaptic level (Crescenzi et al., 2017). It was also reported that a decrease in gluCEST correlates with reduced cerebral blood flow (CBF) in the 5xFAD mice model meaning that gluCEST pattern can also explain the hypoperfusion found in AD (Igarashi et al., 2020). Hypoperfusion in AD is a consequence of earlier aberrant neuronal excitability and increased glucose consumption. A strong coupling between glutamatergic activity and cerebral glucose metabolism has been described in AD patients. Indeed, synthesis of glutamate requires glucose, hence, impaired glucose metabolism found in AD slow down glutamate synthesis. Measuring the glucose concentration in the brain using glucose CEST (glucoCEST) can also be an accurate indicator of altered metabolism in AD. To conclude, gluCEST can be used for staging AD, exploring glial metabolism and revealing synaptic loss prior to neurodegeneration. This approach can be used to explore the impact of Aβ on these three components.

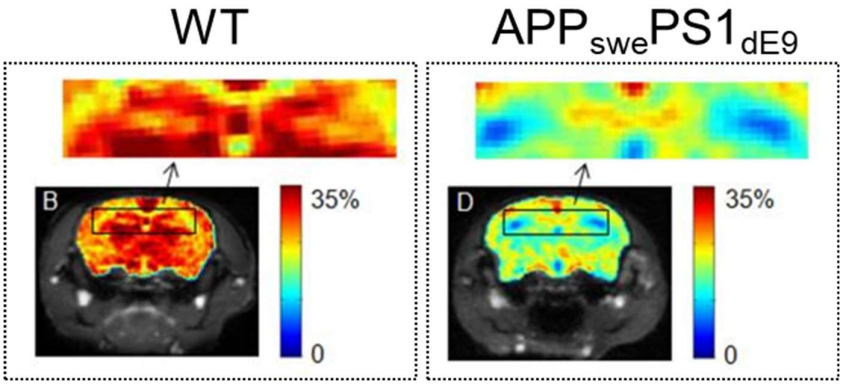

Figure 50: Decreased gluCEST signal in the hippocampus of WT and $APP_{swe}/PS1_{dE9}$ mice

The hippocampus sub-regions are shown in a rectangular box in both WT and AD mouse (arrows).

OBJECTIVES & RESEARCH PROJECT

In the last decade, extensive research effort has been dedicated to understanding whether Aβ represents a trigger or a driver of AD, or both. The discovery of mutations on APP at the origin of the FADs has brought a lot to our understanding of the disease and placed Aβ peptides at the center of the pathophysiological process. Different Aβ forms issued from different APP mutations were described leading to very distinct clinical outcomes in humans due to the influence of these mutations on Aβ secondary/tertiary structures. The $A\beta_{osa}$ variant was reported to strongly increase oligomerization process responsible for severe dementia in the absence of amyloid plaques. On the contrary, some mutated forms, like $A\beta_{ice}$, can associate to $A\beta_{wt}$ and promote the formation of Aβ heterodimers ($A\beta_{ice}/A\beta_{wt}$) that exhibit protective characteristics. Transmission of AD-related pathology was developed in mouse models through the intracerebral inoculation of minimal amounts of misfolded Aβ (described as Aβ "seeds") isolated from AD brains. Hence, several experimental transmission studies have been conducted to decipher the prion-like mechanism of amyloidosis explaining the disease propagation. However, the low level of sample purity prevents the direct association of these changes with the unique effect of Aβ. To understand the role of Aβ in AD downstream events, inoculation of synthetic or recombinant Aβ have been conducted in rodents. However, these studies mainly indicated the acute effect of Aβ without addressing the long-term and widespread effects of Aβ. **Determining how subtle changes in the primary structure of Aβ translate into dramatic or beneficial changes in the clinical expression and distinct neuropathology will provide greater insight into the mechanisms of this disease.**

Our hypothesis is that Aβ species are key-regulators of brain function that can be either protective or toxic. The objectives of this research project are to decipher how different forms of Aβ affect key events of AD pathophysiology including amyloid synthesis and spreading, synaptic dysfunctions, neuroinflammation, Tau pathology and neuronal network dysfunctions. The project proposes a holistic approach and relies on hypotheses that specific Aβ seeds as well as AD-brain extracts can exhibit long-term and wide impacts on cerebral lesions and brain functions leading to different phenotypes (benefic or toxic) and promoting different pathophysiological mechanisms. The research project aims:

(1) To produce, by using a recombinant strategy, specific Aβ species that promote aggressive or protective clinical outcomes mimicking human pathological features;
(2) To decipher the pathological cascades triggered by three different Aβ seeds, protective $A\beta_{ice}$, aggressive $A\beta_{osa}$ and $A\beta_{1-42}$;

Answering to these questions is critical since it may explain heterogeneity of AD phenotypes and may highlight new targets for personalized treatments in AD. This work will lay the foundation for future projects designed to propose new therapeutic approaches able to modulate Aβ impacts in AD pathology.

RESULTS

1. Developing tools to process MR images

1.1 Context, objectives & abstract

Resting-state fMRI is a non-invasive *in vivo* exploration methodology of large-scale brain networks. Yet, whole-brain fMRI imaging in rodents suffers from non-linear geometric and intensity distortions caused by static magnetic field inhomogeneity that worsens at the higher field strengths. In the last decade, novel tools have emerged to analyze small animal fMRI data, including correct preprocessing, but current software remain less powerful than the available tools that process human brain data. Thus, we developed an adaptive protocol that perform data preprocessing using flexible and efficient pipelines encompassed in the python library SmAll-MaMmal BrAin MRI (Sammba-MRI). This protocol allowed registering resting-state fMRI data from numerous subjects while applying artifact correction such as slice-timing correction, head-motion correction and susceptibility distortion correction.

1.2 Article

CELESTINE M., Nadkarni, Garin C., Bougacha S. and Dhenain M. Sammba-MRI: a library for processing small mammals' brain MRI data in Python. Frontiers in Neuroinformatics. 2020.
https://doi.org/10.3389/fninf.2020.00024

frontiers in Neuroinformatics

TECHNOLOGY AND CODE
published: 28 May 2020
doi: 10.3389/fninf.2020.00024

Sammba-MRI: A Library for Processing SmAll-MaMmal BrAin MRI Data in Python

Marina Celestine[1,2†], *Nachiket A. Nadkarni*[1,2†], *Clément M. Garin*[1,2], *Salma Bougacha*[1,2,3,4†] *and Marc Dhenain*[1,2*]

[1] UMR9199 Laboratory of Neurodegenerative Diseases, Centre National de la Recherche Scientifique (CNRS), Fontenay-aux-Roses, France, [2] MIRCen, Institut de Biologie François Jacob, Commissariat à l'Energie Atomique et aux Energies Alternatives (CEA), Fontenay-aux-Roses, France, [3] UMR-S U1237 Physiopathologie et imagerie des troubles Neurologiques (PhIND), INSERM, Université de Caen-Normandie, GIP Cyceron, Caen, France, [4] Normandie Université, UNICAEN, PSL Research University, EPHE, Inserm, U1077, CHU de Caen, Neuropsychologie et Imagerie de la Mémoire Humaine, Caen, France

Small-mammal neuroimaging offers incredible opportunities to investigate structural and functional aspects of the brain. Many tools have been developed in the last decade to analyse small animal data, but current softwares are less mature than the available tools that process human brain data. The Python package Sammba-MRI (SmAll-MaMmal BrAin MRI in Python; http://sammba-mri.github.io) allows flexible and efficient use of existing methods and enables fluent scriptable analysis workflows, from raw data conversion to multimodal processing.

Keywords: processing pipeline, MRI, registration, small animal neuroimaging, Python

OPEN ACCESS

Edited by:
Jan G. Bjaalie,
University of Oslo, Norway

Reviewed by:
Luz María Alonso-Valerdi,
Monterrey Institute of Technology and Higher Education (ITESM), Mexico
Eszter Agnes Papp,
University of Oslo, Norway

****Correspondence:***
Marc Dhenain
marc.dhenain@cea.fr

†These authors have contributed equally to this work

Received: *31 May 2019*
Accepted: *23 April 2020*
Published: *28 May 2020*

Citation:
Celestine M, Nadkarni NA, Garin CM, Bougacha S and Dhenain M (2020) Sammba-MRI: A Library for Processing SmAll-MaMmal BrAin MRI Data in Python. Front. Neuroinform. 14:24. doi: 10.3389/fninf.2020.00024

1. INTRODUCTION

The use of magnetic resonance imaging (MRI) methods in animals provides considerable benefits for improving our understanding of brain structure and function in health and diseases. The greatest advantages of preclinical MRI include group homogeneity and the opportunity to acquire a high amount of information repeated as needed. This added value, together with practical and ethical considerations, resulted in an increase of the use of small-mammal MRI in research. In human brain imaging, a large variety of high level software solutions is available for MRI preprocessing and analysis (e.g., SPM[1], FSL[2], or AFNI[3]). Less Free and Open Source Software (FOSS) are already available to analyse animal MRI. Atlas-based Imaging Data Analysis of structural and functional mouse brain MRI (AIDAmri) (Pallast et al., 2019) package allows registration of functional and diffusion mouse brain MRI with the Allen Mouse Brain Atlas (Allen Institute for Brain Science, 2004; Lein et al., 2007). The SAMRI (Small Animal Magnetic Resonance Imaging) package provides fMRI preprocessing, metadata parsing, and data analysis functions optimized for mouse brains (Ioanas et al., 2020). Today, there is still a need for other efficient and collaborative tools that would facilitate the adoption and dissemination of standardized pre-processing strategies for small animal MRI. Sammba-MRI was designed to process MR images, including anatomical, functional, and perfusion images. It allows to preprocess image dataset (conversion to NIfTI, bias correction), register images to templates or atlases, and perform perfusion measures.

[1] https://www.fil.ion.ucl.ac.uk/spm/software/
[2] http://freesurfer.net/
[3] https://afni.nimh.nih.gov/

2. WORKFLOW

2.1. Tools: Python Ecosystem and Neuroimaging Software Packages

With its FOSS dependency stack and its growing neuroimaging community Python has been naturally the language of choice for our package. The scientific Python libraries used inSammba-MRI are NumPy (Oliphant, 2006), SciPy (Millman and Aivazis, 2011), the neuroimaging data analysis tools nibabel[4], Nilearn (Abraham et al., 2014) and Nipype (Gorgolewski et al., 2011). Visualization functionality depends on Matplotlib (Hunter, 2007) or Graphviz (Gansner and North, 2000), but neither is required to perform MRI data processing.

Via Nipype, we utilize basic MRI preprocessing functions from AFNI (Cox, 1996), FSL (Jenkinson et al., 2012) and ANTs (Avants et al., 2009) packages. The dependency on the efficient but non open-source brain segmentation RATs tool (Oguz et al., 2014) is optional.

More specifically, Sammba-MRI and the examples provided in its manual depends on the following libraries: Nipype $\geq$ 1.0.4; Nilearn $\geq$ 0.4.0; Numpy $\geq$ 1.14; SciPy $\geq$ 0.19; Nibabel $\geq$ 2.0.2; Sklearn $\geq$ 0.19; matplotlib $\geq$ 1.5.1; nose $\geq$ 1.2.1; doctest-ignore-unicode; DICOM ToolKit package as well as FSL (version 5.0), AFNI, ANTs, and RATS.

2.2. Code Design

Sammba-MRI is developed within GitHub development platform[5]. Coding guidelines follow the model of Nilearn and other successfully adopted packages (e.g., Scikit-learn Pedregosa et al., 2011) to make the codebase understandable and easily maintainable[6]. Objects are used with parsimony: the different registration classes share all the same interface, and the brain extraction classes comply to the Nipype `BaseInterface`.

Effort is made to keep the code uniformly formatted and to use consistent naming for the functions and parameters following the coding conventions of Nilearn. Preprocessing building blocks and pipelines are automatically tested on light MRI data samples to ensure code quality. Finally, the user is guided through Sammba-MRI with extensive documentation including installation instructions, application programming interface (API) reference, pipeline graphs, and practical examples based on publicly available small animal neuroimaging datasets.

An overview of the modules used to manipulate images is presented in **Figure 1**. These modules are implemented either as "stand-alone" (i.e., `bias_correction`) or as ready-to-use pipelines (i.e., `TemplateRegistrator`).

2.3. DICOM to NIfTI Conversion

Sammba-MRI allows to convert Bruker DICOM (digital imaging and communications in medicine) files to the standard Neuroimaging Informatics Technology Initiative format (NIfTI-1) and extracts extensive information using DCMTK package (Eichelberg et al., 2004). Bruker files conversion is an active development field, with various available tools handling DICOM (e.g., dicomifier[7]) or not (e.g., bru2nii[8], Bruker2nifti[9], bruker2nifti[10]). Finally, ParaVision 360 with the latest patch 1.1 can export the NIFTI format since February 2019. Our implementation is meant to be a light helper function, allowing to handle the conversion on the fly. It has been tested only for Paravision 6 and a limited number of imaging sequences.

2.4. Bias Field Correction

Intensity non-uniformity modeling is essential in preclinical studies because the intensity gradient corrupting MR images becomes particularly pronounced at high field strengths (Boyes et al., 2008). Sammba-MRI relies on AFNI's `3dUnifize` to correct for intensity bias in anatomical images, and on `N4BiasFieldCorrection` function of the ANTs package (Tustison et al., 2010) for the other modalities. `3dUnifize` is also used to aid brain extraction, as detailed in the following paragraph.

2.5. Skull-Stripping

Skull-stripping is a critical early step in processing MR images from small animals. Various automatic rodent-specific softwares (Chou et al., 2011; Oguz et al., 2014) or adaptations of human algorithms (Wood et al., 2013; AFNI's 3dskullstrip -rat) are freely available for research purposes. We choose to rely on the LOGISMOS-based graph segmentation (Yin et al., 2010) based on grayscale mathematical morphology RATS software (Oguz et al., 2014) because of its good performance across a wide range of datasets (Sargolzaei et al., 2018). An alternative to the free but non-open source RATS tool is also available, based on an adaptation of the human histogram-based brain extraction method of Nilearn. This method can be used in any pipeline by setting the parameter `use_rats_tool` to `False`. Because intensity inhomogeneity can hamper the performance of automatic skull-stripping, prior bias field correction is usually recommended (Sled et al., 1998) and is performed by default with `3dUnifize`. The helper function `brain_segmentation_report` from Sammba-MRI `segmentation` module allows to efficiently tune the initial intensity threshold used in bias correction by producing for a given set of thresholds 5 informative measures characterizing the extracted mask to bypass time consuming repetitive visual checks. The returned features consist of the total volume of the extracted mask, its anteroposterior length, its right-left width, and its inferior-superior height as well as the sample Pearson's product-moment correlation coefficient between the brain mask image and its reflection with respect to the estimated mid-sagittal plane (Powell et al., 2016).

2.6. Registrations

Several registration algorithms are implemented within Sammba-MRI. First, rigid-body registration can be performed to roughly align individual images from the same modality or from different modalities. It minimizes normalized mutual information between brain extracted images. This registration

[4]https://nipy.org/nibabel/
[5]https://github.com/sammba-mri/sammba-mri
[6]http://gael-varoquaux.info/programming/software-design-for-maintainability.html
[7]https://github.com/lamyj/dicomifier
[8]https://github.com/neurolabusc/Bru2Nii
[9]https://github.com/CristinaChavarrias/Bruker2nifti
[10]https://github.com/SebastianoF/bruker2nifti

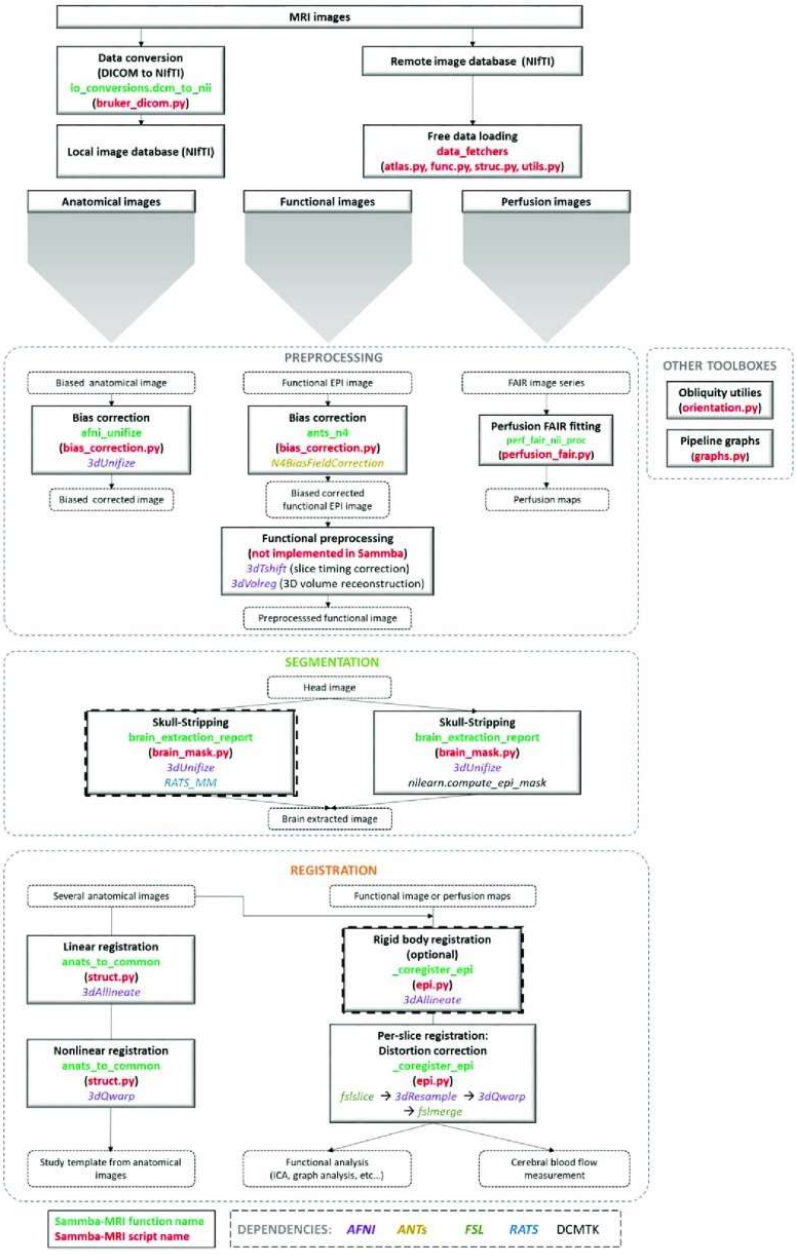

FIGURE 1 | Sammba-MRI workflow. Anatomical, functional, or perfusion images are imported from MRI local scanners or databases. They are analyzed using different preprocessing, segmentation and registration modules. Each function (green) and python-scripts (red) of Sammba-MRI are presented. Library dependencies are specified with color codes.

is finally estimated and applied to the whole head images. Second, linear registration estimates linear transforms between a source image and a reference image. It relies on AFNI's 3dAllineate function. Linear registration is more efficient when performed on brain-extracted rather than on whole head images. Third, non-linear registration (piecewise polynomial C^1 diffeomorphism) between a source image and a reference image can also performed. It relies on AFNI's 3dQwarp and iterations toward patch size reduction until a maximum refinement "level" is reached. Unlike linear registration, it is more efficient when computed using whole head images.

2.6.1. Group-Wise Registration and Study-Template

Group-wise registration aims to align all images from different animals within a common space, resulting in an average brain (study template) that represents the commonalities among individual brain anatomies of a particular population. Using a study template eliminates possible bias toward external features and improves subsequent analyses (De Feo and Giove, 2019). Sammba-MRI implements the multi-level, iterative scheme proposed by Kovačević et al. (2005) to create a fine anatomical template from individual anatomical MRI scans. A first rough template is obtained by averaging bias corrected head images centered on their respective brain mask centroids. Then the individual images are registered to this template. This process of successive averaging/registration is iterated while increasing the number of degrees of freedom of the estimated transform and updating the target template (see Nadkarni et al., 2019 for a detailed description of the pipeline).

2.6.2. Inter-Modality Registration

Several multimodal images can be recorded from a single animal, including structural imaging with different contrasts, blood-oxygenation-level-dependent (BOLD) and arterial spin labeling (ASL) MRI. BOLD imaging is largely used to investigate brain function in response to specific tasks or in the absence of explicit tasks (i.e., in resting state conditions) (Glover, 2011). ASL is an attractive method to image the vascular system by directly measuring blood flow (Kober et al., 2008).

In addition to the inherent difficulties in intermodality registration (Ashburner and Friston, 1997), severe image artifacts can corrupt BOLD or ASL scans resulting in a low signal-to-noise ratio (SNR). For instance, the echo planar imaging (EPI) technique widely used in functional and perfusion imaging suffers from non-linear geometric and intensity distortions caused by static magnetic field inhomogeneity that worsen at higher field strengths (Hong et al., 2015).

Thus a specific module called `_coregister_epi` was developed to register anatomical and EPI scans from individual animals. Anatomical images are first reoriented to match EPI images. Next, the reoriented anatomical images and the EPI scans are split into 2D slices along the z-direction (according to the slice geometry of EPI). Each EPI slice then undergoes a non-linear registration to match the corresponding anatomical slice. This per-slice registration corrects for EPI distortion while being more conservative than a global 3D non-linear registration.

3. PIPELINES

Sammba-MRI proposes two ready-to-use pipelines to perform spatial registrations to a population or standard reference template as well as inter-modalities registration between anatomical, functional, or perfusion images. These pipelines have been tested throughout the different stages of their development process on various datasets from mice, rats and mouse lemurs and used in several publications from our lab (Garin et al., 2018, 2019; Nadkarni et al., 2019). The two pipelines are called `Coregistrator` and `TemplateRegistrator`.

All pipelines start with bias field correction for the individual images, involve skull-stripping and specific registration algorithms depending on image modality.

3.1. Registration Between Anatomical Images and Another Modality: `Coregistrator`

Intra-subject registration between an anatomical scan and another modality (BOLD or ASL) is handled in the individual space through the `Coregistrator` class from the `registration` module (**Figure 2**).

```
from sammba.registration import
    Coregistrator
coregistrator = Coregistrator(
brain_volume=400)
```

Multimodal processing slightly differs between modality. Thus, user can choose modality of interest and the critical parameters that lead to the best registration.

BOLD scans are preprocessed using the same usual steps for human data with optional slice timing correction, bias field correction, realignment to the first volume and computation of the temporal mean of all the volumes. The corresponding structural scan is then registered to the average BOLD scan. Since this is a critical step, the user can choose either to pursue with human-like pipeline by estimating a rigid body functional-to-structural transform and applying its inverse to the structural image, or to assume that the head motion between the two scans is negligible. In all cases, it is better to only reorient the anatomical image to match the modality of interest. Finally, per-slice-based registration is performed as described in *section 2.6.2*.

```
coregistrator.fit_anat(
    'mouse01_t1.nii.gz')
coregistrator.fit_modality(
    'mouse01_t2.nii.gz',
    'func',
    slice_timing=True,
    reorient_only=True)
```

Sammba-MRI was also designed to analyse ASL scans to perform perfusion measures. This analysis relies on Bruker-FAIR (Flow-sensitive Alternating Inversion Recovery) EPI sequences. Quantitative CBF maps are first estimated using `perf_fair_nii_proc` function from the `modality_processor` module. Then Sammba-MRI allows to preprocess functional ASL scans with the equilibrium magnetization maps (M0) used as the representative volume for

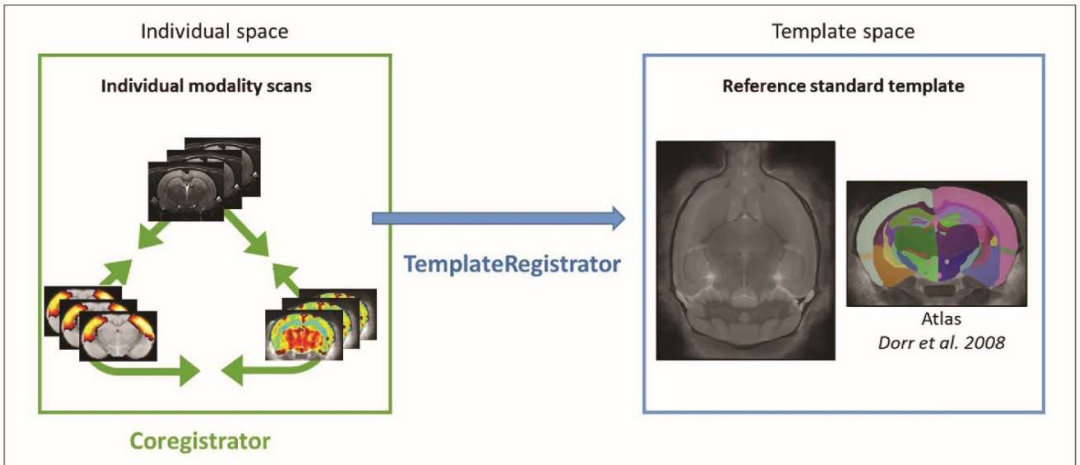

FIGURE 2 | Sammba-MRI pipelines. Color box represents spaces in which individual images are registered. Registration between individual modalities is performed by Coregistrator class (green arrow). Registration of individual modality images to a reference standard template space is performed by TemplateRegistrator class (blue arrow).

registration. The M0 volume is aligned to the anatomical, first with a rigid body registration and then on a per-slice basis.

```
coregistrator.fit_anat(
    'mouse01_t1.nii.gz')
coregistrator.fit_modality(
    'mouse01_t2.nii.gz',
    'perf',
    reorient_only=True)
```

3.2. Template-Based Multi-Modal Processing: `TemplateRegistrator`

Multimodal images (anatomical, functional, or perfusion MRI) can be handled in the template space through the `TemplateRegistrator` class. This pipeline matches individual images to a reference template, a necessary step for group studies (**Figure 2**).

3.2.1. Template Matching

Sammba-MRI proposes to download reference templates both for mouse and rat brains. The user needs to specify the path to the template of his choice to the `TemplateRegistrator` class from the `registration` module.

```
from sammba.registration import
TemplateRegistrator
registrator=TemplateRegistrator(
'dorr_t2.nii.gz',
brain_volume=400)
registrator.fit('mouse01_t1.nii.gz')
```

3.2.2. BOLD and ASL Preprocessing

BOLD and ASL preprocessing can also be performed in template space with `TemplateRegistrator`. The structural-to-template warp, the functional-to-structural rigid body transform and the perslice functional-to-structural warps are combined and applied in a one-big-step transformation to the functional data to minimize interpolation errors. The `TemplateRegistrator` class encompasses an `inverse_transform_towards_modality` method to bring an image from the reference space to the individual's space.

4. RESULTS

Sammba-MRI is available through the GitHub platform[11] and was tested using different image datasets.

4.1. Group-Wise Registration, Registration of Anatomical Images to a Common Space, and Template Creation

First, we evaluated group-wise registration and template creation using a dataset of *in vivo* T2-weighted images of 10 Sprague-Dawley rat brains (Lancelot et al., 2014). The scans were acquired using a 7.0 T Bruker scanner at 100 × 100 × 500 μm resolution using 30 different slices. We used `anats_to_common` to register images from the different animals and create a group average template (**Figure 3**).

For comparison purposes, the registration between images from each animal was also performed using algorithms from SPM8[12] with the SPMMouse toolbox[13] (Sawiak et al., 2009), a reference method for image-registrations. The brain images were segmented into gray (GM) and white matter (WM) tissue

[11] https://sammba-mri.github.io/introduction.html#installation
[12] www.fil.ion.ucl.ac.uk/spm
[13] http://spmmouse.org

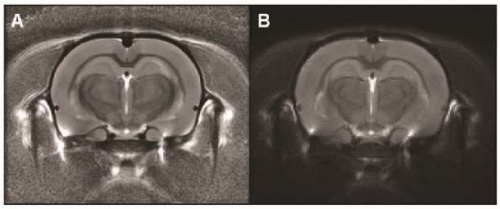

FIGURE 3 | Rat templates issued from Sammba-MRI **(A)** or SPM-based **(B)** registrations. These templates were calculated from anatomical images of 10 animals. Visual observation suggests similar quality of the two templates.

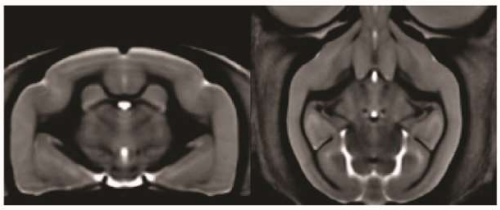

FIGURE 4 | Mouse lemur template from 34 animals. Coronal section of the mouse lemur MRI template (level of hippocampus).

probability maps using locally developed priors, then spatially transformed to a standard space. Priors were based on 100 × 100 × 100 µm resolution images and 134 slices. Affine regularization was set for an average-sized template, with a bias non-uniformity FWHM cut off of 10mm, a 5mm basis-function cut off and sampling distance of 0.3 mm. The resulting GM and WM portions were output in rigid template space, and DARTEL (Ashburner, 2007) was used to create non-linearly registered maps for each animal and common templates for the cohort of animals. The deformation fields were applied to the MR images of each animal and the resulting images were averaged to create a template. **Figure 3** shows the template obtained with SPM/Dartel. No obvious difference could be identified between the two templates.

Sammba-MRI adapts to different small animal species. **Figure 4** shows a template of mouse lemurs as another example (Nadkarni et al., 2018).

4.2. Validation of Template Matching

The Sprague-Dawley dataset is associated to brain segmentations into 28 regions for each animal (Lancelot et al., 2014). It also includes a study-template and an atlas based on segmentation of this template into 28 regions. Each image of the 12 individual animal was registered to the template using Sammba-MRI and the deformation fields were applied to the segmented images of each animal. We then measured the regional overlap between each region of the transformed atlases of each animal and the template-segmentation using Dice similarity coefficient ($2\frac{|A\cap B|}{|A|+|B|}$).

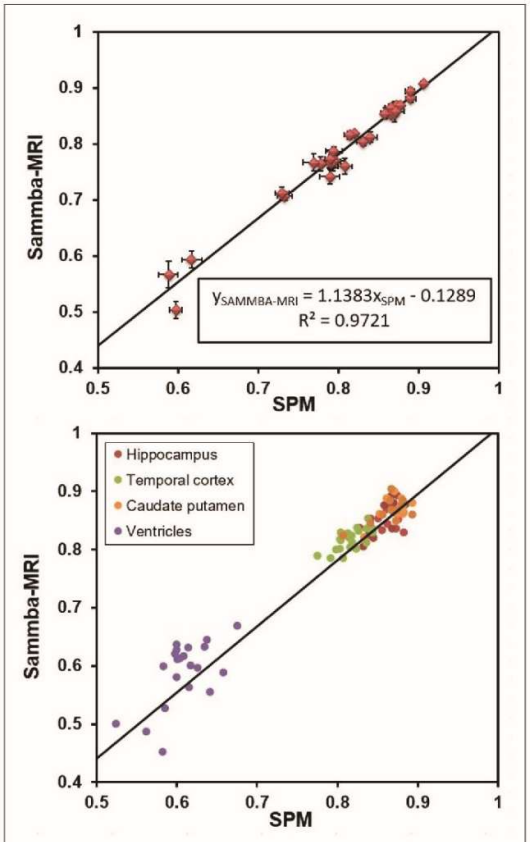

FIGURE 5 | Dice coefficients obtained after registering individual images to a rat brain templates with Sammba-MRI and SPM/Dartel. **(Top)** Comparisons showing 27 brains regions. Bars represents standard error of the mean. **(Bottom)** Individual measures for four different brain regions.

The deformation fields calculated with SPM were also applied to the MR and segmented images of each animal. We also measured the regional overlap between each region of the SPM-transformed segmentations of each animal and the template-segmentation also using Dice similarity coefficient.

Figure 5 shows that Dice coefficients obtained with Sammba-MRI were highly correlated with those obtained using SPM mouse and outperformed those of SPM in several cases (points above the line). Regions with lower Dice values correspond to ventricles.

4.3. fMRI and Perfusion Modalities

Resting state fMRI allows to study temporally synchronized BOLD oscillations reflecting functionally connected brain

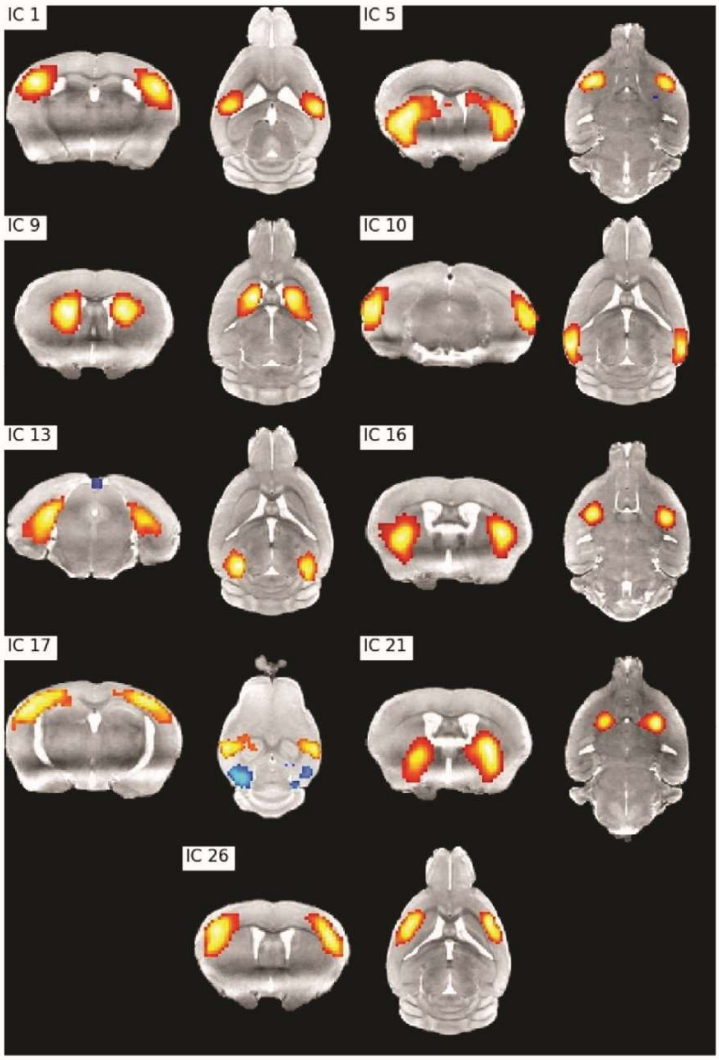

FIGURE 6 | ICA bilateral components. IC 1: Barrel field (i) cortex, IC 5: Lateral striatum, IC 9: Dorsal striatum (i), IC 10: Visual cortex, IC1 3: Hippocampus, IC 16: Dorsal striatum (ii), IC 17: Barrel field (ii) cortex, IC 21: Ventral striatum, IC 26: Supplementary cortex.

networks. As in human resting state fMRI, spatial networks can be extracted using Independent Components Analysis (ICA) (Zerbi et al., 2015; Grandjean et al., 2020). We preprocessed the publicly shared functional data from 15 mice (2–3 months old) from (Zerbi et al., 2015) paper with Sammba-MRI and performed a group ICA (Varoquaux et al., 2010) with 30 components. Relevant bilateral regions related to somatosensory, hippocampal, visual, basal ganglia, and sensorimotor networks were obtained without additional data post-processing (**Figure 6**).

To illustrate the perfusion processing pipeline, we used perfusion FAIR images from 30 C57BL/6J mice (6–8 months) to quantify CBF. **Figure 7** shows regional absolute CBF values. Perfusion values of 152±22 and 143±26 ml/100g/min in the hippocampus and temporal cortex, respectively. These values are lower than those reported by Kober et al. (208±20 and

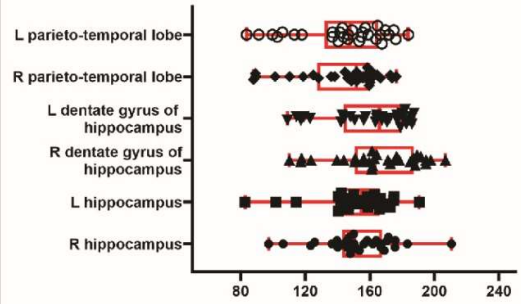

FIGURE 7 | CBF from 30 C57BL/6J mice. Boxplot shows median, interquartile range, upper and lower adjacent values for six brain region. Each dot represents regional CBF in ml/100g/min from one animal.

243±35 ml/100g/min in the hippocampus and cortex) with FAIR method (Kober et al., 2008). They are higher than those (118±6 ml/100g/min in the cortex) reported with the same method by (Zheng et al., 2010).

5. BIG DATA, REPRODUCIBILITY, COLLABORATION

The package design facilitates big data exploration: the user is able to run an entire analysis in a single Python script. Rerunning pipelines are optimized through Nipype caching mechanism and long lasting steps (non-linear warping, perfusion fitting) are executed in parallel. We believe that reproducibility in the neuroimaging field is not possible without making the acquired images and the preprocessing code available to the community. For this reason, Sammba-MRI promotes the sharing of MRI data by providing utility functions to download public small animal brain MRI datasets and relies on it for demonstrating the package capabilities. In order to encourage external contributions, our library source code is hosted on the open collaborative GitHub platform and distributed under the CeCILL v2.1 license, a FOSS license adapted to both international and French legal matters allowing anyone to make changes and redistribute it. Sammba-MRI supports GNU/Linux and Mac OS X operating systems (OS), used by over 70% of neuroimagers (Hanke and Halchenko, 2011). So far, Sammba-MRI is designed for advanced users but documentation is provided to help novices.

6. CONCLUSION

By efficiently combining different existing human and animal neuroimaging tools, Sammba-MRI allows to tackle common processing issues in a fully automated fashion. High quality spatial registration can be easily performed, including template matching, between modalities registration as well as the creation of cohort-specific templates. Sammba-MRI also implements functional and perfusion MRI preprocessing methods and cerebral blood flow estimation for FAIR perfusion images. Emphasis is put on code readability and ease of use to favor contributions from the community.

DATA AVAILABILITY STATEMENT

The mouse lemur dataset can be automatically loaded through Sammba-MRI or directly from https://nitrc.org/projects/mouselemuratlas for the template and https://openneuro.org/datasets/ds001945 for the original anatomical images. The perfusion dataset will be made publicly available following publication.

ETHICS STATEMENT

The animal study was reviewed and approved by local ethics committees CEtEA-CEA DSV IdF.

AUTHOR CONTRIBUTIONS

SB designed the Sammba-architecture and its implementation on Github. SB, NN, and MC contributed code to the project. NN, CG, and MD contributed to data acquisition. SB wrote the first version of the manuscript with input from CG and NN. MC and MD wrote the final version of the manuscript.

FUNDING

This work was funding by French Public Investment Bank's ROMANE program.

ACKNOWLEDGMENTS

We thank the France-Alzheimer Association, Plan Alzheimer Foundation, the Foundation Vaincre-Alzheimer, and the French Public Investment Bank's ROMANE program for funding this study.

REFERENCES

Abraham, A., Pedregosa, F., Eickenberg, M., Gervais, P., Mueller, A., Kossaifi, J., et al. (2014). Machine learning for neuroimaging with scikit-learn. *Front. Neuroinform.* 8:14. doi: 10.3389/fninf.2014.00014

Allen Institute for Brain Science (2004). *Allen Mouse Brain Atlas*. Available online at: http://mouse.brain-map.org

Ashburner, J. (2007). A fast diffeomorphic image registration algorithm. *Neuroimage* 38, 95–113. doi: 10.1016/j.neuroimage.2007.07.007

Ashburner, J., and Friston, K. (1997). Multimodal image coregistration and partitioning-a unified framework. *Neuroimage* 6, 209–217. doi: 10.1006/nimg.1997.0290

Avants, B. B., Tustison, N., and Song, G. (2009). Advanced normalization tools (ANTS). *Insight J.* 2, 1–35.

Boyes, R. G., Gunter, J. L., Frost, C., Janke, A. L., Yeatman, T., Hill, D. L., et al. (2008). Intensity non-uniformity correction using N3 on 3-T scanners with multichannel phased array coils. *Neuroimage* 39, 1752–1762. doi: 10.1016/j.neuroimage.2007.10.026

Chou, N., Wu, J., Bingren, J. B., Qiu, A., and Chuang, K.-H. (2011). Robust automatic rodent brain extraction using 3-D pulse-coupled neural networks (PCNN). *IEEE Trans. Image Process.* 20, 2554–2564. doi: 10.1109/TIP.2011.2126587

Cox, R. W. (1996). AFNI: software for analysis and visualization of functional magnetic resonance neuroimages. *Comput. Biomed. Res.* 29, 162–173. doi: 10.1006/cbmr.1996.0014

De Feo, R., and Giove, F. (2019). Towards an efficient segmentation of small rodents brain: a short critical review. *J. Neurosci. Methods* 323, 82–89. doi: 10.1016/j.jneumeth.2019.05.003

Eichelberg, M., Riesmeier, J., Wilkens, T., Hewett, A. J., Barth, A., and Jensch, P. (2004). "Ten years of medical imaging standardization and prototypical implementation: the DICOM standard and the OFFIS DICOM toolkit (DCMTK)," in *Medical Imaging 2004: PACS and Imaging Informatics*, Vol. 5371 (International Society for Optics and Photonics), 57–69. doi: 10.1117/12.534853

Gansner, E. R., and North, S. C. (2000). An open graph visualization system and its applications to software engineering. *Softw. Pract. Exp.* 30, 1203–1233. doi: 10.1002/1097-024X(200009)30:11<1203::AID-SPE338>3.0.CO;2-N

Garin, C. M., Nadkarni, N. A., Bougacha, S., Picq, J.-L., Pepin, J., Flament, J., et al. (2018). "Resting state, gluCEST and anatomical MRI approaches at 11.7T for brain aging studies in a non-human primate," in *Proceedings of the Joint Annual Meeting of the International Society for Magnetic Resonance in Medicine and European Society for Magnetic Resonance in Medicine and Biology* (Paris).

Garin, C. M., Nadkarni, N. A., Landeau, B., Chetelat, G., Picq, J.-L., Bougacha, S., et al. (2019). Resting state cerebral networks in mouse lemur primates: from multilevel validation to comparison with humans. *bioRixv*. doi: 10.1101/599423

Glover, G. H. (2011). Overview of functional magnetic resonance imaging. *Neurosurg. Clin. N. Am.* 22, 133–139. doi: 10.1016/j.nec.2010.11.001

Gorgolewski, K., Burns, C. D., Madison, C., Clark, D., Halchenko, Y. O., Waskom, M. L., et al. (2011). Nipype: a flexible, lightweight and extensible neuroimaging data processing framework in python. *Front. Neuroinform.* 5:13. doi: 10.3389/fninf.2011.00013

Grandjean, J., Canella, C., Anckaerts, C., Ayranci, G., Bougacha, S., Bienert, T., et al. (2020). Common functional networks in the mouse brain revealed by multi-centre resting-state fMRI analysis. *Neuroimage*, 205:116278. doi: 10.1016/j.neuroimage.2019.116278

Hanke, M., and Halchenko, Y. O. (2011). Neuroscience runs on GNU/Linux. *Front. Neuroinform.* 5:8. doi: 10.3389/fninf.2011.00008

Hong, X., To, X. V., Teh, I., Soh, J. R., and Chuang, K.-H. (2015). Evaluation of EPI distortion correction methods for quantitative MRI of the brain at high magnetic field. *Mag. Reson. Imaging* 33, 1098–1105. doi: 10.1016/j.mri.2015.06.010

Hunter, J. D. (2007). Matplotlib: A 2D graphics environment. *Comput. Sci. Eng.* 9:90. doi: 10.1109/MCSE.2007.55

Ioanas, H.-I., Marks, M., Garin, C., Dhenain, M., Yanik, M. F., and Rudin, M. (2020). An automated open-source workflow for standards-compliant integration of small animal magnetic resonance imaging data. *Front. Neuroinform.* 14:5. doi: 10.3389/fninf.2020.00005

Jenkinson, M., Beckmann, C. F., Behrens, T. E., Woolrich, M. W., and Smith, S. M. (2012). Fsl. *Neuroimage* 62, 782–790. doi: 10.1016/j.neuroimage.2011.09.015

Kober, F., Duhamel, G., and Cozzone, P. J. (2008). Experimental comparison of four FAIR arterial spin labeling techniques for quantification of mouse cerebral blood flow at 4.7 T. *NMR Biomed.* 21, 781–792. doi: 10.1002/nbm.1253

Kovačević, N., Henderson, J., Chan, E., Lifshitz, N., Bishop, J., Evans, A., et al. (2005). A three-dimensional MRI atlas of the mouse brain with estimates of the average and variability. *Cereb. Cortex* 15, 639–645. doi: 10.1093/cercor/bhh165

Lancelot, S., Roche, R., Slimen, A., Bouillot, C., Levigoureux, E., Langlois, J., et al. (2014). A multi-atlas based method for automated anatomical rat brain MRI segmentation and extraction of PET activity. *PLoS ONE* 9:e109113. doi: 10.1371/journal.pone.0109113

Lein, E. S., Hawrylycz, M. J., Ao, N., Ayres, M., Bensinger, A., Bernard, A., et al. (2007). Genome-wide atlas of gene expression in the adult mouse brain. *Nature* 445, 168–176. doi: 10.1038/nature05453

Millman, K. J., and Aivazis, M. (2011). Python for scientists and engineers. *Comput. Sci. Eng.* 13, 9–12. doi: 10.1109/MCSE.2011.36

Nadkarni, N. A., Bougacha, S., Garin, C., Dhenain, M., and Picq, J.-L. (2018). Digital templates and brain atlas dataset for the mouse lemur primate. *Data Brief* 21, 1178–1185. doi: 10.1016/j.dib.2018.10.067

Nadkarni, N. A., Bougacha, S., Garin, C., Dhenain, M., and Picq, J.-L. (2019). A 3D population-based brain atlas of the mouse lemur primate with examples of applications in aging studies and comparative anatomy. *Neuroimage* 185, 85–95. doi: 10.1016/j.neuroimage.2018.10.010

Oguz, I., Zhang, H., Rumple, A., and Sonka, M. (2014). RATS: rapid automatic tissue segmentation in rodent brain MRI. *J. Neurosci. Methods* 221, 175–182. doi: 10.1016/j.jneumeth.2013.09.021

Oliphant, T. E. (2006). *A Guide to NumPy*. Vol. 1. Trelgol Publishing.

Pallast, N., Diedenhofen, M., Blaschke, S., Wieters, F., Wiedermann, D., Hoehn, M., et al. (2019). Processing pipeline for atlas-based imaging data analysis of structural and functional mouse brain MRI (AIDAmri). *Front. Neuroinform.* 13:42. doi: 10.3389/fninf.2019.00042

Pedregosa, F., Varoquaux, G., Gramfort, A., Michel, V., Thirion, B., Grisel, O., et al. (2011). Scikit-learn: Machine learning in Python. *J. Mach. Learn. Res.* 12, 2825–2830.

Powell, N. M., Modat, M., Cardoso, M. J., Ma, D., Holmes, H. E., Yu, Y., et al. (2016). Fully-automated μMRI morphometric phenotyping of the Tc1 mouse model of Down syndrome. *PLoS ONE* 11:e0162974. doi: 10.1371/journal.pone.0162974

Sargolzaei, S., Cai, Y., Wolahan, S. M., Gaonkar, B., Sargolzaei, A., Giza, C. C., et al. (2018). "A comparative study of automatic approaches for preclinical MRI-based brain segmentation in the developing rat," in *2018 40th Annual International Conference of the IEEE Engineering in Medicine and Biology Society (EMBC)* (Honolulu, HI: IEEE), 652–655. doi: 10.1109/EMBC.2018.8512402

Sawiak, S., Wood, N., Williams, G., Morton, A., and Carpenter, T. (2009). Voxel-based morphometry in the R6/2 transgenic mouse reveals differences between genotypes not seen with manual 2D morphometry. *Neurobiol. Dis.* 33, 20–27. doi: 10.1016/j.nbd.2008.09.016

Sled, J. G., Zijdenbos, A. P., and Evans, A. C. (1998). A nonparametric method for automatic correction of intensity nonuniformity in MRI data. *IEEE Trans. Med. Imaging* 17, 87–97. doi: 10.1109/42.668698

Tustison, N. J., Avants, B. B., Cook, P. A., Zheng, Y., Egan, A., Yushkevich, P. A., et al. (2010). N4ITK: improved N3 bias correction. *IEEE Trans. Med. Imaging* 29:1310. doi: 10.1109/TMI.2010.2046908

Varoquaux, G., Sadaghiani, S., Pinel, P., Kleinschmidt, A., Poline, J.-B., and Thirion, B. (2010). A group model for stable multi-subject ICA on fMRI datasets. *Neuroimage* 51, 288–299. doi: 10.1016/j.neuroimage.2010.02.010

Wood, T. C., Lythgoe, D. J., and Williams, S. C. (2013). "rBET: making BET work for rodent brains," in *Proceedings of the 21th Meeting of the International Society for Magnetic Resonance in Medicine* (Salt Lake City, UT), Vol. 21, 2706.

Yin, Y., Zhang, X., Williams, R., Wu, X., Anderson, D. D., and Sonka, M. (2010). LOGISMOS - Layered Optimal Graph Image Segmentation of Multiple Objects and Surfaces: cartilage segmentation in the knee joint. *IEEE Trans. Med. Imaging* 29, 2023–2037. doi: 10.1109/TMI.2010.2058861

Zerbi, V., Grandjean, J., Rudin, M., and Wenderoth, N. (2015). Mapping the mouse brain with Rs-fMRI: an optimized pipeline for functional network identification. *Neuroimage* 123, 11–21. doi: 10.1016/j.neuroimage.2015.07.090

Zheng, B. W., Lee, P. T. H., and Golay, X. (2010). High-sensitivity cerebral perfusion mapping in mice by kbGRASE-fair at 9.4 t. *NMR Biomed.* 23, 1061–1070. doi: 10.1002/nbm.1533

Conflict of Interest: The authors declare that the research was conducted in the absence of any commercial or financial relationships that could be construed as a potential conflict of interest.

2. Toxic effects of Aβ seeds

2.1 Context, objectives & abstract

AD is characterized by intracerebral accumulation of abnormal proteinaceous assemblies made of Aβ peptides or Tau proteins. These pathological events are associated with synaptic damage and neural network dysfunctions that are strongly correlated with the cognitive decline. Even if the relationship between AD-associated lesions is still unknown, soluble Aβ accumulation has been proposed to govern this pathological cascade (Edwards, 2019; Hardy and Higgins, 1992; Karran et al., 2011; Karran and De Strooper, 2022). However, it still unclear whether focal events that modulate Aβ accumulation can change the pathology outcome and the clinical fate of AD. Previous attempts to elucidate the effect of Aβ on downstream events have mainly implicated transgenic mice overexpressing human Aβ. Several studies have suggested that intracerebral infusion of well-defined Aβ seeds from synthetic or recombinant non-mutated $Aβ_{1-40}$ or $Aβ_{1-42}$ peptides can increase Aβ plaque deposition several months after the infusion (Ruiz-Riquelme et al., 2018; Stöhr et al., 2014, 2012; Ulm et al., 2021). However, to our knowledge, long-term effects of synthetic or recombinant non-mutated Aβ seeds on synaptic or cognitive impairments have not been reported yet.

In this first article, we aimed at evaluating the impact of highly synaptotoxic Aβ seeds, bearing the *Osaka* mutation (E693Δ) (Tomiyama et al., 2008), on downstream events in the time-course of AD. We showed that intracerebral infusion of $Aβ_{osa}$ increases Aβ plaque depositions and modifies Aβ oligomeric patterns, 4 months post-inoculation in a mouse model of amyloidosis. More interestingly, we showed for the first time that $Aβ_{osa}$ induces memory disturbances, worsens synaptic pathology and subsequently reduces the connectivity between different brain regions. This study clearly shows long-term functional toxicity of $Aβ_{osa}$ seeds. It shows that a single, sporadic event as $Aβ_{osa}$ inoculation can aggravate the fate of the pathology and clinical outcome several months after the event. Extrapolation of this discovery suggests that any event that focally modulates Aβ aggregation process in the time-course of AD can be responsible for the heterogeneity of AD clinical outcome.

2.2 Article

CELESTINE M., Jacquier-Sarlin M., Borel E., Petit F., Perot JB., Hérard AS., Bousset L., Buisson A., Dhenain M. Long term worsening of Alzheimer pathology and clinical outcome by a single inoculation of mutated beta-amyloid seeds. (*Submitted)*

Long term worsening of Alzheimer pathology and clinical outcome by a single inoculation of mutated beta-amyloid seeds

Marina Célestine[1,2], Muriel Jacquier-Sarlin[3], Eve Borel[3], Fanny Petit[1,2], Jean-Baptiste Perot[1,2], Anne-Sophie Hérard[1,2], Luc Bousset[1,2], Alain Buisson[3], Marc Dhenain[1,2]

Author affiliations:

[1] Université Paris-Saclay, CEA, CNRS, Laboratoire des Maladies Neurodégénératives, 18 Route du Panorama, F-92265 Fontenay-aux-Roses, France.

[2] Commissariat à l'Energie Atomique et aux Énergies Alternatives (CEA), Direction de la Recherche Fondamentale (DRF), Institut François Jacob, MIRCen, 18 Route du Panorama, F-92265 Fontenay-aux-Roses, France

[3] Université Grenoble Alpes, Inserm, U1216, Grenoble Institut Neurosciences, GIN, 38000 Grenoble, France

Author emails:

Marina.Celestine: Marina.Celestine@cea.fr;

Muriel Jackier-Sarlin: Muriel.Jacquier-Sarlin@univ-grenoble-alpes.fr;

Eve Borel: Eve.Borel@univ-grenoble-alpes.fr;

Fanny Petit: Fanny.Petit@cea.fr;

Jean-Baptiste Perot: Jean-Baptiste.Perot@icm-institute.org;

Anne-Sophie Hérard: Anne-Sophie.Herard@cea.fr;

Luc Bousset: Luc.Bousset@cnrs.fr;

Alain Buisson: Alain.Buisson@univ-grenoble-alpes.fr;

Marc Dhenain: Marc.Dhenain@cnrs.fr

Correspondence to: Marc Dhenain, DVM, PhD

Université Paris-Saclay, CEA, CNRS, Laboratoire des Maladies Neurodégénératives, MIRCen, 18 Route du Panorama, F-92265 Fontenay-aux-Roses, France

E-mail: marc.dhenain@cnrs.fr

ABSTRACT

Background

Alzheimer's disease (AD) is characterized by intracerebral accumulation of abnormal proteinaceous assemblies made of amyloid-β (Aß) peptides or tau proteins. These lesions induce synaptic dysfunctions that are strongly correlated with cognitive decline. Intracerebral infusion of well-defined Aβ seeds from synthetic or recombinant non-mutated $Aβ_{1-40}$ or $Aβ_{1-42}$ peptides can increase Aβ plaque depositions several months after the infusion. Familial forms of AD are associated with mutations in the amyloid precursor protein (APP) that induce the production of Aβ peptides with different structures. The $Aβ_{osa}$ mutation (E693Δ) is located within the Aβ sequence and thus the $Aβ_{osa}$ peptides have different structures and properties as compared to non-mutated $Aβ_{1-42}$ peptides ($Aβ_{wt}$). Here, we wondered if a single exposure to this mutated Aβ can worsen AD pathology as well as downstream events including cognition, cerebral connectivity and synaptic health several months after the inoculation compared to non-mutated Aβ.

Method

To answer this question we inoculated $Aβ_{1-42}$-bearing Osaka mutation ($Aβ_{osa}$) in the dentate gyrus of $APP_{swe}/PS1_{dE9}$ mice at the age of two months. The inoculated mice were analyzed at 4 months post-inoculation by cognitive evaluation and functional MRI to assess cerebral connectivity. Aβ and tau lesions as well as synaptic density were evaluated by histology. The impact of $Aβ_{osa}$ peptides on synaptic health was also measured on primary cortical neurons.

Results

Remarkably, compared to $Aβ_{wt}$, the intracerebral administration of $Aβ_{osa}$ induced cognitive impairments, synaptic impairments and a reduction of the connectivity between different brain regions, 4 months post-inoculation. Aβ plaque depositions but not tau lesions were increased and Aβ oligomeric patterns were modified.

Conclusion

This is the first study showing long-term functional toxicity of Aβ seeds. It shows that a single, sporadic event as $Aβ_{osa}$ inoculation can worsen the fate of the pathology and clinical outcome several months after the event. Extrapolation of this discovery suggests that any event that modulates focally Aβ aggregation process in the time-course of AD can be responsible for the heterogeneity of AD clinical outcome.

KEYWORDS

Alzheimer's disease, Cerebral connectivity, Amyloid-β, Aβ Osaka, Memory, Synapses, Transmission

GRAPHICAL ABSTRACT

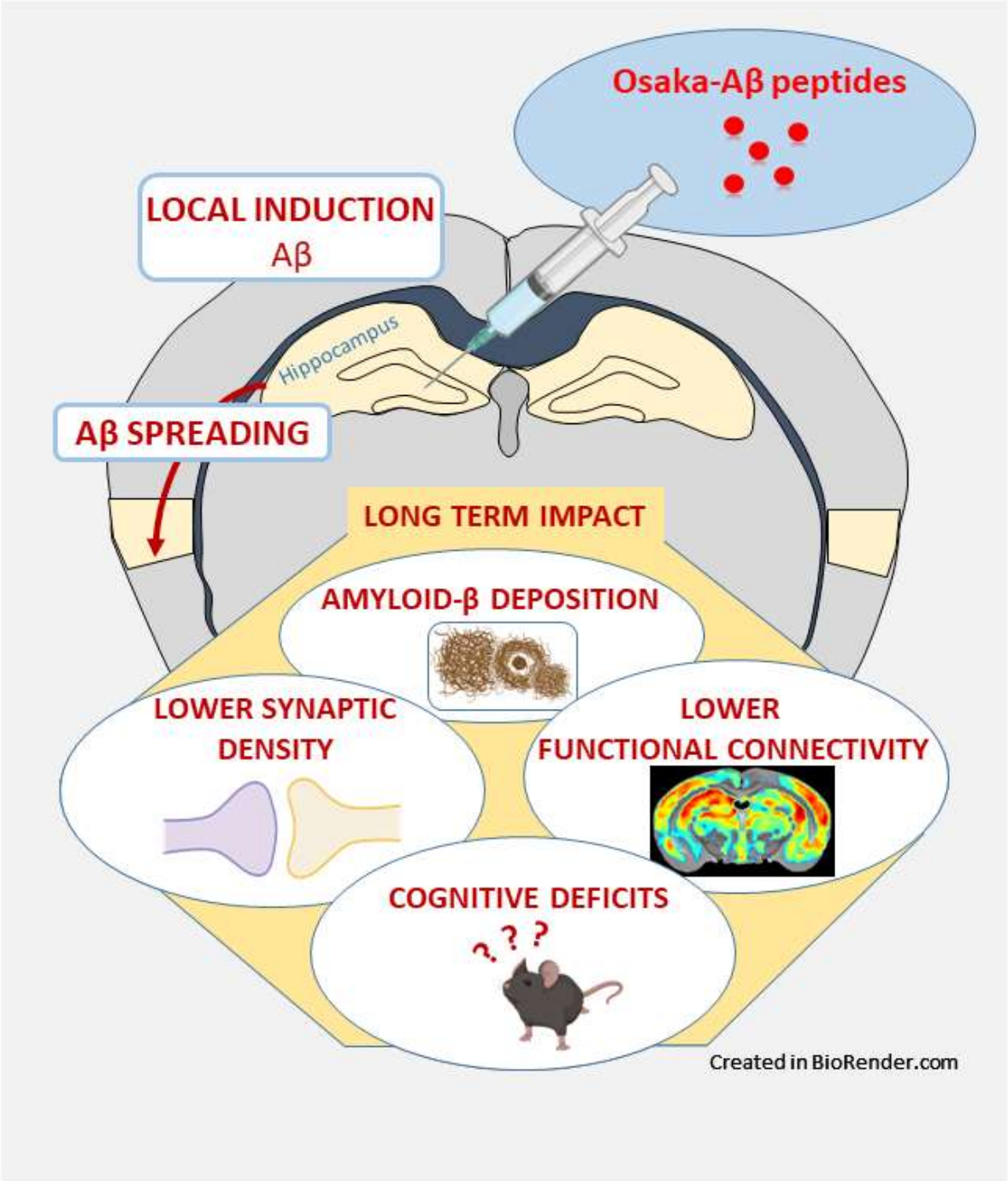

BACKGROUND

Alzheimer's disease (AD) is a clinical entity leading to cognitive deficits. It is characterized by intracerebral accumulation of abnormal proteinaceous assemblies made of amyloid-β (Aß) peptides or tau proteins. These lesions induce synaptic dysfunctions that are strongly correlated with the cognitive decline [1]. Aβ peptides arise from the proteolytic cleavage of the Aβ precursor protein (APP), leading to monomeric Aβ peptides that progressively aggregate to form fibrillary deposits (Aβ plaques). Tau lesions occur as neuropil threads, neurofibrillary tangles (NFTs), and neuritic plaques *i.e.* tau aggregates and hyperphosphorylation within neurites surrounding Aβ deposits.

Several publications in humans [2-4] as well as studies in experimental animal models of AD [5-8] indicate that intracerebral inoculation of minimal amounts of misfolded Aβ present within AD brain extracts induces build-up of Aβ deposits in their host. The intracerebral infusion of well-defined synthetic or recombinant non-mutated $A\beta_{1-40}$ or $A\beta_{1-42}$ peptides can also increase Aβ plaque depositions several months after the infusion [9, 10]. Mechanistic models explaining prion diseases are used to interpret this Aβ deposition. As prion proteins, Aβ proteins can adopt a β-sheet or "amyloid" conformation during which they can form bundles of twisted, unbranched filaments. Each filament is composed of parallel β-strands that are hydrogen-bonded by their backbones. It is suggested that amyloid formation starts with a slow nucleation phase consisting of protein oligomerization leading to seeds of aggregation. This nucleation process is associated with conformation changes of Aβ peptide. Newly produced monomers or oligomers can assemble onto preformed seeds following conformational conversion. With increasing length, fibril can eventually break and generate new seeds that will enhance the conversion either locally or at a distant point following spreading of seeds. This process is thus self-propagating. The kinetics of amyloid fibril formation are a function of the rates of nucleation, growth, and fragmentation. The lag time that precedes protein aggregation *in vitro* can be greatly shortened by the addition of pre-formed exogenous seeds [11].

In addition to Aβ lesions, the inoculation of AD-brain extracts can induce long-term cognitive alterations as well as synaptic impairments in rodents [12] or primates [8, 13]. As inoculation of AD-brain extracts can induce both Aβ and tau pathologies [12], it is difficult to dissociate the role of Aβ or tau on cognitive or synaptic impairments induced by this inoculation [12]. Thus, inoculation of Aβ oligomers was proposed to evaluate the impact of Aβ seeds on brain function. However, although intracerebral infusion of synthetic Aβ oligomers was shown to induce acute memory impairments in wild-type mice [14, 15], to our knowledge, long term effects of synthetic or recombinant Aβ seeds not issued from brain extracts have not been reported on cognition or synaptic impairments.

Some familial forms of AD are associated with mutations in the Aβ fragment of the APP. Given the different structures of Aβ peptides issued from these mutations, we wondered if exposure to mutated

Aβ can worsen AD lesions as well as downstream events including cognition, cerebral connectivity and synaptic health as well as tau pathologies several months after the inoculation. To answer these questions we focused on the Osaka mutation (E693Δ, "Osa"). This mutation, found in a Japanese pedigree of familial AD, corresponds to amino acid 693 deletion from APP gene, resulting in mutant Aβ peptide lacking a glutamic amino acid residue at the 22nd position. Thus, as the mutation is located within the Aβ fragment, the $Aβ_{osa}$ peptides have a different structure and properties as compared to $Aβ_{wt}$ [16]. In particular, they exhibit preferred conformational states that allow higher hydrophobicity resulting in faster oligomerization [17]. The long-term effect of a single intra-hippocampal inoculation of each $Aβ_{osa}$ seed was evaluated four months post inoculation in transgenic mice ($APP_{swe}/PS1_{dE9}$) overexpressing $Aβ_{1-42}$ peptide and presenting Aβ plaques and neuritic plaques [12]. We provide evidence that exposure to $Aβ_{osa}$ induces cognitive and functional impairments, including reduced hippocampal connectivity compared to mice inoculated with non-mutated $Aβ_{1-42}$ peptide ($Aβ_{wt}$). $Aβ_{osa}$-inoculated animals also displayed lower synaptic density and increased Aβ plaque load as well as different Aβ oligomeric patterns without change of tau-positive neuritic plaque burden. Our results suggest that a single exposure to $Aβ_{osa}$ worsen the fate of Aβ lesions and clinical outcome several months after.

RESULTS

Characterization of inoculated Aβ peptides: from structures to synapse-modifying properties

We used a recombinant approach to produce non-mutated $Aβ_{1-42}$ ($Aβ_{wt}$) or $Aβ_{osa}$ (E693Δ also called E22Δ). We characterized by Dynamic Light Scattering (DLS) the size distributions of Aβ assemblies in solutions prior to inoculation in mouse brains. We observed a single population with large polydispersity of particles for both $Aβ_{wt}$ and $Aβ_{osa}$. The size distributions observed for $Aβ_{wt}$ solutions revealed a size distribution between 30 and ~150 nm with an average particle size of 55 nm. $Aβ_{osa}$ solutions had size distribution at higher values (between 70 and ~500 nm) with an average particle size of 271 nm **(Fig. 1A)**. Monomeric forms of Aβ have a hydrodynamic radius of ~2nm, thus $Aβ_{wt}$ and $Aβ_{osa}$ have much larger hydrodynamic radiuses. Aβ structures observed in electron micrographs reflected the diversity seen with DLS as exemplified in **(Fig. 1B)** showing small and large particles of $Aβ_{wt}$ that formed small fibrils whereas $Aβ_{osa}$ showed larger structures.

Aβ aggregation is a nucleation-dependent polymerization process, with a slow initial nucleation phase, called lag-phase, followed by a rapid growth phase [11]. We investigated the assembly properties of different forms of Aβ *in vitro* using thioflavin fluorescence assay [18, 19]. First, synthetic monomeric $Aβ_{1-42}$ was incubated at 37 °C, the ThT fluorescence signal displayed a sigmoidal shape characterized

by a 6 hours lag time followed by an 8 hours elongation step **(Fig. 1C)**. When synthetic monomeric $A\beta_{1-42}$ was seeded with recombinant $A\beta_{wt}$ [10%, v/v] at 37 °C, assembly kinetic was not affected while Aβ fibrils were formed **(Fig. 1C)**. On the contrary, addition of $A\beta_{osa}$ seeds [2 and 10%, v/v] shortened the lag time to 2 and 4 hours respectively **(Fig. 1C)**. Thus, $A\beta_{osa}$ displayed increased seeding effects. At steady state, the Aβ fibrils assembled from synthetic $A\beta_{1-42}$ alone or seeded with $A\beta_{wt}$ or $A\beta_{osa}$ displayed undistinguishable shape when observed by electron microscopy **(not shown)**.

Exogenous application of $A\beta_{osa}$ and $A\beta_{wt}$ impaired synaptic plasticity and induced different mushroom spine changes

As Aβ has been shown to induce synaptic dysfunction [20], we compared the direct impact of $A\beta_{osa}$ and $A\beta_{wt}$ seeds on synaptic health by assessing spine morphology of primary cortical neuron cultures. Cortical neurons were co-transfected with LifeActin-GFP (LA-GFP), a small peptide that specifically binds to F-actin to visualize the dendritic arbor and spines. LA-GFP expressing cortical neurons display characteristic dendrites with a high density of spines **(Fig. 2A)**. Then, we incubated the neurons with 100 nM of either $A\beta_{osa}$ or $A\beta_{wt}$ for 24 hours, and analyzed thin, stubby, mushroom spine density **(Fig. 2B-F)**. Compared to PBS, the total spine density of neurons treated with $A\beta_{osa}$ or $A\beta_{wt}$ was reduced at 24 hours ($p<0.0001$ for $A\beta_{osa}$; $p<0.05$ for $A\beta_{wt}$, **Fig. 2C**). The spine loss was significantly more severe in $A\beta_{osa}$ compared to $A\beta_{wt}$ ($p<0.05$, **Fig. 2C**). The spine loss was mainly due to a strong reduction in mushroom spine density ($p<0.0001$ for $A\beta_{osa}$; $p<0.005$ for $A\beta_{wt}$, **Fig. 2D**) and in thin spine density ($p<0.5$ for $A\beta_{osa}$, **Fig. 2E**) while stubby spine density was not significantly affected by Aβ compared to PBS **(Fig. 2F)**.

Inoculation of $A\beta_{osa}$ impairs long-term memory

We then evaluated the long-term impact of $A\beta_{osa}$ and $A\beta_{wt}$ *in vivo*. 2-month-old $APP_{swe}/PS1_{de9}$ mice were inoculated bilaterally with 0.5µg of Aβ in the molecular layer of the dentate gyrus (MoDG) of the hippocampus. Behavioral assessment was performed at 4 months post-inoculation (mpi) and compared to a PBS-inoculated $APP_{swe}/PS1_{de9}$ and wild-type (WT) littermate groups. Memory impairment of mice inoculated with $A\beta_{osa}$ was detected using a novel object recognition task in a V-maze test **(Fig. 3)**. First, the mice underwent a habituation to the test in an empty arena (day 1) followed by a training phase where two identical objects were added to the V-maze platform (day 2). Comparable discrimination index was observed during the training phase indicating similar exploratory activity between groups **(Fig. 3A)**. The probe test (day 3) was performed the day following the training phase. During this task, a novel object replaced one of the objects. The traveled distance decreased throughout the three days of the test, but was comparable between groups **(Fig. 3B)**. During the probe

test, all groups of $APP_{swe}/PS1_{de9}$ mice had comparable exploratory activity **(Fig. 3C)**. During the discrimination task, mice inoculated with $A\beta_{osa}$ spent less time exploring the novel object compared to control mice (PBS-inoculated WT or $APP_{swe}/PS1_{dE9}$ mice), suggesting memory impairments **(Fig. 3D)**.

$A\beta_{osa}$ inoculation leads to long-term functional impairments

To further evaluate brain function, we performed resting-state functional magnetic resonance imaging studies (fMRI) at 4-months post-inoculation. First, we analyzed the strength of the hippocampus functional connectivity (FC) to the whole-brain. The correlation coefficient between the hippocampus and other brain areas was lower in $A\beta_{osa}$-inoculated animals compared to PBS and $A\beta_{wt}$-inoculated mice **(Fig. 4A)**. This indicates a decreased hippocampus connectivity in $A\beta_{osa}$-inoculated mice. To further identify specific networks impaired by $A\beta_{osa}$ inoculation, we evaluated FC of three selected brain regions (right hemisphere) to the whole-brain: the MoDG (inoculation site), the CA1 area (which contains the pyramidal cell layer (CAPy)) and the entorhinal cortex **(Fig. 4B)**. We used a "Seed-based analysis" (SBA), to identify regions functionally associated with each selected brain region in the $APP_{swe}/PS1_{dE9}$ mice **(Fig. 4C)**. The individual correlation maps were averaged for each group to highlight connected areas in each group of animals **(Fig. 4D)**. Homotopic functional connectivity of MoDG was abolished in the contralateral dorsal dentate gyrus of $A\beta_{osa}$-inoculated mice while unaffected in $A\beta_{wt}$-inoculated animals **(Fig. 4D)**. The MoDG and the CA1 of $A\beta_{osa}$-inoculated mice had also lower FC with the peri-hippocampal area, amygdalar area, temporal area and ventral CA1. The entorhinal cortex of $A\beta_{osa}$-inoculated mice had lower FC with the posterior cingulate, amygdala areas and the hippocampus area compared to PBS-inoculated mice **(Fig. 4D)**. The alterations reported in $A\beta_{osa}$ animals concerned both left-to-right changes (displayed figures) as well as right to left connectivity (not shown).

The individual correlation maps between groups were compared by performing voxel-wise statistical analysis. **Fig. 4E** displays differences between $A\beta_{osa}$- and PBS-inoculated $APP_{swe}/PS1_{dE9}$ mice. As expected, it confirmed changes observed in $A\beta_{osa}$ connectivity maps. Voxel-wise analysis comparing $A\beta_{wt}$- and PBS-inoculated $APP_{swe}/PS1_{dE9}$ mice were also computed. They did not display any changes between the two groups **(not shown)**. The FC alterations in $A\beta_{osa}$-inoculated animals that involve memory circuits are consistent with cognitive impairments reported in transgenic animals expressing $A\beta_{osa}$ variant.

$A\beta_{osa}$ inoculation reduces synaptic density

Mice were sacrificed 4 months post-inoculation (mpi) to evaluate cerebral lesions. We measured synaptic density at the inoculation site (hippocampus) and at a distant place (entorhinal cortex). Double immunolabeling of presynaptic (Bassoon) and postsynaptic (Homer) markers was performed

(Fig. 5A-B) and the amount of synapses was quantified from colocalized puncta. Inoculation of $A\beta_{osa}$ led to decreased **(Fig. 5C-D)** compared to $APP_{swe}/PS1_{dE9}$ mice inoculated either with PBS or $A\beta_{wt}$. Unlike $A\beta_{osa}$, $A\beta_{wt}$. did not modulate synaptic densities in these regions compared with PBS-inoculated animals **(Fig. 5C-D)**. Synapses in the CA2/3 region and the entorhinal cortex were not affected by $A\beta_{osa}$ or $A\beta_{wt}$ **(Fig. 5E-F)**. Taken together, these results indicate that a single inoculation of $A\beta_{osa}$ has a long-term effect on synapse while $A\beta_{wt}$ does not have such long term effect. Altogether our results suggest that inoculation of $A\beta_{osa}$ increases a cascade of events leading to synaptic impairments, neuronal networks disorganization and cognitive impairments.

$A\beta_{osa}$ inoculation increases long-term Aβ plaque deposition without affecting tau pathology within neuritic plaques

Four months post-inoculation (mpi), Aβ plaque load was increased at the inoculation site *i.e.* in the dentate gyrus of mice inoculated with $A\beta_{osa}$ compared to $APP_{swe}/PS1_{dE9}$ inoculated with PBS or $A\beta_{wt}$ **(Fig. 6A-C, 6J)**. Interestingly, in regions connected to the dentate gyrus as the subiculum **(Fig. 6L)** and the entorhinal cortex **(Fig. 6D-F, 5G)**, Aβ plaque load was also increased in animals inoculated with $A\beta_{osa}$ compared to those inoculated with PBS or $A\beta_{wt}$. The Aβ load was similar in the CA1 **(not shown)** and CA2/3 **(not shown)** of the three experimental groups. We did not find differences in plaque morphology **(Fig. 6A-I)**. Taken together, these results indicate that inoculation of $A\beta_{osa}$ increases Aβ pathology at 4 mpi.

At 4 mpi, we detected tau-positive neuritic plaques (NPs) in the hippocampus **(Fig. 7A-C)** and the cortex **(data not shown)** of all groups of inoculated $APP_{swe}/PS1_{dE9}$ mice. Tau lesion loads and morphology were similar between groups in the hippocampus **(Fig. 7D-E)**, the subiculum **(Fig. 7F)** and the entorhinal cortex **(Fig. 7G)**. Thus, the inoculation of $A\beta_{osa}$ or $A\beta_{wt}$ does not modulate tau pathology.

Aβ seeds inoculation modulates Aβ oligomerization patterns and APP processing

As we showed different Aβ deposit load induced by Aβ variants in mice, we wondered if oligomers composition is affected by the inoculation of Aβ variants. We fractionated soluble and insoluble Aβ aggregates from the hippocampus by sarkosyl detergent extraction. Western blot analysis of sarkosyl-soluble fraction showed that inoculation of $A\beta_{osa}$ led to an increase of 15kDa and 12KDa bands (also referred as 4-mer and 3-mer forms of Aβ oligomers [21]) **(Fig. 8A)**. On the contrary, $A\beta_{wt}$ did not affect amyloid oligomers profiles as compared to PBS. The enrichment in multimeric/assembled forms of Aβ were confirmed by dot blot analysis using conformational antibodies against oligomers (A11) and fibrils (OC). We observed that both species increased in the hippocampus of $A\beta_{osa}$-inoculated $APP_{swe}/PS1_{dE9}$

mice compared to WT mice **(Fig. 8B-D)**. Taken together, these results support the hypothesis that different $A\beta_{osa}$ seeds are able to modulate Aβ aggregation processes up to 4 mpi.

An alternative hypothesis is that $A\beta_{osa}$ modulated APP processing [22]. To test this hypothesis, we assessed APP proteolytic profiles caused by α- or β- secretase pathways in the hippocampus at 4 mpi. We quantified by Western blot α-CTF (C83, 9kDA) and β-CTF (C99, 11kDa) **(Fig. 8E-F)**. We found an increase of α-CTF and β-CTF following $A\beta_{osa}$ inoculation compared to PBS and $A\beta_{wt}$-inoculation in $APP_{swe}/PS1d_{E9}$ mice, suggesting that $A\beta_{osa}$ seeds modulate APP processing *in vivo* **(Fig. 8 E-F)**.

DISCUSSION

We showed that intracerebral inoculation of $A\beta_{osa}$ seeds in the hippocampus of a mouse model of amyloidosis worsen the clinical outcome associated with Aβ deposition 4 months post-inoculation. This leads to cognitive and synaptic impairments, reduced functional connectivity between brain regions involved in memory circuits, increased focal Aβ plaque deposition at the inoculation site and spreading of Aβ in the brain as well as reorganization of Aβ oligomers patterns and APP processing. These results suggest that a single, sporadic event as $A\beta_{osa}$ inoculation can worsen the fate of the pathology and clinical outcome several months after the event. In addition, we outlined that distinct Aβ seeds have different impacts on the pathology as toxic effects were detected after inoculation of $A\beta_{osa}$ but not with $A\beta_{wt}$ seeds.

Pathological cascades induced by $A\beta_{osa}$

$A\beta_{osa}$ have different structures and properties as compared to $A\beta_{wt}$ [16]. Here, we showed that it leads to higher molecular species than $A\beta_{wt}$ in solution. Using Thioflavin binding aggregation assay, we showed that it has pro-aggregative properties in presence of $A\beta_{1-42}$ and reduces the lag time to accelerate Aβ aggregation. Our *in vivo* study was performed in $APP_{swe}/PS1_{dE9}$ transgenic mice that express human-like $A\beta_{1-40}$ and $A\beta_{1-42}$ peptides [23]. Thus, in these mice, $A\beta_{osa}$ increased aggregation of endogenous $A\beta_{1-40}$ or $A\beta_{1-42}$ peptides. It is reasonable to assume that this effect of $A\beta_{osa}$ was acute, just after the inoculation. This acute effect could be related to a reduced lag time as shown with thioflavin T assay. It could also be related to a direct impact of $A\beta_{osa}$ on synaptic health leading to modulation of APP processing, as we showed that $A\beta_{osa}$ impairs synapses in neuron cultures.

The long-term effects of the single inoculation of $A\beta_{osa}$ on increased Aβ plaque deposition can be explained by an early increase of Aβ deposition leading to a long term prion-like effect. As we detected changes of APP processing, another non-exclusive hypothesis is that APP processing was shifted towards increased Aβ production and deposition. It is interesting to outline that the effect of $A\beta_{osa}$ on

Aβ aggregation and downstream events was stronger than for $A\beta_{wt}$. Further studies are now required to evaluate links between the structure of $A\beta_{osa}$ and its toxic effects.

To our knowledge, long-term effects of synthetic or recombinant Aβ seeds on cognition or synaptic impairments had not been reported. In our study, we found that the ability to induce cognitive and synaptic impairments was related to the use of mutated $A\beta_{osa}$ while $A\beta_{wt}$ did not have an effect on these outcomes. As Aβ is known to induce synaptic deficits either *ex vivo* or in transgenic mouse models [24-26], it seems reasonable to consider that the increased Aβ plaque deposition and reorganization of oligomeric patterns induced by $A\beta_{osa}$ was, at least in part, responsible for the cognitive and synaptic impairments detected in $A\beta_{osa}$-inoculated $APP_{swe}/PS1_{dE9}$ mice. As the tau pathology within neuritic plaques was correlated with synaptic impairments in $APP_{swe}/PS1_{dE9}$ mice [12], we investigated tau pathology and found that different Aβ seeds did not modulate tau lesion occurrence. This rules out the role of tau pathology on the synaptic changes observed in the $A\beta_{osa}$-inoculated animals.

Taken together, our results suggest that a single inoculation of $A\beta_{osa}$ induced a cascade of events leading to increased Aβ aggregation and modified Aβ oligomeric patterns in the brain. These events would impair synaptic health, leading to cerebral network reorganization and cognitive impairments.

Spreading of Aβ

Inoculation of $A\beta_{osa}$ in the dentate gyrus at 2 months induced increased Aβ deposition 4 months after the inoculation in the proximity of the inoculum site but also at distance, in the entorhinal cortex. The spreading of Aβ from the inoculum site to interconnected brains regions has already been reported in mice inoculated with Aβ-positive brain extract into different brain regions (including olfactory bulb, entorhinal cortex, hippocampus, parietal cortex) [27, 28]. Although this result indicated that Aβ seeds contribute to the spreading of β-amyloidosis, the origin of the Aβ deposition found in the spreading area raises some questions. Indeed, Aβ deposition can come from either the materials injected or the Aβ expressed by the host that would self-propagate in a prion-like manner. Our study cannot decipher between these two hypotheses.

Clinical fate in Alzheimer's

AD is a heterogeneous disease as regard to its origin, clinical course or its lesions [29]. Today, factors modulating the clinical course of pathology are still poorly understood. Several studies have outlined that tau pathology is associated with the heterogeneity of disease evolution [30], although this is not reported in all studies [31, 32]. Modulation of Aβ structures is another potential culprit to explain different fate of AD evolution in particular to explain rapidly progressive forms of AD [33]. Here we

clearly outline that sporadic events that lower lag time of Aβ aggregation can change the pathology outcome and be one of the causes for disease heterogeneity. Of course, an event as $A\beta_{osa}$ intracerebral inoculation is not clinically relevant. However our study outlines that a single event regulating Aβ aggregation and synaptic health can have long term impacts. Previous studies had already shown that a focal seeding event can alter the morphology of resultant Aβ deposits and the age of pathology onset. In particular, Stohr et al showed that intracerebral inoculations of synthetic $A\beta_{1-40}$ or $A\beta_{1-42}$ have different impacts on lesion outcomes [9]. Here we show that cognitive function can also be altered, and more importantly, we isolate $A\beta_{osa}$ as a single form of Aβ that can be responsible for pathology fate changes. Further studies are now required to determine relationships between structural changes of $A\beta_{osa}$ and functional outcomes.

Differences between the impact of a single $A\beta_{osa}$ inoculation in transgenic mice and pathologies developed by $A\beta_{osa}$ in patients

The increased Aβ depositions observed in mice following $A\beta_{osa}$ inoculation was unexpected as patients with $A\beta_{osa}$ mutations display low levels of extracellular Aβ plaques. Moreover, transgenic mice overexpressing the $A\beta_{osa}$ mutations did not show any Aβ plaques even at 24 months [34]. This evidence suggests that Aβ triggers different pathways when it is intracellularly secreted and when it is used as an exogenous seed. However, we also found common features between secreted Aβ and Aβ seeds. Indeed, APP_{osa} transgenic mice display an age-dependent accumulation of Aβ oligomers within neurons in the hippocampus causing alteration of synaptic plasticity and memory impairment [34, 35]. In our western blot analysis of hippocampus extract of $A\beta_{osa}$-inoculated mice, we also found modified Aβ oligomeric patterns as compared to control animals. Moreover, *ex vivo* and *in vivo* data show a clear contribution of $A\beta_{osa}$ in synapto-pathology responsible for memory alteration. Taken together, these results indicate the up-holding of the role of Aβ when it is used as a seed.

Limitations of the study

$APP_{swe}/PS1_{dE9}$ mice were inoculated at 2 months. In the absence of any inoculum, Aβ is continuously secreted and the first senile plaques occur in 4-month-old animals, while in 6 month-old animals, they have reached the cortex and the hippocampus. In our study, we chose to study the impact of $A\beta_{osa}$ inoculation in 6-month-old mice. At this stage, while $A\beta_{wt}$ inoculation had no effect on Aβ plaque deposition, $A\beta_{osa}$ accelerated the development of the plaques. Our interpretation for the lack of impact of $A\beta_{wt}$ on Aβ plaques is that mice were too young to detect the impact of $A\beta_{wt}$, and only strong effects as the one of $A\beta_{osa}$ were detected. Consistently with this suggestion, the induction of Aβ plaques by synthetic or recombinant $A\beta_{1-42}$ (corresponding to $A\beta_{wt}$) seeds has been reported in mice [9].

CONCLUSION

As a conclusion, we showed that a single inoculation of $A\beta_{osa}$ induces long term increased of Aβ plaque deposition, reorganization of cerebral Aβ oligomeric patterns and APP processing, synaptic impairments, reduced hippocampal connectivity with different brain regions involved in memory circuits, and cognitive impairments. This is the first study showing long-term functional toxicity of Aβ seeds. These results suggest that a single, sporadic event as $A\beta_{osa}$ inoculation can worsen the fate of the pathology and clinical outcome several months after the event. Extrapolation of this discovery suggests that any event that modulates focally Aβ aggregation process in the time-course of AD can be responsible for the heterogeneity of AD clinical outcome.

METHODS

Production of recombinant Aβ proteins

To make the plasmids for the fusion protein Aβ(His) of wild-type human β-amyloid 1-42 protein ($A\beta_{wt}$) or $A\beta_{osa}$ mutant (E22Δ), the cDNA containing the sequence for human $A\beta_{1-42}$ was obtained from synthetic oligonucleotides (Sigma, Lyon, France) (containing a Nde1 restriction site as forward primers and a PspXI restriction site as reverse primers) using overlapping PCR. PCR products were then cloned into a pet28a-vector (Novagen, Paris, France) and subsequently constructed as various mutant HIS-$A\beta_{1-42}$ expressing plasmid (pet28a-$A\beta(His)_{wt}$ or pet28a-$A\beta(His)_{osa}$ (E22Δ). The resulting plasmids were verified by sequencing. Escherichia Coli BL21 (DE3) was transformed with the fusion protein plasmids and a single colony was chosen to grow in a 250 mL starter culture in Luria broth (LB medium) overnight at 37°C. The next day, 10 mL of culture was diluted in 1L LB culture medium. When the culture reached an OD600nm of 0.8, isopropyl-beta-D-thiogalactopyranoside (IPTG) was added to 1 mM for induction. The culture was grown for an additional 4 h and the cells harvested by centrifugation at 4000g for 20 min. The pellet was re-suspended in 10 mL ice-cold PBS and lysed by sonication at ice-cold temperature. The cell extract was then centrifuged at 20,000g for 15 min at 4°C. The pellet was re-suspended in 10 mL of 8 M urea in PBS and sonicated as previously described before centrifugation at 20,000g for 15 min at 4°C. The supernatant (5 mL) was diluted with 15 mL of binding buffer (PBS with 10 mM imidazole at pH 8.0). Before affinity purification using nickel-nitriloacetic acid (NTA) column purification, samples were filtered on 0.45 µm. The Ni-NTA column (3 mL of protino Ni-NTA Agarose from Macherey Nagel) was equilibrated with binding buffer prior to loading the sample on the column. Then the column was washed with the washing buffer (PBS with 30 mM imidazole at pH 8.0) with 5-10 column volumes. The protein was then eluted with the elution buffer (PBS with 500 mM imidazole

at pH 7.4). The absorbance at 280 nm was used to monitor the elution but the concentration of the fusion proteins was estimated by comparing the intensity of the band of the protein on SDS-PAGE with that of a known quantity of BSA (Sigma, Lyon, France). A final concentration of 100 µM was obtained and aliquots were stored at -80°C. Aliquots from all subsequent purification steps were analyzed by SDS-PAGE [37], and the identity of $A\beta_{1-42}$ and mutants was verified by western blots using 4G8 monoclonal antibodies against Aβ sequence (4G8).

Endotoxin assay

Endotoxin content of Aβ solutions was detected using a kinetic Limulus amebocyte lysate (LAL) chromogenic endotoxin quantitation kit (Thermo Scientific). In brief, 50 µM of Aβ solution was prepared in PBS and was transferred to a sterile 96-well plate prewarmed to 37°C. LAL (0.1 mL, room temperature) was quickly added to each well. Detection relied on standards supplied in the kit with the range from 0.10 to 1 EU/ml and on positive and negative controls that were performed at the same time as the samples. Endotoxin concentrations were determined by measuring kinetic absorbance at 405 nm at 37°C following the instructions of the manufacturer, in a Spark plate reader (Tecan).

DLS measurements

$A\beta_{wt}$ and $A\beta_{osa}$ solutions were rapidly thawed out and were diluted to 50µM in water. DLS measurements were recorded on a Zetasizer Instrument (Nano ZS; Malvern Instruments) operating at a laser wavelength of 633 nm equipped with a Peltier temperature controller set to 20°C in a 3 x 3 mm quartz cuvette. Malvern DTS software was used to calculate mean hydrodynamic diameters.

Thioflavin T (ThT) binding assay

The aggregative properties of different forms of Aβ can be evaluated *in vitro* with the well-characterized thioflavin dye binding assay [18]. First, the lyophilized synthetic $A\beta_{42}$ was purchased from Covalb (Villeurbanne, France). It was dissolved at a concentration of 1 mM in DMSO. Aβ monomers stock solutions were generated by dilution of the peptides to a concentration of 100 µM in phosphate buffer, pH 7.4.

Spontaneous fibril formation was evaluated by incubating 8 µM of Aβ monomer solutions at 37 °C for 24 hours in presence of 10 µM ThT (Wako Chemical Industries Ltd, Osaka, Japan) in phosphate buffer, pH 7.4. Fibril formation was followed by monitoring ThT fluorescence with shaking using a Hitachi F-2500 fluorometer. The excitation and emission wavelengths were 445 nm and 485 nm, respectively. Fluorescence was determined by averaging the three readings and subtracting the ThT blank.

To perform the seeding experiments, $A\beta_{wt}$ and $A\beta_{osa}$ solutions were rapidly thaw out and were added to the synthetic $A\beta_{1-42}$ + ThT solution previously described. All seeding experiments were performed with 10% or 2% of freshly prepared seeds and 90% or 98% of soluble Aβ monomers, resulting in a total of 8 µM. $A\beta_{wt}$ was used at 10% and $A\beta_{osa}$ at 2 and 10%.

Electron microscopy

Aβ solutions (100 µl sample of 8 µM) were concentrated 10 fold by centrifugation at 50,000g for 10 minutes and suspended in MilliQ water. Assemblies were layered on glow discharged carbon coated 400 mesh copper grid, and stained with 1% uranyl acetate. The assemblies were observed under Jeol 1400 electron microscope at 80kV and 10K magnification. Images were recorded on Rios CCD camera (Gatan).

Primary cultures of cortical neurons

Mouse cortical neurons were cultured from 14- to 15-day-old OF1 embryos (Charles River) as described previously [38]. After extraction of the embryonic brains, the cerebral membranes were removed and the cortices were dissected, mechanically dissociated and cultured in Dulbecco's Modified Eagle's Medium supplemented with 5% horse serum, 5% fetal bovine serum and 1mM glutamine (all from Sigma) on 24-well plates (Falcon; Becton Dickinson) for biochemical experiments.

Neurons were seeded on 35 mm glass-bottom dishes (MatTek) at a final concentration of two cortical hemispheres per dish for confocal experiments. All plates, dishes, and coverslips were coated with 0.1 mg/mL poly-D-lysine and 0.02 mg/mL laminin (Sigma). Cultures were maintained at 37°C in a humidified atmosphere containing 5% CO2/95% air. After 3–4 days in vitro (DIV), cytosine arabinoside (AraC, 10 µM; Sigma) was added to inhibit proliferation of non-neuronal cells in cultures used for biochemistry experiments; 98% of the cells were considered as neuronal. The day before the experiments, cells were washed in DMEM. Treatments were performed on neuronal cultures at 14–15 DIV.

Quantification and morphological characterisation of dendritic spine density

Neurons were visualized using a Nikon Ti C2 confocal microscope with a Nikon 60X water-immersion objective and NIS-Elements software (Nikon, Melville, NY, USA). Excitation of GFP and mCherry fluorophores was performed with an argon laser at 488 nm (emission filtered at 504-541 nm) and at 543 nm (emission filtered at 585-610 nm) respectively. Images (1024x1024 pixels) were acquired as Z-stacks (tridimensional section) with 0.3 µM per step. The acquired images were then deconvoluted using AutoQuantX3 software (Media Cybernetics, Abingdon, Oxon, UK). For analysis of spines, serial image files corresponding to z-stacks of 20–30 optical sections per dendritic segment were directly

processed with NeuronStudio, a software package specifically designed for spine detection and analysis (http://www.mssm.edu/cnic/tools.html). Voxel size was 0.3x0.3x0.300 µm. After modeling of the dendrite surface, protrusions with a minimum volume of 5 voxels, length of between 0.2 µm and 4 µm and a maximal width of 3 µm were retained as spines. Following default settings of the program and the empirical classification rule previously described, spines with a minimum head diameter of 0.35 µm and minimum head vs neck ratio of 1.1 were classified as mushroom spines. Non-mushroom spines with minimum volume of 10 voxels (0.040 μm^3) were classified as stubby spines. All other spines were considered thin.

Transgenic mice

Mouse experiments involved the $APP_{swe}/PS1_{dE9}$ mouse model of amyloidosis (C57Bl6 background) [39]. Aβ plaques can be detected as early as 4 months of age in these mice and increase in number and total area with age [39]. This model expresses endogenous murine tau protein isoforms and is not transgenic for any human tau. At the time of the inoculation of $A\beta_{wt}$, $A\beta_{osa}$ or PBS, at 2 months of age, these mice did not have Aβ plaques. Animals were studied for four months after intracerebral inoculation (at 4 post-inoculation (mpi) respectively, $n_{APP/PS1\text{-}A\beta wt}$=10, $n_{APP/PS1\text{-}A\beta osa}$=10, $n_{APP/PS1\text{-}PBS}$=10). Wild-type littermates injected with the PBS were used as controls for the behavioral tests ($n_{WT\text{-}PBS}$=10). All $APP_{swe}/PS1_{dE9}$ and littermate WT mice were born and bred in our center (Commissariat à l'Energie Atomique, Fontenay-aux-Roses; European Institutions Agreement #B92-032-02). Females were exclusively used in this study in order to optimize group homogeneity (Aβ plaque load is known to vary between males and females). Mice were injected during different inoculation sessions and each group was randomly inoculated at each session to avoid an "order of treatment" confounding effect. All animals were randomly assigned to the experimental groups using a simple procedure: They were identified using increasing numbers based on their birthdate. Animals with increasing numbers were alternatively assigned to the *APP/PS1*-$A\beta_{wt}$ (animal 1, 4, 7…), *APP/PS1*-$A\beta_{osa}$ (animal 2, 5, 8…) and *APP/PS1-*$_{PBS}$ groups (animal 3, 6, 9…). All experimental procedures were conducted in accordance with the European Community Council Directive 2010/63/UE and approved by local ethics committees (CEtEA-CEA DSV IdF N°44, France) and the French Ministry of Education and Research, and in compliance with the 3R guidelines. Animal care was supervised by a dedicated in-house veterinarian and animal technicians. Human endpoints concerning untreatable continuous suffering signs and prostrations were taken into account and not reached during the study. Animals were housed under standard environmental conditions (12-hours light-dark cycle, temperature: 22 ± 1°C and humidity: 50%) with *ad libitum* access to food and water. The design and reporting of animal experiments were based on the ARRIVE reporting guidelines [40]. Sample size was based on previous experiments for Aβ induction in $APP_{swe}/PS1_{dE9}$ mice after inoculation of human brain extracts (estimated with significance

level of 5%, a power of 80%, and a two-sided test) [8] and increased to take into account uncertainties for new markers (tau lesion load, memory and synaptic changes). No animals were excluded from the study. MC was aware of initial group allocation, but further analyses (memory evaluations and post-mortem studies) were performed blindly.

Stereotaxic surgery

Fifty micromolar of $A\beta_{wt}$, $A\beta_{osa}$ solution were rapidly thawed out before stereotaxic injection.

Two month-old $APP_{swe}/PS1_{dE9}$ and wild-type littermates were anesthetized by an intraperitoneal injection of ketamine (1mg/10g; Imalgène 1000, Merial) and xylazine (0.1mg/10g; 2% Rompun, Bayer Healthcare). Local anesthesia was also performed by a subcutaneous injection of lidocaine at the incision site (1 µL/g; 0.5% Xylovet, Ceva). Mice were placed in the stereotaxic frame (Phymep) and bilateral injections of brain samples were performed in the dentate gyrus (AP -2 mm, DV 1.8 mm, L +/- 2 mm from bregma). Two µl/site of sample were administered using 34-gauge needles and Hamilton syringes, at a rate of 0.2µl/min. After the injection, needles were kept in place for 5 more minutes before removal and the incision was sutured. The surgical area was cleaned before and after the procedure using povidone iodine (Vétédine, Vétoquinol). Respiration rate was monitored and body temperature was maintained at 37±0.5°C with a heating pad during the surgery. Anesthesia was reversed with a subcutaneous injection of atipamezole (0.25 mg/kg; Antisedan, Vetoquinol). Mice were placed in a ventilated heating box (25°C) and monitored until full recovery from anesthesia. Postoperative anticipatory pain management consisted of paracetamol administration in drinking water (1.45 mL/20mL of water; Doliprane, Sanofi) during 48 hours.

Behavioral evaluations

A novel object recognition task in a V-maze was used to investigate cognition at 4 mpi on $A\beta_{wt}$-, $A\beta_{osa}$- and PBS-inoculated $APP_{swe}/PS1_{dE9}$ mice. Wild-type littermates injected with PBS were used as controls for the tests. Mice were handled for 2 minutes per day, for 5 days prior to any test to prevent stress effects during tasks. Prior to each test, mice were habituated to the experimental room for 30 minutes. The experimenter was blind to mouse groups. Performances were recorded using a tracking software (EthoVision XT14, Noldus).

The V-maze arena consisted of two 6 cm-wide, 33.5 cm-long and 15 cm-high black arms forming a V shape and exposed to 50 lux-lighting. The test was divided into three phases, each one separated by 24 hours. At the beginning of each session, mice were placed at the center of the arena, *i.e.* at the intersection of the arms. During the habituation phase (day 1), mice were free to explore the empty arena for 9 minutes. The distance traveled was automatically recorded as an indicator of their exploratory activity. For the training phase (day 2), two identical objects (bicolor plastic balls) were

placed at the end of each arm. Exploratory activity was evaluated as the time spent exploring the objects (manually recorded) and the distance traveled during the 9-minute trial. On the test day (day 3), one familiar object (a bicolor plastic ball) was replaced by a novel one of a different shape and material (a transparent glass flask). Recognition was assessed using a discrimination index, calculated as follows:

$$Discrimination\ index = \frac{Time\ exploring\ the\ novel\ object - Time\ exploring\ the\ familiar\ object}{Total\ exploration\ time}$$

It reflects the time spent exploring each object, and therefore, the ability to discriminate a novel object from a familiar, previously explored one. A low discrimination index score reveals that mice spent less time exploring the new object, *i.e.* still had marked interest in the familiar object, and suggests that memory was impaired. Between each run, the V-maze was cleaned with 10% ethanol, effectively eliminating any scents from previous visits.

Animal preparation and MRI acquisition

Animals were scanned four months post-inoculations. Acquisitions were performed on anesthetized mice with a combination of isoflurane 0.5% in a mix 0.5:0.5 of air:O_2 and medetomidine 0.3 mg/kg bolus and 0.1 mg/kg/h infusion. Animals were freely-breathing and respiratory rate was monitored to confirm animal stability until the end of the experiment. Body temperature was maintained by a water heating system at 37°C. The MRI system was an 11.7 Tesla Bruker BioSpec (Bruker, Ettlingen, Germany) using a Cryoprobe surface and running ParaVision 6.0.1. First, anatomical images were acquired using a T2-weighted multi-slice multi-echo (MSME) sequence: TR = 1000 ms, TE = 5 ms, 6 echoes, inter-echo time = 5 ms, FOV = 16 × 16 mm, 100 slices of 0.2 mm thickness, resolution = 200 µm isotropic, acquisition duration 10 minutes. Then, resting-state functional MRI (rs-fMRI) was acquired using a gradient-echo echo planar imaging (EPI) sequences with repetition time (TR) =1000 ms, echo time (TE) =10 ms, flip angle = 90°, volumes = 500, Field of view (FOV) = 22.5 × 15.4 mm, 12 slices of 0.5 mm thickness, acquisition duration 7 minutes 30 seconds. Animals were scanned twice with this sequence. For analysis, the two scans were merged.

MRI pre-processing and analysis

Scanner data were exported as DICOM files then converted into NIfTI-1 format. Then spatial pre-processing was performed using the python module sammba-mri (SmAll MaMmals BrAin MRI; http://sammba-mri.github.io, [41]). First, spatial normalization of the anatomical images was performed to generate a high-resolution template. Rs-fMRI images were corrected for slice timing (interleaved), motion, and B0 distortion (per-slice registration to respective anatomicals). Then, rs-fMRI images were co-registered to the high-resolution template of the DSURQE anatomical atlas (Dorr-

Steadman-Ulman-Richards-Qiu-Egan (DSURQE) atlas, 182 structures, freely available at: https://wiki.mouseimaging.ca/display/MICePub/Mouse+Brain+Atlases) [42-45]. Functional images were further pretreated using Nilearn [46]. Nuisance signal regression was applied including a linear trend as well as 24-motion confounds (6 motion parameters, those of the preceding volume, plus each of their squares [47]). Images were then spatially smoothed with a 0.4 mm full-width at half-maximum Gaussian filter. The first 10 volumes were excluded from analysis after the preprocessing to ensure steady-state magnetization.

MRI analysis and statistics

Seeds in the right hemisphere were defined based on the DSURQE Dorr atlas using 0.3 mm^3 spheres, corresponding to 25 voxels. The mean BOLD signal time-series within a seed were extracted and regressed into individual scans to obtain correlation z-statistic maps using Nilearn. Voxelwise statistics were carried out in FSL using nonparametric permutation tests (randomize) for comparison between PBS- inoculated $APP_{swe}/PS1_{dE9}$ and either $A\beta_{wt}$- or $A\beta_{osa}$-inoculated $APP_{swe}/PS1_{dE9}$ (5000 permutations and voxelwise correction). 3D representation of voxelwise statistical maps are shown as color-coded t-statistics overlays on the DSURQE template at $0.04 \times 0.04 \times 0.04\ mm^3$ using MRIcroGL (https://www.nitrc.org/projects/mricrogl/).

Animal euthanasia and brain preparation

Mice were sacrificed at 4 mpi, after MRI acquisition, with an intraperitoneal injection of a lethal dose of pentobarbital (100 mg/kg; Exagon, Axience). They were perfused intracardially with cold sterile 0.1M PBS for 4 minutes, at a rate of 8 ml/min. The brain was extracted and separated in two hemispheres. The left hemisphere was dissected in order to take out the hippocampus and the cortex. Samples were directly deep-frozen into liquid nitrogen and stored at −80 °C for biochemical analysis. For histology using, the right hemisphere was post-fixed in 4% paraformaldehyde for 48 hours at +4°C, transferred into a 15% sucrose solution for 24 hours and in a 30% sucrose solution for 48 hours at +4°C for cryoprotection. Serial coronal sections of 40 µm were performed with a microtome (SM2400, Leica Microsystem) and stored at -20°C in a storing solution (glycerol 30%, ethylene glycol 30%, distilled water 30%, phosphate buffer 10%).

Mouse brain sample preparation for biochemical analyses

For amyloid protein extraction, deep-frozen brain tissue was dissociated with Collagenase D (2 mg/mL) in Tris-buffer saline (20 mM Tris-HCl, 150 mM NaCl, pH 7.4) at 1:10 TBS volume:brain wet weight and incubated at 37°C. Brains were further homogenized using a Dounce homogenizer with 20 strokes in ice-cold quench buffer containing protease inhibitors (Complete, PMSF 1 mM) and phosphatase

inhibitors (Na_3VO_4 1 mM, NaF 10 mM). Sarkosyl (2%) were added to homogenates. Samples were centrifuged for 30 min at 10,000 x g at 4°C. The resulting supernatant was further centrifuged for 1 hour at 100,000g in a 4°C TLA100.2 rotor on Beckman TL 100. The resulting supernatant called S100K contained the sarkosyl-soluble fraction. Pellet (P100K) was washed twice in TBS and finally resuspended in TBS at 1:10 TBS volume:brain wet weight. All samples were stored at -80°C until analysis.

Western blotting and dot blotting

For western blot, samples were diluted in LDS (Lithium Dodecyl Sulfate) sample buffer (NuPage) and sampling reducing agent in order to load 20 µg of proteins. After heating, samples were loaded on a 4-12% Criterion™ XT Bis-Tris gel (Bio-Rad), migrated in XT MES Running Buffer (Bio-Rad) for 1 hour at 110 V and transferred onto 0.2 µm nitrocellulose. For dot blot, 2µL of samples were directly loaded onto 0.2 µm nitrocellulose. After 1 hour of blocking at room temperature, membranes were blotted overnight at 4°C with primary antibodies 6E10 (Against human $A\beta_{1-16}$; Biolegend), APP-Cter-17 (against the last 17 amino acids of the human APP sequence [36, 48], A11 (against oligomeric species, ThermoFisher) and OC (anti-amyloid fibrils, Rockland). After rinse in TBS-T, membranes were incubated with secondary antibodies for 1 hour at room temperature. Proteins were revealed using horseradish peroxidase (HRP) and ECL™ Western Blotting Detection Reagent (G&E Healthcare). Quantifications of protein expression levels were performed on ImageJ Software.

Immunohistochemistry

Aβ deposits were evaluated using a 4G8 labeling. Tau was evaluated using labeling with AT8 directed against hyperphosphorylated tau. Free-floating brain sections were rinsed in a 0.1M PBS solution (10% Sigma-Aldrich® phosphate buffer, 0.9% Sigma-Aldrich® NaCl, distilled water) before use. Washing and incubation steps were performed on a shaker at room temperature unless indicated otherwise.

4G8 labeling was performed after pretreating brain sections with 70% formic acid (VWR®) for 20 minutes at room temperature. AT8 labeling was performed after a pre-treatment with EDTA 1X citrate (Diagnostic BioSystems®) for 30 minutes at 95°C. All tissues were then incubated in 30% hydrogen peroxide (Sigma-Aldrich®) diluted 1/100 for 20 minutes to inhibit endogenous peroxidases. Blocking of non-specific antigenic sites was achieved over 1 hour using a 0.2% Triton X-100/0.1M PBS (Sigma-Aldrich®) (PBST) solution containing 4.5% normal goat serum or 5% bovine serum albumin. Sections were then incubated at +4°C with the 4G8 (Biolegend 800706, 1/500) antibody diluted in a 3%NGS/PBST solution for 48h, or with the AT8 (Thermo MN1020B, 1/500) antibody diluted in a 3%NGS/PBST solution for 96h. After rinsing, an incubation with the appropriate biotinylated secondary antibody diluted to 1/1000 in PBST was performed for 1h at room temperature, followed by a 1h

incubation at room temperature with a 1:250 dilution of an avidin-biotin complex solution (ABC Vectastain kit, Vector Laboratories®). Revelation was performed using the DAB Peroxidase Substrate Kit (DAB SK4100 kit, Vector Laboratories®). Sections were mounted on Superfrost Plus slides (Thermo-Scientific®). For the AT8 labellings, a cresyl violet counterstain was performed. All sections were then dehydrated in successive baths of ethanol at 50°, 70°, 96° and 100° and in xylene. Slides were mounted with the Eukitt® mounting medium (Chem-Lab®).

Stained sections were scanned using an Axio Scan.Z1 (Zeiss® - Z-stack images acquired at 20× (z-stacks with 16 planes, 1µm steps with extended depth of focus)). Each slice was extracted individually in the .czi format using the Zen 2.0 (Zeiss®) software. Image processing and analysis were performed with the ImageJ 1.53i software. Macros were developed for each staining in order to attain a reproducible semi-automated quantification. Images were imported with a 50% reduction in resolution (0.44 µm/pixel), converted to the RGB format and saved as .tif. The 4G8 immunostaining was highlighted by color deconvolution with the H DAB vectors and by selecting the resulting DAB image. Then, segmentation was performed through an automatic local thresholding using the Phansalkar method (radius = 50). Aβ load was evaluated after quantification of the 4G8-labeled particles between 7 and 5,000 µm², and normalization to the surface area of each region of interest (ROI). The AT8 immunostaining was highlighted - after background subtraction (rolling ball, radius = 50) and contrast enhancement (saturated pixels = 0.5%) - by color deconvolution with the H DAB vectors and by selecting the resulting DAB image. Then, segmentation of the whole staining was performed through an automatic local thresholding using the Phansalkar method (radius = 90). Non-specific staining from vessels was also removed by performing a mask using the Sauvola (radius = 5) automatic local threshold. Finally, the vessel mask was subtracted to the whole staining image to provide an AT8-positive image from which tau loads were assessed by an evaluation of the percentage of AT8-positive surface area in each ROI.

All quantifications were performed on adjacent slices between 1.98 mm and -4.36 mm from bregma. Eighteen adjacent slices were analyzed for the 4G8 and AT8 staining. All ROIs were manually segmented using ImageJ/FIJI, according to the Paxinos and Franklin neuro-anatomical atlas of mouse brain [49].

Evaluation of synaptic density

Synaptic density was evaluated in the hippocampus (CA1) and the perirhinal/entorhinal cortex of all inoculated mice using a double immunolabeling of presynaptic (Bassoon) and postsynaptic (Homer1) markers. Free-floating sections were permeabilized in a 0.5% Triton X-100/0.1M PBS (Sigma-Aldrich®) solution for 15 min. Slices were incubated with Bassoon (Abcam Ab82958, 1/200) and Homer1 (Synaptic systems 160003, 1/400) antibodies diluted in 3% BSA/PBST solution for 24 hours at RT.

Incubation with secondary antibodies coupled to a fluorochrome (Alexa Fluor) diluted in a 3% BSA/0.1M PBS solution was then performed for 1h at room temperature. Sections were rinsed and mounted on Superfrost Plus (Thermo-Scientific®) slides with the Vectashield® mounting medium with a refractive index of 1.45. Images of stained sections were acquired using a Leica DMI6000 confocal optical microscope (TCS SPE) with a 40x oil-immersion objective (refractive index 1.518) and the Leica Las X software. A confocal zoom of 3 and a pinhole aperture fixed at 1 Airy were applied. Acquisition was performed in sequential mode with a sampling rate of 1024 x 1024 and a scanning speed of 700 Hz. Image resolution was 80 nm/pixel and the optical section was 0.896 µm. 26 separate planes with a 0.2 µm step were acquired. The excitation wavelengths were 594 nm or 633 nm. Image acquisition in the dentate gyrus, CA1 and CA2/3 region was performed on 5 adjacent slices located between -1.58 mm and -3.40 mm from the bregma, with 3 images per slice. For the entorhinal cortex, 3 adjacent slices located between -2.98 mm and -3.40 mm from the bregma were analyzed, with 2 images acquired per slice. 3D deconvolution of the images was performed using the AutoQuant X3 software. The deconvoluted 8-bit images were analyzed using the ImageJ software, as described in Gilles et al [50]. Briefly, automated 3D segmentation of the presynaptic (Bassoon) and postsynaptic (Homer1) stained deconvoluted images was performed using "3D spots segmentation" from ImageJ (with "gaussian fit", "block" and "no watershed" options; https://imagej.net/plugins/3d-segmentation). Co-localization of overlapping objects was evaluated using "DiAna" from imageJ (https://imagej.net/plugins/distance-analysis). The percentage of colocalized objects was quantified as an index of synaptic density.

Statistical analysis

Statistical analysis was performed using the GraphPad Prism software 9. For the behavioral tasks analysis, Kruskal-Wallis tests with Dunn's multiple comparisons were performed except when repeated measures were acquired, in which case, a two-way repeated measures ANOVA with the Geisser-Greenhouse correction and Dunnett's multiple comparisons was carried out. For the post-mortem analysis, Kruskal-Wallis tests with Dunn's multiple comparisons tests were performed in order to compare differences between inoculated mice. The significance level was set at $p<0.05$. Data are shown on scattered dot plots with mean ± standard error of the mean (SEM).

Data availability

The data that support the findings of this study are available from the corresponding author, upon request.

List of abbreviations

Aβ = amyloid-β; NFTs = Neurofibrillary tangles; AD = Alzheimer's disease; mpi = months post-inoculation; APP = Amyloid precursor protein; PS1 = Presenilin 1; WT = wild-type; ThT= Thioflavine T; SBA = Seed-based analysis

Declarations

Ethics approval and consent to participate

All experimental procedures were conducted in accordance with the European Community Council Directive 2010/63/UE and approved by local ethics committees (CEtEA-CEA DSV IdF N°44, France) and the French Ministry of Education and Research, and in compliance with the 3R guidelines. Animal care was supervised by a dedicated veterinarian and animal technicians.

Consent for publication

Does not apply to the content of this article.

Availability of data and materials

The data that support the findings of this study are available from the corresponding author.

Competing interests

The authors declare that they have no competing interests.

Funding

The project was funded by the Fondation Vaincre Alzheimer 2018 and the Association France-Alzheimer 2021. It was performed in a core facility supported by/member of NeurATRIS - ANR-11-INBS-0011. It was also supported by internal funds from the Laboratory of Neurodegenerative Diseases and MIRCen. MC was financed by the French Ministère de l'Enseignement Supérieur, de la Recherche, et de l'Innovation. The funding sources had no role in the design of the study, in the collection, analysis, and interpretation of data, nor in writing the manuscript.

Author's contributions

M.C., A.S.H., A.B., and M.D. contributed to the study conception and design. M.J.S., E. B., A.B. provided the recombinant Aβ proteins. M.C. performed the inoculations in mice. M.C. designed and performed memory evaluations, M.C., J.B.P., M.D. designed and performed connectivity studies, M.C., A.S.H., F.P., designed and performed the immunohistological analysis in animals. M.C., M.J.S., and A.B. performed biochemical analysis. M.C., L.B. performed Thioflavin aggregation assays and electron microscopy.

M.J.S., E. B., A.B. performed ex vivo experiments on cell cultures. M.C., A.B., and M.D. wrote the manuscript. All authors commented on previous versions of the manuscript. All authors read and approved the final manuscript.

Acknowledgements

We thank Martine Guillermier and Mylène Gaudin for surgical expertise during inoculation of proteins to animals. We thank Nicolas Heck for his help in synapse quantification. This work has benefited from the platform and expertise of the Electron Microscopy Facility of
I2BC. We thank Nicolas Sergeant for providing the APP-Cter-17 antibody.

REFERENCES

1. Koffie RM, Hyman BT, Spires-Jones TL. Alzheimer's disease: synapses gone cold. Mol Neurodegener 2011; 6: Artn 63. https://doi.org/10.1186/1750-1326-6-63.

2. Jaunmuktane Z, Mead S, Ellis M, Wadsworth JD, Nicoll AJ, Kenny J*, et al.* Evidence for human transmission of amyloid-beta pathology and cerebral amyloid angiopathy. Nature 2015; 525(7568): 247-50. https://doi.org/10.1038/nature15369.

3. Duyckaerts C, Sazdovitch V, Ando K, Seilhean D, Privat N, Yilmaz Z*, et al.* Neuropathology of iatrogenic Creutzfeldt-Jakob disease and immunoassay of French cadaver-sourced growth hormone batches suggest possible transmission of tauopathy and long incubation periods for the transmission of Abeta pathology. Acta Neuropathol 2018; 135(2): 201-12. https://doi.org/10.1007/s00401-017-1791-x.

4. Herve D, Porche M, Cabrejo L, Guidoux C, Tournier-Lasserve E, Nicolas G*, et al.* Fatal Abeta cerebral amyloid angiopathy 4 decades after a dural graft at the age of 2 years. Acta Neuropathol 2018; 135(5): 801-3. https://doi.org/10.1007/s00401-018-1828-9.

5. Kane MD, Lipinski WJ, Callahan MJ, Bian F, Durham RA, Schwarz RD*, et al.* Evidence for seeding of beta-amyloid by intracerebral infusion of Alzheimer brain extracts in beta -amyloid precursor protein-transgenic mice. J Neurosci 2000; 20(10): 3606-11. https://doi.org/10.1523/JNEUROSCI.20-10-03606.2000.

6. Meyer-Luehmann M, Coomaraswamy J, Bolmont T, Kaeser S, Schaefer C, Kilger E*, et al.* Exogenous induction of cerebral beta-amyloidogenesis is governed by agent and host. Science 2006; 313(5794): 1781-4. https://doi.org/10.1126/science.1131864.

7. Novotny R, Langer F, Mahler J, Skodras A, Vlachos A, Wegenast-Braun BM*, et al.* Conversion of Synthetic A beta to In Vivo Active Seeds and Amyloid Plaque Formation in a Hippocampal Slice Culture Model. J Neurosci 2016; 36(18): 5084-93. https://doi.org/10.1523/Jneurosci.0258-16.2016.

8. Gary C, Lam S, Herard AS, Koch JE, Petit F, Gipchtein P*, et al.* Encephalopathy induced by Alzheimer brain inoculation in a non-human primate. Acta Neuropathol Commun 2019; 7(1): 126. https://doi.org/10.1186/s40478-019-0771-x.

9. Stohr J, Condello C, Watts JC, Bloch L, Oehler A, Nick M*, et al.* Distinct synthetic Abeta prion strains producing different amyloid deposits in bigenic mice. Proc Natl Acad Sci USA 2014; 111(28): 10329-34. https://doi.org/10.1073/pnas.1408968111.

10. Ulm BS, Borchelt DR, Moore BD. Remodeling Alzheimer-amyloidosis models by seeding. Mol Neurodegener 2021; 16(1): ARTN 8. https://doi.org/10.1186/s13024-021-00429-4.

11. Jucker M, Walker LC. Self-propagation of pathogenic protein aggregates in neurodegenerative diseases. Nature 2013; 501(7465): 45-51. https://doi.org/10.1038/nature12481.

12. Lam S, Herard AS, Boluda S, Petit F, Eddarkaoui S, Cambon K*, et al.* Pathological changes induced by Alzheimer's brain inoculation in amyloid-beta plaque-bearing mice. Acta Neuropathol Commun 2022; 10(1): ARTN 112. https://doi.org/10.1186/s40478-022-01410-y.

13. Lam S, Petit F, Hérard A-S, Boluda S, Eddarkaoui S, Guillermier M*, et al.* Transmission of amyloid-beta and tau pathologies is associated with cognitive impairments in a primate. Acta Neuropathol Commun 2021; 9: 165. https://doi.org/10.1186/s40478-021-01266-8.

14. Balducci C, Beeg M, Stravalaci M, Bastone A, Sclip A, Biasini E*, et al.* Synthetic amyloid-beta oligomers impair long-term memory independently of cellular prion protein. Proc Natl Acad Sci USA 2010; 107(5): 2295-300. https://doi.org/10.1073/pnas.0911829107.

15. Epelbaum S, Youssef I, Lacor PN, Chaurand P, Duplus E, Brugg B*, et al.* Acute amnestic encephalopathy in amyloid-beta oligomer-injected mice is due to their widespread diffusion in vivo. Neurobiol Aging 2015; 36: 2043-52. https://doi.org/10.1016/j.neurobiolaging.2015.03.005.

16. Schutz AK, Vagt T, Huber M, Ovchinnikova OY, Cadalbert R, Wall J*, et al.* Atomic-resolution three-dimensional structure of amyloid beta fibrils bearing the Osaka mutation. Angew Chem Int Edit 2015; 54(1): 331-5. https://doi.org/10.1002/anie.201408598.

17. Jang H, Arce FT, Ramachandran S, Kagan BL, Lal R, Nussinov R. Disordered amyloidogenic peptides may insert into the membrane and assemble into common cyclic structural motifs. Chemical Society reviews 2014; 43(19): 6750-64. https://doi.org/10.1039/c3cs60459d.

18. LeVine H. Quantification of beta-sheet amyloid fibril structures with thioflavin T. Method Enzymol 1999; 309: 274-84. https://doi.org/10.1016/S0076-6879(99)09020-5.

19. Ono K, Takahashi R, Ikeda T, Mizuguchi M, Hamaguchi T, Yamada M. Exogenous amyloidogenic proteins function as seeds in amyloid beta-protein aggregation. Biochim Biophys Acta 2014; 1842(4): 646-53. https://doi.org/10.1016/j.bbadis.2014.01.002.

20. Lacor PN, Buniel MC, Chang L, Fernandez SJ, Gong Y, Viola KL*, et al.* Synaptic targeting by Alzheimer's-related amyloid beta oligomers. J Neurosci 2004; 24(45): 10191-200. https://doi.org/10.1523/JNEUROSCI.3432-04.2004.

21. Lutzenberger M, Burwinkel M, Riemer C, Bode V, Baier M. Ablation of CCAAT/enhancer-binding protein delta (C/EBPD): Increased plaque burden in a murine Alzheimer's disease model. PLoS ONE 2015; 10(7): ARTN e0134228. https://doi.org/10.1371/journal.pone.0134228.

22. Rolland M, Powell R, Jacquier-Sarlin M, Boisseau S, Reynaud-Dulaurier R, Martinez-Hernandez J*, et al.* Interaction of Aβ oligomers with neuronal APP triggers a vicious cycle leading to the propagation of synaptic plasticity alterations to healthy neurons. J Neurosci 2020; 40(27): 5161-76. https://doi.org/10.1523/Jneurosci.2501-19.2020.

23. Jankowsky JL, Fadale DJ, Anderson J, Xu GM, Gonzales V, Jenkins NA*, et al.* Mutant presenilins specifically elevate the levels of the 42 residue beta-amyloid peptide in vivo: evidence for

augmentation of a 42-specific gamma secretase. Hum Mol Genet 2004; 13(2): 159-70. https://doi.org/10.1093/hmg/ddh019.

24. Selkoe DJ. Alzheimer's disease is a synaptic failure. Science 2002; 298(5594): 789-91. https://doi.org/10.1126/science.1074069.

25. Sivanesan S, Tan A, Rajadas J. Pathogenesis of abeta oligomers in synaptic failure. Curr Alzh Res 2013; 10(3): 316-23. https://doi.org/10.2174/1567205011310030011.

26. Spires-Jones TL, Hyman BT. The intersection of amyloid beta and tau at synapses in Alzheimer's disease. Neuron 2014; 82(4): 756-71. https://doi.org/10.1016/j.neuron.2014.05.004.

27. Eisele YS, Bolmont T, Heikenwalder M, Langer F, Jacobson LH, Yan ZX*, et al.* Induction of cerebral beta-amyloidosis: intracerebral versus systemic Abeta inoculation. Proc Natl Acad Sci USA 2009; 106(31): 12926-31. https://doi.org/ 10.1073/pnas.0903200106.

28. Ye L, Hamaguchi T, Fritschi SK, Eisele YS, Obermuller U, Jucker M*, et al.* Progression of seed-induced Abeta deposition within the limbic connectome. Brain Pathol 2015; 25(6): 743-52. https://doi.org/10.1111/bpa.12252.

29. Ferreira D, Nordberg A, Westman E. Biological subtypes of Alzheimer disease A systematic review and meta-analysis. Neurology 2020; 94(10): 436-48. https://doi.org/10.1212/Wnl.0000000000009068.

30. Dujardin S, Commins C, Lathuiliere A, Beerepoot P, Fernandes AR, Kamath TV*, et al.* Tau molecular diversity contributes to clinical heterogeneity in Alzheimer's disease. Nat Med 2020; 26(8): 1256-+. https://doi.org/10.1038/s41591-020-0938-9.

31. Sirkis DW, Bonham LW, Johnson TP, La Joie R, Yokoyama JS. Dissecting the clinical heterogeneity of early-onset Alzheimer's disease. Mol Psychiatry 2022; 27(6): 2674-88. https://doi.org/10.1038/s41380-022-01531-9.

32. Singleton E, Hansson O, Pijnenburg YAL, La Joie R, Mantyh WG, Tideman P*, et al.* Heterogeneous distribution of tau pathology in the behavioural variant of Alzheimer's disease. J Neurol Neurosur Psy 2021; 92(8): 872-80. https://doi.org/10.1136/jnnp-2020-325497.

33. Cohen ML, Kim C, Haldiman T, ElHag M, Mehndiratta P, Pichet T*, et al.* Rapidly progressive Alzheimer's disease features distinct structures of amyloid-beta. Brain 2015; 138(Pt 4): 1009-22. https://doi.org/10.1093/brain/awv006.

34. Tomiyama T, Matsuyama S, Iso H, Umeda T, Takuma H, Ohnishi K*, et al.* A mouse model of amyloid beta oligomers: Their contribution to synaptic alteration, abnormal tau phosphorylation, glial activation, and neuronal loss in vivo. J Neurosci 2010; 30(14): 4845-56. https://doi.org/10.1523/Jneurosci.5825-09.2010.

35. Matsuyama S, Teraoka R, Mori H, Tomiyama T. Inverse correlation between amyloid precursor protein and synaptic plasticity in transgenic mice. Neuroreport 2007; 18(10): 1083-7. https://doi.org/Doi 10.1097/Wnr.0b013e3281e72b18.

36. Sergeant N, David JP, Champain D, Ghestem A, Wattez A, Delacourte A. Progressive decrease of amyloid precursor protein carboxy terminal fragments (APP-CTFs), associated with tau pathology stages, in Alzheimer's disease. J Neurochem 2002; 81(4): 663-72. https://doi.org/DOI 10.1046/j.1471-4159.2002.00901.x.

37. Laemmli UK. Cleavage of structural proteins during assembly of head of bacteriophage-T4. Nature 1970; 227(5259): 680-+. https://doi.org/Doi 10.1038/227680a0.

38. Leveille F, El Gaamouch F, Gouix E, Lecocq M, Lobner D, Nicole O*, et al.* Neuronal viability is controlled by a functional relation between synaptic and extrasynaptic NMDA receptors. Faseb Journal 2008; 22(12): 4258-71. https://doi.org/10.1096/fj.08-107268.

39. Garcia-Alloza M, Robbins EM, Zhang-Nunes SX, Purcell SM, Betensky RA, Raju S*, et al.* Characterization of amyloid deposition in the APPswe/PS1dE9 mouse model of Alzheimer disease. Neurobiol Dis 2006; 24(3): 516-24. https://doi.org/10.1016/j.nbd.2006.08.017.

40. du Sert NP, Hurst V, Ahluwalia A, Alam S, Avey MT, Baker M*, et al.* The ARRIVE guidelines 2.0: Updated guidelines for reporting animal research. Bmc Vet Res 2020; 16(1): Article 242. https://doi.org/10.1186/s12917-020-02451-y.

41. Celestine M, Nadkarni NA, Garin C, Bougacha S, Dhenain M. Sammba-MRI, a library for small animal neuroimaging data processing in Python. Front Neuroinform 2020; 14:24. https://doi.org/10.3389/fninf.2020.00024.

42. Dorr AE, Lerch JP, Spring S, Kabani N, Henkelman RM. High resolution three-dimensional brain atlas using an average magnetic resonance image of 40 adult C57Bl/6J mice. Neuroimage 2008; 42(1): 60-9. https://doi.org/10.1016/j.neuroimage.2008.03.037.

43. Steadman PE, Ellegood J, Szulc KU, Turnbull DH, Joyner AL, Henkelman RM*, et al.* Genetic effects on cerebellar structure across mouse models of autism using a magnetic resonance imaging atlas. Autism Res 2014; 7(1): 124-37. https://doi.org/10.1002/aur.1344.

44. Ullmann JFP, Watson C, Janke AL, Kurniawan ND, Reutens DC. A segmentation protocol and MRI atlas of the C57BL/6J mouse neocortex. Neuroimage 2013; 78: 196-203. https://doi.org/10.1016/j.neuroimage.2013.04.008.

45. Richards K, Watson C, Buckley RF, Kurniawan ND, Yang ZY, Keller MD*, et al.* Segmentation of the mouse hippocampal formation in magnetic resonance images. Neuroimage 2011; 58(3): 732-40. https://doi.org/10.1016/j.neuroimage.2011.06.025.

46. Abraham A, Pedregosa F, Eickenberg M, Gervais P, Mueller A, Kossaifi J, *et al.* Machine learning for neuroimaging with scikit-learn. Front Neuroinform 2014; 8(14). https://doi.org/10.3389/fninf.2014.00014.

47. Friston KJ, Holmes AP, Worsley KJ, Poline JP, Frith CD, Frackowiak RSJ. Statistical parametric maps in functional imaging: a general linear approach. Human Brain Mapping 1994; 2(4): 189-210. https://doi.org/10.1002/hbm.460020402.

48. Vingtdeux V, Hamdane M, Gompel M, Begard S, Drobecq H, Ghestem A, *et al.* Phosphorylation of amyloid precursor carboxy-terminal fragments enhances their processing by a gamma-secretase-dependent mechanism. Neurobiol Dis 2005; 20(2): 625-37. https://doi.org/10.1016/j.nbd.2005.05.004.

49. Paxinos G, Franklin KBJ. The mouse brain in stereotaxic coordinates. second ed. San Diego: Academic Press; 2001.

50. Gilles JF, Dos Santos M, Boudier T, Bolte S, Heck N. DiAna, an ImageJ tool for object-based 3D co-localization and distance analysis. Methods 2017; 115: 55-64. https://doi.org/10.1016/j.ymeth.2016.11.016.

FIGURES

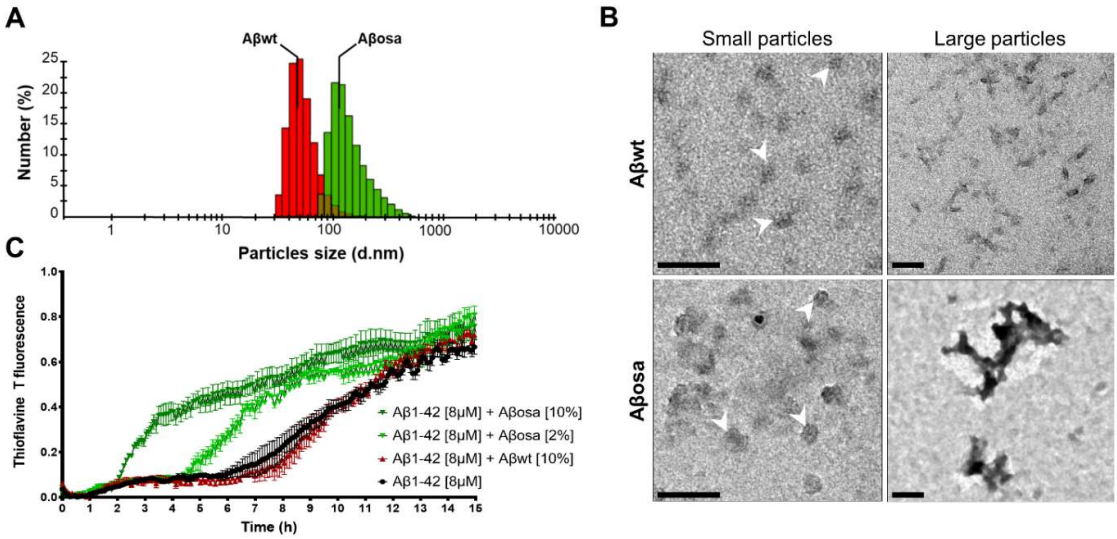

Figure 1. Properties of wt and mutated Aβ assemblies. **A.** Overlay of DLS particle size distribution of $A\beta_{wt}$ (red histogram) and $A\beta_{osa}$ (green histogram). **B.** Representative electron microscopy images of small and large particles in $A\beta_{wt}$ and $A\beta_{osa}$ solution. $A\beta_{wt}$ assembles into small fibrils whereas $A\beta_{osa}$ assembles into larger structures. Scale bars: 100 nm. **C.** Kinetics of synthetic $A\beta_{1\text{-}42}$ aggregation monitored by thioflavin T fluorescence in the absence and presence of $A\beta_{wt}$ and $A\beta_{osa}$ seeds.

Aggregation experiments were performed in triplicates. $A\beta_{1-42}$ monomer concentration is 8 µM, in a PBS buffer at 37°C with continuous agitation. The aggregation curves were normalized to maximal values of ThT fluorescence at plateau. Symbols and error bars are the average and standard deviation, respectively, of three independent kinetics experiments.

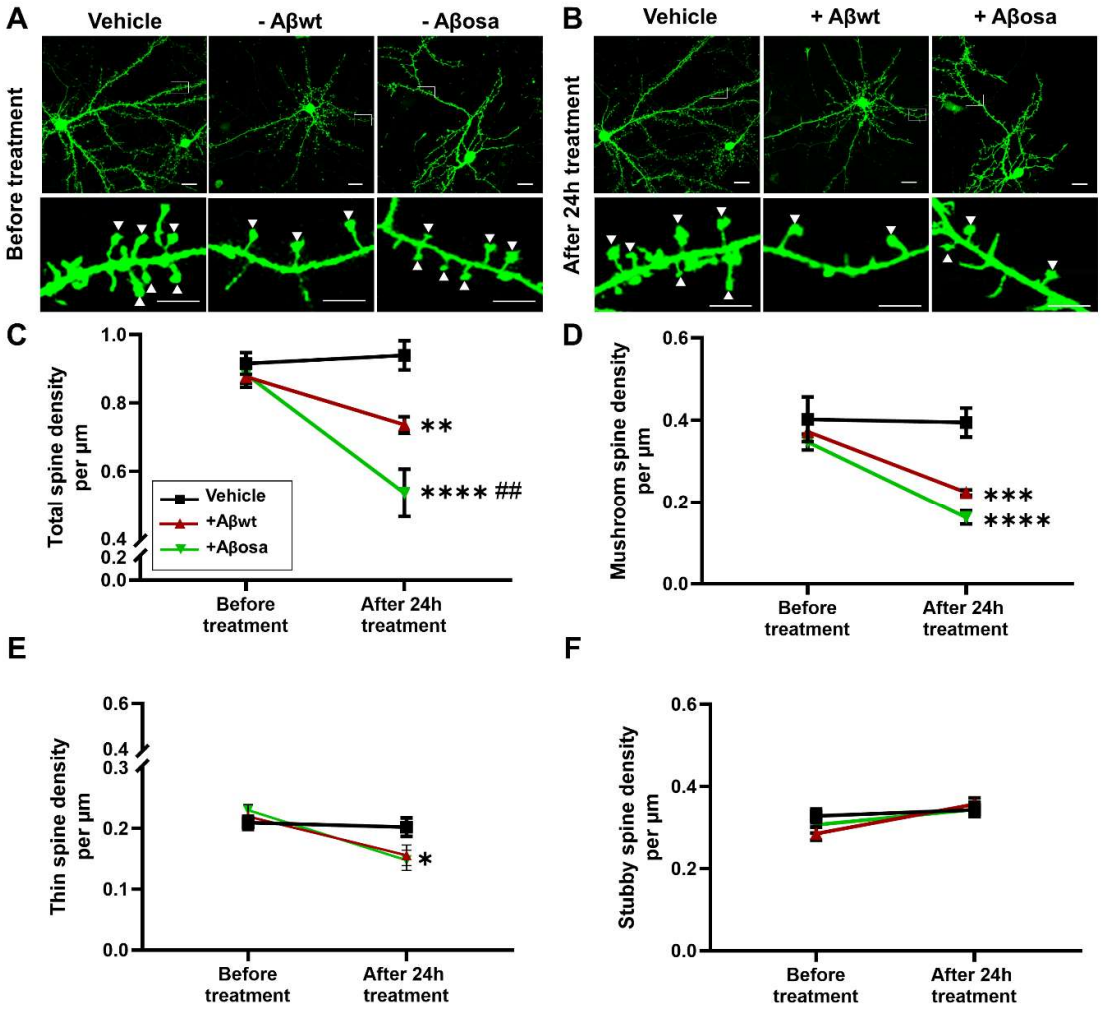

Figure 2. Exposure to exogenous $A\beta_{osa}$ and $A\beta_{wt}$ differentially impaired synapses. **A-B.** Representative images of primary cultures of cortical neurons expressing LA-GFP before (A), and after treatment for 24 hours with 100 nM of $A\beta_{osa}$ or $A\beta_{wt}$ (B). Top row wide field view, scale bar = 10 µm; bottom row: dendrite portions with mushroom spines (white arrows, scale bar = 5 µm). **C.** Quantification of total spine density showed a reduction of total number of spines after treatment with $A\beta_{osa}$ and $A\beta_{wt}$, compared to PBS (34.7±3.1% for $A\beta_{osa}$, $p<0.0001$; 14.1±3.4% for $A\beta_{wt}$, $p=0.0049$). The spine loss was significantly more severe in $A\beta_{osa}$ compared to $A\beta_{wt}$ ($p=0.0048$). **D.** Quantification of mushroom spine density showed a reduction of the number of mushroom spines after treatment with $A\beta_{wt}$ and $A\beta_{osa}$ (respectively $p=0.0005$ and $p<0.0001$). **E.** Quantification of thin spine density showed a reduction of the number of mushroom spines after treatment with $A\beta_{osa}$ ($p<0.1$) **F.** Stubby spine density was not modified after treatment with the different Aβ seeds. n = 6 neurons from at least 3 different cultures. Data are shown as mean ± s.e.m. Kruskal-Wallis with Dunn's multiple comparisons. *p<0.5, ** or ## p<0.05, ***p<0.005, ****p<0.0005.

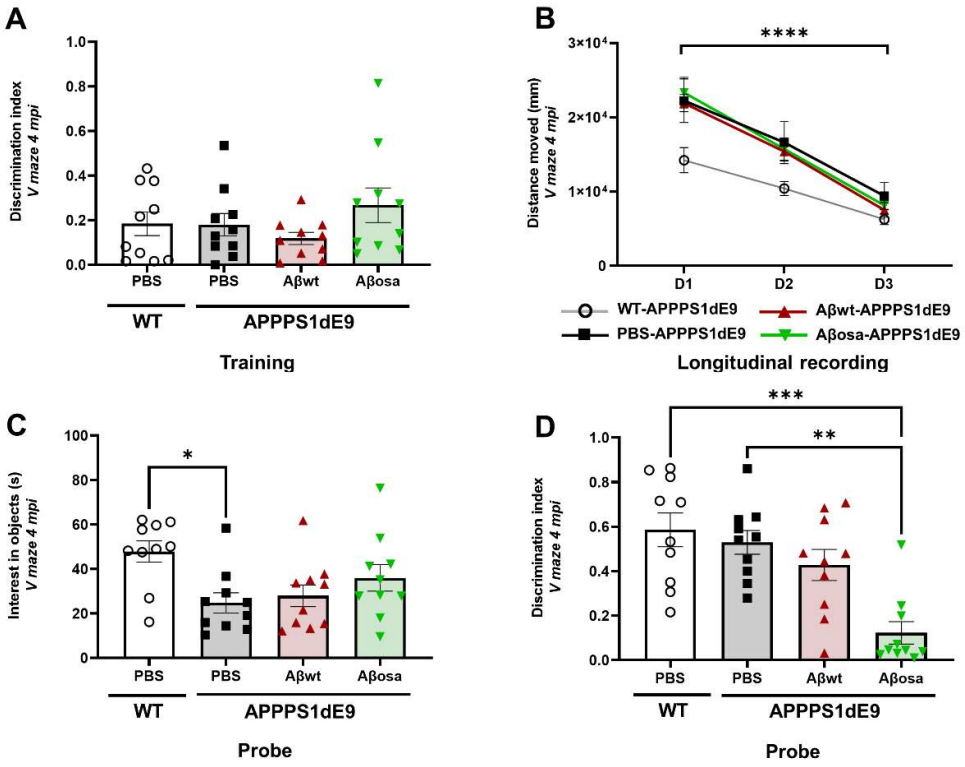

Figure 3. Memory impairment of $APP_{swe}/PS1_{de9}$ mice following Aβ inoculation. Novel object recognition was evaluated in a V-maze at 4 months post-inoculation. **A**. Mice performance during the training phase. Similar discrimination indexes were found for all groups when mice had to discriminate two identical objects ($p>0.05$, Kruskal-Wallis with Dunn's multiple comparisons). **B**. Distance moved throughout 3 days of tests (exploration, training and probe-test days). Measurements revealed a time-effect from day 1 to day 3 ($F_{(1.49,\ 53.95)} = 123.8$, $p<0.0005$), but no differences between experimental groups ($p>0.05$) (two-way repeated measures ANOVA with the Geisser-Greenhouse correction and Dunnett's multiple comparisons). **C**. Novel object recognition evaluated by the time spent on exploring the objects (in seconds) highlighted group effects ($p=0.02$). Post-hoc analysis showed that the PBS-inoculated wild-type mice group had a higher exploratory activity than PBS-inoculated $APP_{swe}/PS1_{dE9}$ ($p=0.02$) while all groups of $APP_{swe}/PS1_{de9}$ mice had comparable exploratory activity (Kruskal-Wallis with Dunn's multiple comparisons). **D**. Object discrimination index. $APP_{swe}/PS1_{de9}$ mice inoculated with $Aβ_{osa}$ spent less time exploring the novel object compared to PBS-inoculated WT mice or $APP_{swe}/PS1_{dE9}$ mice (group analysis using Kruskal-Wallis ($p=0.0006$) with post-hoc analysis using Dunn's multiple comparisons $p=0.0008$ and $p=0.0046$, for $Aβ_{osa}$ versus PBS-inoculated WT and $APP_{swe}/PS1_{dE9}$ mice, respectively). $n_{WT\text{-}PBS}=10$, $n_{APP/PS1\text{-}PBS}=10$, $n_{Aβwt}=10$, $n_{Aβosa}=10$ mice. Data are shown as mean ± s.e.m.

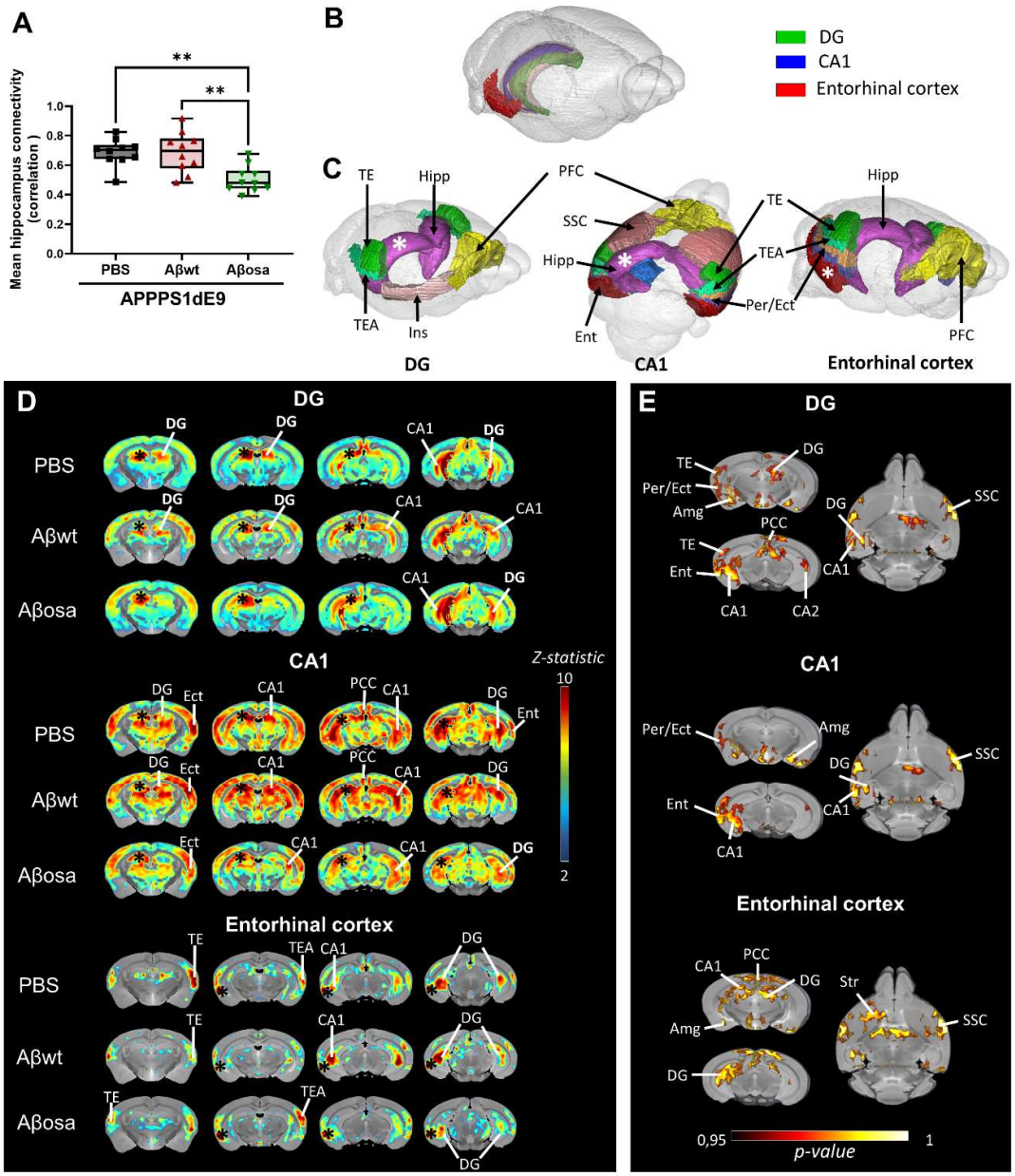

Figure 4. $A\beta_{osa}$ inoculated animals displayed abnormal brain connectivity within hippocampal-memory circuits. A. Mean hippocampus connectivity changes measured by resting-state functional MRI. $A\beta_{osa}$-inoculated group displayed a decreased hippocampus connectivity compared to PBS and $A\beta_{wt}$-inoculated mice at 4mpi (Kruskal-Wallis with Dunn's multiple comparisons. group effect p=0.002; p=0.006 and p=0.01 for $A\beta_{osa}$-inoculated group versus PBS or $A\beta_{wt}$-inoculated mice). **B**. 3D representation of the three brain regions -DG, CA1 and the entorhinal cortex- used for the seed-based analyses (SBA). **C**. SBA-derived resting state networks found in PBS-inoculated $APP_{swe}/PS1_{dE9}$ are shown for each seed (the white asterisk represents the location of the seeds where the signal was extracted). **D**. Correlation maps of each seed. The color scale bar represents the strength of the functional

correlation normalized with a fisher z-transformation. Black asterisks represent the location of the seeds. Differences are found between groups in inter-hemispheric homotopic FC. **E**. Voxelwise nonparametric permutation tests of FC correlation maps. $A\beta_{osa}$-inoculated mice have a lower FC in the hippocampus compared to PBS-inoculated mice ($p < 0.001$)**.** The color scale bar represents the statistical significant p-value. DG = dentate gyrus, Hipp = hippocampus, TE = temporal area, TEA= temporal associative area, Per/Ect = perirhinal + ectorhinal cortex, Ins = Insular, Amg = amygdalar area, Ent = entorhinal cortex, PCC = posterior cingulate cortex, SSC = primary somatosensory area, Str = striatum. $n_{APP/PS1\text{-}PBS}$=10, $n_{A\beta wt}$=10, $n_{A\beta osa}$=10 mice.

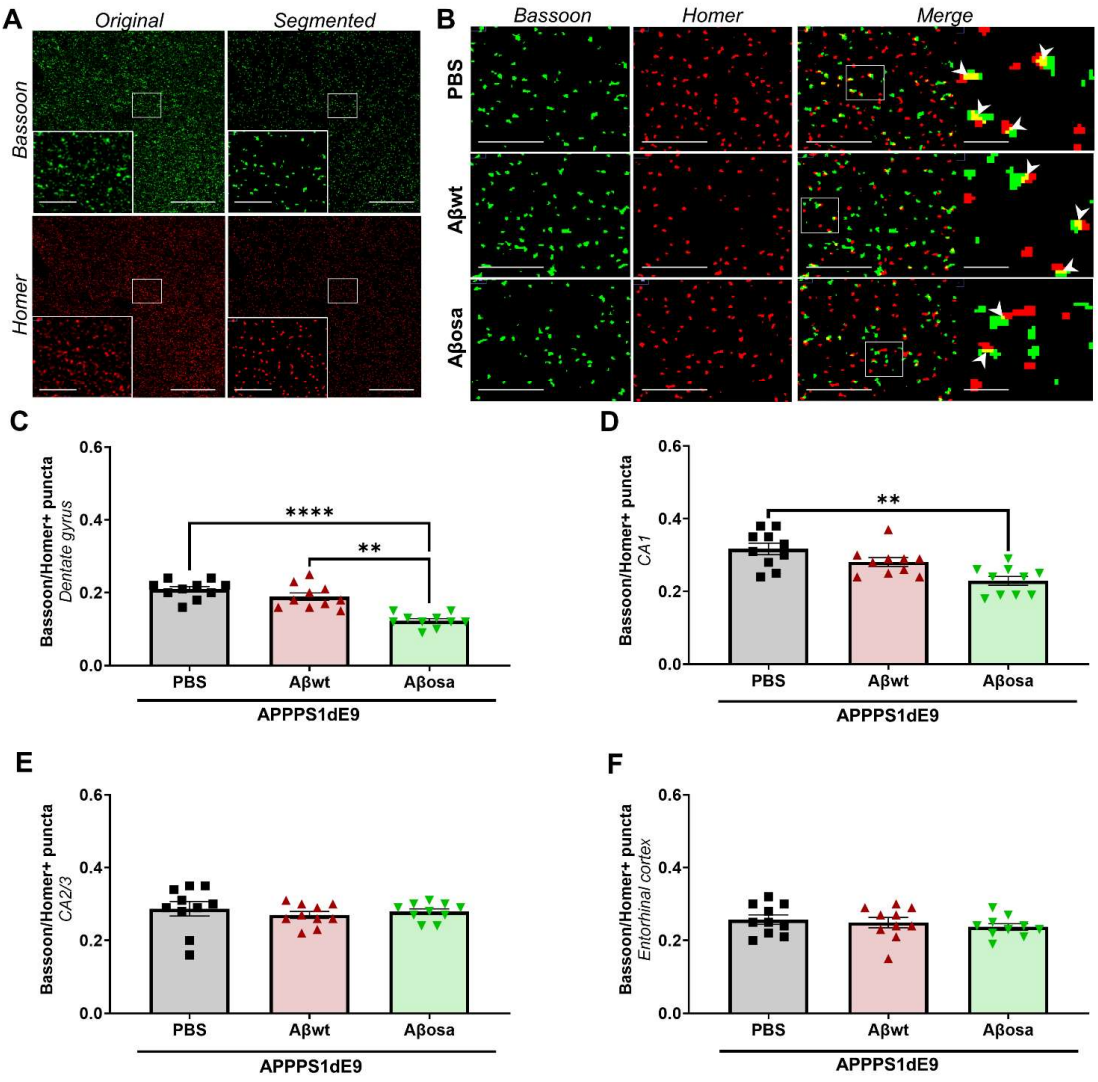

Figure 5. $A\beta_{osa}$ exacerbates long-term synaptotoxicity *in vivo*. A. Representative views of original Bassoon/Homer images and segmented puncta in $APP_{swe}/PS1_{dE9}$ mice. Scale bars main images: 20 µm; Insets: 5 µm. **B.** Co-localisation puncta of Bassoon/Homer labels (white arrow). Scale bars main images: 5 µm; Insets: 1 µm. Quantification of synaptic density from Bassoon/Homer colocalization in the dentate gyrus showed decrease of synaptic density in the dentate gyrus of $A\beta_{osa}$-inoculated $APP_{swe}/PS1_{dE9}$ mice (**C**, overall effect: $p<0.0001$ (Kruskal-Wallis). Post-hoc evaluation with Dunn's multiple comparisons: $A\beta_{osa}$- versus PBS-inoculated $APP_{swe}/PS1_{dE9}$: $p<0.0001$; $A\beta_{wt}$- versus $A\beta_{osa}$-inoculated $APP_{swe}/PS1_{dE9}$: $p=0.003$), and in their CA1 (**D**, overall effect: $p=0.002$ (Kruskal-Wallis). Post-hoc evaluation with Dunn's multiple comparisons: $A\beta_{osa}$- versus PBS-inoculated animals: $p=0.002$).

There were no changes in the different groups in the CA2/3 (**E**) and in the entorhinal cortex (**F**). $n_{APP/PS1-PBS}$=10, $n_{A\beta wt}$=10, $n_{A\beta osa}$=10 mice. Data are shown as mean ± s.e.m.

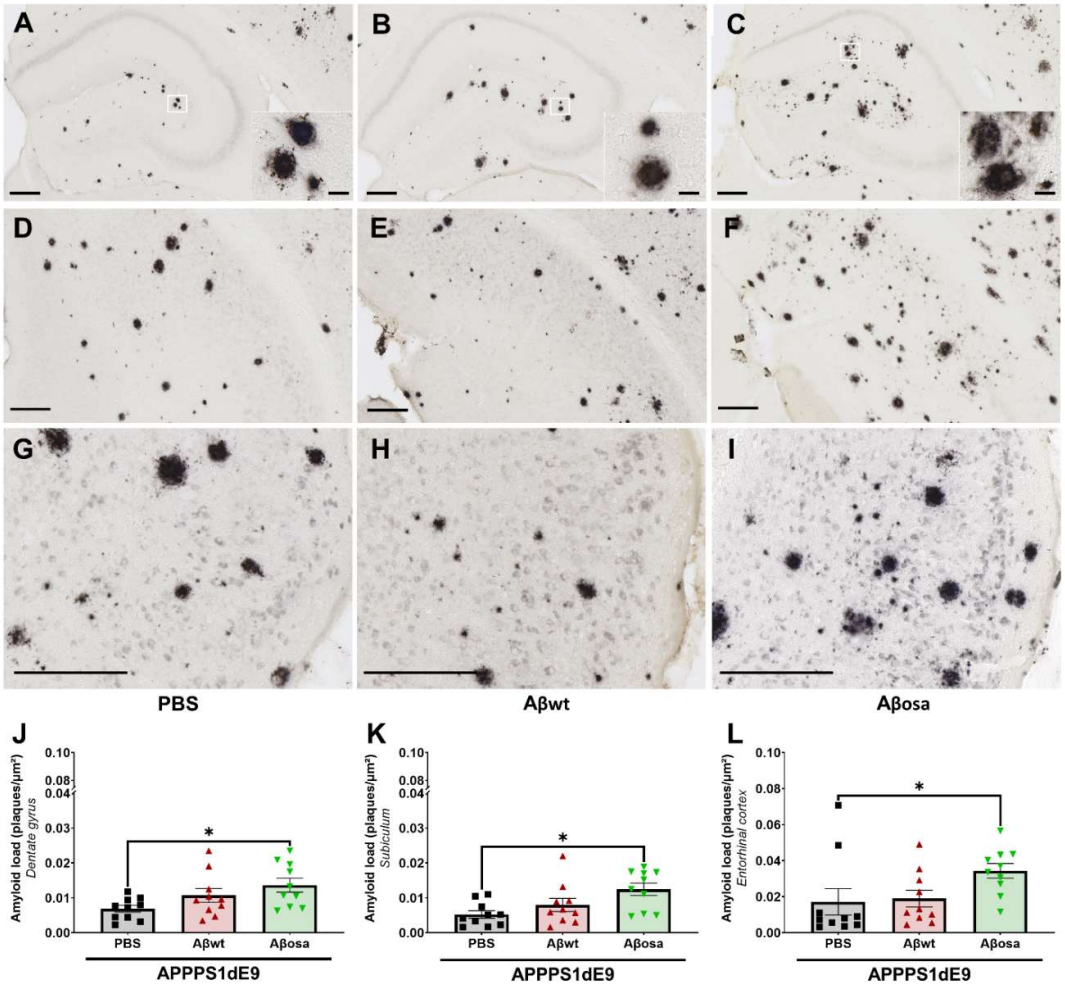

Figure 6. Modulation of Aβ plaque load following inoculation of Aβ variants. Representative images of 4G8 immunolabeling showing Aβ plaque deposition in the dorsal hippocampus (**A-C**), subiculum (**D-F**) and entorhinal cortex (**G-I**) of $APP_{swe}/PS1_{dE9}$ mice after PBS, $Aβ_{wt}$ or $Aβ_{osa}$ inoculation in the dentate gyrus. **J-L**. Quantification of amyloid load (4G8-positive amyloid plaques per µm²) in the dentate gyrus (**J**), in the subiculum (**K**), and in the entorhinal cortex (**L**). $Aβ_{osa}$ increases Aβ plaque deposition in the dentate gyrus (p=0.04), in the subiculum (p=0.02), in the entorhinal cortex (p=0.02). Kruskal-Wallis with Dunn's multiple comparisons. $n_{APP/PS1-PBS}$=10, $n_{Aβwt}$=10, $n_{Aβosa}$=10 mice. Data are shown as mean ± s.e.m. Scale bars main images: 200 µm; Insets: 20 µm.

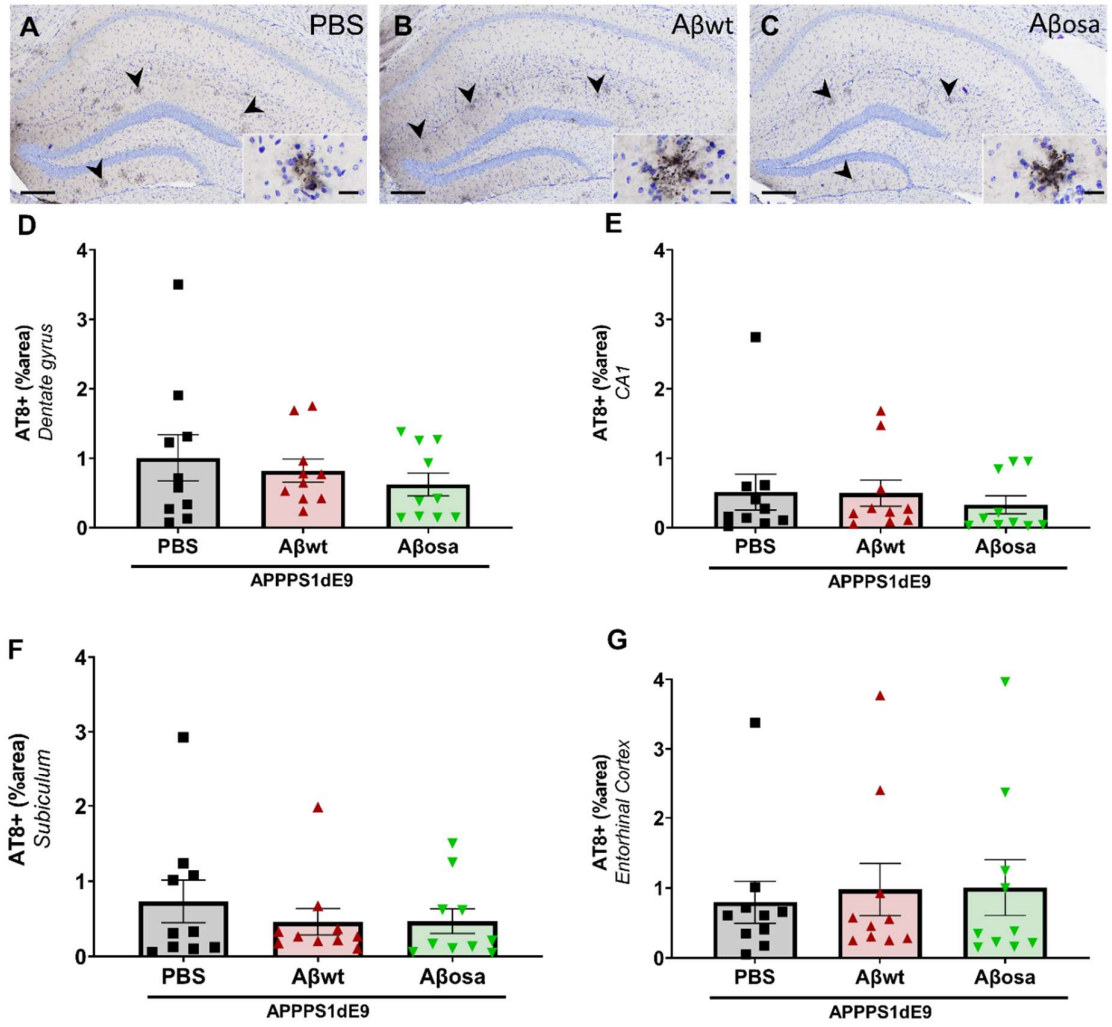

Figure. 7. Tau pathology quantification at 4 mpi. Representative images of AT8 immunolabeling showing neuritic plaques in the dorsal hippocampus (**A-C,** arrows) of $APP_{swe}/PS1_{dE9}$ mice after PBS, $A\beta_{wt}$ or $A\beta_{osa}$ inoculation in the dentate gyrus. Scale bars: 200 µm. Magnified views show no difference in the morphology of neuritic plaques between groups. Scale bars: 20 µm. **D-G**. Quantification of AT8 staining (percentage of AT8-positive area). AT8-positive areas are similar between all groups in the dentate gyrus (**D**), in the CA1 (**E**), in the subiculum (**F**) and in the entorhinal cortex (**G**). Kruskal-Wallis with Dunn's multiple comparisons. $nAPP/PS1_{PBS}=10$, $n_{A\beta wt}=10$, $n_{A\beta osa}=10$ mice. Data are shown as mean ± s.e.m.

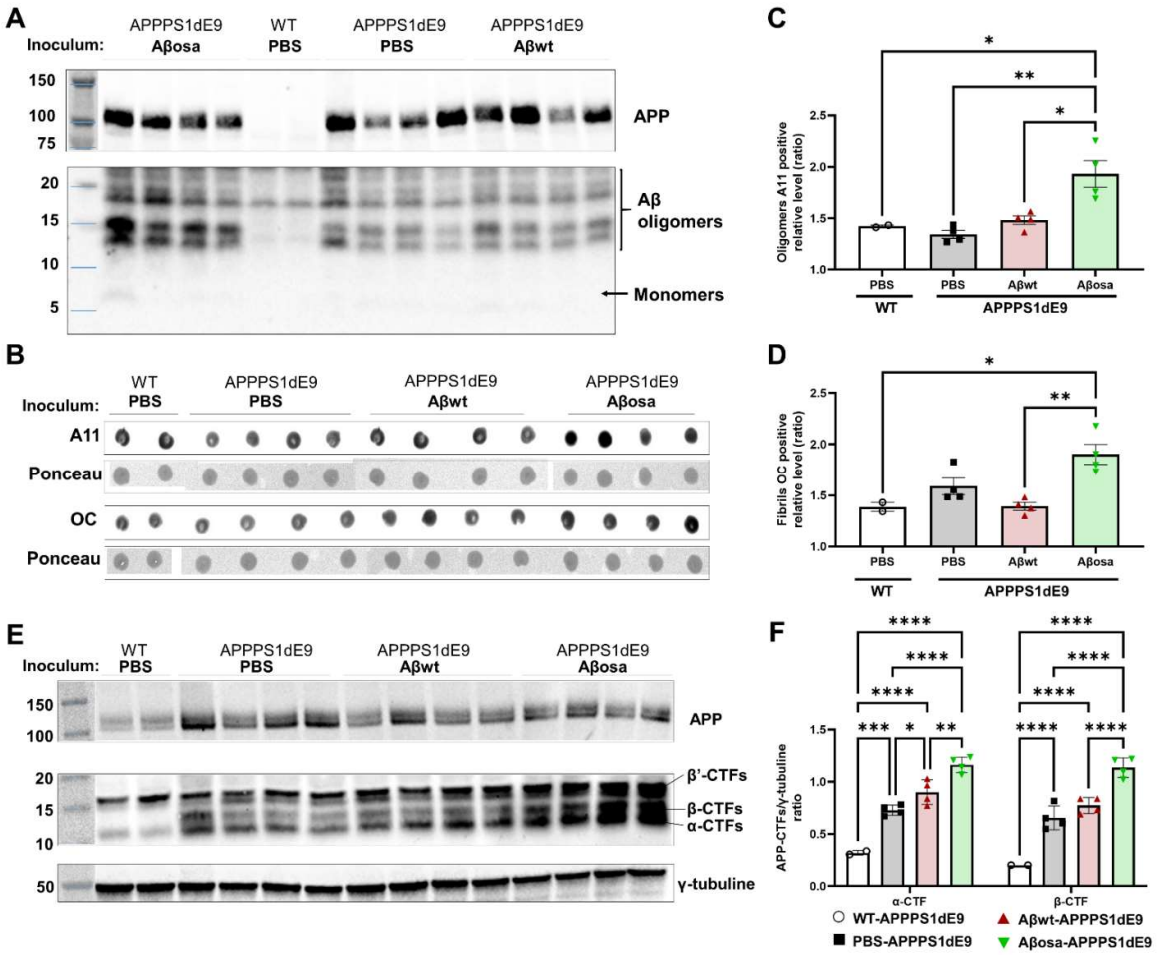

Figure 8. APP proteolysis profiles and oligomerization of amyloid-β peptides at 4 mpi. **A.** Western-blot analysis (6E10 Antibody) of total human APP and Aβ oligomeric species in sarkosyl-soluble extracts of the hippocampus of $APP_{swe}/PS1_{dE9}$ mice after PBS, $Aβ_{wt}$ or $Aβ_{osa}$ inoculation at 4mpi. Full length APP runs at an apparent molecular size of 110kDa, oligomeric forms of Aβ are detected at 15kDa and 12kDa **B.** Dot blot analysis for oligomeric species (A11) and fibrils (OC) in sarkosyl-soluble extract from the hippocampus. **C.** Quantification of relative expression levels of A11 are presented. $Aβ_{osa}$ increased oligomer forms compared to PBS- (p=0.0019), $Aβ_{wt}$-inoculated (p=0.0106) $APP_{swe}/PS1_{dE9}$ and WT mice (p=0.0142). **D.** Quantification of relative expression levels of OC are presented. $Aβ_{osa}$ increased fibrils compared to $Aβ_{wt}$-inoculated (p=0.0038) $APP_{swe}/PS1_{dE9}$ and WT mice (p=0.0118) **E.** Western-blot analysis (APP-Cter-17 antibody) of total endogenous APP, APP-CTFs and tubulin in hippocampus lysates (S100K fractions) obtained from wild-type and $APP_{swe}/PS1_{dE9}$ mice after PBS, $Aβ_{wt}$ or $Aβ_{osa}$ inoculation. Tubulin staining was used as a marker and loading control. **F.** Semi-quantification of β-CTF/C99 and α-CTF/C83 (APP-Cter-C17 Antibody) [36]. Kruskal-Wallis with Dunn's multiple comparisons. *p<0.5,

**p<0.05, ***p<0.005, ****p<0.0005. nWT_{PBS}=2, $nAPP/PS1_{PBS}$=4, $n_{A\beta wt}$=4, $n_{A\beta osa}$ =4 mice. Data are shown as mean ± s.e.m.

3. Protective effects of Aβ seeds

3.1 Context, objectives & abstract

Because of the clear implication of Aβ as the key initiator of the pathogenic process, at least in familial AD, targeting Aβ in various ways has been the major strategy in developing therapeutic approaches. These include anti-Aβ antibodies, β- and □-secretase inhibitors, □ -secretase modulators to selectively lower $Aβ_{42}$, and Aβ aggregation inhibitors (Chen et al., 2017; Karran and De Strooper, 2022). None of the above therapeutic strategies has led to substantial beneficial clinical effects. The discovery of mutations on APP at the origin of the FAD has brought a lot to our understanding of the disease. The *Icelandic* mutation (A673T), leading to a protective $Aβ_{ice}$ expression, is characterized by the substitution A to T of the second amino acid in the sequence of Aβ. This mutation protects humans from AD and improves cognition in the elderly (Jonsson et al., 2012). $Aβ_{ice}$ can associate with $Aβ_{wt}$ and promote the formation of Aβ heterodimers ($Aβ_{ice}$/$Aβ_{wt}$) that exhibit protective characteristic (Das et al., 2017, 2015). Other mutations on the same amino-acid (A673V mutations) are also protective (Di Fede et al., 2016). Mechanisms by which this mutation shifts toxicity profiles remain unknown. Understanding how particular mutations on Aβ can modulate the cascade of events (including synaptic loss and Tau pathologies) associated with AD is critical to investigate potential new therapies against AD.

In this second article, we aimed at evaluating the beneficial effect of protective Aβ on AD-associated lesions in a transgenic mouse model of AD that produces high levels of Aβ. We reported that a single intrahippocampal inoculation of protective $Aβ_{ice}$ can reverse the detrimental effect of endogenous Aβ four months post-inoculation. The amount of Tau-positive neuritic plaques was significantly reduced and spatial memory alteration were rescued. The beneficial effects were more associated with a protective role of $Aβ_{ice}$ on synapses than with changes in amyloidosis levels. This finding mainly raises the question about the relationship between $Aβ_{ice}$ and Tau, that needs to be further investigated in future studies. These questions are critical as they may shed light on the molecular mechanisms involving Aβ in AD pathophysiology and may unveil new AD therapeutic targets.

3.2 Article

CELESTINE M., Jacquier-Sarlin M., Borel E., Petit F., Bousset L., Hérard AS., Buisson A., Dhenain M. A protective form of Aβ rescues synaptic and cognitive impairments by reducing tau pathology in an Alzheimer's disease mouse model *(In preparation)*

A protective form of Aβ rescues synaptic and cognitive impairments by reducing tau pathology in an Alzheimer's disease mouse model

Marina Célestine[1,2], Muriel Jackier-Sarlin[3], Eve Borel[3], Fanny Petit[1,2], Luc Bousset[1,2], Anne-Sophie Hérard[1,2] , Alain Buisson[3], Marc Dhenain[1,2]

Author affiliations:

[1] Université Paris-Saclay, CEA, CNRS, Laboratoire des Maladies Neurodégénératives, 18 Route du Panorama, F-92265 Fontenay-aux-Roses, France.

[2] Commissariat à l'Energie Atomique et aux Energies Alternatives (CEA), Direction de la Recherche Fondamentale (DRF), Institut François Jacob, MIRCen, 18 Route du Panorama, F-92265 Fontenay-aux-Roses, France

[3] Université Grenoble Alpes, Inserm, U1216, Grenoble Institut Neurosciences, GIN, 38000 Grenoble, France

Author emails:

Marina.Celestine: Marina.Celestine@cea.fr;

Muriel Jackier-Sarlin: Muriel.Jacquier-Sarlin@univ-grenoble-alpes.fr;

Eve Borel: Eve.Borel@univ-grenoble-alpes.fr;

Fanny Petit: Fanny.Petit@cea.fr;

Anne-Sophie Hérard: Anne-Sophie.Herard@cea.fr;

Luc Bousset: Luc.Bousset@cnrs.fr;

Alain Buisson: Alain.Buisson@univ-grenoble-alpes.fr;

Marc Dhenain: Marc.Dhenain@cnrs.fr

Correspondence to: Marc Dhenain, DVM, PhD

Université Paris-Saclay, CEA, CNRS, Laboratoire des Maladies Neurodégénératives, MIRCen, 18 Route du Panorama, F-92265 Fontenay-aux-Roses, France

E-mail: marc.dhenain@cnrs.fr

ABSTRACT

Background

In Alzheimer's disease (AD), focal sporadic events can modulate the downstream pathology. A particular mutation (A673T) of the amyloid precursor protein (APP) was identified among Icelandic population, providing a protective effect against AD and age-related cognitive decline to APP_{ice} carriers. This APP mutation leads to reduced Aβ production. In addition, Aβ (with A2T change) issued from APP_{ice} has the capacity to form protective heterodimers in association with wild type $Aβ_{42.}$ Despite the emerging interest in $Aβ_{ice}$ during the last decade, the impact of $Aβ_{ice}$ on events associated with the amyloid cascade has never been reported.

Method

To address $Aβ_{ice}$ impact we evaluated its effect on cortical neurons and the long-term effects of a single inoculation of $Aβ_{ice}$ in the hippocampus of transgenic mice ($APP_{swe}/PS1_{dE9}$) overexpressing $Aβ_{1-42}$ peptide and presenting with Aβ plaques and Tau-positive neuritic plaques.

Results

Remarkably, $Aβ_{ice}$ protects against endogenous Aβ-mediated synaptotoxicity. Interestingly, the single intra-hippocampal inoculation of $Aβ_{ice}$ rescued synaptic density and spatial memory losses four months post-inoculation, compared to $Aβ_{wt}$ inoculation. Although Aβ load was not modulated by $Aβ_{ice}$ intracerebral infusion, the amount of Tau-positive neuritic plaques was significantly reduced.

Conclusion

These results suggest that a single event as $Aβ_{ice}$ inoculation can improve the fate of the pathology and clinical outcome several months after the event. These new insights into $Aβ_{ice}$ influence on AD pathological features open unexpected fields to develop innovative therapeutic strategies.

KEYWORDS

Alzheimer's disease, Cerebral connectivity, Amyloid-β, Aβ Icelandic Memory, Synapses, Transmission

BACKGROUND

Alzheimer's disease (AD) is the most widespread cause of dementia in the world. The number of patients has been predicted to double every 20 years. Thus, developing therapeutic strategies is an urgent need for public health. AD is characterized by intracerebral accumulation of abnormal proteinaceous assemblies made of amyloid-β (Aβ) peptides or Tau proteins. Aβ peptides arise from the proteolytic cleavage of the amyloid precursor protein (APP), leading to monomers of Aβ that progressively aggregate to form fibrillary Aβ deposits (Aβ plaques). Tau lesions occur in the form of neuropil threads, neurofibrillary tangles (NFTs), and neuritic plaques, *i.e.* Tau aggregates within neurites surrounding Aβ deposits. AD is also characterized by a progressive synaptic dysfunction leading to cognitive deficits.

Recently, the whole-genome sequencing of the Icelander population revealed an "Icelandic" mutation (A673T, "Ice") which protects against AD and age-related cognitive decline (Jonsson et al., 2012). The alanine to threonine substitution in the codon 693 of APP gene occurs within the Aβ sequence close to the β-secretase cleavage site of the APP. A widely advanced hypothesis to explain the protective effect of APP_{ice} is that the APP mutation leads to reduced Aβ production (Benilova et al., 2014; Jonsson et al., 2012; Maloney et al., 2014). An alternative hypothesis relies on the capacity of $Aβ_{ice}$ that displays with A2T change to form protective heterodimers with wild type $Aβ_{42}$. Indeed, the $Aβ_{ice}$ N-terminus is engaged in interactions with central and C-terminal hydrophobic residues, leading to hydrophobic burial which prevents Aβ aggregation and toxic oligomer formation (Das et al., 2017). Despite the emerging interest in $Aβ_{ice}$ during the last decade, the impact of $Aβ_{ice}$ on events associated with the amyloid cascade has never been reported.

Previous studies in animal models indicated that the intracerebral infusion of either Aβ-positive AD brain extracts (Eisele et al., 2009; Gary et al., 2019; Kane et al., 2000; Lam et al., 2022, 2021; Meyer-Luehmann et al., 2006; Watts et al., 2014) or well-defined synthetic or recombinant $Aβ_{1-40}$ or $Aβ_{1-42}$ peptides (Stöhr et al., 2014, 2012) induces build-up of Aβ deposits in their host several months after the infusion. Long-term cognitive alterations and synaptic impairments were also shown in inoculated animals (Gary et al., 2019; Lam et al., 2022, 2021). Taken together, these findings indicate that focal sporadic events can modulate the downstream pathology. Here, the effects of $Aβ_{ice}$ were evaluated on cortical neurons and in transgenic mice ($APP_{swe}/PS1_{dE9}$) overexpressing $Aβ_{1-42}$ peptide and presenting with Aβ plaques and Tau-positive neuritic plaques (Lam et al., 2022). First, we showed that $Aβ_{ice}$ protects against endogenous Aβ-mediated synaptotoxicity. Interestingly, the single intra-hippocampal inoculation of $Aβ_{ice}$ rescued synaptic density and spatial memory, four months post-inoculation, compared with $Aβ_{wt}$ inoculation. Although Aβ load was not modulated by $Aβ_{ice}$ intracerebral infusion, the amount of Tau-positive neuritic plaques was significantly reduced. These results suggest that a

single event as $A\beta_{ice}$ inoculation can improve the fate of the pathology and clinical outcome several months after the event and could pave the way for new therapeutic approaches.

RESULTS

$A\beta_{ice}$ rescues synapses in vitro

Several studies have shown that Aβ induces synaptic dysfunction by altering synaptic activity (Ortiz-Sanz et al., 2020; Tomiyama et al., 2010). We wondered whether $A\beta_{ice}$ also modulate synaptic activity. Long-term potentiation (LTP) was evaluated in wild-type mouse hippocampal slices after exogenous application of Aβ seeds. $A\beta_{wt}$ and $A\beta_{ice}$ were pre-incubated with slices for 15 min before the induction of the LTP. One hour after 100 Hz electric stimulation-induced LTP, we observed an increase of 160±5% in the average fEPSP slope in PBS (control) and $A\beta_{ice}$–exposed slices, compared to a moderate increase in $A\beta_{wt}$-exposed slices (120±5%; p = 0.0017). Thus, Aβ loses its toxicity when it bears the Icelandic mutation, since $A\beta_{wt}$ acutely impaired synaptic functions *in vitro*, while $A\beta_{ice}$ does not **(Fig. 1A).**

Then, we wondered if $A\beta_{ice}$ modulates synapse morphology and density. To model *in vitro* Aβ-associated AD-like pathology, we used primary cortical neurons that overexpress APP transgene bearing the Swedish mutation (APP_{swe}) leading to an overproduction of endogenous $A\beta_{wt}$. We compared spine morphology of APP_{swe} expressing cortical neurons alone and after a 24 hours $A\beta_{ice}$ exposition. As a control, we also imaged LifeActin-GFP (LA-GFP) cultured cortical neurons that do not express the transgene **(Fig. 1B)**. We analyzed thin, stubby and mushroom spine density **(Fig. 1C-G)**. While APP_{swe} expressing neurons exhibited a decrease in spine density, the exogenous application of $A\beta_{ice}$ led to an increase in the total spine density (**Fig. 1C**). This gain of spines was mainly due to a strong increase in thin and stubby spine density **(Fig. D-E)** and was associated with an increase in mushroom spine volume **(Fig. 1G)**. These results indicate that a 24 hours exposition to $A\beta_{ice}$ rescues the synaptotoxicity induced by the secreted Aβ in APP_{swe} neurons.

A single inoculation of $A\beta_{ice}$ promotes increase of synaptic density and spatial memory in mice

$A\beta_{wt}$ and $A\beta_{ice}$ were inoculated in the dentate gyrus of the hippocampus of $APP_{swe}/PS1_{dE9}$ mice at the age of 2 months. Behavioral assessment of mice was performed 4 months post-inoculation (mpi). An additional group of PBS-inoculated wild-type (WT) littermates was used as control. Spatial memory of inoculated mice was evaluated using the Morris water maze. Because the purpose of this task is to learn the location of a hidden escape platform thanks to stationary geometric cues, we ensure that mice did not have visual deficiency using a visible platform **(Fig. 2A)**. Then, 4-days training phase allowed mice to learn the location of the hidden platform (training phase). The day of the probe test,

we removed the platform to assess mouse recall and we recorded the time spent in the quadrant of the platform (target quadrant) versus the other quadrants. Mice from each group showed similar spatial learning as suggested by comparable reduction of the time spent to find the hidden platform over the training days **(Fig. 2B)**. Spatial memory was evaluated 24 hours after training. Interestingly, $A\beta_{ice}$-inoculated $APP_{swe}/PS1_{dE9}$ and WT mice significantly spent more time in the target quadrant than the other quadrants compared to PBS- or $A\beta_{wt}$-inoculated $APP_{swe}/PS1_{dE9}$. These results suggest that spatial memory is impaired in 6-month-old $APP_{swe}/PS1_{dE9}$ mice and that a single inoculation of $A\beta_{ice}$ leads to a rescue of spatial memory four months following the inoculation **(Fig. 2E-F)**.

Mice were euthanized 4 mpi to evaluate cerebral lesions. First, we investigated synaptic density at the inoculation site (hippocampus). Double immunolabeling of presynaptic (Bassoon) and postsynaptic (Homer) markers was performed and the amount of colocalized puncta was quantified as an indicator of synaptic integrity **(Fig. 2G)**. The inoculation of $A\beta_{wt}$ had no impact on synaptic integrity, we showed an increase of synaptic densities in the dentate gyrus and CA1 of $A\beta_{ice}$-inoculated $APP_{swe}/PS1_{dE9}$ mice **(Fig. 2H-I)** compared to $APP_{swe}/PS1_{dE9}$ mice inoculated either with PBS or $A\beta_{wt}$. Synapses in the CA2/3 region were not modulated **(Fig. 2J)**. Taken together, these results indicate that the synapto-protective effect of $A\beta_{ice}$ shown on neurons *in vitro* is also detected after a single intra-hippocampal inoculation and is associated with a recovery of spatial memory.

$A\beta_{ice}$ reduces Tau pathology without affecting Aβ plaque deposition

At 4 mpi, we detected Aβ deposits **(Fig. 3A)** and Tau-positive neuritic plaques (NPs) **(Fig. 3E)** in the hippocampus and the cortex of all inoculated $APP_{swe}/PS1_{dE9}$ mice. Aβ plaque load and morphology were similar between groups in the hippocampus **(Fig. 3B-C)** and the cortex **(Fig. 3D)**. Remarkably, the quantification of overall AT8-labelled phospho-Tau (percentage of AT8-positive area) significantly decreased in the hippocampus of $A\beta_{ice}$-inoculated $APP_{swe}/PS1_{dE9}$ mice compared to $APP_{swe}/PS1_{dE9}$ inoculated with PBS or $A\beta_{wt}$ **(Fig. 3F-G)**. The amount of Tau lesions in the cortex was similar between groups **(Fig. 3H)**. Taken together, these results suggest that protective effect of $A\beta_{ice}$ involves mechanisms associated with a reduction of Tau pathology without affecting Aβ aggregation.

DISCUSSION

We showed that intracerebral inoculation of $A\beta_{ice}$ seeds in the hippocampus of a mouse model of amyloidosis rescues synaptic damages and spatial memory 4 months post-inoculation. Interestingly, while the amyloid loads in the inoculum site or in the cortex was similar in $A\beta_{ice}$ and other experimental groups, a significant reduction of Tau within the neuritic plaques was observed in $A\beta_{ice}$-inoculated

mice. These findings provide new insights into the ability of Aβ seeds to exhibit positive effects on the course of AD-associated pathology and counteracts the negative effects induced by the overproduction of endogenous Aβ.

Abolition of anti-amyloidogenic properties of $A\beta_{ice}$

In vitro studies have revealed that the Icelandic mutation makes APP a less favorable substrate for cleavage by BACE1 resulting in the reduction of amyloidogenic processing of APP and consequently a reduction of Aβ production described in human carrier (Kokawa et al., 2015; Maloney et al., 2014). Additionally, it was reported that $A\beta_{ice}$ decreases Aβ aggregation causing the absence of amyloid plaque in human carrier and experimental models (Benilova et al., 2014; Lin et al., 2017). In our study, we did not find changes in cerebral amyloid load following a single $A\beta_{ice}$ inoculation at the inoculation site or in others brain areas. Interestingly, we found beneficial effect on cognitive performance and tau pathology four months post-inoculation. The mechanism by which $A\beta_{ice}$ shifts wild type Aβ toxicity involved heterodimers formation with cross-interaction of both peptide (Das et al., 2017). Here, we cannot decipher whether such a mechanism has occurred, therefore further investigations on the biological process of $A\beta_{ice}$-inoculated $APP_{swe}/PS1_{dE9}$ are needed.

$A\beta_{ice}$ inoculum confers neuroprotection

The main findings of our study is that $A\beta_{ice}$ modulates synapses. First, we showed that $A\beta_{ice}$ is not neurotoxic as it did not modulate synaptic transmission. This result is consistent with several reports showing nontoxic formation of small $A\beta_{ice}$ oligomers and inhibition of dodecamer formation (Zheng et al., 2015). First, using in vitro methods, we showed that $A\beta_{ice}$ protects synapses against Aβ-mediated synaptoxicity in neuron cultures overexpressing wild type Aβ. One study has shown lower binding affinity of $A\beta_{ice}$ oligomers on synaptic receptors (Limegrover et al., 2021). Results from our *in vivo* study highlighted a long-term synaptic protection induced by a single $A\beta_{ice}$ inoculation. As we did not observed changes in amyloidosis, we suggested that protection associated with $A\beta_{ice}$ is not linked with changes of Aβ plaque load. Still, we cannot completely abolish the possibility that Aβ-$A\beta_{ice}$ exert protective impact on synapse just after inoculation. *In vitro* incubation of Aβice with wild type $A\beta_{40}$ and $A\beta_{42}$ has been demonstrated to form smallest oligomeric aggregates that showed a decrease of neurotoxicity (Benilova et al., 2014).

As we detected changes in Tau within neuritic plaque, another non-exclusive hypothesis is that synaptic damage was shifted towards decreased Tau-mediated synaptic toxicity. Studies in animal models have suggested that tau can induce synaptic deficits (Dejanovic et al., 2018; Hoover et al., 2010; Pooler et al., 2014). Previously, our team has shown that the inoculation of AD-brain extracts in our

mouse model worsens synaptic defects that were associated with the severity of Tau lesion (Lam et al., 2022). Thus, in our study, reduction of Tau pathology induced by $A\beta_{ice}$ inoculation can be the culprit event that changes the outcome of the disease progression. Further investigations will have to decipher the relationships between $A\beta_{ice}$, Tau pathology and synapses.

CONCLUSION

As a conclusion we showed that a single inoculation of $A\beta_{ice}$ induces long term protection of synaptic damage that were associated with rescue of spatial memory performance and reduction of Tau pathology in a mouse model of amyloidosis. These results suggest that a single, sporadic event as $A\beta_{ice}$ inoculation can modulate the fate of the pathology and clinical outcome several months after the event. Extrapolation of this discovery suggests that any event that modulates focally synaptotoxicity and Tau-associated pathology in the time-course of AD can protect against AD. This study provides new insights into new therapeutic approaches that could counteract Aβ-mediated toxicity

METHODS

Production of recombinant Aβ proteins

cDNAs of WT human APP_{695} and the Swedish mutant (APP_{swe}) were cloned into pmcherry-N1 vector (Snapgene) using the BamHI and AgeI restriction sites. Then, using overlapping PCR and the Infusion Kit (Thermo Scientific) we generated the various APP mutant-mCherry plasmids as described by manufacturer's instructions. All constructions in pmCherry vector were verified by sequencing.

To make the plasmids for the fusion protein Aβ(His) of wild-type human β-amyloid 1-42 protein (Aβwt) or $A\beta_{ice}$ mutant (A2T), the cDNA containing the sequence for human $A\beta_{1-42}$ was obtained from synthetic oligonucleotides (Sigma, Lyon, France) - containing a Nde1 restriction site as forward primers and a PspXI restriction site as reverse primers - using overlapping PCR. PCR products were then cloned into a pet28a-vector (Novagen, Paris, France) and subsequently constructed as various mutant HIS-$A\beta_{1-42}$ expressing plasmids (pet28a-AβHis or pet28a-Aβ(His)ice: A2T). The resulting plasmids were verified by sequencing. Escherichia Coli BL21 (DE3) was transformed with the fusion protein plasmids and a single colony was chosen to grow in a 250 mL starter culture in Luria broth (LB medium) overnight at 37°C. The next day, 10 mL of culture was diluted in 1L LB culture medium. When the culture reached an OD600nm of 0.8, isopropyl-beta-D-thiogalactopyranoside (IPTG) was added to 1 mM for induction. The culture was grown for an additional 4 h and the cells harvested by centrifugation at 4000g for 20 min. The pellet was re-suspended in 10 mL ice-cold PBS and lysed by sonication at ice-cold temperature. The cell extract was then centrifuged at 20,000g for 15 min at 4°C. The pellet was re-suspended in 10

mL of 8 M urea in PBS and sonicated as previously described before centrifugation at 20,000g for 15 min at 4°C. The supernatant (5 mL) was diluted with 15 mL of binding buffer (PBS with 10 mM imidazole at pH 8.0). Before affinity purification using nickel-nitriloacetic acid (Ni-NTA) column (3 mL of protino Ni-NTA Agarose from Macherey Nagel), samples were filtered on 0.45 µm. The Ni-NTA column was equilibrated with binding buffer prior to loading the sample on the column. Then the column was washed with the washing buffer (PBS with 30 mM imidazole at pH 8.0) with 5-10 column volumes. The protein was then eluted with the elution buffer (PBS with 500 mM imidazole at pH 7.4). The absorbance at 280 nm was used to monitor the elution but the concentration of the fusion proteins was estimated by comparing the intensity of the band of the protein on SDS-PAGE with that of known quantity of BSA (Sigma, Lyon, France). A final concentration of 100 µM was obtained and aliquots were stored at -80°C. Aliquots from all subsequent purification steps were analysed by SDS-PAGE, and the identity of $A\beta_{1-42}$ and mutants was verified by western blots using 4G8 monoclonal antibodies against Aβ sequence (4G8).

Lentivirus production

Lentiviruses were produced in HEK293T cells from the following plasmids: pLenti-APPswe-mCherry, . To generate infectious lentiviral particles, sequences of various human APP695 mutants were cloned into pLenti-C-mCherry vector. pLenti-C mCherry vector was a gift from Dr Christophe Bosc (Grenoble Institute of Neuroscience) and was derived from pLenty-C-mGFP (Snapgene). psPAX2 is a packaging plasmid encoding HIV-1 gag/pol sequences under the control of a SV40 promoter (Addgene plasmid # 12259). pCMV-VSV-G is an envelope-expressing plasmid encoding for VSV-G glycoprotein under the control of a CMV promoter (Addgene plasmid # 8454).

For the virus production, cells were transfected using Ca2+- phosphate in cell culture dishes (100 x 15 mm) with a given lentiviral plasmid and the two helper plasmids psPAX2 and pCMV-VSV-G. Six hours after transfection, the medium was changed to remove transfection reagent in the conditioned medium to which the virus is secreted. 48 h after transfection conditioned medium was spun at 250g for 5 min at 4°C before being collected and filtered using a 0.45 µm sterile filter (Sarstedt, Nuembrecht, Germany). Then virus particles were pelleted by ultra-centrifugation for 2 h at 4 °C and 20,000 rpm in a Beckman SW32Ti swinging bucket rotor. Supernatant was discarded and virus was suspended in PBS (X100 concentrated according to the initial volume of supernatant) and aliquots of the viral solution were snap-frozen in liquid nitrogen before storage at -80°C until use. Lentivirus titration was performed by FACS analysis after viral transduction of HEK293T and was estimated around 2 108 UI/mL.

For viral transduction, lentiviral solutions were diluted (1:10) in complete culture medium and 50 µL of the diluted preparation were added to the culture medium of a 24-well plate (for human neuronal cultures). Cell culture supernatant or lysates were harvested 48 h to 72 h post-infection.

Primary cultures of cortical neurons

Mouse cortical neurons were cultured from 14- to 15-d-old OF1 embryos (Charles River) as described previously (Léveillé et al., 2008). After extraction of the embryonic brains, the cerebral membranes were removed and the cortices were dissected, mechanically dissociated and cultured in Dulbecco's Modified Eagle's Medium supplemented with 5% horse serum, 5% foetal bovine serum and 1mM glutamine (all from Sigma) on 24-well plates (Falcon; Becton Dickinson) for biochemical experiments. Neurons were seeded on 35 mm glass-bottom dishes (MatTek) for confocal experiments. All plates, dishes, and coverslips were coated with 0.1 mg/mL poly-D-lysine and 0.02 mg/mL laminin (Sigma). Cultures were maintained at 37°C in a humidified atmosphere containing 5% CO2/95% air. After 3–4 days in vitro (DIV), cytosine arabinoside (AraC, 10 µM; Sigma) was added to inhibit proliferation of non-neuronal cells in cultures used for biochemistry experiments; 98% of the cells were considered as neuronal. The day before the experiments, cells were washed in DMEM. Treatments were performed on neuronal cultures at 14–15 DIV.

Endotoxin assay

Endotoxin content of Aβ solutions was detected using a kinetic Limulus amebocyte lysate (LAL) chromogenic endotoxin quantitation kit (Thermo Scientific). In brief, 50 µM of Aβ solution was prepared in PBS and was transferred to a sterile 96-well plate prewarmed to 37°C. LAL (0.1 mL, room temperature) was quickly added to each well. Detection relied on standards supplied in the kit with the range from 0.10 to 1 EU/ml and on positive and negative controls that were performed at the same time as the samples. Endotoxin concentrations were determined by measuring kinetic absorbance at 405 nm at 37°C following the instructions of the manufacturer, in a Spark plate reader (Tecan).

Transgenic mice

Mouse experiments involved the $APP_{swe}/PS1_{dE9}$ mouse model of amyloidosis (C57Bl6 background) (Garcia-Alloza et al., 2006). Aβ plaques can be detected as early as 4 months of age in these mice and increase in number and total area with age (Garcia-Alloza et al., 2006). This model expresses endogenous murine Tau protein isoforms and is not transgenic for any human Tau. At the time of the inoculation of $Aβ_{wt}$, $Aβ_{ice}$ or PBS, at 2 months of age, these mice did not have Aβ plaques. Animals were studied for 4 months after intracerebral inoculation of the peptides (at 4 post-inoculation (mpi) respectively, $n_{APP/PS1\text{-}wt}$=10, $n_{APP/PS1\text{-}osa}$=12, $n_{APP/PS1\text{-}pbs}$=12). Wild-type littermates injected with the PBS

were used as controls for the behavioral tests ($n_{WT\text{-}pbs}$=10). All $APP_{swe}/PS1_{dE9}$ and WT littermates were born and bred in our center (Commissariat à l'Energie Atomique, centre de Fontenay-aux-Roses; European Institutions Agreement #B92-032-02). Females were exclusively used in this study in order to optimize group homogeneity (Aβ plaque load is known to vary between males and females). Mice were injected during different inoculation sessions and each group was randomly inoculated at each session to avoid an "order of treatment" confounding effect. All animals were randomly assigned to the experimental groups using a simple procedure, they were identified using increasing numbers based on their birthdate. Animals with increasing numbers were alternatively assigned to the *APP/PS1-wt* (animal 1, 4, 7…), *APP/PS1-ice* (animal 2, 5, 8…) and *APP/PS1-pbs* groups (animal 3, 6, 9…). All experimental procedures were conducted in accordance with the European Community Council Directive 2010/63/UE and approved by local ethics committees (CEtEA-CEA DSV IdF N°44, France) and the French Ministry of Education and Research (A20_017 authorization), and in compliance with the 3R guidelines. Animal care was supervised by a dedicated in-house veterinarian and animal technicians. Human endpoints concerning untreatable continuous suffering signs and prostrations were taken into account and not reached during the study. Animals were housed under standard environmental conditions (12-h light-dark cycle, temperature: 22 ± 1°C and humidity: 50%) with *ad libitum* access to food and water. The design and reporting of animal experiments were based on the ARRIVE reporting guidelines (Percie du Sert et al., 2020). Sample size was based on previous experiments for Aβ induction in $APP_{swe}/PS1_{dE9}$ mice after inoculation of human brain (estimated with significance level of 5%, a power of 80%, and a two-sided test) (Gary et al., 2019) and increased to take into account uncertainties for new markers (Tau lesion load, memory and synaptic changes). No animals were excluded from the study. MC was aware of initial group allocation, but further analyses (memory evaluations and post-mortem studies) were performed blinded.

Stereotaxic surgery

Fifty micromolar of $Aβ_{wt}$, $Aβ_{ice}$ solution were rapidly thaw out before stereotaxic injection.

Two month-old $APP_{swe}/PS1_{dE9}$ and wild-type littermates were anesthetized by an intraperitoneal injection of ketamine (1mg/10g; Imalgène 1000, Merial) and xylazine (0.1mg/10g; 2% Rompun, Bayer Healthcare). Local anesthesia was also performed by a subcutaneous injection of lidocaine at the incision site (1 µl/g; 0.5% Xylovet, Ceva). Mice were placed in the stereotaxic frame (Phymep) and bilateral injections of brain samples were performed in the dentate gyrus (AP -2 mm, DV 1.8 mm, L +/- 2 mm from bregma). Two µl/site of sample were administered using 34-gauge needles and Hamilton syringes, at a rate of 0.2µl/min. After the injection, needles were kept in place for 5 more minutes before removal and the incision was sutured. The surgical area was cleaned before and after the procedure using povidone iodine (Vétédine, Vétoquinol). Respiration rate was monitored and body

temperature was maintained at 37±0.5°C with a heating pad during the surgery. Anesthesia was reversed with a subcutaneous injection of atipamezole (0.25 mg/kg; Antisedan, Vetoquinol). Mice were placed in a ventilated heating box (25°C) and monitored until full recovery from anesthesia. Postoperative anticipatory pain management consisted of paracetamol administration in drinking water (1.45 ml/20ml of water; Doliprane, Sanofi) during 48 hours.

Behavioral evaluations

The Morris water maze task was used to investigate spatial memory at 4 mpi on $A\beta_{wt}$-, $A\beta_{ice}$-, and PBS-inoculated $APP_{swe}/PS1_{dE9}$ mice. Wild-type littermates injected with PBS were used as controls for the tests. Mice were handled for 2 minutes per day, for 5 days prior to any test to prevent stress effects during tasks. An open 122 cm-wide circular swimming arena was maintained at 22°C and exposed to a 400 lux-lighting. The test consisted of three phases during which the arena was divided into four artificial quadrants. At the end of each session, mice were dried with a heated towel before returning to their home cages. During the habituation phase (day 1), mice were trained to find a visible platform to escape from the water. To facilitate its detection, the platform was emerged 0.5 cm above the surface of the water and a colorful cue was placed on it. This phase consisted in fou 60-second trials, with an inter-trial interval (ITI) of 20-30 minutes. For each trial, the starting point was different as well as the location of the platform. When the mice did not find the platform within the 60 seconds, they were guided to its location and were left on the platform to rest for 30 seconds. The training phase (day 2 to 5) consisted in three daily 60-seconds trials, with 20-30 minutes ITI, for four days. For each trial, the starting point was different whereas the location of the platform remained the same. The platform was hidden 0.5 cm beneath the water surface and the cue previously placed on it was removed. Visual cues were placed around the maze so that mice could spatially navigate to the platform. When the mice did not find the platform within the 60 seconds, they were guided to its location and were left on the platform to rest for 30 seconds. All trials lasts 60 seconds or until the animal located the platform. Escape latency, i.e the time required to find the platform, was evaluated during the habituation and the training phases to assess learning abilities. A probe test (day 6) was performed 24 hours after the last training session to assess spatial long-term memory. During this phase, the platform was removed from the maze. Mice were placed in the water for 60 seconds from a position opposite to the platform. The time spent in each virtual quadrant of the maze was recorded.

Animal euthanasia and brain preparation

Mice were euthanized at 4 mpi, after the behavioral tests, with an intraperitoneal injection of a lethal dose of pentobarbital (100 mg/kg; Exagon, Axience). They were perfused intracardiacally with cold sterile 0.1M PBS for 4 minutes, at a rate of 8 ml/min. The brain was extracted and separate in two

hemisphere. The left hemisphere was dissected in order to take out the hippocampus and the cortex. Samples were directly deep-frozen into liquid nitrogen and stored at −80 °C for biochemical analysis. For histology using, the right hemisphere was post-fixed in 4% paraformaldehyde for 48 hours at +4°C, transferred into a 15% sucrose solution for 24 hours and in a 30% sucrose solution for 48 hours at +4°C for cryoprotection. Serial coronal sections of 40 µm were performed with a microtome (SM2400, Leica Microsystem) and stored at -20°C in a storing solution (glycerol 30%, ethylene glycol 30%, distilled water 30%, phosphate buffer 10%).

Immunohistochemistry

Aβ deposits were evaluated using a 4G8 labelling. Tau was evaluated using labelling with AT8 directed against hyperphosphorylated Tau. Free-floating brain sections were rinced in a 0.1M PBS solution (10% Sigma-Aldrich® phosphate buffer, 0.9% Sigma-Aldrich® NaCl, distilled water) before use. Washing and incubation steps were performed on a shaker at room temperature unless indicated otherwise.

4G8 labelling was performed after pretreating brain sections with 70% formic acid (VWR®) for 20 min at room temperature. AT8 labellings were performed after a pre-treatment with EDTA 1X citrate (Diagnostic BioSystems®) for 30 min at 95°C. All tissues were then incubated in 30% hydrogen peroxide (Sigma-Aldrich®) diluted 1/100 for 20 min to inhibit endogenous peroxidases. Blocking of non-specific antigenic sites was achieved over 1 hour using a 0.2% Triton X-100/0.1M PBS (Sigma-Aldrich®) (PBST) solution containing 4.5% normal goat serum or 5% bovine serum albumin. Sections were then incubated at +4°C with the 4G8 (Biolegend 800706, 1/500) antibody diluted in a 3%NGS/PBST solution for 48h, or with the AT8 (Thermo MN1020B, 1/500) antibody diluted in a 3%NGS/PBST solution for 96h. After rinsing, an incubation with the appropriate biotinylated secondary antibody diluted to 1/1000 in PBST was performed for 1h at room temperature, followed by a 1h incubation at room temperature with a 1:250 dilution of an avidin-biotin complex solution (ABC Vectastain kit, Vector Laboratories®). Revelation was performed using the DAB Peroxidase Substrate Kit (DAB SK4100 kit, Vector Laboratories®). Sections were mounted on Superfrost Plus slides (Thermo-Scientific®). For the AT8 labellings, a cresyl violet counterstain was performed. All sections were then dehydrated in successive baths of ethanol at 50°, 70°, 96° and 100° and in xylene. Slides were mounted with the Eukitt® mounting medium (Chem-Lab®).

Stained sections were scanned using an Axio Scan.Z1 (Zeiss® - Z-stack images acquired at 20× (z-stacks with 16 planes, 1µm steps with extended depth of focus)). Each slice was extracted individually in the .czi format using the Zen 2.0 (Zeiss®) software. Image processing and analysis were performed with the ImageJ software. Macros were developed for each staining in order to attain a reproducible semi-

automated quantification. Images were imported with a 50% reduction in resolution (0.44 µm/pixel), converted to the RGB format and compressed in .tif format. For the 4G8 immunostainings, segmentation was performed through an automatic local thresholding using the Phansalkar method (radius = 15). Aβ load was evaluated after quantification of the 4G8-labelled particles between 8 and 2,000 µm², and normalization to the surface area of each ROI. For the AT8 staining, the blue component of each image was extracted to remove the cresyl violet counter-staining from the analysis. AT8-positive tau loads were assessed following an automatic local thresholding of the staining with the Phansalkar method followed by an evaluation of the percentage of AT8-positive surface area in each ROI.

In $APP_{swe}/PS1_{dE9}$ mice, tau lesions occur in the form of neuritic plaques *i.e.* tau aggregates within neurites surrounding Aβ deposits. In addition for the AT8 immunostaining, a quantification of neuritic plaques and NFTs was performed by manual counting. The AT8-positive area stained within neuritic plaques was evaluated by drawing circular regions of interest (with a constant area of 6µm²), and by quantifying the percentage of tau-positive regions within each ROI, using the same thresholding method as previously described. A semi-quantitative analysis of neuropil threads was also performed by assigning a severity score based on the intensity and extent of AT8-positive staining in each ROI. All quantifications were performed on adjacent slices between -0.34 mm and -4.36 mm from bregma. Ten adjacent slices were analyzed for the 4G8 and AT8 staining. All ROIs were manually segmented using the Paxinos and Franklin neuro-anatomical atlas of mouse brain (Paxinos, 2001).

Evaluation of synaptic density

Synaptic density was evaluated in the hippocampus (CA1) and the perirhinal/entorhinal cortex of all inoculated mice using a double immunolabelling of presynaptic (Bassoon) and postsynaptic (Homer1) markers. Free-floating sections were permeabilized in a 0.5% Triton X-100/0.1M PBS (Sigma-Aldrich®) solution for 15min. Slices were incubated with Bassoon (Abcam Ab82958, 1/200) and Homer1 (Synaptic systems 160003, 1/400) antibodies diluted in 3% BSA/PBST solution for 24 hours at +4°C. Incubation with secondary antibodies coupled to a fluorochrome (Alexa Fluor) diluted in a 3% BSA/0.1M PBS solution was then performed for 1h at room temperature. Sections were rinsed and mounted on Superfrost Plus (Thermo-Scientific®) slides with the Vectashield® mounting medium with a refractive index of 1.45. Images of stained sections were acquired using a Leica DMI6000 confocal optical microscope (TCS SPE) with a 63x oil-immersion objective (refractive index 1.518) and the Leica Las X software. A confocal zoom of 3 and a pinhole aperture fixed at 1 Airy were applied. Acquisition was performed in sequential mode with a sampling rate of 1024 x 1024 and a scanning speed of 700 Hz. Image resolution was 60 nm/pixel and the optical section was 0.896 µm. 26 separate planes with a 0.2 µm step were acquired. The excitation wavelengths were 594 nm or 633 nm. Image acquisition

in the CA1 region was performed on 4 adjacent slices located between -1.82 mm and -3.28 mm from the bregma, with 2 images per slice. For the perirhinal/entorhinal cortex, 3 adjacent slices located between -3.28 mm and -4.24 mm from the bregma were analyzed, with 2 images acquired per slice. 3D deconvolution of the images was performed using the AutoQuant X3 software. The deconvoluted 8-bit images were analyzed using the ImageJ software. Briefly, automated 3D segmentation of the presynaptic (Bassoon) and postsynaptic (Homer1) stained deconvoluted images was performed using "3D spots segmentation" from ImageJ (with "gaussian fit", "block" and "no watershed" options; https://imagej.net/plugins/3d-segmentation). Co-localization of overlapping objects was evaluated using "DiAna" from imageJ (https://imagej.net/plugins/distance-analysis). The percentage of colocalized objects was quantified as an index of synaptic density.

Electrophysiology recordings

Horizontal brain slices containing the somatosensory cortex were prepared from 20 to 30 day-old SWISS mice. Mice were cervically dislocated and immediately decapitated. Their cortices were dissected out and 300 µm thick transverse slices were cut in ice-cold cutting solution (in mM: KCl 2.5, NaH2PO4 1.25, MgSO4 10, CaCl2 0.5, NaHCO3 26, Sucrose 234, and Glucose 11, saturated with 95% O2 and 5% CO2) with a Leica VT1200 blade microtome. After the dissection, slices were kept in oxygenated ACSF at 37±1 °C for at least 1 h.

Slices were visualized in a chamber on an upright microscope with transmitted illumination and continuously perfused at 2 ml/min with oxygenated Artificial Cerebro-Spinal Fluid (ACSF in mM: 119 NaCl, 2.5 KCl, 1.25 NaH2PO4, 1.3 MgSO4, 2.5 CaCl2, 26 NaHCO3, and 11 Glucose) at room temperature. Stimulating electrodes (bipolar microelectrodes) were placed in the stratum radiatum to stimulate the Schaffer collaterals pathway. Field EPSPs (fEPSPs) were recorded in the stratum radiatum using a recording glass pipette filled with ACSF and were amplified with an EPC 10 Amplifier Patchmaster Multi-channel (HEKA Elektronik Dr. Schulze GmbH, Wiesenstrasse, Germany). Recordings were filtered at 1 kHz using the Patchmaster Multi-channel data acquisition software (HEKA Elektronik Dr. Schulze GmbH, Wiesenstrasse, Germany. The initial slope of the fEPSPs was measured to avoid population spike contamination. For LTP experiments, test stimuli (0.2 ms pulse width) were delivered once every 15 s and the stimulus intensity was set to give baseline fEPSP slopes that were 50% of maximal evoked slopes. Slices that showed maximal fEPSP sizes < 1mV were rejected. Long-term potentiation (LTP) in the hippocampal CA1 region was induced by delivering two 100 Hz protocols (2 x 100 Hz) with an interval of 20 seconds to the Schaffer collateral/commissural pathway. Aβx peptides were added to the ACSF bath (final concentration of Aβx: 100 nM) 15 minutes prior to recording. 2 x 100 Hz was delivered after 15 minutes of stable baseline.

Statistical analysis

Statistical analysis was performed using the GraphPad Prism software 9. For the behavioral tasks analysis, Kruskal-Wallis tests with Dunn's multiple comparisons were performed except when repeated measures were acquired, in which case, a two-way repeated measures ANOVA with the Geisser-Greenhouse correction and Dunnett's multiple comparisons was carried out. For the post-mortem analysis, Kruskal-Wallis tests with Dunn's multiple comparisons tests were performed in order to compare differences between inoculated mice. The significance level was set at $p<0.05$. Data are shown on scattered dot plots with mean ± standard error of the mean (s.e.m).

Data availability

The data that support the findings of this study are available from the corresponding author, upon request.

List of abbreviations

Aβ = amyloid-β; AD = Alzheimer's disease; mpi = months post-inoculation; WT = wild-type.

Declarations

Ethics approval and consent to participate

All experimental procedures were conducted in accordance with the European Community Council Directive 2010/63/UE and approved by local ethics committees (CEtEA-CEA DSV IdF N°44, France) and the French Ministry of Education and Research (APAFIS#21333-2019062611099838 v2 authorization given after depositing the research protocol and associated ethic issues), and in compliance with the 3R guidelines. Animal care was supervised by a dedicated veterinarian and animal technicians.

Consent for publication

Does not apply to the content of this article.

Availability of data and materials

The data that support the findings of this study are available from the corresponding author.

Competing interests

The authors declare that they have no competing interests.

Funding

The project was funded by the Fondation Vaincre Alzheimer 2018 and the Association France-Alzheimer 2021. It was performed in a core facility supported by/member of NeurATRIS - ANR-11-INBS-0011. It was also supported by internal funds from the Laboratory of Neurodegenerative Diseases and MIRCen. MC was financed by the French Ministère de l'Enseignement Supérieur, de la Recherche, et de l'Innovation. The funding sources had no role in the design of the study, in the collection, analysis, and interpretation of data, nor in writing the manuscript.

Author's contributions

M.C., A.S.H., A.B., and M.D. contributed to the study conception and design. M.J.S., E. B., A.B. provided the recombinant Aβ proteins. M.C. performed the inoculations in mice. M.C. designed and performed memory evaluations, M.C., A.S.H., F.P., designed and performed the immunohistological analysis in animals. M.C., M.J.S., and A.B. performed biochemical analysis. M.J.S., E. B., A.B. performed ex vivo experiments on cell cultures. M.C., A.B., and M.D. wrote the manuscript. All authors commented on previous versions of the manuscript. All authors read and approved the final manuscript.

Acknowledgements

We thank Martine Guillermier and Mylène Gaudin for surgical expertise during inoculation of proteins to animals. We thank Nicolas Heck for his help in synapse quantification.

FIGURES

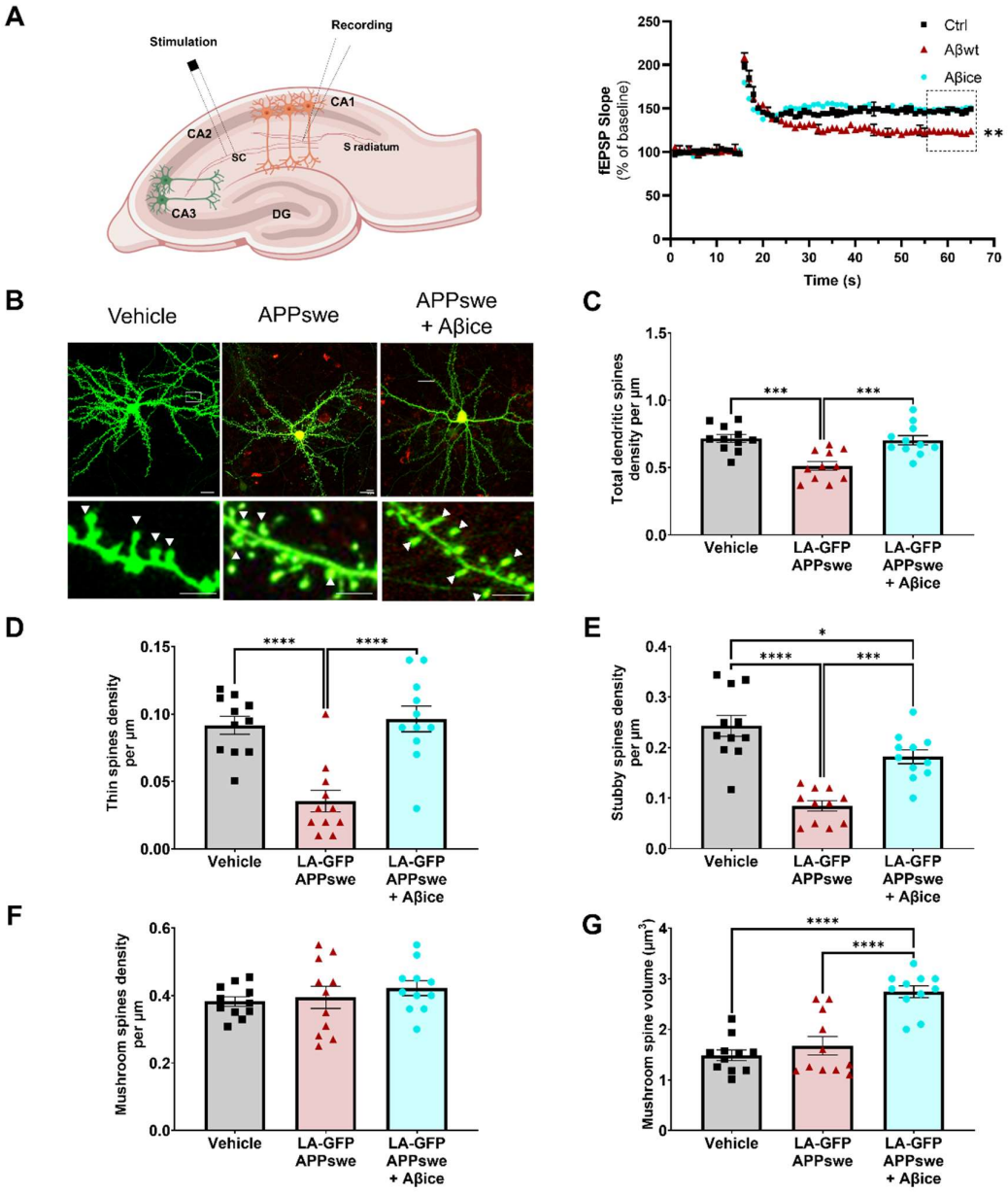

Figure 1. Exogenous application of $A\beta_{ice}$ protected against Aβ-mediated synaptic alterations. A. Left panel: Long-term potentiation (LTP) in the hippocampal CA1 region was induced by delivering two 100 Hz protocols (2 x 100 Hz) with an interval of 20 seconds to the Schaffer collateral/commissural (sc) pathway. $A\beta_x$ peptides were added to the artificial CSF bath 15 minutes prior to recording. Right panel: The 2 x 100 Hz was delivered after 15 minutes of stable baseline. Each point on the graph represents the mean ± SEM. While $A\beta_{ice}$ did not modulate LTP ($p>0.9999$), $A\beta_{wt}$

decreased LTP (**p=0.0017) when comparing the last 10 time points of fEPSP slope (% of baseline) to control conditions (Ctrl; without Aβ treatment). n = at least 5 slices per condition. **B.** Top row: Representative images of cultured cortical neurons expressing LA-GFP, respectively from left to right, after a 24 hours incubation with buffer (vehicle, APP_{swe}) or 100 nM of $Aβ_{ice}$ (scale bar = 10 µm). Bottom row: Dendrite portions with less mushroom spines (white arrows) in APP_{swe} neurons but not after 24 hours incubation with $Aβ_{ice}$ (scale bar = 5 µm). **C.** Quantification of total spine density (mean ± SEM) showing a reduction of total number of spines in APP_{swe} (****p<0.0001 compared to vehicle) and a recovery after treatment with $Aβ_{ice}$ (****p<0.0001 compared to vehicle; *p<0.01 compared to APP_{swe}). Quantification of **(D)** thin spine and **(E)** stubby spine density showing a reduction of thin and stubby spine number in APP_{swe} (****p<0.0001 compared to vehicle) and an increase of both after treatment with $Aβ_{ice}$ (****p<0.0001 compared to vehicle). **F.** Quantification of mushroom spine density being similar between conditions. **G.** Quantification of mushroom spine volume showing an increase after treatment with $Aβ_{ice}$ (****p<0.0001 compared to APP_{swe}). Kruskal-Wallis with Dunn's multiple comparisons. N = 6 neurons from at least 3 different cultures. Data are shown as mean ± s.e.m.

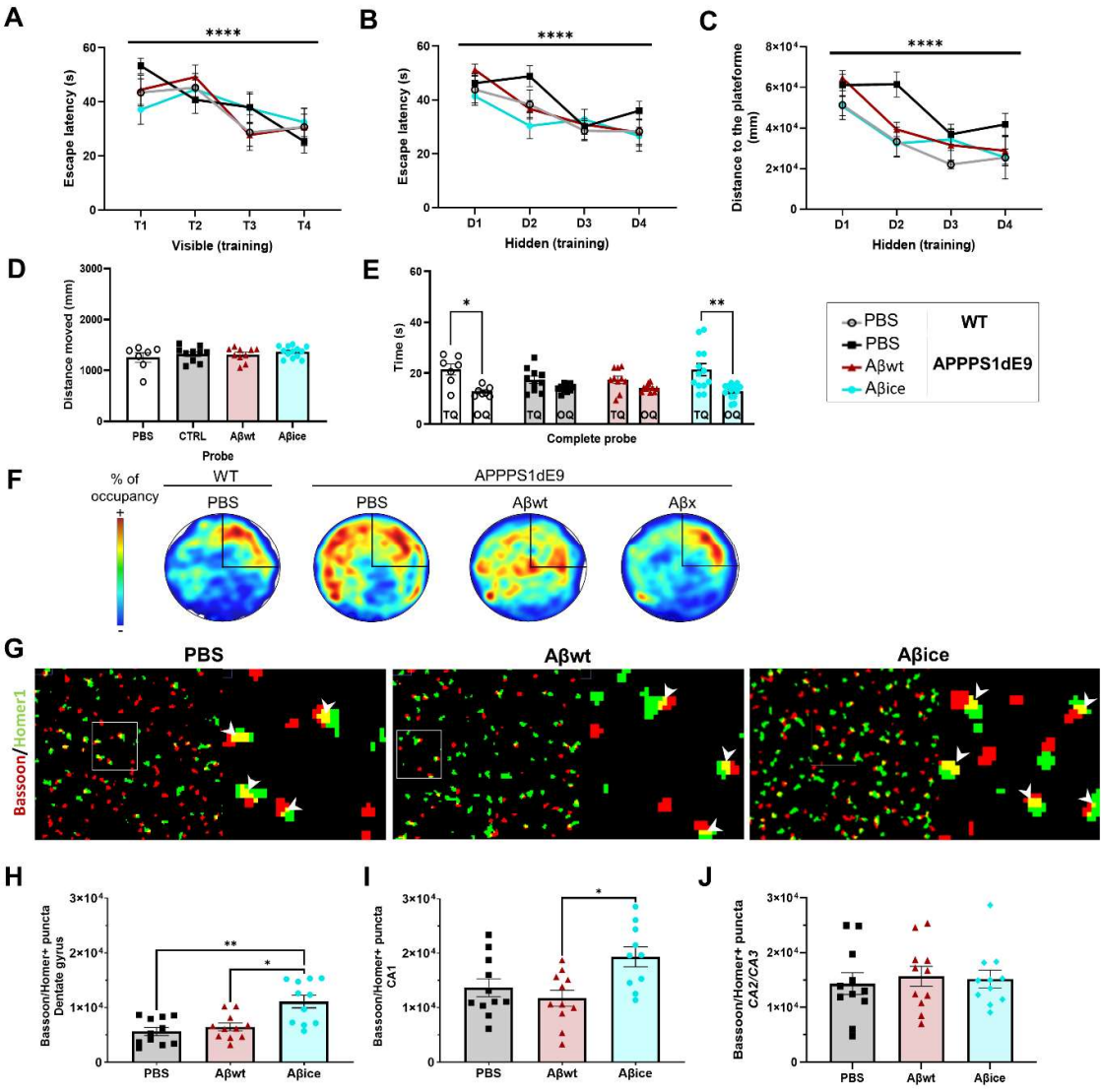

Figure 2. $A\beta_{ice}$ intra-hippocampal infusion rescued spatial memory and increased synaptic density. Spatial memory was evaluated using Morris water maze task at 4 months post-inoculation. **A.** During the visible platform phase, escape latencies decreased across the four trials ($F_{(2.950, 177.0)}$ = 11.76, p<0.0001****; two-way repeated measures ANOVA with the Geisser-Greenhouse correction and Dunnett's multiple comparisons). No difference was observed between the groups ($F_{(4, 63)}$ = 0.07, p=0.9891; two-way repeated measures ANOVA with the Geisser-Greenhouse correction and Dunnett's multiple comparisons). (**B-C**) WT mice and $APP_{swe}/PS1_{dE9}$ mice inoculated with PBS, $A\beta_{wt}$ or $A\beta_{ice}$ had comparable learning abilities, as suggested by the decrease of time to find the platform (**B**) (for the days: $F_{(1.69, 82.98)}$ =18.65; p<0.0005***; two-way repeated measures ANOVA with the Geisser-Greenhouse correction and Dunnett's multiple comparisons) and the distance moved (**C**) (for the days: $F_{(2.894, 101.3)}$ = 20.74, p<0.0005***; two-way repeated measures ANOVA with the

Geisser-Greenhouse correction and Dunnett's multiple comparisons) throughout the 4 training day. **D**. The distance moved during the probe test was similar between groups. **E.** During the probe test evaluating spatial memory, the time spent in the target quadrant (TQ) was significantly higher than the time spent in the opposite one (OQ) in WT mice (p=0.0379*) and $A\beta_{ice}$-inoculated $APP_{swe}/PS1_{dE9}$ mice (p=0.0031**). **F.** Representative heatmap images of probe test. Increased red color intensity represents increased time spent in a given location. Conversely, a cooler color indicates a shorter time spent in the location. The target quadrant is represented. Unlike WT animals, PBS and $A\beta_{wt}$-inoculated $APP_{swe}/PS1_{dE9}$ mice were unable to find the target platform. $A\beta_{ice}$ rescued this phenotype. **G.** Representative views of original Bassoon/Homer segmented and co-localized puncta (white arrow). (**H-J).** An increase in synaptic density is observed in $A\beta_{ice}$-inoculated mice in the dentate gyrus (**H**) and the CA1 (**I**), compared to PBS- and $A\beta_{wt}$-inoculated mice as suggested by a higher co-localized puncta ratio between Bassoon and Homer synaptic markers. (**H**; p<0.0001**** Kruskal-Wallis with Dunn's multiple comparisons: PBS- versus $A\beta_{ice}$-inoculated $APP_{swe}/PS1_{dE9}$: p=0,0052** and $A\beta_{wt}$- versus $A\beta_{ice}$-inoculated $APP_{swe}/PS1_{dE9}$: p=0,0316*) (**I**; p=0,0132* Kruskal-Wallis with Dunn's multiple comparisons: $A\beta_{wt}$- versus $A\beta_{ice}$-inoculated $APP_{swe}/PS1_{dE9}$: p=0,0131*). Synaptic density in the CA2/3 (**J**) are similar between groups (p=0,0104; Kruskal-Wallis with Dunn's multiple comparisons).

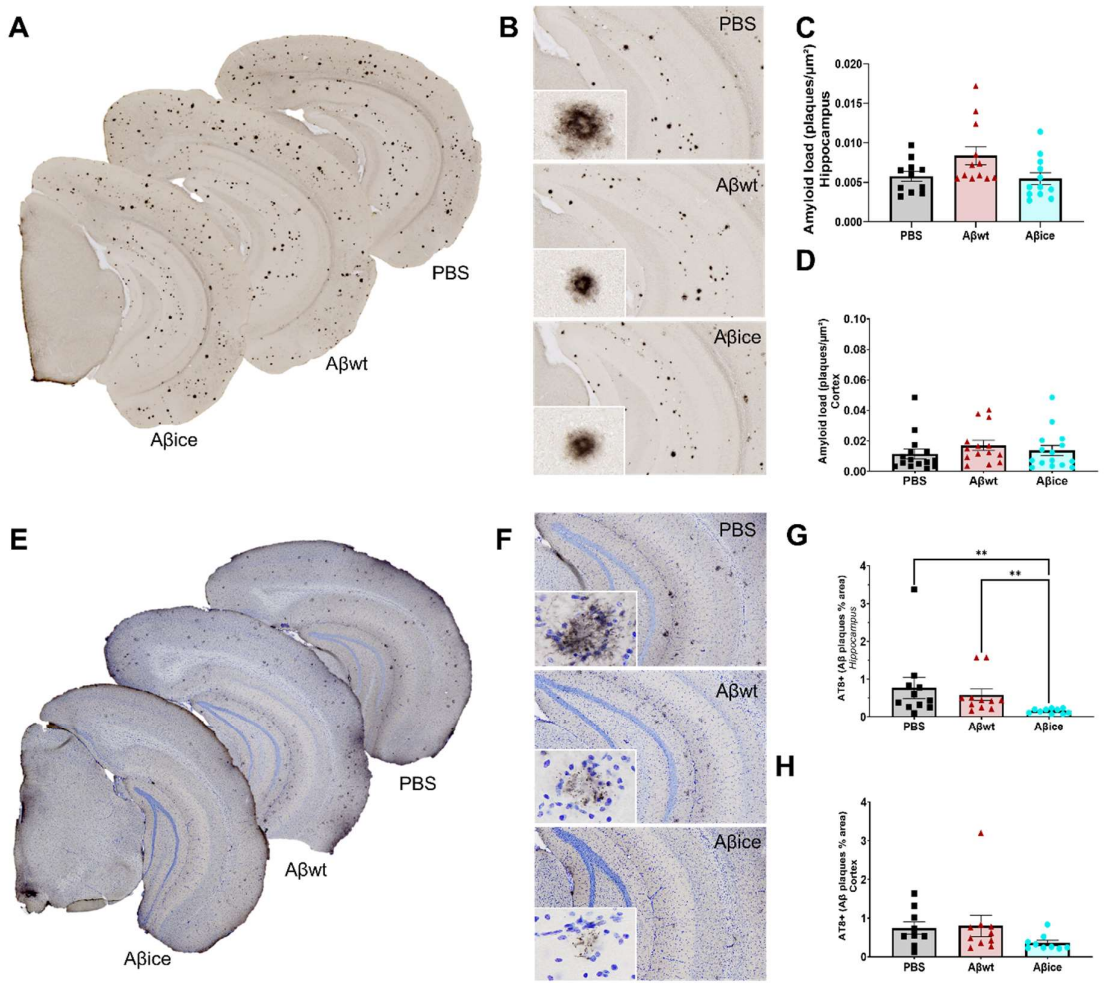

Figure. 3. $A\beta_{ice}$ reduced tau pathology without affecting amyloid load. A. Representative images of 4G8 immunolabelling showing Aβ plaque deposition in the brain of $APP_{swe}/PS1_{dE9}$ mice after PBS, $A\beta_{wt}$ or $A\beta_{ice}$ inoculation in the dentate gyrus. **B.** Representative images of Aβ plaque deposition in the hippocampus. Magnified views showed no difference in the morphology of Aβ plaques between groups. (**C-D**) Quantification of amyloid load (4G8-positive Aβ plaques per µm²) revealed no difference between groups in the hippocampus (**C**, p=0.0874) and in the cortex (**D**, p=0.2315). **E.** Representative images of AT8 immunolabelling showing neuritic plaques in the brain of $APP_{swe}/PS1_{dE9}$ mice after PBS, $A\beta_{wt}$ or $A\beta_{ice}$ inoculation in the dentate gyrus. **F.** Representative images of Tau-positive neuritic plaque in the hippocampus. Magnified views showed no difference in the morphology of neuritic plaques between groups. (**G-H**) Quantification of overall AT8-labelled phospho-tau (percentage of AT8-positive area) revealed decrease of AT8-positive area in the hippocampus (**G**) of $A\beta_{ice}$-inoculated $APP_{swe}/PS1_{dE9}$ mice compared to PBS- (p=0.0018) and $A\beta_{wt}$-inoculated (p=0.0029) $APP_{swe}/PS1_{dE9}$ mice. Kruskal-Wallis with Dunn's multiple comparisons. $nAPP/PS1_{PBS}$=14, $n_{A\beta wt}$=14, $n_{A\beta ice}$ =14 mice. Data are shown as mean ± s.e.m.

4. Complementary data

4.1 Context, objectives & abstract

In this section, we integrated complementary data that were not included in the two last articles. We first confirmed the modulation of β-amyloidosis by Aβ seeds using different amyloid immunolabelling that target Aβ fibrils and dense-core plaques. We conducted a multimodal MRI study that allows to evaluate the impact of different Aβ seeds on (i) neuronal networks, (ii) structural connectivity, and (iii) glutamate distribution. As AD-like lesions - including Aβ plaques, Tau-containing neuritic plaques and synapses - were shown to be impacted by Aβ seeds, we investigated the role of neuroinflammatory actors in the maintenance of the microenvironment induced by the inoculation of Aβ seeds. Finally, we wondered whether the modulation of β-amyloidosis and cognition were maintained with aging.

4.2 Supplementary material

4.2.1 Co-staining of thioflavine and OC-fibrils

In order to evaluate OC-positive fibril load surrounding dense-core amyloid plaques, the co-staining of thioflavine and OC was performed. Free-floating brain sections were rinsed in a 0.1M PBS solution (10% Sigma-Aldrich® phosphate buffer, 0.9% Sigma-Aldrich® NaCl, distilled water) before use. Washing and incubation steps were performed on a shaker at room temperature unless otherwise indicated. Free-floating sections were permeabilized in a 0.5% Triton X-100/0.1M PBS (Sigma-Aldrich®) solution for 30 min. Sections were incubated with the OC antibody (Rabbit, 200-401-E87, ROCKLAND, 1/500) in 3%BSA, 0.2% Triton X-100/0.1M PBS (Sigma-Aldrich®) solution, overnight at 4°C. On the next day, sections were rinsed in 0.1M PBS and incubated for 1h at RT with the appropriate secondary antibody diuted to 1/500 (anti-rat AlexaFluor 633) 3%BSA, 0.2% Triton X-100/0.1M PBS (Sigma-Aldrich®) solution. OC-immunolabeled sections were rinsed and stained with 0.02% Thioflavin-S (Sigma-Aldrich) in 50% ethanol. Sections were mounted on Superfrost Plus (Thermo-Scientific®) slides with the Vectashield® mounting medium with a refractive index of 1.45. Images of stained sections were scanned using an Axio Scan.Z1 (Zeiss® - Z-stack images acquired at 20× (z-stacks with 16 planes, 1µm steps with extended depth of focus)). Each slice was extracted individually in the .czi format using the Zen 2.0 (Zeiss®) software. Image processing and analysis were performed with the ImageJ 1.53i software. Images were imported with a 50% reduction in resolution (0.44 µm/pixel), converted to the 8bit format and saved as .tif. For both staining, segmentation was performed through an automatic local thresholding using the Phansalkar method (radius = 200). Aβ load was evaluated after quantification of the thioflavine and OC-labelled particles between 8 and 2,000 µm², and normalization

to the surface area of each ROI. All ROIs were manually segmented using the Paxinos and Franklin neuro-anatomical atlas of mouse brain (Franklin and Paxinos, 2019). Images of stained sections were also acquired using a Leica DMI6000 confocal optical microscope (TCS SPE) with a 63x oil-immersion objective (refractive index 1.518) and the Leica Las X software. A confocal zoom of 3 and a pinhole aperture fixed at 1 Airy were applied. Acquisition was performed in sequential mode with a sampling rate of 1024 x 1024 and a scanning speed of 700 Hz. Image resolution was 80 nm/pixel and the optical section was 0.896 µm. Twenty-one separate planes with a 0.2 µm step were acquired. The excitation wavelengths were 488 nm (Thioflavine), or 633 nm (OC-fibrils). Image acquisition in the hippocampus was performed on 4 adjacent slices located between -1.58 mm and -3.40 mm from bregma, with 5 images per slice.

4.2.2 fMRI data preprocessing and analysis

The SAMMBA-MRI preprocessing workflow gathers fundamental fMRI preprocessing steps prior to functional analysis (**Figure 51**). Structural images were acquired along with functional images, each in its own space. Prior to common space alignment, structural images were initially corrected for inhomogeneities due to the high magnetic field. Then, individual structural images were co-registered to allow their alignment. This registration was performed by iterative non linear registration of each image to an average image. The average was updated at each iteration providing a high quality template image, which better represents the dataset. This newly-generated template, called the study template, was automatically segmented into 48 bilateral regions based on the Dorr mouse brain atlas DSURQE anatomical atlas (Dorr-Steadman-Ulman-Richards-Qiu-Egan (DSURQE) atlas, 182 structures) (Dorr et al., 2008) providing a common space comparable across several studies. The remaining preprocessing step involved the functional images. First, functional volume was aligned to the anatomical images from the same MRI session using a rigid body registration. During this registration, head motion parameters were estimated and inhomogeneity correction was performed. Then, a per-slice basis registration was performed allowing the correction of susceptibility distortions arising from the EPI acquisition and the slice timing correction. Finally, the rigid body transform and the per-slice warps were combined and applied to the initial volume to minimize interpolation errors. In order to meet the common space and particularly the atlas space, the nonlinear transform of anatomical images to the template and to the atlas was applied to the functional images that were in the native space. Proper co-registration of preprocessed functional images in the atlas space was confirmed by checking the alignment of atlas edges on preprocessed functional images.

Multi-subject ICA was performed with Nilearn (Abraham et al., 2014) on preprocessed rsfMRI using 10 sparse components. Atlas-based correlation analysis was performed between 20 bilateral key ROIs

involved in AD extracted from Dorr atlas. Mean correlation matrices of resting state FC, one for each group, were compared using a two-sample t-test ($p<0.05$) corrected for multiple comparisons (Bonferroni).

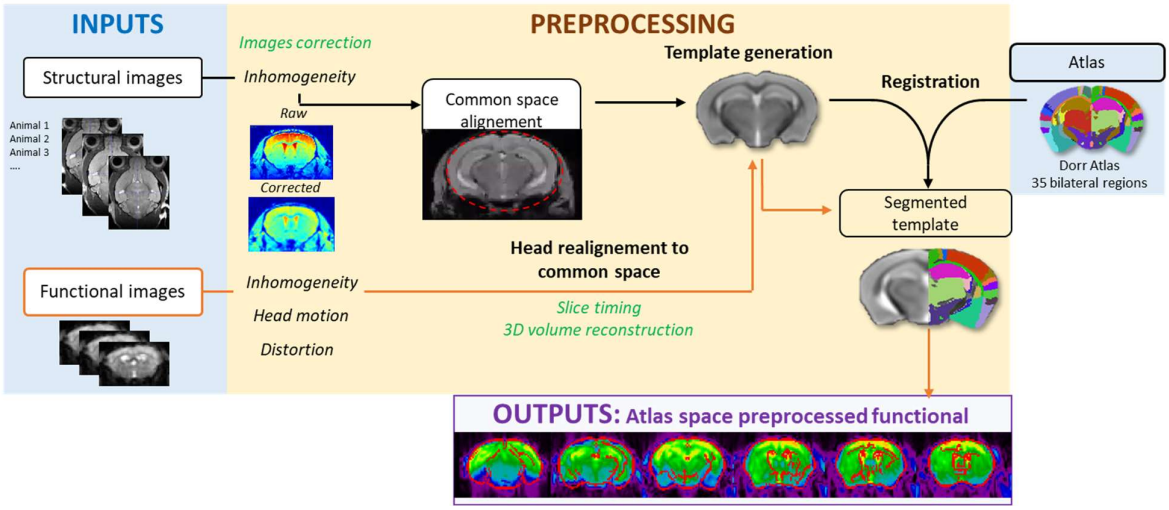

Figure 51: Pre-processing pipeline of MRI

4.2.3 Diffusion

The diffusion-weighted MRI data were acquired using EPI sequence (TE/TR = 30/3200 ms, in-plane resolution = 112 × 112 µm2, 500 µm slice thickness, 10 slices, b-value = 1000 s/mm2, 35 directions). FA maps were generated using ParaVision 6.1 software (Bruker, Ettlingen, Germany). FA images were co-registered using Sammba-MRI pipeline (**Figure 52**). Voxelwise analysis of FA was carried out in *FSL* (Smith et al., 2004) using the Tract-Based Spatial Statistics (TBSS) pipeline (Smith et al., 2006) home-adapted for mouse brain. Mean FA map was generated over the entire animal cohort and the skeleton template of white matter tracts was extracted. Individual skeleton from each animal was calculated using the same process and then projected to the skeleton template to yield a good co-registration of WM tracts. TBSS group comparison were performed using a permutation test (Threshold-Free Cluster Enhancement) ($p<0.05$, 5000 permutations) with false discovery rate correction.

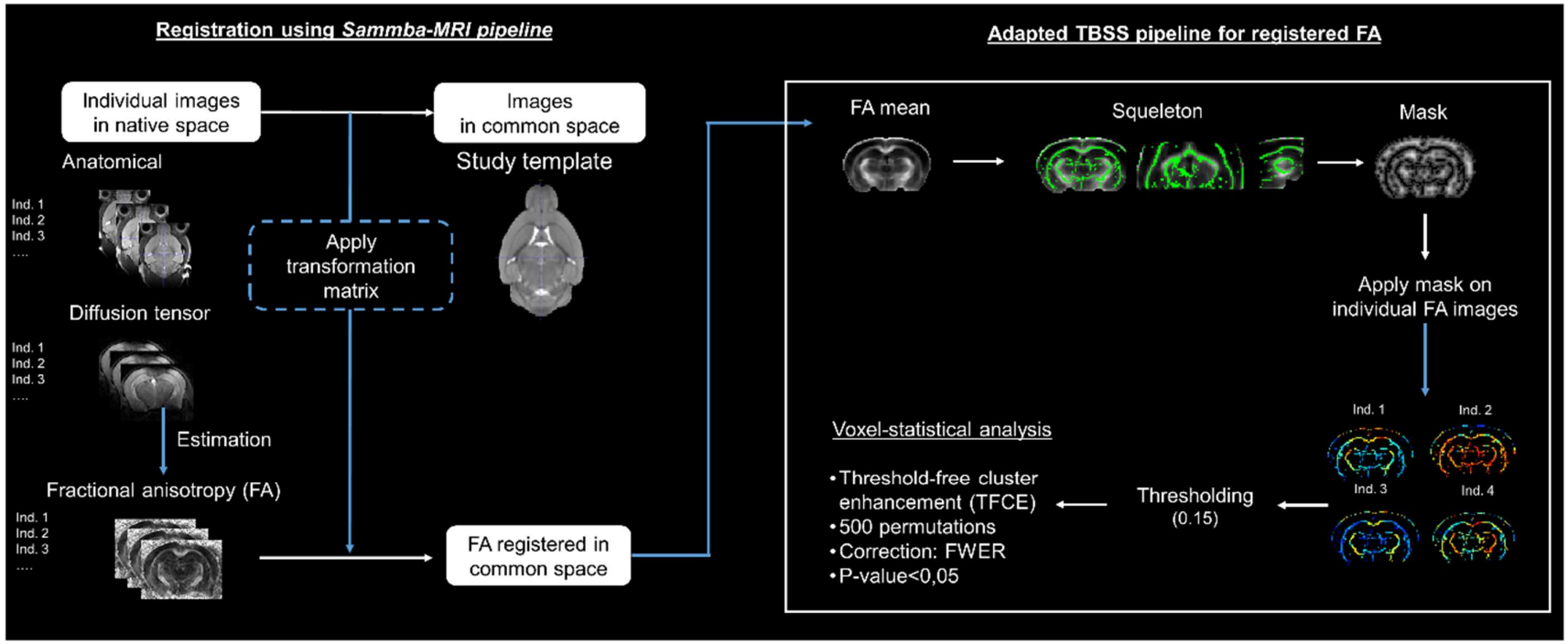

Figure 52: Pipeline used for analyzing diffusion images.

Individual anatomical images were registered to the study template using Sammba-MRI pipeline allowing to obtain transformation matrices. Individual fractional anisotropy (FA) images were calculated from the diffusion tensor. Transformation matrices were applied to FA images in order to get all FA images in a common space. Once FA images were registered, they enter in the TBSS pipeline from FSL that has been adapted to the mouse brain. Voxel-based statistical analysis then was performed to compare white mater FA signal between groups.

4.2.4 CEST

GluCEST images were acquired and processed as previously describe in (Pérot et al., 2022). Briefly, three gluCEST images centered on the hippocampus were acquired with a 2D fast spin-echo sequence preceded by a frequency-selective continuous wave saturation pulse (TE/TR = 6/5000 ms, in-plane resolution = 150 × 150 µm2, 0.8 mm slice thickness). MAPSHIM routine was applied in a voxel encompassing the slices of interest and gluCEST images were acquired with a saturation pulse applied with a frequence ranging from from −5 to 5 ppm (parts per million) with a step of 0.5 ppm. High magnetic field inhomogeneities were corrected using the WASSR method. CEST images were processed pixel-by-pixel and analyzed using in-house programs developed with MATLAB software (MathWorks Inc., Natick, MA) used to generate Z-spectra by plotting the longitudinal magnetization as a function of saturation frequency. WASSR method was used to generate absolute B0 map by finding the actual frequency within each voxel. Z-spectrum in each voxel was interpolated using a cubic spline and B0 map was used to correct for B0 inhomogeneities. Finally, calculated gluCEST images in the hippocampus were manually segmented and mean gluCEST signal was statistically compared between groups using Kruskal-Wallis with post-hoc analysis using Dunn's multiple comparisons.

4.2.5 Microglial engulfment of synapse analysis

In order to evaluate microglial engulfment of synapse, the co-staining of microglia (anti-CD68), presynaptic (Bassoon) and postsynaptic (Homer1) markers were performed. Free-floating sections were permeabilized in a 0.3% Triton X-100/0.1M PBS (Sigma-Aldrich®) solution for 30 min. Slices were then rinced in a 0.02% Tween/0.1M PBS (Sigma-Aldrich®) solution for 5 min following by further permeabilization in 0.3% Triton X-100/0.1M PBS (Sigma-Aldrich®) solution for 3X5min. Sections were blocked in a 3% NGS, 3%BSA, 0.3% Triton X-100/0.1M PBS (Sigma-Aldrich®) solution for 1h at RT before being incubated with the CD68 antibody (MCA1957, Biorad, 1/500) overnight at 4°C. On the next day, sections were rinsed in 0.1M PBS and incubated for 2h at RT with the appropriate secondary antibody diluted to 1/1000 in PBS (anti-rat AlexaFluor 488). Sections were rinsed in 0.1M PBS and permeabilized in a 0.5% Triton X-100/0.1M PBS (Sigma-Aldrich®) solution for 15 min. Slices were incubated with Bassoon (Abcam Ab82958, 1/200) and Homer1 (Synaptic systems 160003, 1/400) antibodies diluted in 3% BSA/PBST solution for 24 hours at RT. Incubation with appropriate secondary antibodies coupled to a fluorochrome (Alexa Fluor) diluted in a 3% BSA/0.1M PBS solution was then performed for 1h at room temperature. Sections were rinsed and mounted on Superfrost Plus (Thermo-Scientific®) slides with the Vectashield® mounting medium with a refractive index of 1.45. Images of stained sections were acquired using a Leica DMI6000 confocal optical microscope (TCS SPE) with a 63x oil-immersion objective (refractive index 1.518) and the Leica Las X software. A confocal zoom of 1.28 and a pinhole

aperture fixed at 1 Airy were applied. Acquisition was performed in sequential mode with a sampling rate of 1024 x 1024 and a scanning speed of 700 Hz. Image resolution was 80 nm/pixel and the optical section was 0.896 µm. Seventy three separate planes with a 0.2 µm step were acquired. The excitation wavelengths were 488 nm (microglia), 594 nm (Basson) or 633 nm (Homer). Image acquisition in the hippocampus was performed on 2 adjacent slices located between -1.58 mm and -3.40 mm from bregma, with 4 images per slice. 3D reconstruction of microglia and synaptic spots was performed with Imaris (9.0.0). First, confocal images were converted in Imaris supported file by Imaris File Converter (9.0.0). While mean filter gradients were applied to CD68 images, subtraction background was performed on synaptic images. Then, the plug-in "surface" was used to reconstruct the CD68 volume and the plug-in "spot" to reconstruct Homer and Basson volume. Finally, the XTension file "Split spots into surface objects" (Matlab) was used to calculate the number of synaptic spots in CD68 positive surface.

4.3 Additional data

4.3.1 Plaque-associated Aβ fibrilar oligomers

In our studies, while $A\beta_{osa}$-inoculated mice displayed an increase in amyloid deposition in the hippocampus and connected regions, the inoculation of $A\beta_{ice}$ did not change the amyloid outcome. We further described the amyloid deposition using co-immunolabelling of Thioflavine that stained dense-core plaques, and OC that revealed fibrillar Aβ and amyloid fibrils (**Figure 53A-B**). We quantified each type of amyloid deposition in the hippocampus of inoculated mice (**Figure 53C-D**). We found an increase in thioflavine and OC-positive plaques in the dentate gyrus of $A\beta_{osa}$-inoculated mice compared to PBS-inoculated mice. Using confocal microscopy, we showed that amyloid fibrils were mostly found around dense-core plaques, which is consistent with previous reports (**Figure 53B**). This structure called plaque-associated fibrillar Aβ oligomers, is mainly involved in AD-associated pathology. One interesting feature of fibrillar Aβ oligomers is their capacity for spreading. Thus, we quantified the amount of plaque-associated fibrillar Aβ oligomers in the entorhinal cortex which is known to be highly connected to the hippocampus. Interestingly, we found that the increased of amyloid load in the entorhinal cortex of $A\beta_{osa}$-inoculated mice, described in Article 2 (**Section 1.2**), was more associated to an increase in fibrillar amyloid than in dense-core plaques, as suggested by the significant increased level of OC-positive plaques in $A\beta_{osa}$-inoculated mice (**Figure 54**).

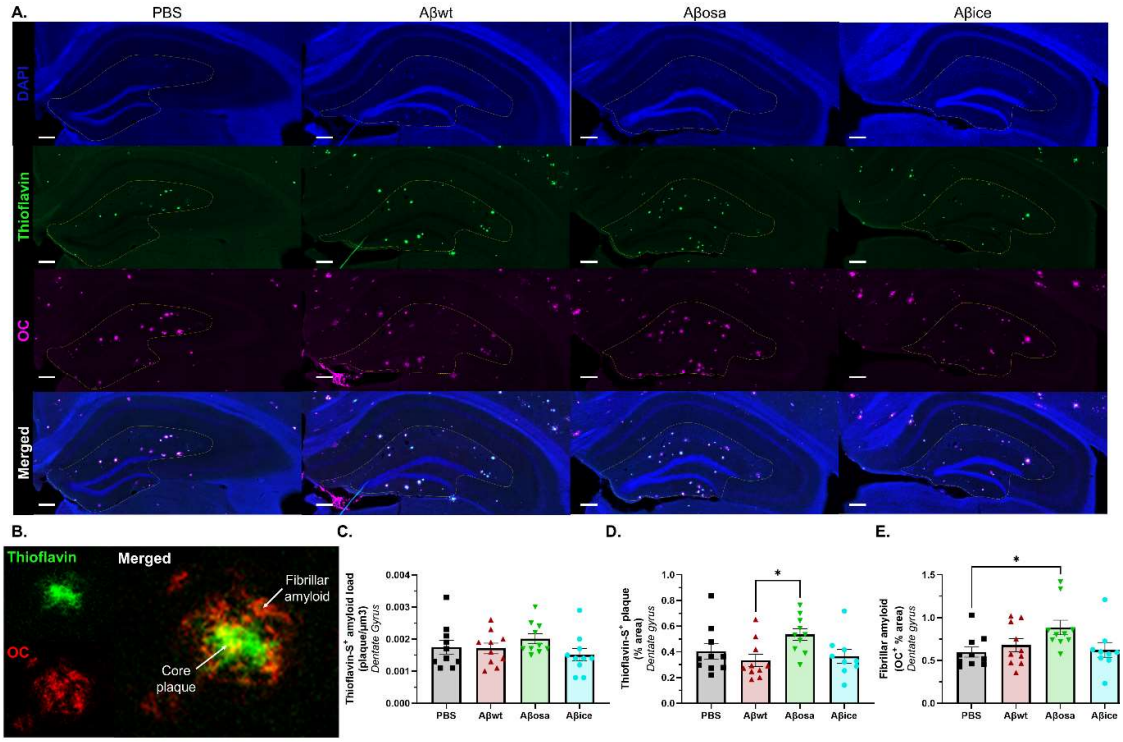

Figure 53: Modulation of plaque-associated Aβ fibrillar oligomer load in the hippocampus following inoculation of Aβ variants at 4 mpi

A. Representative images of OC and Thioflavine S immunolabeling showing respectively Aβ fibrils and dense core plaque deposition in the brain of $APP_{swe}/PS1_{dE9}$ mice after PBS, $Aβ_{wt}$ or $Aβ_{osa}$ inoculation in the dentate gyrus. **B.** Representative image of the co-immunolabelling. Aβ fibrils and fibrilar oligomers (red) are located around the dense core plaque (green). Quantification of amyloid load (**C**: Thioflavin-positive amyloid plaques per µm²; **D**: Thioflavine-positive % area) and Aβ fibrils load (**E:** OC-positive % area) in the hippocampus. $Aβ_{osa}$ inoculation increases Aβ plaque deposition (**D**, p=0.0162) and Aβ fibrillar oligomers (**E**, p=0.0268) in the hippocampus compared to respectively $Aβ_{wt}$-and PBS-inoculated $APP_{swe}/PS1_{dE9}$ mice. Kruskal-Wallis with Dunn's multiple comparisons. $n_{APP/PS1-PBS}$=10, $n_{Aβwt}$=10, $n_{Aβosa}$=10, $n_{Aβice}$=10 mice. Data are shown as mean ± s.e.m.

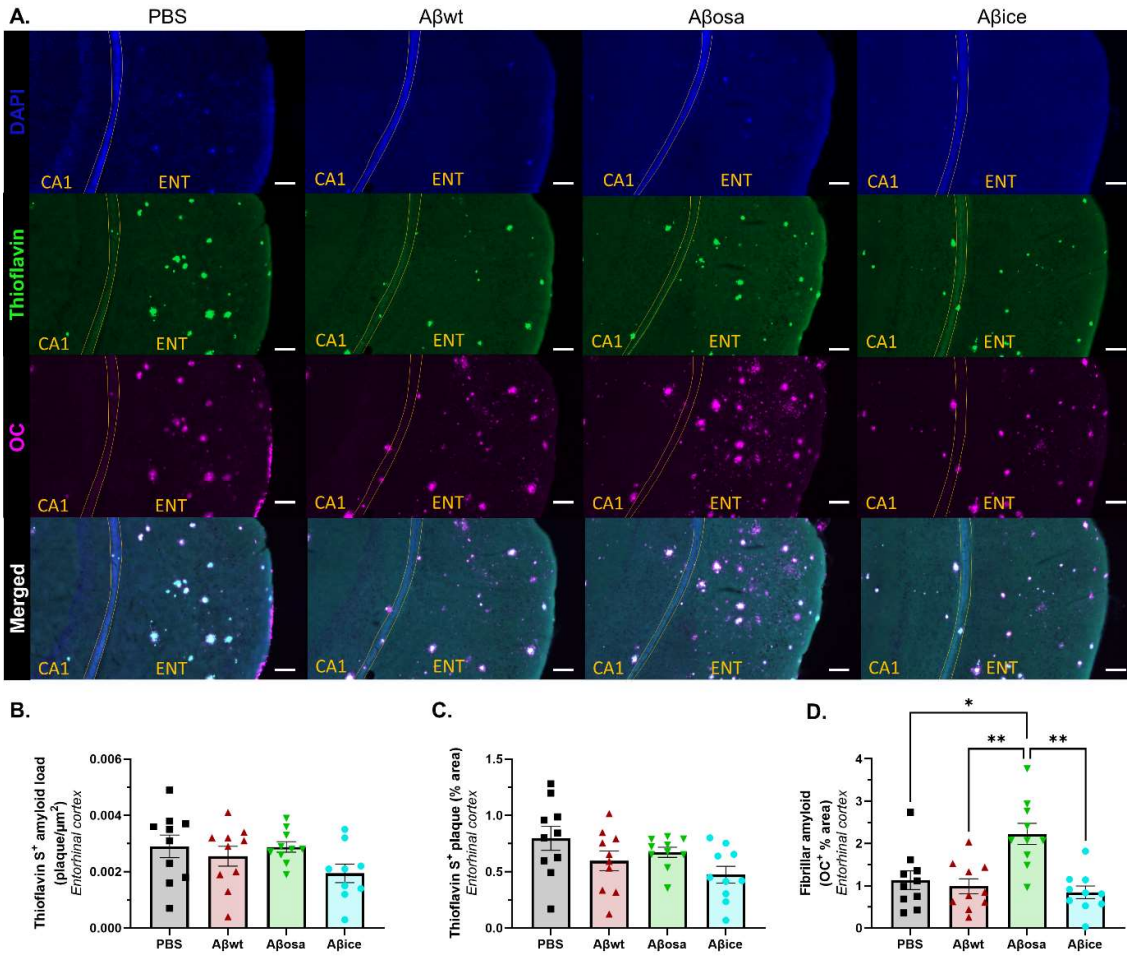

Figure 54: Modulation of plaque-associated Aβ fibrillar oligomer load in the entorhinal cortex following inoculation of Aβ variants at 9 mpi

A. Representative images of OC and Thioflavine S immunolabeling showing respectively Aβ fibrils and dense core plaque deposition in the brain of $APP_{swe}/PS1_{dE9}$ mice after PBS, $Aβ_{wt}$ or $Aβ_{osa}$ inoculation in the dentate gyrus. Quantification of amyloid load (**B**: Thioflavin-positive amyloid plaques per µm²; **C**: Thioflavine-positive % area) and Aβ fibrils load (**D:** OC-positive % area) in the entorhinal cortex. $Aβ_{osa}$ inoculation increases Aβ fibrillar oligomers (**D**, p=0.0216) without changing dense core plaque load in the entorhinal cortex compared to PBS- (p=0,0179); $Aβ_{wt}$- (p=0,0084) and $Aβ_{ice}$-(p=0,0030) inoculated $APP_{swe}/PS1_{dE9}$ mice. Kruskal-Wallis with Dunn's multiple comparisons. $n_{APP/PS1-PBS}$=**10**, $n_{Aβwt}$=**10**, $n_{Aβosa}$=**10**, $n_{Aβice}$=**10** mice. Data are shown as mean ± s.e.m.

4.3.2 Aβ-mediated neuronal networks dysfunction

In our study, we described an accumulation of Aβ deposition in the hippocampus following $Aβ_{osa}$ inoculation associated with a hippocampal network disconnection and a reduction of memory performance. Other Aβ seeds did not have any impact on FC. Seed-based analysis with a seed in the hippocampus and the entorhinal cortex mainly supported evidence of a dissociation of the hippocampus-involving network. We confirmed these findings using the atlas-based correlation analysis where FC between 28 bilateral regions were assessed. We generated connectivity matrices that compared brain regions FC correlation in Aβ-inoculated mice and in PBS-inoculated mice. Reduced FC were observed within the laterality communication and among hippocampal-related area in $Aβ_{osa}$-inoculated mice compared to PBS-inoculated mice (**Figure 55A**).

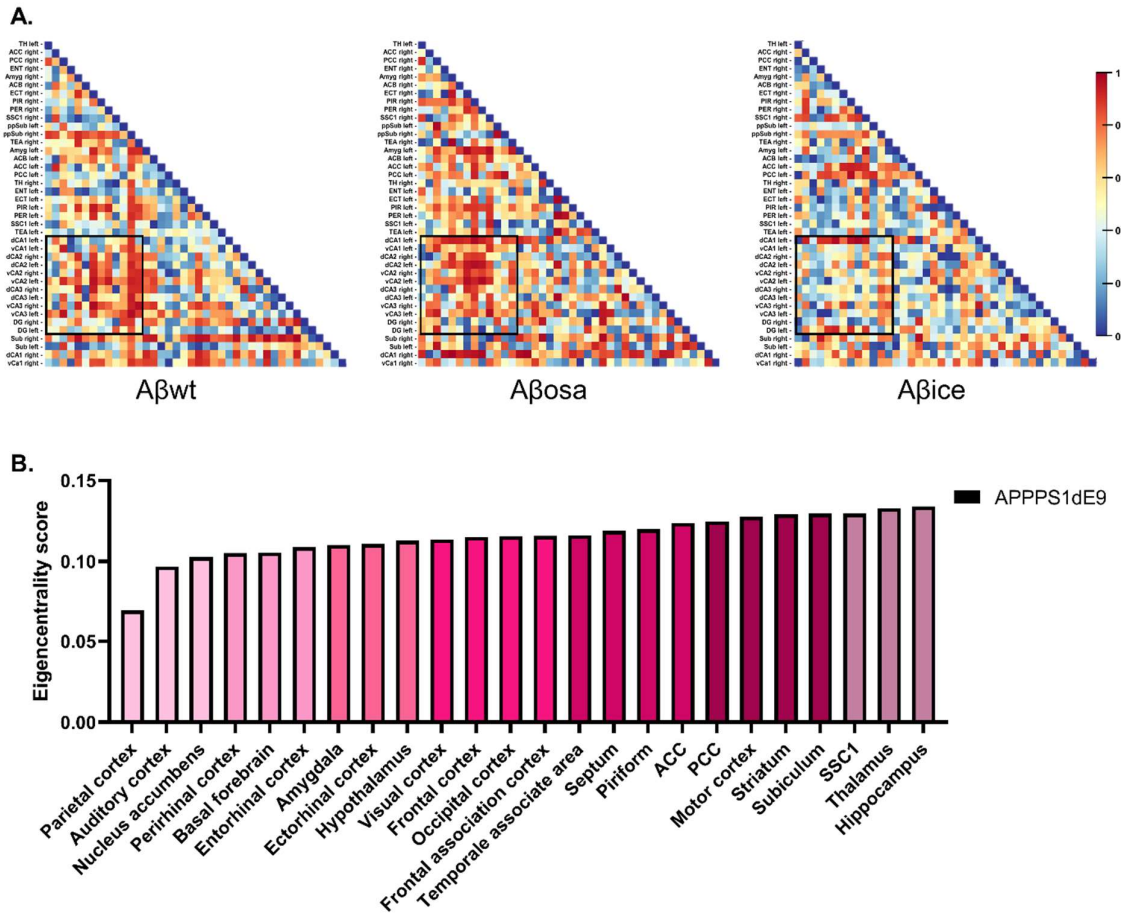

Figure 55: Atlas-based connectivity matrices

A. Functional connectivity (FC) matrices of significant p-value represented ($p<0.0001$) FC differences between Aβ-inoculated mice and PBS-inoculate mice. Main differences occur within the laterality communication particularly in hippocampal-related area (black boxes) networks. **B.** Eigencentrality

score in the different brain areas of PBS-inoculated $APP_{swe}/PS1_{dE9}$ mice. Abbreviations: ACC, anterior cingulate cortex; PCC, posterior cingulate cortex; SSC1, primary secondary somatosensory cortex.

Another way for measuring the ability of a given brain area to functionally communicate with others brain areas, is to assess the "hubness" which describes the degree of inter-region connectivity which is supposedly related to its importance for brain function. The eigencentrality score give a score according to the number of connections that a given brain area has with other brain areas. The hippocampus was shown to be a high connectivity hub in $APP_{swe}/PS1_{dE9}$ as suggested by the higher eigencentrality score (**Figure 55B**). Compelling evidence in human and animal studies have proven that the accumulation of Aβ occurs through regions that shown high neuronal activity which is consistent with our observation. We hypothesize that the dissociation of the hippocampus-involving network may contribute to the alteration of larger networks involved in cognitive process. Using group ICA with presets of 15 components, we identified nine components that detect meaningful anatomical regions of anesthetized mouse brain and considered as rs-fMRI networks (**Figure 56**). Among these networks, we identified one network that displayed high overlap with areas included in the DMN-like activation pattern for mice (Sforazzini et al., 2014; Stafford et al., 2014; Zerbi et al., 2015). The somatosensory and the basal ganglia networks were each found unilaterally divided in two components. The remaining subcortical network was bilateral. The ventral hippocampus was found highly connected to the septum, resulting in the septo-hippocampic network.

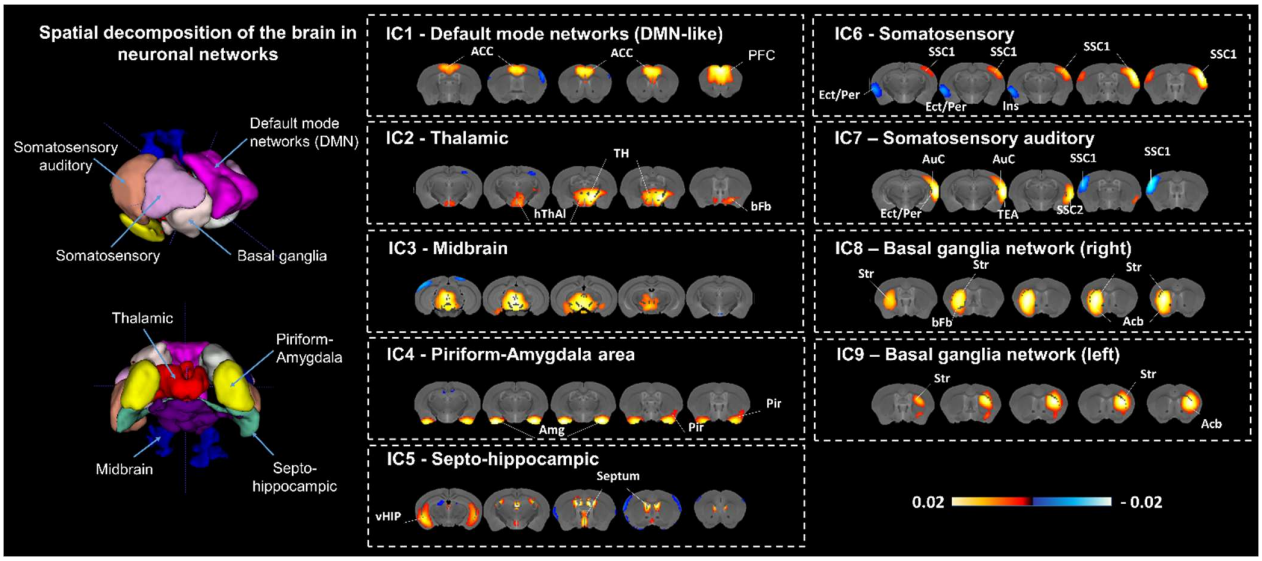

Figure 56: Functional regions identified in the mouse brain using 9 ICA-related components

Individual ICA components are represented overlaid on anatomical template in the coronal view. Functionally-correlated and anti-correlated oscillation signals are shown in red/yellow and blue, respectively. Abbreviations: ACC, anterior cingulate cortex; PFC, prefrontal cortex, TH, thalamus,

hThAl, hypothalamus, bFb, basal forebrain; Amg, amygdala; Pir, piriform cortex; vHIP, ventral hippocampus; Ect/Per, Ectorhinal/Perirhinal cortex; SSC1/2, primary and secondary somatosensory cortex; Ins, insula; AuC, auditory cortex; TEA, temporal association area; Str, striatum; Acb, nucleus accumbens.

To further investigate the impact of Aβ seeds on rs-fMRI network, we compared the connectivity within the ICA network across subject. Dual regression analyses were performed and enabled to create subject-specific maps of FC from the group networks. These maps contain values reflecting the degree to which a voxel's time series is correlated with the mean time series of a given network. In other words, we analyzed how each subject contributed to the final shape of network connectivity. FC network changes were only observed in $A\beta_{osa}$-inoculated mice. Reduction of connectivity within the DMN, somatosensory and septo-hippocampic networks has been identified in these mice compared to PBS-inoculated mice (**Figure 57**). While few voxels showed a reduction of FC in the somatosensory and septo-hippocampic networks, the DMN is almost completely altered. Thus, $A\beta_{osa}$ inoculation led to a disconnection of the hippocampus which is associated with alterations of large-scale brain networks connected to this structure such as DMN and septo-hippocampic networks. The negative effect of Aβ on network functional connectivity has been shown to cause memory disturbance in several studies of animal models.

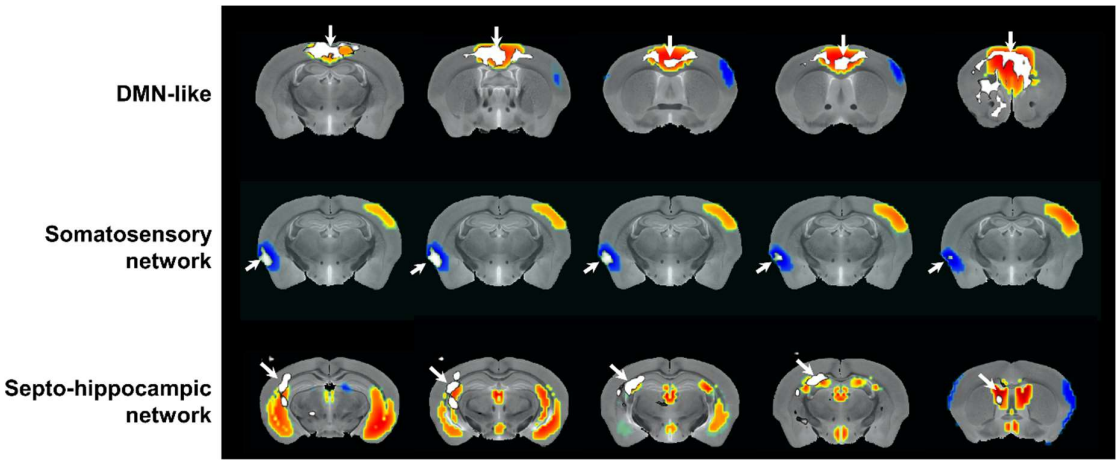

Figure 57: $A\beta_{osa}$-inoculated mice showed decreased rs-fMRI networks

Group-ICA dual regression analysis of rs-fMRI networks are represented as an overlay on ICA-related networks. The differences in resting state networks are showed in white color.

4.3.3 Diffusion

Several evidences in AD have shown that functional connectivity is associated with changes in the microstructure of white matter that can be measured by evaluating the distribution of water diffusivity

in DTI images. The role of Aβ in diffusional changes is mainly controversial. Both increase and decrease of fractional anisotropy were reported in different transgenic mouse models that produce high levels of Aβ. We hypothesized that different Aβ seeds can differently modulate diffusivity by changing the pathological outcome, which contributes to the diversity reported in FA data. FA images were skeletonized using TBSS pipeline, which enabled to obtain an accurate representation of white matter fiber in the mouse brain (**Figure 58**). For example, corpus callosum, fimbria of the hippocampus and amygdalar capsule were readily discriminated from these images. To visualize the distribution of water diffusivity differences between groups, we performed a statistical voxel-based analysis of each subject's skeleton (**Figure 59A**). Significant voxels were differentiated in areas where $A\beta_{wt}$-, $A\beta_{osa}$-, $A\beta_{ice}$-inoculated $APP_{swe}/PS1_{dE9}$ mice showed lower FA values (**Figure 59B**) and higher FA values (**Figure 59C**) compared with PBS-inoculated $APP_{swe}/PS1_{dE9}$ mice. Non-significant voxels were not represented. In several clusters in the corpus callosum and fornix system, a decrease in FA was visible in $A\beta_{ice}$-inoculated $APP_{swe}/PS1_{dE9}$ mice (**Figure 59B**). While in the external capsule, unilateral clusters of voxels showed a large increase in FA in $A\beta_{osa}$-inoculated $APP_{swe}/PS1_{dE9}$ mice. Similar changes were observed in the amygdalar capsule (**Figure 59C**). $A\beta_{wt}$-inoculated $APP_{swe}/PS1_{dE9}$ mice showed a slight decrease of FA in the corpus callosum (**Figure 59B**). This finding revealed multiple regions where higher FA was associated with greater amyloid deposition on $A\beta_{osa}$-inoculated $APP_{swe}/PS1_{dE9}$ mice. Surprisingly, altered cortico-hippocampal connections, such as the fornix, were shown in $A\beta_{ice}$-inoculated $APP_{swe}/PS1_{dE9}$, which raise the question whether this diffusional changes are associated with beneficial effects instead of detrimental effects in those mice.

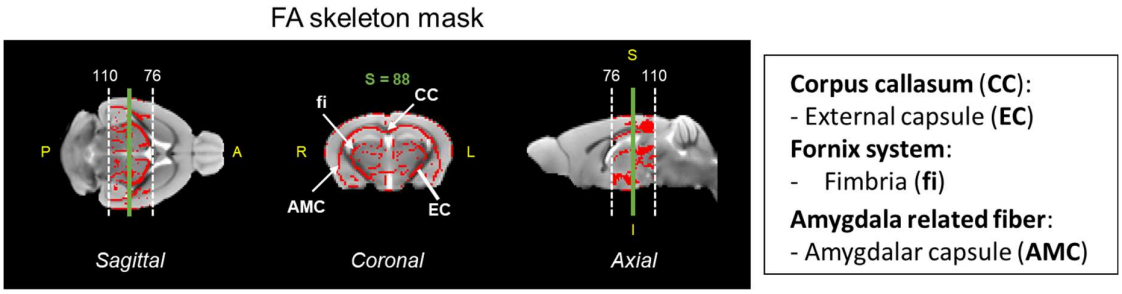

Figure 58: Mean FA skeleton mask used for group comparison analysis

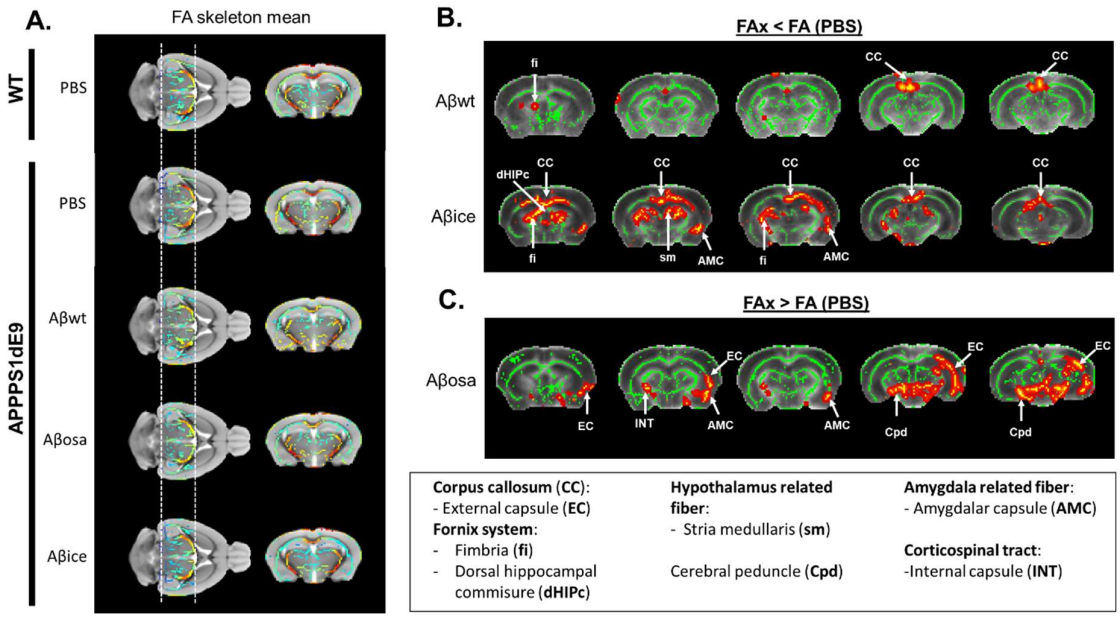

Figure 59: Microstructural white matter changes in inoculated mice at 4 months post-inoculation

A. Fractional anisotropy (FA) skeleton means obtained after TBSS pipeline for each group are shown overlaid on the study template. **B-C**. FA alterations in white matter as revealed by TBSS analysis for each group, overlaid on the mean FA map. Green regions represent mean white matter skeleton as used in TBSS pipeline. Red–yellow zones show clusters of voxels with significant decrease (**B**) or increase (**C**) of FA compared to PBS-inoculated mice (threshold-free cluster enhancement, $P < 0.05$).

4.3.4 Aβ seeds regulate glutamate metabolism and neuroinflammation process

In our study, we found that, while $A\beta_{osa}$ inoculation was associated with an early loss of hippocampal synapses, $A\beta_{ice}$ increased synaptic density. The direct impact of Aβ seeds on synapse integrity was confirmed as we also showed detrimental and beneficial effects on cortical neurons after treatment with $A\beta_{osa}$ and $A\beta_{ice}$ respectively. However, the mechanism by which synaptic changes were maintained four months after the inoculation remains unclear. One possibility is that Aβ seeds regulate the metabolism of glutamate that is the major excitatory neurotransmitter found at low levels in AD, resulting in defects in synaptic transmission and cognitive abilities. Glutamate can be measured using the non-invasive gluCEST imaging. Previous studies in transgenic mouse models of AD have demonstrated an age-dependent decrease in gluCEST signal that strongly correlates with synaptic changes (Igarashi et al., 2020). While decreased glutamate levels specific to the hippocampal region have been reported at late stage of the disease in 18 months-old $APP_{swe}PS1_{dE9}$, elevated glutamate levels have been described in the hippocampus prior to Aβ accumulation resulting in aberrant excitatory phenomenon (Haris et al., 2013). To see whether Aβ seeds are able to modulate the switch of cerebral glutamate level, we investigated glutamate alterations in inoculated mice four month post-

inoculation. As we detected Aβ-mediated alteration mainly in the DG, we chose three slices that span the hippocampus from rostral to caudal. GluCEST maps that illustrated the distribution of glutamate in different regions were obtained for each group (**Figure 60A**). An increased gluCEST signal was found in $APP_{swe}PS1_{dE9}$ compared to WT mice that is in contradiction with what was observed in the literature. In addition, we demonstrated a statistically significant decrease in gluCEST signal in $APP_{swe}PS1_{dE9}$ inoculated with $A\beta_{osa}$ and $A\beta_{wt}$. Inoculation of $A\beta_{ice}$ did not change the distribution of glutamate in the hippocampus (**Figure 60B**). These results indicate that toxic Aβ seeds can modulate the metabolism of glutamate, which may contribute to the alteration of synapses in the hippocampus. However, the protective impact on synapses is not related to glutamate level modifications.

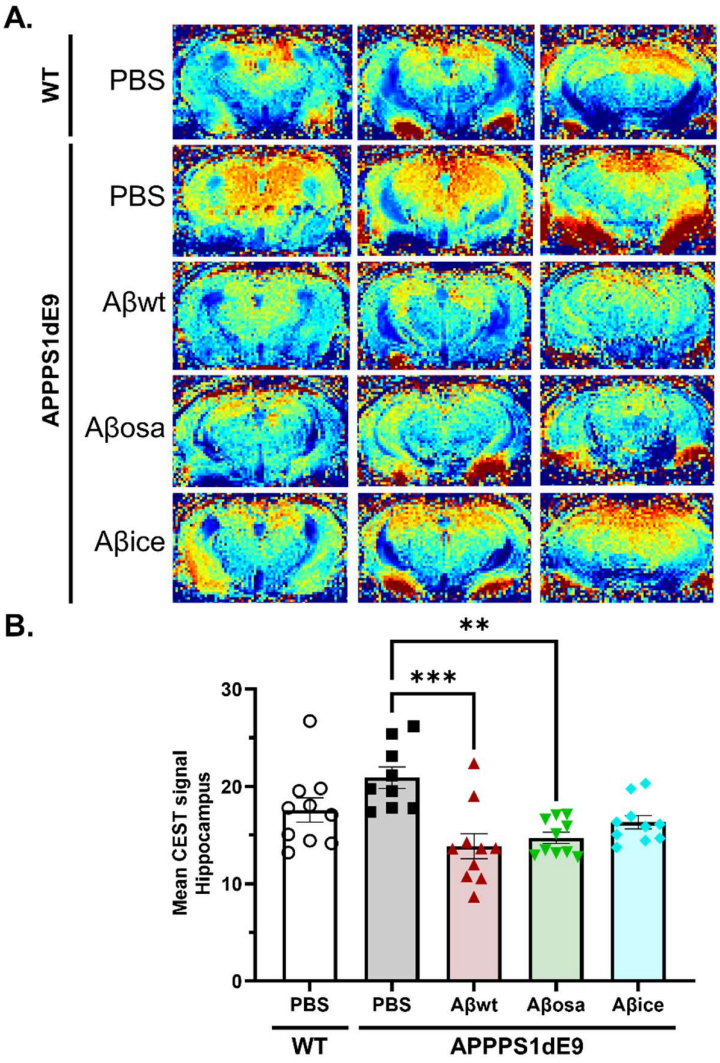

Figure 60: Decreased glutamate levels after inoculation of $A\beta_{wt}$ and $A\beta_{osa}$ in $APP_{swe}/PS1_{de9}$ mice

A. Whole-brain GluCEST average signal is shown in PBS-inoculated WT, PBS-, $A\beta_{wt}$- and $A\beta_{osa}$-inoculated $APP_{swe}/PS1_{de9}$ mice. **B**. A decrease of mean GluCEST signal in the hippocampus is shown in $APP_{swe}/PS1_{de9}$

mice inoculated with $A\beta_{wt}$- and $A\beta_{osa}$- compared to PBS-inoculated $APP_{swe}/PS1_{de9}$ mice. Group analysis using Kruskal-Wallis (p=0.0005) with post-hoc analysis using Dunn's multiple comparisons p=0.0008 and p=0.0038, for $A\beta_{osa}$- and $A\beta_{wt}$- versus PBS-inoculated $APP_{swe}/PS1_{de9}$ mice, respectively). **p<0.05, ***p<0.005; $n_{WT\text{-}PBS}$=10, $n_{APP/PS1\text{-}PBS}$=10, $n_{A\beta wt}$=10, $n_{A\beta osa}$=10 mice, $n_{A\beta ice}$=10 mice. Data are shown as mean ± s.e.m

The switch from elevated to decreased glutamate concentration is highly dependent on glial activity in mouse models of AD resulting in an early neuroinflammation process prior to neurodegeneration. Thus, we assessed the neuroinflammatory response following the inoculation of Aβ seeds by staining brain tissues using GFAP and Iba1, general markers for astrocyte and microglia respectively. Quantification of GFAP and Iba1 immunoreactivity showed similar astrocyte and microglia load in the hippocampus of inoculated $APP_{swe}PS1_{dE9}$ mice (**Figure 61**). Visual observation of the stained sections did not demonstrate morphological difference of glial cells between the groups. However, microglia clusters surrounding amyloid plaques displayed high level of Iba1 immunoreactivity. Abundant activated microglia was characterized by spherical and enlarged cell body with dystrophic ramifications also described in the literature.

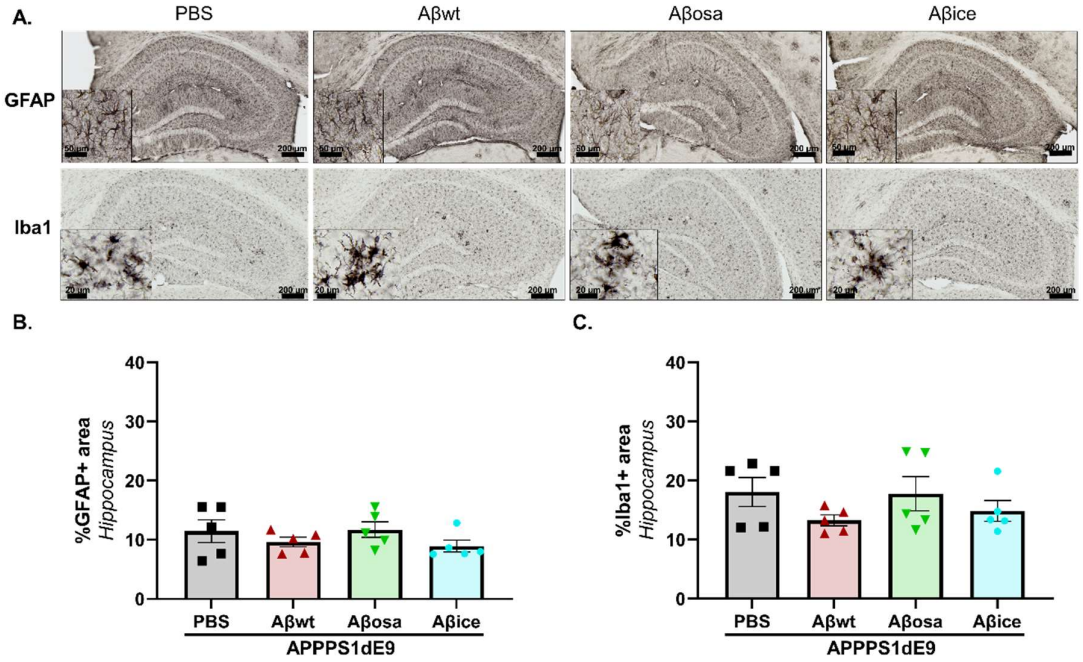

Figure 61: Astrocyte and microglia coverage was similar in the hippocampus of Aβ seeds inoculated mice at 4mpi.

A. Representative images of GFAP and Iba1 immunolabeling showing respectively astrocytes and microglia in the dorsal hippocampus of $APP_{swe}/PS1_{dE9}$ mice after PBS, $A\beta_{wt}$, $A\beta_{osa}$, or $A\beta_{ice}$ inoculation in the dentate gyrus. GFAP and Iba1 staining revealed similar astrocytic (**B**) and microglial (**C**) loads in the

hippocampus at 4mpi. Kruskal-Wallis with Dunn's multiple comparisons. $n_{APP/PS1-PBS}$=10, $n_{A\beta wt}$=10, $n_{A\beta osa}$=10, $n_{A\beta ice}$=10 mice. Data are shown as mean ± s.e.m. Scale bars in main images: 200 µm; Insets: 20 µm.

Controversial role of microglia during AD, from neuroprotective to detrimental role, has been described in AD. Microglial-associated plaque form a barrier to protect the brain against Aβ-associated neurotoxicity (Condello et al., 2015). Microglia was also proposed to remove synaptic damage in order to limit the spreading of the disease and not to lose the entire axon (Edwards, 2019). In another hand, at later stages of AD, excessive synaptic pruning of microglia causes neuronal loss, network dysfunction and cognitive alterations. Microglia phagocytosis performance is highly dependent on Aβ accumulation and the stage of the disease. As we showed an early accumulation of Aβ associated with an acceleration of pathological process in $A\beta_{osa}$-inoculated mice, we wondered whether microglial synaptic engulfment could be an indirect target of $A\beta_{osa}$-mediated detrimental regulation. Furthermore, we hypothesized that the mechanism by which $A\beta_{ice}$ protects against synaptic damage rely on the capacity of microglia to phagocyte synapses. To investigate microglial synaptic engulfment, we performed immunofluorescence coupling CD68 labelling of microglia lysosomes, presynaptic Bassoon marker and post-synaptic Homer marker in a small cohort of inoculated mice. Using confocal microscopy, we imaged activated microglia near amyloid plaques, which generate blue autofluorescence propertie. (**Figure 62A**). Unfortunately, we observed a co-localization between Basson and CD68 indicating that Basson is expressed in microglia, which made impossible microglia-mediated Basson engulfment analysis. Thus, we quantified the number of post-synaptic spots (Homer) inside CD68-positive microglial vesicles (**Figure 62B**). We found an increased amount of Homer spot engulfment in $A\beta_{osa}$-inoculated mice. In contrast, decreased phagocytosis was observed in $A\beta_{ice}$-inoculated mice (**Figure 62C**). These primary results indicated the possibility to modulate neuroinflammation response following Aβ seeds. This findings need to be further confirmed by co-labelling of CD68 and Iba1 marker to ensure that observed vesicles are localized inside microglia.

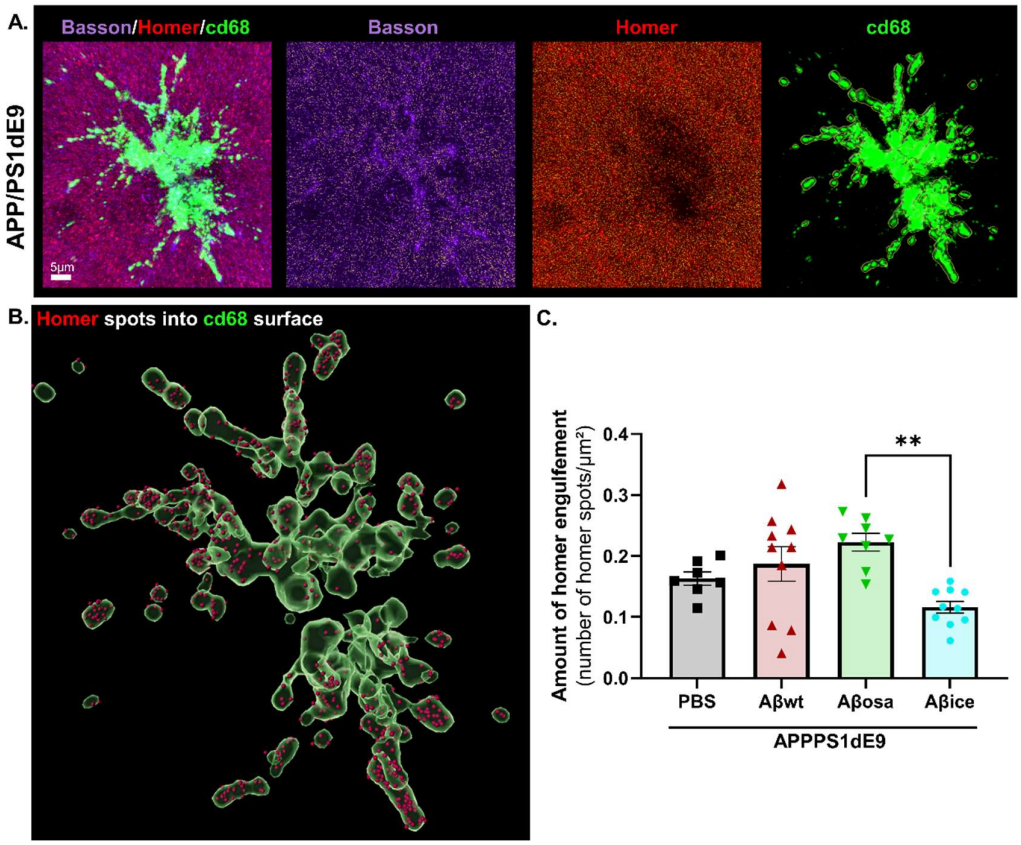

Figure 62: Increased microglial phagocytosis of synapses in $A\beta_{osa}$-inoculated $APP_{swe}/PS1_{dE9}$ mice

A. Co-immunolabeling of lysosomal microglia (CD68, green), pre-synaptic (Basson, magenta) and post-synaptic (Homer, red) marker. Unexpected labelling of microglia is observed in Basson immunolabelling. **B.** CD68 positive lysosomes (green) and Homer spot (red) are 3D-reconstructed to assess the phagocytose of post-synaptic compartment. **C**. Homer spot inside CD68+ lysosomes are quantified and represents the amount of microglial engulfement of synapse. Phagocytosis of synapse was higher in $A\beta_{osa}$-inoculated $APP_{swe}/PS1_{dE9}$ mice mice than $A\beta_{ice}$-inoculated $APP_{swe}/PS1_{dE9}$ mice. Kruskal-Wallis with Dunn's multiple comparisons ($A\beta_{osa}$- versus $A\beta_{ice}$-inoculated $APP_{swe}/PS1_{dE9}$: p=0.0017). $n_{APP/PS1\text{-}PBS}$=7, $n_{A\beta wt}$=10, $n_{A\beta osa}$=8, $n_{A\beta ice}$=10 mice. Data are shown as mean ± s.e.m.

4.3.5 The effect of Aβ seeds disappears with aging

Different clinical outcomes were found in six-month-old $APP_{swe}/PS1_{dE9}$ mice following the inoculation of different mutated Aβ seeds. $A\beta_{osa}$ inoculation led to increased amyloid deposition associated with cerebral function impairments, synaptic defects and activation of phagocytic microglia. In contrast, $A\beta_{ice}$ inoculation protected against synaptic damage through a Tau-dependent mechanism, which allowed to rescue spatial memory. A crucial question is to assess whether these different effects persist with aging. Mutated Aβ seeds were compared with a non-mutated $A\beta_{1\text{-}42}$ that have shown moderate

impact four months post-inoculation. This moderate effect was unexpected as several experimental transmission of Aβ studies have proven the amyloidogenic properties and synaptotoxicity of $A\beta_{1-42}$ (Stöhr et al., 2014). We hypothesized that the time-lapse to observe pathological effect of Aβwt was too short in our previous study. Thus, another cohort of $APP_{swe}/PS1_{dE9}$ mice was inoculated bilaterally in the hippocampus with Aβ seeds as previously described. Behavioral assessment was performed at 9 months post-inoculation (mpi) and compared to PBS-inoculated $APP_{swe}/PS1_{dE9}$ and wild-type (WT) littermate groups. In the V-maze, the traveled distance decreased throughout the three days of the test, but was comparable between groups (**Figure 63A**). Additionally, comparable discrimination index was observed during the training phase, indicating similar exploratory activity between groups (**Figure 63B**). During the probe test, all groups of $APP_{swe}/PS1_{dE9}$ mice had comparable exploratory activity (**Figure 63C**). During the discrimination task, all groups had comparable exploratory activity of the novel object. However, mice inoculated with $A\beta_{osa}$ and $A\beta_{wt}$ had a tendency to spend less time exploring the novel object compared to control mice (PBS-inoculated WT or $APP_{swe}/PS1_{dE9}$ mice) but it was not statistically significant. Spatial memory of inoculated mice was also evaluated using the Morris water maze. First, we ensure that mice did not have visual deficiency using a visible platform (**Figure 63D**). Except for $A\beta_{osa}$-inoculated, mice from each other group showed similar spatial learning as suggested by comparable reduction of the time spent to find the hidden platform over the training days (**Figure 63E**). Spatial memory was evaluated 24 hours after training. Interestingly, only WT mice significantly spent more time in the target quadrant than the other quadrants compared to PBS- or Aβseed-inoculated $APP_{swe}/PS1_{dE9}$. These results suggest that the beneficial effects of $A\beta_{ice}$ inoculation on spatial memory recovery have disappear with aging. Together, these results demonstrated that memory performance cannot be distinguish across groups with aging.

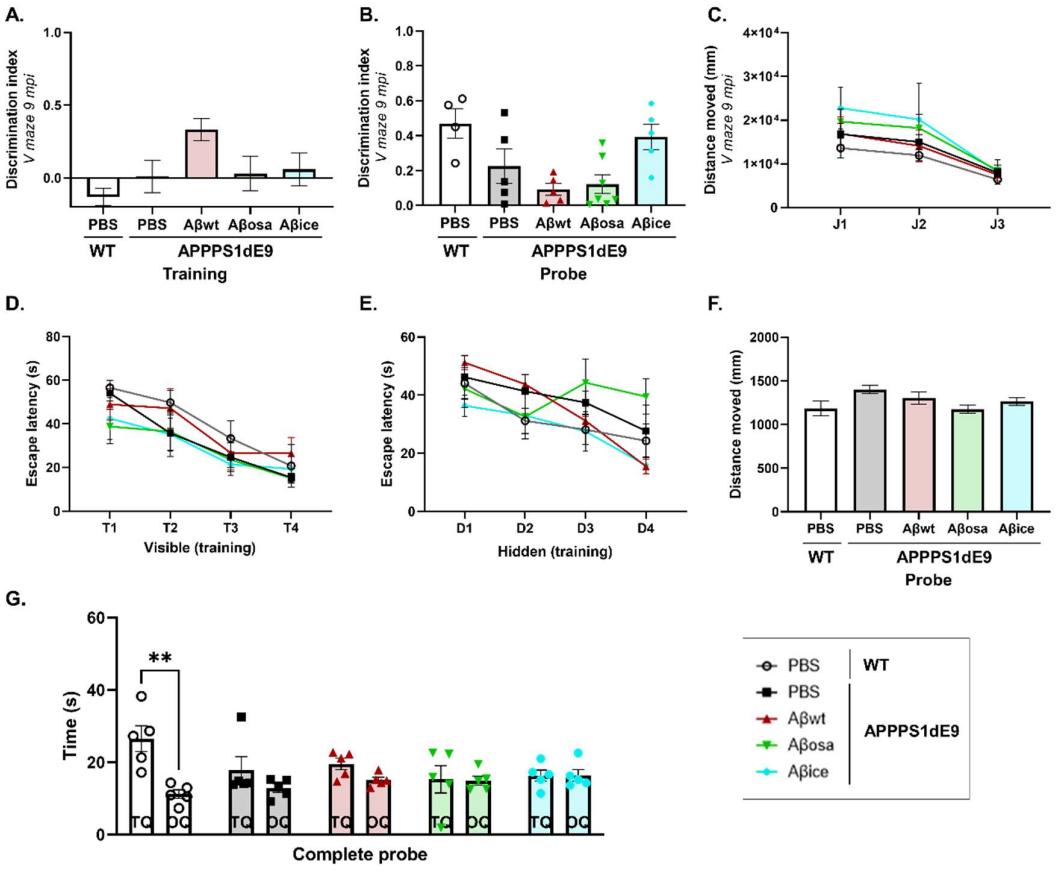

Figure 63: Similar memory performances were observed in inoculated $APP_{swe}/PS1_{dE9}$ at 9 mpi

Novel object recognition was evaluated in a V-maze (A-C) at 9 months post-inoculation. **A**. Mice performance during the training phase. Similar discrimination indexes were found for all groups when mice had to discriminate two identical objects ($p>0.05$, Kruskal-Wallis with Dunn's multiple comparisons). **B.** Object discrimination index. Similar discrimination indexes were found for all groups when mice had to discriminate between familiar and novel objects ($p>0.05$, Kruskal-Wallis with Dunn's multiple comparisons). $APP_{swe}/PS1_{dE9}$ mice inoculated with $A\beta_{osa}$ and $A\beta_{wt}$ had a tendency to spent less time exploring the novel object compared to PBS-inoculated WT mice or $APP_{swe}/PS1_{dE9}$ mice. **C**. Distance moved throughout 3 days of tests (exploration, training and probe-test days). Measurements revealed a time-effect from day 1 to day 3 ($F(1,896, 39,81) = 30,77$, $p<0.0001$), but no differences between experimental groups ($p>0.05$) (two-way repeated measures ANOVA with the Geisser-Greenhouse correction and Dunnett's multiple comparisons). Spatial memory was evaluated using Morris water maze (D-G) task at 4 months post-inoculation. **D**. During the visible platform phase, escape latencies decreased across the four trials ($p<0.0001$****; two-way repeated measures ANOVA with the Geisser-Greenhouse correction and Dunnett's multiple comparisons). No difference was observed between the groups ($p=0.9891$; two-way repeated measures ANOVA with the Geisser-

Greenhouse correction and Dunnett's multiple comparisons). **E.** WT mice and $APP_{swe}/PS1_{dE9}$ mice inoculated with PBS, $A\beta_{wt}$ or $A\beta_{ice}$ had comparable learning abilities, as suggested by the decrease of time to find the platform (for the days: p<0.0001****; two-way repeated measures ANOVA with the Geisser-Greenhouse correction and Dunnett's multiple comparisons) throughout the 4 training day. **F**. The distance moved during the probe test was similar between groups. **G**. During the probe test evaluating spatial memory, the time spent in the target quadrant (TQ) was significantly higher than the time spent in the opposite one (OQ) in WT mice (p=0.0036**). $n_{WT\text{-}PBS}$=5, $n_{APP/PS1\text{-}PBS}$=5, $n_{A\beta wt}$=5, $n_{A\beta osa}$=7, $n_{A\beta ice}$=7 mice. Data are shown as mean ± s.e.m.

As memory performances remained unchanged by the inoculation of Aβ seeds at 9 mpi, we assessed the cerebral amyloid deposition in those mice (**Figure 64A**). Aβ plaque load was assessed in the cortex (**Figure 64B**) and the hippocampus (**Figure 64C**). We showed a tendency toward an increased Aβ deposition in $A\beta_{wt}$-, $A\beta_{osa}$-inoculated $APP_{swe}/PS1_{dE9}$ and a decrease in $A\beta_{ice}$-inoculated $APP_{swe}/PS1_{dE9}$ compared to PBS-inoculated $APP_{swe}/PS1_{dE9}$ in both structures. Significant difference in amyloid load were only observed between $A\beta_{ice}$- and $A\beta_{osa}$-inoculated $APP_{swe}/PS1_{dE9}$. Thus, we quantified the amyloid load in hippocampal subregions: DG (**Figure 64E-F**), CA1 (**Figure 64G-H**) and CA2/3 (**Figure 64I-J**). We found a similar pattern in all subregions. Interestingly, a stronger decrease/increase of amyloid load in the entorhinal cortex was observed in respectively, $A\beta_{ice}$-inoculated $APP_{swe}/PS1_{dE9}$ and $A\beta_{wt}$-, $A\beta_{osa}$-inoculated $APP_{swe}/PS1_{dE9}$ (**Figure 64K-L**). These results suggest a potential persistence of Aβ seeds 9 months after their inoculation.

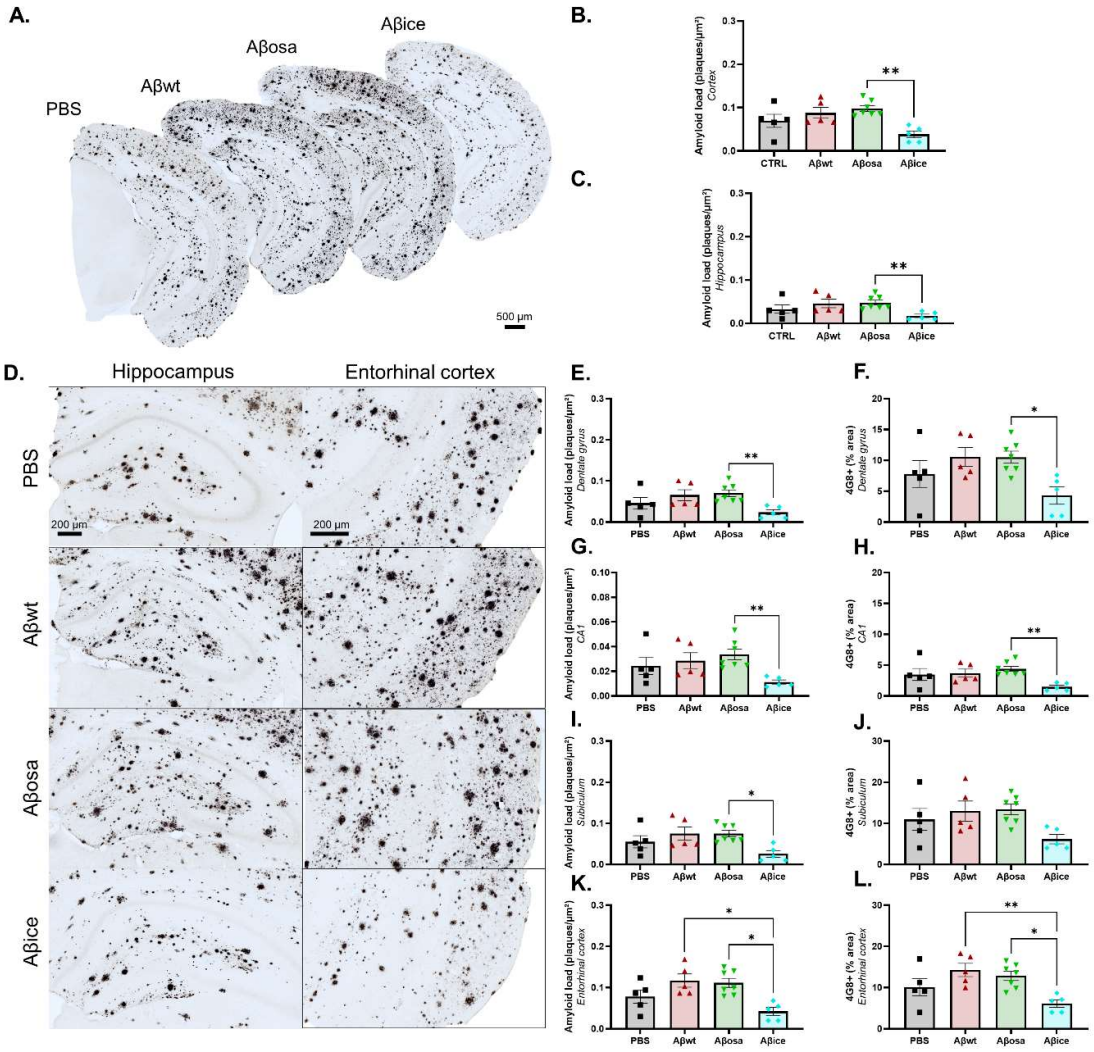

Figure 64: Modulation of Aβ plaque load following inoculation of Aβ variants at 9 mpi

A. Representative images of 4G8 immunolabeling showing Aβ plaque deposition in the brain of $APP_{swe}/PS1_{dE9}$ mice after PBS, $Aβ_{wt}$ or $Aβ_{osa}$ inoculation in the dentate gyrus. Quantification of amyloid load (4G8-positive amyloid plaques per µm²) in the cortex (p=0.0061) (**B**) and hippocampus (p=0.0034) (**C**). $Aβ_{osa}$ increases Aβ plaque deposition in both regions. **D**. Representative images of 4G8 immunolabeling showing Aβ plaque deposition in the dorsal hippocampus and entorhinal cortex. $Aβ_{osa}$-inoculated $APP_{swe}/PS1_{dE9}$ mice showed a higher amyloid load (4G8-positive amyloid plaques per µm²) in the dentate gyrus (**E: p=0.0071 ;F: p=0.0318**), in the CA1 (**G: p=0.0032 ;H: p=0.0039**), in the subiculum (**I: p=0.0208; J**), and in the entorhinal cortex (**K: p=0.0218 ;L: p=0.0438**) compared to $Aβ_{ice}$-inoculated $APP_{swe}/PS1_{dE9}$ mice. $Aβ_{wt}$-inoculated $APP_{swe}/PS1_{dE9}$ mice showed a higher amyloid load in the entorhinal cortex compared to $Aβ_{ice}$-inoculated $APP_{swe}/PS1_{dE9}$ mice (K: p=0.0152; L: p=0.0093).

Kruskal-Wallis with Dunn's multiple comparisons. $n_{APP/PS1\text{-}PBS}$=5, $n_{A\beta wt}$=5, $n_{A\beta osa}$=7, $n_{A\beta ice}$=5 mice. Data are shown as mean ± s.e.m. Scale bars = 500 µm (A), 200 µm (D).

DISCUSSION & PERSPECTIVES

The deleterious effect of Aβ on AD-associated pathology has been widely studied in cellular and animal models. In this study, we found that the degree of toxicity is not equal between Aβ variants and some Aβ forms are protective. To assess the role of Aβ on the progression of AD *in vivo*, highly purified brain-derived Aβ and synthetic Aβ were inoculated in transgenic mouse model of amyloidosis. Some previous studies of synthetic Aβ inoculation in WT mice were focused on the acute negative effects of Aβ on the brain function (Epelbaum et al., 2015). Other studies on long-term impact of synthetic Aβ were focused mainly on Aβ lesions without assessing the other features of AD (Stöhr et al., 2014, 2012). Additionally, the dual effects of Aβ (deleterious or beneficial) on brain functions and associated pathology have never been investigated in mice.

In the studies reported here, we described the long-term impact of different Aβ seeds on brain pathology and physiology. We provided a critical insight into the AD-like pathological fingerprints of distinct recombinant Aβ seeds following their inoculation *in vivo*. We showed that a single inoculation of Aβ seeds leads to a diversity of toxicity degrees, which allows dissociating them into: highly deleterious, moderate and beneficial. Inoculation of $A\beta_{osa}$ led to memory dysfunctions and whole brain disconnection syndrome associated with synaptic loss without affecting Tau pathology (**Table 4**). These functional alterations were induced by an acceleration of endogenous Aβ pathology resulting from an increase of soluble and insoluble Aβ species and by an excessive APP processing leading to an increase of CTFs. Conversely, the inoculation of $A\beta_{ice}$ rescued the AD-like associated pathology by preserving spatial memory, cerebral connectivity and synaptic density. Interestingly, instead of modulating amyloidosis, the inoculation of $A\beta_{ice}$ provoked a reduction of Tau within neuritic plaques (**Table 4**). Thus, in our study, Aβ is seen as a regulator that can steer toward either deleterious or beneficial pathways.

	Aβosa	Aβwt	Aβice
	Aggravation of AD	Moderate	Protection against AD
Self-assembly	Yes	Yes	Yes
Neurotoxicity *in vitro*	Yes	Yes	No
Cognition	Alteration	-	Restoration
Neuronal networks	Alteration	-	-
Synaptic density	↓↓	-	↑↑
Amyloidosis	↑↑↑	-	-
APP processing	↑	-	-
Tau pathology	-	-	↓

Table 4: Summary table of Aβ seeds *in vitro* and *in vivo* impacts

1. Aβ as a regulator of AD-like downstream events

According to the amyloid cascade hypothesis, soluble Aβ initiates the AD pathology. Mounting evidences have suggested that the different aggregation properties of Aβ may result in the existence of distinct Aβ strains that exhibit different conformations with pathological signatures that could lead to the phenotypic polymorphism observed in patients (Condello et al., 2018; Eisele, 2013; Eisele et al., 2010, 2009; Ladiwala et al., 2012; Meyer-Luehmann et al., 2006; Stöhr et al., 2014, 2012; Watts et al., 2014; Ye et al., 2015) . The concepts of Aβ strains was mainly supported by the inoculation of transgenic mice with brain samples from patients with two different heritable forms of AD (*Swedish* and *Artic*) known to produce two distinct patterns of cerebral Aβ deposition, that were maintained upon serial passages (Watts et al., 2014). Although brain samples are highly bioactive and relevant to understand the link between Aβ strains and AD heterogeneity, many co-factors as Tau or neuroinflammation participate to the "strain effect". Therefore, the strain-inducing neuropathology polymorphism cannot be associated to the unique effect of Aβ. As it was also suggested that Aβ governs the pathological cascade of events, questions about how different Aβ "strains" can induce different outcomes of the pathology and which are their pathological fingerprints remain unanswered. In our study, we demonstrated that in addition to acting like a strain, Aβ is a regulator of AD-like downstream events. We showed that the focal seeding of different mutated Aβ can either aggravate the pathology ($Aβ_{osa}$), have moderate effects ($Aβ_{wt}$) or protect against the disease ($Aβ_{ice}$). The regulating effect of Aβ may occur directly following its inoculation as suggested by the acute changes in synaptic density and synaptic transmission, as observed in cortical neurons after exogenous application of the Aβ seeds. *In vivo*, the regulating effects were observed four months post-inoculations and we hypothesized that, accordingly with a prion-like effect, the inoculum was not present anymore in the brain at the time of neuropathology studies. Our data strongly support the possibility that Aβ seeds induce different cascades of pathological events that allow maintaining an effect during four months and even more. For $Aβ_{osa}$-related pathological cascade, it is noteworthy that the accumulation of Aβ is the key event in the pathogenic mechanism. $Aβ_{wt}$ seems also to modulate the amyloidosis pathology but more slowly, as suggested by the increase of amyloid load not observed before 9 months post-inoculation. In contrast, $Aβ_{ice}$ regulates the Tau pathology and the synapses in a way that protects against the toxicity of the endogenous overexpressed Aβ. Although Aβ seeds were inoculated in the hippocampus, their impacts were observed in different brain areas either close to or far from the inoculum site. This strongly supports a global regulation of the pathology in multiple sites of the brain leading to changes in the outcome of the disease. Thus, the early regulation associated with Aβ seeds is responsible for brain function modifications including cognition and brain connectivity.

A critical question in our study is whether $A\beta_{osa}$ acts like a strain by misfolding other Aβ proteins leading to a shift in the dominant shape of Aβ proteins present in the mice. Further investigations to determine the existence of "strain effects" will be conducted using conformation stability assay or conformational-binding dye such as luminescent conjugated oligothiophenes (LCO).

2. Modulation of Aβ pathology by Aβ seeds

The $APP_{swe}/PS1_{dE9}$ mice were inoculated bilaterally in the dorsal hippocampus (dentate gyrus) at 2 months. At this age, mice produce high levels of Aβ leading to the formation of the first senile plaques around 4 months of age with a progressive increase in plaque deposition until 12 months of age in the cortex and hippocampus (Garcia-Alloza et al., 2006). We also showed that our model spontaneously develops murine Tau-containing neuritic plaques in the cortex and the hippocampus at 6 months. In this model, compared to PBS-inoculated $APP_{swe}/PS1_{dE9}$ mice, amyloid load in the hippocampus was increased in $A\beta_{osa}$ and $A\beta_{wt}$ respectively at 4 and 9 months after the inoculation, while it remained unchanged following the inoculation of $A\beta_{ice}$. The increase in amyloid load is consistent with several experimental transmission studies in transgenic mice showing that intracerebral inoculation of minimal amounts of misfolded Aβ contained in AD brain extracts or synthetic Aβ can induce premature build-up of Aβ deposits in their host (Eisele et al., 2009; Meyer-Luehmann et al., 2006; Stöhr et al., 2014, 2012; Watts et al., 2014). Notably, we found that local $A\beta_{osa}$ seeding induces widespread Aβ depositions in the host suggesting that focal seeding $A\beta_{osa}$ reduces the lag phase of senile plaque development. This may lead to an acceleration of the overall pathology and clinical outcome. We also demonstrated that β-amyloidosis appears in neuroanatomically connected brain regions in $A\beta_{osa}$-inoculated $APP_{swe}/PS1_{dE9}$ mice. Inoculation into the dentate gyrus increases Aβ deposits in the entorhinal cortex and the subiculum, which are interconnected regions. Interestingly, the increase of amyloid load in the entorhinal cortex was more associated to an increase of Aβ fibrils than Aβ dense-core plaques. In the absence of β-amyloidosis changes in the inoculum site, we did not observe changes in other brain areas. Taken together, these findings further support the hypothesis that Aβ aggregates spread to neighboring and interconnected brain areas that have been described in the literature (Eisele, 2013; Eisele et al., 2009; Ye et al., 2015), although we assume that only the endogenous Aβ and not Aβ seed inoculum was responsible for the spreading.

In our study, the modulation of Aβ pathology by Aβ seeds did not only affect amyloid load but also modulated oligomerization pattern and APP processing. We hypothesize that the β-amyloidosis outcome changes are due to local changes of Aβ compositions that may favor the fast development of amyloid plaques in $A\beta_{osa}$-inoculated $APP_{swe}/PS1_{dE9}$ mice at 4mpi. An increase of prefibrillar and fibrillar oligomers and CTFs fragments was shown in these mice compared to PBS-inoculated animals. Our

results highlight that a single inoculation of $A\beta_{osa}$ is able to regulate the endogenous Aβ oligomer secretion s and APP processing, which facilitates the occurrence of Aβ pathology four months post-inoculation. These results are consistent with several studies showing the properties of $A\beta_{osa}$ in inducing high levels of Aβ oligomers compared to $A\beta_{wt}$ responsible for the disease in AD patients and APP_{osa} transgenic mice (Tomiyama et al., 2008). Thus, we can postulate that $A\beta_{osa}$ transfers its properties to the endogenous Aβ. However, this is not true for $A\beta_{ice}$. While co-incubation of $A\beta_{ice}$ and $A\beta_{wt}$ was reported to reduce Aβ pathology *in vitro* (Lin et al., 2017; Nguyen et al., 2016; Zheng et al., 2015), we did not observe any change in the mice. Thus, in this case, there is a likely dissociation between the peptide itself and the mutation that will be further discussed in **Section 7.**

3. Modulation of Tau pathology by Aβ seeds

AD-associated neuropathological lesions gathers amyloid plaques and misfolded Tau-containing NFTs. Tau was the first lesion described to propagate in a prion-like manner. It induces neurodegeneration and synaptic loss that highly correlate with cognitive alterations in AD patients (Arnsten et al., 2021; Clavaguera et al., 2009; Duyckaerts et al., 2009; Goedert et al., 2014). Even if Aβ was widely suggested to govern Tau pathology, accumulation of Tau is likely to exert the main pathological functions in AD dementia (Hardy and Higgins, 1992; Karran et al., 2011; Ricciarelli and Fedele, 2017b). In our study, we showed that Tau pathology occurs in the form of neuritic plaques and neither NTs nor NFTs were described in our mouse model, even after the inoculation of Aβ seeds. As our mouse model is not transgenic for human Tau, the unique Tau pathology is related to the endogenously expressed murine Tau protein isoform (0N4R) that is thought not to aggregate unlike the human Tau. Thus, we assessed the impact of the different Aβ seeds in the recruitment of Tau within neuritic plaques, which has been described to form a corona in the immediate vicinity of amyloid plaques (**Section 1.5**). The co-occurrence of Tau pathology was recently reported by our group, in $APP_{swe}/PS1_{dE9}$ following the inoculation of Aβ and Tau positive AD brain extracts. Our group showed that the severity of Tau pathology in the inoculated mice is strongly associated with long-term cognitive alterations and synaptic impairment (Lam et al., 2022). Interestingly, when using the same mouse model but with recombinant Aβ inoculum (*e.g.* $A\beta_{wt}$, $A\beta_{osa}$ or $A\beta_{ice}$), we obtained various effects on Tau pathology and associated clinical outcomes depending on the Aβ seeds supporting that Aβ may or may not govern the development of Tau-associated lesions. Tau pathology remains unchanged after the inoculation of $A\beta_{wt}$ and $A\beta_{osa}$ while focal seeding of $A\beta_{ice}$ induced a reduction of neuritic plaques at the inoculum site. Interestingly, we found opposite pathways of deleterious $A\beta_{osa}$ and protective $A\beta_{ice}$: $A\beta_{osa}$ did not modulate Tau and induced cognitive alterations and synaptic damages while $A\beta_{ice}$ significantly reduced Tau and rescued cognitive alterations by protecting against synapse damages. Our study does not allow

yet to decipher the underlying mechanisms involved in the recruitment of Tau within the neuritic plaques but we can argue that this mechanism is highly dependent of the Aβ seed properties.

4. Modulation of cognition and synapses by Aβ seeds

Synaptic damages are associated with cognitive impairments in AD patients and transgenic mouse models (Jacobsen et al., 2006; Selkoe, 2002). In our study, behavioral evaluation and assessment of synaptic density were carried out on inoculated mice at 4 months post-inoculation. We found that reduction of synaptic density occurred in mice that exhibit recognition memory dysfunctions. Conversely, mice showing increased synaptic density did not present memory dysfunctions. In the absence of inoculum and at 6 months, our mice did not develop synaptic alterations but can present subtle cognitive impairments depending on the memory task. Thus, Aβ seeds strongly contribute to the pathological polymorphism observed in inoculated mice. In line with this hypothesis, mounting evidences postulate that soluble Aβ links the synaptic failure to memory dysfunction (Ma and Klann, 2012). Our study highlights that the primary sequence of Aβ can be a predictor of synaptic changes. We showed that the exogenous application of Aβ seeds on cultured cortical neurons and acute mouse hippocampal slices leads to different impacts of Aβ seeds on spine morphology and synaptic transmission. While $A\beta_{wt}$ and $A\beta_{osa}$ induce reduction on spine density, in particular mature spines, with different levels of toxicity, $A\beta_{ice}$ rescues from the synaptotoxicity exerted by overproduced Aβ, preserves synaptic transmission and do not affect LTP. Interestingly, we showed that the properties of Aβ seeds were conserved after inoculation in mice. Taken together, we demonstrated that a single inoculation of Aβ seed is sufficient to either accelerate or reverse the synaptotoxicity of endogenous Aβ, which was associated with modulation of memory performances. Our data strongly support that the regulation of synapses by toxic Aβ triggers a vicious circle leading to the propagation of synaptic alterations that promote cognitive disturbances. A contrario, protective Aβ may create a microenvironment that counteracts the deleterious effect of endogenous Aβ. Mechanisms associated with the propagation of the synaptic effects are still unclear and will need to be elucidated in further studies.

5. Modulation of brain function by Aβ seeds

The interplay between Aβ and synapses, which had been hinted by others, led us to wonder whether the presence or absence of neuronal network modulation is a consequence of the synaptoprotection/synaptotoxicity induced by Aβ seeds. Inoculation of $A\beta_{osa}$ was found to affect both local hippocampus connectivity and global connections within networks contributing to the assumption of an AD-like disconnection syndrome in the inoculated mice. This disconnection occurs in

some brain regions and hubs that are particularly vulnerable because of the accumulation of Aβ deposits such as the hippocampus and the entorhinal cortex. It is now well established that Aβ toxicity arises from pathological amounts of Aβ. Notably, we showed that modulation of hippocampus connectivity and network organization are abolished when $APP_{swe}/PS1_{dE9}$ are inoculated with Aβ seeds that did not induce Aβ build-up four months post-inoculation, confirming that Aβ build-up is required for brain disconnections. Thus, we demonstrated here a potential link between seed-specific Aβ build-up and network dysfunctions. However, it is unclear whether the accumulation of Aβ occurs prior to network dysfunctions or if network dysfunctions favor the accumulation and the spreading of Aβ. In human, the distribution of PiB-amyloid uptake was shown to recapitulate the spatial pattern of hubs with more topographic fidelity in some networks such as the DMN. High degree of neuronal activity in these brain areas was postulated to favor the production of Aβ. In our study, Aβ build-up was restricted to hippocampal area and interconnected regions at 4 months whereas functional impairment was found in other brain areas such as the cingulate cortex. Further longitudinal studies of $Aβ_{osa}$-inoculated $APP_{swe}/PS1_{dE9}$ will allow investigating whether the propagation of Aβ pathology occurs following functional networks alteration and will allow to define network fingerprints of $Aβ_{osa}$.

As no difference in brain connectivity was found between $Aβ_{wt}$-, $Aβ_{ice}$- and PBS-inoculated $APP_{swe}/PS1_{dE9}$, our study further suggests that Aβ sequence is important in inducing deleterious effects. Further investigations will be interesting to clearly identify why Aβ seeds target specific neuronal networks.

6. Acute neurotoxicity of Aβ seeds and their preparations

As it was demonstrated that synthetic or recombinant Aβ are less bioactive and proteinase K-resistant than brain-derived Aβ seeds (Langer et al., 2011), we inoculated high amounts of Aβ peptide (~1µg) to avoid an important loss of material once into the brain. This concentration range was defined according to the literature, where high concentrations were shown to be highly toxic and low concentrations do not show any effects (Meyer-Luehmann et al., 2006). However, even with moderate concentrations, inoculation of highly purified proteins is more neurotoxic than brain-derived Aβ seeds. We observed 20% of mortality in our mice following the inoculation of Aβ seeds. One way to preserve Aβ, without increasing the amount of inoculated peptide, is to encapsulate the peptide into small extracellular vesicles such as the exosome to avoid excessive degradation in the brain. As exogenous application of Aβ-containing exosomes from AD patients was shown to contribute to the propagation of the pathology in neurons (Sardar Sinha et al., 2018), they can be a good candidate to propagate Aβ seeds-associated pathology.

When comparing different Aβ seeds, the peptide preparation method is vital to the biological relevance of the study. We prepared well-characterized recombinant Aβ that reproduce different Aβ aggregation states *in vitro* (from oligomers to protofibrils) and exert distinct degree of synaptotoxicity. *In vivo*, in our study, $A\beta_{wt}$ showed a moderate impact on the development of AD pathology. This result seems inconsistent with the widely reported toxicity and seeding activity of synthetic or recombinant misfolded $A\beta_{1-42}$ in mouse models. Our first hypothesis to explain this discrepancy was based on the preparation of $A\beta_{wt}$. We showed both the presence of oligomers and protofibrils in our solution of $A\beta_{wt}$ whereas $A\beta_{osa}$ solutions did not have protofibrils and showed more globular structures. Thus, $A\beta_{wt}$ solution may not contain enough toxic materials to exert its pathogenicity. Another hypothesis is that the incubation period (4 months) was not sufficient for Aβ misfolding replication.

7. Link with human pathology

In our study, we assumed that inoculation of Aβ seeds cannot reproduce all the pathological features present in FAD patients due to the important lag between APP genetic mutations occurring in a biological microenvironment and a single mutated Aβ in solution. For example, in humans, the Osaka mutation prevents the formation of amyloid plaques and favors the development of Tau pathology (Shimada et al., 2020; Tomiyama et al., 2008). In our study, we found the opposite since $A\beta_{osa}$ increases Aβ deposits without affecting Tau pathology. Similarly, in humans, the Icelandic mutation significantly decreases the amyloid pathology while, in our hands, $A\beta_{ice}$ inoculation had no effect on mouse brain amyloidoisis. Taken together, our study suggests that Aβ triggers different pathways when it is intracellularly secreted and when it is used as an exogenous seed. A critical question arising from this study is to know whether highly purified brain-derived Aβ seeds would exhibit features similar to synthetic Aβ or to APP mutations.

8. Could we use Aβ as a therapy against AD?

Our study provides some insights into the conservation of Aβ protective effects following its inoculation in transgenic mice. We identified that reduction of disease progression by $A\beta_{ice}$ is associated with its impact on synapses and Tau. Although this appears to be a unique opportunity to counteract AD-pathology, the underlying mechanism is unknown. Further investigations must aim to decipher these mechanisms.

REFERENCES

2020 Alzheimer's disease facts and figures. Alzheimers Dement 2020;16:391–460. https://doi.org/10.1002/alz.12068.

Abraham A, Pedregosa F, Eickenberg M, Gervais P, Mueller A, Kossaifi J, et al. Machine learning for neuroimaging with scikit-learn. Front Neuroinformatics 2014;8.

Adhikari MH, Belloy ME, Linden AV der, Keliris GA, Verhoye M. Resting-State Co-activation Patterns as Promising Candidates for Prediction of Alzheimer's Disease in Aged Mice. Front Neural Circuits 2020;14. https://doi.org/10.3389/fncir.2020.612529.

Afifi AK. The basal ganglia: A neural network with more than motor function. Semin Pediatr Neurol 2003;10:3–10. https://doi.org/10.1016/S1071-9091(02)00003-7.

Agosta F, Pievani M, Geroldi C, Copetti M, Frisoni GB, Filippi M. Resting state fMRI in Alzheimer's disease: beyond the default mode network. Neurobiol Aging 2012;33:1564–78. https://doi.org/10.1016/j.neurobiolaging.2011.06.007.

Aguzzi A, Heikenwalder M, Polymenidou M. Insights into prion strains and neurotoxicity. Nat Rev Mol Cell Biol 2007;8:552–61. https://doi.org/10.1038/nrm2204.

Albers MW, Gilmore GC, Kaye J, Murphy C, Wingfield A, Bennett DA, et al. At the interface of sensory and motor dysfunctions and Alzheimer's Disease. Alzheimers Dement J Alzheimers Assoc 2015;11:70–98. https://doi.org/10.1016/j.jalz.2014.04.514.

Alexander AL, Hurley SA, Samsonov AA, Adluru N, Hosseinbor AP, Mossahebi P, et al. Characterization of cerebral white matter properties using quantitative magnetic resonance imaging stains. Brain Connect 2011;1:423–46. https://doi.org/10.1089/brain.2011.0071.

Alexander AL, Lee JE, Lazar M, Field AS. Diffusion tensor imaging of the brain. Neurother J Am Soc Exp Neurother 2007;4:316–29. https://doi.org/10.1016/j.nurt.2007.05.011.

Alves GS, Oertel Knöchel V, Knöchel C, Carvalho AF, Pantel J, Engelhardt E, et al. Integrating Retrogenesis Theory to Alzheimer's Disease Pathology: Insight from DTI-TBSS Investigation of the White Matter Microstructural Integrity. BioMed Res Int 2015;2015:e291658. https://doi.org/10.1155/2015/291658.

Alzheimer A, Stelzmann RA, Schnitzlein HN, Murtagh FR. An English translation of Alzheimer's 1907 paper, "Uber eine eigenartige Erkankung der Hirnrinde." Clin Anat N Y N 1995;8:429–31. https://doi.org/10.1002/ca.980080612.

Andreasen N, Hesse C, Davidsson P, Minthon L, Wallin A, Winblad B, et al. Cerebrospinal Fluid β-Amyloid(1-42) in Alzheimer Disease: Differences Between Early- and Late-Onset Alzheimer Disease and Stability During the Course of Disease. Arch Neurol 1999;56:673–80. https://doi.org/10.1001/archneur.56.6.673.

Andrews-Hanna JR, Snyder AZ, Vincent JL, Lustig C, Head D, Raichle ME, et al. Disruption of large-scale brain systems in advanced aging. Neuron 2007;56:924–35. https://doi.org/10.1016/j.neuron.2007.10.038.

Armstrong RA, Nochlin D, Bird TD. Neuropathological heterogeneity in Alzheimer's disease: a study of 80 cases using principal components analysis. Neuropathol Off J Jpn Soc Neuropathol 2000;20:31–7. https://doi.org/10.1046/j.1440-1789.2000.00284.x.

Arnsten AFT, Datta D, Del Tredici K, Braak H. Hypothesis: Tau pathology is an initiating factor in sporadic Alzheimer's disease. Alzheimers Dement 2021;17:115–24. https://doi.org/10.1002/alz.12192.

Arnsten AFT, Datta D, Leslie S, Yang S-T, Wang M, Nairn AC. Alzheimer's-like pathology in aging rhesus macaques: Unique opportunity to study the etiology and treatment of Alzheimer's disease. Proc Natl Acad Sci 2019;116:26230–8. https://doi.org/10.1073/pnas.1903671116.

Asai H, Ikezu S, Tsunoda S, Medalla M, Luebke J, Haydar T, et al. Depletion of microglia and inhibition of exosome synthesis halt tau propagation. Nat Neurosci 2015;18:1584–93. https://doi.org/10.1038/nn.4132.

Ashe KH. The biogenesis and biology of amyloid β oligomers in the brain. Alzheimers Dement 2020;16:1561–7. https://doi.org/10.1002/alz.12084.

Attems J, Jellinger KA. The overlap between vascular disease and Alzheimer's disease--lessons from pathology. BMC Med 2014;12:206. https://doi.org/10.1186/s12916-014-0206-2.

Axelman K, Basun H, Winblad B, Lannfelt L. A large Swedish family with Alzheimer's disease with a codon 670/671 amyloid precursor protein mutation. A clinical and genealogical investigation. Arch Neurol 1994;51:1193–7. https://doi.org/10.1001/archneur.1994.00540240037013.

Bai F, Watson DR, Shi Y, Wang Y, Yue C, YuhuanTeng null, et al. Specifically progressive deficits of brain functional marker in amnestic type mild cognitive impairment. PloS One 2011;6:e24271. https://doi.org/10.1371/journal.pone.0024271.

Balducci C, Beeg M, Stravalaci M, Bastone A, Sclip A, Biasini E, et al. Synthetic amyloid-beta oligomers impair long-term memory independently of cellular prion protein. Proc Natl Acad Sci U S A 2010;107:2295–300. https://doi.org/10.1073/pnas.0911829107.

Bales KR, Verina T, Dodel RC, Du Y, Altstiel L, Bender M, et al. Lack of apolipoprotein E dramatically reduces amyloid beta-peptide deposition. Nat Genet 1997;17:263–4. https://doi.org/10.1038/ng1197-263.

Bardai FH, Wang L, Mutreja Y, Yenjerla M, Gamblin TC, Feany MB. A Conserved Cytoskeletal Signaling Cascade Mediates Neurotoxicity of FTDP-17 Tau Mutations In Vivo. J Neurosci Off J Soc Neurosci 2018;38:108–19. https://doi.org/10.1523/JNEUROSCI.1550-17.2017.

Barth M, Poser BA. Advances in High-Field BOLD fMRI. Materials 2011;4:1941–55. https://doi.org/10.3390/ma4111941.

Bartus RT, Dean RL, Beer B, Lippa AS. The cholinergic hypothesis of geriatric memory dysfunction. Science 1982;217:408–14. https://doi.org/10.1126/science.7046051.

Bayer TA, Wirths O. Intracellular Accumulation of Amyloid-Beta – A Predictor for Synaptic Dysfunction and Neuron Loss in Alzheimer's Disease. Front Aging Neurosci 2010;2:8. https://doi.org/10.3389/fnagi.2010.00008.

Beckmann CF, DeLuca M, Devlin JT, Smith SM. Investigations into resting-state connectivity using independent component analysis. Philos Trans R Soc Lond B Biol Sci 2005;360:1001–13. https://doi.org/10.1098/rstb.2005.1634.

Behzadi Y, Restom K, Liau J, Liu TT. A component based noise correction method (CompCor) for BOLD and perfusion based fMRI. NeuroImage 2007;37:90–101. https://doi.org/10.1016/j.neuroimage.2007.04.042.

Bell RD, Winkler EA, Singh I, Sagare AP, Deane R, Wu Z, et al. Apolipoprotein E controls cerebrovascular integrity via cyclophilin A. Nature 2012;485:512–6. https://doi.org/10.1038/nature11087.

Benilova I, Gallardo R, Ungureanu A-A, Castillo Cano V, Snellinx A, Ramakers M, et al. The Alzheimer disease protective mutation A2T modulates kinetic and thermodynamic properties of amyloid-β (Aβ) aggregation. J Biol Chem 2014;289:30977–89. https://doi.org/10.1074/jbc.M114.599027.

Berchtold NC, Cotman CW. Evolution in the Conceptualization of Dementia and Alzheimer's Disease: Greco-Roman Period to the 1960s. Neurobiol Aging 1998;19:173–89. https://doi.org/10.1016/S0197-4580(98)00052-9.

Bero AW, Yan P, Roh JH, Cirrito JR, Stewart FR, Raichle ME, et al. Neuronal activity regulates the regional vulnerability to amyloid-β deposition. Nat Neurosci 2011;14:750–6. https://doi.org/10.1038/nn.2801.

Bi C, Bi S, Li B. Processing of Mutant β-Amyloid Precursor Protein and the Clinicopathological Features of Familial Alzheimer's Disease. Aging Dis 2019;10:383–403. https://doi.org/10.14336/AD.2018.0425.

Biffi A. Main features of hereditary cerebral amyloid angiopathies: A systematic review. Cereb Circ - Cogn Behav 2022;3:100124. https://doi.org/10.1016/j.cccb.2022.100124.

Billings LM, Green KN, McGaugh JL, LaFerla FM. Learning Decreases Aβ*56 and Tau Pathology and Ameliorates Behavioral Decline in 3xTg-AD Mice. J Neurosci 2007;27:751–61. https://doi.org/10.1523/JNEUROSCI.4800-06.2007.

Binder LI, Guillozet-Bongaarts AL, Garcia-Sierra F, Berry RW. Tau, tangles, and Alzheimer's disease. Biochim Biophys Acta 2005;1739:216–23. https://doi.org/10.1016/j.bbadis.2004.08.014.

Binnewijzend MAA, Schoonheim MM, Sanz-Arigita E, Wink AM, van der Flier WM, Tolboom N, et al. Resting-state fMRI changes in Alzheimer's disease and mild cognitive impairment. Neurobiol Aging 2012;33:2018–28. https://doi.org/10.1016/j.neurobiolaging.2011.07.003.

Biswal B, Yetkin FZ, Haughton VM, Hyde JS. Functional connectivity in the motor cortex of resting human brain using echo-planar MRI. Magn Reson Med 1995;34:537–41. https://doi.org/10.1002/mrm.1910340409.

Biswal BB, Van Kylen J, Hyde JS. Simultaneous assessment of flow and BOLD signals in resting-state functional connectivity maps. NMR Biomed 1997;10:165–70. https://doi.org/10.1002/(sici)1099-1492(199706/08)10:4/5<165::aid-nbm454>3.0.co;2-7.

Blennow K, Hampel H, Weiner M, Zetterberg H. Cerebrospinal fluid and plasma biomarkers in Alzheimer disease. Nat Rev Neurol 2010;6:131–44. https://doi.org/10.1038/nrneurol.2010.4.

Bohrmann B, Baumann K, Benz J, Gerber F, Huber W, Knoflach F, et al. Gantenerumab: a novel human anti-Aβ antibody demonstrates sustained cerebral amyloid-β binding and elicits cell-mediated removal of human amyloid-β. J Alzheimers Dis JAD 2012;28:49–69. https://doi.org/10.3233/JAD-2011-110977.

Boumenir A, Cognat E, Sabia S, Hourregue C, Lilamand M, Dugravot A, et al. CSF level of β-amyloid peptide predicts mortality in Alzheimer's disease. Alzheimers Res Ther 2019;11:29. https://doi.org/10.1186/s13195-019-0481-4.

Braak H, Alafuzoff I, Arzberger T, Kretzschmar H, Del Tredici K. Staging of Alzheimer disease-associated neurofibrillary pathology using paraffin sections and immunocytochemistry. Acta Neuropathol (Berl) 2006;112:389–404. https://doi.org/10.1007/s00401-006-0127-z.

Braak H, Braak E. Neuropathological stageing of Alzheimer-related changes. Acta Neuropathol (Berl) 1991;82:239–59. https://doi.org/10.1007/BF00308809.

Braak H, Del Tredici K. Are cases with tau pathology occurring in the absence of Aβ deposits part of the AD-related pathological process? Acta Neuropathol (Berl) 2014;128:767–72. https://doi.org/10.1007/s00401-014-1356-1.

Brier MR, Thomas JB, Snyder AZ, Benzinger TL, Zhang D, Raichle ME, et al. Loss of intranetwork and internetwork resting state functional connections with Alzheimer's disease progression. J Neurosci Off J Soc Neurosci 2012;32:8890–9. https://doi.org/10.1523/JNEUROSCI.5698-11.2012.

Brion J-P. Immunological demonstration of tau protein in neurofibrillary tangles of Alzheimer's disease. J Alzheimers Dis JAD 2006;9:177–85. https://doi.org/10.3233/jad-2006-9s321.

Brion JP, Couck AM, Passareiro E, Flament-Durand J. Neurofibrillary tangles of Alzheimer's disease: an immunohistochemical study. J Submicrosc Cytol 1985;17:89–96.

Buckner RL, DiNicola LM. The brain's default network: updated anatomy, physiology and evolving insights. Nat Rev Neurosci 2019;20:593–608. https://doi.org/10.1038/s41583-019-0212-7.

Buckner RL, Krienen FM. The evolution of distributed association networks in the human brain. Trends Cogn Sci 2013;17:648–65. https://doi.org/10.1016/j.tics.2013.09.017.

Buckner RL, Sepulcre J, Talukdar T, Krienen FM, Liu H, Hedden T, et al. Cortical Hubs Revealed by Intrinsic Functional Connectivity: Mapping, Assessment of Stability, and Relation to Alzheimer's Disease. J Neurosci 2009;29:1860–73. https://doi.org/10.1523/JNEUROSCI.5062-08.2009.

Buckner RL, Vincent JL. Unrest at rest: Default activity and spontaneous network correlations. NeuroImage 2007;37:1091–6. https://doi.org/10.1016/j.neuroimage.2007.01.010.

Buerger K, Ewers M, Pirttilä T, Zinkowski R, Alafuzoff I, Teipel SJ, et al. CSF phosphorylated tau protein correlates with neocortical neurofibrillary pathology in Alzheimer's disease. Brain J Neurol 2006;129:3035–41. https://doi.org/10.1093/brain/awl269.

Busche MA, Eichhoff G, Adelsberger H, Abramowski D, Wiederhold K-H, Haass C, et al. Clusters of hyperactive neurons near amyloid plaques in a mouse model of Alzheimer's disease. Science 2008;321:1686–9. https://doi.org/10.1126/science.1162844.

Bussy A, Snider BJ, Coble D, Xiong C, Fagan AM, Cruchaga C, et al. Effect of apolipoprotein E4 on clinical, neuroimaging, and biomarker measures in noncarrier participants in the Dominantly Inherited Alzheimer Network. Neurobiol Aging 2019;75:42–50. https://doi.org/10.1016/j.neurobiolaging.2018.10.011.

Butters MA, Lopez OL, Becker JT. Focal temporal lobe dysfunction in probable Alzheimer's disease predicts a slow rate of cognitive decline. Neurology 1996;46:687–92. https://doi.org/10.1212/wnl.46.3.687.

Cabrales Fontela Y, Kadavath H, Biernat J, Riedel D, Mandelkow E, Zweckstetter M. Multivalent cross-linking of actin filaments and microtubules through the microtubule-associated protein Tau. Nat Commun 2017;8:1981. https://doi.org/10.1038/s41467-017-02230-8.

Cai K, Haris M, Singh A, Kogan F, Greenberg JH, Hariharan H, et al. Magnetic resonance imaging of glutamate. Nat Med 2012;18:302–6. https://doi.org/10.1038/nm.2615.

Calhoun VD, Adali T, Pearlson GD, Pekar JJ. A method for making group inferences from functional MRI data using independent component analysis. Hum Brain Mapp 2001;14:140–51. https://doi.org/10.1002/hbm.1048.

Carbone I, Lazzarotto T, Ianni M, Porcellini E, Forti P, Masliah E, et al. Herpes virus in Alzheimer's disease: relation to progression of the disease. Neurobiol Aging 2014;35:122–9. https://doi.org/10.1016/j.neurobiolaging.2013.06.024.

Castano EM, Prelli F, Wisniewski T, Golabek A, Kumar RA, Soto C, et al. Fibrillogenesis in Alzheimer's disease of amyloid beta peptides and apolipoprotein E. Biochem J 1995;306 (Pt 2):599–604. https://doi.org/10.1042/bj3060599.

Catania M, Colombo L, Sorrentino S, Cagnotto A, Lucchetti J, Barbagallo MC, et al. A novel bio-inspired strategy to prevent amyloidogenesis and synaptic damage in Alzheimer's disease. Mol Psychiatry 2022:1–8. https://doi.org/10.1038/s41380-022-01745-x.

Celestine M, Nadkarni NA, Garin CM, Bougacha S, Dhenain M. Sammba-MRI: A Library for Processing SmAll-MaMmal BrAin MRI Data in Python. Front Neuroinformatics 2020;14:24. https://doi.org/10.3389/fninf.2020.00024.

Chen G, Xu T, Yan Y, Zhou Y, Jiang Y, Melcher K, et al. Amyloid beta: structure, biology and structure-based therapeutic development. Acta Pharmacol Sin 2017;38:1205–35. https://doi.org/10.1038/aps.2017.28.

Cheng IH, Scearce-Levie K, Legleiter J, Palop JJ, Gerstein H, Bien-Ly N, et al. Accelerating amyloid-beta fibrillization reduces oligomer levels and functional deficits in Alzheimer disease mouse models. J Biol Chem 2007;282:23818–28. https://doi.org/10.1074/jbc.M701078200.

Chong S-H, Yim J, Ham S. Structural heterogeneity in familial Alzheimer's disease mutants of amyloid-beta peptides. Mol Biosyst 2013;9:997–1003. https://doi.org/10.1039/c2mb25457c.

Clavaguera F, Bolmont T, Crowther RA, Abramowski D, Frank S, Probst A, et al. Transmission and spreading of tauopathy in transgenic mouse brain. Nat Cell Biol 2009;11:909–13. https://doi.org/10.1038/ncb1901.

Clayton K, Delpech JC, Herron S, Iwahara N, Ericsson M, Saito T, et al. Plaque associated microglia hyper-secrete extracellular vesicles and accelerate tau propagation in a humanized APP mouse model. Mol Neurodegener 2021;16:18. https://doi.org/10.1186/s13024-021-00440-9.

Cohen ML, Kim C, Haldiman T, ElHag M, Mehndiratta P, Pichet T, et al. Rapidly progressive Alzheimer's disease features distinct structures of amyloid-β. Brain J Neurol 2015;138:1009–22. https://doi.org/10.1093/brain/awv006.

Cohen SIA, Linse S, Luheshi LM, Hellstrand E, White DA, Rajah L, et al. Proliferation of amyloid-β42 aggregates occurs through a secondary nucleation mechanism. Proc Natl Acad Sci U S A 2013;110:9758–63. https://doi.org/10.1073/pnas.1218402110.

Colby DW, Prusiner SB. Prions. Cold Spring Harb Perspect Biol 2011;3:a006833. https://doi.org/10.1101/cshperspect.a006833.

Coletta L. Network structure of the mouse brain connectome with voxel resolution | Science Advances 2020. https://www.science.org/doi/10.1126/sciadv.abb7187 (accessed January 27, 2023).

Collinge J. Molecular neurology of prion disease. J Neurol Neurosurg Psychiatry 2005;76:906–19. https://doi.org/10.1136/jnnp.2004.048660.

Collinge J, Clarke AR. A general model of prion strains and their pathogenicity. Science 2007;318:930–6. https://doi.org/10.1126/science.1138718.

Colombo L, Gamba A, Cantù L, Salmona M, Tagliavini F, Rondelli V, et al. Pathogenic Aβ A2V versus protective Aβ A2T mutation: Early stage aggregation and membrane interaction. Biophys Chem 2017;229:11–8. https://doi.org/10.1016/j.bpc.2017.05.001.

Condello C, Lemmin T, Stöhr J, Nick M, Wu Y, Maxwell AM, et al. Structural heterogeneity and intersubject variability of Aβ in familial and sporadic Alzheimer's disease. Proc Natl Acad Sci U S A 2018;115:E782–91. https://doi.org/10.1073/pnas.1714966115.

Condello C, Yuan P, Schain A, Grutzendler J. Microglia constitute a barrier that prevents neurotoxic protofibrillar Aβ42 hotspots around plaques. Nat Commun 2015;6:6176. https://doi.org/10.1038/ncomms7176.

Connolly J, McNulty JP, Boran L, Roche RAP, Delany D, Bokde ALW. Identification of Resting State Networks Involved in Executive Function. Brain Connect 2016;6:365–74. https://doi.org/10.1089/brain.2015.0399.

Copanaki E, Chang S, Vlachos A, Tschäpe J-A, Müller UC, Kögel D, et al. sAPPalpha antagonizes dendritic degeneration and neuron death triggered by proteasomal stress. Mol Cell Neurosci 2010;44:386–93. https://doi.org/10.1016/j.mcn.2010.04.007.

Corder EH, Saunders AM, Risch NJ, Strittmatter WJ, Schmechel DE, Gaskell PC, et al. Protective effect of apolipoprotein E type 2 allele for late onset Alzheimer disease. Nat Genet 1994;7:180–4. https://doi.org/10.1038/ng0694-180.

Cordes D, Haughton VM, Arfanakis K, Carew JD, Turski PA, Moritz CH, et al. Frequencies contributing to functional connectivity in the cerebral cortex in "resting-state" data. AJNR Am J Neuroradiol 2001;22:1326–33.

Cox RW. AFNI: software for analysis and visualization of functional magnetic resonance neuroimages. Comput Biomed Res Int J 1996;29:162–73. https://doi.org/10.1006/cbmr.1996.0014.

Crescenzi R, DeBrosse C, Nanga RPR, Byrne MD, Krishnamoorthy G, D'Aquilla K, et al. Longitudinal imaging reveals subhippocampal dynamics in glutamate levels associated with histopathologic events in a mouse model of tauopathy and healthy mice. Hippocampus 2017;27:285–302. https://doi.org/10.1002/hipo.22693.

Dai M-H, Zheng H, Zeng L-D, Zhang Y. The genes associated with early-onset Alzheimer's disease. Oncotarget 2018;9:15132–43. https://doi.org/10.18632/oncotarget.23738.

Damoiseaux JS. Resting-state fMRI as a biomarker for Alzheimer's disease? Alzheimers Res Ther 2012;4:8. https://doi.org/10.1186/alzrt106.

Damoiseaux JS, Prater KE, Miller BL, Greicius MD. Functional connectivity tracks clinical deterioration in Alzheimer's disease. Neurobiol Aging 2012;33:828.e19-30. https://doi.org/10.1016/j.neurobiolaging.2011.06.024.

Damoiseaux JS, Rombouts S a. RB, Barkhof F, Scheltens P, Stam CJ, Smith SM, et al. Consistent resting-state networks across healthy subjects. Proc Natl Acad Sci U S A 2006;103:13848–53. https://doi.org/10.1073/pnas.0601417103.

Das P, Chacko AR, Belfort G. Alzheimer's Protective Cross-Interaction between Wild-Type and A2T Variants Alters Aβ42 Dimer Structure. ACS Chem Neurosci 2017;8:606–18. https://doi.org/10.1021/acschemneuro.6b00357.

Das P, Murray B, Belfort G. Alzheimer's protective A2T mutation changes the conformational landscape of the $A\beta_{1-42}$ monomer differently than does the A2V mutation. Biophys J 2015;108:738–47. https://doi.org/10.1016/j.bpj.2014.12.013.

Davies CA, Mann DM, Sumpter PQ, Yates PO. A quantitative morphometric analysis of the neuronal and synaptic content of the frontal and temporal cortex in patients with Alzheimer's disease. J Neurol Sci 1987;78:151–64. https://doi.org/10.1016/0022-510x(87)90057-8.

Davies P, Maloney AJ. Selective loss of central cholinergic neurons in Alzheimer's disease. Lancet Lond Engl 1976;2:1403. https://doi.org/10.1016/s0140-6736(76)91936-x.

De Rossi P, Harde E, Dupuis JP, Martin L, Chounlamountri N, Bardin M, et al. A critical role for VEGF and VEGFR2 in NMDA receptor synaptic function and fear-related behavior. Mol Psychiatry 2016;21:1768–80. https://doi.org/10.1038/mp.2015.195.

De Strooper B, Karran E. The Cellular Phase of Alzheimer's Disease. Cell 2016;164:603–15. https://doi.org/10.1016/j.cell.2015.12.056.

Dejanovic B, Huntley MA, De Mazière A, Meilandt WJ, Wu T, Srinivasan K, et al. Changes in the Synaptic Proteome in Tauopathy and Rescue of Tau-Induced Synapse Loss by C1q Antibodies. Neuron 2018;100:1322-1336.e7. https://doi.org/10.1016/j.neuron.2018.10.014.

Dematteos RB, Lu J, Tang Y, Racke MM, Delong CA, Tzaferis JA, et al. A plaque-specific antibody clears existing β-amyloid plaques in Alzheimer's disease mice. Neuron 2012;76:908–20. https://doi.org/10.1016/j.neuron.2012.10.029.

Desrosiers-Gregoire G, Devenyi GA, Grandjean J, Chakravarty MM. Rodent Automated Bold Improvement of EPI Sequences (RABIES): A standardized image processing and data quality platform for rodent fMRI 2022:2022.08.20.504597. https://doi.org/10.1101/2022.08.20.504597.

DeTure MA, Dickson DW. The neuropathological diagnosis of Alzheimer's disease. Mol Neurodegener 2019;14:32. https://doi.org/10.1186/s13024-019-0333-5.

Di Fede G, Catania M, Maderna E, Ghidoni R, Benussi L, Tonoli E, et al. Molecular subtypes of Alzheimer's disease. Sci Rep 2018;8:3269. https://doi.org/10.1038/s41598-018-21641-1.

Di Fede G, Catania M, Maderna E, Morbin M, Moda F, Colombo L, et al. Tackling amyloidogenesis in Alzheimer's disease with A2V variants of Amyloid-β. Sci Rep 2016;6:20949. https://doi.org/10.1038/srep20949.

Di Fede G, Catania M, Morbin M, Giaccone G, Moro ML, Ghidoni R, et al. Good gene, bad gene: new APP variant may be both. Prog Neurobiol 2012;99:281–92. https://doi.org/10.1016/j.pneurobio.2012.06.004.

Di Fede G, Catania M, Morbin M, Rossi G, Suardi S, Mazzoleni G, et al. A recessive mutation in the APP gene with dominant-negative effect on amyloidogenesis. Science 2009;323:1473–7. https://doi.org/10.1126/science.1168979.

Dickerson BC, Salat DH, Greve DN, Chua EF, Rand-Giovannetti E, Rentz DM, et al. Increased hippocampal activation in mild cognitive impairment compared to normal aging and AD. Neurology 2005;65:404–11. https://doi.org/10.1212/01.wnl.0000171450.97464.49.

Dickson TC, Vickers JC. The morphological phenotype of β-amyloid plaques and associated neuritic changes in Alzheimer's disease. Neuroscience 2001;105:99–107. https://doi.org/10.1016/S0306-4522(01)00169-5.

Diociaiuti M, Bonanni R, Cariati I, Frank C, D'Arcangelo G. Amyloid Prefibrillar Oligomers: The Surprising Commonalities in Their Structure and Activity. Int J Mol Sci 2021;22:6435. https://doi.org/10.3390/ijms22126435.

Dorr AE, Lerch JP, Spring S, Kabani N, Henkelman RM. High resolution three-dimensional brain atlas using an average magnetic resonance image of 40 adult C57Bl/6J mice. NeuroImage 2008;42:60–9. https://doi.org/10.1016/j.neuroimage.2008.03.037.

Douaud G, Jbabdi S, Behrens TEJ, Menke RA, Gass A, Monsch AU, et al. DTI measures in crossing-fibre areas: increased diffusion anisotropy reveals early white matter alteration in MCI and mild Alzheimer's disease. NeuroImage 2011;55:880–90. https://doi.org/10.1016/j.neuroimage.2010.12.008.

Dubois B, Villain N, Frisoni GB, Rabinovici GD, Sabbagh M, Cappa S, et al. Clinical diagnosis of Alzheimer's disease: recommendations of the International Working Group. Lancet Neurol 2021;20:484–96. https://doi.org/10.1016/S1474-4422(21)00066-1.

van Duinen SG, Castaño EM, Prelli F, Bots GT, Luyendijk W, Frangione B. Hereditary cerebral hemorrhage with amyloidosis in patients of Dutch origin is related to Alzheimer disease. Proc Natl Acad Sci 1987;84:5991–4. https://doi.org/10.1073/pnas.84.16.5991.

Duyckaerts C, Delatour B, Potier M-C. Classification and basic pathology of Alzheimer disease. Acta Neuropathol (Berl) 2009;118:5–36. https://doi.org/10.1007/s00401-009-0532-1.

Duyckaerts C, Sazdovitch V, Ando K, Seilhean D, Privat N, Yilmaz Z, et al. Neuropathology of iatrogenic Creutzfeldt-Jakob disease and immunoassay of French cadaver-sourced growth hormone batches suggest possible transmission of tauopathy and long incubation periods for the transmission of Abeta pathology. Acta Neuropathol (Berl) 2018;135:201–12. https://doi.org/10.1007/s00401-017-1791-x.

Edwards FA. A Unifying Hypothesis for Alzheimer's Disease: From Plaques to Neurodegeneration. Trends Neurosci 2019;42:310–22. https://doi.org/10.1016/j.tins.2019.03.003.

Eisele YS. From soluble aβ to progressive aβ aggregation: could prion-like templated misfolding play a role? Brain Pathol Zurich Switz 2013;23:333–41. https://doi.org/10.1111/bpa.12049.

Eisele YS, Bolmont T, Heikenwalder M, Langer F, Jacobson LH, Yan Z-X, et al. Induction of cerebral beta-amyloidosis: intracerebral versus systemic Abeta inoculation. Proc Natl Acad Sci U S A 2009;106:12926–31. https://doi.org/10.1073/pnas.0903200106.

Eisele YS, Obermüller U, Heilbronner G, Baumann F, Kaeser SA, Wolburg H, et al. Peripherally applied Abeta-containing inoculates induce cerebral beta-amyloidosis. Science 2010;330:980–2. https://doi.org/10.1126/science.1194516.

Eisenberg D, Jucker M. The Amyloid State of Proteins in Human Diseases. Cell 2012;148:1188–203. https://doi.org/10.1016/j.cell.2012.02.022.

Ella A, Barrière DA, Adriaensen H, Palmer DN, Melzer TR, Mitchell NL, et al. The development of brain magnetic resonance approaches in large animal models for preclinical research. Anim Front Rev Mag Anim Agric 2019;9:44–51. https://doi.org/10.1093/af/vfz024.

Elman JA, Oh H, Madison CM, Baker SL, Vogel JW, Marks SM, et al. Neural compensation in older people with brain amyloid-β deposition. Nat Neurosci 2014;17:1316–8. https://doi.org/10.1038/nn.3806.

Epelbaum S, Youssef I, Lacor PN, Chaurand P, Duplus E, Brugg B, et al. Acute amnestic encephalopathy in amyloid-β oligomer–injected mice is due to their widespread diffusion in vivo. Neurobiol Aging 2015;36:2043–52. https://doi.org/10.1016/j.neurobiolaging.2015.03.005.

Esler WP, Wolfe MS. A portrait of Alzheimer secretases--new features and familiar faces. Science 2001;293:1449–54. https://doi.org/10.1126/science.1064638.

Ezzat K, Pernemalm M, Pålsson S, Roberts TC, Järver P, Dondalska A, et al. The viral protein corona directs viral pathogenesis and amyloid aggregation. Nat Commun 2019;10:2331. https://doi.org/10.1038/s41467-019-10192-2.

Ferreira D, Nordberg A, Westman E. Biological subtypes of Alzheimer disease. Neurology 2020;94:436–48. https://doi.org/10.1212/WNL.0000000000009058.

Ferreira D, Pereira J, Volpe G, Westman E. Subtypes of Alzheimer's Disease Display Distinct Network Abnormalities Extending Beyond Their Pattern of Brain Atrophy. Front Neurol 2019;in–press. https://doi.org/10.3389/fneur.2019.00524.

Ferreira D, Verhagen C, Hernández-Cabrera JA, Cavallin L, Guo C-J, Ekman U, et al. Distinct subtypes of Alzheimer's disease based on patterns of brain atrophy: longitudinal trajectories and clinical applications. Sci Rep 2017;7:46263. https://doi.org/10.1038/srep46263.

Flores R de, Das SR, Xie L, Wisse LEM, Lyu X, Shah P, et al. Medial Temporal Lobe Networks in Alzheimer's Disease: Structural and Molecular Vulnerabilities. J Neurosci 2022;42:2131–41. https://doi.org/10.1523/JNEUROSCI.0949-21.2021.

Fol R, Braudeau J, Ludewig S, Abel T, Weyer SW, Roederer J-P, et al. Viral gene transfer of APPsα rescues synaptic failure in an Alzheimer's disease mouse model. Acta Neuropathol (Berl) 2016;131:247–66. https://doi.org/10.1007/s00401-015-1498-9.

Forest KH, Alfulaij N, Arora K, Taketa R, Sherrin T, Todorovic C, et al. Protection against β-amyloid neurotoxicity by a non-toxic endogenous N-terminal β-amyloid fragment and its active hexapeptide core sequence. J Neurochem 2018;144:201–17. https://doi.org/10.1111/jnc.14257.

Forest KH, Taketa R, Arora K, Todorovic C, Nichols RA. The Neuroprotective Beta Amyloid Hexapeptide Core Reverses Deficits in Synaptic Plasticity in the 5xFAD APP/PS1 Mouse Model. Front Mol Neurosci 2021;14:576038. https://doi.org/10.3389/fnmol.2021.576038.

Fox MD, Raichle ME. Spontaneous fluctuations in brain activity observed with functional magnetic resonance imaging. Nat Rev Neurosci 2007;8:700–11. https://doi.org/10.1038/nrn2201.

Franklin KBJ, Paxinos G. Paxinos and Franklin's the Mouse Brain in Stereotaxic Coordinates, Compact: The Coronal Plates and Diagrams. Academic Press; 2019.

Fransson P. Spontaneous low-frequency BOLD signal fluctuations: an fMRI investigation of the resting-state default mode of brain function hypothesis. Hum Brain Mapp 2005;26:15–29. https://doi.org/10.1002/hbm.20113.

Friston KJ, editor. Statistical parametric mapping: the analysis of funtional brain images. 1st ed. Amsterdam ; Boston: Elsevier/Academic Press; 2007.

Frost GR, Li Y-M. The role of astrocytes in amyloid production and Alzheimer's disease. Open Biol 2017;7:170228. https://doi.org/10.1098/rsob.170228.

Fu L, Sun Y, Guo Y, Chen Y, Yu B, Zhang H, et al. Comparison of neurotoxicity of different aggregated forms of Aβ40, Aβ42 and Aβ43 in cell cultures. J Pept Sci Off Publ Eur Pept Soc 2017;23:245–51. https://doi.org/10.1002/psc.2975.

Fulga TA, Elson-Schwab I, Khurana V, Steinhilb ML, Spires TL, Hyman BT, et al. Abnormal bundling and accumulation of F-actin mediates tau-induced neuronal degeneration in vivo. Nat Cell Biol 2007;9:139–48. https://doi.org/10.1038/ncb1528.

Fuller S, Münch G, Steele M. Activated astrocytes: a therapeutic target in Alzheimer's disease? Expert Rev Neurother 2009;9:1585–94. https://doi.org/10.1586/ern.09.111.

Gajdusek DC, Gibbs CJ, Alpers M. Experimental Transmission of a Kuru-like Syndrome to Chimpanzees. Nature 1966;209:794–6. https://doi.org/10.1038/209794a0.

Garcia-Alloza M, Robbins EM, Zhang-Nunes SX, Purcell SM, Betensky RA, Raju S, et al. Characterization of amyloid deposition in the APPswe/PS1dE9 mouse model of Alzheimer disease. Neurobiol Dis 2006;24:516–24. https://doi.org/10.1016/j.nbd.2006.08.017.

Gary C, Lam S, Hérard A-S, Koch JE, Petit F, Gipchtein P, et al. Encephalopathy induced by Alzheimer brain inoculation in a non-human primate. Acta Neuropathol Commun 2019;7:126. https://doi.org/10.1186/s40478-019-0771-x.

Gitter BD, Cox LM, Rydel RE, May PC. Amyloid beta peptide potentiates cytokine secretion by interleukin-1 beta-activated human astrocytoma cells. Proc Natl Acad Sci U S A 1995;92:10738–41. https://doi.org/10.1073/pnas.92.23.10738.

Glabe CG. Structural Classification of Toxic Amyloid Oligomers*. J Biol Chem 2008;283:29639–43. https://doi.org/10.1074/jbc.R800016200.

Glenner GG, Wong CW. Alzheimer's disease: initial report of the purification and characterization of a novel cerebrovascular amyloid protein. Biochem Biophys Res Commun 1984a;120:885–90. https://doi.org/10.1016/s0006-291x(84)80190-4.

Glenner GG, Wong CW. Alzheimer's disease and Down's syndrome: sharing of a unique cerebrovascular amyloid fibril protein. Biochem Biophys Res Commun 1984b;122:1131–5. https://doi.org/10.1016/0006-291x(84)91209-9.

Goate A, Chartier-Harlin MC, Mullan M, Brown J, Crawford F, Fidani L, et al. Segregation of a missense mutation in the amyloid precursor protein gene with familial Alzheimer's disease. Nature 1991;349:704–6. https://doi.org/10.1038/349704a0.

Goedert M, Falcon B, Clavaguera F, Tolnay M. Prion-like Mechanisms in the Pathogenesis of Tauopathies and Synucleinopathies. Curr Neurol Neurosci Rep 2014;14:495. https://doi.org/10.1007/s11910-014-0495-z.

Goedert M, Jakes R, Vanmechelen E. Monoclonal antibody AT8 recognises tau protein phosphorylated at both serine 202 and threonine 205. Neurosci Lett 1995;189:167–9. https://doi.org/10.1016/0304-3940(95)11484-e.

Golby A, Silverberg G, Race E, Gabrieli S, O'Shea J, Knierim K, et al. Memory encoding in Alzheimer's disease: an fMRI study of explicit and implicit memory. Brain J Neurol 2005;128:773–87. https://doi.org/10.1093/brain/awh400.

Goldgaber D, Harris HW, Hla T, Maciag T, Donnelly RJ, Jacobsen JS, et al. Interleukin 1 regulates synthesis of amyloid beta-protein precursor mRNA in human endothelial cells. Proc Natl Acad Sci U S A 1989;86:7606–10. https://doi.org/10.1073/pnas.86.19.7606.

Gong C-X, Iqbal K. Hyperphosphorylation of microtubule-associated protein tau: a promising therapeutic target for Alzheimer disease. Curr Med Chem 2008;15:2321–8. https://doi.org/10.2174/092986708785909111.

Gore JC. Principles and practice of functional MRI of the human brain. J Clin Invest 2003;112:4–9. https://doi.org/10.1172/JCI200319010.

Gorno-Tempini ML, Brambati SM, Ginex V, Ogar J, Dronkers NF, Marcone A, et al. The logopenic/phonological variant of primary progressive aphasia. Neurology 2008;71:1227–34. https://doi.org/10.1212/01.wnl.0000320506.79811.da.

Gouras GK, Tampellini D, Takahashi RH, Capetillo-Zarate E. Intraneuronal beta-amyloid accumulation and synapse pathology in Alzheimer's disease. Acta Neuropathol (Berl) 2010;119:523–41. https://doi.org/10.1007/s00401-010-0679-9.

Gouras GK, Tsai J, Naslund J, Vincent B, Edgar M, Checler F, et al. Intraneuronal Abeta42 accumulation in human brain. Am J Pathol 2000;156:15–20. https://doi.org/10.1016/s0002-9440(10)64700-1.

Gozzi A, Schwarz AJ. Large-scale functional connectivity networks in the rodent brain. NeuroImage 2016;127:496–509. https://doi.org/10.1016/j.neuroimage.2015.12.017.

Grabowski TJ, Cho HS, Vonsattel JP, Rebeck GW, Greenberg SM. Novel amyloid precursor protein mutation in an Iowa family with dementia and severe cerebral amyloid angiopathy. Ann Neurol 2001;49:697–705. https://doi.org/10.1002/ana.1009.

Grandjean J, Canella C, Anckaerts C, Ayrancı G, Bougacha S, Bienert T, et al. Common functional networks in the mouse brain revealed by multi-centre resting-state fMRI analysis. NeuroImage 2020;205:116278. https://doi.org/10.1016/j.neuroimage.2019.116278.

Grandjean J, Preti MG, Bolton TAW, Buerge M, Seifritz E, Pryce CR, et al. Dynamic reorganization of intrinsic functional networks in the mouse brain. NeuroImage 2017a;152:497–508. https://doi.org/10.1016/j.neuroimage.2017.03.026.

Grandjean J, Schroeter A, He P, Tanadini M, Keist R, Krstic D, et al. Early Alterations in Functional Connectivity and White Matter Structure in a Transgenic Mouse Model of Cerebral Amyloidosis. J Neurosci 2014a;34:13780–9. https://doi.org/10.1523/JNEUROSCI.4762-13.2014.

Grandjean J, Schroeter A, He P, Tanadini M, Keist R, Krstic D, et al. Early alterations in functional connectivity and white matter structure in a transgenic mouse model of cerebral amyloidosis. J Neurosci Off J Soc Neurosci 2014b;34:13780–9. https://doi.org/10.1523/JNEUROSCI.4762-13.2014.

Grandjean J, Zerbi V, Balsters JH, Wenderoth N, Rudin M. Structural Basis of Large-Scale Functional Connectivity in the Mouse. J Neurosci 2017b;37:8092–101. https://doi.org/10.1523/JNEUROSCI.0438-17.2017.

Gratuze M, Chen Y, Parhizkar S, Jain N, Strickland MR, Serrano JR, et al. Activated microglia mitigate Aβ-associated tau seeding and spreading. J Exp Med 2021;218:e20210542. https://doi.org/10.1084/jem.20210542.

Greenberg SM, Bacskai BJ, Hernandez-Guillamon M, Pruzin J, Sperling R, van Veluw SJ. Cerebral amyloid angiopathy and Alzheimer disease — one peptide, two pathways. Nat Rev Neurol 2020;16:30–42. https://doi.org/10.1038/s41582-019-0281-2.

Greicius MD, Krasnow B, Reiss AL, Menon V. Functional connectivity in the resting brain: a network analysis of the default mode hypothesis. Proc Natl Acad Sci U S A 2003;100:253–8. https://doi.org/10.1073/pnas.0135058100.

Greicius MD, Srivastava G, Reiss AL, Menon V. Default-mode network activity distinguishes Alzheimer's disease from healthy aging: evidence from functional MRI. Proc Natl Acad Sci U S A 2004;101:4637–42. https://doi.org/10.1073/pnas.0308627101.

Grundke-Iqbal I, Iqbal K, Tung YC, Quinlan M, Wisniewski HM, Binder LI. Abnormal phosphorylation of the microtubule-associated protein tau (tau) in Alzheimer cytoskeletal pathology. Proc Natl Acad Sci 1986;83:4913–7. https://doi.org/10.1073/pnas.83.13.4913.

Guo T, Noble W, Hanger DP. Roles of tau protein in health and disease. Acta Neuropathol (Berl) 2017;133:665–704. https://doi.org/10.1007/s00401-017-1707-9.

Gusnard DA, Akbudak E, Shulman GL, Raichle ME. Medial prefrontal cortex and self-referential mental activity: relation to a default mode of brain function. Proc Natl Acad Sci U S A 2001;98:4259–64. https://doi.org/10.1073/pnas.071043098.

Gutierrez-Barragan D, Singh NA, Alvino FG, Coletta L, Rocchi F, De Guzman E, et al. Unique spatiotemporal fMRI dynamics in the awake mouse brain. Curr Biol CB 2022;32:631-644.e6. https://doi.org/10.1016/j.cub.2021.12.015.

Guyon A, Rousseau J, Lamothe G, Tremblay JP. The protective mutation A673T in amyloid precursor protein gene decreases Aβ peptides production for 14 forms of Familial Alzheimer's Disease in SH-SY5Y cells. PloS One 2020;15:e0237122. https://doi.org/10.1371/journal.pone.0237122.

Haan J, Lanser JB, Zijderveld I, van der Does IG, Roos RA. Dementia in hereditary cerebral hemorrhage with amyloidosis-Dutch type. Arch Neurol 1990;47:965–7. https://doi.org/10.1001/archneur.1990.00530090035010.

Haass C, Kaether C, Thinakaran G, Sisodia S. Trafficking and proteolytic processing of APP. Cold Spring Harb Perspect Med 2012;2:a006270. https://doi.org/10.1101/cshperspect.a006270.

Haass C, Selkoe DJ. Soluble protein oligomers in neurodegeneration: lessons from the Alzheimer's amyloid beta-peptide. Nat Rev Mol Cell Biol 2007;8:101–12. https://doi.org/10.1038/nrm2101.

Habib N, McCabe C, Medina S, Varshavsky M, Kitsberg D, Dvir-Szternfeld R, et al. Disease-associated astrocytes in Alzheimer's disease and aging. Nat Neurosci 2020;23:701–6. https://doi.org/10.1038/s41593-020-0624-8.

Halliday M, Radford H, Mallucci GR. Prions: Generation and Spread Versus Neurotoxicity. J Biol Chem 2014;289:19862–8. https://doi.org/10.1074/jbc.R114.568477.

Halpert BP. Development of the term “senility” as a medical diagnosis. Minn Med 1983;66:421–4.

Hämäläinen A, Pihlajamäki M, Tanila H, Hänninen T, Niskanen E, Tervo S, et al. Increased fMRI responses during encoding in mild cognitive impairment. Neurobiol Aging 2007;28:1889–903. https://doi.org/10.1016/j.neurobiolaging.2006.08.008.

Hampel H, Hardy J, Blennow K, Chen C, Perry G, Kim SH, et al. The Amyloid-β Pathway in Alzheimer’s Disease. Mol Psychiatry 2021;26:5481–503. https://doi.org/10.1038/s41380-021-01249-0.

Hampel H, Mesulam M-M, Cuello AC, Khachaturian AS, Vergallo A, Farlow MR, et al. Revisiting the Cholinergic Hypothesis in Alzheimer’s Disease: Emerging Evidence from Translational and Clinical Research. J Prev Alzheimers Dis 2019;6:2–15. https://doi.org/10.14283/jpad.2018.43.

Hansen DV, Hanson JE, Sheng M. Microglia in Alzheimer’s disease. J Cell Biol 2018;217:459–72. https://doi.org/10.1083/jcb.201709069.

Hanyu H, Sakurai H, Iwamoto T, Takasaki M, Shindo H, Abe K. Diffusion-weighted MR imaging of the hippocampus and temporal white matter in Alzheimer’s disease. J Neurol Sci 1998;156:195–200. https://doi.org/10.1016/S0022-510X(98)00043-4.

Hardy J. The discovery of Alzheimer-causing mutations in the APP gene and the formulation of the “amyloid cascade hypothesis.” FEBS J 2017;284:1040–4. https://doi.org/10.1111/febs.14004.

Hardy JA, Higgins GA. Alzheimer’s Disease: The Amyloid Cascade Hypothesis. Science 1992;256:184–5. https://doi.org/10.1126/science.1566067.

Haris M, Nath K, Cai K, Singh A, Crescenzi R, Kogan F, et al. Imaging of Glutamate Neurotransmitter Alterations in Alzheimer’s Disease. NMR Biomed 2013;26:386–91. https://doi.org/10.1002/nbm.2875.

Hatami A, Monjazeb S, Milton S, Glabe CG. Familial Alzheimer’s Disease Mutations within the Amyloid Precursor Protein Alter the Aggregation and Conformation of the Amyloid-β Peptide. J Biol Chem 2017;292:3172–85. https://doi.org/10.1074/jbc.M116.755264.

Hayashi Y, Majewska AK. Dendritic spine geometry: functional implication and regulation. Neuron 2005;46:529–32. https://doi.org/10.1016/j.neuron.2005.05.006.

He X, Qin W, Liu Y, Zhang X, Duan Y, Song J, et al. Abnormal salience network in normal aging and in amnestic mild cognitive impairment and Alzheimer’s disease. Hum Brain Mapp 2014;35:3446–64. https://doi.org/10.1002/hbm.22414.

Heilbronner G, Eisele YS, Langer F, Kaeser SA, Novotny R, Nagarathinam A, et al. Seeded strain-like transmission of β-amyloid morphotypes in APP transgenic mice. EMBO Rep 2013;14:1017–22. https://doi.org/10.1038/embor.2013.137.

Heneka MT, Carson MJ, El Khoury J, Landreth GE, Brosseron F, Feinstein DL, et al. Neuroinflammation in Alzheimer’s Disease. Lancet Neurol 2015;14:388–405. https://doi.org/10.1016/S1474-4422(15)70016-5.

van den Heuvel MP, Hulshoff Pol HE. Exploring the brain network: A review on resting-state fMRI functional connectivity. Eur Neuropsychopharmacol 2010;20:519–34. https://doi.org/10.1016/j.euroneuro.2010.03.008.

Hohman TJ, Bell SP, Jefferson AL, Alzheimer’s Disease Neuroimaging Initiative. The role of vascular endothelial growth factor in neurodegeneration and cognitive decline: exploring interactions with biomarkers of Alzheimer disease. JAMA Neurol 2015;72:520–9. https://doi.org/10.1001/jamaneurol.2014.4761.

Hong W, Wang Z, Liu W, O’Malley TT, Jin M, Willem M, et al. Diffusible, highly bioactive oligomers represent a critical minority of soluble Aβ in Alzheimer’s disease brain. Acta Neuropathol (Berl) 2018;136:19–40. https://doi.org/10.1007/s00401-018-1846-7.

Hoover BR, Reed MN, Su J, Penrod RD, Kotilinek LA, Grant MK, et al. Tau mislocalization to dendritic spines mediates synaptic dysfunction independently of neurodegeneration. Neuron 2010;68:1067–81. https://doi.org/10.1016/j.neuron.2010.11.030.

Hopp SC, Lin Y, Oakley D, Roe AD, DeVos SL, Hanlon D, et al. The role of microglia in processing and spreading of bioactive tau seeds in Alzheimer’s disease. J Neuroinflammation 2018;15:269. https://doi.org/10.1186/s12974-018-1309-z.

Huang H, Nie S, Cao M, Marshall C, Gao J, Xiao N, et al. Characterization of AD-like phenotype in aged APPSwe/PS1dE9 mice. Age 2016;38:303–22. https://doi.org/10.1007/s11357-016-9929-7.

Huang J, Beach P, Bozoki A, Zhu DC. Alzheimer's Disease Progressively Reduces Visual Functional Network Connectivity. J Alzheimers Dis Rep 2021;5:549–62. https://doi.org/10.3233/ADR-210017.

Hughes C, Choi ML, Yi J-H, Kim S-C, Drews A, George-Hyslop PS, et al. Beta amyloid aggregates induce sensitised TLR4 signalling causing long-term potentiation deficit and rat neuronal cell death. Commun Biol 2020;3:1–7. https://doi.org/10.1038/s42003-020-0792-9.

Huilgol D, Tole S. Cell migration in the developing rodent olfactory system. Cell Mol Life Sci CMLS 2016;73:2467–90. https://doi.org/10.1007/s00018-016-2172-7.

Hurtado DE, Molina-Porcel L, Iba M, Aboagye AK, Paul SM, Trojanowski JQ, et al. A{beta} accelerates the spatiotemporal progression of tau pathology and augments tau amyloidosis in an Alzheimer mouse model. Am J Pathol 2010;177:1977–88. https://doi.org/10.2353/ajpath.2010.100346.

Hyman BT, Phelps CH, Beach TG, Bigio EH, Cairns NJ, Carrillo MC, et al. National Institute on Aging–Alzheimer's Association guidelines for the neuropathologic assessment of Alzheimer's disease. Alzheimers Dement 2012;8:1–13. https://doi.org/10.1016/j.jalz.2011.10.007.

Hyman BT, Van Hoesen GW, Damasio AR, Barnes CL. Alzheimer's disease: cell-specific pathology isolates the hippocampal formation. Science 1984;225:1168–70. https://doi.org/10.1126/science.6474172.

Hyvärinen A, Oja E. Independent component analysis: algorithms and applications. Neural Netw 2000;13:411–30. https://doi.org/10.1016/S0893-6080(00)00026-5.

Iadanza MG, Jackson MP, Hewitt EW, Ranson NA, Radford SE. A new era for understanding amyloid structures and disease. Nat Rev Mol Cell Biol 2018;19:755–73. https://doi.org/10.1038/s41580-018-0060-8.

Igarashi H, Ueki S, Kitaura H, Kera T, Ohno K, Ohkubo M, et al. Longitudinal GluCEST MRI Changes and Cerebral Blood Flow in 5xFAD Mice. Contrast Media Mol Imaging 2020;2020:e8831936. https://doi.org/10.1155/2020/8831936.

Ilievski V, Zuchowska PK, Green SJ, Toth PT, Ragozzino ME, Le K, et al. Chronic oral application of a periodontal pathogen results in brain inflammation, neurodegeneration and amyloid beta production in wild type mice. PloS One 2018;13:e0204941. https://doi.org/10.1371/journal.pone.0204941.

Iliff JJ, Chen MJ, Plog BA, Zeppenfeld DM, Soltero M, Yang L, et al. Impairment of Glymphatic Pathway Function Promotes Tau Pathology after Traumatic Brain Injury. J Neurosci 2014;34:16180–93. https://doi.org/10.1523/JNEUROSCI.3020-14.2014.

Itzhaki RF. Herpes simplex virus type 1 and Alzheimer's disease: increasing evidence for a major role of the virus. Front Aging Neurosci 2014;6:202. https://doi.org/10.3389/fnagi.2014.00202.

Iwanowski P, Kozubski W, Losy J. Iowa-type hereditary cerebral amyloid angiopathy in a Polish family. J Neurol Sci 2015;356:202–4. https://doi.org/10.1016/j.jns.2015.06.020.

Jack CR, Bennett DA, Blennow K, Carrillo MC, Dunn B, Haeberlein SB, et al. NIA-AA Research Framework: Toward a biological definition of Alzheimer's disease. Alzheimers Dement J Alzheimers Assoc 2018;14:535–62. https://doi.org/10.1016/j.jalz.2018.02.018.

Jacobsen JS, Wu C-C, Redwine JM, Comery TA, Arias R, Bowlby M, et al. Early-onset behavioral and synaptic deficits in a mouse model of Alzheimer's disease. Proc Natl Acad Sci U S A 2006;103:5161–6. https://doi.org/10.1073/pnas.0600948103.

Jagust WJ, Mormino EC. Lifespan brain activity, β-amyloid, and Alzheimer's disease. Trends Cogn Sci 2011;15:520–6. https://doi.org/10.1016/j.tics.2011.09.004.

James TW, Culham J, Humphrey GK, Milner AD, Goodale MA. Ventral occipital lesions impair object recognition but not object-directed grasping: an fMRI study. Brain 2003;126:2463–75. https://doi.org/10.1093/brain/awg248.

Janelidze S, Mattsson N, Palmqvist S, Smith R, Beach TG, Serrano GE, et al. Plasma P-tau181 in Alzheimer's disease: relationship to other biomarkers, differential diagnosis, neuropathology and longitudinal progression to Alzheimer's dementia. Nat Med 2020;26:379–86. https://doi.org/10.1038/s41591-020-0755-1.

Jang H, Arce FT, Ramachandran S, Kagan BL, Lal R, Nussinov R. Familial Alzheimer's disease Osaka mutant (ΔE22) β-barrels suggest an explanation for the different Aβ1-40/42 preferred conformational states observed by experiment. J Phys Chem B 2013;117:11518–29. https://doi.org/10.1021/jp405389n.

Jankowsky JL, Slunt HH, Gonzales V, Jenkins NA, Copeland NG, Borchelt DR. APP processing and amyloid deposition in mice haplo-insufficient for presenilin 1. Neurobiol Aging 2004;25:885–92. https://doi.org/10.1016/j.neurobiolaging.2003.09.008.

Jaunmuktane Z, Mead S, Ellis M, Wadsworth JDF, Nicoll AJ, Kenny J, et al. Evidence for human transmission of amyloid-β pathology and cerebral amyloid angiopathy. Nature 2015;525:247–50. https://doi.org/10.1038/nature15369.

Jay TR, von Saucken VE, Landreth GE. TREM2 in Neurodegenerative Diseases. Mol Neurodegener 2017;12:56. https://doi.org/10.1186/s13024-017-0197-5.

Jin M, Shepardson N, Yang T, Chen G, Walsh D, Selkoe DJ. Soluble amyloid β-protein dimers isolated from Alzheimer cortex directly induce Tau hyperphosphorylation and neuritic degeneration. Proc Natl Acad Sci 2011;108:5819–24. https://doi.org/10.1073/pnas.1017033108.

Johnson KA, Schultz A, Betensky RA, Becker JA, Sepulcre J, Rentz D, et al. Tau positron emission tomographic imaging in aging and early Alzheimer disease. Ann Neurol 2016;79:110–9. https://doi.org/10.1002/ana.24546.

Jongsiriyanyong S, Limpawattana P. Mild Cognitive Impairment in Clinical Practice: A Review Article. Am J Alzheimers Dis Other Demen 2018;33:500–7. https://doi.org/10.1177/1533317518791401.

Jonsson T, Atwal JK, Steinberg S, Snaedal J, Jonsson PV, Bjornsson S, et al. A mutation in APP protects against Alzheimer's disease and age-related cognitive decline. Nature 2012;488:96–9. https://doi.org/10.1038/nature11283.

Jucker M, Walker LC. Pathogenic protein seeding in Alzheimer disease and other neurodegenerative disorders. Ann Neurol 2011;70:532–40. https://doi.org/10.1002/ana.22615.

Kane MD, Lipinski WJ, Callahan MJ, Bian F, Durham RA, Schwarz RD, et al. Evidence for Seeding of β-Amyloid by Intracerebral Infusion of Alzheimer Brain Extracts in β-Amyloid Precursor Protein-Transgenic Mice. J Neurosci 2000;20:3606–11. https://doi.org/10.1523/JNEUROSCI.20-10-03606.2000.

van der Kant R, Goldstein LSB. Cellular Functions of the Amyloid Precursor Protein from Development to Dementia. Dev Cell 2015;33:240. https://doi.org/10.1016/j.devcel.2015.04.004.

Kantarci K, Senjem ML, Avula R, Zhang B, Samikoglu AR, Weigand SD, et al. Diffusion tensor imaging and cognitive function in older adults with no dementia. Neurology 2011;77:26–34. https://doi.org/10.1212/WNL.0b013e31822313dc.

Karran E, De Strooper B. The amyloid hypothesis in Alzheimer disease: new insights from new therapeutics. Nat Rev Drug Discov 2022;21:306–18. https://doi.org/10.1038/s41573-022-00391-w.

Karran E, Mercken M, Strooper BD. The amyloid cascade hypothesis for Alzheimer's disease: an appraisal for the development of therapeutics. Nat Rev Drug Discov 2011;10:698–712. https://doi.org/10.1038/nrd3505.

Kayed R, Head E, Sarsoza F, Saing T, Cotman CW, Necula M, et al. Fibril specific, conformation dependent antibodies recognize a generic epitope common to amyloid fibrils and fibrillar oligomers that is absent in prefibrillar oligomers. Mol Neurodegener 2007;2:18. https://doi.org/10.1186/1750-1326-2-18.

Kent SA, Spires-Jones TL, Durrant CS. The physiological roles of tau and Aβ: implications for Alzheimer's disease pathology and therapeutics. Acta Neuropathol (Berl) 2020;140:417–47. https://doi.org/10.1007/s00401-020-02196-w.

Kero M, Paetau A, Polvikoski T, Tanskanen M, Sulkava R, Jansson L, et al. Amyloid precursor protein (APP) A673T mutation in the elderly Finnish population. Neurobiol Aging 2013;34:1518.e1-3. https://doi.org/10.1016/j.neurobiolaging.2012.09.017.

Kinney JW, Bemiller SM, Murtishaw AS, Leisgang AM, Salazar AM, Lamb BT. Inflammation as a central mechanism in Alzheimer's disease. Alzheimers Dement Transl Res Clin Interv 2018;4:575–90. https://doi.org/10.1016/j.trci.2018.06.014.

Kokawa A, Ishihara S, Fujiwara H, Nobuhara M, Iwata M, Ihara Y, et al. The A673T mutation in the amyloid precursor protein reduces the production of β-amyloid protein from its β-carboxyl terminal fragment in cells. Acta Neuropathol Commun 2015;3:66. https://doi.org/10.1186/s40478-015-0247-6.

Kulic L, McAfoose J, Welt T, Tackenberg C, Späni C, Wirth F, et al. Early accumulation of intracellular fibrillar oligomers and late congophilic amyloid angiopathy in mice expressing the Osaka intra-Aβ APP mutation. Transl Psychiatry 2012;2:e183–e183. https://doi.org/10.1038/tp.2012.109.

Kulikova AA, Makarov AA, Kozin SA. Roles of zinc ions and structural polymorphism of β-amyloid in the development of Alzheimer's disease. Mol Biol 2015;49:217–30. https://doi.org/10.1134/S0026893315020065.

Kvartsberg H, Duits FH, Ingelsson M, Andreasen N, Öhrfelt A, Andersson K, et al. Cerebrospinal fluid levels of the synaptic protein neurogranin correlates with cognitive decline in prodromal Alzheimer's disease. Alzheimers Dement 2015;11:1180–90. https://doi.org/10.1016/j.jalz.2014.10.009.

Ladiwala ARA, Litt J, Kane RS, Aucoin DS, Smith SO, Ranjan S, et al. Conformational differences between two amyloid β oligomers of similar size and dissimilar toxicity. J Biol Chem 2012;287:24765–73. https://doi.org/10.1074/jbc.M111.329763.

LaFerla FM, Green KN, Oddo S. Intracellular amyloid-β in Alzheimer's disease. Nat Rev Neurosci 2007;8:499–509. https://doi.org/10.1038/nrn2168.

Lam AR, Teplow DB, Stanley HE, Urbanc B. Effects of the Arctic (E22→G) Mutation on Amyloid β-Protein Folding: Discrete Molecular Dynamics Study. J Am Chem Soc 2011;133:2789–2789. https://doi.org/10.1021/ja111314d.

Lam B, Masellis M, Freedman M, Stuss DT, Black SE. Clinical, imaging, and pathological heterogeneity of the Alzheimer's disease syndrome. Alzheimers Res Ther 2013;5:1. https://doi.org/10.1186/alzrt155.

Lam S, Hérard A-S, Boluda S, Petit F, Eddarkaoui S, Cambon K, et al. Pathological changes induced by Alzheimer's brain inoculation in amyloid-beta plaque-bearing mice. Acta Neuropathol Commun 2022;10:112. https://doi.org/10.1186/s40478-022-01410-y.

Lam S, Petit F, Hérard A-S, Boluda S, Eddarkaoui S, Guillermier M, et al. Transmission of amyloid-beta and tau pathologies is associated with cognitive impairments in a primate. Acta Neuropathol Commun 2021;9:165. https://doi.org/10.1186/s40478-021-01266-8.

Lambert JC, Ibrahim-Verbaas CA, Harold D, Naj AC, Sims R, Bellenguez C, et al. Meta-analysis of 74,046 individuals identifies 11 new susceptibility loci for Alzheimer's disease. Nat Genet 2013;45:1452–8. https://doi.org/10.1038/ng.2802.

Langer F, Eisele YS, Fritschi SK, Staufenbiel M, Walker LC, Jucker M. Soluble Aβ Seeds Are Potent Inducers of Cerebral β-Amyloid Deposition. J Neurosci 2011;31:14488–95. https://doi.org/10.1523/JNEUROSCI.3088-11.2011.

Lannfelt L, Basun H, Wahlund L-O, Rowe BA, Wagner SL. Decreased α-secretase-cleaved amyloid precursor protein as a diagnostic marker for Alzheimer's diseas. Nat Med 1995;1:829–32. https://doi.org/10.1038/nm0895-829.

LaRocca TJ, Cavalier AN, Roberts CM, Lemieux MR, Ramesh P, Garcia MA, et al. Amyloid beta acts synergistically as a pro-inflammatory cytokine. Neurobiol Dis 2021;159:105493. https://doi.org/10.1016/j.nbd.2021.105493.

Larson-Prior LJ, Zempel JM, Nolan TS, Prior FW, Snyder AZ, Raichle ME. Cortical network functional connectivity in the descent to sleep. Proc Natl Acad Sci U S A 2009;106:4489–94. https://doi.org/10.1073/pnas.0900924106.

Lashley T, Schott JM, Weston P, Murray CE, Wellington H, Keshavan A, et al. Molecular biomarkers of Alzheimer's disease: progress and prospects. Dis Model Mech 2018;11:dmm031781. https://doi.org/10.1242/dmm.031781.

Lauritzen I, Pardossi-Piquard R, Bourgeois A, Pagnotta S, Biferi M-G, Barkats M, et al. Intraneuronal aggregation of the β-CTF fragment of APP (C99) induces Aβ-independent lysosomal-autophagic pathology. Acta Neuropathol (Berl) 2016;132:257–76. https://doi.org/10.1007/s00401-016-1577-6.

Lawrence JLM, Tong M, Alfulaij N, Sherrin T, Contarino M, White MM, et al. Regulation of presynaptic Ca2+, synaptic plasticity and contextual fear conditioning by a N-terminal β-amyloid fragment. J Neurosci Off J Soc Neurosci 2014;34:14210–8. https://doi.org/10.1523/JNEUROSCI.0326-14.2014.

Lazo ND, Grant MA, Condron MC, Rigby AC, Teplow DB. On the nucleation of amyloid β-protein monomer folding. Protein Sci 2005;14:1581–96. https://doi.org/10.1110/ps.041292205.

Ledig C, Schuh A, Guerrero R, Heckemann RA, Rueckert D. Structural brain imaging in Alzheimer's disease and mild cognitive impairment: biomarker analysis and shared morphometry database. Sci Rep 2018;8:11258. https://doi.org/10.1038/s41598-018-29295-9.

Lee SJC, Nam E, Lee HJ, Savelieff MG, Lim MH. Towards an understanding of amyloid-β oligomers: characterization, toxicity mechanisms, and inhibitors. Chem Soc Rev 2017;46:310–23. https://doi.org/10.1039/c6cs00731g.

Leqembi | ALZFORUM. n.d. https://www.alzforum.org/therapeutics/leqembi (accessed January 23, 2023).

Leuzy A, Mattsson-Carlgren N, Palmqvist S, Janelidze S, Dage JL, Hansson O. Blood-based biomarkers for Alzheimer's disease. EMBO Mol Med 2022;14:e14408. https://doi.org/10.15252/emmm.202114408.

Léveillé F, El Gaamouch F, Gouix E, Lecocq M, Lobner D, Nicole O, et al. Neuronal viability is controlled by a functional relation between synaptic and extrasynaptic NMDA receptors. FASEB J Off Publ Fed Am Soc Exp Biol 2008;22:4258–71. https://doi.org/10.1096/fj.08-107268.

Levy E, Carman MD, Fernandez-Madrid IJ, Power MD, Lieberburg I, van Duinen SG, et al. Mutation of the Alzheimer's Disease Amyloid Gene in Hereditary Cerebral Hemorrhage, Dutch Type. Science 1990;248:1124–6. https://doi.org/10.1126/science.2111584.

Leyns CEG, Holtzman DM. Glial contributions to neurodegeneration in tauopathies. Mol Neurodegener 2017;12:50. https://doi.org/10.1186/s13024-017-0192-x.

Li Binyin, Zhang M, Jang I, Ye G, Zhou L, He G, et al. Amyloid-Beta Influences Memory via Functional Connectivity During Memory Retrieval in Alzheimer's Disease. Front Aging Neurosci 2021;13.

Li J, Martin S, Tricklebank MD, Schwarz AJ, Gilmour G. Task-Induced Modulation of Intrinsic Functional Connectivity Networks in the Behaving Rat. J Neurosci 2015;35:658–65. https://doi.org/10.1523/JNEUROSCI.3488-14.2015.

Li R, Wu X, Fleisher AS, Reiman EM, Chen K, Yao L. Attention-related networks in Alzheimer's disease: A resting functional MRI study. Hum Brain Mapp 2011;33:1076–88. https://doi.org/10.1002/hbm.21269.

Li S, Jin M, Koeglsperger T, Shepardson NE, Shankar GM, Selkoe DJ. Soluble Aβ oligomers inhibit long-term potentiation through a mechanism involving excessive activation of extrasynaptic NR2B-containing NMDA receptors. J Neurosci Off J Soc Neurosci 2011;31:6627–38. https://doi.org/10.1523/JNEUROSCI.0203-11.2011.

Liang Z, King J, Zhang N. Intrinsic Organization of the Anesthetized Brain. J Neurosci 2012;32:10183–91. https://doi.org/10.1523/JNEUROSCI.1020-12.2012.

Liang Z, King J, Zhang N. Uncovering Intrinsic Connectional Architecture of Functional Networks in Awake Rat Brain. J Neurosci 2011;31:3776–83. https://doi.org/10.1523/JNEUROSCI.4557-10.2011.

Liebsch F, Kulic L, Teunissen C, Shobo A, Ulku I, Engelschalt V, et al. Aβ34 is a BACE1-derived degradation intermediate associated with amyloid clearance and Alzheimer's disease progression. Nat Commun 2019;10:2240. https://doi.org/10.1038/s41467-019-10152-w.

Limegrover CS, LeVine H, Izzo NJ, Yurko R, Mozzoni K, Rehak C, et al. Alzheimer's protection effect of A673T mutation may be driven by lower Aβ oligomer binding affinity. J Neurochem 2021;157:1316–30. https://doi.org/10.1111/jnc.15212.

Lin T-W, Chang C-F, Chang Y-J, Liao Y-H, Yu H-M, Chen Y-R. Alzheimer's amyloid-β A2T variant and its N-terminal peptides inhibit amyloid-β fibrillization and rescue the induced cytotoxicity. PloS One 2017;12:e0174561. https://doi.org/10.1371/journal.pone.0174561.

Liu P, Reed MN, Kotilinek LA, Grant MKO, Forster CL, Qiang W, et al. Quaternary Structure Defines a Large Class of Amyloid-β Oligomers Neutralized by Sequestration. Cell Rep 2015;11:1760–71. https://doi.org/10.1016/j.celrep.2015.05.021.

Liu P-P, Xie Y, Meng X-Y, Kang J-S. History and progress of hypotheses and clinical trials for Alzheimer's disease. Signal Transduct Target Ther 2019;4:1–22. https://doi.org/10.1038/s41392-019-0063-8.

Liu Y, Li J, Ji H, Zhuang J. Comparisons of Glutamate in the Brains of Alzheimer's Disease Mice Under Chemical Exchange Saturation Transfer Imaging Based on Machine Learning Analysis. Front Neurosci 2022;16:838157. https://doi.org/10.3389/fnins.2022.838157.

Long JM, Holtzman DM. Alzheimer Disease: An Update on Pathobiology and Treatment Strategies. Cell 2019;179:312–39. https://doi.org/10.1016/j.cell.2019.09.001.

Lowe MJ, Beall EB, Sakaie KE, Koenig KA, Stone L, Marrie RA, et al. Resting state sensorimotor functional connectivity in multiple sclerosis inversely correlates with transcallosal motor pathway transverse diffusivity. Hum Brain Mapp 2008;29:818–27. https://doi.org/10.1002/hbm.20576.

Lu J-X, Qiang W, Yau W-M, Schwieters CD, Meredith SC, Tycko R. Molecular structure of β-amyloid fibrils in Alzheimer's disease brain tissue. Cell 2013;154:1257–68. https://doi.org/10.1016/j.cell.2013.08.035.

Lue L-F, Kuo Y-M, Roher AE, Brachova L, Shen Y, Sue L, et al. Soluble Amyloid β Peptide Concentration as a Predictor of Synaptic Change in Alzheimer's Disease. Am J Pathol 1999;155:853–62. https://doi.org/10.1016/S0002-9440(10)65184-X.

Luyendijk W, Bots GT, Vegter-van der Vlis M, Went LN, Frangione B. Hereditary cerebral haemorrhage caused by cortical amyloid angiopathy. J Neurol Sci 1988;85:267–80. https://doi.org/10.1016/0022-510x(88)90186-4.

Ma T, Klann E. Amyloid β: Linking Synaptic Plasticity Failure to Memory Disruption in Alzheimer's Disease. J Neurochem 2012;120:140–8. https://doi.org/10.1111/j.1471-4159.2011.07506.x.

Machulda MM, Ward HA, Borowski B, Gunter JL, Cha RH, O'Brien PC, et al. Comparison of memory fMRI response among normal, MCI, and Alzheimer's patients. Neurology 2003;61:500–6. https://doi.org/10.1212/01.wnl.0000079052.01016.78.

Makaretz SJ, Quimby M, Collins J, Makris N, McGinnis S, Schultz A, et al. Flortaucipir tau PET imaging in semantic variant primary progressive aphasia. J Neurol Neurosurg Psychiatry 2018;89:1024–31. https://doi.org/10.1136/jnnp-2017-316409.

Maloney JA, Bainbridge T, Gustafson A, Zhang S, Kyauk R, Steiner P, et al. Molecular mechanisms of Alzheimer disease protection by the A673T allele of amyloid precursor protein. J Biol Chem 2014;289:30990–1000. https://doi.org/10.1074/jbc.M114.589069.

Mandino F, Vrooman RM, Foo HE, Yeow LY, Bolton TAW, Salvan P, et al. A triple-network organization for the mouse brain. Mol Psychiatry 2022;27:865–72. https://doi.org/10.1038/s41380-021-01298-5.

Marcello E, Musardo S, Vandermeulen L, Pelucchi S, Gardoni F, Santo N, et al. Amyloid-β Oligomers Regulate ADAM10 Synaptic Localization Through Aberrant Plasticity Phenomena. Mol Neurobiol 2019;56:7136–43. https://doi.org/10.1007/s12035-019-1583-5.

Marchant NL, Reed BR, DeCarli CS, Madison CM, Weiner MW, Chui HC, et al. Cerebrovascular disease, beta-amyloid, and cognition in aging. Neurobiol Aging 2012;33:1006.e25-1006.e36. https://doi.org/10.1016/j.neurobiolaging.2011.10.001.

Marquié M, Normandin MD, Vanderburg CR, Costantino IM, Bien EA, Rycyna LG, et al. Validating novel tau positron emission tomography tracer [F-18]-AV-1451 (T807) on postmortem brain tissue. Ann Neurol 2015;78:787–800. https://doi.org/10.1002/ana.24517.

Martin L, Bouvet P, Chounlamountri N, Watrin C, Besançon R, Pinatel D, et al. VEGF counteracts amyloid-β-induced synaptic dysfunction. Cell Rep 2021;35:109121. https://doi.org/10.1016/j.celrep.2021.109121.

Martiskainen H, Herukka S-K, Stančáková A, Paananen J, Soininen H, Kuusisto J, et al. Decreased plasma β-amyloid in the Alzheimer's disease APP A673T variant carriers. Ann Neurol 2017;82:128–32. https://doi.org/10.1002/ana.24969.

Mattsson N, Zetterberg H, Janelidze S, Insel PS, Andreasson U, Stomrud E, et al. Plasma tau in Alzheimer disease. Neurology 2016;87:1827–35. https://doi.org/10.1212/WNL.0000000000003246.

Maurer K, Volk S, Gerbaldo H. Auguste D and Alzheimer's disease. Lancet Lond Engl 1997;349:1546–9. https://doi.org/10.1016/S0140-6736(96)10203-8.

McDonald C. Clinical Heterogeneity in Senile Dementia. Br J Psychiatry 1969;115:267–71. https://doi.org/10.1192/bjp.115.520.267.

McKhann G, Drachman D, Folstein M, Katzman R, Price D, Stadlan EM. Clinical diagnosis of Alzheimer's disease: Report of the NINCDS-ADRDA Work Group* under the auspices of Department of Health and Human Services Task Force on Alzheimer's Disease. Neurology 1984;34:939–939. https://doi.org/10.1212/WNL.34.7.939.

McLean CA, Cherny RA, Fraser FW, Fuller SJ, Smith MJ, Beyreuther K, et al. Soluble pool of Abeta amyloid as a determinant of severity of neurodegeneration in Alzheimer's disease. Ann Neurol 1999;46:860–6. https://doi.org/10.1002/1531-8249(199912)46:6<860::aid-ana8>3.0.co;2-m.

McNamara J, Murray TA. Connections Between Herpes Simplex Virus Type 1 and Alzheimer's Disease Pathogenesis. Curr Alzheimer Res 2016;13:996–1005. https://doi.org/10.2174/1567205013666160314150136.

Menon V, Uddin LQ. Saliency, switching, attention and control: a network model of insula function. Brain Struct Funct 2010;214:655–67. https://doi.org/10.1007/s00429-010-0262-0.

Meyer-Luehmann M, Coomaraswamy J, Bolmont T, Kaeser S, Schaefer C, Kilger E, et al. Exogenous induction of cerebral beta-amyloidogenesis is governed by agent and host. Science 2006;313:1781–4. https://doi.org/10.1126/science.1131864.

Mirza Z, Pillai VG, Kamal MA. Protein interactions between the C-terminus of Aβ-peptide and phospholipase A2--a structure biology based approach to identify novel Alzheimer's therapeutics. CNS Neurol Disord Drug Targets 2014;13:1224–31. https://doi.org/10.2174/1871527313666140917112248.

Mitchell AJ, Shiri-Feshki M. Rate of progression of mild cognitive impairment to dementia - meta-analysis of 41 robust inception cohort studies. Acta Psychiatr Scand 2009;119:252–65. https://doi.org/10.1111/j.1600-0447.2008.01326.x.

Moir RD, Lathe R, Tanzi RE. The antimicrobial protection hypothesis of Alzheimer's disease. Alzheimers Dement J Alzheimers Assoc 2018;14:1602–14. https://doi.org/10.1016/j.jalz.2018.06.3040.

Mok T, Chalissery AJ, Byrne S, Costelloe L, Galvin L, Vinters HV, et al. Familial Cerebral Amyloid Angiopathy Due to the Iowa Mutation in an Irish Family. Can J Neurol Sci 2014;41:512–7. https://doi.org/10.1017/S031716710001859X.

Morales R, Bravo-Alegria J, Duran-Aniotz C, Soto C. Titration of biologically active amyloid–β seeds in a transgenic mouse model of Alzheimer's disease. Sci Rep 2015;5:9349. https://doi.org/10.1038/srep09349.

Müller H-P, Kassubek J, Vernikouskaya I, Ludolph AC, Stiller D, Rasche V. Diffusion Tensor Magnetic Resonance Imaging of the Brain in APP Transgenic Mice: A Cohort Study. PLOS ONE 2013;8:e67630. https://doi.org/10.1371/journal.pone.0067630.

Murray B, Sorci M, Rosenthal J, Lippens J, Isaacson D, Das P, et al. A2T and A2V Aβ peptides exhibit different aggregation kinetics, primary nucleation, morphology, structure, and LTP inhibition. Proteins 2016;84:488–500. https://doi.org/10.1002/prot.24995.

Murray ME, Graff-Radford NR, Ross OA, Petersen RC, Duara R, Dickson DW. Neuropathologically defined subtypes of Alzheimer's disease with distinct clinical characteristics: a retrospective study. Lancet Neurol 2011;10:785–96. https://doi.org/10.1016/S1474-4422(11)70156-9.

Myers N, Pasquini L, Göttler J, Grimmer T, Koch K, Ortner M, et al. Within-patient correspondence of amyloid-β and intrinsic network connectivity in Alzheimer's disease. Brain J Neurol 2014;137:2052–64. https://doi.org/10.1093/brain/awu103.

Nakamura A, Kaneko N, Villemagne VL, Kato T, Doecke J, Doré V, et al. High performance plasma amyloid-β biomarkers for Alzheimer's disease. Nature 2018;554:249–54. https://doi.org/10.1038/nature25456.

Nassi JJ, Callaway EM. Parallel processing strategies of the primate visual system. Nat Rev Neurosci 2009;10:360–72. https://doi.org/10.1038/nrn2619.

Nguyen PH, Sterpone F, Pouplana R, Derreumaux P, Campanera JM. Dimerization Mechanism of Alzheimer Aβ40 Peptides: The High Content of Intrapeptide-Stabilized Conformations in A2V and A2T Heterozygous Dimers Retards Amyloid Fibril Formation. J Phys Chem B 2016;120:12111–26. https://doi.org/10.1021/acs.jpcb.6b10722.

Nilsberth C, Westlind-Danielsson A, Eckman CB, Condron MM, Axelman K, Forsell C, et al. The "Arctic" APP mutation (E693G) causes Alzheimer's disease by enhanced Abeta protofibril formation. Nat Neurosci 2001;4:887–93. https://doi.org/10.1038/nn0901-887.

Nobis L, Husain M. Apathy in Alzheimer's disease. Curr Opin Behav Sci 2018;22:7–13. https://doi.org/10.1016/j.cobeha.2017.12.007.

Noh Y, Jeon S, Lee JM, Seo SW, Kim GH, Cho H, et al. Anatomical heterogeneity of Alzheimer disease: based on cortical thickness on MRIs. Neurology 2014;83:1936–44. https://doi.org/10.1212/WNL.0000000000001003.

Nordberg A. Amyloid imaging in Alzheimer's disease. Neuropsychologia 2008;46:1636–41. https://doi.org/10.1016/j.neuropsychologia.2008.03.020.

Olsson B, Lautner R, Andreasson U, Öhrfelt A, Portelius E, Bjerke M, et al. CSF and blood biomarkers for the diagnosis of Alzheimer's disease: a systematic review and meta-analysis. Lancet Neurol 2016;15:673–84. https://doi.org/10.1016/S1474-4422(16)00070-3.

Ono K, Condron MM, Teplow DB. Structure–neurotoxicity relationships of amyloid β-protein oligomers. Proc Natl Acad Sci 2009;106:14745–50. https://doi.org/10.1073/pnas.0905127106.

Orre M, Kamphuis W, Osborn LM, Melief J, Kooijman L, Huitinga I, et al. Acute isolation and transcriptome characterization of cortical astrocytes and microglia from young and aged mice. Neurobiol Aging 2014;35:1–14. https://doi.org/10.1016/j.neurobiolaging.2013.07.008.

Ortiz-Sanz C, Gaminde-Blasco A, Valero J, Bakota L, Brandt R, Zugaza JL, et al. Early Effects of Aβ Oligomers on Dendritic Spine Dynamics and Arborization in Hippocampal Neurons. Front Synaptic Neurosci 2020;12:2. https://doi.org/10.3389/fnsyn.2020.00002.

Ossenkoppele R, Jansen WJ, Rabinovici GD, Knol DL, van der Flier WM, van Berckel BNM, et al. Prevalence of Amyloid PET Positivity in Dementia Syndromes: A Meta-analysis. JAMA 2015;313:1939–50. https://doi.org/10.1001/jama.2015.4669.

Ovchinnikova OYu, Finder VH, Vodopivec I, Nitsch RM, Glockshuber R. The Osaka FAD Mutation E22Δ Leads to the Formation of a Previously Unknown Type of Amyloid β Fibrils and Modulates Aβ Neurotoxicity. J Mol Biol 2011;408:780–91. https://doi.org/10.1016/j.jmb.2011.02.049.

Päiviö A, Jarvet J, Gräslund A, Lannfelt L, Westlind-Danielsson A. Unique physicochemical profile of beta-amyloid peptide variant Abeta1-40E22G protofibrils: conceivable neuropathogen in arctic mutant carriers. J Mol Biol 2004;339:145–59. https://doi.org/10.1016/j.jmb.2004.03.028.

Pallas-Bazarra N, Jurado-Arjona J, Navarrete M, Esteban JA, Hernández F, Ávila J, et al. Novel function of Tau in regulating the effects of external stimuli on adult hippocampal neurogenesis. EMBO J 2016;35:1417–36. https://doi.org/10.15252/embj.201593518.

Palmqvist S, Janelidze S, Quiroz YT, Zetterberg H, Lopera F, Stomrud E, et al. Discriminative Accuracy of Plasma Phospho-tau217 for Alzheimer Disease vs Other Neurodegenerative Disorders. JAMA 2020;324:772–81. https://doi.org/10.1001/jama.2020.12134.

Paolicelli RC, Bolasco G, Pagani F, Maggi L, Scianni M, Panzanelli P, et al. Synaptic Pruning by Microglia Is Necessary for Normal Brain Development. Science 2011;333:1456–8. https://doi.org/10.1126/science.1202529.

Paravastu AK, Qahwash I, Leapman RD, Meredith SC, Tycko R. Seeded growth of beta-amyloid fibrils from Alzheimer's brain-derived fibrils produces a distinct fibril structure. Proc Natl Acad Sci U S A 2009;106:7443–8. https://doi.org/10.1073/pnas.0812033106.

Pascoal TA, Mathotaarachchi S, Shin M, Benedet AL, Mohades S, Wang S, et al. Synergistic interaction between amyloid and tau predicts the progression to dementia. Alzheimers Dement J Alzheimers Assoc 2017;13:644–53. https://doi.org/10.1016/j.jalz.2016.11.005.

Paspalas CD, Carlyle BC, Leslie S, Preuss TM, Crimins JL, Huttner AJ, et al. The aged rhesus macaque manifests Braak stage III/IV Alzheimer's-like pathology. Alzheimers Dement 2018;14:680–91. https://doi.org/10.1016/j.jalz.2017.11.005.

Pépin J, Francelle L, Carrillo-de Sauvage M-A, de Longprez L, Gipchtein P, Cambon K, et al. In vivo imaging of brain glutamate defects in a knock-in mouse model of Huntington's disease. NeuroImage 2016;139:53–64. https://doi.org/10.1016/j.neuroimage.2016.06.023.

Percie du Sert N, Hurst V, Ahluwalia A, Alam S, Avey MT, Baker M, et al. The ARRIVE guidelines 2.0: Updated guidelines for reporting animal research. PLoS Biol 2020;18:e3000410. https://doi.org/10.1371/journal.pbio.3000410.

Perea JR, Bolós M, Avila J. Microglia in Alzheimer's Disease in the Context of Tau Pathology. Biomolecules 2020;10:1439. https://doi.org/10.3390/biom10101439.

Pérot J-B, Célestine M, Palombo M, Dhenain M, Humbert S, Brouillet E, et al. Longitudinal multimodal MRI characterization of a knock-in mouse model of Huntington's disease reveals early gray and white matter alterations. Hum Mol Genet 2022;31:3581–96. https://doi.org/10.1093/hmg/ddac036.

Petkova AT, Leapman RD, Guo Z, Yau W-M, Mattson MP, Tycko R. Self-propagating, molecular-level polymorphism in Alzheimer's beta-amyloid fibrils. Science 2005;307:262–5. https://doi.org/10.1126/science.1105850.

Piaceri I, Nacmias B, Sorbi S. Genetics of familial and sporadic Alzheimer's disease. Front Biosci Elite Ed 2013;5:167–77. https://doi.org/10.2741/e605.

Poduslo JF, Howell KG. Unique molecular signatures of Alzheimer's disease amyloid β peptide mutations and deletion during aggregate/oligomer/fibril formation. J Neurosci Res 2015;93:410–23. https://doi.org/10.1002/jnr.23507.

Pontecorvo MJ, Devous MD, Kennedy I, Navitsky M, Lu M, Galante N, et al. A multicentre longitudinal study of flortaucipir (18F) in normal ageing, mild cognitive impairment and Alzheimer's disease dementia. Brain J Neurol 2019;142:1723–35. https://doi.org/10.1093/brain/awz090.

Pooler AM, Noble W, Hanger DP. A role for tau at the synapse in Alzheimer's disease pathogenesis. Neuropharmacology 2014;76 Pt A:1–8. https://doi.org/10.1016/j.neuropharm.2013.09.018.

Pooler AM, Polydoro M, Maury EA, Nicholls SB, Reddy SM, Wegmann S, et al. Amyloid accelerates tau propagation and toxicity in a model of early Alzheimer's disease. Acta Neuropathol Commun 2015;3:14. https://doi.org/10.1186/s40478-015-0199-x.

Portelius E, Bogdanovic N, Gustavsson MK, Volkmann I, Brinkmalm G, Zetterberg H, et al. Mass spectrometric characterization of brain amyloid beta isoform signatures in familial and sporadic Alzheimer's disease. Acta Neuropathol (Berl) 2010;120:185–93. https://doi.org/10.1007/s00401-010-0690-1.

Prusiner SB. Novel Proteinaceous Infectious Particles Cause Scrapie. Science 1982;216:136–44. https://doi.org/10.1126/science.6801762.

Qiang W, Yau W-M, Lu J-X, Collinge J, Tycko R. Structural variation in amyloid-β fibrils from Alzheimer's disease clinical subtypes. Nature 2017;541:217–21. https://doi.org/10.1038/nature20814.

Qin S, Hermans EJ, van Marle HJF, Luo J, Fernández G. Acute psychological stress reduces working memory-related activity in the dorsolateral prefrontal cortex. Biol Psychiatry 2009;66:25–32. https://doi.org/10.1016/j.biopsych.2009.03.006.

Qin Y-Y, Li M-W, Zhang S, Zhang Y, Zhao L-Y, Lei H, et al. In vivo quantitative whole-brain diffusion tensor imaging analysis of APP/PS1 transgenic mice using voxel-based and atlas-based methods. Neuroradiology 2013;55:1027–38. https://doi.org/10.1007/s00234-013-1195-0.

Quintanilla RA, Orellana DI, González-Billault C, Maccioni RB. Interleukin-6 induces Alzheimer-type phosphorylation of tau protein by deregulating the cdk5/p35 pathway. Exp Cell Res 2004;295:245–57. https://doi.org/10.1016/j.yexcr.2004.01.002.

Racine AM, Adluru N, Alexander AL, Christian BT, Okonkwo OC, Oh J, et al. Associations between white matter microstructure and amyloid burden in preclinical Alzheimer's disease: A multimodal imaging investigation. NeuroImage Clin 2014;4:604–14. https://doi.org/10.1016/j.nicl.2014.02.001.

Rahman MA, Rahman MS, Uddin MJ, Mamum-Or-Rashid ANM, Pang M-G, Rhim H. Emerging risk of environmental factors: insight mechanisms of Alzheimer's diseases. Environ Sci Pollut Res 2020;27:44659–72. https://doi.org/10.1007/s11356-020-08243-z.

Raichle ME. The Restless Brain. Brain Connect 2011;1:3–12. https://doi.org/10.1089/brain.2011.0019.

Raichle ME. A Paradigm Shift in Functional Brain Imaging. J Neurosci 2009;29:12729–34. https://doi.org/10.1523/JNEUROSCI.4366-09.2009.

Raichle ME, MacLeod AM, Snyder AZ, Powers WJ, Gusnard DA, Shulman GL. A default mode of brain function. Proc Natl Acad Sci 2001;98:676–82. https://doi.org/10.1073/pnas.98.2.676.

Rasmussen J, Mahler J, Beschorner N, Kaeser SA, Häsler LM, Baumann F, et al. Amyloid polymorphisms constitute distinct clouds of conformational variants in different etiological subtypes of Alzheimer's disease. Proc Natl Acad Sci U S A 2017;114:13018–23. https://doi.org/10.1073/pnas.1713215114.

Ricciarelli R, Fedele E. The Amyloid Cascade Hypothesis in Alzheimer's Disease: It's Time to Change Our Mind. Curr Neuropharmacol 2017a;15:926–35. https://doi.org/10.2174/1570159X15666170116143743.

Ricciarelli R, Fedele E. The Amyloid Cascade Hypothesis in Alzheimer's Disease: It's Time to Change Our Mind. Curr Neuropharmacol 2017b;15:926–35. https://doi.org/10.2174/1570159X15666170116143743.

Ridler C. BACE1 inhibitors block new Aβ plaque formation. Nat Rev Neurol 2018;14:126–126. https://doi.org/10.1038/nrneurol.2018.12.

Ripoli C, Cocco S, Li Puma DD, Piacentini R, Mastrodonato A, Scala F, et al. Intracellular Accumulation of Amyloid-β (Aβ) Protein Plays a Major Role in Aβ-Induced Alterations of Glutamatergic Synaptic Transmission and Plasticity. J Neurosci 2014;34:12893–903. https://doi.org/10.1523/JNEUROSCI.1201-14.2014.

Rodríguez JJ, Verkhratsky A. Neurogenesis in Alzheimer's disease. J Anat 2011;219:78–89. https://doi.org/10.1111/j.1469-7580.2011.01343.x.

Rodríguez-Arellano JJ, Parpura V, Zorec R, Verkhratsky A. Astrocytes in physiological aging and Alzheimer's disease. Neuroscience 2016;323:170–82. https://doi.org/10.1016/j.neuroscience.2015.01.007.

Rolland M, Powell R, Jacquier-Sarlin M, Boisseau S, Reynaud-Dulaurier R, Martinez-Hernandez J, et al. Effect of Aβ oligomers on neuronal APP triggers a vicious cycle leading to the propagation of synaptic plasticity alterations to healthy neurons. J Neurosci 2020. https://doi.org/10.1523/JNEUROSCI.2501-19.2020.

Rombouts SARB, Barkhof F, Goekoop R, Stam CJ, Scheltens P. Altered resting state networks in mild cognitive impairment and mild Alzheimer's disease: An fMRI study. Hum Brain Mapp 2005;26:231–9. https://doi.org/10.1002/hbm.20160.

Ruiz-Riquelme A, Lau HHC, Stuart E, Goczi AN, Wang Z, Schmitt-Ulms G, et al. Prion-like propagation of β-amyloid aggregates in the absence of APP overexpression. Acta Neuropathol Commun 2018;6:26. https://doi.org/10.1186/s40478-018-0529-x.

Ryan NS, Keihaninejad S, Shakespeare TJ, Lehmann M, Crutch SJ, Malone IB, et al. Magnetic resonance imaging evidence for presymptomatic change in thalamus and caudate in familial Alzheimer's disease. Brain 2013;136:1399–414. https://doi.org/10.1093/brain/awt065.

Salloway S, Sperling R, Fox NC, Blennow K, Klunk W, Raskind M, et al. Two phase 3 trials of bapineuzumab in mild-to-moderate Alzheimer's disease. N Engl J Med 2014;370:322–33. https://doi.org/10.1056/NEJMoa1304839.

Sanz-Arigita EJ, Schoonheim MM, Damoiseaux JS, Rombouts SARB, Maris E, Barkhof F, et al. Loss of "small-world" networks in Alzheimer's disease: graph analysis of FMRI resting-state functional connectivity. PloS One 2010;5:e13788. https://doi.org/10.1371/journal.pone.0013788.

Sardar Sinha M, Ansell-Schultz A, Civitelli L, Hildesjö C, Larsson M, Lannfelt L, et al. Alzheimer's disease pathology propagation by exosomes containing toxic amyloid-beta oligomers. Acta Neuropathol (Berl) 2018;136:41–56. https://doi.org/10.1007/s00401-018-1868-1.

Savage MJ, Kalinina J, Wolfe A, Tugusheva K, Korn R, Cash-Mason T, et al. A Sensitive A Oligomer Assay Discriminates Alzheimer's and Aged Control Cerebrospinal Fluid. J Neurosci 2014;34:2884–97. https://doi.org/10.1523/JNEUROSCI.1675-13.2014.

Scheltens P, Blennow K, Breteler MMB, de Strooper B, Frisoni GB, Salloway S, et al. Alzheimer's disease. The Lancet 2016;388:505–17. https://doi.org/10.1016/S0140-6736(15)01124-1.

Schenk D, Barbour R, Dunn W, Gordon G, Grajeda H, Guido T, et al. Immunization with amyloid-beta attenuates Alzheimer-disease-like pathology in the PDAPP mouse. Nature 1999;400:173–7. https://doi.org/10.1038/22124.

Schindler SE, Bollinger JG, Ovod V, Mawuenyega KG, Li Y, Gordon BA, et al. High-precision plasma β-amyloid 42/40 predicts current and future brain amyloidosis. Neurology 2019;93:e1647–59. https://doi.org/10.1212/WNL.0000000000008081.

Schöll M, Lockhart SN, Schonhaut DR, O'Neil JP, Janabi M, Ossenkoppele R, et al. PET Imaging of Tau Deposition in the Aging Human Brain. Neuron 2016;89:971–82. https://doi.org/10.1016/j.neuron.2016.01.028.

Schwarz AJ, Gass N, Sartorius A, Risterucci C, Spedding M, Schenker E, et al. Anti-Correlated Cortical Networks of Intrinsic Connectivity in the Rat Brain. Brain Connect 2013;3:503–11. https://doi.org/10.1089/brain.2013.0168.

Scialò C, De Cecco E, Manganotti P, Legname G. Prion and Prion-Like Protein Strains: Deciphering the Molecular Basis of Heterogeneity in Neurodegeneration. Viruses 2019;11:261. https://doi.org/10.3390/v11030261.

Seeley WW, Crawford RK, Zhou J, Miller BL, Greicius MD. Neurodegenerative diseases target large-scale human brain networks. Neuron 2009;62:42–52. https://doi.org/10.1016/j.neuron.2009.03.024.

Selkoe DJ. Alzheimer's Disease Is a Synaptic Failure. Science 2002;298:789–91. https://doi.org/10.1126/science.1074069.

Selkoe DJ. Alzheimer's disease: genes, proteins, and therapy. Physiol Rev 2001;81:741–66. https://doi.org/10.1152/physrev.2001.81.2.741.

Sforazzini F, Schwarz AJ, Galbusera A, Bifone A, Gozzi A. Distributed BOLD and CBV-weighted resting-state networks in the mouse brain. NeuroImage 2014;87:403–15. https://doi.org/10.1016/j.neuroimage.2013.09.050.

Sgourakis NG, Merced-Serrano M, Boutsidis C, Drineas P, Du Z, Wang C, et al. Atomic-level characterization of the ensemble of the Aβ(1-42) monomer in water using unbiased molecular dynamics simulations and spectral algorithms. J Mol Biol 2011;405:570–83. https://doi.org/10.1016/j.jmb.2010.10.015.

Shah D, Jonckers E, Praet J, Vanhoutte G, Palacios RD y, Bigot C, et al. Resting State fMRI Reveals Diminished Functional Connectivity in a Mouse Model of Amyloidosis. PLOS ONE 2013;8:e84241. https://doi.org/10.1371/journal.pone.0084241.

Shah D, Praet J, Latif Hernandez A, Höfling C, Anckaerts C, Bard F, et al. Early pathologic amyloid induces hypersynchrony of BOLD resting-state networks in transgenic mice and provides an early therapeutic window before amyloid plaque deposition. Alzheimers Dement J Alzheimers Assoc 2016;12:964–76. https://doi.org/10.1016/j.jalz.2016.03.010.

Shankar GM, Li S, Mehta TH, Garcia-Munoz A, Shepardson NE, Smith I, et al. Amyloid-beta protein dimers isolated directly from Alzheimer's brains impair synaptic plasticity and memory. Nat Med 2008;14:837–42. https://doi.org/10.1038/nm1782.

Shen J, Kelleher RJ. The presenilin hypothesis of Alzheimer's disease: evidence for a loss-of-function pathogenic mechanism. Proc Natl Acad Sci U S A 2007;104:403–9. https://doi.org/10.1073/pnas.0608332104.

Shiino A, Watanabe T, Maeda K, Kotani E, Akiguchi I, Matsuda M. Four subgroups of Alzheimer's disease based on patterns of atrophy using VBM and a unique pattern for early onset disease. NeuroImage 2006;33:17–26. https://doi.org/10.1016/j.neuroimage.2006.06.010.

Shimada Hiroyuki, Minatani S, Takeuchi J, Takeda A, Kawabe J, Wada Y, et al. Heavy Tau Burden with Subtle Amyloid β Accumulation in the Cerebral Cortex and Cerebellum in a Case of Familial Alzheimer's Disease with APP Osaka Mutation. Int J Mol Sci 2020;21:4443. https://doi.org/10.3390/ijms21124443.

Shu X, Qin Y-Y, Zhang S, Jiang J-J, Zhang Y, Zhao L-Y, et al. Voxel-Based Diffusion Tensor Imaging of an APP/PS1 Mouse Model of Alzheimer's Disease. Mol Neurobiol 2013;48:78–83. https://doi.org/10.1007/s12035-013-8418-6.

Sjogren T, Sjogren H, Lindgren AG. Morbus Alzheimer and morbus Pick; a genetic, clinical and patho-anatomical study. Acta Psychiatr Neurol Scand Suppl 1952;82:1–152.

Sleegers K, Brouwers N, Gijselinck I, Theuns J, Goossens D, Wauters J, et al. APP duplication is sufficient to cause early onset Alzheimer's dementia with cerebral amyloid angiopathy. Brain J Neurol 2006;129:2977–83. https://doi.org/10.1093/brain/awl203.

Smith SM, Jenkinson M, Johansen-Berg H, Rueckert D, Nichols TE, Mackay CE, et al. Tract-based spatial statistics: Voxelwise analysis of multi-subject diffusion data. NeuroImage 2006;31:1487–505. https://doi.org/10.1016/j.neuroimage.2006.02.024.

Smith SM, Jenkinson M, Woolrich MW, Beckmann CF, Behrens TEJ, Johansen-Berg H, et al. Advances in functional and structural MR image analysis and implementation as FSL. NeuroImage 2004;23:S208–19. https://doi.org/10.1016/j.neuroimage.2004.07.051.

Sokolowski K, Corbin JG. Wired for behaviors: from development to function of innate limbic system circuitry. Front Mol Neurosci 2012;5:55. https://doi.org/10.3389/fnmol.2012.00055.

Song M, Zhou Y, Li J, Liu Y, Tian L, Yu C, et al. Brain spontaneous functional connectivity and intelligence. NeuroImage 2008;41:1168–76. https://doi.org/10.1016/j.neuroimage.2008.02.036.

Song S-K, Kim JH, Lin S-J, Brendza RP, Holtzman DM. Diffusion tensor imaging detects age-dependent white matter changes in a transgenic mouse model with amyloid deposition. Neurobiol Dis 2004;15:640–7. https://doi.org/10.1016/j.nbd.2003.12.003.

Sontag J-M, Wasek B, Taleski G, Smith J, Arning E, Sontag E, et al. Altered protein phosphatase 2A methylation and Tau phosphorylation in the young and aged brain of methylenetetrahydrofolate reductase (MTHFR) deficient mice. Front Aging Neurosci 2014;6:214. https://doi.org/10.3389/fnagi.2014.00214.

Spangenberg EE, Green KN. Inflammation in Alzheimer's disease: Lessons learned from microglia-depletion models. Brain Behav Immun 2017;61:1–11. https://doi.org/10.1016/j.bbi.2016.07.003.

Speciale L, Ruzzante S, Calabrese E, Saresella M, Taramelli D, Mariani C, et al. 1-40 Beta-amyloid protein fragment modulates the expression of CD44 and CD71 on the astrocytoma cell line in the presence of IL1beta and TNFalpha. J Cell Physiol 2003;196:190–5. https://doi.org/10.1002/jcp.10295.

Sperling RA, Dickerson BC, Pihlajamaki M, Vannini P, LaViolette PS, Vitolo OV, et al. Functional Alterations in Memory Networks in Early Alzheimer's Disease. Neuromolecular Med 2010;12:27–43. https://doi.org/10.1007/s12017-009-8109-7.

Srinivasan K, Friedman BA, Larson JL, Lauffer BE, Goldstein LD, Appling LL, et al. Untangling the brain's neuroinflammatory and neurodegenerative transcriptional responses. Nat Commun 2016;7:11295. https://doi.org/10.1038/ncomms11295.

Stafford JM, Jarrett BR, Miranda-Dominguez O, Mills BD, Cain N, Mihalas S, et al. Large-scale topology and the default mode network in the mouse connectome. Proc Natl Acad Sci U S A 2014;111:18745–50. https://doi.org/10.1073/pnas.1404346111.

Stam CJ, Jones BF, Nolte G, Breakspear M, Scheltens P. Small-world networks and functional connectivity in Alzheimer's disease. Cereb Cortex N Y N 1991 2007;17:92–9. https://doi.org/10.1093/cercor/bhj127.

Stöhr J, Condello C, Watts JC, Bloch L, Oehler A, Nick M, et al. Distinct synthetic Aβ prion strains producing different amyloid deposits in bigenic mice. Proc Natl Acad Sci 2014;111:10329–34. https://doi.org/10.1073/pnas.1408968111.

Stöhr J, Watts JC, Mensinger ZL, Oehler A, Grillo SK, DeArmond SJ, et al. Purified and synthetic Alzheimer's amyloid beta (Aβ) prions. Proc Natl Acad Sci U S A 2012;109:11025–30. https://doi.org/10.1073/pnas.1206555109.

Suárez-Calvet M, Belbin O, Pera M, Badiola N, Magrané J, Guardia-Laguarta C, et al. Autosomal-dominant Alzheimer's disease mutations at the same codon of amyloid precursor protein differentially alter Aβ production. J Neurochem 2014;128:330–9. https://doi.org/10.1111/jnc.12466.

Sun S-W, Liang H-F, Mei J, Xu D, Shi W-X. In vivo Diffusion Tensor Imaging of Amyloid-β-Induced White Matter Damage in Mice. J Alzheimers Dis JAD 2014;38:93–101. https://doi.org/10.3233/JAD-130236.

Sunde M, Serpell LC, Bartlam M, Fraser PE, Pepys MB, Blake CC. Common core structure of amyloid fibrils by synchrotron X-ray diffraction. J Mol Biol 1997;273:729–39. https://doi.org/10.1006/jmbi.1997.1348.

Supekar K, Menon V, Rubin D, Musen M, Greicius MD. Network analysis of intrinsic functional brain connectivity in Alzheimer's disease. PLoS Comput Biol 2008;4:e1000100. https://doi.org/10.1371/journal.pcbi.1000100.

Syková E, Voříšek I, Antonova T, Mazel T, Meyer-Luehmann M, Jucker M, et al. Changes in extracellular space size and geometry in APP23 transgenic mice: A model of Alzheimer's disease. Proc Natl Acad Sci U S A 2005;102:479–84. https://doi.org/10.1073/pnas.0408235102.

Tai LM, Bilousova T, Jungbauer L, Roeske SK, Youmans KL, Yu C, et al. Levels of soluble apolipoprotein E/amyloid-β (Aβ) complex are reduced and oligomeric Aβ increased with APOE4 and Alzheimer disease in a transgenic mouse model and human samples. J Biol Chem 2013;288:5914–26. https://doi.org/10.1074/jbc.M112.442103.

Tambini MD, Norris KA, D'Adamio L. Opposite changes in APP processing and human Aβ levels in rats carrying either a protective or a pathogenic APP mutation. ELife 2020;9:e52612. https://doi.org/10.7554/eLife.52612.

Teipel SJ, Grothe MJ, Filippi M, Fellgiebel A, Dyrba M, Frisoni GB, et al. Fractional anisotropy changes in Alzheimer's disease depend on the underlying fiber tract architecture: a multiparametric DTI study using joint independent component analysis. J Alzheimers Dis JAD 2014;41:69–83. https://doi.org/10.3233/JAD-131829.

Terry RD, Masliah E, Salmon DP, Butters N, DeTeresa R, Hill R, et al. Physical basis of cognitive alterations in alzheimer's disease: Synapse loss is the major correlate of cognitive impairment. Ann Neurol 1991;30:572–80. https://doi.org/10.1002/ana.410300410.

Thal DR, Rüb U, Orantes M, Braak H. Phases of Aβ-deposition in the human brain and its relevance for the development of AD. Neurology 2002;58:1791–800. https://doi.org/10.1212/WNL.58.12.1791.

Thal DR, Walter J, Saido TC, Fändrich M. Neuropathology and biochemistry of Aβ and its aggregates in Alzheimer's disease. Acta Neuropathol (Berl) 2015;129:167–82. https://doi.org/10.1007/s00401-014-1375-y.

Thiessen ED. Effects of Visual Information on Adults' and Infants' Auditory Statistical Learning. Cogn Sci 2010;34:1093–106. https://doi.org/10.1111/j.1551-6709.2010.01118.x.

Thijssen EH, La Joie R, Wolf A, Strom A, Wang P, Iaccarino L, et al. Diagnostic value of plasma phosphorylated tau181 in Alzheimer's disease and frontotemporal lobar degeneration. Nat Med 2020;26:387–97. https://doi.org/10.1038/s41591-020-0762-2.

Thomas Yeo BT, Krienen FM, Sepulcre J, Sabuncu MR, Lashkari D, Hollinshead M, et al. The organization of the human cerebral cortex estimated by intrinsic functional connectivity. J Neurophysiol 2011;106:1125–65. https://doi.org/10.1152/jn.00338.2011.

Tian Q, Wang J. Role of serine/threonine protein phosphatase in Alzheimer's disease. Neurosignals 2002;11:262–9. https://doi.org/10.1159/000067425.

Tomic JL, Pensalfini A, Head E, Glabe CG. Soluble fibrillar oligomer levels are elevated in Alzheimer's disease brain and correlate with cognitive dysfunction. Neurobiol Dis 2009;35:352–8. https://doi.org/10.1016/j.nbd.2009.05.024.

Tomiyama T, Matsuyama S, Iso H, Umeda T, Takuma H, Ohnishi K, et al. A mouse model of amyloid beta oligomers: their contribution to synaptic alteration, abnormal tau phosphorylation, glial activation, and neuronal loss in vivo. J Neurosci Off J Soc Neurosci 2010;30:4845–56. https://doi.org/10.1523/JNEUROSCI.5825-09.2010.

Tomiyama T, Nagata T, Shimada H, Teraoka R, Fukushima A, Kanemitsu H, et al. A new amyloid beta variant favoring oligomerization in Alzheimer's-type dementia. Ann Neurol 2008;63:377–87. https://doi.org/10.1002/ana.21321.

Tomiyama T, Shimada H. APP Osaka Mutation in Familial Alzheimer's Disease—Its Discovery, Phenotypes, and Mechanism of Recessive Inheritance. Int J Mol Sci 2020;21:1413. https://doi.org/10.3390/ijms21041413.

Tournier J-D, Yeh C-H, Calamante F, Cho K-H, Connelly A, Lin C-P. Resolving crossing fibres using constrained spherical deconvolution: Validation using diffusion-weighted imaging phantom data. NeuroImage 2008;42:617–25. https://doi.org/10.1016/j.neuroimage.2008.05.002.

Tremblay JP, Tremblay G, Guyon A, Joël R, Happi-Mbakam C. Insertion of the Icelandic mutation (A673T) in the APP gene using the CRISPR/Cas9 base editing and Prime editing technologies, a preventive treatment for Alzheimer? Alzheimers Dement 2021;17:e058710. https://doi.org/10.1002/alz.058710.

Tuch DS, Reese TG, Wiegell MR, Makris N, Belliveau JW, Wedeen VJ. High angular resolution diffusion imaging reveals intravoxel white matter fiber heterogeneity. Magn Reson Med 2002;48:577–82. https://doi.org/10.1002/mrm.10268.

Tustison NJ, Cook PA, Klein A, Song G, Das SR, Duda JT, et al. Large-scale evaluation of ANTs and FreeSurfer cortical thickness measurements. NeuroImage 2014;99:166–79. https://doi.org/10.1016/j.neuroimage.2014.05.044.

Tv B, Gl C. A synaptic model of memory: long-term potentiation in the hippocampus. Nature 1993;361. https://doi.org/10.1038/361031a0.

Ueno M, Chiba Y, Matsumoto K, Nakagawa T, Miyanaka H. Clearance of beta-amyloid in the brain. Curr Med Chem 2014;21:4085–90. https://doi.org/10.2174/09298673216614101194256.

Ulm BS, Borchelt DR, Moore BD. Remodeling Alzheimer-amyloidosis models by seeding. Mol Neurodegener 2021;16:8. https://doi.org/10.1186/s13024-021-00429-4.

Ulrich JD, Ulland TK, Colonna M, Holtzman DM. Elucidating the Role of TREM2 in Alzheimer's Disease. Neuron 2017;94:237–48. https://doi.org/10.1016/j.neuron.2017.02.042.

Umeda T, Kimura T, Yoshida K, Takao K, Fujita Y, Matsuyama S, et al. Mutation-induced loss of APP function causes GABAergic depletion in recessive familial Alzheimer's disease: analysis of Osaka mutation-knockin mice. Acta Neuropathol Commun 2017;5:59. https://doi.org/10.1186/s40478-017-0461-5.

Valacyclovir | ALZFORUM. n.d. https://www.alzforum.org/therapeutics/valacyclovir (accessed December 6, 2022).

Van Broeckhoven C, Haan J, Bakker E, Hardy JA, Van Hul W, Wehnert A, et al. Amyloid beta protein precursor gene and hereditary cerebral hemorrhage with amyloidosis (Dutch). Science 1990;248:1120–2. https://doi.org/10.1126/science.1971458.

Van der Jeugd A, Hochgräfe K, Ahmed T, Decker JM, Sydow A, Hofmann A, et al. Cognitive defects are reversible in inducible mice expressing pro-aggregant full-length human Tau. Acta Neuropathol (Berl) 2012;123:787–805. https://doi.org/10.1007/s00401-012-0987-3.

van de Ven VG, Formisano E, Prvulovic D, Roeder CH, Linden DEJ. Functional connectivity as revealed by spatial independent component analysis of fMRI measurements during rest. Hum Brain Mapp 2004;22:165–78. https://doi.org/10.1002/hbm.20022.

Verkhratsky A, Olabarria M, Noristani HN, Yeh C-Y, Rodriguez JJ. Astrocytes in Alzheimer's disease. Neurother J Am Soc Exp Neurother 2010;7:399–412. https://doi.org/10.1016/j.nurt.2010.05.017.

Viana da Silva S, Haberl MG, Zhang P, Bethge P, Lemos C, Gonçalves N, et al. Early synaptic deficits in the APP/PS1 mouse model of Alzheimer's disease involve neuronal adenosine A2A receptors. Nat Commun 2016;7:11915. https://doi.org/10.1038/ncomms11915.

Villemagne VL, Pike KE, Darby D, Maruff P, Savage G, Ng S, et al. Abeta deposits in older non-demented individuals with cognitive decline are indicative of preclinical Alzheimer's disease. Neuropsychologia 2008;46:1688–97. https://doi.org/10.1016/j.neuropsychologia.2008.02.008.

Vossel S, Geng JJ, Fink GR. Dorsal and Ventral Attention Systems. The Neuroscientist 2014;20:150–9. https://doi.org/10.1177/1073858413494269.

Walker LC. Aβ Plaques. Free Neuropathol 2020;1:31. https://doi.org/10.17879/freeneuropathology-2020-3025.

Walker LC, Schelle J, Jucker M. The Prion-Like Properties of Amyloid-β Assemblies: Implications for Alzheimer's Disease. Cold Spring Harb Perspect Med 2016;6:a024398. https://doi.org/10.1101/cshperspect.a024398.

Wang H, Kulas JA, Wang C, Holtzman DM, Ferris HA, Hansen SB. Regulation of beta-amyloid production in neurons by astrocyte-derived cholesterol. Proc Natl Acad Sci 2021;118:e2102191118. https://doi.org/10.1073/pnas.2102191118.

Wang W, Yang Y, Ying C, Li W, Ruan H, Zhu X, et al. Inhibition of glycogen synthase kinase-3β protects dopaminergic neurons from MPTP toxicity. Neuropharmacology 2007;52:1678–84. https://doi.org/10.1016/j.neuropharm.2007.03.017.

Ward A, Tardiff S, Dye C, Arrighi HM. Rate of Conversion from Prodromal Alzheimer's Disease to Alzheimer's Dementia: A Systematic Review of the Literature. Dement Geriatr Cogn Disord Extra 2013;3:320–32. https://doi.org/10.1159/000354370.

Watts JC, Condello C, Stöhr J, Oehler A, Lee J, DeArmond SJ, et al. Serial propagation of distinct strains of Aβ prions from Alzheimer's disease patients. Proc Natl Acad Sci U S A 2014;111:10323–8. https://doi.org/10.1073/pnas.1408900111.

Whalen BM, Selkoe DJ, Hartley DM. Small non-fibrillar assemblies of amyloid β-protein bearing the Arctic mutation induce rapid neuritic degeneration. Neurobiol Dis 2005;20:254–66. https://doi.org/10.1016/j.nbd.2005.03.007.

Whitehouse PJ, Price DL, Struble RG, Clark AW, Coyle JT, Delon MR. Alzheimer's disease and senile dementia: loss of neurons in the basal forebrain. Science 1982;215:1237–9. https://doi.org/10.1126/science.7058341.

Whitesell JD, Liska A, Coletta L, Hirokawa KE, Bohn P, Williford A, et al. Regional, Layer, and Cell-Type-Specific Connectivity of the Mouse Default Mode Network. Neuron 2021;109:545-559.e8. https://doi.org/10.1016/j.neuron.2020.11.011.

Whitson JS, Selkoe DJ, Cotman CW. Amyloid beta protein enhances the survival of hippocampal neurons in vitro. Science 1989;243:1488–90. https://doi.org/10.1126/science.2928783.

Whitwell JL. Alzheimer's disease neuroimaging. Curr Opin Neurol 2018;31:396–404. https://doi.org/10.1097/WCO.0000000000000570.

Winkler EA, Sagare AP, Zlokovic BV. The pericyte: a forgotten cell type with important implications for Alzheimer's disease? Brain Pathol Zurich Switz 2014;24:371–86. https://doi.org/10.1111/bpa.12152.

Wu J, Anwyl R, Rowan MJ. beta-Amyloid-(1-40) increases long-term potentiation in rat hippocampus in vitro. Eur J Pharmacol 1995;284:R1-3. https://doi.org/10.1016/0014-2999(95)00539-w.

Wu Y-C, Mustafi SM, Harezlak J, Kodiweera C, Flashman LA, McAllister TW. Hybrid Diffusion Imaging in Mild Traumatic Brain Injury. J Neurotrauma 2018;35:2377–90. https://doi.org/10.1089/neu.2017.5566.

Xiong Y, Ye C, Chen Y, Zhong X, Chen H, Sun R, et al. Altered Functional Connectivity of Basal Ganglia in Mild Cognitive Impairment and Alzheimer's Disease. Brain Sci 2022;12:1555. https://doi.org/10.3390/brainsci12111555.

Yang HD, Kim DH, Lee SB, Young LD. History of Alzheimer's Disease. Dement Neurocognitive Disord 2016;15:115. https://doi.org/10.12779/dnd.2016.15.4.115.

Yang M, Teplow DB. Amyloid beta-protein monomer folding: free-energy surfaces reveal alloform-specific differences. J Mol Biol 2008;384:450–64. https://doi.org/10.1016/j.jmb.2008.09.039.

Yang T, Li S, Xu H, Walsh DM, Selkoe DJ. Large Soluble Oligomers of Amyloid β-Protein from Alzheimer Brain Are Far Less Neuroactive Than the Smaller Oligomers to Which They Dissociate. J Neurosci Off J Soc Neurosci 2017;37:152–63. https://doi.org/10.1523/JNEUROSCI.1698-16.2016.

Yang Y-W, Liou S-H, Hsueh Y-M, Lyu W-S, Liu C-S, Liu H-J, et al. Risk of Alzheimer's disease with metal concentrations in whole blood and urine: A case–control study using propensity score matching. Toxicol Appl Pharmacol 2018;356:8–14. https://doi.org/10.1016/j.taap.2018.07.015.

Ye L, Hamaguchi T, Fritschi SK, Eisele YS, Obermüller U, Jucker M, et al. Progression of Seed-Induced Aβ Deposition within the Limbic Connectome. Brain Pathol Zurich Switz 2015;25:743–52. https://doi.org/10.1111/bpa.12252.

Yeh FL, Hansen DV, Sheng M. TREM2, Microglia, and Neurodegenerative Diseases. Trends Mol Med 2017;23:512–33. https://doi.org/10.1016/j.molmed.2017.03.008.

Yeh FL, Wang Y, Tom I, Gonzalez LC, Sheng M. TREM2 Binds to Apolipoproteins, Including APOE and CLU/APOJ, and Thereby Facilitates Uptake of Amyloid-Beta by Microglia. Neuron 2016;91:328–40. https://doi.org/10.1016/j.neuron.2016.06.015.

Yuan P, Condello C, Keene CD, Wang Y, Bird TD, Paul SM, et al. TREM2 Haplodeficiency in Mice and Humans Impairs the Microglia Barrier Function Leading to Decreased Amyloid Compaction and Severe Axonal Dystrophy. Neuron 2016;90:724–39. https://doi.org/10.1016/j.neuron.2016.05.003.

Yuede CM, Lee H, Restivo JL, Davis TA, Hettinger JC, Wallace CE, et al. Rapid in vivo measurement of β-amyloid reveals biphasic clearance kinetics in an Alzheimer's mouse model. J Exp Med 2016;213:677–85. https://doi.org/10.1084/jem.20151428.

Yuste R, Bonhoeffer T. Morphological changes in dendritic spines associated with long-term synaptic plasticity. Annu Rev Neurosci 2001;24:1071–89. https://doi.org/10.1146/annurev.neuro.24.1.1071.

Zempel H, Mandelkow E. Lost after translation: missorting of Tau protein and consequences for Alzheimer disease. Trends Neurosci 2014;37:721–32. https://doi.org/10.1016/j.tins.2014.08.004.

Zerbi V, Grandjean J, Rudin M, Wenderoth N. Mapping the mouse brain with rs-fMRI: An optimized pipeline for functional network identification. NeuroImage 2015;123:11–21. https://doi.org/10.1016/j.neuroimage.2015.07.090.

Zerbi V, Kleinnijenhuis M, Fang X, Jansen D, Veltien A, Van Asten J, et al. Gray and white matter degeneration revealed by diffusion in an Alzheimer mouse model. Neurobiol Aging 2013;34:1440–50. https://doi.org/10.1016/j.neurobiolaging.2012.11.017.

Zerbi V, Wiesmann M, Emmerzaal TL, Jansen D, Van Beek M, Mutsaers MPC, et al. Resting-State Functional Connectivity Changes in Aging apoE4 and apoE-KO Mice. J Neurosci 2014;34:13963–75. https://doi.org/10.1523/JNEUROSCI.0684-14.2014.

Zetterberg H. Plasma amyloid β—quo vadis? Neurobiol Aging 2015;36:2671–3. https://doi.org/10.1016/j.neurobiolaging.2015.07.021.

Zhang F, Zhong R, Qi H, Li S, Cheng C, Liu X, et al. Impacts of Acute Hypoxia on Alzheimer's Disease-Like Pathologies in APPswe/PS1dE9 Mice and Their Wild Type Littermates. Front Neurosci 2018;12:314. https://doi.org/10.3389/fnins.2018.00314.

Zhang G, Xie Y, Wang W, Feng X, Jia J. Clinical characterization of an APP mutation (V717I) in five Han Chinese families with early-onset Alzheimer's disease. J Neurol Sci 2017;372:379–86. https://doi.org/10.1016/j.jns.2016.10.039.

Zhang W, Lv J, Li X, Zhu D, Jiang X, Zhang S, et al. Experimental Comparisons of Sparse Dictionary Learning and Independent Component Analysis for Brain Network Inference From fMRI Data. IEEE Trans Biomed Eng 2019;66:289–99. https://doi.org/10.1109/TBME.2018.2831186.

Zheng X, Liu D, Roychaudhuri R, Teplow DB, Bowers MT. Amyloid β-Protein Assembly: Differential Effects of the Protective A2T Mutation and Recessive A2V Familial Alzheimer's Disease Mutation. ACS Chem Neurosci 2015;6:1732–40. https://doi.org/10.1021/acschemneuro.5b00171.

Zhou J, Greicius MD, Gennatas ED, Growdon ME, Jang JY, Rabinovici GD, et al. Divergent network connectivity changes in behavioural variant frontotemporal dementia and Alzheimer's disease. Brain J Neurol 2010;133:1352–67. https://doi.org/10.1093/brain/awq075.

Zhu B, Liu Y, Hwang S, Archuleta K, Huang H, Campos A, et al. Trem2 deletion enhances tau dispersion and pathology through microglia exosomes. Mol Neurodegener 2022;17:58. https://doi.org/10.1186/s13024-022-00562-8.

Zlokovic BV. Neurovascular pathways to neurodegeneration in Alzheimer's disease and other disorders. Nat Rev Neurosci 2011;12:723–38. https://doi.org/10.1038/nrn3114.

ANNEXES

ANNEXE I – PUBLICATIONS

Pérot JB., **CELESTINE M.**, Palombo M., Dhenain M., Humbert S., Brouillet E., Flament J. Longitudinal multimodal MRI characterization of a knock-in mouse model of Huntington's disease reveals early grey and white matter alterations. Human Molecular Genetics. 2022
https://doi.org/10.1093/hmg/ddac036

OXFORD

Human Molecular Genetics, 2022, Vol. 31, 21, 3581–3596
https://doi.org/10.1093/hmg/ddac036
Advance access publication date 11 February 2022
Original Article

Longitudinal multimodal MRI characterization of a knock-in mouse model of Huntington's disease reveals early gray and white matter alterations

Jean-Baptiste Pérot[1], Marina Célestine[1], Marco Palombo[2], Marc Dhenain[1], Sandrine Humbert[3], Emmanuel Brouillet[1] and Julien Flament[1,*]

[1]Laboratoire des Maladies Neurodégénératives, Molecular Imaging Research Center (MIRCen), Université Paris-Saclay, Commissariat à l'Energie Atomique et aux Energies Alternatives (CEA), Centre National de la Recherche Scientifique (CNRS), Fontenay -aux-Roses 92260, France
[2]Department of Computer Science, Centre for Medical Image Computing, University College London, London WC1E 6BT, UK
[3]Université Grenoble Alpes, INSERM, U1216, Grenoble Institut Neurosciences, Grenoble 38000 , France

*To whom correspondence should be addressed. Tel: +33 146548146; Email: julien.flament@cea.fr

Abstract

Pathogenesis of the inherited neurodegenerative disorder Huntington's disease (HD) is progressive with a long presymptomatic phase in which subtle changes occur up to 15 years before the onset of symptoms. Thus, there is a need for early, functional biomarker to better understand disease progression and to evaluate treatment efficacy far from onset. Recent studies have shown that white matter may be affected early in mutant HTT gene carriers. A previous study performed on 12 months old Ki140CAG mice showed reduced glutamate level measured by Chemical Exchange Saturation Transfer of glutamate (gluCEST), especially in the corpus callosum. In this study, we scanned longitudinally Ki140CAG mice with structural MRI, diffusion tensor imaging, gluCEST and magnetization transfer imaging, in order to assess white matter integrity over the life of this mouse model characterized by slow progression of symptoms. Our results show early defects of diffusion properties in the anterior part of the corpus callosum at 5 months of age, preceding gluCEST defects in the same region at 8 and 12 months that spread to adjacent regions. At 12 months, frontal and piriform cortices showed reduced gluCEST, as well as the pallidum. MT imaging showed reduced signal in the septum at 12 months. Cortical and striatal atrophy then appear at 18 months. Vulnerability of the striatum and motor cortex, combined with alterations of anterior corpus callosum, seems to point out the potential role of white matter in the brain dysfunction that characterizes HD and the pertinence of gluCEST and DTI as biomarkers in HD.

Introduction

Huntington's disease (HD) is an inherited neurodegenerative disease characterized by a triad of symptoms. While the disease is well known for its most prominent motor symptoms (chorea, dyskinesia and dystonia), many non-motor manifestations also occur early including olfactory deficits, sleep disorders, psychiatric signs such as depression, perturbation of emotivity and irritability. Cognitive deficits are also observed including loss of mental flexibility/adaptation and defective procedural memory (1). Despite tremendous efforts made, there is currently no therapy to cure the disease or to slow its progression, resulting in a fatal outcome 10–15 years after the onset of symptoms in young individuals. The disease is caused by a mutation consisting of an abnormal expansion of CAG repeats in the exon 1 of the HTT gene coding the protein huntingtin (htt) (2). This leads to an expansion of a poly-glutamine tract in the N-terminal part of the protein. Mutant htt (m-htt) is toxic to brain cells through combination of gain and loss of function mechanisms (3).

Non-motor manifestations in m-HTT gene carriers are among the earliest to occur and are very disabling features in young individuals. Several studies suggested that they could occur many years before the onset of the motor symptoms of the disease (4,5). However, these manifestations can be highly variable from one patient to the other and their use as clinical readouts for future treatment evaluation is difficult, as it requires large cohort sizes. Similarly, the intra- and inter-subject variability of motor symptoms, although lower than that of non-motor signs, also limits their use to monitor disease progression (6,7).

In addition to symptoms, neuroimaging methods likely represent a crucial non-invasive approach to characterize in a quantitative manner the progression of the disease at the individual level. The preferential atrophy and dysfunction of the striatum first evidenced as the

Received: July 23, 2021. **Revised:** January 19, 2022. **Accepted:** January 31, 2022

most striking neuropathological finding in post-mortem HD brain samples (8,9) was confirmed more than two decades ago by founding studies using CT, MRI and PET scanners even in patients at early stages of the disease (10,11). Recent work showed that the atrophy of the striatum as measured by MRI is currently the best biomarker of disease progression in HD gene carriers (12,13). However, despite a good correlation between striatal atrophy and disease severity (14), atrophy provides only limited information about HD pathogenesis and is probably the long-term consequence of subtle biological modifications that occur many years before macroscopic alterations. In addition, numerous studies suggested that volume alterations could occur simultaneously in several other brain structures such as cortical and subcortical regions (15,16) as well as white matter (WM) (17,18). Therefore, focusing only on striatal atrophy is too limiting to capture the extent of different biological processes involved in HD. Thus, there is a need to find more predictive, functional and earlier biomarkers for a better understanding of disease pathogenesis and to monitor its progression. Moreover, in the perspective of future therapeutic interventions aiming at slowing down disease progression before onset of disabling symptoms, such biomarkers would be extremely useful to evaluate drug engagement and biological efficacy.

Interestingly, recent studies pointed out early alterations of WM and fiber tracks in HD concomitantly with atrophy measured in gray matter (GM) (17,19). Furthermore, longitudinal studies performed in large cohorts of HD gene carriers such as TRACK-HD identified a good correlation between atrophy measured in frontal and posterior WM and disease progression in presymptomatic HD patients (14,20). Early WM changes have also been reported in animal models of HD where anomalies of WM tracks were found using MRI (21,22). In addition, the presence of m-htt in oligodendrocytes of knock-in mice has been shown to lead to abnormal myelination and apparition of neurological symptoms (23,24). Although WM changes have been considered as a consequence of GM loss for many years, numerous studies provided strong evidence of the major role of WM alterations in HD physiopathology, independently of neuronal cell loss (25–27). Therefore, WM modifications might be one of the early hallmarks of the disease and could constitute a key biomarker, especially during the presymptomatic phase of the disease.

Further investigations are needed to characterize WM changes induced by HD pathological processes, and neuroimaging methods can provide valuable tools to address this question. MRI can be used to assess non-invasively several aspects of the pathology, going from neuro-metabolic modifications to macrostructural changes.

Numerous studies have used diffusion tensor imaging (DTI) to analyze WM modifications (28). Quantitative indexes such as fractional anisotropy (FA), mean diffusivity (MD), radial diffusivity (RD, diffusivity perpendicular to axonal fibers) and axial diffusivity (AD, diffusivity along axonal fibers) can be derived to assess microstructural properties of WM (29). FA describes the degree of anisotropy within a voxel so a decrease of FA value represents a loss of tissue organization that can be associated with alteration of cellular integrity (30). AD and RD are usually considered to be increased in pathological conditions due respectively to axonal degeneration and demyelinating processes (31). However, several studies have shown inconsistent results in the context of HD so interpretation of these variations remains ambiguous (27,32,33). Such heterogeneity may be explained by the variability of symptoms within HD patients or due to different characteristics of animal models.

Complementarily to diffusion MRI, magnetization transfer (MT) imaging can capture changes of macromolecular content of tissues with a good spatial resolution, especially myelin content (34). The MT contrast relies on decrease of water signal intensity due to exchange of magnetization between fast exchanging protons bound to macromolecules and free water after an off-resonance radio frequency (RF) pulse (35). This method has been shown to be sensitive to myelin concentration with a good specificity and several studies used it to explore both WM and GM changes in HD patients (36,37).

In vivo ^{1}H magnetic resonance spectroscopy (^{1}H-MRS) can monitor alterations of metabolic profiles, providing key biological insights of pathological pathways involved in different cell types (38,39). Previous studies demonstrated metabolic changes that occur in the brain of either human HD patients or transgenic mouse models of HD (40–42). In particular, decreased concentrations of N-acetyl-aspartate (NAA) and glutamate (Glu), two metabolites mainly located in neurons, were measured in HD patients and animal models (43). Other metabolite concentrations such as glutamine (Gln), myo-inositol (Ins) and choline (Cho) have been reported to be altered in HD mouse models, even if variations were not consistently reported depending on the model (44,45). However, in spite of the rich biological information provided by ^{1}H-MRS, this method suffers from its inherently low sensitivity. Measurement of metabolic profiles within small and thin structures such as the corpus callosum would be very difficult without strong contamination by surrounding structures.

Recently, chemical exchange saturation transfer (CEST) has been proposed to address this limitation by using indirect detection of dilute molecules through their exchange of labile protons with the bulk water (46–48). Exchangeable protons such as amine (-NH_2) or amide (-NH) exhibit a resonance frequency that is shifted from the water resonance frequency so they can be selectively saturated using RF pulse. The decrease of water signal due to magnetization exchange being directly correlated to the concentration of exchanging protons, it is possible to map the spatial distribution of the molecule of interest. Several studies already

demonstrated the potential of CEST imaging to map glutamate with a good spatial resolution in both rodent and human brains (49–51), including in the context of HD (52).

The Ki140CAG mouse model (53) is a knock-in model of HD containing 140 CAG repeats inserted in the murine huntingtin gene. It is characterized by the slowly progressive appearance of the symptoms and is considered to mimic more closely clinical form of HD than severe and rapid mouse models (53,54). These mice present early locomotor abnormalities and huntingtin aggregates in the striatum as early as 4 months of age (53). Homozygous mice for the HTT gene present early impairments of motor functions, such as hypokinesia at 4 months of age and reduced performances in rotarod test (55). In a recent study performed on heterozygous and homozygous Ki140CAG mice, we showed a progression of the severity of locomotor activity defects with genotype when compared to age-matched wild-type littermates (52). Previously, we detected early brain changes using neuroimaging in this model. Structural MRI revealed significant striatal atrophy at 12 months of age in small cohorts of homozygous mice (52). ^{1}H-MRS in the same mice showed metabolic modifications including reduced levels of taurine and NAA in the striatum, in both homozygous and heterozygous Ki140CAG mice. Concentration of Glu was also found to be reduced while Gln was increased. These alterations were associated with a decrease of gluCEST signal in the striatum and piriform cortex of homozygous mice. Surprisingly, the most affected structure was the corpus callosum in both heterozygous and homozygous mice, suggesting that this structure was very early affected in this mouse model. However, whereas all changes we observed tended to be stronger in homozygous than in heterozygous Ki140CAG mice, they were obtained only at one age, so that the progression of the disease in this model remained to be investigated.

In the present study, we developed a multimodal MRI protocol combining anatomical, diffusion weighted, gluCEST and MT imaging in order to monitor longitudinally Ki140CAG mice and their wild-type (WT) littermates. Indeed, multimodal MRI characterization provides complementary and mutually relevant insights to probe several aspects of disease progression and to better understand physiopathology of HD. Data pointed toward early changes affecting the function and tissue organization of different extra-striatal brain regions providing new insights on the progression of brain perturbations in this slowly progressive model of HD that could be reminiscent of those occurring in m-HTT human gene carriers.

Results

Long-term and evolving cortico-striatal atrophy in Ki140CAG mice

The mean volume of each of the 34 brain regions was calculated at each timepoint for WT littermates and Ki140CAG mice. Volume variation between mice groups was calculated for all brain structures and reported in a variation map in order to highlight hypertrophied (shades of pink) and atrophied (shades of green) structures (Fig. 1, variation expressed in percentage referred to WT littermates). At 18 months, significant atrophy of the striatum (−4.3%, $P < 0.05$), frontal cortex (−5.3%, $P < 0.01$), retrosplenial cortex (−5.8%, $P < 0.05$) and motor cortex (−3.3%, $P < 0.05$) was measured in Ki140CAG mice (Fig. 1, last column). At earlier timepoints, we saw a clear trend toward cerebral atrophy particularly in cortical regions in association with dilation of ventricles that reached statistical significance at 18 months (+9.0%, $P < 0.05$). Although volume variations were not significant, the atrophy trend seemed increased with aging.

Early deficiencies of cortico-striatal pathway revealed by metabolic imaging

Variations of mean gluCEST contrast (Fig. 2A, increase of gluCEST contrast in shades of red, decrease in shades of blue) measured in each brain region at each timepoint were calculated between Ki140CAG mice and WT littermates and reported on a variation map. The most affected structure in Ki140CAG mice was the corpus callosum (CC) where a significant decrease of gluCEST contrast was measured at 8 and 12 months (−10.8%, $P < 0.05$ and −19%, $P < 0.01$, respectively, Fig. 2A). The time courses of MTRasym measured in WT and Ki140CAG mice were shown for this particular structure (Fig. 2B). Significant decreases of gluCEST contrast were also measured in the frontal (−7.3%, $P < 0.05$) and piriform (−16.7%, $P < 0.05$) cortices and in the pallidum (−21.0%, $P < 0.05$) of Ki140CAG mice at 12 months, confirming our previous results acquired in this mouse model (52). A non-significant decrease of gluCEST contrast (−12%, $P = 0.12$) was measured in the striatum of 12 months old mice, as already reported in heterozygous Ki140CAG mice.

Similar maps of MT contrast variations (Fig. 3, increase of MT contrast in shades of orange, decrease in shades of purple) revealed significant decrease of MT contrast in the septum (Fig. 3, −21.7%, $P < 0.05$) and a trend in the striatum (−12.5%, $P = 0.12$) at 12 months only.

Surprisingly, at 18 months, neither gluCEST nor MT imaging showed significant variation of MTRasym values between WT littermates and Ki140CAG mice. This could be attributed to normal aging of control mice with the decrease of gluCEST and MT contrast for those mice (56).

Alteration of structural connectivity and microstructure in Ki140CAG mice

Microstructural properties and neuronal fiber integrity were investigated using DTI. Variations of FA, AD and RD between HD and WT mice were calculated and showed for the anterior brain slices (Fig. 4, increase of FA, AD or RD in shades of brown, decrease in shades of cyan). Despite a clear tendency of decreased FA, AD and RD

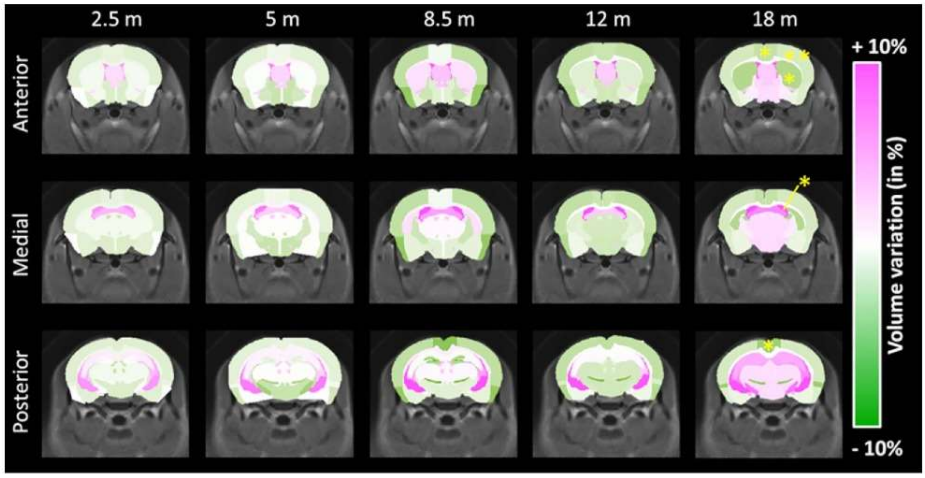

Figure 1. Volume variation maps between WT and Ki140CAG mice, at each timepoint, on three slices of the mouse brain, overlaid on the study template. Hypertrophied structures are reported in shades of pink and atrophied structures in shades of green. Yellow stars represent significant atrophy (RM-ANOVA + Bonferroni, *$P < 0.05$, **$P < 0.01$).

values over time in Ki140CAG in most of GM structures, no variation reached statistical significance.

We hypothesized that the relevance of atlas-based approach might be limiting for examination of the WM. Indeed, due to small CC thickness and imprecise realignment of WM structures, atlas-based analysis was not able to detect any change. Interestingly, both HD and WT groups showed increase of FA values during the first 8 months and then reached a plateau (Fig. 5A). Nonetheless, both time courses were not identical and a delay of FA increase was observed in Ki140CAG mice. Consequently, we performed tract-based spatial statistics (TBSS) (57) analysis to improve DTI data analysis for WM structures. Thanks to TBSS approach, several clusters of voxels with significant decrease of FA values were identified in the anterior CC of Ki140CAG mice as early as 5 months (Fig. 5B). Clusters of reduced FA values were also observed in the anterior CC at 8 and 12 months in very precise locations confirming the local alteration of the anterior CC that could not be detected with atlas-based approach.

Integration of affected structures within anatomical networks

In order to further explore the importance of the connections between brain regions, we analyzed our results using the Allen Connectivity Atlas (58). Precisely, the matrix assessing the normalized strength of axonal projections between all the regions of the mouse brain, available from Oh *et al.* (58), was represented using graph theory. Figure 6 represents physical connections in the mouse brain as derived from Oh *et al.* (58) as a network of structures linked with axonal projections. Nodes represent mouse brain structures as presented in the Allen Connectivity Atlas. The size of each node represents the connectivity degree of each structure with surrounding structures. Arrows' size represents the value of normalized projection from one structure to another as reported in the Allen Connectivity Atlas. Position of the regions was determined in an unbiased way by force atlas algorithm. Large structures, similar to those we used in our MRI atlas, were identified in this graph (Fig. 6, encircled areas). Interestingly, the striatum showed high degree of connectivity and is central in the graph, showing its importance in terms of connections with surrounding structures such as frontal cortex, motor cortex or pallidum. In order to summarize findings of this study, we superimposed on this network all structures that were found to be altered in one of the MRI modalities (Fig. 6, in blue for gluCEST defects, violet for MT defects and green for atrophy). One can observe that the striatum exhibited alteration in the three modalities. Colored arrows, representing projection from an affected region, seem to highlight cortico-striatal connections. This representation merging brain connectivity and altered regions identified using our multimodal MRI approach indicates that damaged/dysfunctional structures/pathways in the HD model belong to a relevant anatomical network.

Discussion

Ki140CAG as a slowly progressive mouse model of HD

Knock-in models of HD, especially the Ki140CAG model, have been designed and generated through homologous

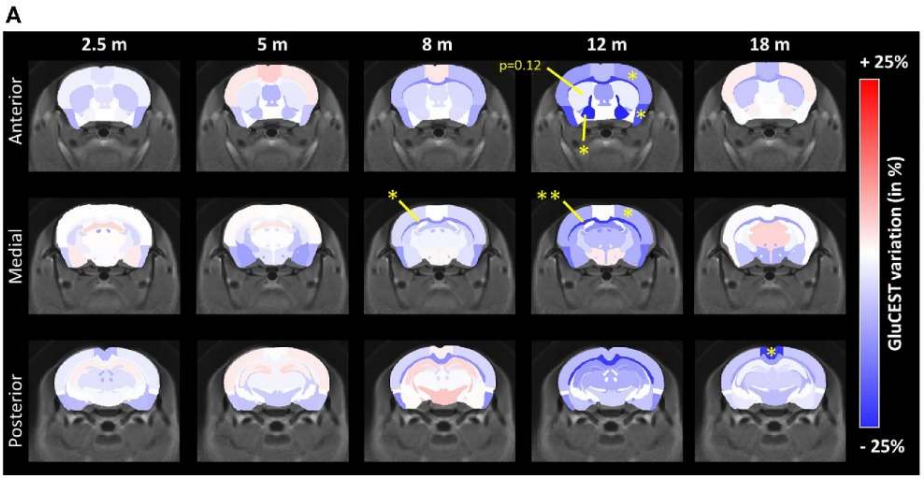

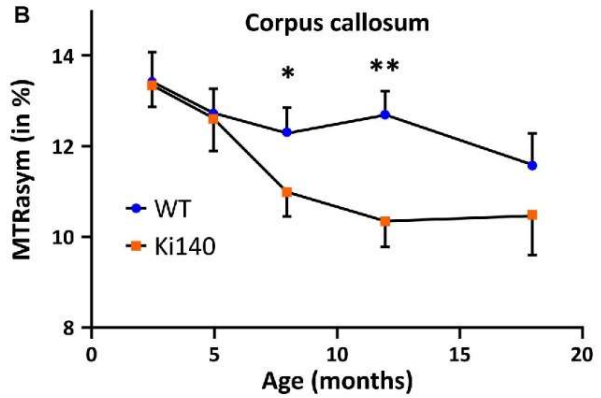

Figure 2. (**A**) GluCEST variation maps between WT and Ki140CAG mice, at each timepoint, on three slices of the mouse brain, overlaid on the study template. Structures with increased gluCEST contrast are reported in shades of red and structures with decreased gluCEST contrast in shades of blue. Yellow stars represent significant difference (RM-ANOVA + Bonferroni, *$P < 0.05$, **$P < 0.01$). (**B**) MTRasym measured in CC of WT and Ki140CAG mice as a function of time (blue dots and orange squares, respectively, mean ± SEM).

recombination to faithfully replicate the human genetic defect in the mouse HdH gene. This model, along other knock-in models, is characterized by a mild progression of the disease, as compared to transgenic models where a short fragment of the mutant human HTT gene is inserted randomly in the mouse genome (e.g. R6/2, R6/1 and 171-82Q mice) (54,59). The Ki140CAG model has already been characterized by slow progression of locomotor performances, behavioral, cellular and molecular abnormalities associated with neurodegeneration (53). Moreover, we demonstrated in a previous study that both heterozygous and homozygous Ki140CAG mice exhibit a significant alteration of their metabolic profiles in the striatum as compared to WT littermate controls at 12 months of age. More interestingly, gluCEST imaging revealed that the CC is the most affected structure in both genotypes, suggesting that this structure is preferentially affected in HD and might play a major role in the physiopathology of the disease as suggested by our previous study (52). However, this study only focused on 12-month-old mice, while numerous studies demonstrated that variations of MRI/MRS indexes or biomarkers are not constant overtime (60). Consequently, we thought it was crucial to characterize these changes longitudinally to identify the most relevant biomarkers to monitor disease progression. Indeed, such biomarkers could be of high value to assess the efficacy of experimental therapeutics over time in preclinical trials in genetic rodent models of

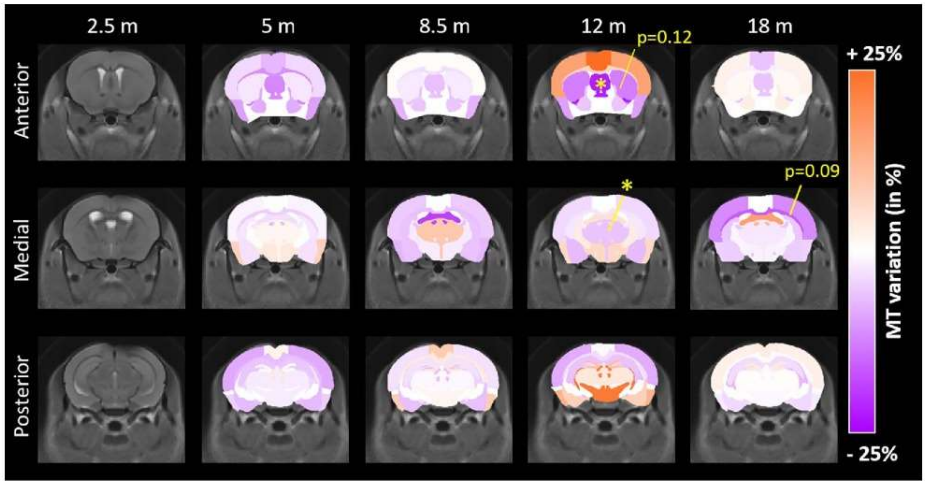

Figure 3. MT variation maps between WT and Ki140CAG mice, at each timepoint, on three slices of the mouse brain, overlaid on the study template. Structures with increased MT contrast are reported in shades of orange and structures with decreased MT contrast in shades of violet. Yellow stars represent significant difference (RM-ANOVA + Bonferroni, *$P < 0.05$).

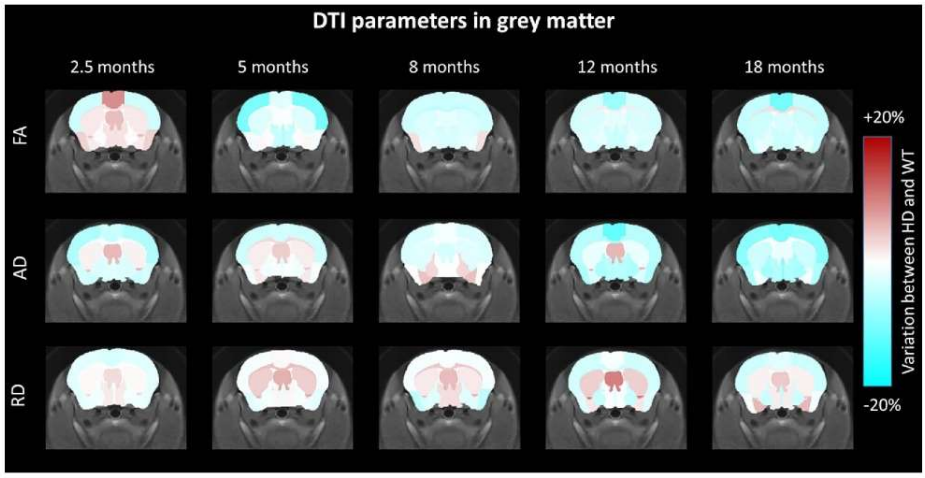

Figure 4. FA, AD and RD variation maps between WT and Ki140CAG mice, at each timepoint, on an anterior slice of the mouse brain, overlaid on the study template. Structures with increased diffusion parameters are reported in shades of brown and structures with decreased diffusion parameters in shades of cyan.

HD, and if translatable to clinical setups, they could be a great help in clinical trials.

In the present study, we monitored longitudinally several potential biomarkers to better understand the physiopathology in this particular mouse model of HD. The most commonly used biomarker to characterize HD progression in m-HTT gene carriers is striatal atrophy. In our knock-in model, striatal atrophy is detected only at 18 months (~5% range with approximately 10 animals per group). Based on our results, we could estimate the sample size to compare groups of control and Ki140CAG models assuming a significance level of 5%, a power of 80% and two-sided tests. Our results showed that 120 animals would be necessary to detect an effect at 12 months.

Similarly, in human studies, the number of premanifest mutant HTT gene carriers or early stage HD patients to be included to observe a significant atrophy of their

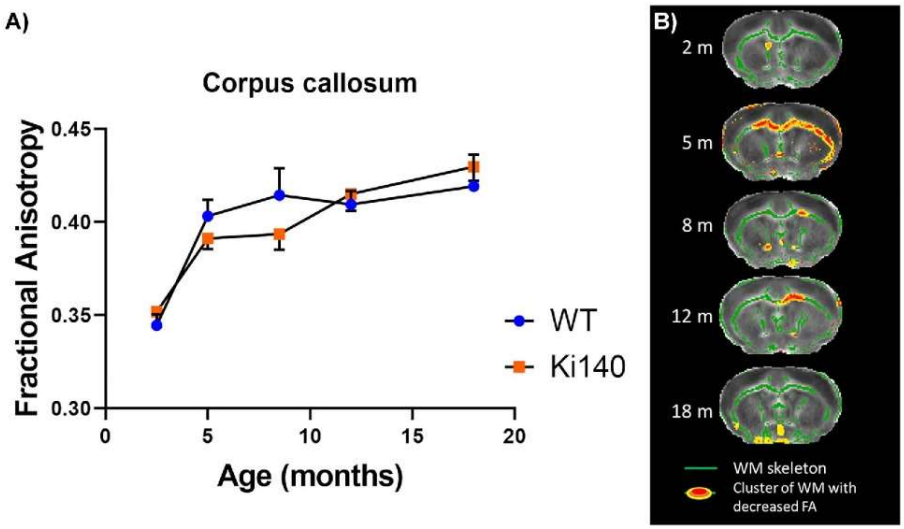

Figure 5. (**A**) FA values measured in CC of WT and Ki140CAG mice as a function of time (blue dots and orange squares, respectively, mean ± SEM). (**B**) FA alterations in white matter as revealed by TBSS analysis, at each timepoint, on an anterior slice of the mouse brain, overlaid on the mean FA map. Green regions represent mean white matter skeleton as used in TBSS pipeline. Red–yellow zones show clusters of voxels with significant decrease of FA (threshold-free cluster enhancement, $P < 0.05$).

striatum is high (>30) (61). Apart from striatal atrophy, we found other indexes that seem to be more sensitive with first FA alterations measured with the TBSS approach as early as 5 months of age in the anterior CC, followed with gluCEST defect at 8 months in the same structure. In a previous study, we showed that Ki140CAG mice exhibited very mild phenotype at 12 months. Indeed, except reduced latency to fall measured in the rotarod test, heterozygous Ki140CAG mice showed no significant difference of rearing behavior, duration of grooming behavior and total distance traveled measured during the open-field test compared to WT mice (52). Thus, FA alteration and gluCEST decrease measured in the current study at 5 and 8 months occurred several months before behavioral symptoms onset and macrostructural changes. Our results support the progressivity of the pathogenesis in the Ki140CAG model and highlight the slight progression of the disease in heterozygous mice, making it a great model for the study of early phase of the disease and for the evaluation of new experimental therapeutics with reasonable number of animal per groups. Indeed, transposed to clinical HD time course, such model with such biomarkers would be relevant to study the pre-symptomatic phase of HD gene carriers.

Identification of molecular biomarkers of HD

From the perspective of identifying relevant and early biological markers of HD, molecules related to energy metabolism and neurotransmission are likely good candidates since it is conceivable that their alteration could occur before actual neurodegeneration associated with major cell shrinkage and/or death of brain cells (62). Glutamate is an amino acid present in high concentrations in the brain. It is involved in numerous brain functions and plays a major role in brain energy metabolism. [Glu] as measured using ^{1}H-MRS has been reported to be affected in the striatum and cortex of HD patients, with conflicting results on whether it increases or decreases (63,64). [Glu] decreases in the striatum have also been observed in zQ175 and R6/2 mice (44,45,65,66). We found similar reduction in [Glu] in the striatum of Ki140 mice (52,67). However, due to inherently low spatial resolution of ^{1}H-MRS, observations have been limited to striatum and cortex. Here, we could evaluate glutamate changes at the whole-brain level using gluCEST imaging. This method is able to capture subtle variations of [Glu] with a high spatial resolution and a rather good specificity. Indeed, previous studies demonstrated that approximately 70% of gluCEST contrast originates from Glu (49). In a previous study, we showed that gluCEST imaging is able to map deficiencies linked to glutamate content in 12-month-old Ki140CAG mice (52). In particular, it detected reduced contrast in the CC of 12 months old heterozygous mice, with increased severity in age-matched homozygous mice. In the present study, with a new cohort of Ki140 mice, we confirmed the 18.8% decrease of gluCEST contrast measured at 12 months in the CC when compared to wild-type littermates confirming the good reproducibility of such measurements. We also show that a significant 10.8%

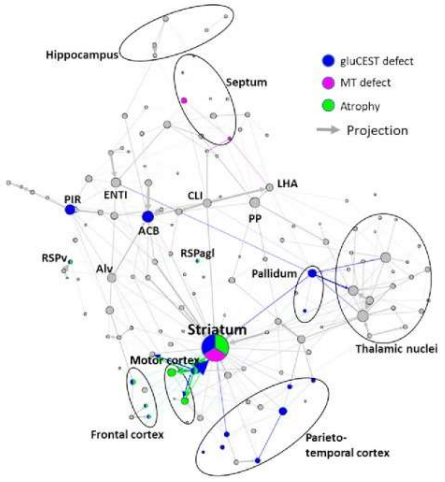

Figure 6. Summary of main results overlaid with graph–theory representation of axonal projection atlas of the mouse brain. Gray arrows and dots represent axonal projections and regions, respectively. Colored dots represent affected regions according to our results. Colored arrows represent axonal projections between affected regions and can be associated with white matter alterations. For clarity, only highest degree nodes and affected nodes are labeled. ACB: Nucleus accumbens; Alv: Alveus; CLI: Central linear nuclei raphe; ENTl: Lateral entorhinal area; LHA: Lateral hypothalamic area; PIR: Piriform area; PP: Peripeduncular nucleus; RSPv: Ventral retrosplenial area; RSPagl: Lateral agranular retrosplenial area.

decrease of gluCEST contrast can be observed earlier in the anterior part of the CC at 8 months of age. Noticeably, this reduction in gluCEST signal does not result from a 'partial volume' bias, since morphometric measures showed the CC volume was similar in Ki140 mice and controls. Interestingly, following timepoints showed a spreading of gluCEST decrease to surrounding structures, such as the motor and piriform cortices, and subcortical nuclei, including the pallidum and the striatum. We hypothesize that this defect is an early manifestation of alteration of the axonal projections between motor cortex and striatum that pass through the anterior corpus callosum as shown in Figure 7. Indeed, Fig. 7A shows the cortico-striatal and inter-hemispheric tracts isolated using locally constrained tractography on a representative dataset from this study. Out of 100 000 total streamlines used in whole-brain tractography, 8575 were part of the CC, while 5320 were part of both the CC and the cortico-striatal tract. Thus, we can estimate a proportion of about 5320/8575 ~62% of streamlines in the CC going through the cortico-striatal tract. The estimation of streamlines belonging to cortico-striatal tract passing through the CC suggests that this specific tract is not negligible in this area of the CC and alterations may be picked out by our measurements. In addition, Figure 7B supports this idea by showing the projections from primary motor area of motor cortex, using more precise cell tracking technique (Allen Connectivity Atlas) with a good correlation to tractography shown in Figure 7A.

Complementarily to gluCEST, MT is based on the exchange of magnetization between free-water protons and protons of water bound to proteins such as myelin (36). Thus, MT signal can be another potential candidate for biomarker identification. Reduced MT contrast can be symptomatic of disruption of myelin sheath or axonal loss (36,68). In HD, decreased MT contrast was found in gray matter and white matter of pre-symptomatic gene carriers and HD patients, with correlation between MT loss and disease severity (69,70).

In this study, we reported for the first time MT defects in a mouse model of HD, especially in the septum and in the striatum. Such decrease of MT contrast could reflect alteration of myelin contents in affected brain structures as already reported in pre-symptomatic and symptomatic m-HTT gene carriers (71).

Altered diffusion in corpus callosum suggests a potential role of white matter defects in HD physiopathology

FA is the most commonly used index to study defects related to microstructural organization. Diffusion of water molecules within WM is highly anisotropic due to strong organization of highly myelinated fibers tracks, providing high FA values. In this study, we observed several clusters of reduced FA values in the anterior part of the CC of Ki140CAG mice at different ages (Fig. 5A). Such results argue in favor of preferential alteration of WM integrity, especially in the anterior part of the CC. Even if interpretation of FA changes is not straightforward (72), several studies have already showed similar decrease of FA values in the WM of HD patients (33,73). Significant alteration of FA and other diffusion parameters were also observed in premanifest HD gene carriers, with a good correlation with WM atrophy (74). Similar decrease of FA value was also observed in WM of YAC128CAG mice as early as 2 weeks of age (21,22,75). In our study, we only observed a relatively small part of the CC with reduced FA value. Besides, no variation of CC volume or RD and AD was measured in Ki140CAG mice contrarily to YAC128CAG mice. Such discrepancy may be partly due to limited size of our animal cohorts or to anisotropic voxels used in our study that could bring partial volume effect. In addition, comparison of different animal models of a same pathology is not always straightforward and differences in the model itself may result in inconsistent observations. For instance, Ki140CAG mice are known to develop very mild phenotype, especially heterozygous mice (52,53,55,76). This could explain the absence of significant difference in FA, AD or RD parameters with the classical atlas-based approach.

In our study, we observed clusters of reduced FA values in the anterior CC at 5 months of age. One possible explanation is the difference in WM maturation between

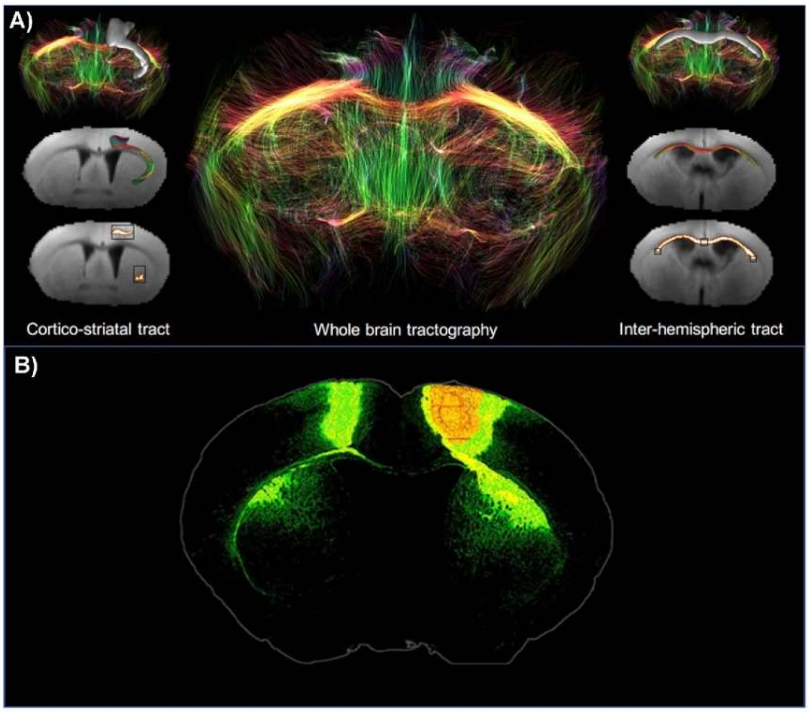

Figure 7. (**A**) White matter tracts isolated from the whole-brain tractography of a representative dataset using locally constrained tractography. Black boxes show starting and ending regions of interest (ROIs) used for isolation of cortico-striatal (left panel) or interhemispheric (right panel) tracts. White voxels show fibers satisfying starting and ending ROIs. (**B**) Axonal projections from primary motor area. Extracted from Allen Connectivity Atlas (https://connectivity.brain-map.org/projection).

Ki140CAG mice and their WT littermates. Indeed, development of cortico-striatal tracts was shown affected in Ki111CAG animals (77,78), so FA values at early timepoints may be reduced as compared with control animals. Recently, developmental origin of HD has been thoroughly discussed (77–80). Cortical progenitor cells from Ki111CAG mice and human gene carriers have shown impaired division in the developmental phase (77,81). Compensatory mechanisms may occur in the early life of mice to compensate maturation/developmental defects. However, cortico-striatal projections may remain vulnerable and could explain metabolic impairments observed at 8 months of age.

The molecular and cellular mechanisms underlying WM alteration in HD mouse models and mutant HTT human gene carriers are unknown. However, hypotheses have been recently supported by experimental evidence. It has been shown that selective inactivation of mutant HTT in progenitors of oligodendrocytes in the YAC128CAG mouse model of HD was sufficient to alleviate motor symptoms and defects in myelination, supporting the hypothesis of a cell autonomous mechanism of WM defects in HD (82). A transcriptional analysis in this work also pointed to underlying mechanisms involving the transcriptional regulatory complex PRC2 (polycomb repressive complex 2), which acts through epigenetic modifications, one of its subunit being the histone H3 methyl-transferase EZH2 that methylates lysine 9 and 27 residues of histone H3, producing repression of the target gene. Huang and collaborators generated a genetic mouse model of HD where mutant HTT (150 CAG repeats) was expressed selectively in oligodendrocytes using the promoter driving the expression of the proteolipid protein (PLP), which is specific of myelinated cells (23). They found that PLP-150Q mice show progressive neurological symptoms, reduced expression of myelin genes, demyelination and early death. Further analysis indicated that these changes were related to defects of the transcription factor myelin regulatory factor (MYRF). Experiments also showed that MYRF is an interactor of mutant HTT. Interestingly, mutant HTT was found to change the transcriptional activity of MYRF. In line with these observations, recent observations showed that interaction between MYRF and mutant HTT depended

on the phosphorylation of MYRF (83). In HD cells, phosphorylation of MYRF was increased, leading to reduced expression of myelin-associated genes (83). Results of this recent study indicated that the increase in MYRF phosphorylation in HD resulted, at least in part, from an increase in the activity of the cGMP-activated protein kinase subunit II (PRKG2). Knocking down PGKG2 ameliorates expression of myelin genes in HD. Thus WM defects would not be a secondary consequence of neuronal dysfunction or loss but could result from a mutant HTT-induced deregulation of oligodendrocyte homeostasis (mature or at the early stage of development in the adult brain) involving MYRF and PRC2.

Identification of a vulnerable network of brain structures in Ki140CAG mice

In the present study, we performed a longitudinal follow-up of heterozygous Ki140CAG mice with several MRI modalities in order to monitor potential alterations of tissue microstructure, metabolic or energetic defects, and morphological changes of brain structures. Rather than taking these results separately, integrating both structural and functional data may result in a better understanding of the pathogenesis of HD in the Ki140CAG mouse model.

We observed that cortical and striatal regions were vulnerable in terms of both atrophy and metabolic changes. In addition, DTI and gluCEST highlighted early WM changes in the anterior part of the CC. Interestingly, striatum and frontal cortex are anatomically connected through the anterior part of the CC and cortico-striatal connections have been shown to be impaired in HD patients as well as in animal models (84–87). Our findings corroborate these results and could reflect specific alteration of such connections in the Ki140CAG mouse model.

Thanks to the representation on Figure 6, one can observe that striatum seems to be particularly vulnerable as it appears to be affected on several MRI indexes. Moreover, this vulnerability seems to be associated with its centrality in the network and connection strength to cortical tissues that are also affected, through white matter tracts that are affected early.

Based on temporality of the observed modifications and from results found in the literature, we hypothesize that our longitudinal, multiparametric MRI protocol was able to image the vulnerability of the cortico-striato-thalamic glutamatergic pathway (88), which is known to be impaired in HD. Metabolic and diffusion deficiencies that appear in the white matter might be related to alterations found at the cortico-striatal synapse between cortical pyramidal neurons (CPNs) and medium spiny neurons (MSNs). These alterations include diminished brain-derived neurotrophic factor (BDNF) transport, increased glutamate neurotransmission, altered NMDA receptor transcription and reduced Ca^{2+} uptake from mitochondria, that together lead to vulnerability of MSNs to excitotoxicity (89). Such hypothesis would need further validations with histopathological study to confirm the status of WM tracks at different ages.

Conclusion

In this study, we developed a multimodal MRI protocol to identify biomarkers of HD pathogenesis. This protocol was applied to monitor longitudinally heterozygous Ki140CAG mice, a slowly progressive mouse model of HD. Thanks to this multimodal approach, we identified early defects in striatal and cortical tissues. Interestingly, DTI, MT and gluCEST modalities seemed to be earlier indicators of pathology progression than structure atrophy. Moreover, a combination of all results obtained with different MRI modalities was integrated to propose a specific brain network that would be particularly vulnerable in this animal model. As most of these modalities have already been applied on clinical scanners, such approach would be particularly interesting to assess disease progression in a clinical context of HD. This might help identify more relevant and early biomarkers in premanifest HD patients and could provide relevant information about disease pathogenesis.

Materials and Methods

Ki140CAG and wild-type littermate mice

Knock-in mice express chimeric mouse/human exon 1 containing 140 CAG repeats inserted in the murine HTT gene (Ki140CAG) (53). Ki140CAG mice colony was maintained by breeding heterozygous Ki140CAG males and WT females. Heterozygous mice ($n = 11$ males, Ki140CAG) were compared to their relative age-matched littermates ($n = 12$ males, WT). Mice were housed in a temperature-controlled room maintained on a 12-h light/dark cycle. Food and water were available ad libitum. All animal studies were conducted according to the French regulation (EU Directive 2010/63/EU—French Act Rural Code R 214–87 to 126). The animal facility was approved by veterinarian inspectors (authorization n° A 92-032-02) and complies with Standards for Humane Care and Use of Laboratory Animals of the Office of Laboratory Animal Welfare (OLAW—n°#A5826-01). All procedures received approval from the ethical committee (APAFIS #21335-201907031642584 v2).

MRI protocol

Animals were scanned longitudinally (2.5, 5, 8, 12 and 18 months of age) on a horizontal 11.7 T Bruker scanner (Bruker, Ettlingen, Germany). Mice were first anesthetized using 3% isoflurane in a 1:1 gas mixture of air/O_2 and positioned in a dedicated stereotaxic frame with mouth and ear bars to prevent any movements during MR acquisitions. Mice temperature was monitored with a rectal probe and maintained at 37°C with regulated water flow. Respiratory rate was continuously monitored using PC SAM software (Small Animal Instruments, Inc., Stony Brook, NY, USA) during scanning. The isoflurane level

was adjusted around 1.5% to keep the respiratory rate in the range of 60–80 per min. A quadrature cryoprobe (Bruker, Ettlingen, Germany) was used for radiofrequency transmission and reception.

High-resolution anatomical images (turbo spin-echo sequence, TE/TR = 5/10 000 ms, Turbo factor = 10, effective TE = 45 ms, in-plane resolution = 100 × 100 μm^2, 200 μm slice thickness, 100 slices) were used for structures volumetry.

Three gluCEST images centered on the mid-striatum were acquired with a 2D fast spin-echo sequence preceded by a frequency-selective continuous wave saturation pulse (TE/TR = 6/5000 ms, 10 echoes and effective TE = 30 ms, in-plane resolution = 150 × 150 μm^2, 0.6 mm slice thickness). The MAPSHIM routine was applied in a voxel encompassing the slices of interest in order to reach a good shim on gluCEST images. GluCEST images were acquired with a saturation pulse applied during T_{sat} = 1 s, composed by 10 broad pulse of 100 ms, with 20 μs inter-delay and an amplitude B_1 = 5 μT. The frequency of the saturation pulse $\Delta\omega$ was applied in a range from −5 to 5 ppm with a step of 0.5 ppm. The WASSR method (90) was used to correct for B_0 inhomogeneities (B_1 = 0.2 μT, $\Delta\omega$ in a range from −1 to 1 ppm with a step of 0.1 ppm). A variability of gluCEST values of 0.5% and 0.8% was measured in the striatum and in the CC respectively in a test–retest experiment performed in a WT animal at two consecutive days. The same sequence than gluCEST was used for MT images acquisition with optimized parameters to assess macromolecular compounds ($\Delta\omega$ = ±16 ppm, B_1 = 10 μT, T_{sat} = 800 ms). MT images were not acquired during the first timepoint (2.5 months).

The diffusion-weighted MRI data were acquired using Echo Planar Imaging (EPI) sequence (TE/TR = 30/3200 ms, in-plane resolution = 112 × 112 μm^2, 500 μm slice thickness, 10 slices, *b*-value = 1000 s/mm^2, 30 directions). A variability of FA values of 0.7% and 1.2% was measured in the striatum and in the CC respectively in a test–retest experiment performed in a WT animal at two consecutive days.

Data processing and statistical analyses

Images acquired using each of the MRI modalities were co-registered and automatically segmented using an in-house python library (Sammba-MRI (91), Fig. 8). In a first step, anatomical images were co-registered to generate an average of all anatomical images, called the study template. This template was segmented using an atlas composed of 34 regions (Fig. 8) derived from the Allen Mouse Brain Atlas (92). Then, transformations to match the atlas to the study template and to match the study template to all high-resolution anatomical images were calculated. Finally, transformations were computed to project the atlas onto the images acquired using each of the MRI modalities. Outputs of the Sammba-MRI pipeline are the volume of each of the 34 structures and mean gluCEST contrast, MT contrast and FA, RD and AD within each structure for each animal.

CEST images were processed pixel-by-pixel and analyzed using in-house programs developed on MATLAB software (MathWorks Inc., Natick, MA) used to generate Z-spectra by plotting the longitudinal magnetization as a function of saturation frequency. WASSR method was used to generate absolute B_0 map by finding the actual frequency within each voxel. Z-spectrum in each voxel was interpolated using a cubic spline and B_0 map was used to correct for B_0 inhomogeneities. The specific glutamate contribution was isolated using Asymmetrical Magnetization Transfer Ratio (MTRasym) (93) and was calculated as follows: $MTRasym(\Delta\omega) = 100 \times (M_{sat}(-\Delta\omega) - M_{sat}(+\Delta\omega))/M_{sat}(-5\text{ ppm})$ where $M_{sat}(\pm\Delta\omega)$ is the magnetization acquired with saturation pulse applied at '+' or '−'$\Delta\omega$ ppm. GluCEST images were calculated with $\Delta\omega$ centered at ±3 ppm.

FA, AD and RD maps were generated using ParaVision 6.1 software (Bruker, Ettlingen, Germany). FA images underwent the TBSS pipeline (57) using FSL software (94). For that, FA maps were first co-registered to the study template. Then, the mean FA map over the whole animal cohort was generated and the skeleton template of WM tracks was extracted. Individual skeleton from each animal was calculated using the same process and then projected to skeleton template to have a good co-registration of WM tracks.

Variation of each index *Ind* (with *Ind* being structure volume, gluCEST contrast or MT contrast) between WT littermates and Ki140CAG mice was calculated in each brain region as follows: Variation = 100 × (Ind(WT)—*Ind*(Ki140CAG))/Ind(WT).

Statistical analyses were performed using GraphPad Prism 8.0 (GraphPad Software, San Diego, California, USA). The Shapiro–Wilk test was used to test the data for normality and no deviation from normality was observed for any data. One-way ANOVA with repeated measures was used for statistical analysis. The significant threshold was set to 0.05. ANOVA was followed by a Bonferroni *post-hoc* test to determine individual significant differences between groups. Sample size to compare HD and WT mice that would have been needed for detection of significant change was estimated assuming a significance level of 5%, a power of 80% and two-sided tests (BiostaTGV module, https://biostatgv.sentiweb.fr/?module=etudes/sujets#). The standard deviation used for this estimation was the square root of the pooled variance from each group. All data used in this study can be made available upon request after signing a transfer agreement required by authors' institution. All codes of the in-house python library Sammba-MRI are freely available (https://sammba-mri.github.io/index.html).

Graph theory

Normalized projection data from the Allen Connectivity Atlas (Oh *et al.* (58)) was processed using graph theory. This method has been widely used for representation

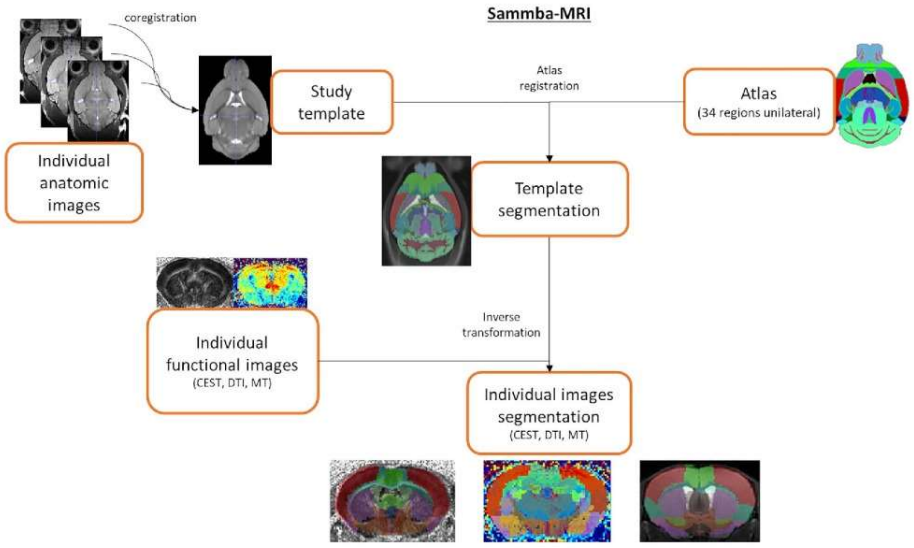

Figure 8. Automated co-registration and segmentation pipeline using in-house python library Sammba-MRI.

of functional networks as measured by resting-state functional MRI. A threshold was applied at 1 of normalized projection strength to remove irrelevant projections. Thresholded projection matrix was then loaded in Gephi 0.9.2 and a Force Atlas spatialization algorithm was applied. This algorithm iteratively forms clusters of regions based on their connectivity. Correspondence between subregions from connectivity atlas and large structures used in MRI atlas was established based on the Allen Mouse Brain Atlas (92) (http://atlas.brain-map.org/).

Tractography

Acquired diffusion-weighted MRI data were reconstructed with the generalized q-sampling imaging (GQI) method (95), which models diffusion patterns in each voxel with an orientation distribution function (ODF) that can detect simultaneous diffusion in multiple directions, using the DSI Studio software (http://dsi-studio.labsolver.org). For tractography, the generalized deterministic tracking algorithm implemented in DSI Studio (96) was used. Whole-brain tractography was first performed to assess overall data quality and to decide appropriate values for global parameters (e.g. the anisotropy threshold used as a stopping criterion in tractography) by tracking streamlines with a whole-brain seed. Then, locally constrained tractography was used to isolate the tract connecting the cortex to the striatum, namely the cortico-striatal tract, and those connecting the two hemispheres, namely inter-hemispheric tract, by making use of ROI-based Boolean operations. For the cortico-striatal tract, ROIs were defined by specifying the volume of the motor cortex from which streamlines must start and the volume of the striatum where streamlines must terminate. For the inter-hemispheric tract, ROIs were defined by specifying the volume of the left end of the corpus callosum from which streamlines must start and the volume of the right end of the corpus callosum where streamlines must terminate, with an additional ROI in the middle of the corpus callosum that streamlines must cross. A threshold on the FA at 0.15, maximum streamline length 20 mm, random maximum angle and trilinear interpolation were used as global parameters. For whole-brain tractography, 100 000 streamlines were generated with random seeds in the whole brain; these streamlines where then filtered in the locally constrained tractography step, where only the streamlines satisfying the ROI-based Boolean conditions were retained to define the cortico-striatal tract and the inter-hemispheric tract.

Conflict of Interest statement. The authors have no financial interest or connection to disclose related to this study.

Funding

Agence Nationale pour la Recherche ('HDeNERGY' project [ANR-14-CE15-0007-01] and 'epiHD' project

[ANR-17-CE12-0027]); the ERA-Net for Research Programs on Rare Diseases ('TreatPolyQ' project [ANR-17-RAR3-0008-01]). The 11.7T MRI scanner was funded by a grant from NeurATRIS: A Translational Research Infrastructure for Biotherapies in Neurosciences ('Investissements d'Avenir', [ANR-11-INBS-0011]); UKRI Future Leaders Fellowship MR/T020296/1 to M.P.

References

1. Walker, F.O. (2007) Huntington's disease. *Lancet Lond. Engl.*, **369**, 218–228.
2. Liot, G., Valette, J., Pépin, J., Flament, J. and Brouillet, E. (2017) Energy defects in Huntington's disease: why "in vivo" evidence matters. *Biochem. Biophys. Res. Commun.*, **483**, 1084–1095.
3. Dubinsky, J.M. (2017) Towards an understanding of energy impairment in Huntington's disease brain. *J. Huntingt. Dis.*, **6**, 267–302.
4. Paoli, R.A., Botturi, A., Ciammola, A., Silani, V., Prunas, C., Lucchiari, C., Zugno, E. and Caletti, E. (2017) Neuropsychiatric burden in Huntington's disease. *Brain Sci.*, **7**.
5. Stout, J.C., Paulsen, J.S., Queller, S., Solomon, A.C., Whitlock, K.B., Campbell, J.C., Carlozzi, N., Duff, K., Beglinger, L.J., Langbehn, D.R. *et al.* (2011) Neurocognitive signs in prodromal Huntington disease. *Neuropsychology*, **25**, 1–14.
6. Hogarth, P., Kayson, E., Kieburtz, K., Marder, K., Oakes, D., Rosas, D., Shoulson, I., Wexler, N.S., Young, A.B. and Zhao, H. (2005) Interrater agreement in the assessment of motor manifestations of Huntington's disease. *Mov. Disord.*, **20**, 293–297.
7. Tabrizi, S.J., Reilmann, R., Roos, R.A.C., Durr, A., Leavitt, B., Owen, G., Jones, R., Johnson, H., Craufurd, D., Hicks, S.L. *et al.* (2012) Potential endpoints for clinical trials in premanifest and early Huntington's disease in the TRACK-HD study: analysis of 24 month observational data. *Lancet Neurol.*, **11**, 42–53.
8. Bird, E.D. and Iversen, L.L. (1974) Huntington's chorea: post-mortem measurement of glutamic acid decarboxylase, choline acetyltransferase and dopamine in basal ganglia. *Brain*, **97**, 457–472.
9. Vonsattel, J.-P., Myers, R.H., Stevens, T.J., Ferrante, R.J., Bird, E.D. and Richardson, E.P., Jr. (1985) Neuropathological classification of Huntington's disease. *J. Neuropathol. Exp. Neurol.*, **44**, 559–577.
10. Kuhl, D.E., Phelps, M.E., Markham, C.H., Metter, E.J., Riege, W.H. and Winter, J. (1982) Cerebral metabolism and atrophy in Huntington's disease determined by 18FDG and computed tomographic scan. *Ann. Neurol.*, **12**, 425–434.
11. Brouillet, E., Condé, F., Beal, M.F. and Hantraye, P. (1999) Replicating Huntington's disease phenotype in experimental animals. *Prog. Neurobiol.*, **59**, 427–468.
12. Tabrizi, S.J., Scahill, R.I., Owen, G., Durr, A., Leavitt, B.R., Roos, R.A., Borowsky, B., Landwehrmeyer, B., Frost, C., Johnson, H. *et al.* (2013) Predictors of phenotypic progression and disease onset in premanifest and early-stage Huntington's disease in the TRACK-HD study: analysis of 36-month observational data. *Lancet Neurol.*, **12**, 637–649.
13. Aylward, E.H., Sparks, B.F., Field, K.M., Yallapragada, V., Shpritz, B.D., Rosenblatt, A., Brandt, J., Gourley, L.M., Liang, K., Zhou, H. *et al.* (2004) Onset and rate of striatal atrophy in preclinical Huntington disease. *Neurology*, **63**, 66–72.
14. Paulsen, J.S., Langbehn, D.R., Stout, J.C., Aylward, E., Ross, C.A., Nance, M., Guttman, M., Johnson, S., MacDonald, M., Beglinger, L.J. *et al.* (2008) Detection of Huntington's disease decades before diagnosis: the predict-HD study. *J. Neurol. Neurosurg. Psychiatry*, **79**, 874–880.
15. Kipps, C.M., Duggins, A.J., Mahant, N., Gomes, L., Ashburner, J. and McCusker, E.A. (2005) Progression of structural neuropathology in preclinical Huntington's disease: a tensor based morphometry study. *J. Neurol. Neurosurg. Psychiatry*, **76**, 650–655.
16. Gómez-Ansón, B., Alegret, M., Muñoz, E., Monté, G.C., Alayrach, E., Sánchez, A., Boada, M. and Tolosa, E. (2009) Prefrontal cortex volume reduction on MRI in preclinical Huntington's disease relates to visuomotor performance and CAG number. *Parkinsonism Relat. Disord.*, **15**, 213–219.
17. Paulsen, J.S., Nopoulos, P.C., Aylward, E., Ross, C.A., Johnson, H., Magnotta, V.A., Juhl, A., Pierson, R.K., Mills, J., Langbehn, D. *et al.* (2010) Striatal and white matter predictors of estimated diagnosis for Huntington disease. *Brain Res. Bull.*, **82**, 201–207.
18. Crawford, H.E., Hobbs, N.Z., Keogh, R., Langbehn, D.R., Frost, C., Johnson, H., Landwehrmeyer, B., Reilmann, R., Craufurd, D., Stout, J.C. *et al.* (2013) Corpus callosal atrophy in premanifest and early Huntington's disease. *J. Huntingt. Dis.*, **2**, 517–526.
19. Gregory, S., Crawford, H., Seunarine, K., Leavitt, B., Durr, A., Roos, R.A.C., Scahill, R.I., Tabrizi, S.J., Rees, G., Langbehn, D. *et al.* (2018) Natural biological variation of white matter microstructure is accentuated in Huntington's disease. *Hum. Brain Mapp.*, **39**, 3516–3527.
20. Dumas, E.M., van den Bogaard, S.J.A., Ruber, M.E., Reilmann, R., Stout, J.C., Craufurd, D., Hicks, S.L., Kennard, C., Tabrizi, S.J., van Buchem, M.A. *et al.* (2011) Early changes in white matter pathways of the sensorimotor cortex in premanifest Huntington's disease. *Hum. Brain Mapp.*, **33**, 203–212.
21. Teo, R.T.Y., Hong, X., Yu-Taeger, L., Huang, Y., Tan, L.J., Xie, Y., To, X.V., Guo, L., Rajendran, R., Novati, A. *et al.* (2016) Structural and molecular myelination deficits occur prior to neuronal loss in the YAC128 and BACHD models of Huntington disease. *Hum. Mol. Genet.*, **25**, 2621–2632.
22. Garcia-Miralles, M., Hong, X., Tan, L.J., Caron, N.S., Huang, Y., To, X.V., Lin, R.Y., Franciosi, S., Papapetropoulos, S., Hayardeny, L. *et al.* (2016) Laquinimod rescues striatal, cortical and white matter pathology and results in modest behavioural improvements in the YAC128 model of Huntington disease. *Sci. Rep.*, **6**, 31652.
23. Huang, B., Wei, W., Wang, G., Gaertig, M.A., Feng, Y., Wang, W., Li, X.-J. and Li, S. (2015) Mutant huntingtin downregulates myelin regulatory factor-mediated myelin gene expression and affects mature oligodendrocytes. *Neuron*, **85**, 1212–1226.
24. Bartzokis, G., Lu, P.H., Tishler, T.A., Fong, S.M., Oluwadara, B., Finn, J.P., Huang, D., Bordelon, Y., Mintz, J. and Perlman, S. (2007) Myelin breakdown and iron changes in Huntington's disease: pathogenesis and treatment implications. *Neurochem. Res.*, **32**, 1655–1664.
25. Casella, C., Lipp, I., Rosser, A., Jones, D.K. and Metzler-Baddeley, C. (2020) A critical review of white matter changes in Huntington's disease. *Mov. Disord.*, **35**, 1302–1311.
26. Zhang, J., Gregory, S., Scahill, R.I., Durr, A., Thomas, D.L., Lehericy, S., Rees, G., Tabrizi, S.J. and Zhang, H. (2018) In vivo characterization of white matter pathology in premanifest Huntington's disease. *Ann. Neurol.*, **84**, 497–504.
27. Gregory, S., Johnson, E., Byrne, L.M., Rodrigues, F.B., Henderson, A., Moss, J., Thomas, D., Zhang, H., De Vita, E., Tabrizi, S.J. *et al.* (2020) Characterizing white matter in Huntington's disease. *Mov. Disord. Clin. Pract.*, **7**, 52–60.
28. Le Bihan, D. (2003) Looking into the functional architecture of the brain with diffusion MRI. *Nat. Rev. Neurosci.*, **4**, 469–480.
29. Sen, P.N. and Basser, P.J. (2005) A model for diffusion in white matter in the brain. *Biophys. J.*, **89**, 2927–2938.

30. Le Bihan, D. and Johansen-Berg, H. (2012) Diffusion MRI at 25: exploring brain tissue structure and function. *NeuroImage*, **61**, 324–341.
31. Gregory, S., Cole, J.H., Farmer, R.F., Rees, E.M., Roos, R.A.C., Sprengelmeyer, R., Durr, A., Landwehrmeyer, B., Zhang, H., Scahill, R.I. *et al.* (2015) Longitudinal diffusion tensor imaging shows progressive changes in white matter in Huntington's disease. *J. Huntingt. Dis.*, **4**, 333–346.
32. Rosas, H.D., Wilkens, P., Salat, D.H., Mercaldo, N.D., Vangel, M., Yendiki, A.Y. and Hersch, S.M. (2018) Complex spatial and temporally defined myelin and axonal degeneration in Huntington disease. *NeuroImage Clin.*, **20**, 236–242.
33. Poudel, G.R., Stout, J.C., Domínguez D., J.F., Churchyard, A., Chua, P., Egan, G.F. and Georgiou-Karistianis, N. (2015) Longitudinal change in white matter microstructure in Huntington's disease: the IMAGE-HD study. *Neurobiol. Dis.*, **74**, 406–412.
34. Ou, X., Sun, S.-W., Liang, H.-F., Song, S.-K. and Gochberg, D.F. (2009) Quantitative magnetization transfer measured pool size ratio reflects optic nerve myelin content in ex vivo mice. *Magn. Reson. Med. Off. J. Soc. Magn. Reson. Med. Soc. Magn. Reson. Med.*, **61**, 364–371.
35. van Zijl, P.C.M., Lam, W.W., Xu, J., Knutsson, L. and Stanisz, G.J. (2018) Magnetization transfer contrast and chemical exchange saturation transfer MRI. Features and analysis of the field-dependent saturation spectrum. *NeuroImage*, **168**, 222–241.
36. Tambasco, N., Nigro, P., Romoli, M., Simoni, S., Parnetti, L. and Calabresi, P. (2015) Magnetization transfer MRI in dementia disorders, Huntington's disease and parkinsonism. *J. Neurol. Sci.*, **353**, 1–8.
37. Bourbon-Teles, J., Bells, S., Jones, D.K., Coulthard, E., Rosser, A. and Metzler-Baddeley, C. (2019) Myelin breakdown in human Huntington's disease: multi-modal evidence from diffusion MRI and quantitative magnetization transfer. *Neuroscience*, **403**, 79–92.
38. Chaney, A., Williams, S.R. and Boutin, H. (2019) In vivo molecular imaging of neuroinflammation in Alzheimer's disease. *J. Neurochem.*, **149**, 438–451.
39. Graham, S.F., Rey, N.L., Yilmaz, A., Kumar, P., Madaj, Z., Maddens, M., Bahado-Singh, R.O., Becker, K., Schulz, E., Meyerdirk, L.K. *et al.* (2018) Biochemical profiling of the brain and blood metabolome in a mouse model of prodromal Parkinson's disease reveals distinct metabolic profiles. *J. Proteome Res.*, **17**, 2460–2469.
40. Mochel, F., Durant, B., Meng, X., O'Callaghan, J., Yu, H., Brouillet, E., Wheeler, V.C., Humbert, S., Schiffmann, R. and Durr, A. (2012) Early alterations of brain cellular energy homeostasis in Huntington disease models. *J. Biol. Chem.*, **287**, 1361–1370.
41. Sturrock, A., Laule, C., Decolongon, J., Dar Santos, R., Coleman, A.J., Creighton, S., Bechtel, N., Reilmann, R., Hayden, M.R., Tabrizi, S.J. *et al.* (2010) Magnetic resonance spectroscopy biomarkers in premanifest and early Huntington disease. *Neurology*, **75**, 1702–1710.
42. Zacharoff, L., Tkac, I., Song, Q., Tang, C., Bolan, P.J., Mangia, S., Henry, P.-G., Li, T. and Dubinsky, J.M. (2012) Cortical metabolites as biomarkers in the R6/2 model of Huntington's disease. *J. Cereb. Blood Flow Metab.*, **32**, 502–514.
43. Jenkins, B.G., Andreassen, O.A., Dedeoglu, A., Leavitt, B., Hayden, M., Borchelt, D., Ross, C.A., Ferrante, R.J. and Beal, M.F. (2005) Effects of CAG repeat length, HTT protein length and protein context on cerebral metabolism measured using magnetic resonance spectroscopy in transgenic mouse models of Huntington's disease. *J. Neurochem.*, **95**, 553–562.
44. Tkac, I., Dubinsky, J.M., Keene, C.D., Gruetter, R. and Low, W.C. (2007) Neurochemical changes in Huntington R6/2 mouse striatum detected by in vivo 1H NMR spectroscopy. *J. Neurochem.*, **100**, 1397–1406.
45. Heikkinen, T., Lehtimäki, K., Vartiainen, N., Puoliväli, J., Hendricks, S.J., Glaser, J.R., Bradaia, A., Wadel, K., Touller, C., Kontkanen, O. *et al.* (2012) Characterization of neurophysiological and behavioral changes, MRI brain volumetry and 1H MRS in zQ175 knock-in mouse model of Huntington's disease. *PLoS One*, **7**, e50717.
46. Wolff, S.D. and Balaban, R.S. (1990) Regulation of the predominant renal medullary organic solutes in vivo. *Annu. Rev. Physiol.*, **52**, 727–746.
47. Ward, K.M., Aletras, A.H. and Balaban, R.S. (1997) (2000) a new class of contrast agents for MRI based on proton chemical exchange dependent saturation transfer (CEST). *J. Magn. Reson. San Diego Calif*, **143**, 79–87.
48. Ward, K.M. and Balaban, R.S. (2000) Determination of pH using water protons and chemical exchange dependent saturation transfer (CEST). *Magn. Reson. Med.*, **44**, 799–802.
49. Cai, K., Haris, M., Singh, A., Kogan, F., Greenberg, J.H., Hariharan, H., Detre, J.A. and Reddy, R. (2012) Magnetic resonance imaging of glutamate. *Nat. Med.*, **18**, 302–306.
50. Cai, K., Singh, A., Roalf, D.R., Nanga, R.P.R., Haris, M., Hariharan, H., Gur, R. and Reddy, R. (2013) Mapping glutamate in subcortical brain structures using high-resolution GluCEST MRI. *NMR Biomed.*, **26**, 1278–1284.
51. Carrillo-de Sauvage, M.-A., Flament, J., Bramoulle, Y., Ben Haim, L., Guillermier, M., Berniard, A., Aurégan, G., Houitte, D., Brouillet, E., Bonvento, G. *et al.* (2015) The neuroprotective agent CNTF decreases neuronal metabolites in the rat striatum: an in vivo multimodal magnetic resonance imaging study. *J. Cereb. Blood Flow Metab.*, **35**, 917–921.
52. Pépin, J., Francelle, L., Carrillo-de Sauvage, M.-A., de Longprez, L., Gipchtein, P., Cambon, K., Valette, J., Brouillet, E. and Flament, J. (2016) In vivo imaging of brain glutamate defects in a knock-in mouse model of Huntington's disease. *NeuroImage*, **139**, 53–64.
53. Menalled, L.B., Sison, J.D., Dragatsis, I., Zeitlin, S. and Chesselet, M.-F. (2003) Time course of early motor and neuropathological anomalies in a knock-in mouse model of Huntington's disease with 140 CAG repeats. *J. Comp. Neurol.*, **465**, 11–26.
54. Menalled, L.B. and Chesselet, M.-F. (2002) Mouse models of Huntington's disease. *Trends Pharmacol. Sci.*, **23**, 32–39.
55. Hickey, M.A., Kosmalska, A., Enayati, J., Cohen, R., Zeitlin, S., Levine, M.S. and Chesselet, M.-F. (2008) Extensive early motor and non-motor behavioral deficits are followed by striatal neuronal loss in knock-in Huntington's disease mice. *Neuroscience*, **157**, 280–295.
56. Crescenzi, R., DeBrosse, C., Nanga, R.P.R., Byrne, M.D., Krishnamoorthy, G., D'Aquilla, K., Nath, H., Morales, K.H., Iba, M., Hariharan, H. *et al.* (2017) Longitudinal imaging reveals subhippocampal dynamics in glutamate levels associated with histopathologic events in a mouse model of tauopathy and healthy mice. *Hippocampus*, **27**, 285–302.
57. Smith, S.M., Jenkinson, M., Johansen-Berg, H., Rueckert, D., Nichols, T.E., Mackay, C.E., Watkins, K.E., Ciccarelli, O., Cader, M.Z., Matthews, P.M. *et al.* (2006) Tract-based spatial statistics: voxelwise analysis of multi-subject diffusion data. *NeuroImage*, **31**, 1487–1505.
58. Oh, S.W., Harris, J.A., Ng, L., Winslow, B., Cain, N., Mihalas, S., Wang, Q., Lau, C., Kuan, L., Henry, A.M. *et al.* (2014) A mesoscale connectome of the mouse brain. *Nature*, **508**, 207–214.

59. Menalled, L.B. (2005) Knock-in mouse models of Huntington's disease. *NeuroRx J. Am. Soc. Exp. Neurother.*, **2**, 465–470.
60. Tkac, I., Henry, P.-G., Zacharoff, L., Wedel, M., Gong, W., Deelchand, D.K., Li, T. and Dubinsky, J.M. (2012) Homeostatic adaptations in brain energy metabolism in mouse models of Huntington disease. *J. Cereb. Blood Flow Metab.*, **32**, 1977–1988.
61. Scahill, R.I., Zeun, P., Osborne-Crowley, K., Johnson, E.B., Gregory, S., Parker, C., Lowe, J., Nair, A., O'Callaghan, C., Langley, C. *et al.* (2020) Biological and clinical characteristics of gene carriers far from predicted onset in the Huntington's disease young adult study (HD-YAS): a cross-sectional analysis. *Lancet Neurol.*, **19**, 502–512.
62. Bonvento, G., Valette, J., Flament, J., Mochel, F. and Brouillet, E. (2017) Imaging and spectroscopic approaches to probe brain energy metabolism dysregulation in neurodegenerative diseases. *J. Cereb. Blood Flow Metab.*, **37**, 1927–1943.
63. van den Bogaard, S.J.A., Dumas, E.M., Teeuwisse, W.M., Kan, H.E., Webb, A., Roos, R.A.C. and van der Grond, J. (2011) Exploratory 7-tesla magnetic resonance spectroscopy in Huntington's disease provides in vivo evidence for impaired energy metabolism. *J. Neurol.*, **258**, 2230–2239.
64. van den Bogaard, S.J.A., Dumas, E.M., Teeuwisse, W.M., Kan, H.E., Webb, A., van Buchem, M.A., Roos, R.A.C. and van der Grond, J. (2014) Longitudinal metabolite changes in Huntington's disease during disease onset. *J. Huntingt. Dis.*, **3**, 377–386.
65. Jenkins, B.G., Klivenyi, P., Kustermann, E., Andreassen, O.A., Ferrante, R.J., Rosen, B.R. and Beal, M.F. (2000) Nonlinear decrease over time in N-acetyl aspartate levels in the absence of neuronal loss and increases in glutamine and glucose in transgenic Huntington's disease mice. *J. Neurochem.*, **74**, 2108–2119.
66. Peng, Q., Wu, B., Jiang, M., Jin, J., Hou, Z., Zheng, J., Zhang, J. and Duan, W. (2016) Characterization of Behavioral, neuropathological, brain metabolic and key molecular changes in zQ175 knock-in mouse model of Huntington's disease. *PLoS One*, **11**, e0148839.
67. Pépin, J., de Longprez, L., Trovero, F., Brouillet, E., Valette, J. and Flament, J. (2020) Complementarity of gluCEST and 1 H-MRS for the study of mouse models of Huntington's disease. *NMR Biomed.*, **33**, e4301.
68. Anik, Y., Iseri, P., Demirci, A., Komsuoglu, S. and Inan, N. (2007) Magnetization transfer ratio in early period of Parkinson disease. *Acad. Radiol.*, **14**, 189–192.
69. van den Bogaard, S., Dumas, E., van der Grond, J., van Buchem, M. and Roos, R. (2012) MRI biomarkers in Huntington's disease. *Front. Biosci. (Elite Ed.)*, **4**, 1910–1925.
70. van den Bogaard, S.J.A., Dumas, E.M., Hart, E.P., Milles, J., Reilmann, R., Stout, J.C., Craufurd, D., Gibbard, C.R., Tabrizi, S.J., van Buchem, M.A. *et al.* (2013) Magnetization transfer imaging in premanifest and manifest Huntington disease: a 2-year follow-up. *AJNR Am. J. Neuroradiol.*, **34**, 317–322.
71. Di Paola, M., Phillips, O.R., Sanchez-Castaneda, C., Di Pardo, A., Maglione, V., Caltagirone, C., Sabatini, U. and Squitieri, F. (2014) MRI measures of corpus callosum iron and myelin in early Huntington's disease. *Hum. Brain Mapp.*, **35**, 3143–3151.
72. Wheeler-Kingshott, C.A.M. and Cercignani, M. (2009) About "axial" and "radial" diffusivities. *Magn. Reson. Med.*, **61**, 1255–1260.
73. Diana Rosas, H., Lee, S.Y., Bender, A., Zaleta, A.K., Vange, M., Yu, P., Fischl, B., Pappu, V., Cha, J.-H., Salat, D.H. *et al.* (2010) Altered white matter microstructure in the corpus callosum in Huntington's disease: implications for cortical "disconnection.". *NeuroImage*, **49**, 2995–3004.
74. Novak, M.J.U., Seunarine, K.K., Gibbard, C.R., Hobbs, N.Z., Scahill, R.I., Clark, C.A. and Tabrizi, S.J. (2014) White matter integrity in premanifest and early Huntington's disease is related to caudate loss and disease progression. *Cortex. J. Devoted Study Nerv. Syst. Behav.*, **52**, 98–112.
75. Petrella, L.I., Castelhano, J.M., Ribeiro, M., Sereno, J.V., Gonçalves, S.I., Laço, M.N., Hayden, M.R., Rego, A.C. and Castelo-Branco, M. (2018) A whole brain longitudinal study in the YAC128 mouse model of Huntington's disease shows distinct trajectories of neurochemical, structural connectivity and volumetric changes. *Hum. Mol. Genet.*, **27**, 2125–2137.
76. Rising, A.C., Xu, J., Napoli, V.V., Carlson, A., Denovan-Wright, E.M. and Mandel, R.J. (2011) Longitudinal Behavioral, cross-sectional transcriptional and histopathological characterization of a knock-in mouse model of Huntington's disease with 140 CAG repeats. *Exp. Neurol.*, **228**, 173–182.
77. Barnat, M., Capizzi, M., Aparicio, E., Boluda, S., Wennagel, D., Kacher, R., Kassem, R., Lenoir, S., Agasse, F., Braz, B.Y. *et al.* (2020) Huntington's disease alters human neurodevelopment. *Science*, **369**, 787–793.
78. Molina-Calavita, M., Barnat, M., Elias, S., Aparicio, E., Piel, M. and Humbert, S. (2014) Mutant huntingtin affects cortical progenitor cell division and development of the mouse neocortex. *J. Neurosci.*, **34**, 10034–10040.
79. Wiatr, K., Szlachcic, W.J., Trzeciak, M., Figlerowicz, M. and Figiel, M. (2018) Huntington disease as a neurodevelopmental disorder and early signs of the disease in stem cells. *Mol. Neurobiol.*, **55**, 3351–3371.
80. Zhang, C., Wu, Q., Liu, H., Cheng, L., Hou, Z., Mori, S., Hua, J., Ross, C.A., Zhang, J., Nopoulos, P.C. *et al.* (2020) Abnormal brain development in Huntington' disease is recapitulated in the zQ175 knock-in mouse model. *Cereb. Cortex Commun.*, **1**, tgaa044.
81. Barnat, M., Le Friec, J., Benstaali, C. and Humbert, S. (2017) Huntingtin-mediated multipolar-bipolar transition of Newborn cortical neurons is critical for their postnatal neuronal morphology. *Neuron*, **93**, 99–114.
82. Ferrari Bardile, C., Garcia-Miralles, M., Caron, N.S., Rayan, N.A., Langley, S.R., Harmston, N., Rondelli, A.M., Teo, R.T.Y., Waltl, S., Anderson, L.M. *et al.* (2019) Intrinsic mutant HTT-mediated defects in oligodendroglia cause myelination deficits and behavioral abnormalities in Huntington disease. *Proc. Natl. Acad. Sci. U. S. A.*, **116**, 9622–9627.
83. Yin, P., Liu, Q., Pan, Y., Yang, W., Yang, S., Wei, W., Chen, X., Hong, Y., Bai, D., Li, X.-J. *et al.* (2020) Phosphorylation of myelin regulatory factor by PRKG2 mediates demyelination in Huntington's disease. *EMBO Rep.*, **21**, e49783.
84. Hong, S.L., Cossyleon, D., Hussain, W.A., Walker, L.J., Barton, S.J. and Rebec, G.V. (2012) Dysfunctional Behavioral modulation of Corticostriatal communication in the R6/2 mouse model of Huntington's disease. *PLoS One*, **7**, e47026.
85. Naze, S., Humble, J., Zheng, P., Barton, S., Rangel-Barajas, C., Rebec, G.V. and Kozloski, J.R. (2018) Cortico-striatal cross-frequency coupling and gamma genesis disruptions in Huntington's disease mouse and computational models. *eNeuro*, **5**, 1–23.
86. Rebec, G.V. (2018) Corticostriatal network dysfunction in Huntington's disease: deficits in neural processing, glutamate transport, and ascorbate release. *CNS Neurosci. Ther.*, **24**, 281–291.
87. Blumenstock, S. and Dudanova, I. (2020) Cortical and striatal circuits in Huntington's disease. *Front. Neurosci.*, **14**, 82.
88. Schwartz, T.L., Sachdeva, S. and Stahl, S.M. (2012) Glutamate neurocircuitry: theoretical underpinnings in schizophrenia. *Front. Pharmacol.*, **3**.
89. Fan, M.M.Y. and Raymond, L.A. (2007) N-methyl-D-aspartate (NMDA) receptor function and excitotoxicity in Huntington's disease. *Prog. Neurobiol.*, **81**, 272–293.

90. Kim, M., Gillen, J., Landman, B.A., Zhou, J. and van Zijl, P.C.M. (2009) Water saturation shift referencing (WASSR) for chemical exchange saturation transfer (CEST) experiments. *Magn. Reson. Med.*, **61**, 1441–1450.
91. Celestine, M., Nadkarni, N.A., Garin, C.M., Bougacha, S. and Dhenain, M. (2020) Sammba-MRI: a library for processing SmAll-MaMmal BrAin MRI data in python. *Front. Neuroinform.*, **14**, 24.
92. Lein, E.S., Hawrylycz, M.J., Ao, N., Ayres, M., Bensinger, A., Bernard, A., Boe, A.F., Boguski, M.S., Brockway, K.S., Byrnes, E.J. *et al.* (2007) Genome-wide atlas of gene expression in the adult mouse brain. *Nature*, **445**, 168–176.
93. Liu, G., Gilad, A.A., Bulte, J.W.M., Zijl, P.C.M. van and McMahon, M.T. (2010) High-throughput screening of chemical exchange saturation transfer MR contrast agents. *Contrast Media Mol. Imaging*, **5**, 162–170.
94. Smith, S.M., Jenkinson, M., Woolrich, M.W., Beckmann, C.F., Behrens, T.E.J., Johansen-Berg, H., Bannister, P.R., De Luca, M., Drobnjak, I., Flitney, D.E. *et al.* (2004) Advances in functional and structural MR image analysis and implementation as FSL. *NeuroImage*, **23**, S208–S219.
95. Yeh, F.-C., Wedeen, V.J. and Tseng, W.-Y.I. (2010) Generalized q-sampling imaging. *IEEE Trans. Med. Imaging*, **29**, 1626–1635.
96. Yeh, F.-C., Verstynen, T.D., Wang, Y., Fernández-Miranda, J.C. and Tseng, W.-Y.I. (2013) Deterministic diffusion fiber tracking improved by quantitative anisotropy. *PLoS One*, **8**, e80713.

Grandjean J., Desrosiers G.G, Anckaerts C., Angeles-aldez D., Ayad F., Barrière D., Blockx I., Bortel A., Broadwater M., M Cardoso B, **CELESTINE M.**, […] Chakravarty M., Hess A.. StandardRat: A multi-center consensus protocol to enhance functional connectivity specificity in the rat brain. Nature Neuroscience (accepted)
https://doi.org/10.17605/OSF.IO/EMQ4B

StandardRat: A multi-center consensus protocol to enhance functional connectivity specificity in the rat brain

Joanes Grandjean[1, 2], Gabriel Desrosiers-Gregoire[3, 4], Cynthia Anckaerts[5, 6], Diego Angeles-Valdez[7], Fadi Ayad[8, 9, 10], David A Barrière[11], Ines Blockx[5, 6], Aleksandra Bortel[8, 10, 12], Margaret Broadwater[13, 14, 15], Beatriz M Cardoso[16], Marina Célestine[17], Jorge E Chavez-Negrete[18], Sangcheon Choi[18, 20], Emma Christiaen[21], Perrin Clavijo[22], Luis Colon-Perez[23], Samuel Cramer[24], Tolomeo Daniele[25], Elaine Dempsey[26, 27], Yujian Diao[28, 29], Arno Doelemeyer[30], David Dopfel[24], Lenka Dvořáková[31], Claudia Falfán-Melgoza[32], Francisca F Fernandes[16], Caitlin F Fowler[8, 3], Antonio Fuentes-Ibañez[18], Clément Garin[17], Eveline Gelderman[1], Carla EM Golden[33], Chao CG Guo[1], Marloes JAG Henckens[1, 34], Lauren A Hennessy[35, 36], Peter Herman[37, 38], Nita Hofwijks[1], Corey Horien[37], Tudor M Ionescu[39], Jolyon Jones[40], Johannes Kaesser[41], Eugene Kim[42], Henriette Lambers[43], Alberto Lazari[44], Sung-Ho Lee[13, 14, 15], Amanda Lillywhite[45, 46], Yikang Liu[24], Yanyan Y Liu[47], Alejandra López -Castro[7], Xavier López-Gil[48], Zilu Ma[24], Eilidh MacNicol[42], Dan Madularu[8, 49], Francesca Mandino[37], Sabina Marciano[39], Matthew J McAuslan[26], Patrick McCunn[50], Alison McIntosh[26, 27], Xianzong Meng[1], Lisa Meyer-Baese[22], Stephan Missault[5, 6], Federico Moro[51], Daphne MP Naessens[52], Laura J Nava-Gomez[53, 54], Hiroi Nonaka[55], Juan J Ortiz[18], Jaakko Paasonen[31], Lore M Peeters[5, 6], Mickaël Pereira[56], Pablo D Perez[24], Marjory Pompilus[57], Malcolm Prior[58], Rustam Rakhmatullin[59], Henning M Reimann[60], Jonathan Reinwald[61], Rodrigo Triana de Rio[62], Alejandro Rivera-Olvera[1], Daniel Ruiz-Pérez[59], Gabriele Russo[63], Tobias J Rutten[1], Rie Ryoke[55], Markus Sack[32], Piergiorgio Salvan[44], Basavaraju G Sanganahalli[37, 38], Aileen Schroeter[64], Bhedita J Seewoo[35, 36, 65], Erwan Selingue[66], Aline Seuwen[64], Bowen Shi[67], Nikoloz Simpilatze[68, 69, 70], Joanna AB Smith[71, 72, 73], Corrie Smith[22], Filip Sobczak[19, 20], Petteri J Stenroos[74], Milou Straathof[75], Sandra Strobelt[41], Akira Sumiyoshi[55, 76], Kengo Takahashi[19, 20], Maria E Torres-García[18], Raul Tudela[77], Monica van den Berg[5, 6], Kajo van der Marel[75], Aran TB van Hout[1], Roberta Vertullo[1], Benjamin Vidal[56], Roel M Vrooman[1], Victora X Wang[78], Isabel Wank[41], David JG Watson[45], Ting Yin[79], Yongzhi Zhang[80], Stefan Zurbruegg[81], Sophie Achard[82], Sarael Alcauter[18], Dorothee P Auer[83, 58], Emmanuel L Barbier[74], Jürgen Baudewig[68], Christian F Beckmann[1, 44], Nicolau Beckmann[30], Guillaume JPC Becq[84], Erwin LA Blezer[75], Radu Bolbos[85], Susann Boretius[86, 69, 70], Sandrine Bouvard[56], Eike Budinger[26, 87], Joseph D Buxbaum[33], Diana Cash[42], Victoria Chapman[45, 46, 8], Kai-Hsiang Chuang[88], Luisa Ciobanu[66], Bram F Coolen[52], Jeffrey W Dalley[40], Marc Dhenain[17], Rick M Dijkhuizen[75], Oscar Esteban[89], Cornelius Faber[43], Marcelo Febo[57], Kirk W Feindel[65], Gianluigi Forloni[90], Jérémie Fouquet[3], Eduardo A Garza-Villarreal[7], Natalia Gass[32], Jeffrey C Glennon[91], Alessandro Gozzi[82], Olli Gröhn[31], Andrew Harkin[26, 27], Arend Heerschap[2], Xavier Helluy[63, 93], Kristina Herfert[39], Arnd Heuser[94], Judith R Homberg[1], Danielle J Houwing[1], Fahmeed Hyder[37, 38], Giovanna Diletta Ielacqua[94], Ileana O Jelescu[28], Heidi Johansen-Berg[44], Gen Kaneko[95], Ryuta Kawashima[55], Sheila D Keilholz[22], Georgios A Keliris[5, 6], Clare Kelly[27, 96, 97], Christian Kerskens[27, 98], Jibran Y Khokhar[50], Peter C Kind[71, 72, 73, 99], Jean-Baptiste Langlois[85], Jason P Lerch[44, 100], Monica A López-Hidalgo[54], Denise Manahan-Vaughan[83], Fabien Marchand[101], Rogier B Mars[1, 44], Gerardo Marsella[102], Edoardo Micotti[90], Emma Muñoz-Moreno[48], Jamie Near[3, 103], Thoralf Niendorf[60, 104], Willem M Otte[75, 105], Patricia Pais[19, 106], Wen-Ju Pan[22], Roberto A Prado-Alcalá[18], Gina L Quirarte[18], Jennifer Rodger[35, 36], Tim Rosenow[107], Cassandra Sampaio-Baptista[44, 118], Alexander Sartorius[61], Stephen J Sawiak[108], Tom WJ Scheenen[2, 109], Noam Shemesh[16], Yen-Yu Ian Shih[13, 14, 15, 110], Amir Shmuel[8, 9, 10, 12, 111], Guadalupe Soria[112], Ron Stoop[62], Garth J Thompson[67], Sally M Till[71, 72, 73], Nick Todd[80], Annemie Van Der Linden[5, 6], Annette van der Toorn[75], Geralda AF van Tilborg[75], Christian Vanhove[21], Andor Veltien[2], Marleen Verhoye[5, 6], Lydia Wachsmuth[43], Wolfgang Weber-Fahr[32], Patricia Wenk[86], Xin Yu[19, 113], Valerio Zerbi[114, 115], Nanyin Zhang[24], Baogui B Zhang[47], Luc Zimmer[85, 56, 116], Gabriel A Devenyi[3, 117], M Mallar Chakravarty[8, 3, 117], Andreas Hess[41]

1. Donders Institute for Brain, Behaviour, and Cognition, Nijmegen, The Netherlands
2. Department for Medical Imaging, Radboud University Medical Center, PO Box 9101, Nijmegen, The Netherlands
3. Cerebral Imaging Centre, Douglas Mental Health University Institute, 6875 Boulevard LaSalle, Verdun, Canada
4. Integrated Program in Neuroscience, McGill University, Montreal, Canada
5. Bio-imaging lab, University of Antwerp, Universiteitsplein 1, Antwerp, Belgium
6. µNEURO Research Centre of Excellence, University of Antwerp, Antwerp, Belgium
7. Instituto de Neurobiología, Universidad Nacional Autónoma de México campus Juriquilla, Querétaro, Mexico
8. Biological and Biomedical Engineering, McGill University, 3775, rue University, Montreal, Canada
9. McConnell Brain Imaging Centre, McGill University, 3801 University St., Montreal, Canada
10. Montreal Neurological Institute, McGill University, 3801 University St., Montreal, Canada
11. UMR INRAE/CNRS 7247 Physiologie des Comportements et de la Reproduction, Physiologie de la reproduction et des comportements, Centre de recherche INRAE de Nouzilly, Tours, France
12. Department of Neurology and Neurosurgery, McGill University, 3801 University St., Montreal, Canada
13. Center for Animal MRI, The University of North Carolina at Chapel Hill, 125 Mason Farm Rd., Chapel Hill, USA
14. Neurology, The University of North Carolina at Chapel Hill, 125 Mason Farm Rd., Chapel Hill, USA
15. Biomedical Research Imaging Center, The University of North Carolina at Chapel Hill, 125 Mason Farm Rd., Chapel Hill, USA
16. Preclinical MRI, Champalimaud Research, Champalimaud Centre for the Unknown, Avenida de Brasília, Lisbon, Portugal
17. Laboratoire des Maladies Neurodégénératives, Molecular Imaging Research Center (MIRCen), Université Paris-Saclay, Commissariat à l'Énergie Atomique et aux Énergies Alternatives (CEA), CNRS, 18 Route du Panorama, Fontenay-aux-Roses, France
18. Departamento de Neurobiología Conductual y Cognitiva, Instituto de Neurobiología, Universidad Nacional Autónoma de México, Campus Juriquilla, Boulevard Juriquilla 3001, Querétaro, México
19. Translational Neuroimaging and Neural Control Group, High-Field Magnetic Resonance, Max Planck Institute for Biological Cybernetics, 72076, Tuebingen, Germany
20. Graduate Training Centre of Neuroscience, International Max Planck Research School, University of Tuebingen, 72074, Tuebingen, Germany
21. Institute Biomedical Technology (IBiTech), Electronics and Information Systems (ELIS), Ghent University, Corneel Heymanslaan 10, Gent, Belgium
22. Biomedical Engineering, Emory University/Georgia Institute of Technology, 1760 Haygood Dr, Atlanta, USA
23. Dept. of Pharmacology & Neuroscience, University of North Texas Health Science Center, 3500 Camp Bowie Blvd, Fort Worth, USA
24. Translational Neuroimaging and Systems Neuroscience Lab, Biomedical Engineering, Pennsylvania State University, W-341 Millennium Science Complex, University Park, USA
25. Centre for advanced biomedical imaging, University College London, London, UK
26. Neuropsychopharmacology Research Group, School of Pharmacy and Pharmaceutical Sciences, Trinity College Dublin, Dublin, Ireland
27. Trinity College Institute of Neuroscience, Trinity College Dublin, Dublin, Ireland
28. CIBM Center for Biomedical Imaging, Ecole Polytechnique Fédérale de Lausanne, Route des Noyerettes, Lausanne, Switzerland
29. Laboratory for Functional and Metabolic Imaging, Ecole Polytechnique Fédérale de Lausanne, Route des Noyerettes, Lausanne, Switzerland

30. Musculoskeletal Diseases Department, Novartis Institutes for BioMedical Research, Basel, Switzerland
31. Biomedical Imaging Unit, A.I.V. Institute for Molecular Sciences, University of Eastern Finland, Kuopio, Finland
32. Translational Imaging, Department of Neuroimaging, Central Institute of Mental Health, Medical Faculty Mannheim, University of Heidelberg, J5, Mannheim, Germany
33. Seaver Autism Center for Research & Treatment, Department of Psychiatry, Icahn School of Medicine at Mount Sinai, 1468 Madison Avenue, New York City, USA
34. Department of Neuroscience and Pharmacology, Rudolf Magnus Institute of Neuroscience, University Medical Center Utrecht, Heidelberglaan 100, Utrecht, The Netherlands
35. Experimental and Regenerative Neurosciences, School of Biological Sciences, The University of Western Australia, 35 Stirling Highway, Crawley, Australia
36. Brain Plasticity Group, Perron Institute for Neurological and Translational Science, 8 Verdun Street, Nedlands, Australia
37. Radiology and Biomedical Imaging, Yale University School of Medicine, New Haven, USA
38. Quantitative Neuroscience with Magnetic Resonance (QNMR) Core Center, Yale University School of Medicine, New Haven, USA
39. Werner Siemens Imaging Center, Department of Preclinical Imaging and Radiopharmacy, University of Tuebingen, Tuebingen, Germany
40. Department of Psychology, University of Cambridge, Downing Street, Cambridge, UK
41. Institute of Experimental and Clinical Pharmacology and Toxicology, FAU Erlangen-Nürnberg, Fahrstrasse 17, 91054 Erlangen, Germany
42. Biomarker Research And Imaging in Neuroscience (BRAIN) Centre, Department of Neuroimaging, King's College London, Coldharbour Lane, London, UK
43. Experimental Magnetic Resonance Group, Clinic of Radiology, University Hospital Münster, Albert-Schweitzer-Campus 1, Muenster, Germany
44. Nuffield Department of Clinical Neurosciences, Wellcome Centre for Integrative Neuroimaging, FMRIB, University of Oxford, John Radcliffe Hospital, Headington, OX3 9DU, Oxford, UK
45. School of Life Sciences, University of Nottingham, Nottingham, UK
46. Pain Centre Versus Arthritis, University of Nottingham, Nottingham, UK
47. Brainnetome CenterBrainnetome Center. Institute of Automation, Chinese Academy of Sciences, Zhongguancun East Road, Beijing. China
48. Magnetic Imaging Resonance Core Facility, Institut d'Investigacions Biomèdiques August Pi I Sunyer (IDIBAPS), Rosselló, 149-153, Barcelona, Spain
49. Center for Translational Neuroimaging, Northeastern University, 360 Huntington Avenue, Boston, USA
50. Khokhar Lab, Department of Anatomy and Cell Biology, Western University, 1151 Richmond St., London, Canada
51. Laboratory of Acute Brain Injury and Therapeutic Strategies, Neuroscience, Istituto di Ricerche Farmacologiche Mario Negri,IRCCS, via Mario Negri 2, Milan, Italy
52. Biomedical Engineering and Physics, Amsterdam UMC location University of Amsterdam, Amsterdam, The Netherlands
53. Facultad de Medicina, Universidad Autónoma de Querétaro, Querétaro, México
54. Escuela Nacional de Estudios Superiores unidad Juriquilla, Universidad Nacional Autónoma de México, Boulevard Juriquilla 3001, Querétaro, México
55. Institute of Development, Aging and Cancer, Tohoku University, 4-1 Seiryo-machi, Aoba-ku, Sendai, Japan
56. Lyon Neuroscience Research Center, Université Claude Bernard Lyon 1, INSERM, CNRS, Lyon, France
57. Febo Laboratory, Psychiatry, University of Florida, 1149 S. Newell Drive, Gainesville, United States
58. School of Medicine, University of Nottingham, Nottingham, UK
59. Comparative Medicine Unit, Trinity College Dublin, Dublin, Ireland
60. Berlin Ultrahigh Field Facility (B.U.F.F.), Max-Delbrück Center for Molecular Medicine in the Helmholtz Association, Robert-Rössle-Str. 10, Berlin, Germany
61. Translational Imaging, Department of Psychiatry and Psychotherapy, Central Institute of Mental Health, Medical Faculty Mannheim, University of Heidelberg, J5, Mannheim, Germany
62. Psychiatric neurosciences, Center for Psychiatric Neuroscience, Lausanne University and University Hospital Center, Unicentre, Lausanne, Switzerland
63. Department of Neurophysiology, Medical Faculty, Ruhr University Bochum, Universitätsstraße 150, Bochum, Germany
64. Institute for Biomedical Engineering, University and ETH Zurich, Wolfgang-Pauli-Str. 27, Zurich, Switzerland
65. Centre for Microscopy, Characterisation & Analysis, Research Infrastructure Centres, The University of Western Australia, 6 Verdun Street, Nedlands, Australia
66. NeuroSpin, CEA Saclay, Paris, France
67. iHuman Institute, ShanghaiTech University, Shanghai, China
68. Functional Imaging Laboratory, German Primate Center - Leibniz Institute for Primate Research, Kellnerweg 4, Göttingen, Germany
69. Faculty of Biology and Psychology, Georg-August University of Göttingen, Göttingen, Germany
70. DFG Research Center for Nanoscale Microscopy and Molecular Physiology of the Brain (CNMPB), Göttingen, Germany
71. Simons Initiative for the Developing Brain, The University of Edinburgh, Edinburgh, UK
72. Patrick Wild Centre, The University of Edinburgh, Edinburgh, UK
73. Centre for Discovery Brain Sciences, The University of Edinburgh, Edinburgh, UK
74. Grenoble Institut Neurosciences, Univ. Grenoble Alpes, CNRS, Grenoble, France
75. Biomedical MR Imaging and Spectroscopy Group, Center for Image Sciences, University Medical Center Utrecht & Utrecht University, Yalelaan 2, Utrecht, The Netherlands
76. National Institutes for Quantum Science and Technology, 4-9-1 Anagawa, Inage-ku, Chiba, Japan
77. Group of Biomedical Imaging, Consorcio Centro de Investigación Biomédica en Red (CIBER) de Bioingeniería, Biomateriales y Nanomedicina (CIBER-BBN), University of Barcelona, Barcelona, Spain
78. BioMedical Engineering and Imaging Institute, Icahn School of Medicine at Mount Sinai, 1470 Madison Avenue, New York City, USA
79. Animal Imaging and Technology Section, Center for Biomedical Imaging, École polytechnique fédérale de Lausanne, Route Cantonale, Lausanne, Switzerland
80. Focused Ultrasound Laboratory, Radiology, Brigham and Women's Hospital, 221 Longwood Ave, Boston, USA
81. Neurosciences Department, Novartis Institutes for BioMedical Research, Basel, Switzerland
82. Inria, Univ. Grenoble Alpes, CNRS, Grenoble, France
83. NIHR Biomedical Research Centre, University of Nottingham, Nottingham, UK
84. Gipsa-lab, Univ. Grenoble Alpes, CNRS, Grenoble, France
85. CERMEP - Imagerie du vivant, Lyon, France
86. Combinatorial NeuroImaging Core Facility, Leibniz Institute for Neurobiology, Brenneckestreet 6, Magdeburg, Germany
87. Center for Behavioral Brain Sciences, Universitaetsplatz 2, Magdeburg, Germany
88. Queensland Brain Institute and Centre for Advanced Imaging, University of Queensland, Building 79, St Lucia, Australia
89. Centre de recherche en radiologie, Centre Hospitalier Universitaire Vaudois, Rue Centrale 7, Lausanne, Switzerland
90. Biology of Neurodegenerative Disorders, Neuroscience, Istituto di Ricerche Farmacologiche Mario Negri,IRCCS, via Mario Negri 2, Milan, Italy
91. Conway Institute of Biomedical and Biomolecular Sciences, School of Medicine, University College Dublin, Dublin, Ireland
92. Functional Neuroimaging Laboratory, Center for Neuroscience and Cognitive systems, Istituto Italiano di Tecnologia, Rovereto, Italy
93. Department of Biopsychology, Institute of Cognitive Neuroscience, Ruhr University Bochum, Universitätsstraße 150, Bochum, Germany

94. Max-Delbrück Center for Molecular Medicine in the Helmholtz Association, Robert-Rössle-Straße 10, Haus 90, Berlin, Germany
95. School of Arts & Sciences, University of Houston-Victoria, Victoria, USA
96. School of Psychology, Trinity College Dublin, Dublin, Ireland
97. Department of Psychiatry at the School of Medicine, Trinity College Dublin, Dublin, Ireland
98. Trinity Centre for Biomedical Engineering, School of Medicine, Trinity College Dublin, Dublin 2, Ireland
99. Centre for Brain Development and Repair, Institute for Stem Cell Biology and Regenerative Medicine, Bangalore, India
100. Department of Medical Biophysics, University of Toronto, Toronto, Canada
101.Université Clermont Auvergne, Inserm U1107 Neuro-Dol, Pharmacologie Fondamentale et Clinique de la Douleur, Clermont-Ferrand, France
102. Animal Care Unit, Istituto di Ricerche Farmacologiche Mario Negri,IRCCS, via Mario Negri 2, Milan, Italy
103. Physical Sciences Platform, Sunnybrook Research Institute, 2075 Bayview Avenue, Toronto, Canada
104. Experimental and Clinical Research Center, A Joint Cooperation Between the Charité Medical Faculty and the Max-Delbrück Center for Molecular Medicine in the Helmholtz Association, Berlin, Germany
105. Department of Pediatric Neurology, UMC Utrecht Brain Center, University Medical Center Utrecht & Utrecht University, Heidelberglaan 100, Utrecht, The Netherlands
106. Medical Imaging Physics (INM-4), Institute of Neuroscience and Medicine, Forschungszentrum Juelich, 52428, Juellich, Germany
107. Centre for Microscopy, Characterisation and Analysis, The University of Western Australia, 35 Stirling Highway, Crawley, Australia
108. Translational Neuroimaging Laboratory, Physiology, Development and Neuroscience, University of Cambridge, Downing Street, Cambridge, UK
109. Erwin L. Hahn Institute for MR Imaging, University of Duisburg-Essen, Essen, Germany
110. Biomedical Engineering, The University of North Carolina at Chapel Hill, 125 Mason Farm Rd., Chapel Hill, USA
111. Department of Physiology, McGill University, 3655 Promenade Sir-William-Osler, Montreal, Canada
112. Laboratory of Surgical Neuroanatomy, Institute of Neuroscience, University of Barcelona, Casanova, 143, Barcelona, Spain
113. Athinoula A. Martinos Center for Biomedical Imaging, Massachusetts General Hospital and Harvard Medical School, MA 02129, Charlestown, USA
114. Department of Health Sciences and Technology, ETH Zurich, Wolfgang-Pauli-Str. 27, Zurich, Switzerland
115. Neuroscience Center Zürich, ETH Zürich and University of Zürich, Zürich, Switzerland
116. Hospices Civils de Lyon, Lyon, France
117. Department of Psychiatry, McGill University, 1033 Pine Avenue West, Montreal, Canada
118. School of Psychology and Neuroscience, University of Glasgow, Glasgow G61 1QH, UK

Corresponding author:
dr. Joanes Grandjean
PO Box 9101
6500HB Nijmegen
The Netherlands
joanes.grandjean@radboudumc.nl

Abstract
Task-free functional connectivity in animal models provides an experimental framework to examine connectivity phenomena under controlled conditions and allows for comparisons with data modalities collected under invasive or terminal procedures. To date, animal acquisitions are performed with varying protocols and analyses that hamper result comparison and integration. We introduce *StandardRat*, a consensus rat functional MRI acquisition protocol tested across 20 centers. To develop this protocol with optimized acquisition and processing parameters, we initially aggregated 65 functional imaging datasets acquired from rats across 46 centers. We developed a reproducible pipeline for analyzing rat data acquired with diverse protocols and determined experimental and processing parameters associated with the robust detection of functional connectivity across centres. We show that the standardized protocol enhances biologically plausible functional connectivity patterns, relative to previous acquisitions. The protocol and processing pipeline described here are openly shared with the neuroimaging community to promote interoperability and cooperation towards tackling the most important challenges in neuroscience.

Main

Understanding the brain requires a multilevel approach across spatial and temporal scales. Distinct brain network features, as revealed by task-free functional magnetic resonance imaging (fMRI), play a central role in our comprehension of healthy brain function and disorder mechanisms. This hemodynamic readout method relies on spontaneous fluctuations in the blood oxygenation level-dependent contrast signal to infer functional connectivity across the brain.

Human neuroimaging has made great strides in our understanding of the brain through open data-sharing initiatives focused on task-free fMRI data [1–5]. Nonetheless, animal models, particularly small rodents, continue to play an important role in neuroscience discovery, partly due to the feasibility of performing invasive and terminal manipulations on genetically controlled animals [6]. For example, rats are commonly used in pharmacological studies owing to similarities in drug metabolism, as well as in behavioral neuroscience due to their high proficiency in learning complex tasks. By leveraging the same neuroimaging methods and metrics obtained in humans, task-free neuroimaging in rodents may provide a translational bridge from the invasive methods only possible in animal models.

Human neuroimaging sharing initiatives have led to a standardization of fMRI acquisition protocols that aid in the dissemination, aggregation, and reuse of data [4,7,8]. In contrast, preclinical neuroimaging essentially remains without harmonizing guidelines [9]. Animal data acquisitions are performed under diverse protocols that span different strains, restraint and anesthesia conditions, radiofrequency coil designs, and magnetic field strengths. These impact the generalization of the results and conclusions. Efforts to propose acquisition and/or preprocessing protocols rarely extend beyond the confines of single laboratories, thus limiting interoperability and widespread adoption [9,10]. Thanks to the potential of fMRI in rodents to study the biological basis for connectivity phenomena across the whole-brain longitudinally [11], an optimized consensus protocol could potentiate future scientific discoveries.

In this preregistered study, we set out to aggregate and make publicly available representative datasets with various fMRI acquisition protocols in the rat and identify experimental parameters associated with robust and reliable functional connectivity detection. We curated the *Multirat_rest* collection (646 rats from 65 datasets) representing protocols used at 46 institutions. Based on the analysis of the *Multirat_rest* collection, we devised a new consensus protocol and used it to aggregate the *StandardRat* collection (209 rats from 21 datasets). Preprocessing and confound correction were tailored to rodent data of different characteristics using a rodent-adapted fMRI preprocessing and analysis tool. Our primary outcome was the detection of plausible functional connectivity patterns corresponding to the biologically expected models. Collating data from 50 centers and 855 rats, we show that standardized acquisition and the associated preprocessing pipeline optimize the detection of distributed fMRI networks in rats. In line with large-scale studies from other species [12,13], we have freely released all data and the generated code.

Results

We aggregated the *MultiRat_rest* collection of unstandardized fMRI datasets representative of local site acquisition procedures (N = 65 datasets, n = 646 rats). As expected, we found high heterogeneity in all experimental factors recorded, including rat characteristics (sex, strain, **Figure 1a,b,** age, weight, **Figure S1**), in-scan physiology (anesthesia/awake, breathing rates **Figure 1c,e**), and image acquisitions (magnetic field strength, sequence, and sequence parameters **Figure 1d,f,g**). Notably, there was a large sex bias in favor of males (**Figure 1a**). Similarly, the distribution of anesthesia protocols was also in line with current trends in the field (**Figure 1**c) [9]. Despite the heterogeneous distribution of the acquisition parameters and ensuing image quality (**Figure 1g,h,i**), 638/646 of the scans passed preprocessing quality control (one scan with excessive motion, one empty scan, six scans failed image registrations, **Figure 1j,k, Figure S2**). As further quality controls, we described temporal signal-to-noise (**Figure S3**) and motion parameters (**Figure S4**). Overall, we found that the aggregated datasets represent current rodent fMRI acquisition trends [9]. Moreover, given the low exclusion rate due to misregistration,

we concluded that the RABIES toolbox can be effectively employed to preprocess rat datasets despite widely varying acquisition parameters. This paves the way for reproducible and interoperable data processing across sites.

We focused on examining functional connectivity in the sensory cortex, as sensory networks are robust to assess anesthesia effects, in the anesthesia depth range typically used in fMRI [26]. More specifically, we evaluated the specificity of the connectivity of the S1 barrel field area (S1bf) using two complementary criteria as indexes of accurate functional connectivity identification (**Figure 2a,b**) [12]. The first criterion was the strong connectivity between inter-hemispheric sensory cortices (barrel field, S1bf). Indeed, in both humans and animals, dating back to the original description of functional connectivity [27], most networks including sensory-motor networks have a bilateral homotopic organization. The second criterion was a weak or anti-correlation between S1bf and the anterior cingulate area (ACA). The ACA is a major node in the task-negative rodent default-mode network. Task-positive (as the S1bf-associated sensory network [28,29]), and task-negative networks are generally non- or anti-correlated [30].

Functional connectivity was evaluated for each animal and divided into four categories based on these two criteria referred above: specific, nonspecific, spurious, and no connectivity. Five confound correction models were tested (**Table S2, Figure 2c**). The global signal regression nuisance model was the one that performed the best for specific connectivity detection (40.8% of the animals with specific connectivity, 11.8% as nonspecific, 13.6% as spurious, and 33.9% as containing no detectable functional connectivity, **Figure 2c,d,g**). To test the generalizability of the specificity metric to other networks, we implemented the same quality control metric to the cingulate cortex, a node of the rodent default-mode network, whichuncovered lower connectivity specificity (22.1%, **Figure S5**). Because network inference is often assessed at the group-level rather than at the individual-level, we performed a one-sample t-test per dataset to estimate the incidence of contralateral connectivity detected within groups, relative to the S1bf seed, as well as three other seeds (**Figure 3**). Up to 70% of the 65 datasets presented limited evidence of contralateral connectivity relative to the seeds, and 50% of the datasets captured the features of a larger sensory network at the group level. We conclude that rat datasets do not capture functional connectivity equally, similar to what we reported in the mouse [12]. We also found that global signal regression enhances the incidence of specific connectivity of S1bf seeds, so we decided to use this confound model for the remainder of our analysis.

Our observations underline the need for an improved acquisition protocol to maximize individual-level inferences to potentiate discovery in experimental network neuroscience. To address this, we evaluated parameters associated with increased specificity incidence in the *MultiRat_rest* collection. Because our analysis relied on categorical data, we tested for differences against the expected frequency distribution of the four connectivity categories as a function of anesthesia and sequence categories using the X^2 test. Medetomidine/isoflurane anesthesia combination condition was enriched in scans categorized as specific (**Figure 2e**, 92/187 scans, X^2 test *connectivity category ~ anesthesia*: $\varphi = 0.27$, dof = 15, g = 92.38, p = 3.5e-13). The use of gradient echo imaging sequence was also associated with higher specificity incidence (**Figure 2f,** 241/568 scans, X^2 test *connectivity category ~ sequence*: $\varphi = 0.11$, dof = 3, g = 16.00, p = 0.001). Based on these observations, we devised an anesthesia protocol derived from dataset ds01031 (9/10 specific scans), and an imaging sequence based on ds01028 (8/10 specific scans), acquired on a 4.7 T mid-field system. The sequence selection is justified as it allows for the detection of specific connectivity on one of the lower field systems used in this collection and should also perform well for higher field systems. We optimized relevant sequence parameters (echo time, flip angle, bandwidth) as a function of field strength (Table S1). We hypothesized that this protocol

would enhance functional specificity while being compatible with lower field systems that continue to represent a relevant share of the systems used (**Figure 1d**) [9].

Using this consensus protocol, we curated the *StandardRat* collection of 21 datasets obtained across 20 centers. This consisted of n = 209 rats (93/116 f/m) rats, mainly Wistar (189/209) aged ~ 2 months (**Figure S6**). Dataset acquisitions were performed at magnetic field strengths ranging from 4.7 to 17.2 T. Preprocessing was performed similarly to the unstandardized dataset. 207/209 scans passed quality assurance (two discards due to image misregistration). Interestingly, despite the same anesthesia protocol being used, the respiratory rates reported at the start of fMRI acquisition differed as a function of rat strain (**Figure 4a,b**, ANOVA *breathing rate ~ rat strain*, η^2 = 0.24, $F_{(195,2)}$ = 31.17, p = 1.8e-12,). Finally, there was only a negligible effect on the temporal signal-to-noise ratio as a function of magnetic field strength (**Figure 4c,** linear regression *temporal signal-to-noise ratio ~ field strength*, coef = 0.53 [-0.23, 1.30], r^2 = 0.01, dof = 201, T = 1.37, p = 0.17)**.**

The objective of the StandardRat study was to improve the detection of specific connectivity in the individual datasets. We found that 61.8% of the scans were categorized as exhibiting specific connectivity (**Figure 4d)** against 40.8% in the *MultiRat_rest* dataset with unstandardized acquisitions (**Figure S8a)** when using global signal regression (X^2 test *connectivity category ~ dataset collection*: φ = 0.13, dof = 3, g = 33.01, p = 3.2e-07). The difference remained when we compared datasets from centers that contributed to both collections exclusively (X^2 test *connectivity category ~ dataset collection*: φ = 0.17, dof = 3, g = 28.37, p = 3.0e-06). This is going against the notion that the *StandardRat* collection outperforms due to characteristics of the contributing laboratories (e.g., magnet type or strength; greater experience in data collection). Intriguingly, we could not establish a field strength effect on connectivity specificity (X^2 test *connectivity category ~ field strength*: φ = 0.19, dof = 12, g = 14.89, p-value = 0.25), suggesting acquisition systems are not the limiting factor in this protocol. We conclude that the newly standardized protocol outperforms, on average, previously used protocols within the community for the detection of biologically plausible connectivity patterns. Finally, to explore whole-brain connectivity patterns, we examined connectivity incidence at the dataset level for four selected seeds (**Figure S7**) and group independent component analysis (**Figure 4e, Figure S10**). We found improvement in distal connectivity detection at the dataset level compared to the MultiRat_rest dataset, as well as evidence for previously described rodent networks spanning across the whole brain [22].

Intriguingly, there remained differences in the connectivity patterns between datasets from the *StandardRat* collection. Indeed, 5/21 datasets achieved 90% specificity or above. This underlines the potential of our protocol, but also the need to understand what factors hamper other datasets. We next sought to identify the variables associated with greater incidences of specific connectivity patterns. Importantly, we could not establish strain, sex, or magnetic field strength effects, suggesting the protocol is applicable for a large range of conditions (**Table S3**). Next, we examined breathing rate and temporal signal-to-noise ratio as indicators of acquisition variability (**Figure S9**). Overall, scans with breathing rates ranging 84-114 breaths-per-minutes and cortical temporal signal-to-noise ratio >53 achieved higher incidences of connectivity specificity among the *StandardRat* collection. These provide the first line of evidence to refine the *StandardRat* protocol by identifying practices that can further enhance connectivity outcomes. The importance of these observations will require confirmations in new datasets, preferably across multiple centers, before the StandardRat protocol can be updated with new guidelines.

Discussion

In summary, we curated two dataset collections (*Multirat_rest* and *StandardRat)*, analyzed them, and made them an open-access resource. These are the largest rodent fMRI datasets currently available. We developed and deployed a preprocessing and confound correction strategy generalizable to most scans and every dataset. Using information from the *MultiRat_rest* collection, we provide useful population parameter estimates to enhance the comparison of rat fMRI datasets. We proposed and evaluated a new standardized protocol and found that this consensus acquisition and preprocessing pipeline outperformed the previous acquisitions for connectivity specificity. To allow replication and to inspire new analyses we release all raw and processed data to the broader community.

On average, the standardized protocol yielded improvements over previous acquisitions gathered in the *MultiRat_rest* collection. However, individual-level inferences remain limited to 61.8% of the scans acquired. For comparison, we estimated 55% specificity in the 7T Human Connectome Project dataset (based on 184 scans) using the same quality assurance metrics [5]. This underlines the importance of implementing sound quality assurance metrics based on assumptions of biologically-plausible functional connectivity. Improving output quality, either through understanding the factors leading to successful acquisitions, enhanced protocols, preprocessing, or nuisance regression models would lead to tangible outcomes capable of further potentiating future data acquisitions and reducing animal use by reducing discards.

Importantly, our new protocol relies on light sedation to restrain the animals. While optimized for fMRI, this protocol may not generalize to other procedures such as electrophysiology. We also found that existing awake restraining protocols, on average, lead to a lower incidence of specific connectivity patterns (**Figure S8b**). A previous report has indicated similar values in a dataset in awake rats [16], which we confirmed with preprocessing using the RABIES pipeline (**Figure S8b**) Due to the impact of anesthesia on networks [9,10], it remains central to develop awake imaging as an alternative. However, these protocols should be examined through the lens of quality control metrics to ensure plausible connectivity patterns are achieved consistently. Further, physiological factors, such as heart rate, were scarcely reported. This limited our ability to examine the possible contribution of these factors on connectivity outcomes. We take this opportunity to encourage the community to acquire these data and report them in ensuing publications. Finally, the acquisition sequence in *StandardRat* is designed to run on many systems. The effectiveness of new sequences should be examined against the current protocol, e.g., isotropic resolution [32] or multiband acquisition [33].

Our project's methodological and conceptual advancements are the first step toward large multi-site rat neuroimaging acquisitions. Coordinated open-science projects in neuroimaging and other disciplines are transforming the scientific landscape [34]. Through the concerted efforts of our centers and potentiated by a substantially improved protocol, rat functional brain imaging is set to tackle urgent questions in neuroscience and mental health research.

References

1. Elam, J. S. *et al.* The Human Connectome Project: A retrospective. *NeuroImage* **244**, 118543 (2021).
2. Mennes, M., Biswal, B., Castellanos, F. X. & Milham, M. P. Making data sharing work: The FCP/INDI experience. *NeuroImage* **82**, 683 (2013).
3. Miller, K. L. *et al.* Multimodal population brain imaging in the UK Biobank prospective

epidemiological study. *Nat. Neurosci.* **19**, 1523–1536 (2016).

4. Smith, S. M. *et al.* Resting-state fMRI in the Human Connectome Project. *NeuroImage* **80**, 144–168 (2013).
5. Van Essen, D. C. *et al.* The WU-Minn Human Connectome Project: an overview. *NeuroImage* **80**, 62–79 (2013).
6. Homberg, J. R. *et al.* The continued need for animals to advance brain research. *Neuron* **109**, 2374–2379 (2021).
7. Alfaro-Almagro, F. *et al.* Image processing and Quality Control for the first 10,000 brain imaging datasets from UK Biobank. *NeuroImage* **166**, 400–424 (2018).
8. Esteban, O. *et al.* FMRIPrep: a robust preprocessing pipeline for functional MRI. *Nat. Methods* **16**, 111–116 (2019).
9. Mandino, F. *et al.* Animal Functional Magnetic Resonance Imaging: Trends and Path Toward Standardization. *Front. Neuroinformatics* **13**, 78 (2019).
10. Reimann, H. M. & Niendorf, T. The (Un)Conscious Mouse as a Model for Human Brain Functions: Key Principles of Anesthesia and Their Impact on Translational Neuroimaging. *Front. Syst. Neurosci.* **14**, 8 (2020).
11. Pais-Roldán, P. *et al.* Contribution of animal models toward understanding resting state functional connectivity. *NeuroImage* **245**, 118630 (2021).
12. Grandjean, J. *et al.* Common functional networks in the mouse brain revealed by multi-centre resting-state fMRI analysis. *NeuroImage* **205**, 116278 (2020).
13. Milham, M. P. *et al.* An Open Resource for Non-human Primate Imaging. *Neuron* **100**, 61-74.e2 (2018).
14. Desrosiers-Gregoire, G., Devenyi, G. A., Grandjean, J. & Chakravarty, M. M. Rodent Automated Bold Improvement of EPI Sequences (RABIES): A standardized image processing and data quality platform for rodent fMRI. 2022.08.20.504597 Preprint at https://doi.org/10.1101/2022.08.20.504597 (2022).

15. Barrière, D. A. *et al.* The SIGMA rat brain templates and atlases for multimodal MRI data analysis and visualization. *Nat. Commun.* **10**, 5699 (2019).
16. Papp, E. A., Leergaard, T. B., Calabrese, E., Johnson, G. A. & Bjaalie, J. G. Waxholm Space atlas of the Sprague Dawley rat brain. *NeuroImage* **97**, 374–386 (2014).
17. Liu, Y. *et al.* An open database of resting-state fMRI in awake rats. *NeuroImage* **220**, 117094 (2020).
18. Gorgolewski, K. J. *et al.* The brain imaging data structure, a format for organizing and describing outputs of neuroimaging experiments. *Sci. Data* **3**, 160044 (2016).
19. Cox, R. W. AFNI: Software for Analysis and Visualization of Functional Magnetic Resonance Neuroimages. *Comput. Biomed. Res.* **29**, 162–173 (1996).
20. Avants, B., Tustison, N. J. & Song, G. Advanced Normalization Tools: V1.0. *Insight J.* (2009) doi:10.54294/uvnhin.
21. Pruim, R. H. R. *et al.* ICA-AROMA: A robust ICA-based strategy for removing motion artifacts from fMRI data. *NeuroImage* **112**, 267–277 (2015).
22. Zerbi, V., Grandjean, J., Rudin, M. & Wenderoth, N. Mapping the mouse brain with rs-fMRI: An optimized pipeline for functional network identification. *NeuroImage* **123**, 11–21 (2015).
23. Abraham, A. *et al.* Machine learning for neuroimaging with scikit-learn. *Front. Neuroinformatics* **8**, (2014).
24. Virtanen, P. *et al.* SciPy 1.0: fundamental algorithms for scientific computing in Python. *Nat. Methods* **17**, 261–272 (2020).
25. Vallat, R. Pingouin: statistics in Python. *J. Open Source Softw.* **3**, 1026 (2018).
26. Paasonen, J., Stenroos, P., Salo, R. A., Kiviniemi, V. & Gröhn, O. Functional connectivity under six anesthesia protocols and the awake condition in rat brain. *NeuroImage* **172**, 9–20 (2018).
27. Biswal, B., Yetkin, F. Z., Haughton, V. M. & Hyde, J. S. Functional connectivity in the motor cortex of resting human brain using echo-planar MRI. *Magn. Reson. Med.* **34**, 537–541

(1995).

28. Gozzi, A. & Schwarz, A. J. Large-scale functional connectivity networks in the rodent brain. *NeuroImage* **127**, 496–509 (2016).

29. Mandino, F. *et al.* A triple-network organization for the mouse brain. *Mol. Psychiatry* (2021) doi:10.1038/s41380-021-01298-5.

30. Fox, M. D. *et al.* The human brain is intrinsically organized into dynamic, anticorrelated functional networks. *Proc. Natl. Acad. Sci.* **102**, 9673–9678 (2005).

31. Gutierrez-Barragan, D., Basson, M. A., Panzeri, S. & Gozzi, A. Infraslow State Fluctuations Govern Spontaneous fMRI Network Dynamics. *Curr. Biol. CB* **29**, 2295-2306.e5 (2019).

32. Lee, S.-H. *et al.* An isotropic EPI database and analytical pipelines for rat brain resting-state fMRI. *NeuroImage* **243**, 118541 (2021).

33. Lee, H.-L., Li, Z., Coulson, E. J. & Chuang, K.-H. Ultrafast fMRI of the rodent brain using simultaneous multi-slice EPI. *NeuroImage* **195**, 48–58 (2019).

34. Milham, M. P. *et al.* Assessment of the impact of shared brain imaging data on the scientific literature. *Nat. Commun.* **9**, 2818 (2018).

Figure legends

Figure 1. ***MultiRat_rest dataset description. a.*** *Sex,* ***b.*** *Strain,* ***c.*** *Anesthesia,* ***d.*** *Magnetic field strength,* ***e.*** *Breathing rate as a function of anesthesia,* ***f.*** *Repetition time,* ***g.*** *Echo time as a function of magnetic field strength,* ***h.*** *Slice position for the examples,* ***i.*** *Example of representative raw functional images. Arrows indicate different susceptibility artifact-related geometric distortions in the amygdala.* ***j.*** *Successful anatomical (top) to standard (bottom) space registration. Red lines indicate the outlines of the standard image (top) and the anatomical (bottom).* ***k.*** *Successful functional (top) to anatomical (bottom) registration. Red lines indicate the outlines of the anatomical image (top) and the functional (bottom).*

Figure 2. ***Functional connectivity specificity. a.*** *Diagram illustrating the logic behind functional connectivity specificity. The sensory (barrel field, S1bf) area (blue) chiefly projects to the contralateral homotopic area (light blue), but not to the anterior cingulate area (ACA) area (purple)* ***b.*** *Example of temporal dynamics in the resting-state signal. Correlated signal between the ipsi- and contralateral S1bf, and anti-correlated signal from the ACA.* ***c.*** *Distribution of functional connectivity (FC) categories as a function of confound correction models.* ***d.*** *Functional connectivity in left S1bf relative to specific (right S1bf) and nonunspecific (ACA) ROIs using the global regression correction model. Dots represent scans (n = 638 rats), dotted lines indicate the*

thresholds used to delineate the categories. ***e.*** *Distribution of connectivity categories as a function of anesthesia.Example of individual seed-based analysis maps for each connectivity category.* ***f.*** *Distribution of connectivity categories as a function of imaging sequence (SE = spin echo, GE = gradient echo, EPI = echo-planar imaging).Group-level functional connectivity incidence map (N = 65 datasets).* ***g.*** *Example of individual seed-based analysis maps for each connectivity category.*

Figure 3. ***Incidence of functional connectivity at the group level*** *(N=65 datasets of n ~ 10 subjects per dataset) for four seeds. S1bf: Somatosensory Barrel field; ACA: Anterior cingulate area; Cpu: caudate-putamen; MOp: primary motor area. (MOp) and caudoputamen (CPu) seeds, were generally observed in 50 - 75% of the datasets.*

Figure 4. ***StandardRat*** **dataset description. a.** Breathing rate (breath per minute, bpm) as a function of strain. **b.** Mean framewise displacement (MFW) as a function of strain. **c.** Temporal signal-to-noise ratio in the sensory cortex as a function of field strength. **d.** *Functional connectivity in left S1bf relative to specific (right S1bf) and nonunspecific (ACA) ROIs using the global regression correction model. Dots represent scans (n = 207 rats), dotted lines indicate the thresholds used to delineate the categories.* ***e.*** *Representative independent components.*

Methods

Preregistration: The study was pre-registered (https://doi.org/10.17605/OSF.IO/EMQ4B). Here are notable deviations. We used the SIGMA rat template [15] instead of the Papp et al. 2014 template [16], due to fewer artifacts, additional relevant assets, and improved *in vivo* contrast. Some datasets had field-of-view cropped to ease image registration. Some datasets had time-series cropped to ease the computational load. We used temporal signal-to-noise instead of signal-to-noise ratio as these were shown to be correlated [12]. Detailed deviations are listed here: https://github.com/grandjeanlab/MultiRat.

Animals: All acquisitions were performed following approval from the respective local and national ethical authorities. Participating laboratories were instructed to provide n = 10 rat imaging acquisitions consisting of one anatomical and one resting-state functional run. Exclusion criteria were unsuitability for RABIES preprocessing (*e.g.*, dedicated image reconstruction needs, restricted field-of-view). The *MultiRat_rest* collection consists of N = 65 datasets from 46 research centers, n = 646 rats (141/505 f/m). *StandardRat* consists of N = 21 datasets, n = 209 rats (93/116 f/m) from 20 research centers. For comparison, 224 scans (n = 39 rats) from a single-center awake rat dataset were included [17]. Exclusions were based on the following criteria: image misregistration **(Figure S2)**, excessive motion, and missing or corrupted data.

Standardized fMRI acquisition protocol: The standardized protocol was determined based on the outcomes of the analysis of *MultiRat_rest* and used to acquire the *StandardRat* dataset. Acquisitions were performed chiefly in ~2 months old free-breathing Wistar rats, mixed-sex, and anesthetized using 4% isoflurane and 0.05 mg/kg medetomidine s.c. bolus for induction, and 0.4% isoflurane and 0.1 mg/kg/h medetomidine s.c. for maintenance. Imaging with a gradient-echo echo-planar imaging technique was conducted 40 min post-anesthesia induction, with repetition time = 1000 ms, echo time / flip angle / bandwidth defined as a function of field strength (**Table S1**), repetitions = 1000, matrix size [64 x 64], field-of-view (25.6 x 25.6) mm^2, 18 interleaved axial slices of 1 mm with 0.1 mm gap. The full protocol is available here: https://github.com/grandjeanlab/StandardRat.

Data preprocessing and confound correction: Scans were organized according to the BIDS format[18]. Preprocessing was performed on each scan session separately using a reproducible containerized software environment for RABIES 0.3.5 (Singularity 3.7.3-1.el7, Sylabs, California, USA). The preprocessing was performed using autobox [19], N4 inhomogeneity correction [20], motion correction [20], a rigid registration between functional and anatomical scans [20], non-linear registration between anatomical scan and template, and a common space resampling to (0.3 x 0.3 x 0.3) mm^3. A volumetric image registration and brain masking workflow wereas developed to address discrepancies in brain size, image contrast and susceptibility distortions that are found in rodent images. Visual inspection was performed on preprocessing outputs for all scans for quality control. Five confound correction models were tested, using three approaches based on ICA-AROMA [21], white-matter and ventricle signal, or global signal regression (**Table S2**). These were done together with motion regression, spatial smoothing to $(0.5\ mm)^3$, a high-pass filter of 0.01 Hz, and a low-pass filter of either 0.1 or 0.2 Hz. The ICA-AROMA method was adapted from humans to rats by using dedicated rat cerebrospinal fluid and brain edge masks, and by training the classifier parameters based on a set of rodent images [14]. A visual inspection of the components and their classifications indicated that < 5% of the plausible signal components were erroneously labeled as noise.

Data analysis: To determine functional connectivity in individual rats, seed-based analysis was performed with RABIES in template-space using spherical seeds of 0.9 mm diameter located on the S1 barrel field area (S1bf), and anterior cingulate area (ACA), caudate-putamen, and primary motor area. Functional connectivity was calculated as the Pearson's correlation coefficient between regional time-courses. Functional connectivity specificity was defined relative to the left S1bf seed, using the contralateral right S1bf region-of-interest as the specific region-of-interest, and the ACA as the nonspecific region-of-interest[12]. Functional connectivity was evaluated for each animal and divided into four categories: specific ($r_{S1bf\ left\ to\ right} > 0.1$ AND $r_{S1bf\ left\ to\ ACA} < 0.1$), nonspecific ($r_{S1bf\ left\ to\ right} > 0.1$ AND $r_{S1bf\ left\ to\ ACA} > 0.1$), no ($r_{S1bf\ left\ to\ right}$ [-0.1, 0.1] AND $r_{S1bf\ left\ to\ ACA}$ [-0.1, 0.1]), and spurious connectivity (remaining cases). To assess connectivity specificity in the default-mode network, the same approach was implemented with a seed in the ACA., tThe specific region-of-interest was located in the ACA (3.3 mm posterior to the seed), and the nonspecific region-of-interest was located in the S1bf. To assess whole-brain connectivity, group independent component analysis was performed with n = 20 components using Nilearn (https://github.com/grandjeanlab/MultiRat/blob/master/assets/nifti/canica_resting_state_clean.nii.gz). Components' biological plausibility was assessed using criteria defined in Zerbi et al. 2015 [22]. For comparison against humans, the same quality control metric was implemented on the 7T Human Connectome Project dataset [5]. The FIX-denoised scans (n = 184 participants) were bandpass corrected (0.01 to 0.1 Hz) and smoothed ($2.5\ mm^2$) using 3dTproject. Region-of-interest were positioned in the sensory cortex and ACA.

Statistical analysis: One sample t-test voxel-wise maps and group independent component analysis were estimated using Nilearn 0.7.1 [23]. Comparisons between functional connectivity specificity and categorical variables (e.g., magnetic field strength, strain, sex) were determined using X^2 tests, as implemented in SciPy 1.6.2 [24]. Continuous variables (e.g., mean framewise displacement) were transformed into six categorical bins to allow comparison with □2 tests. Linear regression and ANOVA were performed using Pingouin 0.5 [25]. Individual seed-based maps are represented as color-coded overlays thresholded at r > 0.1. Given the emphasis on detection of functional connectivity and the factors that affect it, we mitigated against false negatives by applying a liberal threshold of $p_{uncorrected} < 0.05$ to the one-sample t-test maps, following preregistration specifications. This thresholding is justified sinceas we did not want to exclude any datasets with weakpotential traces of functional connectivity. Slice positions are indicated in mm relative to the anterior commissure.

Code availability: Jupyter notebooks demonstrating the analysis code are available under the terms of the Apache-2.0 license (https://github.com/grandjeanlab/MultiRat).

Data availability: The raw datasets are available here: Unstandardized resting-state fMRI (*MultiRat_rest*) (https://doi.org/10.18112/openneuro.ds004114.v1.0.0); Standardized resting-state fMRI (*StandardRat*) (https://doi.org/10.18112/openneuro.ds004116.v1.0.0). The preprocessed volumes, time-series, and quality control files are available here (https://doi.org/10.34973/1gp6-gg97). Image preprocessing, confound correction and connectivity analysis were performed using RABIES 0.3.5 (https://github.com/CoBrALab/RABIES [14]).

Acknowledgments: This research was enabled in part by support provided by Compute Ontario https://www.computeontario.ca/ and Compute Canada (www.computecanada.ca). For the purpose of Open Access, the author has applied a CC BY public copyright license to any Author Accepted Manuscript version arising from this submission.This research was funded by: the National Institute of Health (K01EB023983, R03DA042971, R21AG065819, K25DA047458, I01S10CX000642-04, R01NS085200, R01MH098003, RF1MH114224, T32AA007573, R01MH067528, P30NS05219, T32GM007205, R01MH111416, R01NS078095, R01EB029857, F31 MH115656, 1R21MH116473-01A1), The Wellcome Trust (212934/Z/18/Z, 109062/Z/15/Z, 110027/Z/15/Z, 203139/Z/16/Z), The Dutch Research Council (OCENW.KLEIN.334, 021.002.053, 016.130.662, 016.168.038), The German Research Foundation (SA 1869/15-1, SA 2897/2-1, SFB 874/B3, SFB 1280/A01, SFB 1436/B06), The French National Research Agency (ANR-15-IDEX-02, ANR-11-INBS-0006), Programa de Apoyo a Proyectos de Investigación e Innovación Tecnológica (IN212219, IA202120, IA201622), UK Medical Research Council (MR/N013700/1, 1653552), Portuguese Foundation for Science and Technology (LISBOA-01-0145-FEDER-022170, 275-FCT-PTDC/BBB/IMG/5132/2014), the Swiss National Science Foundation (PCEFP3_203005, PCEFP2_194260), King's College London, Biotechnology and Biological Sciences Research Council (BB/N009088/1), European Community's Seventh Framework Program (FP7/2007-2013), TACTICS (278948), the Brain and Behaviour Foundation (NARSAD, 25861), The Dutch Brain Foundation (F2014(1)-06), The National Science Foundation (DMR-1644779, 1533260), Human Brain Project (945539), Canadian Institutes of Health Research (PJT-148751, PJT-173442, MOP-102599), The Natural Sciences and Engineering Research Council of Canada (RGPIN-2020-05917, RGPIN-375457-09, RGPIN-2015-05103), Horizon 2020 Framework Programme of the European Union (740264, 802371), Academy of Finland (298007), European Research Council (ERC, 679058, 802371), Innosuisse (18546.1), The Research Foundation – Flanders (12W1619N, FWO-G048917N, G045420N), the Stichting Alzheimer Onderzoek (SAO-FRA-20180003), Special Research Programmes (1158), CIBER-BBN, Instituto de Salut Carlos III - FEDER (PI18/00893), Versus Arthritis (20777), The Brain Behavior Foundation (25861), Telethon Foundation (GGP19177), Eurostars (E!114985), Brain Canada Foundation platform support grant (PSG15-3755), the National Natural Science Foundation of China (81950410637), Fonds de recherche du Québec – Nature et technologies, the Forrest Research Foundation, Australian National Imaging Facility, University of Western Australia, National Health and Medical Research Council of the Australian Government, Perron Institute for Neurological and Translational Science, McGill University's Faculty of Medicine, Seaver Foundation, Autism Speaks, the Centre d'Imagerie BioMédicale of the UNIL, UNIGE, HUG, CHUV, EPFL, the Leenaards and Louis-Jeantet Foundations, DFG Research Center for Nanoscale Microscopy and Molecular Physiology of the Brain, the Synapsis foundation, Simons Initiative for the Developing Brain, the Patrick Wild Centre, Department of Biotechnology India, Utrecht University High Potential Program, ERA-NET NEURON Neuromarket, Mannheim Advanced Clinician Scientist Program, ICON - Interfaces and Interventions in Complex Chronic Conditions, Werner Siemens Foundation, Lisboa Regional Operational Programme. The Japan Ministry of Education,

Culture, Sports, Science and Technology (MEXT), ShanghaiTech University, the Shanghai Municipal Government. Interdisciplinary Center for Clinical Research Münster (PIX)

Author contributions: JG designed, planned, and executed the study, and wrote the manuscript. GDG, GAD, and MMC provided the software and hardware environment for the analysis. All authors contributed experimental data and edited the manuscript. AH initiated the study.

Competing interest: Aline Seuwen is an employee of Bruker, the manufacturer of preclinical MRI systems used for the acquisition of the majority of the datasets in this collection. Emmanuel L. Barbier is a consultant for Bruker. Benjamin Vidal is an employee of Theranexus company. Stefan Zurbruegg, Arno Doelemeyer, and Nicolau Beckmann are employees of Novartis Pharma AG. Thoralf Niendorf is founder and CEO of MRI.TOOLS GmbH.

Figure 1

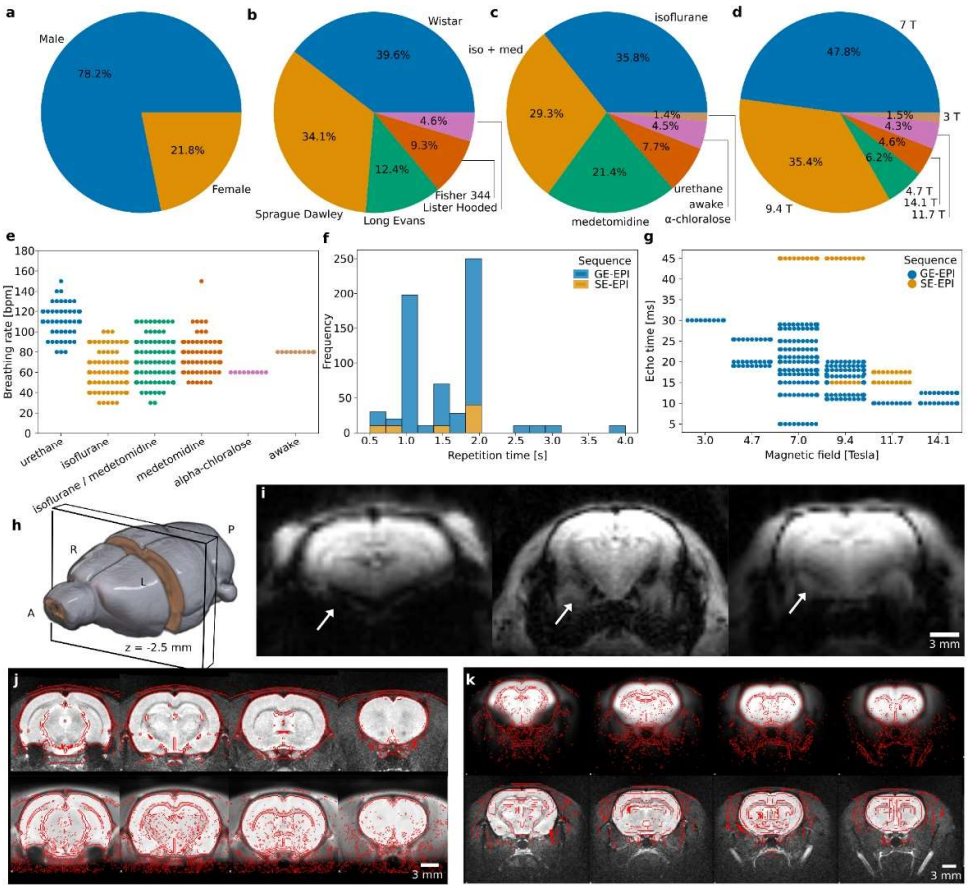
a
Male
78.2%
21.8%
Female
b
Wistar
39.6%
34.1%
4.6%
9.3%
12.4%
Fisher 344
Lister Hooded
Sprague Dawley
Long Evans
c
isoflurane
iso + med
35.8%
29.3%
1.4%
4.5%
7.7%
21.4%
urethane
awake
α-chloralose
medetomidine
d
7 T
47.8%
3 T
1.5%
4.3%
4.6%
6.2%
35.4%
4.7 T
14.1 T
11.7 T
9.4 T
e
Breathing rate [bpm]
urethane
isoflurane
isoflurane / medetomidine
medetomidine
alpha-chloralose
awake
f
Frequency
Sequence
GE-EPI
SE-EPI
Repetition time [s]
g
Echo time [ms]
Sequence
GE-EPI
SE-EPI
Magnetic field [Tesla]
h
R
L
P
A
z = -2.5 mm
i
3 mm
j
3 mm
k
3 mm

Figure 2

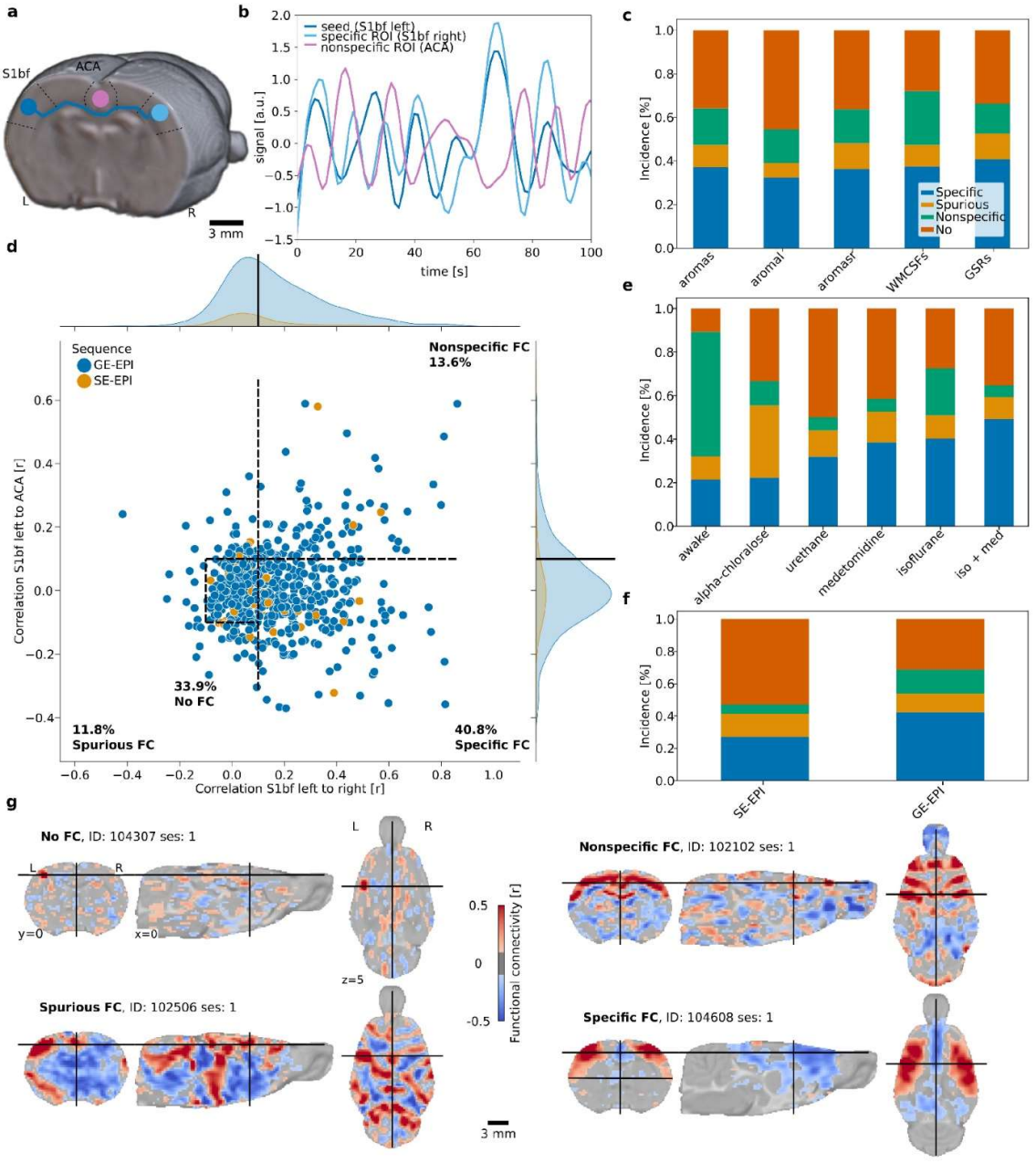
a
S1bf
ACA
L
R
3 mm
b
seed (S1bf left)
specific ROI (S1bf right)
nonspecific ROI (ACA)
signal [a.u.]
time [s]
c
Incidence [%]
Specific
Spurious
Nonspecific
No
aromas
aromal
aromasr
WMCSFs
GSRs
d
Sequence
GE-EPI
SE-EPI
Nonspecific FC
13.6%
33.9%
No FC
11.8%
Spurious FC
40.8%
Specific FC
Correlation S1bf left to ACA [r]
Correlation S1bf left to right [r]
e
Incidence [%]
awake
alpha-chloralose
urethane
medetomidine
isoflurane
iso + med
f
Incidence [%]
SE-EPI
GE-EPI
g
No FC, ID: 104307 ses: 1
Spurious FC, ID: 102506 ses: 1
Nonspecific FC, ID: 102102 ses: 1
Specific FC, ID: 104608 ses: 1
y=0
x=0
z=5
Functional connectivity [r]
3 mm

Figure 3

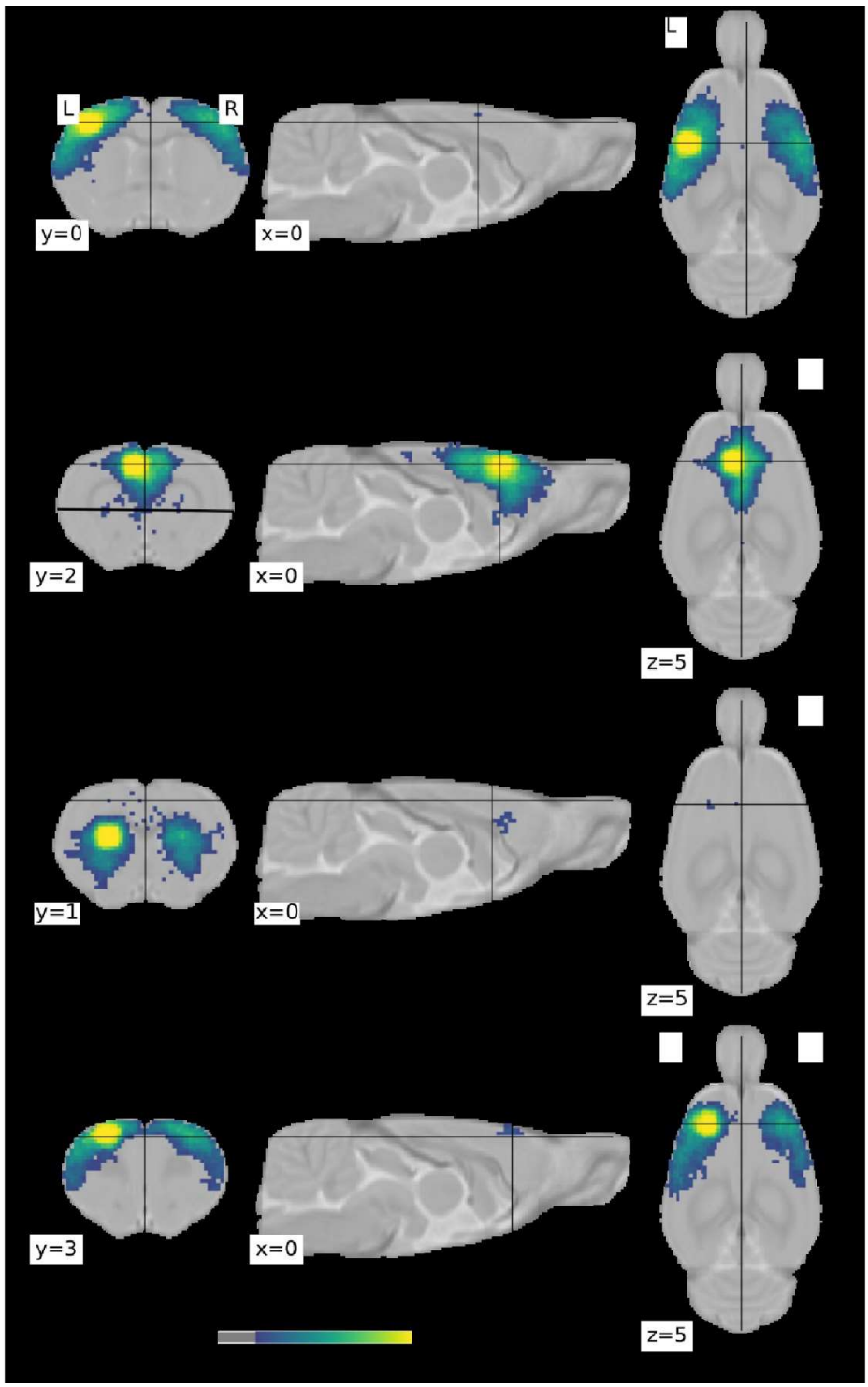

Figure 4

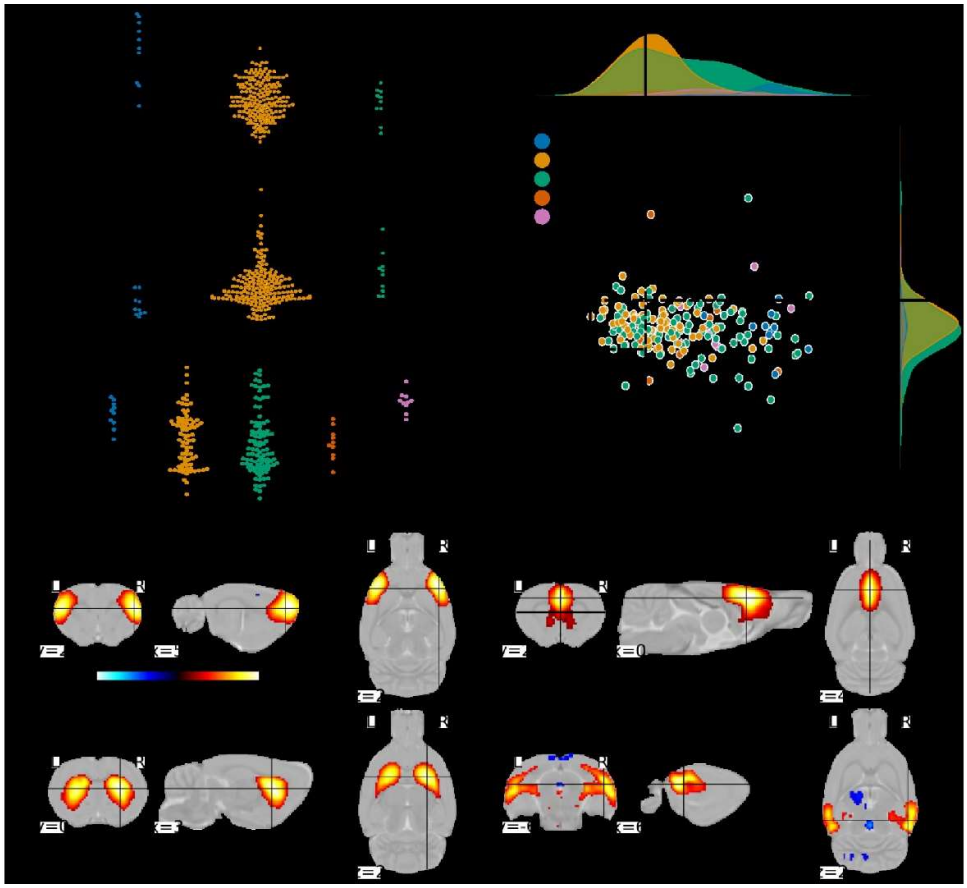

Supplementary material

Table S1 | Magnetic field strength-dependent parameters for the StandardRat acquisition protocol.

	3T	4.7T	7T	9.4T	11.7T	14.1T	17.2T
TE [ms]	30	25	17	15	12	10	9
Flip angle [degree]	64	61	55	53	52	51	50
Receiver bandwidth [kHz]	180	200	220	250	250	300	300

Table S2 | Confound correction model.

Confound model	Low-pass filter	Nuisance regression	Other	RABIES arguments
aromas	0.1 Hz	ICA-AROMA	-	--lowpass 0.1 --run_aroma --aroma_dim 10
aromal	0.2 Hz	ICA-AROMA	-	--lowpass 0.2 --run_aroma --aroma_dim 10
aromasr	0.1 Hz	ICA-AROMA	Framewise displacement censoring together with 1 back and 2 forward frames at FD threshold 0.05	--lowpass 0.1 --run_aroma --aroma_dim 10 --FD_censoring
WMCSFs	0.1 Hz	White matter + Cerebrospinal fluid + motion	-	-lowpass 0.1 --conf_list WM_signal CSF_signal mot_6
GSRs	0.1 Hz	Global signal regression + motion	-	--lowpass 0.1 --conf_list global_signal mot_6

Table S3 | Frequency test ($\square^2$) for connectivity categories in the StandardRat collection

Effect	Effect size (φ)	Degrees of freedom	g-value	p-value
Strain	0.15	6	8.77	0.19
Sex	0.07	3	2.16	0.54
Field strength	0.19	12	14.89	0.25

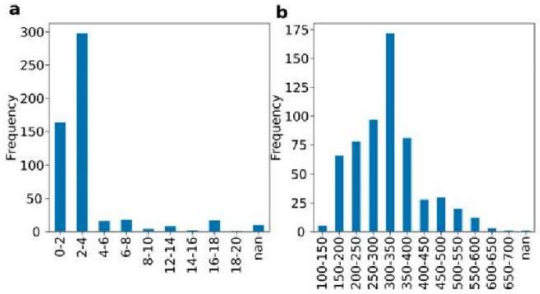

Figure S1. *Age (**a**) and weight (**b**) distribution for the rats in the multiRat_rest collection.*

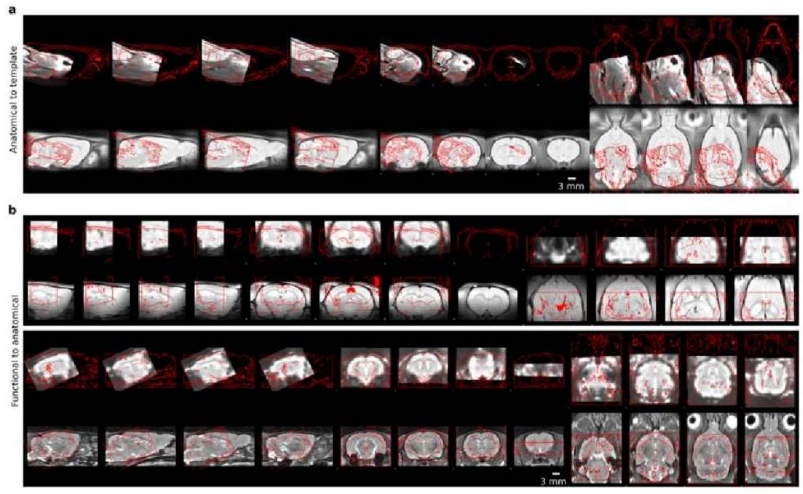

Figure S2. *Failed quality controls for anatomical to template registrations (**a**) and functional to anatomical registrations (**b**). The top rows are the moving objects, bottom rows are the reference objects. The red lines indicate the outlines of the other object. Four slices along the sagittal, axial, and coronal axis are shown for each case.*

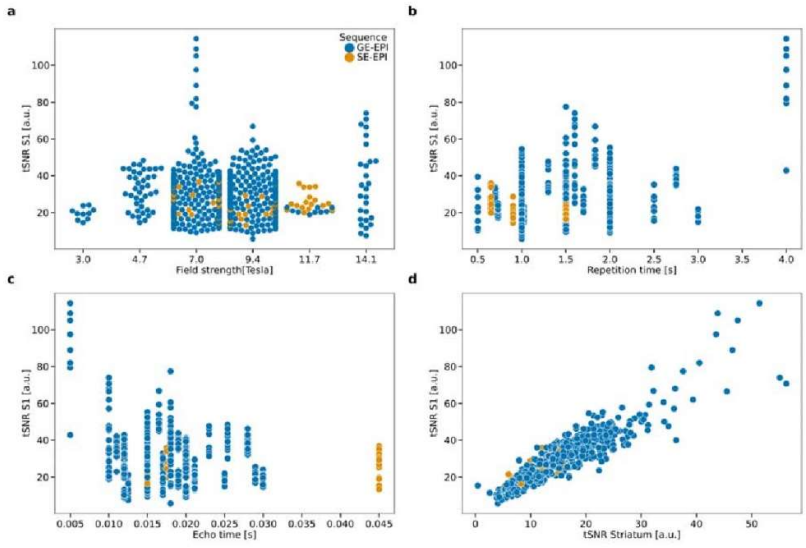

Figure S3. *Temporal signal-to-noise ratio in the sensory cortex (tSNR S1) in the multiRat_rest dataset collection as a function of (**a**) magnetic field strength, (**b**) repetition time, (**c**) echo time, (**d**) temporal signal-to-noise ratio in the striatum.*

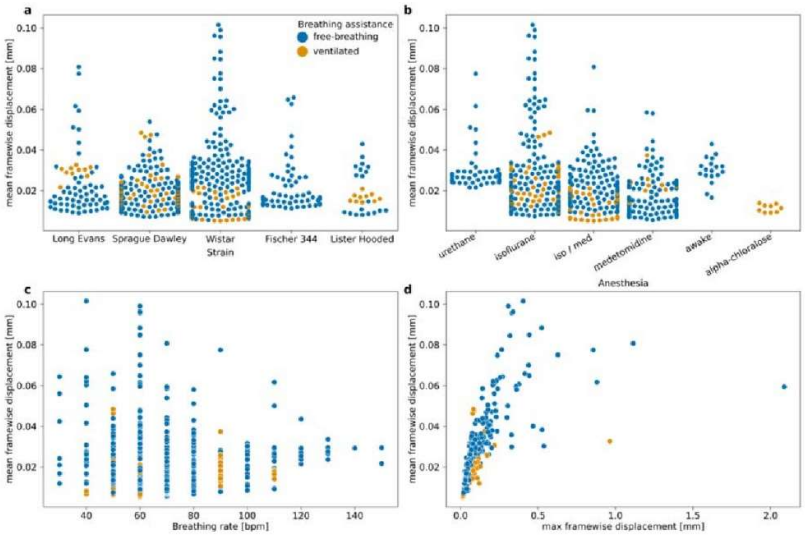

Figure S4. *Mean framewise displacement in the multiRat_rest dataset collection as a function of (**a**) strain, (**b**) anesthesia, (**c**) breathing rate, (**d**) maximal framewise displacement.*

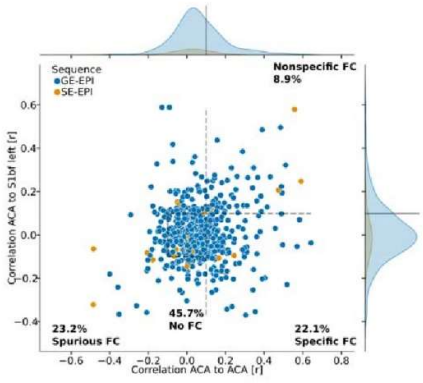

Figure S5 *Functional connectivity in the default-mode network. The reference seed is positioned in the anterior cingulate cortex (**Figure 2a**), the specific region-of-interest is positioned 3.3 mm posterior in the cingulate cortex and the nonspecific region-of-interest is positioned in the S1bf.*

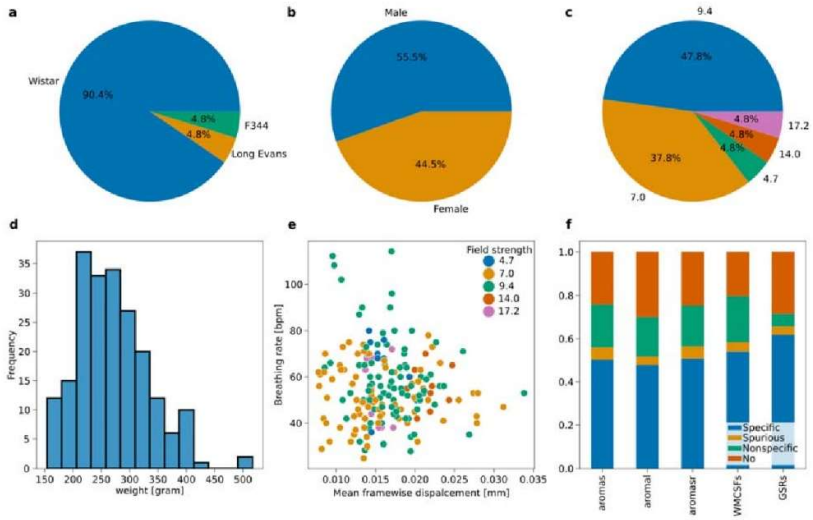

34

35 **Figure S6**. *StandardRat dataset description.* ***a.*** *Strain.* ***b.*** *Sex.* ***c.*** *Field strength.* ***d.*** *Weight.* ***e.***
36 *Breathing rate as a function of mean framewise displacement.* ***f.*** *Functional connectivity specificity*
37 *as a function of confound correction models.*

38

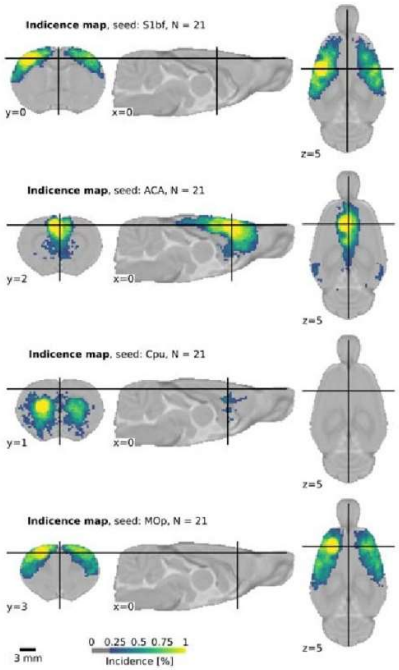

Figure S7. *Incidence of functional connectivity at the group level in the StandardRat collection for four selected seeds (N = 21 datasets, n ~ 10 subjects per dataset). Connectivity incidence is improved in the StandardRat collection relative to Multirat_rest (***Figure 3***)*

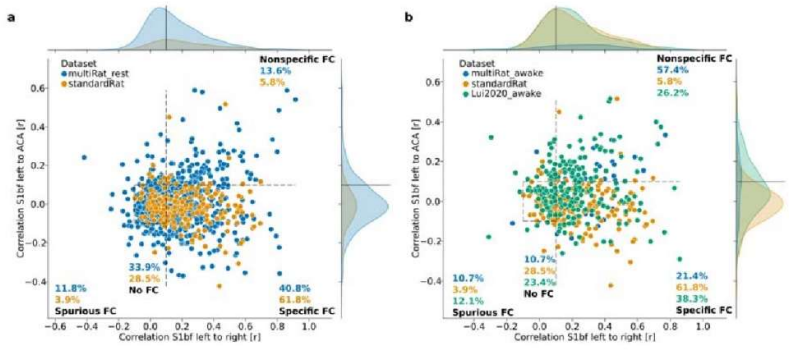

Figure S8. *Functional connectivity category comparison between MultiRat_rest and StandardRat (**a**) and between the awake datasets of MultiRat_rest and the awake dataset from Lui et al. 2020 (**b**).*

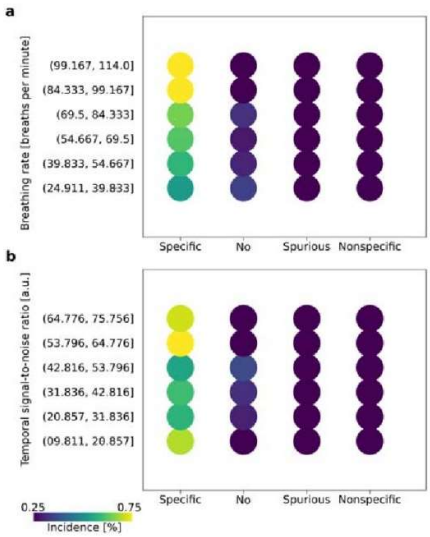

Figure S9. *Functional connectivity specificity as a function of binned breathing rate (**a**) AND temporal signal-to-noise ratio (**b**) in the standardRat collection. The percentage of each condition is size and color-coded. High levels of connectivity specificity were achieved in scans where the breathing rates were in the 84 to 114 bpm range. Similarly, higher connectivity specificity incidences were found when the cortical temporal signal-to-noise ratio was > 53. These observations support the notion of an optimal breathing rate when applying the standardRat protocol, along with temporal signal-to-noise ratio and movement targets.*

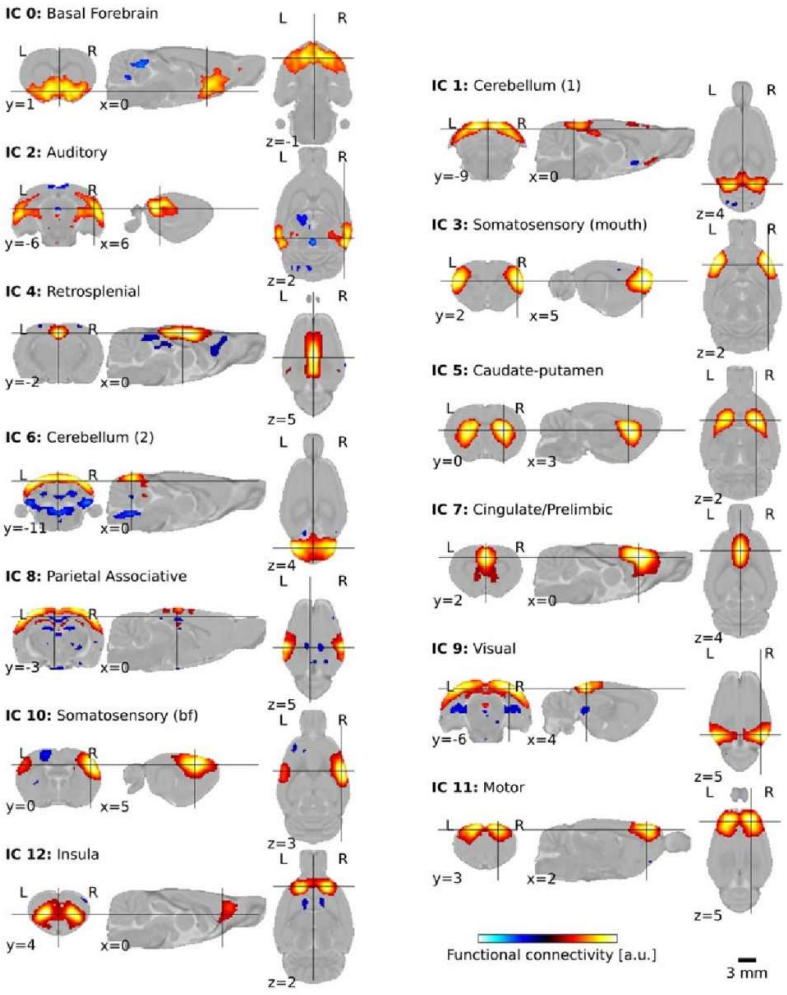

57

58 **Figure S10**. *Plausible independent components overlapping with known rodent networks, obtained*
59 *after group-level decomposition with n = 20 components. Labels are based on the SIGMA*
60 *anatomical atlas.*

ANNEXE II – SCIENTIFIC PRODUCTION

1.1 Publications

CELESTINE M., Jacquier-Sarlin M., Borel E., Petit F., Perot JB., Hérard AS., Bousset L., Buisson A., Dhenain M. Long term worsening of Alzheimer pathology and clinical outcome by a single inoculation of mutated beta-amyloid seeds. Submitted

Grandjean J., Desrosiers G.G, Anckaerts C., Angeles-aldez D., Ayad F., Barrière D., Blockx I., Bortel A., Broadwater M., M Cardoso B, **CELESTINE M.**, […] Chakravarty M., Hess A.. StandardRat: A multi-center consensus protocol to enhance functional connectivity specificity in the rat brain. Nature Neuroscience (accepted)
https://doi.org/10.17605/OSF.IO/EMQ4B
Prepublication in bioRxiv
https://www.biorxiv.org/content/10.1101/2022.04.27.489658v1

Pérot JB., **CELESTINE M.**, Palombo M., Dhenain M., Humbert S., Brouillet E., Flament J. Longitudinal multimodal MRI characterization of a knock-in mouse model of Huntington's disease reveals early grey and white matter alterations. Human Molecular Genetics. 2022
https://doi.org/10.1093/hmg/ddac036

CELESTINE M., Nadkarni, Garin C., Bougacha S. and Dhenain M. Sammba-MRI: a library for processing small mammals' brain MRI data in Python. Frontiers in Neuroinformatics. 2020.
https://doi.org/10.3389/fninf.2020.00024

1.2 Posters

CELESTINE M., Jacquier-Sarlin M., Borel E., Petit F., Perot JB., Hérard AS., Bousset L., Buisson A., Dhenain M. Long term modulation of Alzheimer pathology and clinical outcome by a single inoculation of mutated amyloid seeds. **Cold Spring Habor Laboratory: Neurodegenerative Diseases: Biology & Therapeutics conference.** November 2022

CELESTINE M., Jacquier-Sarlin M., Borel E., Cambon K., Hérard AS., Buisson A. and Dhenain M. Regulation of Alzheimer pathology by amyloid seeds: from toxic effects to therapeutic opportunities. **13th Forum of Neuroscience** (FENS) July 2022, Paris

CELESTINE M., Pérot J., Jacquier-Sarlin M., Flament J., Borel E., Hérard AS., Buisson A. and Dhenain M. Can familial Alzheimer variability affect brain networks? Exploration through Osaka Aβ variant inoculation in mice. **29th Annual Meeting of the International Society for Magnetic Resonance in Medicine** (ISMRM) conference, May 2021, Vancouver.

Pérot JB, **CELESTINE M.**, Dhenain M., Humbert S., Brouillet E., Flament J. DTI and gluCEST imaging reveal the key role of white matter alteration in the pathogenesis in a mouse model of Huntington's Disease. **29th Annual Meeting of the International Society for Magnetic Resonance in Medicine** (ISMRM) conference, May 2021, Vancouver.

Perot JB, **CELESTINE M.**, Riquelme-Pérez M, Escartin C, Dhenain M, Brouillet E, Flament J. Brain connectivity impairments revealed by DTI and resting-state fMRI in a mouse model of Huntington's disease. **29th Annual Meeting of the International Society for Magnetic Resonance in Medicine** (ISMRM) conference, May 2021, Vancouver.

CELESTINE M., Jacquier-Sarlin M., Borel E., Cambon K., Hérard AS., Buisson A. and Dhenain M. Regulation of Alzheimer pathology by amyloid seeds: from toxic effects to therapeutic opportunities. **BRAIN** Conference. March 2021.

CELESTINE M., Jacquier-Sarlin M., Borel E., Cambon K., Hérard AS., Buisson A. and Dhenain M. Effect of Alzheimer's disease-related β-amyloid variants in transgenic mouse models of β-amyloidosis. **Alzheimer's and Parkinson's Diseases** (AD/PD) Conference. March 2021, Barcelone

CELESTINE M., Jacquier-Sarlin M., Borel E., Cambon K., Hérard AS., Buisson A. and Dhenain M. Impact des variants de l'amyloïdes-β (Aβ) dans la maladie d'Alzheimer chez un modèle murin d'amyloïdose. **Club Alzheimer de Montpellier** (CALM). November 2020, Montpellier.

CELESTINE M., Jacquier-Sarlin M., Borel E., Hérard AS., Buisson A. and Dhenain M. Effect of Alzheimer's disease-related β-amyloid peptide conformations in transgenic mouse models of β-amyloidosis. **Alzheimer's Association International Conference** (AAIC). July 2020, Amsterdam.

1.3 Oral communications

CELESTINE M., Grandjean J., Novel approaches in transpecies whole-brain network analysis. (**Workshop chairperson**) **13th Forum of Neuroscience** (FENS) July 2022, Paris

CELESTINE M., Perot J., Nadkarni, Garin C., Bougacha S. and Dhenain M. Resting-State Functional MRI: processing and analysis in rodent. **13th Forum of Neuroscience** (FENS) July 2022, Paris

université PARIS-SACLAY

ÉCOLE DOCTORALE
Signalisations et réseaux intégratifs en biologie (BIOSIGNE)

Titre : Régulation de la pathologie Alzheimer par des variants de l'amyloïde-β : des effets toxiques et des opportunités thérapeutiques, dans un modèle murin de l'amyloïdose.

Mots clés : maladie d'Alzheimer (MA), β-amyloïde, mutations, connectivité cérébrale, mémoire, synapses

Résumé : La maladie d'Alzheimer (MA) est caractérisée par l'accumulation cérébrale de peptides β-amyloïdes (Aβ) et de protéine tau mal conformés, ainsi qu' une neuroinflammation excessive et des altérations synaptiques, menant au déclin cognitif. Les mutations dans la séquence de l'$Aβ_{1-42}$ induisent des variations de sa structure et de ses propriétés biochimiques qui peuvent être délétères ($Aβ_{1-42}$ -Osaka, $Aβ_{osa}$) ou protectrices ($Aβ_{1-42}$ -muté, $Aβ_{ice}$). L'origine de ces effets variables est, cependant, encore mal connue. Ce travail étudie l'impact fonctionnel à long terme de ces variants sur une cascade d'évènements pathologiques de la MA. Premièrement, nous avons montré qu'à une même concentration, l'inoculation de l'Aβ a des impacts fonctionnels différents dépendant de sa structure primaire. L'inoculation d'$Aβ_{OSA}$ entraîne de sévères déficits mnésiques et une perte de connectivité cérébrale associés à une perte synaptique, induis par une accélération de la pathologie amyloïde. A l'inverse, l'inoculation de l'$Aβ_{ice}$ restaure un phénotype normal en préservant la mémoire spatiale, la connectivité cérébrale et la densité synaptique; et en réduisant la pathologie Tau. En conclusion, un unique évènement sporadique peut modifier le décours de la pathologie. Ces travaux suggèrent que l'inoculation de l'Aβ peut avoir un effet régulateur délétère ou protecteur sur la pathologie. Nos données expérimentales mettent en évidence diverses cibles de l'Aβ en fonction de sa séquence primaire, expliquant en partie l'hétérogénéité de la MA. Finalement, en utilisant des variants protecteurs d' Aβ, nous mettons en évidence des mécanismes d'action pouvant être utilisés comme des outils thérapeutiques.

Title : Regulation of Alzheimer pathology by amyloid seeds: from toxic effects to therapeutic opportunities, in mouse model of amyloidosis.

Keywords : Alzheimer's disease, β-amyloid, mutations, cerebral connectivity, memory, synapses

Abstract : Alzheimer's disease (AD) is characterized by intracerebral accumulation of misfolded β-amyloid (Aβ) peptides and Tau along with excessive neuroinflammation and synaptic alteration leading to cognitive decline. Mutations in $Aβ_{1-42}$ sequence induce differents structures and biochemical properties that can be either deleterious ($Aβ_{1-42}$ -Osaka, $Aβ_{osa}$) or protective ($Aβ_{1-42}$ -muté, $Aβ_{ice}$). The origin of these different effects is unclear. The current work evaluates the functional impact of these mutated forms on dowstream events of AD. First, we showed that at a same concentration, inoculation of Aβ has different functional impact depending on its primary sequence. Inoculation of $Aβ_{OSA}$ lead to severe amnestic defects and loss of brain functional connectivity associated with loss of synapses, induced by the accelaration of amyloid pathology. Conversely, the inoculation of $Aβ_{ice}$ rescues the normal phenotype by preserving spatial memory, brain connectivity and synaptic density; and by reducing Tau pathology. To conclude, a single, sporadic events can modify the time-course of the disease. The current work suggests that Aβ inoculation can have a deleterious or benefical regulator effect on the pathology. Our experimental data outline numerous targets of Aβ depending on its primary sequence, explaining in part the heterogeneity of AD. Finally, by using protective forms of Aβ, we highlight mechanisms of action that can be used as therapeutic tools .